

University of Strathclyde

Doctoral Thesis

**Optical Tweezer and Particle Control of
Nucleation and Growth at the Microscale**



James Michael Flannigan

**A thesis submitted in the fulfilment of the requirements for the
degree of Doctor of Philosophy**

in the

Department of Chemical and Process Engineering

05 April 2023

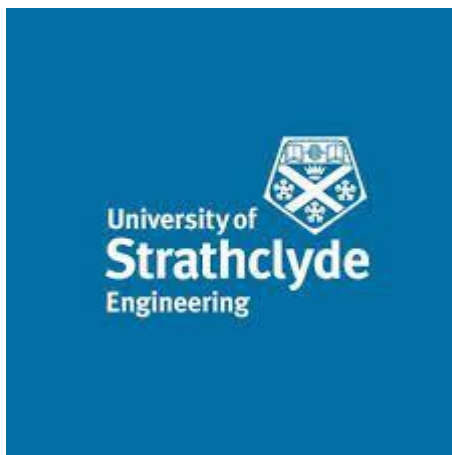
Declaration of Authorship

This thesis is the result of the author's original research. It has been composed by the author and has not been previously submitted for examination which has led to the award of a degree.

The copyright of this thesis belongs to the author under the terms of the United Kingdom Copyright Acts as qualified by University of Strathclyde Regulation 3.50. Due acknowledgement must always be made of the use of any material contained in, or derived from, this thesis.

Signed: _____

Date: _____



*“... the most profound discoveries are not
necessarily beyond that next star.”*

Jonathan Archer

Acknowledgements

The people who I need to thank begins with my supervisors Mark Haw and Jan Sefcik, without whose guidance and support I would not have been able to complete this project. And to the other members of my research group Praveen Parthasarathi, Aditi Mukhopadhyay, Chris Boyle, and Daniel MacIver whose discussions have proved invaluable in the completion of my PhD.

And to all the friends that I have made during my time as a PhD student, that have made this period so memorable, there are so many but special mention goes out to the Andrews Manson and Cashmore, Thomas Cadden, David McKechnie, Magdalena Hudek, Connaire McCready, Robert Sait-Stewart, Michaela McFadden, and Samira Anker.

I would also like to thank my friends Sara Letham, Pierce-Patrick Hynes, Simon McLaughlin, and Matthew Wong for all the good times that we had over many years and your continued support.

And finally, to my family who have made this all possible.

Abstract

Nucleation and growth of crystalline substances from solution is ubiquitous in the production of active pharmaceutical ingredients. However, a basic understanding of nucleation is still lacking after many years of study. One major problem in studies is due to the stochastic nature of nucleation, causing direct observation to be challenging. One possible solution to this is to use optical tweezers to promote nucleation localised to the tweezer focus. Although temporospatial influence and control over nucleation is achievable, some secondary considerations not usually part of the design of crystallisation processes must be considered, with a focus on optical properties with the aim of limiting laser induced heating.

A preliminary study was conducted to allow crystal nucleation and growth experiments performed using the optical tweezer setup to be fully understood within context, examining nucleation and growth kinetics up to a scale of 3 mL on high throughput platforms. This study examined the effect of deuterated solvent and doping with spherical microparticles. The use of deuterated solvents resulted in the reduction of primary nucleation rates. Its impact on secondary nucleation and growth depended on the crystallising material. Doping with spherical microparticles was particle material dependent, with silica promoting nucleation and polystyrene's effect being system and solvent isotopologue dependent.

Optical tweezers allow direct control over localised growth of macroscopic crystals with the effect being dependent upon the solvent isotopologue, when using low laser power. Higher laser power allows the time and position of nucleation to be controlled within certain conditions of supersaturation, laser power and relative location of the tweezing focus within the solution. As well as allowing the growth rates of crystals nucleated from bulk undersaturated solutions to be measured, suggesting the enhancement of the local solute concentration in the region surrounding the optical tweezing focus.

Table of Contents

| | |
|---|---------------|
| Declaration of Authorship | ii |
| Acknowledgements | iv |
| Abstract | v |
| Table of Contents | vi |
| List of Figures | xiii |
| List of Tables | xxix |
| List of Symbols | xxxi |
| List of Common Abbreviations | xxxiii |
| 1 Introduction | 1 |
| 1.1 IMPORTANCE AND HISTORY OF CRYSTALLISATION | 1 |
| 1.2 THESIS GOAL AND LAYOUT | 1 |
| 2 Crystallisation | 3 |
| 2.1 CRYSTALLINE MATERIALS | 3 |
| 2.2 WHY CRYSTALS FORM FROM SOLUTION | 3 |
| 2.3 CRYSTAL FORMATION METHODS | 5 |
| 2.3.1 COOLING CRYSTALLISATION | 5 |
| 2.3.2 EVAPORATIVE CRYSTALLISATION | 7 |
| 2.3.3 PRECIPITATION | 7 |
| 2.3.4 ANTI-SOLVENT CRYSTALLISATION | 7 |
| 2.4 FORMS OF CRYSTALS | 7 |
| 2.4.1 CRYSTAL LATTICE | 7 |
| 2.4.2 CRYSTAL HABIT | 9 |
| 2.4.3 POLYMORPHISM | 9 |
| 2.5 NUCLEATION | 11 |
| 2.5.1 PRIMARY NUCLEATION | 11 |
| 2.5.1.1 Homogeneous Nucleation | 11 |
| 2.5.1.2 Heterogeneous Nucleation | 15 |
| 2.5.2 SECONDARY NUCLEATION | 15 |
| 2.5.2.1 Initial Breeding | 17 |
| 2.5.2.2 Attrition | 17 |

| | | |
|------------|--|-----------|
| 2.5.2.3 | Polycrystalline Breeding | 17 |
| 2.5.2.4 | Dendritic | 17 |
| 2.5.2.5 | Fragmentation | 17 |
| 2.5.2.6 | Contact | 18 |
| 2.6 | MEASUREMENT OF PRIMARY NUCLEATION | 18 |
| 2.7 | INDUCEMENT OF NUCLEATION | 19 |
| 2.7.1 | LASER-INDUCED NUCLEATION | 19 |
| 2.7.2 | SONOCRYSTALLISATION | 20 |
| 2.8 | CRYSTALLISATION IN THE PRESENCE OF IMPURITIES | 20 |
| 2.8.1 | TEMPLATE IMPACTED CRYSTALLISATION | 20 |
| 2.8.2 | NUCLEATION AND GROWTH ALTERED BY ADDITIONAL COMPONENTS | 22 |
| 2.9 | CRYSTAL GROWTH AND DISSOLUTION | 24 |
| 3 | <u>Optical Tweezing</u> | 27 |
| 3.1 | DEVELOPMENT | 27 |
| 3.2 | PRINCIPLES OF OPERATION | 28 |
| 3.2.1 | RAY OPTICS REGIME | 28 |
| 3.2.2 | RAYLEIGH REGIME | 31 |
| 3.3 | MAKING MEASUREMENTS | 32 |
| 3.3.1 | POSITION CALIBRATION AND DETERMINATION | 32 |
| 3.3.2 | FORCE CALIBRATION | 33 |
| 3.3.2.1 | Equipartition Method | 33 |
| 3.3.2.2 | Power Spectral Density Method | 34 |
| 3.3.3 | APPLICABILITY OF HOOKE'S LAW | 35 |
| 3.4 | LASER-INDUCED HEATING | 36 |
| 3.4.1 | HEATING MODELS | 36 |
| 3.4.2 | SOLVENT CHOICE CONSIDERATIONS | 37 |
| 3.5 | CORRECTION FOR NON-ISOTHERMAL SURROUNDINGS | 39 |
| 3.6 | ALTERNATIVE TRAPS | 40 |
| 3.6.1 | TIME-SHARING TRAPS | 40 |
| 3.6.2 | BEAM SPLITTING TRAPS | 41 |
| 3.6.3 | OPTOELECTRONIC TWEEZERS | 41 |
| 3.7 | ALTERNATIVE USES OF OPTICAL TWEEZERS | 42 |
| 3.8 | OPTICAL TWEEZING AND CRYSTALLISATION | 43 |
| 3.8.1 | OPTICAL TWEEZING-INDUCED NUCLEATION | 43 |
| 3.8.1.1 | Theory and Proposed Mechanism | 43 |
| 3.8.1.2 | Experimental Observations | 46 |
| 3.8.1.3 | Heating Effects | 46 |
| 3.8.1.4 | Polymorph and Pseudopolymorph Control | 46 |
| 3.8.2 | CRYSTAL GROWTH INFLUENCED BY OPTICAL TWEEZING | 47 |
| 3.8.3 | INDIRECTLY INFLUENCED NUCLEATION WITH OPTICAL TWEEZERS | 48 |
| 4 | <u>Methodology and Materials</u> | 49 |

| | | |
|-------------|--|-----------|
| 4.1 | CRYSTAL16 | 49 |
| 4.2 | CRYSTALLINE | 49 |
| 4.3 | THORLABS MODULAR OPTICAL TWEEZERS | 50 |
| 4.4 | OPTICAL TWEEZERS ADDITIONAL UNITS | 51 |
| 4.5 | MODIFIED OPTICAL TWEEZERS | 53 |
| 4.6 | CRYSTAL CELL | 53 |
| 4.7 | POLAR BEAR PLUS CRYSTAL | 55 |
| 4.8 | CARY5000 | 56 |
| 4.9 | MATRIX-F | 58 |
| 4.10 | SENSOR II | 59 |
| 4.11 | XRPD | 60 |
| 4.12 | POWER METER | 60 |
| 4.13 | CONTACT ANGLE | 61 |
| 4.14 | MATERIALS | 61 |
| 4.14.1 | GLYCINE | 61 |
| 4.14.2 | SODIUM CHLORIDE | 61 |
| 4.14.3 | SODIUM BROMATE | 62 |
| 4.14.4 | SILICA PARTICLES | 62 |
| 4.14.5 | POLYSTYRENE PARTICLES | 62 |
| 4.14.6 | WATER | 62 |
| 4.14.7 | DEUTERIUM OXIDE | 62 |
| 5 | <u>Heat Absorption of Tweezing Beams and Trapping Particles</u> | 63 |
| 5.1 | IMPACT OF TEMPERATURE ON SOLUBILITY | 63 |
| 5.2 | SOLUBILITY IMPACTED BY SOLVENT ISOTOPOLOGUE | 65 |
| 5.3 | SOLVENT AND PARTICLE ABSORPTION | 67 |
| 5.4 | REFRACTIVE INDEX OF SOLVENTS AND PARTICLES | 69 |
| 5.5 | IMPACT OF SOLUTE ON REFRACTIVE INDEX AND ABSORPTION COEFFICIENT | 71 |
| 5.6 | PETERMAN HEATING MODEL | 72 |
| 5.7 | PREDICTED TEMPERATURE EFFECTS IN TWEEZER EXPERIMENTS FROM MEASUREMENT OF ABSORPTION | 78 |
| 5.7.1 | ABSORPTION OF SOLUTIONS | 78 |
| 5.7.2 | IMPACT OF CHANGING SOLVENT | 82 |
| 5.7.3 | IMPACT OF TRAPPING MATERIAL AND TRAPPING DISTANCE | 85 |
| 5.8 | CONCLUSIONS | 90 |
| 6 | <u>Comparison of Nucleation and Growth Kinetics in Water and Deuterium Oxide</u> | 92 |
| 6.1 | EXPERIMENTAL | 92 |
| 6.1.1 | SOLUBILITY AND METASTABLE ZONE WIDTH | 92 |
| 6.1.2 | INDUCTION TIME MEASUREMENTS | 93 |
| 6.1.2.1 | Agitated Induction Time Measurements | 93 |
| 6.1.2.2 | Quiescent Induction Time Measurements | 95 |
| 6.1.3 | SEED PRODUCTION | 96 |

| | | |
|------------|--|------------|
| 6.1.4 | SEEDED SECONDARY NUCLEATION AND GROWTH EXPERIMENTS | 96 |
| 6.2 | SOLUBILITY AND METASTABLE ZONE WIDTHS | 98 |
| 6.2.1 | SODIUM CHLORIDE | 98 |
| 6.2.2 | GLYCINE | 100 |
| 6.2.3 | POLYMORPHIC EFFECTS | 101 |
| 6.3 | INDUCTION TIME MEASUREMENTS | 107 |
| 6.3.1 | SODIUM CHLORIDE | 107 |
| 6.3.1.1 | Crystal16 Scale Agitated | 108 |
| 6.3.1.2 | Crystal16 Scale Quiescent | 108 |
| 6.3.1.3 | Crystalline Scale | 109 |
| 6.3.1.4 | Primary Nucleation Rate and Growth Times | 116 |
| 6.3.1.5 | Issues with Analysis | 119 |
| 6.3.2 | GLYCINE | 120 |
| 6.3.2.1 | Crystal16 Scale | 121 |
| 6.3.2.2 | Crystalline Scale | 122 |
| 6.4 | CRYSTAL GROWTH RATES | 126 |
| 6.4.1 | GLYCINE | 127 |
| 6.4.2 | SODIUM CHLORIDE | 129 |
| 6.4.2.1 | Unseeded | 129 |
| 6.4.2.2 | Seeded | 130 |
| 6.4.2.3 | Literature Comparison | 131 |
| 6.5 | SECONDARY NUCLEATION RATE | 133 |
| 6.5.1 | GLYCINE | 134 |
| 6.5.2 | SODIUM CHLORIDE | 135 |
| 6.5.2.1 | Unseeded NaCl Secondary Nucleation | 135 |
| 6.5.2.2 | Seeded NaCl Secondary Nucleation | 136 |
| 6.5.2.3 | Secondary Nucleation from Attrition | 138 |
| 6.6 | CONNECTION BETWEEN GROWTH AND NUCLEATION | 140 |
| 6.7 | CONCLUSIONS | 142 |
| 7 | <u>Impact of Particles on Nucleation Characteristics</u> | 143 |
| 7.1 | EXPERIMENTAL | 143 |
| 7.1.1 | SOLVENT PARTICLE SUSPENSION PREPARATION | 143 |
| 7.1.2 | METASTABLE ZONE WIDTH IMPACTED BY PARTICLES | 144 |
| 7.1.3 | INDUCTION TIME DISTRIBUTIONS IMPACTED BY PARTICLES. | 145 |
| 7.2 | IMPACT OF PARTICLES ON MSZW | 147 |
| 7.2.1 | MSZW OF GLYCINE IN H ₂ O AND D ₂ O WITH SILICA AND POLYSTYRENE PARTICLES | 147 |
| 7.2.2 | MSZW OF NaCl IN H ₂ O AND D ₂ O WITH SILICA AND POLYSTYRENE PARTICLES | 149 |
| 7.3 | IMPACT OF PARTICLES ON INDUCTION TIME DISTRIBUTIONS | 151 |
| 7.3.1 | INDUCTION TIME DISTRIBUTIONS OF GLYCINE IN H ₂ O AND D ₂ O WITH SILICA AND POLYSTYRENE PARTICLES | 151 |
| 7.3.2 | INDUCTION TIME DISTRIBUTIONS OF NaCl IN H ₂ O AND D ₂ O WITH SILICA AND POLYSTYRENE PARTICLES | 153 |
| 7.4 | MEASUREMENT ISSUES FOR SYSTEMS WITH ADDED PARTICLES | 156 |

| | | |
|------------|--|------------|
| 7.4.1 | HIGH CONCENTRATION OF SILICA PARTICLES | 156 |
| 7.4.2 | POLYSTYRENE PARTICLES | 159 |
| 7.5 | INDUCTION TIMES DETERMINED USING INDIVIDUAL VIAL TEMPERATURE. | 160 |
| 7.6 | CONCLUSIONS | 164 |
| 8 | <u>Effects of the Proximity of an Optical Tweezing Focus near a Pre-existing Crystal.</u> | 165 |
| 8.1 | EXPERIMENTAL | 165 |
| 8.1.1 | SEED WASHING | 165 |
| 8.1.2 | MEASUREMENT OF SINGLE CRYSTAL GROWTH RATES IN PROXIMITY TO TWEEZING FOCUSES | 166 |
| 8.2 | SEED WASHING | 166 |
| 8.3 | NACL CRYSTAL GROWTH AND DISSOLUTION RATE | 167 |
| 8.4 | GROWTH IN PROXIMITY TO TWEEZING FOCUSES | 168 |
| 8.4.1 | IMPACT OF TWEEZING FOCUS POWER AND PROXIMITY ON CRYSTAL GROWTH RATE | 169 |
| 8.5 | GROWTH THROUGH TWEEZING FOCUSES | 176 |
| 8.5.1 | CRYSTAL GROWTH OF NACL FROM SOLUTION THROUGH THE FOCUS OF AN OPTICAL TRAP | 176 |
| 8.5.2 | INHIBITION OF NACL CRYSTAL GROWTH | 177 |
| 8.5.3 | GROWTH THROUGH AN OPTICAL TRAP CONTAINING A SILICA PARTICLE | 182 |
| 8.6 | IMPACT ON SECONDARY NUCLEATION BY OPTICAL TWEEZING FOCUSES | 184 |
| 8.6.1 | SEEDED AGITATION TESTING | 184 |
| 8.6.1.1 | Growth of Seed Crystals in Supersaturated Solutions Impacted by Agitated Particles | 185 |
| 8.6.1.2 | Well Filling Testing | 187 |
| 8.7 | CONCLUSIONS | 188 |
| 9 | <u>Nucleation from Solution Induced by Optical Tweezing</u> | 189 |
| 9.1 | TWEEZING SET-UP | 189 |
| 9.2 | EXPERIMENTAL | 189 |
| 9.2.1 | CONTACT ANGLE MEASUREMENTS | 189 |
| 9.2.2 | TWEEZED DROPLET SET-UP | 190 |
| 9.3 | SUSPENDING COVER GLASS CHARACTERISATION | 193 |
| 9.4 | CONTACT ANGLES OF TESTED SOLUTIONS | 195 |
| 9.5 | INDUCED NUCLEATION FROM GLYCINE SOLUTIONS USING OPTICAL TWEEZERS | 197 |
| 9.5.1 | EFFECT OF SOLUTION SUPERSATURATION | 197 |
| 9.5.1.1 | Nucleation Time Distributions | 197 |
| 9.5.1.2 | Form of Nucleation Observed | 203 |
| 9.5.2 | EFFECT OF FOCUS POSITION | 206 |
| 9.5.2.1 | Nucleation Time Distribution | 206 |
| 9.5.2.2 | Form of Nucleation Observed | 211 |
| 9.5.3 | EFFECT OF LIGHT POLARISATION | 212 |
| 9.5.3.1 | Nucleation Time Distributions | 212 |
| 9.5.3.2 | Form of Nucleation Observed | 215 |
| 9.5.4 | EFFECT OF THE PRESENCE OF TRAPPED SILICA PARTICLES | 216 |
| 9.5.4.1 | Nucleation Time Distributions | 216 |

| | | |
|-------------------|--|------------|
| 9.5.4.2 | Form of Nucleation Observed | 218 |
| 9.6 | QUADRANT PHOTODIODE RESULTS | 220 |
| 9.7 | SODIUM CHLORIDE SOLUTIONS | 221 |
| 9.8 | SODIUM BROMATE SOLUTIONS | 222 |
| 9.9 | DISCUSSION OF EVIDENCE ABOUT NUCLEATION MECHANISM MODELS | 224 |
| 9.10 | GROWTH RATE OF CRYSTALS THAT NUCLEATED FROM SOLUTION USING OPTICAL TWEEZERS | 226 |
| 9.10.1 | MODEL TRAINING | 227 |
| 9.10.2 | DETERMINED GROWTH RATES | 227 |
| 9.10.3 | MACHINE LEARNING ISSUES | 231 |
| 9.10.4 | COMPARISON TO EXISTING GROWTH RATES OF GLYCINE CRYSTALS | 231 |
| 9.11 | CONCLUSIONS | 236 |
| 10 | Final Remarks | 237 |
| 10.1 | HEAT ABSORPTION OF TWEEZING BEAMS AND TRAPPING PARTICLES | 237 |
| 10.2 | COMPARISON OF NUCLEATION AND GROWTH CHARACTERISTICS IN WATER AND DEUTERIUM OXIDE | 237 |
| 10.3 | IMPACT OF PARTICLES ON NUCLEATION CHARACTERISTICS | 238 |
| 10.4 | EFFECT OF PROXIMITY OF AN OPTICAL TWEEZING FOCUS NEAR A PRE-EXISTING CRYSTAL | 238 |
| 10.5 | NUCLEATION FROM SOLUTION INDUCED BY OPTICAL TWEEZING | 238 |
| 10.6 | FUTURE WORK | 239 |
| | References | 241 |
| Appendix A | Personal Outputs | A |
| A.1 | EVENTS ATTENDED | A |
| A.2 | PAPERS | B |
| Appendix B | COVID-19 Impact Statement | C |
| Appendix C | Images of Washed Seeds | D |
| C.1 | SEEDS WASHED IN H ₂ O | D |
| C.2 | SEEDS WASHED IN D ₂ O | H |
| Appendix D | Crystalline Particle Number and Size Distribution Examples | M |
| Appendix E | Machine Learning Workspace | O |
| Appendix F | Alternative Frequency Distributions of Nucleation from Solution. | P |
| F.1 | CUMULATIVE PROBABILITY DISTRIBUTIONS | P |

| | | |
|------------|--|----------|
| F.1.1 | NUCLEATION OF NA ₂ CO ₃ FROM H ₂ O AND D ₂ O | P |
| F.1.2 | EFFECT OF MICROPARTICLES ON INDUCTION TIME DISTRIBUTIONS | R |
| F.2 | PERIOD INDICATION GRAPHS | S |
| F.2.1 | NUCLEATION OF NA ₂ CO ₃ FROM H ₂ O AND D ₂ O | S |
| F.2.2 | EFFECT OF MICROPARTICLES ON INDUCTION TIME DISTRIBUTIONS | T |

Appendix G **Alternative Frequency Distributions of Nucleation from Solution when induced by Optical Tweezers** **U**

Appendix H **Beer-Lambert Law** **Y**

Appendix I **Hot Brownian Motion Calculation Outcomes** **Z**

Appendix J **Predicted Effect on Supersaturation with Laser Power** **AA**

| | | |
|-----|---|----|
| J.1 | LASER POWER DELIVERED | AA |
| J.2 | EFFECT ON SUPERSATURATION WHEN ALTERING LASER POWER AT FIXED DISPLACEMENT | BB |
| J.3 | EFFECT ON SUPERSATURATION WHEN ALTERING TRAP DISPLACEMENT FROM THE HEATSINK | DD |

List of Figures

| | |
|--|----|
| Figure 2:1: Basic Solubility Diagram. The progress of an elementary cooling crystallisation detailed by the green arrows and letter labelled points are detailed in the text below. | 6 |
| Figure 2:2: Example of Crystal Lattice Unit Cell [11]..... | 8 |
| Figure 2:3: Free Energy Barriers in the Formation of Crystal Polymorphs[17]. See accompanying text above for details of description of diagram. | 11 |
| Figure 2:4: Free Energy Change Associated with Spherical Nuclei Formation according to Classical Nucleation Theory. Adapted from [20]. Black; surface excess free energy. Red Solid; volume excess free energy at high supersaturation. Red Dashed; volume excess free energy at low supersaturation. Blue Solid; free energy change at high supersaturation and Blue Dashed; free energy change at low supersaturation. | 13 |
| Figure 2:5: Nucleation Model Formation Pathways | 13 |
| Figure 2:6: Energy Barriers Associated with the Two-Step Model [23]. Detailed description of free energy diagram given in text above..... | 14 |
| Figure 2:7: Secondary Nucleation Classification by Agrawal and Paterson [31]..... | 16 |
| Figure 3:1: Radial Stability Example [87] | 29 |
| Figure 3:2: Axial Stability Example [86] | 30 |
| Figure 3:3: Coordinate system typically employed in particle trapping. Showing the Cartesian axes (Blue Arrows), Tweezing Beam (Red Hyperbola) which follows the path of the z-axis and the trapped particle (Magenta Circle) located at the origin..... | 32 |
| Figure 3:4: Example Power spectral Density graph. Computed PSD of pairwise voltage signal (Red), fitting of Equation 3:8 (Black). Spectrum produced by trapping a 3 micron diameter polystyrene bead [99]. Low frequency plateau value also indicated. <i>fc can also be written as f0</i> | 34 |
| Figure 3:5: Absorption Spectrum of Water in the visible and NIR regions [110]. | 38 |
| Figure 3:6: Setup required to operate optoelectronic tweezers [121]. | 42 |
| Figure 3:7: Schematic diagram of the forces operating at flat solution interface. Solution air interface (Blue), tweezing beam focus (Red Hyperbola), Gradient force direction (Black Arrows) and Scattering force direction (Orange Arrows). The gradient force would operate rotationally around the axis of the beam, this cannot be shown in this 2D diagram, this would have the effect of drawing objects into the plane shown from in front and behind the plane of this diagram.. | 44 |
| Figure 4:1: The Crystal16 Apparatus. | 49 |
| Figure 4:2: The Crystalline Apparatus. | 50 |
| Figure 4:3: The Base setup of the ThorLabs OTKB/M modular optical tweezers. | 50 |
| Figure 4:4: Schematic diagram of base optical tweezers OTKB/M, OTKBFM and OTKBFM-CAL | 51 |
| Figure 4:5: ThorLabs OTKBFM. | 52 |
| Figure 4:6: ThorLabs OTKBFM-CAL..... | 52 |
| Figure 4:7: 2 W CNI 1064 nm Gaussian Laser. | 53 |
| Figure 4:8: Crystal Cell Apparatus within a custom 3D-printed mount. | 54 |
| Figure 4:9: Schematic diagram of silicon isolator used. | 54 |
| Figure 4:10: Schematic diagram of the wider trap set-up. Number 1, Objective Lens (Nikon x100 NA=1.25) used for focusing trapping laser; Number 2, Condensing Lens (x10); Yellow Solid, Immersion Oil; Blue Diagonal Stripes, Number 1.5 thickness silica microscope coverslips | |

| | |
|--|----|
| and Brown Vertical Stripe, Silicone Gasket. Red Solid Arrow, Path of Trapping Laser and Blue Dashed Arrow, Path of Light Source for Imaging Illumination. | 55 |
| Figure 4:11: The Polar Bear Apparatus..... | 56 |
| Figure 4:12: The Cary5000 Photospectrometer. | 57 |
| Figure 4:13: Hellma Optical Glass Cuvette (1 cm Path length). | 57 |
| Figure 4:14: The Matrix-F Spectrometer. | 58 |
| Figure 4:15: Falcata XP 12 Transflectance Probe. | 59 |
| Figure 4:16: The TensorII FTIR Infrared Spectrometer. | 59 |
| Figure 4:17: ThorLabs PT160T Power Meter. | 60 |
| Figure 4:18: The Kruss DSA30 Contact Angle. | 61 |
| Figure 5:1: Impact of Temperature on Supersaturation of Alpha Glycine in Deuterium Oxide (Calculated using Solubility data from [161]) | 64 |
| Figure 5:2: Impact of Temperature on Supersaturation on Sodium Chloride in Deuterium Oxide (Calculated using solubility data from [162]) | 65 |
| Figure 5:3: Comparison of Solubility of NaCl in Normal Water and Heavy Water (Data from Perry's [180]; Eddy [162]; Antropoff [181]; Blasdale [182] & de Coppet [183]). Hollow symbols indicate solubility in water, and filled symbols indicate deuterium oxide. | 66 |
| Figure 5:4: Comparison of Solubility of glycine in different isotopes of water (Data from Jelińska-Kazimierczuk [161] and Park [184]) Hollow symbols indicate solubility in water, and filled symbols indicate deuterium oxide. | 66 |
| Figure 5:5: Absorption Coefficient of Selected Common Solvents (Water , Heavy Water, Toluene and Ethanol) [110]. The two trapping laser wavelengths used are indicated..... | 67 |
| Figure 5:6: Absorption Coefficient of Selected Common Trapping Materials. Silica [163]. Polystyrene [164]. Soda Lime [165]. PMMA [166]. | 68 |
| Figure 5:7: Refractive Index of Selected Solvents [110] | 69 |
| Figure 5:8: Refractive indices of selected trapping materials. (Data from Silica [170]; Polystyrene [171]; PMMA [171]; Soda-Lime [165])..... | 70 |
| Figure 5:9: Absorption coefficient of aqueous sodium chloride solution at a range of concentrations between 0 and 0.360 g/g [172]. Determined by examining the transmissivity and reflected light through a sample of a known thickness of a solution of known concentration..... | 71 |
| Figure 5:10: Refractive Index of Aqueous Sodium Chloride Solution [172] (Determined by examining the transmissivity and reflected light through a sample of a known thickness of a solution of known concentration.)..... | 72 |
| Figure 5:11: Geometry Used by Peterman Heating Model [105]. Green Circle, Particle trapped by Laser; Blue Line, Interior Surface of Glass Coverslip acting as a heat sink; Black Curves, Focused Trapping Laser and Red Rhombus, centre of Trap Geometry. T_0 , temperature at the trap's centre and T_D , the temperature at the coverslips inside surface acting as the heatsink. Diagram not to scale. A larger-scale diagram of the trapping apparatus is shown in Figure 4:10. | 74 |
| Figure 5:12: Simulated temperature profile as a function of ρ (lateral plane (x-y plane from Figure 3:3) displacement) from the centre of the trap geometry of 2-micron diameter particles of selected materials. Also shown are measurements of the temperature rise when trapping particles of various material, Filled squares. Orange Solid, Melamine Resin (MR); Green Solid, Polystyrene (PS); Blue Solid, Silica (Si); Red Solid (Water), absence of particle. | |

The grey band indicates the standard deviation observed in the polystyrene measurements [176]. B is a measurement of the temperature rise.76

Figure 5:13: Comparison between the Peterman model and actual temperature measurements made through viscosity measurements via Stokes drag [176]. Orange lines are predictions made using the Peterman model trapping polystyrene particles of varying sizes with two solvents: upper; glycerol, and lower water. Individual points are physical measurement of temperature rises when polystyrene particles of a selection of radii were suspended in water trapping using an objective with a NA = 1.2 (Triangles) and NA = 1.3 (Inverted Triangles) and when suspended in glycerol and trapped using a NA = 1.2 objective (Circles).77

Figure 5:14: Left; Absorption Coefficient of Solutions of Sodium Chloride in Deionised water between concentrations of 0 g/g and 0.3 g/g at 975 nm and 1064 nm. Right: relative change of absorption coefficient from the pure solvent with increasing solute concentration.78

Figure 5:15: Left; Absorption Coefficient of Solutions of Sodium Chloride in Deuterium Oxide between concentrations of 0 g/g and 0.3 g/g at 975 nm and 1064 nm. Right: relative change of absorption coefficient from the pure solvent with increasing solute concentration.79

Figure 5:16: Left; Absorption Coefficient of glycine solutions in deionised water between concentrations of 0 g/g and 0.2 g/g at 975 nm and 1064 nm. Right: relative change of absorption coefficient from the pure solvent with increasing solute concentration.80

Figure 5:17: Left; Absorption Coefficient of glycine solutions in deuterium oxide between concentrations of 0 g/g and 0.2 g/g at wavelengths of 975 nm and 1064 nm. Right: relative change of absorption coefficient from the pure solvent with increasing solute concentration.81

Figure 5:18: Left; Predicted temperature rise from Peterman model at the interface of silica particles in suspension medium of a sodium chloride solution in deuterium oxide at different concentrations of sodium chloride (0-0.30 $\frac{g_{solute}}{g_{solvent}}$). Trapped using a 975 nm laser (Solid Lines) and 1064 nm laser (Dashed Lines). Right; Predicted temperature rise from Peterman model at the interface of silica particles in suspension medium of a glycine solution in deuterium oxide at different concentrations of glycine (0-0.15 $\frac{g_{solute}}{g_{solvent}}$). Trapped using a 975 nm laser (Solid Lines) and 1064 nm laser (Dashed Lines)82

Figure 5:19: Left; Predicted temperature rise from Peterman model at the interface of silica particles in suspension medium of a sodium chloride solution in water at different concentrations of sodium chloride (0-0.30 $\frac{g_{solute}}{g_{solvent}}$). Trapped using a 975 nm laser (Solid Lines) and 1064 nm laser (Dashed Lines). Right; Predicted temperature rise from Peterman model at the interface of Silica Particles in suspension medium of a glycine solution in water at different glycine concentrations (0-0.20 $\frac{g_{solute}}{g_{solvent}}$). Trapped using a 975 nm laser (Solid Lines) and 1064 nm laser (Dashed Lines)83

Figure 5:20: Simplified Geometry of the thermal system of a trapped particle and its surrounding suspension material. Blue Vertical Grid Area, solute subject to soda lime thermal conductivity (K) and Red Diagonal Grid Area, volume subject to suspension materials thermal conductivity of the suspension material. Explanation of Dimensions and Temperatures given above in the text. R_1 ; radius of trap centre volume (155 nm for 975 nm laser and 169 nm for 1064 nm). R_2 ; radius of trapped particle. R_3 ; radius of spherical shell at the distance of the coverslip acting as the heat sink, assumed to be 60 μm86

Figure 5:21: Temperature rise predicted at the interfaces of soda lime particles at their interface with the suspension media. Calculated in this case of solutions of NaCl in D₂O up to

| | |
|---|-----|
| a concentration of 0.30 g/g when the focus is located 60 μm from the heatsink with the trapping performed using a 975 nm laser (solid vertical line, giving an $r_1 = 155$ nm) and 1064 nm laser (dashed vertical lines, giving an $r_1 = 169$ nm)..... | 88 |
| Figure 5:22: Left; Comparison between the centre temperature rise from that of the heatsink of a trapped soda-lime particle and the temperature that would exist at the interface with suspension solution when trapped using a 975 nm laser in a 0 and 0.30 $\text{g}_{\text{solute}}/\text{g}_{\text{solvent}}$ solute of NaCl using D2O as a solvent. Right; Comparison between the centre temperature rise from that of the heatsink of a trapped soda-lime particle and the temperature that would exist at the interface with suspension solution when trapped using a 975 nm laser in a 0 and 0.15 $\text{g}_{\text{solute}}/\text{g}_{\text{solvent}}$ solute of Glycine using D2O as a solvent. | 89 |
| Figure 5:23: Left; Predicted Temperature Rise of Differing Radius Silica Particles in Pure Deuterium oxide at various trapping distances trapped using a 975 nm laser (Solid Lines) and a 1064 nm laser (Dashed Lines). Right; Predicted Temperature Rise of Differing Radius Silica Particles in pure water at various trapping distances trapped using a 975 nm laser (Solid Lines) and a 1064 nm laser (Dashed Lines)..... | 90 |
| Figure 6:1: Temperature Cycle used for Solubility and Metastable Zone Width Determinations. | 93 |
| Figure 6:2: Temperature Cycle used for agitated induction time measurements. | 94 |
| Figure 6:3: Quiescent Temperature Cycle for Polar Bear Plus Crystal..... | 95 |
| Figure 6:4: Temperature Cycle used for seeded Secondary Nucleation Studies | 97 |
| Figure 6:5: Left; Solubility, from clear points (Black Hollow Squares) and Metastable Zone Width (MSZW), from cloud points (Red Hollow Circles) of Sodium Chloride in Water. Van't Hoff fitting applied to solubility points (Black Dashed Line). Right; Solubility (Black Squares) and Metastable Zone Width (Red Circles) of NaCl in Deuterium Oxide (Black Line). Van't Hoff fitting applied to solubility points (Black Solid Line) [185]. | 98 |
| Figure 6:6: Comparison of Solubility points and Van't Hoff fittings of NaCl in H ₂ O (Open Symbols and Dashed Line) and D ₂ O (Filled Symbols and Solid Line). Also shown are various sources of solubility data from previously published sources Antropoff [181], Blasdale [182], de Coppet [183], Mullin [3], Bharmoria [193] and Eddy [162]. Methods used to determine solubility from previously published sources are shown in Table 6:1. | 99 |
| Figure 6:7: Left; Solubility from clear points (Black Hollow Squares) and Metastable Zone Width from cloud points (Red Hollow Circles) of Glycine in Water. Van't Hoff fitting applied to solubility points (Black Dashed Line). Right; Solubility (Black Squares) and Metastable Zone Width (Red Circles) of Glycine in Deuterium Oxide. Van't Hoff fitting applied to solubility points (Black Line) [185]..... | 100 |
| Figure 6:8: Left; Comparison of Solubility points and Van't Hoff fittings of Glycine in H ₂ O (Open Symbols and Dashed Line) and D ₂ O (Filled Symbols and Solid Line). Right; Comparison of Solubility points and Van't Hoff fittings of Glycine in H ₂ O (Open Symbols and Dashed Line) and D ₂ O (Filled Symbols and Solid Line). Also shown are various sources of solubility data from previously published sources: Park [184], Seidell [197], Zeng [198] and Jelinska-Kazimierczuk [161]. Measurement techniques of solubility for reference sources are shown in Table 6:2..... | 101 |
| Figure 6:9: FTIR Absorbance of the glycine before dissolution in the solvent, identified as α (Black) and the Glycine recovered from solution in deuterium oxide (Blue). Vertical lines show locations of expected peaks used for non-deuterated polymorph identification of alpha (Red) and gamma (Green). | 102 |

| | |
|--|-----|
| Figure 6:10: Comparison of simulated PXRD curves of alpha glycine (Red), PXRD curve of glycine for electrophoresis, Sigma Aldrich (Black) and Glycine extracted from the end of solubility testing after natural cooling in non-agitated deuterium oxide (Blue). | 104 |
| Figure 6:11: Comparison of simulated PXRD curves of gamma glycine (Green), PXRD curve of glycine for electrophoresis, Sigma Aldrich (Black) and Glycine extracted from the end of solubility testing after natural cooling in non-agitated deuterium oxide (Blue). | 104 |
| Figure 6:12: Comparison of simulated PXRD curves of alpha glycine (Red), PXRD curve of glycine for electrophoresis, Sigma Aldrich (Black) and glycine extracted from the cooling ramp while agitated (Blue). | 106 |
| Figure 6:13: Comparison of simulated PXRD curves of gamma glycine (Green), PXRD curve of glycine for electrophoresis, Sigma Aldrich (Black) and glycine extracted from the cooling ramp while agitated (Blue). | 106 |
| Figure 6:14: Left; Cumulative Probability Distribution Plot of Induction Time Measurements of NaCl in Water, agitated using a stirrer bar at 700 RPM at S at 1.02. Right; Cumulative Probability Distribution Plot of Induction Time Measurements of NaCl in Deuterium Oxide agitated using a stirrer bar at 700 RPM at S between 1.02 and 1.04. Crossed Symbols indicate the proportion of total vials which nucleated before reaching isothermal conditions. Lines indicate fitting according to Jiang and ter Horst [48]. | 108 |
| Figure 6:15: Left; Cumulative Probability Distribution Plot of Induction Time Measurements of NaCl in Water, agitated using a stirrer bar at 700 RPM at S between 1.0025 and 1.02. Right; Cumulative Probability Distribution Plot of Induction Time Measurements of NaCl in Deuterium Oxide agitated using a stirrer bar at 700 RPM at S between 1.0025 and 1.02. Crossed Symbols indicate the proportion of total vials which nucleated before reaching isothermal conditions. Lines indicate fitting according to Jiang and ter Horst [48]. | 109 |
| Figure 6:16: Photographs of NaCl suspended in saturated NaCl solution at different agitation rates using a downward flow three-blade propeller (100 RPM, 250 RPM, 500 RPM, 700 RPM, and 1250 RPM; Left to Right) | 111 |
| Figure 6:17: Photograph of 8 ml crystalline vial agitated at 2200 RPM using a downward flow three-blade propeller. | 112 |
| Figure 6:18: Left; Cumulative Probability Distribution Plot of Induction Time Measurements of NaCl in Water, agitated using an overhead propeller at 1250 RPM at S between 1.0025 and 1.02. Right; Cumulative Probability Distribution Plot of Induction Time Measurements of NaCl in Deuterium Oxide agitated using an overhead propeller at 1250 RPM at S between 1.0025 and 1.02. Lines indicate fitting according to Jiang and ter Horst [48]. | 113 |
| Figure 6:19: Crystalline Camera Images of Sodium Chloride before full dissolution in H ₂ O. Images were taken at 30-second intervals, left to right. Scale bar in each image is 500 microns. | 115 |
| Figure 6:20: Crystalline images of a false positive nucleation event of sodium chloride in H ₂ O, where undissolved NaCl has become suspended in the solution, giving the appearance of nucleation. Images were taken at 30-second intervals left to right in each row, then continuing from the left-hand side of the row below. Scale bar in each image is 500 microns. | 115 |
| Figure 6:21: Crystalline Images of Sodium Chloride, which has nucleated from solution. Images were taken at 30-second intervals from left to right in each row, then descending in rows from top to bottom. Scale bar in each image is 500 microns. | 116 |

Figure 6:22: Comparison of Primary Nucleation Rate of Sodium Chloride as function of relative supersaturation ($\sigma = S - 1$) at Crystalline Scale from previously published data [209]–[213]. Solubility of all points based upon fitted Van't Hoff curves in Figure 6:6.118

Figure 6:23: Left; Cumulative Probability Distribution Plot of Induction Time Measurements of Glycine in Water, agitated using a stirrer bar at 700 RPM at S between 1.16 and 1.22. Right; Cumulative Probability Distribution Plot of Induction Time Measurements of Glycine in Deuterium Oxide agitated using a stirrer bar at 700 RPM at S between 1.18 and 1.22. Lines indicate fitting according to Jiang and ter Horst [48].121

Figure 6:24: Left; Cumulative Probability Distribution Plot of Induction Time Measurements of Glycine in Water, agitated using a stirrer bar at 700 RPM at S between 1.20 and 1.26. Right; Cumulative Probability Distribution Plot of Induction Time Measurements of Glycine in Deuterium Oxide agitated using a stirrer bar at 700 RPM at S between 1.20 and 1.26. Lines indicate fitting according to Jiang and ter Horst [48].122

Figure 6:25: Left; Cumulative Probability Distribution Plot of Induction Time Measurements of Glycine in Water, agitated using an overhead propeller at 700 RPM at S between 1.20 and 1.26. Right; Cumulative Probability Distribution Plot of Induction Time Measurements of Glycine in Deuterium Oxide agitated using an overhead propeller at 700 RPM at S between 1.20 and 1.26. Lines indicate fitting according to Jiang and ter Horst [48].124

Figure 6:26: Growth Rates of Glycine determined through image analysis grown from supersaturated solutions in H₂O and D₂O when agitated using a magnetic stirrer bar agitation (Bar) and overhead stirring agitation (OHS). Trendlines shown are linear best fits of data points. Averages of each set of points at each supersaturation are shown in the insert graph using the same symbols.127

Figure 6:27: Comparison of growth rates of glycine to those previously published. All literature values are for glycine growth in water [219], [220].129

Figure 6:28: Growth Rate of Sodium Chloride Crystals calculated from image analysis of a section of solution where crystallisation occurred, supersaturation between S = 1.0025 and S = 1.02 solvents of deionised water and deuterium oxide. Vessels agitated using Teflon coated stirrer at a speed of 700 RPM and with overhead agitation at 1250 RPM. Averages are shown in the insert graph using the same symbols.129

Figure 6:29: Growth Rate of Sodium Chloride calculated from image analysis of a section of solution where crystallisation was occurring with supersaturations between S = 1.0025-1.01 for the solvents deionised water and deuterium oxide. Solutions used were seeded with a washed crystal. Vessels agitated with overhead stirring propeller at a speed of 1250 RPM. Averages are shown in the insert graph using the same symbols. Linear fitting is constrained to equal 0 growth at S=1.130

Figure 6:30: Comparison of Sodium Chloride crystal growth of a crystal dimension [221]–[224].131

Figure 6:31: Left; Secondary Nucleation rates of glycine nucleating from supersaturated solutions in H₂O and D₂O. Right; Average secondary nucleation rates.134

Figure 6:32: Average Secondary Nucleation rate calculated from multiple supersaturations between S = 1.0025 and 1.02 for both solvents deionised water and deuterium oxide shown on a logarithmic scale. Vials were not seeded and required primary nucleation to occur first. Averages are shown in the insert graph using the same symbols.135

Figure 6:33: Average Secondary Nucleation rate calculated from multiple seeding experiments where a washed crystal was added between supersaturations S = 1.0025 and

| | |
|---|-----|
| 1.02 for both solvents deionised water and deuterium oxide shown on a linear scale. Averages are shown in the insert graph using the same symbols. Linear trendlines shown are of average values. | 136 |
| Figure 6:34: Secondary Nucleation Delay Times for seeded studies in deionised water and deuterium oxide between the supersaturations $S = 1.0025$ and 1.02 . Averages are shown in the insert graph using the same symbols..... | 137 |
| Figure 6:35: Comparison of the average growth rate determined from the trend in D-90s and the corresponding delay time after seeding with a single crystal of sodium chloride in supersaturated sodium chloride solutions in water and deuterium oxide..... | 138 |
| Figure 6:36: Nuclei generated from the attrition of sodium chloride in saturated water. Images taken at five-second intervals; left most image taken first. | 139 |
| Figure 6:37: Nuclei generated from the attrition of sodium chloride in saturated deuterium oxide. Images taken at five-second intervals; left most image taken first. | 139 |
| Figure 6:38: Left; Image of the seed crystal. Right; enlarged view of the section enclosed in red in the left image..... | 140 |
| Figure 6:39: Comparison of Secondary Nucleation Rates and Growth Rates of Glycine from solution in water and deuterium oxide between $S = 1.20$ and $S = 1.26$, when subjected to agitation using magnetic and overhead stirring. Determined at the Crystalline Scale (3 g of solvent). Colour indicates the solvent isotopologue used; H_2O (Black) and D_2O (Red). Shape indicates the supersaturation used; 1.20 (Circles), 1.22 (Triangles), 1.24 (Squares) and 1.26 (Hexagons). The interior state indicates the agitation used; Magnetic Bar Stirring (Filled) and Overhead Stirring (Hollow). | 141 |
| Figure 6:40: Comparison of secondary nucleation rates and growth rates of NaCl from solution in water and deuterium oxide between $S = 1.0025$ and $S = 1.02$ when subjected to magnetic bar agitation and overhead agitation when unseeded, and overhead agitation when seeded. Determined at the Crystalline scale (3 g of solvent). Colour indicates the solvent isotopologue used; H_2O (Black) and D_2O (Red). Shape indicates the supersaturation used; 1.0025 (Circles), 1.005 (Triangles), 1.01 (Squares) and 1.02 (Hexagons). The interior state indicates the agitation used; Magnetic Bar Stirring (Filled) and Overhead Stirring (Hollow). Seeding is indicated by crossed symbols..... | 141 |
| Figure 7:1: Temperature Cycle used to determine the Effect of Microparticles on the MSZW. This is the same profile used in section 6.1.1 as shown in Figure 6:1. | 145 |
| Figure 7:2: Temperature profile used to determine the effects of microparticles on induction time distribution. This is the same profile used in section 6.1.2 as shown in Figure 6:2. | 147 |
| Figure 7:3: Left; Effect of $1 \text{ mg}_{\text{silica}}/\text{g}_{\text{water}}$ 1.57-micron diameter silica microspheres on the MSZW of Glycine nucleating from solution in H_2O . Right; Effect of $1 \text{ mg}_{\text{silica}}/\text{g}_{\text{deuterium oxide}}$ 1.57-micron diameter silica microspheres on the MSZW of Glycine nucleating from solution in D_2O . Addition of silica particles (Black to Red) shrinks the MSZW. | 148 |
| Figure 7:4: Left; $0.5 \text{ mg}_{\text{polystyrene}}/\text{g}_{\text{water}}$ 1.57-micron diameter Polystyrene microspheres on the MSZW of Glycine nucleating from solution in H_2O . Right; $0.5 \text{ mg}_{\text{polystyrene}}/\text{g}_{\text{Deuterium Oxide}}$ 1.57-micron diameter Polystyrene microspheres on the MSZW of Glycine nucleating from solution in D_2O . Addition of particles (Black to Red) induces a shift in the gradient of the MSZW. ... | 149 |
| Figure 7:5: Left; Effect of $0.12 \text{ mg}_{\text{silica}}/\text{g}_{\text{water}}$ 1.57-micron diameter silica microspheres on the MSZW of NaCl nucleating from solution in H_2O . Right; Effect of $0.12 \text{ mg}_{\text{silica}}/\text{g}_{\text{Deuterium Oxide}}$ 1.57-micron diameter silica microspheres on the MSZW of Glycine nucleating from solution in D_2O . | |

Addition of particles (Black to Red) causes both a shrinkage of the MSZW and for this boundary to become steeper.....150

Figure 7:6: 0.06 mg_{polystyrene}/g_{water} 1.57-micron diameter Polystyrene microspheres on the MSZW of NaCl nucleating from solution in H₂O. Addition of particles (Black to Red) cases the MSZW to become narrower at the lower end of the saturation temperatures examined as the gradient of the MSZW is increased.150

Figure 7:7: Both; Cumulative Probability Distribution Plot of Induction Times of Glycine doped and undoped with silica microspheres, agitated using a stirrer bar at 700 RPM at S between 1.16 and 1.22. Pure Solution (Hollow Symbols), 1 mg_{silica}/g_{Solvent} dispersion (Filled Symbols). Jiang and ter Horst fitting [48] only shown in systems doped with silica. Left; Glycine in H₂O. Left; Glycine in D₂O.152

Figure 7:8: Both; Cumulative Probability Distribution Plot of Induction Times of Glycine doped and undoped with polystyrene microspheres, agitated using a stirrer bar at 700 RPM at S between 1.16 and 1.22. Pure Solution (Hollow Symbols), 0.5 mg_{Polystyrene}/g_{Solvent} dispersion (Filled Symbols). Jiang and ter Horst fitting [48] only shown in systems doped with silica. Left; Glycine in H₂O. Left; Glycine in D₂O.....152

Figure 7:9: Effect of Silica and Polystyrene micro-particles on the primary nucleation rates of Glycine from H₂O and D₂O. Calculated using the fitting model published by Jiang and ter Horst [1].....153

Figure 7:10 Both; Cumulative Probability Distribution Plot of Induction Times of NaCl doped and undoped with silica microspheres, agitated using a stirrer bar at 700 RPM at S between 1.0025 and 1.02. Pure Solution (Hollow Symbols), 0.12 mg_{silica}/g_{Solvent} dispersion (Filled Symbols). Jiang and ter Horst fitting [48] only shown in systems doped with silica). At time 0, the proportion of total vials nucleated before isothermal conditions is indicated using the same symbols. Left; NaCl in H₂O. Left; NaCl in D₂O.....154

Figure 7:11: Both; Cumulative Probability Distribution Plot of Induction Times of NaCl doped and undoped with polystyrene microspheres, agitated using a stirrer bar at 700 RPM at S between 1.0025 and 1.02. Pure Solution (Hollow Symbols), 0.06 mg_{Polystyrene}/g_{Solvent} dispersion (Filled Symbols). Jiang and ter Horst fitting [48] only shown in systems doped with silica). At time 0, the proportion of total vials nucleated before isothermal conditions is indicated using the same symbols. Left; NaCl in H₂O. Left; NaCl in D₂O.....155

Figure 7:12: Effect of Silica and Polystyrene micro-particles on the primary nucleation rates of NaCl from H₂O and D₂O. Calculated using the fitting model published by Jiang and ter Horst [1].....156

Figure 7:13: Transmissivity for samples containing added particles at 2 mg/g of glycine in H₂O at different concentrations of glycine 0.245 g/g (Black Solid), 0.265 g/g (Magenta Solid), 0.290 g/g (Green Solid) and 0.313 g/g (Blue Solid). Temperature is shown on the secondary y-axis, temperature profile (Red Dashed).157

Figure 7:14: Transmissivity for samples containing added particles at 1 mg/g of glycine in H₂O at different concentrations of glycine 0.242 g/g (Black Solid), 0.264 g/g (Magenta Solid), 0.288 g/g (Green Solid) and 0.311 g/g (Blue Solid). Temperature is shown on the secondary y-axis, temperature profile (Red Dashed).158

Figure 7:15: Individual transmissivity traces of glycine in H₂O at different concentrations of glycine 0.242 g/g (Black Solid), 0.264 g/g (Magenta Solid), 0.288 g/g (Green Solid) and 0.311 g/g (Blue Solid). Temperature is shown on the secondary y-axis, temperature profile (Red

| | |
|---|-----|
| Dashed). Solutions contained $0.5 \text{ mg}_{\text{Polystyrene}}/\text{g}_{\text{water}}$ of 1.59-micron diameter polystyrene microspheres. | 159 |
| Figure 7:16: Comparison of Induction times as determined using the transmission of light and the monitoring of individual vial temperature. Induction times of glycine solutions in H_2O between the supersaturations of 1.16 and 1.22 at 25°C . The dashed black line indicates the equal time line. | 161 |
| Figure 7:17: Comparison of cumulate probability distributions of glycine solutions in H_2O between $S = 1.16$ and 1.22 when measured in the absence and presence of the temperature probe using light transmission to determine the crystallisation point. | 162 |
| Figure 7:18: Comparison of cumulative probability distributions of glycine solutions in H_2O , between $S = 1.16$ and 1.22 using dopings of $1.57 \mu\text{m}$ diameter silica particles of 1 mg/g , 2 mg/g , and particle free..... | 163 |
| Figure 7:19: Primary nucleation rates of glycine from solution in H_2O under all previously examined conditions when in suspension with silica and polystyrene, measured using light and temperature methods. Hollow Symbols indicated the presence of the temperature probes. | 164 |
| Figure 8:1: Example image showing the surface of a NaCl Crystal prior to immersion washing. Image taken at x20 magnification, Red scale bar is indicative of 200 microns. | 167 |
| Figure 8:2: Growth and Dissolution Rates of NaCl in solutions of NaCl in either H_2O (left) or D_2O (right) at concentrations up to $S = 1.01$. Each point indicates the growth or dissolution calculated by tracking the crystal front over a period of time, extracted from equally time spaced stills from the recoded video. Error bars indicate a 95 % confidence interval of the rate determined from a linear fit of the individual displacements. | 168 |
| Figure 8:3: Growth rate of a NaCl crystal in $S=1.01$ solution made from H_2O (left) and D_2O (right). An optical tweezing focus of various powers is initially located 10 microns from the front of the crystal face. Error bars indicate a 95 % confidence interval calculated by determining a linear fit of the displacement positions of the crystal front, the gradient of this trendline was taken as the growth rate. | 170 |
| Figure 8:4: Growth rate of a NaCl crystal in $S = 1.01$ solution made from H_2O (left) and D_2O (right). An optical tweezing focus set to a power of 300 mW initially at the distance indicated was used. Error bars indicate a 95 % confidence interval calculated by determining a linear fit of the displacement positions of the crystal front, the gradient of this trendline was taken as the growth rate Impact of presence of silica particles in dispersion..... | 171 |
| Figure 8:5: Growth Rates of a NaCl crystal grown from a solution at $S = 1.01$ in H_2O (left) and D_2O (right). The solution used also contains 0.12 mg of silica per g of solvent. Error bars show a 95 % confidence interval of the displacement rate of the crystal front as determined from still images extracted from a video of the growing crystals. | 172 |
| Figure 8:6: Growth rate of a NaCl crystal in $S=1.01$ $0.12 \text{ mg}_{\text{silica}}/\text{g}_{\text{solvent}}$ silica dispersion made from H_2O (left) and D_2O (right). An optical tweezing focus of various powers is initially located 10 microns from the front of the crystal face. Error bars show a 95 % confidence interval calculated from the gradient of the displacement of the crystal front. | 173 |
| Figure 8:7: Growth rate of a NaCl crystal in $S = 1.01$, $0.12 \text{ mg}_{\text{silica}}/\text{g}_{\text{solvent}}$ silica dispersion made H_2O (left) and D_2O (right). An optical tweezing focus set to a power of 300 mW initially at the distance indicated was used. Error bars show a 95 % confidence interval calculated from the gradient of the displacement of the crystal front. | 173 |

Figure 8:8: Growth rate of a NaCl crystal in $S=1.01$, $0.12 \text{ mg}_{\text{silica}}/\text{g}_{\text{solvent}}$ silica dispersion where a single silica particle was held by the tweezers, made from H_2O (left) and D_2O (right). An optical tweezing focus of various powers is initially located 10 microns from the front of the crystal face. Error bars show a 95 % confidence interval calculated from the gradient of the displacement of the crystal front.174

Figure 8:9: Growth rate of a NaCl crystal in $S = 1.01$, $0.12 \text{ mg}_{\text{silica}}/\text{g}_{\text{solvent}}$ silica dispersion where a single silica particle was held by the tweezers, made from H_2O (left) and D_2O (right). An optical tweezing focus set to a power of 300 mW initially at the distance indicated was used. Error bars show a 95 % confidence interval calculated from the gradient of the displacement of the crystal front.175

Figure 8:10: Geometry of crystal growing towards and away from the optical tweezing focus.176

Figure 8:11: Growth rate of NaCl crystal through a focus of an optical tweezer of a NaCl crystal in $S = 1.01$ solution in H_2O at various laser powers. The growth rate was analysed under three circumstances, towards the focus (triangles) and away from the focus (inverted triangles) overall growth rates are shown in the insert; linked runs are indicated using the same symbol colour. Error bars indicate a 95 % confidence interval in the gradient of the points analysed in each scenario. Symbols shown in the same colour at the same laser power were determined from a single experiment. Geometric relationship of towards focus and away from the focus is shown in the diagram in Figure 8:10.177

Figure 8:12: Growth of a NaCl Crystal suspended in $S = 1.01$ solution in H_2O through the Focus of an Optical Trap at 300 mW set power. Images A-I were taken at 30-second intervals where the focus was activated at time 0 when image A was taken. White scale bars show 20 microns. The Position of the tweezing focus in the images is indicated by the red arrow in each image.179

Figure 8:13: Growth of a NaCl Crystal in $S = 1.01$ H_2O based NaCl Solution in H_2O following deactivation of an optical trap with a set laser power of 300 mW. Images A-I were taken at 30-second intervals following activation when image A was taken. White scale bars show 20 microns. Position of where the tweezing focus was located in the image is indicated by the red arrows.....180

Figure 8:14: Growth rate of NaCl crystal through a focus of an optical tweezer of a NaCl crystal in $S = 1.01$ solution in D_2O at various laser powers The growth rate was analysed under three circumstances,) and towards the focus (triangles) and away from the focus (inverted triangles) overall growth rates are shown in the insert; linked runs are indicated using the same symbol colour. Error bars indicate a 95 % confidence interval in the gradient of the points analysed in each scenario. Symbols shown in the same colour at the same laser power were determined from a single experiment.182

Figure 8:15: Growth rate of NaCl crystal through a focus of an optical tweezer of a NaCl crystal in $S = 1.01$ in H_2O with silica in suspension at a concentration of $0.12 \text{ mg}_{\text{silica}}/\text{g}_{\text{solvent}}$ at various laser powers, where a silica particle is held in the focus of the tweezers. The growth rate was analysed under three circumstances,) and towards the focus (triangles) and away from the focus (inverted triangles) overall growth rates are shown in the insert; linked runs are indicated using the same symbol colour. Error bars indicate a 95 % confidence interval in the gradient of the points analysed in each scenario. Symbols shown in the same colour at the same laser power were determined from a single experiment.183

Figure 8:16: Growth rate of NaCl crystal through a focus of an optical tweezer of a NaCl crystal in $S = 1.01$ in D_2O with silica in suspension at a concentration of $0.12 \text{ mg}_{\text{silica}}/\text{g}_{\text{solvent}}$ at various laser powers, where a silica particle is held in the focus of the tweezers. The growth rate was analysed under three circumstances,) and towards the focus (triangles) and away from the focus (inverted triangles) overall growth rates are shown in the insert; linked runs are indicated using the same symbol colour. Error bars indicate a 95 % confidence interval in the gradient of the points analysed in each scenario. Symbols shown in the same colour at the same laser power were determined from a single experiment.184

Figure 8:17: Schematic of agitation applied to the surface of a NaCl seed. Left; Parallel agitation. Right; Perpendicular agitation.185

Figure 8:18: Growth Rates of NaCl Crystals in proximity to an agitated silica microsphere, held using a 975 nm laser at a set power of 300 mW, examined by altering the direction, amplitude, and frequency of agitation. The subdivision of agitation frequency is not shown. Points show individual measurements with 95 % Confidence Intervals. Bars indicate averages of points. Blue lines indicate growth rate of NaCl in $S = 1.01 D_2O$ based solution in absence of any outside influence.186

Figure 8:19: Growth Rates of NaCl Crystals in proximity to an agitated silica microsphere, held using a 975 nm laser at a set power of 300 mW, examined by altering the direction, amplitude, and frequency of agitation. Points show individual measurements with 95 % Confidence Intervals. Bars indicate averages of points. Blue lines indicate growth rate of NaCl in $S = 1.01 D_2O$ based solution in absence of any outside influence.187

Figure 8:20: Pictures taken of Silicon Isolator well-filling tests. Row A; NaCl in H_2O . Row B; NaCl in D_2O . Column 1; Initial appearance. Column 2; Appearance after 24 hours.188

Figure 9:1: Schematic of Modified Optical Tweezer Set-Up. Component library provided by Alexander Franzen [233].189

Figure 9:2: Schematic diagram of the sessile droplet within the silicon isolator and coverslip assembly showing a side view and top-down when the tweezing focus was located at the droplet edge. Wider setup including silicon isolator show. Other non-test droplets placed on to the surface not shown.190

Figure 9:3: Box plot of the contact angle measurements of three liquids to determine the surface energy of the coverslips used in the tweezing experiments. Distributions were determined from 10 measurements of contact angle at $20 \text{ }^\circ\text{C}$. 50 % of points are within the box, outer quartiles are within the bars. The median is indicated with the line, and the mean is highlighted using the indicated point.193

Figure 9:4: Contact angle measurements of sodium chloride solutions in water (Hollow Symbols) and deuterium oxide (Filled Symbols) of a range of supersaturation at $20 \text{ }^\circ\text{C}$ based on a solubility of $0.3623 \text{ g}_{\text{NaCl}}/\text{g}_{\text{Water}}$ and $0.3084 \text{ g}_{\text{NaCl}}/\text{g}_{\text{Deuterium Oxide}}$. Black bars indicate the mean and the standard error for each concentration in each solvent.196

Figure 9:5: Contact angle measurement of glycine solutions in water (Hollow Symbols) and Deuterium Oxide (Filled Symbols) of a range of supersaturation at $20 \text{ }^\circ\text{C}$ using the solubilities of $0.2286 \text{ g}_{\text{glycine}}/\text{g}_{\text{water}}$ and $0.1943 \text{ g}_{\text{glycine}}/\text{g}_{\text{deuterium oxide}}$. Black bars indicate the mean and the standard error for each concentration in each solvent.197

Figure 9:6: Examples of the droplet edge before nucleation, solutions of $S = 1.5$ in H_2O . Solution is located within the darker portion of the image, and the surrounding air is within the lighter half. Scale Bar indicates 10 microns. Red arrows indicate location of tweezing focus.....198

Figure 9:7: Cumulative probability distributions of the nucleation times located at the droplet edge for a range of glycine solutions in H₂O. Trapping power 775 mW (left) and 650 mW (right) of linearly polarised beam. A total of 10 repeat experiments were performed at each power and supersaturation combination.....199

Figure 9:8: Cumulative probability distributions of the nucleation times for a range of glycine solutions in D₂O. Trapping beam 775 mW (left) and 650 mW (right) of linearly polarised 1064 nm. A total of 10 repeat experiments were performed at each power and supersaturation combination.....200

Figure 9:9 Example of model shown in Equation 9:4 fitting to cumulate probability distribution of crystallisation times of glycine in H₂O being induced to nucleate using a 775 mW optical focus located at the droplet edge.202

Figure 9:10 Determined values of K_1 from fittings of Equation 9:4 to the cumulative probability distributions when examining the effect of altering the supersaturation of the solution used for testing while remaining at the droplet edge with the optical tweezers. Points show individual values determined, and lines indicate the averages across the range of supersaturations tested using the same solvent isotopologue and laser power.202

Figure 9:11: Example of Morphology of Glycine nucleating from $S = 1.5$ in D₂O when the focus of the tweezers was no more than 10 microns from the droplet edge. Cluster form (Left), Needle form (Centre) and Plate form (Right). Descending rows show 0.5 s evolution in the morphology of the crystals nucleating. Red scale bars indicate 10 microns. Red arrows indicate the location of the tweezing focus in the first image of each sequence.....204

Figure 9:12: Form of crystal morphology nucleated from a range of supersaturations of glycine in H₂O when acted upon at the droplet edge using optical tweezers generated using a linearly polarised 1064 nm laser at a trapping plane power of 775 mW (left) and 650 mW (right).205

Figure 9:13: Form of crystal morphology nucleated from a range of supersaturations of glycine in D₂O when acted upon at the droplet edge using optical tweezers generated using a linearly polarised 1064 nm laser at a trapping plane power of 775 mW (left) and 650 mW (right).206

Figure 9:14: Cumulative probability distributions of the nucleation times of $S = 1.5$ solutions of glycine in H₂O at selected positions within a sessile drop. Trapping beam 775 mW (left) and 650 mW (right) of linearly polarised 1064 nm. No nucleation was observed for the full 600 seconds of the experiment when focussing trap in bulk (centre of the droplet) or anywhere in the sample when trap was not operated. A total of 10 repeat experiments were performed at each position and power combination.207

Figure 9:15: Cumulative probability distributions of the nucleation times of $S = 1.5$ solutions of glycine in D₂O at selected positions within a sessile drop. Trapping beam 775 mW (left) and 650 mW (right) of linearly polarised 1064 nm. No nucleation was observed when operating in bulk or in the absence of the laser. A total of 10 repeat experiments were performed at each position and power combination.....208

Figure 9:16: Determined values of K_1 from the fitting of Equation 9:4 to the cumulative probability distributions when examining the effect of altering the position of the optical tweezing focus with respect to the droplet edge while keeping the bulk $S = 1.5$. Points show the individual values determined at a range of positions. Lines indicate linear trendlines. 209

Figure 9:17: Schematic diagram of the droplet edge, showing a side view and the approximate position of the tweezing focus when the focus was moved 10 μm horizontally in from the

droplet edge and 10 μm vertically up from the interface of the droplet and the cover glass. Left, H_2O -based solution where the focus would be 2.8 μm above the droplet's surface and right, D_2O -based solution where the focus would be 4.3 μm below the droplet's surface. 210

Figure 9:18: Form of crystal morphology nucleated from $S = 1.5$ glycine in H_2O at a range of positions with reference to the droplet edge when acted upon using optical tweezers generated using a linearly polarised 1064 nm laser at a trapping plane power of 775 mW (left) and 650 mW (right). 211

Figure 9:19: Form of crystal morphology nucleated from $S = 1.5$ glycine in D_2O at a range of positions with reference to the droplet edge when acted upon using optical tweezers generated using a linearly polarised 1064 nm laser at a trapping plane power of 775 mW (left) and 650 mW (right). 212

Figure 9:20: Cumulative probability distribution of nucleation of $S = 1.5$ solutions of glycine in H_2O (left) and D_2O (right) in various positions with the sessile droplets. Trap generated using a power of 650 mW using linearly polarised light (Closed Symbols) and circularly polarised light (Open Symbols). A total of 10 repeat experiments were performed at each polarisation and position combination. 213

Figure 9:21: Cumulative probability distribution of nucleation of solutions of glycine in H_2O (left) and D_2O (right) based solutions examining a range of concentrations where the tweezing focus is located at the edge of the sessile droplet (tri-point interface). Trap generated using a power of 650 mW using linearly polarised light (Closed Symbols) and circularly polarised light (Open Symbols). A total of 10 repeat experiments were performed at each polarisation and supersaturation combination. 214

Figure 9:22: Determined values of K_1 from the fitting of Equation 9:4 to the cumulative probability distributions when examining the effect of altering the polarisation of the laser beam used to generate the tweezing focus. When altering the supersaturation when remaining the droplet edge (left) and altering the horizontal distance between the focus and the droplet edge when keeping the bulk supersaturation at 1.5 (right). Using a laser power of 650 mW. Error bars are smaller than the symbols. 215

Figure 9:23: Form of crystal morphology nucleated when using a circularly polarised 1064 nm laser at a trapping plane power of 650 mW when in solutions of H_2O (left) and D_2O (right). At a range of positions relative to the edge of the droplet at an $S = 1.5$ and at other supersaturations when located at the droplet edge. 215

Figure 9:24: Comparison of the crystal morphology nucleated under a range of conditions varying the supersaturation when located at the droplet edge and $S = 1.5$ solution when in a solution of H_2O (left) and D_2O (right) using circularly polarised, CP, (upper bars) and linearly polarised, LP, (lower bars) of 1064 nm laser at a trapping plane power of 650 mW. 216

Figure 9:25: Cumulative probability distributions of nucleation times of $S = 1.5$ glycine in H_2O (left) and D_2O (right) at selected positions within a sessile drop. The trapping beam had a trapping plane laser power of 650 mW linear polarised 1064 nm laser light holding a 1.57 μm diameter silica particle (Open Symbols). Also shown are particle-free runs for comparison (Filled Symbols). No nucleation was observed when operating in bulk or in the absence of the laser. A total of 10 repeat experiments were performed at each position and particle presence combination. 217

Figure 9:26: Determined values of K_1 from the fitting of Equation 9:4 to the cumulative probability distributions when examining the effect of the presence of a 1.57 μm diameter

| | |
|---|-----|
| silica sphere using a 650 mW trapping beam. Performed in $S = 1.5$ solutions of glycine in H_2O and D_2O . | 218 |
| Figure 9:27: Form of crystal nucleation morphology when $S = 1.5$ of glycine in H_2O (left) and D_2O (right) at various positions with the sessile drop with reference to the edge of the sessile drop tested. The trapping beam held a $1.57 \mu m$ diameter silica spherical particle, trapping laser used linearly polarised 1064 nm with a trapping plane power of 650 mW. | 219 |
| Figure 9:28: Comparison of crystal nucleation morphology of the crystal of glycine formed from an $S = 1.5$ solution in H_2O (left) and D_2O (right). The trapping beam used a linearly polarised 1064 nm laser with a trapping plane power of 650 mW. $1.57 \mu m$ diameter silica spheres were held in the tweezers (Lower Bars) and silica particle free tweezers (Upper Bars). | 219 |
| Figure 9:29: QPD sum voltage extract produced when nucleation was observed using $S = 1.50$ glycine in H_2O (A & B) and D_2O (C) when using a trapping plane power of 775 mW when the focus was located at the droplet edge (0 Micron). A, B and C are the QPD sum voltages for different experiments. | 220 |
| Figure 9:30: Determined growth rates (Open Points) of crystals formed from glycine solutions in H_2O between the supersaturations of 1.5 and 0.85. When the tweezing focus was located at the droplet edge when using a laser power of 775 mW. Crosses indicate averages at each supersaturation. Dashed line indicates linear fitting of average growth rate values at each supersaturation. | 228 |
| Figure 9:31: Determined growth rates of crystals formed from glycine solutions in H_2O between the supersaturations of 1.5 and 1.00. When the tweezing focus was located at the droplet edge when using a laser power of 650 mW. | 229 |
| Figure 9:32: Determined growth rates of crystals formed from glycine solutions in D_2O between the supersaturations of 1.50 and 0.85. When the tweezing focus was located at the droplet edge when using a laser power of 775 mW. | 230 |
| Figure 9:33: Comparison of the growth rate of glycine crystals produced through nucleation via optical tweezing at a range of tweezing conditions using H_2O and D_2O at the two laser powers, 775 mW and 650 mW (Open Squares). Average growth rates were determined using the Crystalline apparatus, previously reported in Chapter 6 (Open Circles). Growth rates from literature sources [219], [220] (Open Triangles). | 232 |
| Figure 9:34: Correlation of the growth rate of glycine crystals at a range of relative supersaturations ($\sigma, S - 1$). Power law fitting is applied to all data shown. Repeat and further analysis of Figure 6:27. Left: showing previous data only. Right: Previously shown data alongside average growth rates induced by the action of the tweezing focus. | 233 |
| Figure 9:35: Comparison of calculated focus relative supersaturation and the bulk relative supersaturation. | 234 |
| Figure 9:36: Average bulk and calculated focus relative superstation. Lines are intended only to guide eyes, elementary power law fitting. Magenta point excluded from fitting of D_2O 775 mW set. | 235 |
| Figure C:1: Impact of Quiescent Immersion Washing in H_2O for 1 second. | E |
| Figure C:2: Impact of Quiescent Immersion Washing in H_2O for 5 seconds. | F |
| Figure C:3: Impact of Quiescent Immersion Washing in H_2O for 10 seconds. | H |
| Figure C:4: Impact of Quiescent Immersion Washing in D_2O for 1 second. | I |
| Figure C:5: Impact of Quiescent Immersion Washing in D_2O for 5 seconds. | K |
| Figure C:6: Impact of Quiescent Immersion Washing in D_2O for 10 seconds. | L |

Figure D:1: Example of the number of particles visible in images captured by a Crystalline camera. Example from a seeded experiment using an $S = 1.01$ solution in H_2O , agitated using an overhead propeller at 1250 RPM. Time from the beginning of isothermal conditions. ... M

Figure D:2: Calculated number concentration of particles in suspension calculated from the number of particles imaged. Example from a seeded experiment using an $S = 1.01$ solution in H_2O , agitated using an overhead propeller at 1250 RPM. The linear fit of points is also shown. Time from the beginning of isothermal conditions. N

Figure D:3: Calculated D-90 from binned particle distributions as determined from the images taken by the internal Crystalline reactor camera. Example from a seeded experiment using an $S = 1.01$ solution in H_2O , agitated using an overhead propeller at 1250 RPM. Linear fit of points is also shown. Time from the beginning of isothermal conditions. N

Figure E:1: Example of the machine learning workspace used CVAT, where an example of a spherical particle is midway through being outlined by the user to allow it to be identified by the algorithm. O

Figure F:1: Left; Cumulative Probability Distribution Plot of Induction Time Measurements of NaCl in Water, agitated using a stirrer bar at 700 RPM at S between 1.0025 and 1.02. Right; Cumulative Probability Distribution Plot of Induction Time Measurements of NaCl in Deuterium Oxide agitated using a stirrer bar at 700 RPM at S between 1.02 and 1.04. P

Figure F:2: Left; Cumulative Probability Distribution Plot of Induction Time Measurements of NaCl in Water, agitated using a stirrer bar at 700 RPM at S between 1.0025 and 1.02. Right; Cumulative Probability Distribution Plot of Induction Time Measurements of NaCl in Deuterium Oxide agitated using a stirrer bar at 700 RPM at S between 1.0025 and 1.02. Q

Figure F:3: Cumulative Probability Distribution Plot of Induction Time Measurements of NaCl in Water, agitated using an overhead propeller at 1250 RPM at S between 1.0025 and 1.02. Right; Cumulative Probability Distribution Plot of Induction Time Measurements of NaCl in Deuterium Oxide agitated using an overhead propeller at 1250 RPM at S between 1.0025 and 1.02. Q

Figure F:4: Cumulative Probability Distribution Plot of Induction Times of NaCl in H_2O , agitated using a stirrer bar at 700 RPM at S between 1.0025 and 1.02. Pure Solution (Hollow Symbols), $0.12 \text{ mg}_{\text{silica}}/\text{g}_{\text{water}}$ dispersion (Filled Symbols). Right; Cumulative Probability Distribution Plot of Induction Times of NaCl in D_2O agitated using a stirrer bar at 700 RPM at S between 1.0025 and 1.02. Pure Solution (Hollow Symbols), $0.12 \text{ mg}_{\text{silica}}/\text{g}_{\text{deuterium oxide}}$ dispersion (Filled Symbols)..... R

Figure F:5: Left; Cumulative Probability Distribution Plot of Induction Times of NaCl in H_2O , agitated using a stirrer bar at 700 RPM at S between 1.0025 and 1.02. Pure Solution (Hollow Symbols), $0.06 \text{ mg}_{\text{polystyrene}}/\text{g}_{\text{water}}$ dispersion (Filled Symbols). Right; Cumulative Probability Distribution Plot of Induction Times of NaCl in D_2O , agitated using a stirrer bar at 700 RPM at S between 1.0025 and 1.02. Pure Solution (Hollow Symbols), $0.06 \text{ mg}_{\text{polystyrene}}/\text{g}_{\text{deuterium oxide}}$ dispersion (Filled Symbols)..... R

Figure F:6: Crystallisation Time Classification Plot. Left: of NaCl in Water, agitated using a stirrer bar at 700 RPM at S between 1.0025 and 1.02. Right: of NaCl in Deuterium Oxide, agitated using a stirrer bar at 700 RPM at S between 1.02 and 1.04. S

Figure F:7: Crystallisation Time Classification Plot. Left: of NaCl in Water, agitated using a stirrer bar at 700 RPM at S between 1.0025 and 1.02. Right: of NaCl in Deuterium Oxide, agitated using a stirrer bar at 700 RPM at S between 1.0025 and 1.02. S

Figure F:8: Crystallisation Time Classification Plot. Left: of NaCl in Water, agitated using an overhead propeller at 1250 RPM at S between 1.0025 and 1.02. Right: of NaCl in Deuterium Oxide, using agitated using an overhead propeller at 1250 RPM at S between 1.0025 and 1.02. T

Figure F:9: Crystallisation Time Classification Plot. Left: NaCl in H₂O, agitated using a stirrer bar at 700 RPM at S between 1.0025 and 1.02 with 0.12 mg_{silica}/g_{water}. Right: NaCl in D₂O, agitated using a stirrer bar at 700 RPM at S between 1.0025 and 1.02 with 0.12 mg_{silica}/g_{Deuterium Oxide}. T

Figure F:10: Crystallisation Time Classification Plot. Left: NaCl in H₂O, agitated using a stirrer bar at 700 RPM at S between 1.0025 and 1.02 with 0.06 mg_{polystyrene}/g_{water}. Right: NaCl in D₂O, agitated using a stirrer bar at 700 RPM at S between 1.0025 and 1.02 with 0.06 mg_{polystyrene}/g_{Deuterium Oxide}. T

Figure G:1: Cumulative probability distributions of the nucleation times located at the droplet edge for a range of glycine solutions in H₂O. Trapping power 775 mW (left) and 650 mW (right) of linearly polarised beam. U

Figure G:2: Cumulative probability distributions of the nucleation times for a range of glycine solutions in D₂O. Trapping beam 775 mW (left) and 650 mW (right) of linearly polarised 1064 nm. U

Figure G:3: Cumulative probability distributions of the nucleation times of S =1.5 solutions of glycine in H₂O at selected positions within a sessile drop. Trapping beam 775 mW (left) and 650 mW (right) of linearly polarised 1064 nm. No nucleation was observed when operating in bulk or in the absence of the laser. V

Figure G:4: Cumulative probability distributions of the nucleation times of S =1.5 solutions of glycine in D₂O at selected positions within a sessile drop. Trapping beam (left) and (right) of linearly polarised 1064 nm. No nucleation was observed when operating in bulk or in the absence of the laser. V

Figure G:5: Cumulative probability distribution of nucleation of S =1.5 solutions of glycine in H₂O (left) and D₂O (right) in various positions with the sessile droplets. Trap generated using a power of 650 mW using linearly polarised light (Closed Symbols) and circularly polarised light (Open Symbols). W

Figure G:6: Cumulative probability distribution of nucleation of solutions of glycine in H₂O (left) and D₂O (right) based solutions examining a range of concentrations where the tweezing focus is located at the edge of the sessile droplet (tri-point interface). Trap generated using a power of mW using linearly polarised light (Closed Symbols) and circularly polarised light (Open Symbols). W

Figure G:7: Cumulative probability distributions of nucleation times of S = 1.5 glycine in H₂O (left) and D₂O (right) at selected positions within a sessile drop. The trapping beam had a trapping plane laser power of mW linear polarised 1064 nm laser light holding a 1.57 μm diameter silica particle (Open Symbols). Also shown are particle-free runs for comparison (Filled Symbols). No nucleation was observed when operating in bulk or in the absence of the laser. X

Figure J:1: Measured Power at the Back of the Objective lens and the associated power delivered at the trapping point. Measurements were taken at the rear of the objective (Black Squares) and calibrated power after the objective (Red Circles), based on transmittance at 975 nm from Figure J:2. AA

Figure J:2: Transmittance of the objective lens, Nikon E Plan 100x NA=1.25, Oil Immersion (Black). Wavelength of the trapping laser (Red Dashed Line). Taken from Nikon [251]. BB

Figure J:3: Left; Bulk and Focus Supersaturation of Solutions of NaCl in H₂O and D₂O using various set powers of a 975 nm trapping laser. Power is set at the point of the driver where the effect of the supersaturation is adjusted to account for losses through the optical components. Predictions were made using H₂O (solid lines) and D₂O (dashed lines). Laser Power is shown by line colour 50 mW set power (black), 100 mW set power (red), 200 mW set power (blue) and 300 mW set power (green). Right; Bulk and Focus Supersaturation of Solutions of NaCl in H₂O and D₂O using various set powers of a 1064 nm trapping laser. Power is set at the point of the driver where the effect of the supersaturation is adjusted to account for losses through the optical components. Predictions were made using H₂O (solid lines) and D₂O (dashed lines). Laser Power is shown by line colour 50 mW set power (black), 100 mW set power (red), 200 mW set power (blue) and 300 mW set power (green). CC

Figure J:4: Left; Trap Supersaturations for Fixed bulk supersaturations in H₂O and D₂O using a 975 nm trapping laser. Predictions were made using H₂O (solid lines) and D₂O (dashed lines). Initial Supersaturation of 1.0025 (black), 1.005 (red), 1.01 (blue) and 1.02 (green). Right; Trap Supersaturations for Fixed bulk supersaturations in H₂O and D₂O using a 1064 nm trapping laser. Predictions were made using H₂O (solid lines) and D₂O (dashed lines). Initial Supersaturation of 1.0025 (black), 1.005 (red), 1.01 (blue) and 1.02 (green). CC

Figure J:5: Left; Predicted Impact of Trapping distance between the trap focus and the internal surface of the coverslip when using bulk S=1.01 based H₂O and D₂O as solvents when using a 975 nm laser. Predictions were made using H₂O (solid lines) and D₂O (dashed lines). Distance between the trap focus and the interior of the coverslip is shown in colour 60 microns distance (black), 30 microns (red) and 16 microns (blue). Right; Predicted Impact of Trapping distance between the trap focus and the internal surface of the coverslip when using H₂O and D₂O as solvents when using a 1064 nm laser. Predictions were made using H₂O (solid lines) and D₂O (dashed lines). Distance between the trap focus and the interior of the coverslip is shown in colour 60 microns distance (black), 30 microns (red) and 16 microns (blue). DD

List of Tables

| | |
|---|-----|
| Table 2:1: Crystal Systems and Lattices [4], [10]. | 8 |
| Table 2:2: Crystal Habits and Associated Shape Factors [4]. | 9 |
| Table 2:3: Secondary Nucleation Classification by Myerson and Ginde [4]. | 16 |
| Table 3:1: Vogel–Fulcher–Tammann Parameters for Deuterium Oxide. Calculated from NIST (National Institute of Standards and Technology) Webbook [115]. | 40 |
| Table 5:1: List of Absorption Coefficients and thermal conductivity at 293 K of solvents and common trapping materials. | 75 |
| Table 5:2: Predicted maximum temperature rises in pure solvent per Watt of laser power used. | 83 |
| Table 5:3 Example Changes in Trap Stiffness with increases in temperature. | 84 |
| Table 6:1: Limited Details of reference papers for solubility of sodium chloride in water and deuterium oxide. | 100 |
| Table 6:2: Details of Glycine solubility in water Sources | 101 |

| | |
|--|-----|
| Table 6:3: Composition of solutions used for induction time measurements of NaCl. | 107 |
| Table 6:4: Time after which 90 % of all samples had nucleated when examining the NaCl nucleating from H ₂ O and D ₂ O at the scale of 3 g of solvent. | 110 |
| Table 6:5: Nucleation Rates and Growth Times of Sodium Chloride Solutions in water and heavy water. Where a cell contains [-], a value cannot be calculated. Tolerances indicate standard error determined from the fitting of the model. 1 mL solvent scale experiments were performed in the Crysatl16, and 3 mL experiments were performed in the Crystalline. | 117 |
| Table 6:6: Comparison of Nucleation Rates of Sodium Chloride from Deionised Water and Deuterium Oxide at the Crystalline scale with bar agitation | 118 |
| Table 6:7: Composition of solutions used for induction time measurements of glycine. | 121 |
| Table 6:8: Time after which 50 % of samples nucleated for glycine in water and deuterium oxide agitated by a magnetic stirrer at a speed of 700 RPM. | 123 |
| Table 6:9: Nucleation Rates and growth times of glycine in water and heavy water. Where a cell contains [-], a value cannot be calculated. Tolerances indicate standard error as determined from the model fitting. | 125 |
| Table 6:10: Comparison of Nucleation Rates and Growth Times of Glycine at the Crystalline Scale agitated using a bar. | 126 |
| Table 7:1: Summary of the particle suspensions used to test the effects of particle dopings on primary nucleation behaviour. | 144 |
| Table 7:2: Concentrations of NaCl in H ₂ O and D ₂ O used to determine the effects of particles on primary nucleation characteristics. | 146 |
| Table 7:3: Concentrations of Glycine in H ₂ O and D ₂ O used to determine the effects of particles on primary nucleation characteristics. | 146 |
| Table 9:1: Compositions of Glycine Solutions used for nucleation testing using optical tweezers. | 191 |
| Table 9:2: Compositions of Sodium Bromate Solutions used for nucleation testing using optical tweezers. | 192 |
| Table 9:3: Surface energy parameters of test liquids [234]. | 194 |
| Table 9:4: Surface Energy Components of the Cover glasses. | 194 |
| Table 9:5: Percentage of times nucleation was observed when focused at the edge of a droplet of glycine solution in D ₂ O at a range of supersaturation at 775 mW and 650 mW. | 200 |
| Table 9:6: Determined values of the K ₁ from the fitting of Equation 9:4 to the cumulative probability distributions when altering the vertical distance when the horizontal distance between the tweezing focus and the droplet edge is 10 microns when the bulk solution is S = 1.5. | 210 |

List of Symbols

| | |
|--------------------|--|
| A | Crystal Surface Area |
| c | Speed of Light |
| C | Concentration |
| $C^*(T)$ | Solubility |
| C_{Real}^* | Experienced Solubility |
| ΔC | Concentration Driving Force |
| D | Diffusion Coefficient |
| E | Electric Field Density |
| F | Force |
| F_{Gr} | Gradient Force |
| F_{Sc} | Scattering Force |
| f | Frequency |
| f_0 | Corner Frequency |
| ΔG | Gibbs Free Energy |
| ΔG_{VU} | Volume Based Gibbs Free Energy |
| ΔG_{Crit} | Critical Gibbs Free Energy |
| $\Delta G'_{Crit}$ | Heterogeneous Critical Gibbs Free Energy |
| h | Diffusion Layer Thickness |
| I_0 | Initial Intensity |
| I | Intensity |
| J | Primary Nucleation Rate |
| K | Thermal Conductivity |
| K_1 | Nucleation Fitting Parameter |
| k_b | Boltzmann's Constant |
| k_i | Trap Stiffness |
| L | Crystal Characteristic Length |
| M | Total Number of Vials |
| $M^*(t)$ | Number of Nucleated Vials |
| N | Number of Nuclei Counted |
| N | Ratio of Refractive Indices |
| N_ρ | Particle Suspension Concentration |

| | |
|--------------|---|
| n | Refractive Index |
| n_i | Complex Component of the Refractive Index |
| $P(t)$ | Cumulative Proportion of Nucleated Vials |
| P | Beam Power |
| Q_i | Trapping Efficiency Parameter |
| R | Universal Gas Constant |
| r | Cluster Radius |
| r_p | Particle Radius |
| S | Supersaturation |
| S_0 | Plateau Value |
| T | Temperature |
| t | Time |
| t_g | Growth Time |
| T_D | Heat Sink Temperature |
| T_0 | Trap Centre Temperature |
| ΔT_B | Beam Component Temperature Rise |
| ΔT_P | Particle Component Temperature Rise |
| ΔT_O | Overall Temperature Rise |
| V | Volume |
| V_{Mol} | Molar Volume |
| x | Path Length |
| x_i | Position in axis i |
| Z | Distance Between Trap Centre and Surface |

| | |
|-------------------|-------------------------------------|
| α | Chemical Activity |
| α | Volume Shape Factor |
| α^* | Chemical Activity at Equilibrium |
| $\alpha_{abs}(i)$ | Absorption Coefficient |
| β | Area Shape Factor |
| Γ_S | Lattice Stress Parameter |
| γ | Activity Coefficient |
| γ^* | Activity Coefficient at Equilibrium |

| | |
|---------------|---|
| γ^+ | Lewis Acid Surface Energy Component |
| γ^- | Lewis Base Surface Energy Component |
| γ^{LW} | Lifshitz van der Waals Surface Energy Component |
| γ_i | Surface Energy |
| η | Viscosity |
| λ | Wavelength |
| θ | Wetting Angle |
| μ | Chemical Potential |
| μ^* | Chemical Potential at Equilibrium |
| $\Delta\mu$ | Difference in Chemical Potential |
| σ | Relative Supersaturation |
| σ_{If} | Interfacial Tension |
| ϕ | Heterogeneous Free Energy Factor |

| | |
|---------|----------------------|
| $Ei(q)$ | Exponential Integral |
| Re | Reynolds Number |
| Sc | Schmidt Number |

List of Common Abbreviations

| | |
|------|--------------------------------|
| MSZW | Metastable Zone Width |
| SNT | Secondary Nucleation Threshold |
| CNT | Classical Nucleation Theory |
| DLS | Dynamic Light Scattering |

1 Introduction

1.1 Importance and History of Crystallisation

Crystallisation is a process which has long been used by humanity to purify substances; early reports suggest this goes as far back as circa 2700 BCE to produce salt from water [1]. Ever since then, crystallisation has grown to play a vital role in the production of a range of products. However, this is especially true of pharmaceuticals as most active ingredients are present within approved drugs in the form of crystals [2].

In spite of how critical crystallisation has become and how long it has been utilised, it has been constantly stated that more study is needed, and this is still true today.

1.2 Thesis Goal and Layout

The overall aim of this thesis is to further the understanding of the influence that optical tweezing and associated particles have over crystallisation (nucleation and growth) from solution. This is accompanied by a body of preparatory work examining the consequences of various tweezing requirements on crystallisation in more commonly studied and better understood setups. Focusing on the use of deuterium oxide (commonly used with optical tweezers to limit laser induced heating) as the base solvent and the addition of tweezing microparticles, to fully contextualise investigations performed using the optical tweezers.

Chapter 1 (this chapter) briefly introduces the thesis and explains its overall structure.

Chapter 2 details the background theory of crystallisation (nucleation and crystal growth) and the impact that other additional materials (chemical and physical additives) can have on these processes.

Chapter 3 details the principles behind optical tweezing, position, and force measurement, uses that optical tweezers have been put to, including some involving crystallisation. This also details some non-basic forms of optical traps where the focus of the optical trap is moved and the ability to have multiple traps in close proximity.

Chapter 4 describes the equipment used for the results presented in the later chapters.

Chapter 5 describes the impact of solute on the optical properties of solutions to estimate the temperature rise that the use of the tweezers would cause. As well as the impact of introducing tweezing particles into the tested systems could also have on temperature and associated key crystallisation process metrics.

Chapter 6 details the effect of solvent isotopologue on nucleation and crystal growth characteristics upon the chosen systems, at various scales and agitation conditions, under commonly studied conditions.

Chapter 7 investigates the impact that microparticles typically used in tweezing (silica and polystyrene) have on nucleation properties, the width of the metastable zone and the induction time distribution when the suspension solvent is made up of different solvent isotopologues. As well as in some cases when the addition of particles interferes with traditional measurement techniques.

Chapter 8 examines the impact that tweezing focuses can have on the growth of macroscopically large crystals, as well as a preliminary look to see what occurs when a particle held with the trap is brought into contact with the surface of a seed crystal by either stage movement or allowing the seed to grow into the position which the trapped bead is occupying.

Chapter 9 explains the effects that optical tweezing focuses can have on substances nucleating from solution at and in proximity to sessile droplet interfaces, including triple phase contact points. Examining the effects of solvent isotopologue, solution supersaturation laser power and polarisation, and lateral displacement from the sessile droplet edge.

Chapter 10 summarises the main findings of the thesis, the conclusions that can be drawn from these findings, and some suggestions for future work to be conducted in this field.

Additional material is contained with the appendices.

2 Crystallisation

This chapter details why and how solid crystalline materials nucleate and grow to larger volumes. In addition to how the formation of crystals is impacted by the presence of existing substances and the typical measurement methods used to determine crystallisation kinetics.

2.1 Crystalline Materials

Three regular states of matter exist: gases, liquids, and solids. Gases take the shape and volume of their container, can be compressed, and have a low viscosity. Liquids have a higher viscosity and may only partially occupy their container; liquid interfaces that are not in contact with the surface of the container are flat. Solids will keep their shape in a larger container as they can resist gravity. Solids can be further divided into two forms: amorphous and crystalline. Crystalline solids differ from amorphous solids in that the most basic units (atoms, molecules, or ions) form a long-range regular fixed pattern, known as the crystal lattice. Crystalline solids are anisotropic, meaning the substance's physical properties depend on the direction of measurement [3]. Amorphous solids can have some short-range ordering of the most basic units. Like liquids and gases, amorphous solids are isotropic. Amorphous material's physical property measurements are not dependent on the measurement direction [4].

Crystallisation has two key stages. Firstly, nucleation, where the "minimum amount of new phase capable of independent existence" [5] is formed. This is followed by the growth phase, where particles that form the crystal structure are transported to the existing surface and incorporated into the crystalline structure.

2.2 Why Crystals Form from Solution

This thesis focuses on crystallisation of a solute from solution, using temperature induced supersaturation, rather than other methods, such as anti-solvent crystallisation or precipitation. However, the basics of these methods are detailed in section 2.3 to provide additional context. The formation of crystals (nucleation and crystal growth) from solution requires the concentration of the crystallising material to be higher than equilibrium conditions would permit. Thus, the chemical potential (μ) would be higher in that case than where dissolved solute would exist in equilibrium with excess solid solute. A supersaturated solution would then return to equilibrium by removing the excess solute from the solution by forming solid phase material. This excess in solution is known as supersaturation, also called supercooling. Cooling below the saturation temperature for the solution of that

composition in a system with standard temperature dependence, is one way to generate supersaturation. To quantify supersaturation, the temperature of the solution must be known as solubility (equilibrium concentration) is temperature-dependent [3]. The relationship between the actual concentration and the equilibrium concentration can be described in several ways. The first is concentration driving force ($\Delta c(T)$) as shown in Equation 2:1. This is equal to the difference between the actual concentration (c) and the solubility at the solution temperature ($c^*(T)$).

$$\Delta c(T) = c - c^*(T)$$

Equation 2:1

The second uses the supersaturation ratio ($S(T)$), also referred to as just 'supersaturation,' which is the ratio of the actual concentration and the solubility, shown in Equation 2:2.

$$S(T) = \frac{c}{c^*(T)}$$

Equation 2:2

The final common way to which this is referred to is the relative supersaturation ($\sigma(T)$), which is the ratio between the concentration driving force and solubility, equivalent to the supersaturation ratio minus 1, shown in Equation 2:3.

$$\sigma(T) = S(T) - 1 = \frac{c - c^*(T)}{c^*(T)} = \frac{\Delta c(T)}{c^*(T)}$$

Equation 2:3

An important note is that the value given to any concentration driving force, supersaturation or the relative supersaturation can depend upon how the solubility is defined by either quantity in reference to the other part or the whole solution. i.e., identical solutions can be given different supersaturation values depending on how the solubility is defined, for example, $g_{\text{solute}}/g_{\text{solvent}}$ and $g_{\text{solute}}/g_{\text{solution}}$. So, care must be taken to ensure what measurement system of solubility is used, especially when performing comparisons from various sources. One method that would be definitive would be to use mole fraction.

The use of supersaturation as a measure is a straightforward way to quantify the composition of the solution. This can be used to determine the difference in chemical potential between the solution conditions (μ) and a saturated solution (μ^*), which is described by the activity,

when making no assumptions, of the solutions in supersaturated and saturated conditions as shown in Equation 2:4

$$\mu - \mu^* = RT \ln \left(\frac{\alpha}{\alpha^*} \right)$$

Equation 2:4

The chemical potential can be linked to the supersaturation using activity coefficients (γ) through activity (α) which describes the effective concentration to account for differences that would be observed in departures from ideality, as seen in Equation 2:5.

$$\frac{\alpha}{\alpha^*} = \frac{\gamma c}{\gamma^* c^*(T)} = \frac{\gamma}{\gamma^*} S(T)$$

Equation 2:5

Assuming that the activity coefficients or their ratio equal unity would be the case in an ideal solution. That assumption allows the supersaturation to be used to determine the difference in chemical potential, shown in Equation 2:6.

$$\mu - \mu^* = RT \ln(S(T))$$

Equation 2:6

Should higher accuracy measurements of the chemical potential be required the activity coefficients would need to be determined. Since these are typically not known, Equation 2:6 is used and for many applications this is suitable [6]. The underlying assumption that allows for the use of this equation only holds at when the relative supersaturation is low. As the supersaturation continues to increase these activity coefficients would drift away from 1 by increasing or decreasing depending on the system being examined [7].

2.3 Crystal Formation Methods

The formation of crystalline solids from solution can be accomplished using several methods discussed in this subsection. These methods include cooling, evaporative, precipitation, and anti-solvent crystallisation [8].

2.3.1 Cooling Crystallisation

Cooling crystallisation is usually performed when a substance has highly temperature-dependent solubility so that small temperature changes result in significant changes in solubility. Therefore, once the temperature is lowered, the solubility falls, causing the system to become liable to crystal nucleation. In industrial processes the temperature dependence

on solubility should be as steep as possible. Upper limits of the mass of crystalline product which can be produced, due to downstream process requirements, may require that a small quantity of solute remain in solution [8]. A simple cooling crystallisation is shown in progress from points A to D, as indicated in Figure 2:1.

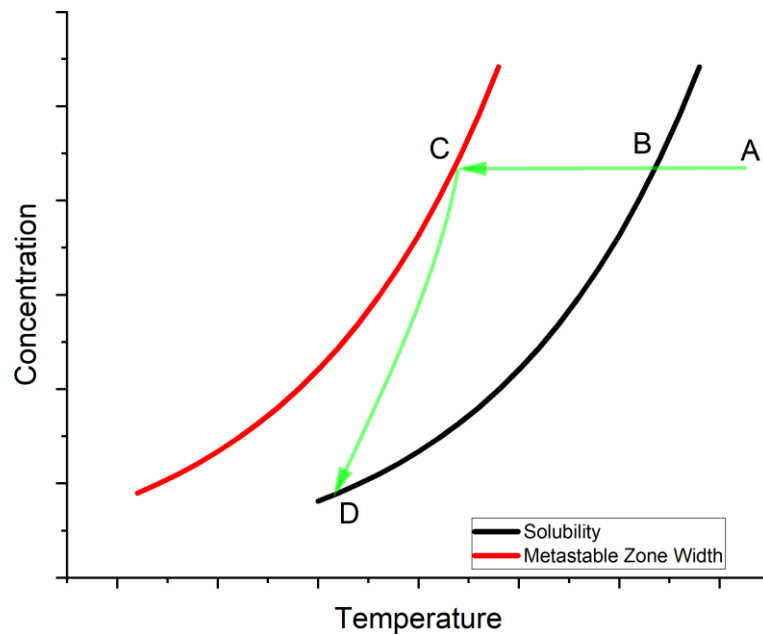


Figure 2:1: Basic Solubility Diagram. The progress of an elementary cooling crystallisation detailed by the green arrows and letter labelled points are detailed in the text below.

A simple cooling crystallisation would begin with an undersaturated solution (Point A). This solution would be subjected to cooling, and once the solution had cooled enough, this solution would become saturated (Point B). Further cooling would make the solution increasingly supersaturated. Crossing the solubility curve would not cause the concentration in solution to fall immediately, as the system is metastable and not liable to crystallisation. Once the solution had cooled down enough to reach the edge of the metastable zone (Point C), crystals would then form immediately. Primary nucleation can occur between the solubility and metastable zone width; however, this could take a long time, depending upon the system[9], causing the nucleation of crystals through primary nucleation. This, alongside the growth of the crystals present in the solution, would reduce the concentration in solution. A possible final concentration is indicated if the solution is slightly further cooled upon nucleation (Point D). The final concentration in solution would depend upon the exact degree of cooling. Further solute extraction may be possible depending on the system undergoing crystallisation; methods to continue extraction are described in the remainder of this section, 2.3.

2.3.2 Evaporative Crystallisation

The heating of a solution can induce the evaporation of the volatile components; in solutions, this is typically the solvent, causing the formation of the solid solute. Evaporative crystallisation is customarily used when there is little temperature dependence on solubility; therefore, cooling crystallisation is not viable. One downside of this method is that non-volatile impurities are also concentrated alongside the target substance [8].

2.3.3 Precipitation

Crystallisation via precipitation occurs when a reaction between at least two soluble substances produces an insoluble product. Precipitation is used when cooling, and evaporative crystallisation would not be suitable due to the low solubility of a crystal-forming substance. Due to the unique way precipitation crystallisation occurs, zones of significantly increased supersaturation can occur, potentially leading to the formation of alternative forms of the crystalline material, such as unwanted alternative polymorphs [8]. Polymorphism is discussed in section 2.4.3.

2.3.4 Anti-Solvent Crystallisation

Crystallisation can occur by adding an anti-solvent to the solution. This anti-solvent causes the solute to have a lower solubility in the new solvent mixture. However, this causes the dilution of the solute in what is now a solvent mixture, as the total mass of solvent is greater while the mass of solute remains unchanged. The decrease in solubility must be enough to compensate for the increased total solvent mass, as the solute is diluted with reference to the total mass of solvent [8].

2.4 Forms of Crystals

Crystals can be described in several different fashions. These descriptions can be based on their external appearance or internal structure.

2.4.1 Crystal Lattice

When considered a geometric solid, a crystal's internal structure can be described as a point lattice, where the crystal-forming units (atoms, molecules, or ions) are lattice points. Six factors, three spatial dimensions (a , b & c) and three angles (α , β & γ), are used to characterise the lattice of any chosen crystal. The repeating units that form the crystal lattice are described in such a way as to allow the lattice to continue indefinitely theoretically. From this, it can be ascertained that a range of different lattice arrangements are possible. It was demonstrated in 1848 by *Bravais* that only 14 such arrangements exist [4]. These 14 structures can be grouped into seven crystal systems or six crystal families [10]. These crystal

systems are shown in Table 2:1, and an example of a simple crystal unit cell is shown in Figure 2:2.

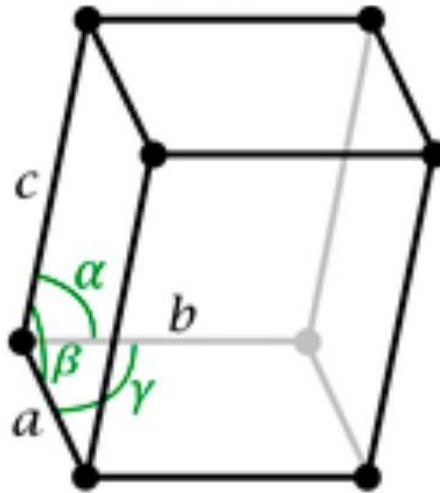


Figure 2:2: Example of Crystal Lattice Unit Cell [11].

Table 2:1: Crystal Systems and Lattices [4], [10].

| Crystal System | Unit Cell Dimensions | Unit Cell Angles | Lattices |
|-------------------------|----------------------|---|--|
| Cubic | $a = b = c$ | $\alpha = \beta = \gamma = 90^\circ$ | <ul style="list-style-type: none"> • Simple • Face Centred • Body Centred |
| Tetragonal | $a = b \neq c$ | $\alpha = \beta = \gamma = 90^\circ$ | <ul style="list-style-type: none"> • Simple • Body Centred |
| Orthorhombic | $a \neq b \neq c$ | $\alpha = \beta = \gamma = 90^\circ$ | <ul style="list-style-type: none"> • Simple • Body Centred • Base Centred • Face Centred |
| Rhombohedral (Trigonal) | $a = b = c$ | $\alpha = \beta = \gamma \neq 90^\circ$ | <ul style="list-style-type: none"> • Simple |
| Hexagonal | $a = b \neq c$ | $\alpha = \beta = 90^\circ$ $\gamma = 120$ | <ul style="list-style-type: none"> • Simple |
| Monoclinic | $a \neq b \neq c$ | $\alpha = \gamma = 90^\circ \neq \beta$ | <ul style="list-style-type: none"> • Simple • Base Centred |
| Triclinic | $a \neq b \neq c$ | $\alpha \neq \beta \neq \gamma \neq 90^\circ$ | <ul style="list-style-type: none"> • Simple |

2.4.2 Crystal Habit

Section 2.4.1, which describes the internal structure of crystals, does not consider the outward physical appearance. This is where the crystal habit becomes useful. The 3D crystalline shapes are described by a type and factors that allow the description of the surface area and volume of the crystal by choosing the characteristic dimension of the crystal observed.

Table 2:2: Crystal Habits and Associated Shape Factors [4].

| Crystal Habit Shape | Volume Shape Factor (α) | Area Shape Factor (β) | β/α |
|---------------------|----------------------------------|-------------------------------|----------------|
| Sphere | 0.524 | 3.142 | 6 |
| Tetrahedron | 0.182 | 2.309 | 12.7 |
| Octahedron | 0.471 | 3.464 | 7.35 |
| Hexagonal Prism | 2.6 | 11.2 | 4.31 |
| Cube | 1 | 6 | 6 |
| Platelet | 0.2 | 2.8 | 14 |
| Needle | 10 | 42 | 4.2 |

The factors (α & β) in Table 2:2 can determine the individual crystals' volume and surface areas using Equation 2:7 and Equation 2:8, respectively, where L is the characteristic length of the crystal in question.

$$V = \alpha L^3$$

Equation 2:7

$$A = \beta L^2$$

Equation 2:8

It is possible for crystals with the same lattice can exhibit different morphologies and vice versa. Multiple factors can impact the crystal habit, such as growth rates, the solvent used, and impurities present.

2.4.3 Polymorphism

Polymorphs exist when a substance can form more than one crystalline form, with polymorphs having different lattice structures. Multiple forms of polymorphism exist, packing and conformational. Packing polymorphs are when rigid molecules that form the

crystal lattice arrange differently. Conformational polymorphs can exist when these molecules are not rigid, as the lattice can be built from the same molecule in different forms. An example is different lattice structures for each of the cis and trans isomers and a third containing a mix of both isomers [12], [13].

The number of polymorphs that exist for substances is not equal, and more are constantly being discovered. However, since some substances are studied more than others, this will influence the number of known polymorphs known for a particular substance. It has been said that the number of known polymorphs depends on the time and effort spent investigating a substance [14].

A commonly studied substance that forms polymorphs is the amino acid glycine. Glycine has three known polymorphic forms (α , β & γ) that can exist at room temperature and pressure. Each of these polymorphs can be produced by changing the conditions from which it is generated. α glycine can be created by dissolution into water and allowing the water to evaporate, γ glycine can be produced using the evaporation method with the addition of sodium chloride. β glycine can be generated using a mixed solvent of water and ethanol. However, any β glycine produced is very short-lived as β quickly transforms to the more stable α polymorph. Given the right humid conditions, α can transform into the more stable again γ form [15].

By no means is there only a single way to produce each polymorph of a crystalline substance, as from more recent work, the γ glycine can be generated from aqueous solutions without the need for other chemical additives by heating the solution near to its boiling point and allowing this to cool down to below ambient temperature in the presence of a magnetic stirrer bar in quiescent conditions, where accompanying experiments performed without the presence of the stirrer bar only a small number of individual samples exhibit nucleation of any kind. Agitation of this solution using the stirrer bar, even at low speeds, produces α form glycine in the vast majority of cases [16].

Metastable polymorphs (such as α glycine) can transform into more stable forms due to a decrease in free energy that occurs with this transformation. Then why do metastable polymorphs form if it is favourable to form a more stable polymorph? Figure 2:3 explains. With the two potential polymorphs that could form, A and B, the formation of the A ($G_A - G_i$) form results in a greater free energy change than the formation of B ($G_B - G_i$). However, the free energy barrier associated with A is greater than B ($G_A^* > G_B^*$). In this case, the B

polymorph would form first, even though this is not thermodynamically the most stable. Given enough time, all the B polymorph present would eventually transform into the A polymorph. The rate at which this would occur would depend on the free energy barrier between the B and A polymorphs, not shown in Figure 2:3 [17].

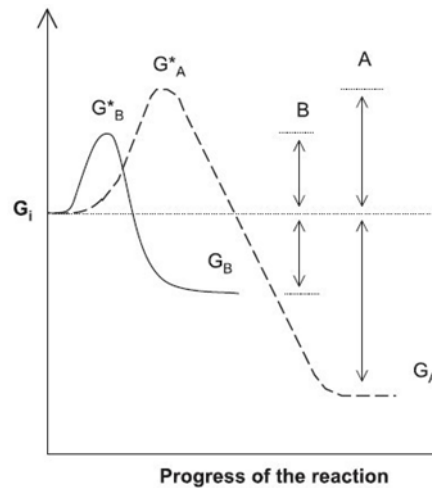


Figure 2:3: Free Energy Barriers in the Formation of Crystal Polymorphs[17]. See accompanying text above for details of description of diagram.

2.5 Nucleation

Nucleation is the first crystallisation stage, where new nuclei are created.

2.5.1 Primary Nucleation

Primary nucleation can be divided into two types based on whether foreign materials are a factor in the nucleation.

2.5.1.1 Homogeneous Nucleation

Homogeneous nucleation is primary nucleation that occurs in the absence and, therefore, free from the influence of third materials.

Classical Nucleation Theory

One model used to explain nucleation is Classical Nucleation Theory (CNT); in a supersaturated solution, it is assumed that the concentration is uniform throughout its volume. However, there will always be statistical fluctuations of the local concentration of solute molecules, and CNT proposes that these fluctuations can lead to the appearance, in more concentrated regions, of ordered collections of molecules, i.e. crystal nuclei [18]. Crystals are assumed to be formed by the serial addition of individual new solute basic units into the crystalline lattice, be those molecules, ions, or atoms [5]. In creating new crystals, the size of these pre-nucleation clusters is critically important in determining their stability.

Once their size reaches a critical point, the nuclei become stable. However, these can dissolve if the nuclei are smaller, as dissolution reduces the cluster size (r) due to the influence of the interfacial tension (σ_{if}), which is favoured as it reduces the Gibbs free energy (ΔG). This free energy change is described by Equation 2:9 if the cluster forming is assumed to be spherical.

$$\Delta G = 4\pi r^2 \sigma_{If} + \frac{4\pi r^3 \Delta G_{VU}}{3}$$

Equation 2:9

Where:

$$\Delta G_{VU} = \frac{\Delta\mu}{V_{Mol}}$$

Equation 2:10

Given:

$\Delta\mu$ Difference in Chemical Potential

V_{Mol} Molar Volume

Once this critical size has been reached, the Gibbs free energy decreases as the crystal continues to grow. This is the case as the size of the cluster increases as the energy change associated with the volume becomes more influential than that of the change in the interfacial area [19], shown in a graphical format in Figure 2:4. The effect of supersaturation on this free energy change helps explain why the nucleation rate is higher at higher supersaturations due to reducing the critical nucleus size with increasing supersaturations. These critical points are shown as stationary points on the blue curves in Figure 2:4, which are shifted to smaller sizes with increasing supersaturation.

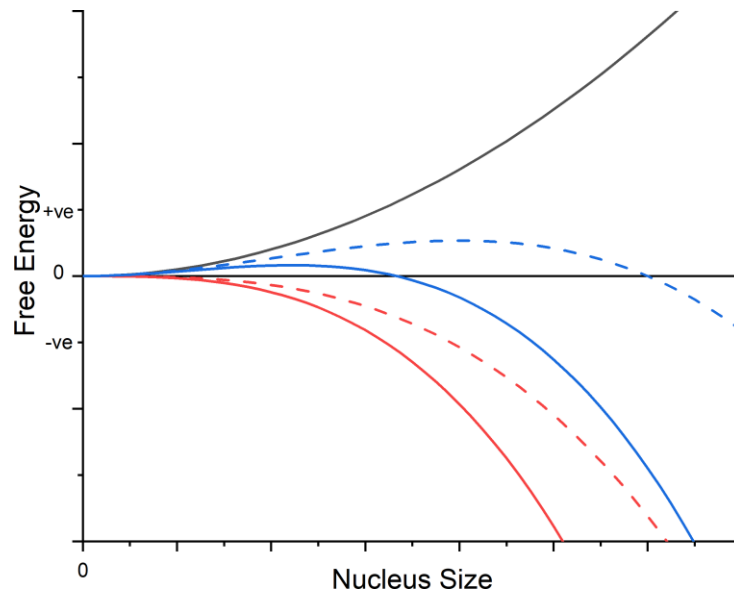


Figure 2:4: Free Energy Change Associated with Spherical Nuclei Formation according to Classical Nucleation Theory. Adapted from [20]. Black; surface excess free energy. Red Solid; volume excess free energy at high supersaturation. Red Dashed; volume excess free energy at low supersaturation. Blue Solid; free energy change at high supersaturation and Blue Dashed; free energy change at low supersaturation.

Two-Step Nucleation Model

Due to the primary nucleation rate predictions of CNT being multiple orders of magnitude higher than physical observations, a new model was sought [8], [21] as this has even been observed in non-solution based crystallisation. This model is supported by the work of *ten Wolde* and *Frenkel*, where the formation of nuclei is a two-stage process is supported by their simulations of homogeneous protein nucleation [22]. Unlike CNT, the crystal does not form directly from the solution but from a pre-existing dense liquid-like cluster [23].

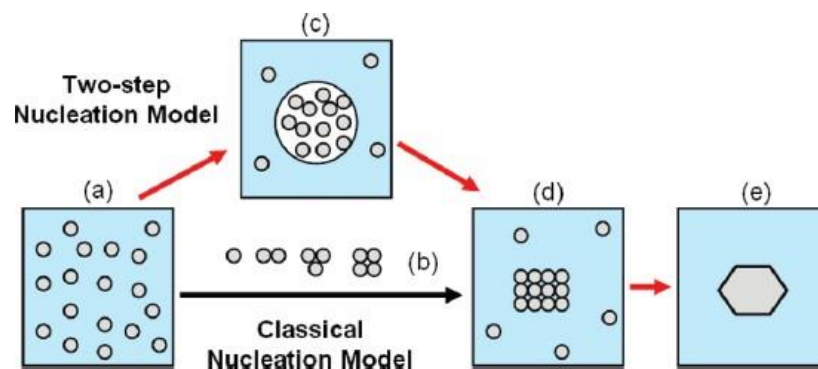


Figure 2:5: Nucleation Model Formation Pathways

Figure 2:5 is a graphical representation of the pathways of the nucleation models described up to this point. In both the CNT and the two-step model, crystals form from semi-ordered clusters. The differences between these theories are based on the source of these nuclei. In

the two-step model, this ordered cluster forms from an already existing “liquid-like cluster” formed from the solute molecules in solution [5].

The free energy barrier associated with the formation of the dense cluster (ΔG_1^*) can be larger than the free energy barrier associated with the formation of the nuclei (ΔG_2^*) as shown in Figure 2:6. The rate of dense cluster formation is faster than the rate at which the dense clusters are transformed into nuclei. This is because the rate-determining step of the whole process is the kinetics involved in forming the nuclei [23], [24]. The dense clusters formed in the first of the two steps can be stable or unstable relative to the original supersaturated solution depending upon the free energy change involved in their formation. In the upper case shown in Figure 2:6, the free energy change is (ΔG_c^0). In this case a decrease in free energy can be achieved by forming a nucleus but also by returning to the non-dense form found in solution. However, in the lower case shown in Figure 2:6, the formation of the dense liquid cluster form is stable relative to the solution as the free energy change involved with this formation (ΔG_{L-L}^0) is negative and the only further decrease in free energy can only be achieved by the formation of a crystal.

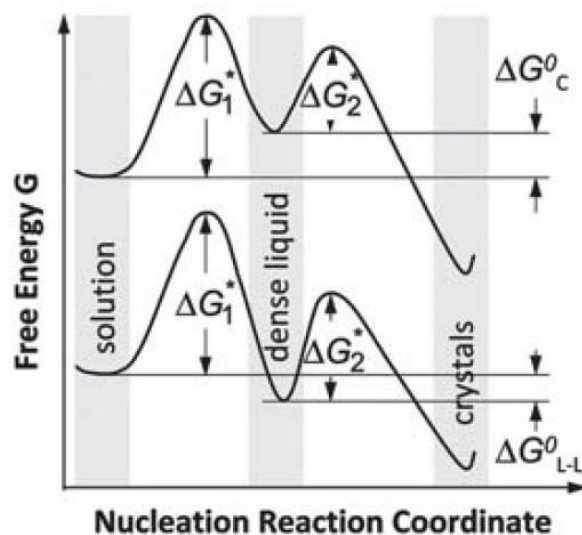


Figure 2:6: Energy Barriers Associated with the Two-Step Model [23]. Detailed description of free energy diagram given in text above.

Alternative Nucleation Models

Although the models discussed in sections 0 and 0 are commonly used to model nucleating systems, they are not all-encompassing. Molecular simulations of nucleating systems (in this case NaCl) of some ionic substances showed similarities with the two-step model as this system was seen to nucleate in “two distinct steps” [25]. However, later simulations have

shown that this does not fit the two-step model completely. The formation of clusters does not require an energy barrier to be overcome, as the ions can be observed to aggregate in solution, modelled as a revised version of CNT, where the magnitude of the energy barrier is reduced depending on the aggregate size [26].

2.5.1.2 Heterogeneous Nucleation

Foreign objects or substances can cause nucleation to occur at greater rates at lower supersaturations than in their absence. Even the surface (e.g., glass vial or the reactor wall) of the object which contains the solution could potentially trigger heterogeneous nucleation. This increase in nucleation is caused by a reduction in the critical free energy, the free energy change observed at the critical nuclei size [3]. This change is given by Equation 2:11.

$$\Delta G'_{crit} = \phi \Delta G_{crit}$$

Equation 2:11

The factor (ϕ) by which this critical free energy is reduced by determined by the wetting angle ($0 \leq \theta \leq 180$), the angle made at the meeting point of all three phases involved, of the liquid phase on the surface of the heterogeneous nucleant from the formula in Equation 2:12.

$$\phi = \frac{1}{4}(2 + \cos\theta)(1 - \cos\theta)^2$$

Equation 2:12

Resulting in a reduction in the free energy barrier associated with nucleation. Therefore, foreign material could be said to be a catalyst for nucleation [3].

2.5.2 Secondary Nucleation

Botsaris defined secondary nucleation in 1976 as nucleation, which only occurs due to the presence of crystals of the material that is being crystallised. If no crystals were present, nucleation would not occur [27]. Secondary nucleation can be further classified; *Myerson and Ginde* presented one classification system that divided secondary nucleation into six mechanisms, shown in Table 2:3. However, it is worth noting that aspects of secondary nucleation are open to interpretation and further investigation to provide more accurate explanations. One aspect open to such speculation is the phenomenon of the secondary nucleation threshold, the level of supersaturation required for secondary nucleation to occur. Previous results have suggested its existence [28], [29]. However, more recent results suggest that this may not exist [30].

Table 2:3: Secondary Nucleation Classification by Myerson and Ginde [4].

| Initial Breeding | Polycrystalline Breeding | Macroabrasion |
|------------------|--------------------------|---------------|
| Dendritic | Fluid Shear | Contact |

However, since no universal system exists, another classification system was developed by *Agrawal and Paterson* for use in industrial crystallisation units [31], based on two overarching mechanism sources, these being mechanical collisions and fluid shear.

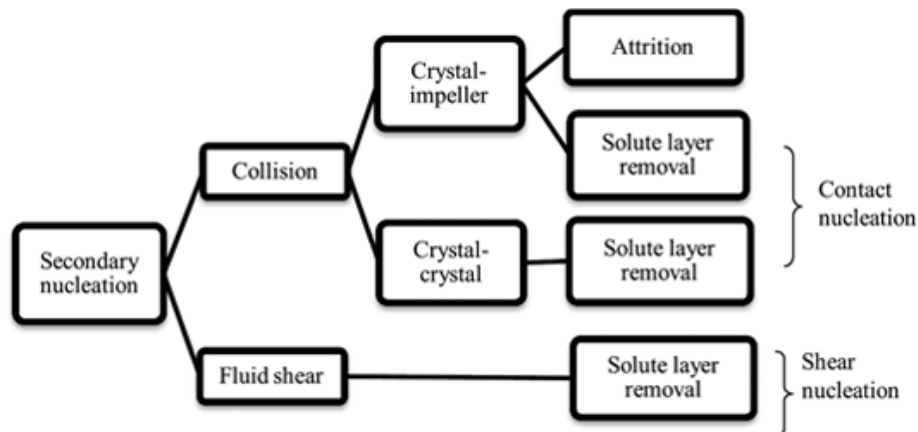


Figure 2:7: Secondary Nucleation Classification by Agrawal and Paterson [31].

Due to the multiple systems that exist classifying individual secondary nucleation mechanisms, some mechanism may be known by multiple names, describing the same or highly similar phenomena.

Molecular simulations of a nucleating system show a mechanism by which a crystal can cause an existing molecular cluster to nucleate once the cluster encounters the crystal. Causing what was the cluster (now a newly formed crystal) to be weakly bonded to the crystal that induced nucleation. These crystals can then be separated, typically from a collision or fluid shear. Allowing that site on the original crystal and the new crystal to “catalyse” further nucleation [32].

Contact with the existing crystal surface is not always required, as multiple clusters can coagulate near its surface. This is possible as the very presence of this crystal attracts clusters through Van der Waals forces. Causing a higher concentration of clusters in the region surrounding the crystal. It is this higher concentration of clusters that leads to their coagulation. Allowing them to grow to a size beyond the critical size, at which point they

become stable. These are then moved to the bulk of the solution through a collision or fluid shear [33], [34].

2.5.2.1 Initial Breeding

Nucleation through initial breeding is caused when small fragments of crystalline material or dust are “washed off” of the surface of the crystal when this is returned to a solution. It is thought that these crystal fragments and/or dust become attached to the main crystal surface during the drying process. When washed off, they can grow in the bulk solution [35], [36].

2.5.2.2 Attrition

Attrition typically occurs within a crystalliser when pre-existing crystals are involved in collisions (with either other crystals or interior parts of the crystalliser) or subjected to fluid shear. Which removes small sections of the crystalline material from the internal structure. As a result, the produced nuclei's size is negligible compared to the crystals from which they are generated [37], [38]. The attrition mechanism is like fragmentation, in that existing parts of the internal structure become the “building blocks” of new crystals. The difference being the relative size of the mother and daughter crystals. See section 2.5.2.5 for an explanation of fragmentation.

2.5.2.3 Polycrystalline Breeding

Growing crystals can sometimes exist in an agglomerated form (where several individual crystal grains are grouped together), where multiple crystals are attached to each other. These aggregates can separate of their own accord and then act as individual crystals. Since this is said to occur during stirring, this can be caused by either a collision or fluid shear [39].

2.5.2.4 Dendritic

Should the supersaturation used for crystallisation be high enough, “dendrite growth,” branch or tree-like growths, appear on the surface of crystals. These growths are broken off from the surface via a collision or mechanical force caused by fluid shear [40], [41]. These would then operate as independent crystals, capable of inducing nucleation independently.

2.5.2.5 Fragmentation

Fragmentation is similar to the case of attrition. However, unlike attrition, when the daughter crystals are small, the crystal is broken into a small number of fragments equal in the order of magnitude in size to the mother crystal [42].

2.5.2.6 Contact

When contact is made between another object and the surface of a crystal, this can cause the further generation of new crystals without generating attrition particles. Testing with γ -glycine crystals being contacted with a rod can cause the generation of α polymorph crystal. Since a less stable polymorph cannot be generated from the existing material of a more stable polymorph, it was thought that the contact with the rod caused disturbances in the boundary surface layer of solute molecules in solution [43]. It is also observed that as the contact force with the surface of the crystal increases, the number of new nuclei generated also rises, up to the point where the contact force is great enough to cause the crystal itself to shatter into multiple independent fragments [44]. Keeping the collision force equal and increasing the supersaturation of the suspending fluid allows for an increasing number of nuclei to be produced from a collision [44], [45]. The similarities between attrition (discussed in section 2.5.2.2) may be the same effect, with fragmentation (section 2.5.2.5) being similar only with forces large enough to break the whole crystal apart [46].

2.6 Measurement of Primary Nucleation

Multiple methods exist for the measurement of primary nucleation rate, the probability per unit time per unit volume of a nucleus being formed from solution. The methods differ in their setup and the conditions that these reflect. This choice of method could depend on what best resembles the configuration in which the nucleation is occurring.

When nucleation studies are performed at small volumes, the observed nucleation process becomes stochastic, allowing primary nucleation rates to be studied [47]. An individual induction time is measured by holding a small volume of solution at a constant supersaturation and measuring the time taken for the solution in the vessel to nucleate since the beginning of the constant supersaturation [48]. This process is repeated many times to provide a statistical estimate of the nucleation rate at the experimental conditions. However, variations can be found between analysis sets, even in large sample sizes (~80). Increasing the number of induction time measurements taken can reduce the width of the probability density function of the nucleation rate [49]. In the *Jiang and ter Horst* model, the proportion of nucleated samples $P(t)$ at time (t) since the beginning of the constant supersaturation is measured, as described by Equation 2:13. Where $M^*(t)$ is the number of nucleated vials a time (t) and M is the total number of vials used for testing.

$$P(t) = \frac{M^*(t)}{M}$$

Equation 2:13

From the points produced by Equation 2:13, a theoretical Poisson distribution model (Equation 2:14) is fitted to determine the primary nucleation rate (J) which has been determined by monitoring multiple individual solution volumes (V). Where a correcting time factor is applied due to the delay between when nucleation occurs and when crystals can be detected; this is termed the growth time (t_g).

$$P(t) = 1 - \exp(-JV(t - t_g))$$

Equation 2:14

Measurements for induction time are typically made via the transmission of light. The formation of crystals causes the solution to become turbid, blocking the transmission of light, possible in crystal-free transparent solutions, allowing the point at which crystals can be detected to be determined. This method would not be able to be used in systems that are not transparent in the absence of crystalline material. An example would be when the impact of added material such as ‘template’ particles on nucleation is studied, if the added material itself interferes with light transmission [50].

2.7 Inducement of Nucleation

Several methods can induce nucleation, some of which expose the crystallising solution to outside phenomena, including electromagnetic radiation and ultrasonic sound waves.

2.7.1 Laser-Induced Nucleation

Pulsed laser light also can induce or enhance nucleation in samples where this would not otherwise be observed. In glycine solutions, this was observed when irradiated with pulsed NIR ($\lambda = 1060$ nm) radiation [51]. This was observed to produce the most stable γ polymorph in most trials, with the metastable α form only being produced in a small percentage of cases. This method required the pulses’ intensity to be relatively high (~ 0.7 GW/cm²). Lower-intensity pulses (~ 0.2 GW/cm²) did not induce nucleation. When this was first discovered, it was required that the samples be aged before being irradiated for the ability of lasers to induce nucleation to be observed. This was believed to be due to the pulses acting upon molecular clusters formed in the ageing process. When non-aged samples were irradiated, nucleation did not occur. However, later work incorporating nanofiltration before the irradiation found that this form of nucleation is partially suppressed, suggesting this is only

part of the effect. Following filtration, irradiated samples were found to have an increased nucleation rate over samples that were only filtered to remove any clusters formed and foreign material. Suggesting the ageing of samples is not a requirement but merely a factor in pulsed laser nucleation inducement [52], [53].

Using NIR radiation wavelengths, continuous lasers can also induce nucleation and influence further crystal growth. This has been observed when the laser beam is highly focused through a high-magnification microscope lens as part of an optical tweezing apparatus. This is discussed in section 3.8.

2.7.2 Sonocrystallisation

Although there is no consensus regarding the mechanism of sonocrystallisation, “the application of ultrasound to the crystallisation process” used to control crystalline product properties, its effects are well documented [54], [55]. Sonocrystallisation is observed to shrink the distance between the metastable zone width and solubility curves as shown in section 2.3.1, reduce induction times observed and produce smaller-sized crystals with a smaller particle size distribution [54], [55].

Sonocrystallisation also can influence the polymorph produced. Altering the sonication length, intensity, or frequency can influence the polymorph [55]. The sonocrystallisation of calcium carbonate is impacted by altering the sonication conditions used as the intensity of sonication increases. With the calcite form being favoured over vaterite when using higher intensities of sonication and for longer sonication times. The sonication frequency also allows for the production of polymorphs that would not be produced in its absence. For example, when paracetamol is crystallised via sonication, the less stable form II is produced, compared with the form I produced when crystallised from solution when stirring [55].

The use of sonication also has an impact on pre-existing crystals including by inducing fragmentation [54], [56]. It is also possible for polycrystalline agglomerate structures to be created and destroyed. These agglomerates are often confused with aggregates which are formed by weak bonds that hold several individual crystals together. Agglomerates are formed from an aggregate that has then been subjected to a period of growth [57]

2.8 Crystallisation in the Presence of Impurities

2.8.1 Template Impacted Crystallisation

Multiple studies have investigated the impact of small solid particulates on crystallisation [58]. For example, one study involved dynamic simulations of hard spheres of different

relative sizes of the 'nucleating' species spheres, which in the simulation were monitored arranging themselves in a fixed regular pattern, and the 'template' sphere, modelling a section of an introduced solid microparticle. When the radius of the template sphere is five times greater than the radius of the nucleating spheres, the free energy barrier associated with nucleation decreased. This reduction in the free energy barrier continued to decrease as the ratio of sizes between the templates and the nucleating spheres increased. In these simulations, it was noted that following the detachment of the nuclei from the template's surface, crystal growth could occur in the direction of the template sphere. This growth could potentially limit that template's ability to act as a catalyst. However, this is unlikely to be the case in any real crystallisation scenario, as a collision would probably cause the separation of the crystal and the template particle [58], [59].

A similar setup was studied using physical microspheres using microscopy. It was noted that the larger the template was compared to the 'nucleating' spheres, the more layers of the nucleating spheres the template was able to support in a crystalline-like structure surrounding the template. When the size ratio of the "template" sphere and the "nucleating" spheres diameter's was 15, the number of layers supportable was on the order of 1. As the ratio reached 38, a small number of layers could be supported. As this ratio reached 1370, the number of layers supportable went beyond the microscopy setup's field of view. This was attributed to the decreasing curvature of the surface that these templates present to the nucleating substance [59].

Studies involving direct crystallisation of tobacco mosaic virus in the presence of polystyrene microspheres found that the virus 'aggregates' growth rate increased with increasing supersaturation. Also, increasing the concentration of polystyrene microspheres found a similar effect that allowed earlier detection of a measurable increase. However, increasing the size of the particles is inconclusive as testing was performed by increasing the size of the spheres while keeping the number concentration equal [60].

However, it is not just the surface area and its curvature that can impact the nucleation characteristics; this surface's roughness can also play a role. Should the surface of a particle deviate from being perfectly smooth, this will further reduce the critical energy barrier that exists for nucleation to occur [61].

It has been argued that template induces nucleation occurs in several stages. First, the new nuclei grow on the template's surface until the crystal reaches a critical size. When this critical

size is reached, the crystal separates from the surface and grows in the bulk solution [62], [63]. Second, the crystal's growth on the surface of the template causes the crystal layers to grow in a curved fashion. Once the crystal reaches a critical size, the elastic force introduced by the curvature of the layers exceeds the adhesive force between the template and the growing crystal. Leading to the separation of the template and crystal, as the elastic force is released when the layers straighten out [64].

It is not just the presence of these particles; interactions involving present surface groups are important. When solutions of calcium sulphate are inoculated with a range of functionalised and non-functionalised silica particles, induction times observed can be altered compared to the non-inoculated samples [65]. Methyl and amino surface groups can reduce the induction times observed. However, some functional groups can act as nucleation inhibitors as the induction time is extended beyond what would be seen in the absence of particles. This inhibition of induction can be seen when the inoculation particles are functionalised with triaminetetraacetic acid. Believed to be caused as these surface groups act as chelating agents capable of trapping the calcium ions present in solution. This is also a concentration-dependent feature as induction time increases proportionally to functional group concentration [65].

The impact can be limited by supersaturation even with these templates' presence. Furthermore, the particles may only have an impact up to a specific supersaturation, where any further increase in template concentration may not have any effect as the induction times observed plateaus in the measurement of nucleation rates[62].

2.8.2 Nucleation and Growth Altered by Additional Components

Surfactants are one series of chemicals that can impact crystallising systems, even at extremely low concentrations. The nucleation rate decreases when the surfactant sodium dodecylbenzene sulfonate (SDBS) is present in a supersaturated solution of vitamin B1 nitrate [66]. A minimum concentration of SDBS must be present for the fall in nucleation rate to occur. At a supersaturation of 2 or 3, little meaningful change in nucleation rate of vitamin B1 nitrate is observed when a concentration of 0.1 mmol l^{-1} of SDBS is used. As the concentration of SDBS is increased beyond 0.1 mmol l^{-1} , the nucleation rate is observed to fall, up to a surfactant concentration of 0.5 mmol l^{-1} . In these cases, since the nucleation rate is measured using the method developed by *Jiang and ter Horst* described in section 2.6,

decreases in nucleation rate were accompanied by increases in growth time. Suggesting the inclusion of this surfactant also partially inhibits crystal growth [66].

However, the presence of surfactants does not always cause a decrease in nucleation rate. For example, adding the surfactant docusate sodium (DOSS) increases the primary nucleation rate when mefenamic acid is crystallised from a 40/60 solvent mixture of dimethylacetamide (DMA) and water [67]. Since this crystallisation was performed from a binary solvent, the proportion of each component of the binary mixture can be altered. When this was performed using a 30/70 solvent mixture, an insignificant effect on the nucleation was observed [67].

From examining these systems, it could be suggested that each system could have a different impact upon adding a surfactant in a sufficient concentration to impact the system. The effect caused by the addition of 'third' chemicals may only be determinable through thorough testing.

The presence of polymers also can affect a nucleating system. For example, polymers can impact the nucleation rate in an aqueous solution of naproxen. This can change upon the polymer added to the system and solution supersaturation [68]. When the polymer PVP was added, an increase in the nucleation rate was observed at all levels of supersaturation tested. However, when a different polymer, HPMC, was added to the solution when $S \lesssim 1.3$, the nucleation rate was higher than in the absence of the polymer. However, when $S \gtrsim 1.3$, the nucleation rate falls below what would be expected in the absence of this polymer [68].

The growth of crystals can also be affected by impurity chemicals. For example, molecular simulations have shown that surfactants can inhibit the growth of crystals by inhibiting the incorporation of new crystal units [67]. These effects can be seen under electron microscopy as the morphology of the crystals is altered by the presence of the surfactant. As the morphology of the mefenamic acid were drastically altered by the presence of the DOSS surfactant [67].

Impurities can also alter the width of the dead zone, the degree of supersaturation required to cause any measurable growth [28]. When low concentrations of potassium ferrocyanide are added to an aqueous sodium chloride solution, increases in the width of the dead zone are shown to increase with the concentration of potassium ferrocyanide. This increase in the dead zone width is two-sided as the magnitude of undersaturation required before the

crystal begins to dissolve also increases. However, the effect on either side of the solubility curve is unequal. The impact on the level of supersaturation required to initiate growth is much higher than the level of undersaturation required to begin the dissolution of the crystal [69].

2.9 Crystal Growth and Dissolution

While solubility is a thermodynamic property, the dissolution of solids into solution is a kinetic property. The rate a solid will dissolve into a solvent depends on a range of factors, including the diffusion coefficient of that solute in that solvent or solvent mixture. The rate at which a solid dissolves into a solution is given by Equation 2:15 [70], [71] where the change in crystal mass over time $\left(\frac{\delta M}{\delta t}\right)$ is determined by not only the concentration (c), the solubility ($c^*(t)$) but also the diffusion coefficient (D), crystal surface area (A) and the thickness of the boundary layer surrounding the crystal (h) as determined by Equation 2:16:

$$\frac{\delta M}{\delta t} = \frac{DA}{h} (c^*(T) - c)$$

Equation 2:15

However, the model described by Equation 2:15 does not acknowledge the existence of the dead zone as Equation 2:15, as this would predict that the mass of crystalline materials would grow or fall in a very slightly super or undersaturated solution, respectively [28], [69].

The thickness of the boundary layer surrounding the dissolving particle depends on the dynamics of the surrounding fluid. The thickness of this diffusion layer is given by Equation 2:16. Which includes dimensionless Reynolds number, used to define the ratio of forces from viscous and inertial components and Schmidt number, used to quantify the ratio of viscosity and diffusivity [74].

From Equation 2:16, it can be deduced that increasing the surrounding fluid's velocity concerning the crystal increases the Reynolds number (Re) and thereby decreases the thickness of this layer (h), increasing the rate at which the solid dissolves. However, this dissolving substance will impact the density and viscosity of the solution [72], where the Schmidt number (Sc) and the characteristic length of the crystal (L) also impact on the thickness of the boundary layer that can be supported.

$$h = \frac{L}{2 + 0.6Re^{0.5}Sc^{0.333}}$$

Equation 2:16

Equation 2:15 can also apply to the growth of crystals if crystal growth is considered the inverse of crystal dissolution by the diffusive theory. Assuming a concentration gradient surrounding any present crystal allowing diffusion to occur from the bulk of the solution to the crystal surface [73]. When dissolution is occurring, this gradient is inverted where the concentration decreases as the distance from the crystal surface increases.

The rate of crystal dissolution can be independent of bulk solute concentration. For example, if the solution is very undersaturated (i.e., $S < 0.15$), then the dissolution rate can be described by Equation 2:17 [74].

$$\frac{\delta M}{\delta t} = \frac{DAc}{h}$$

Equation 2:17

Models developed by *Abegg et al.* allow for the dimension of single crystals to be included into the model describing their growth and dissolution. However, these models are empirical and require that the specific correlation be determined for each solute/solvent system at the tested environmental conditions. The form of the model is given by Equation 2:18 [75]. In this model, the growth rate depends upon the crystal's actual size.

$$r = kS(T)^aL^b$$

Equation 2:18

Where:

- k Growth Rate Constant
- $S(T)$ Supersaturation Ratio
- L Crystal Characteristic Dimension
- a, b Exponential Parameters

However, when in suspension in a solution, the size of particles can influence the solubility these tiny particles experience. This is seen where particles on the scale of attrition particles can be subject to a solubility higher than the thermodynamic solubility. Since this can alter the solubility experienced, this will alter the supersaturation. Therefore, small particles that would typically be expected to grow due to the supersaturated bulk solution could behave

as if suspended in an undersaturated solution and therefore dissolving. The solubility that these particles experience is given by Equation 2:19 [76]–[78].

$$c_{Real}^*(T) = c^*(T) \exp\left(\frac{\Gamma_S}{LRT}\right)$$

Equation 2:19

With attrition particles being produced in collisions involving the crystal and other parts of the suspension or crystalliser, even when the surrounding solution is undersaturated. However, when undersaturated solutions are used, these attrition particles are observed to dissolve [79]. Therefore, even the bulk solution may be supersaturated. Attrition particles could theoretically experience a solubility corresponding to a supersaturation of less than one given a particular bulk concentration, allowing a particle in a supersaturated solution to dissolve. Therefore, increasing the supersaturation would mean that more attrition particles would ‘experience’ a supersaturated solution that would allow these attrition particles to grow in the bulk solution.

3 Optical Tweezing

The late Arthur Ashkin won the 2018 Nobel Prize in Physics “for the optical tweezers and their application to biological systems” [80]. The development of optical tweezers was not a single event but occurred through a series of discoveries and developments over many years.

3.1 Development

The first step in optical tweezers development was in 1970 when *Ashkin* was able to control the position of spherical particles along 2 Cartesian axes on the plane perpendicular to beam propagation. Using a Gaussian beam, which has the brightest point at the centre and decreases in intensity following a Gaussian profile as the radius from the centre of the beam increases. Control was not yet possible in the third axis (the beam path) due to beam induced scattering [81]. This level of control in these circumstances is only possible if the trapped particle acts as a converging lens when the particle has a higher refractive index than its surroundings. If the particle acts as a diverging lens (when the refractive index of the particle is lower than its surrounding material), this will cause the particle to be pushed out of the laser beam. This was checked using air bubbles generated in an 80/20 mixture of glycerol and water. The air bubbles observed were pushed from the centre of the beam while being pushed in the direction of beam propagation [81]. An obvious method to trap a particle in all three Cartesian axes is to use an identical beam propagated opposite to the first, as the scattering forces from each beam would negate each other. Without focusing one beam, any particle that comes into the path of the beam will be propelled by the beam along its path. The ability of a single beam to keep the particle centred is dependent upon the ratio of the refractive indices of the particle and its suspending fluid.

The single laser setup can ‘hold’ a particle in all three axes if the trapping beam is shone from below the particle. This would apply the same gradient force keeping the particle at the centre of the beam at some point along its path. Like previously a scattering force is applied, which in this case is cancelled by the particle’s weight. When this was performed in a vacuum, trapped particles fall to a new equilibrium position compared to trapping performed in a suspending media, indicating that the forces on the system have changed. Since trapped particles are typically only partially absorbing, the top of the sphere is slightly hotter than the bottom, giving rise to a radiometric force operating in the opposite direction to the laser propagation. In non-vacuum cases, the surrounding fluid acts as a coolant, and the magnitude of this radiometric force applied to the trapped object is proportional to the

environmental surrounding the trapped sphere [82], [83]. This setup can study droplet interactions as liquid drops can be supported in gaseous surroundings. Trapped droplets can be struck from above and below by heavier and lighter droplets, respectively [84].

It is possible to induce the trapping along all three Cartesian axes without requiring the weight of the particle to be countered by the beam induced scattering. A resultant force can be applied based upon the conservation of momentum, performed by passing the trapping beam through a highly converging lens before passing through the trapped particle [85]. The lens used in this scenario is a high-magnification microscope lens (x60 or x100) with a high numerical aperture. This is when the wavelength of the trapping laser is smaller than the particle being trapped, discussed in greater detail in section 3.2.1. In the opposite case, where the trapping object is smaller than the wavelength of electromagnetic radiation, this is discussed in section 3.2.2.

3.2 Principles of Operation

The explanation of how the tweezers operate depends on the relative size ratio of the object being trapped and the wavelength of the radiation being used for trapping.

3.2.1 Ray Optics Regime

When Ashkin developed the forerunner of optical tweezers in 1970, this used particle that was larger than the wavelength of the radiation used to trap it ($d_p > \lambda$). Ray optics describe how particles are trapped using pairs of rays passing through the spherical object trapped [81], [86]. A Gaussian beam keeps the particle radially (laterally) stable, where the beam's intensity is highest at the centre and decreases with increasing radius. Should the trapped object drift from the beam's centre, for example when an external net force is applied to the trapped particle, the trapping beam's refraction creates a restoring force that returns the particle to the centre of the beam. This force is generated as the refraction generates the axial momentum of the photons. An example of this is shown in Figure 3:1.

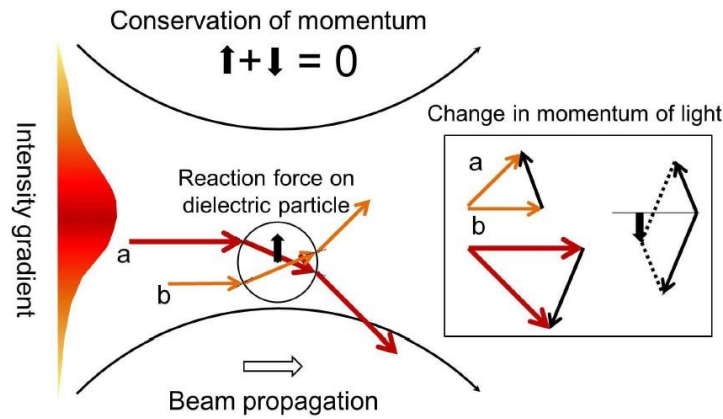


Figure 3:1: Radial Stability Example [87]

In the example shown in Figure 3:1, the particle has drifted out of the centre of the beam by falling below the region of the highest beam intensity. In this scenario, ray “a” is refracted down, and ray “b” is refracted up; however, these rays are not equally intense.

Since the “a” ray comes from nearer the beam’s centre, this ray would have a higher intensity consisting of more photons. Resulting in a net change of radial (lateral) force down on the photons. To obey the conservation of momentum, a net upward momentum must also be created, on the trapped particle. Thus, causing the particle to move up back to the centre of the beam reducing the restoring force applied to the trapped object. This would continue until the net force applied to the sphere is zero, returning the trapped particle to the trap's centre. However, this would still result in the particle being pushed along the centre of the beam.

While a Gaussian beam alone only allows trapping in two Cartesian axes since scattering causes the trapped object to be propelled in the direction of beam propagation, unless countered by another force, e.g., gravity. However, this can be countered by highly focusing the beam before being refracted by the trapped particle. How this highly focused beam interacts with a trapped particle is shown in Figure 3:2.

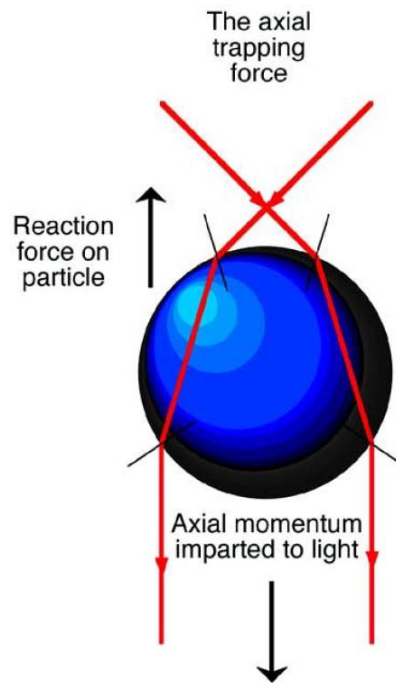


Figure 3:2: Axial Stability Example [86]

In the direction of beam propagation, the axial momentum of the photons is altered by the refraction caused by the trapping particle. The refraction causes the axial momentum of the photons to increase in the beam propagation direction. Like the stability in the radial or lateral axes, the principle of the conservation of momentum must be obeyed, resulting in a net momentum in the direction opposite beam propagation which must be imparted to the trapped particle [85], [86]. The imparted momentum opposes the scattering force generated by the absorption of a small quantity of the photons imparted to the trapped object.

When used in combination, stability in all three Cartesian axes is gained, and the position of the trapped particle can be controlled. Simple equations can be used to quantify the forces applied to the particle by the trap shown in Equation 3:1 [88]–[90]. Using only the refractive index of the suspending medium (n), the speed of light (c), beam power (P) and the trapping efficiency (Q_i), which typically has a value between 0.03 and 0.1 [86]

$$F_i = \frac{nQ_iP}{c}$$

Equation 3:1

Since it is possible for a set of tweezers to have a differing trapping efficiency (allowing the trap to be stronger in one axis than another) in each of the three Cartesian axes (this could be due to a misaligned beam, alteration of the beam profile or if the beam is linearly

polarised), and in each of these three axes, the trapping efficiency can change depending upon the particle's position regarding the equilibrium point of the trapped object [91].

3.2.2 Rayleigh Regime

Unlike the ray optics regime in section 3.2.1, interaction between an object whose size is smaller than the wavelength of electromagnetic radiation that it interacts with ($d_p < \lambda$) [86] is governed by Rayleigh scattering. When operating in the Rayleigh regime the ray optics explanations are no longer suitable due to the differences in scattering that are observed when the relative dimension of the scattering object and wavelength of radiation that is being scattered change. Therefore, the electric field surrounding the trapped particle should be considered for the calculation of the component forces, the first of which is scattering. This propels the particle in the direction of beam propagation. The scattering force can be determined analytically in Equation 3:2 using the beam intensity (I_0), speed of light (c), particle radius (r), beam wavelength (λ), refractive indices ratio ($N = \frac{n_{particle}}{n}$) and the refractive index of the suspending medium (n) [86].

$$F_{Sc} = \frac{I}{c} \frac{128 \pi^5 r^6}{3 \lambda^4} \frac{(N^2 - 1)}{(N^2 + 2)} n$$

Equation 3:2

The gradient force which returns the particle to the equilibrium point can also be determined analytically in Equation 3:3 [86], [92], which requires the addition of the electric field density (E).

$$F_{Gr} = -\frac{n^3 r^3}{2} \frac{N^2 - 1}{N^2 + 2} \nabla |E|^2$$

Equation 3:3

To trap an object, the gradient force applied to a particle must be greater than the scattering force ($F_{Gr} > F_{Sc}$). Since both the scattering force and the gradient force scale linearly with beam power, simply increasing the beam power will not allow a particle to be trapped that cannot be trapped at low power. To achieve trapping in these circumstances, the beam's focusing must be altered, by using a trapping objective lens with a higher numerical aperture (which commonly utilise oil immersion). However, since this is standard practice in the operation of optical tweezers this is unlikely to pose any issues [86].

3.3 Making Measurements

One of the major uses of optical tweezers are for the measurement of force at the microscale. Before forces can be quantified, the instantaneous displacement from the equilibrium position in each axis must be determined. From this measurement of the distance in each axis component parts of the overall force applied to a particle can be determined.

3.3.1 Position Calibration and Determination

Quadrant diodes can be used to determine the trapped object's position from the trap's centre. Each quadrant of the diode produces a voltage based upon the forward scattering (in this case, as backscattering can also be used) of the trapping beam which strikes each section of the diode. These individual voltages can then be combined and compared to determine the displacement from the trap's centre. One calibration method requires that a 'stuck' particle be moved across each axis in the radial (lateral) plane formed by x and y axes indicated in Figure 3:3.

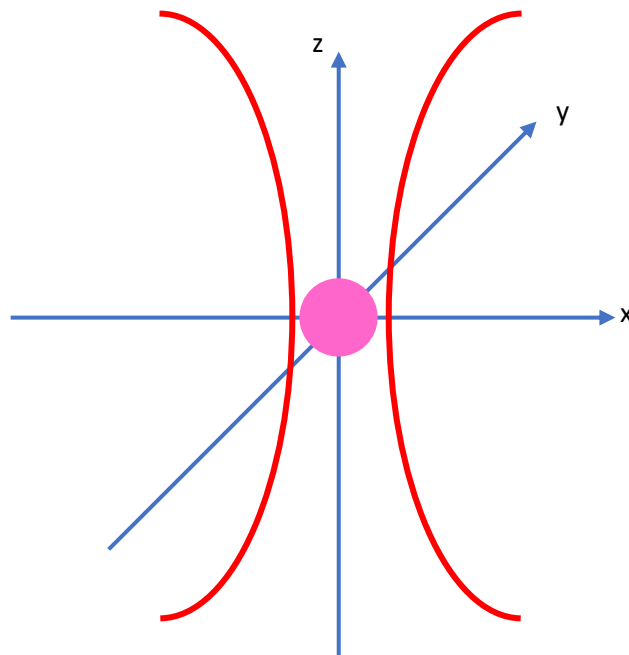


Figure 3:3: Coordinate system typically employed in particle trapping. Showing the Cartesian axes (Blue Arrows), Tweezing Beam (Red Hyperbola) which follows the path of the z-axis and the trapped particle (Magenta Circle) located at the origin.

From this movement the pairwise voltage difference signal produced recorded as the particle is moved through the path of the beam [93], [94]. A region in this trace will form an S-curve that will have a linear region in its centre. The gradient of this linear portion can be used to convert the voltage signal into a displacement [95]. An alternative method allows the position to be determined through secondary analysis of the power spectral density method of force

calibration, this is discussed in detail in section 3.3.2.2. Using the low frequency plateau value of this spectrum (S_0) and the determined corner frequency used to determine the strength of a particular trapping setup (f_0) also written as (f_c), which is the force required per unit distance of the displacement of a trapped bead, shown in Figure 3:4 alongside the temperature (T), Boltzmann's constant (k_B), fluid viscosity (η) and trapped particle radius (r) the position calibration value can be determined by Equation 3:4 allowing the distance voltage conversion factor (δ) to be determined which is used to convert the pair wise sum voltage output from the quadrant photodiode to the displacement experienced by the trapped bead.

$$\delta = \sqrt{\frac{k_B T}{6\pi^3 \eta r S_0 f_0}}$$

Equation 3:4

3.3.2 Force Calibration

Numerous methods exist to calibrate the optical tweezers that allow forces involving the trapped particle to be measured. In addition, methods can be employed simultaneously to check one another to ensure accurate and precise force measurements.

3.3.2.1 Equipartition Method

Since the trapping of particles typically occurs in a medium; causes the particle's motion to be dampened. In any medium, the trapped particle will fluctuate around the focus of the tweezer from the thermal energy of the movement of the medium's molecules. Observations of the trapped particle over a period allow the trap's strength to be determined. The variance particle's position ($\langle x_i \rangle$) in a radial axis allows the trap stiffness (the force required per unit distance to cause the displacement of a particle from its equilibrium position (k_i)) in that axis (indicated by the subscript i) to be determined by Equation 3:5 [96], [97].

$$\frac{1}{2} k_B T = \frac{1}{2} k_i \langle x_i \rangle^2$$

Equation 3:5

Since this method is independent of viscous force measurements, fewer system parameters, such as the fluid viscosity or the distance to the nearest surface, need to be known. The side effect is that since less is required to be known, this also provides fewer outputs, such as the dampening characteristics [93]. However, it is required to track the position of the particles over a period. The more frequently and precisely this can be measured, the more accurate

representation of the trap [94]. However, this method is limited because it is only genuinely applicable when trapping spherical particles due to the dynamics involved [91].

3.3.2.2 Power Spectral Density Method

The power spectral density method is an alternative and one of the most common methods used for determining the trap's stiffness. Where trapped particles are examined, their motion can be described as dampened. Modelled by Equation 3:6 [93], [98] where the speed of the particle (\dot{x}) is also included in the determination of the applied force.

$$k_i x_i + \beta \dot{x} = F$$

Equation 3:6

Where β in Equation 3:6 can be described by Equation 3:7.

$$\beta = 6\pi\eta r$$

Equation 3:7

This allows the variation in the position of the trapped particles to be tracked. In this case, the Lorentzian power spectrum of the pairwise voltage, an example of which is shown in Figure 3:4, observed is fitted to determine the roll-off frequency, also known as the corner frequency, as shown by Equation 3:8.

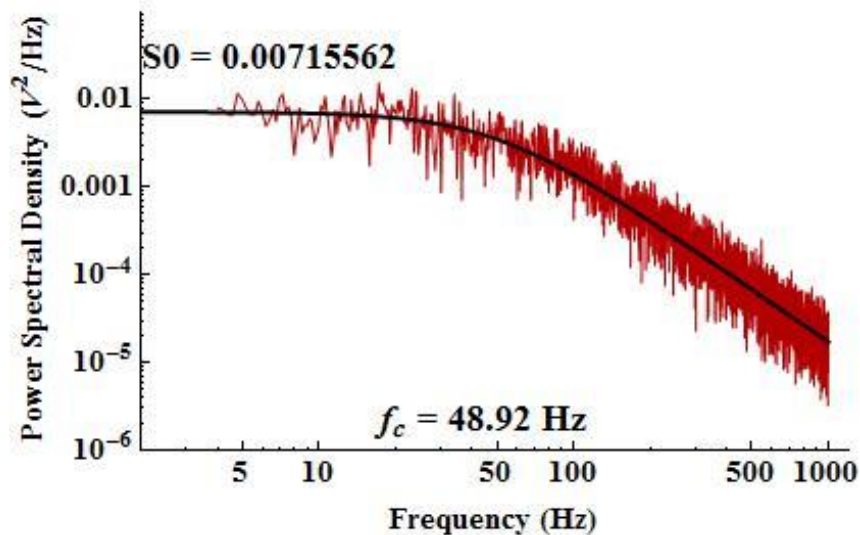


Figure 3:4: Example Power spectral Density graph. Computed PSD of pairwise voltage signal (Red), fitting of Equation 3:8 (Black). Spectrum produced by trapping a 3 micron diameter polystyrene bead [99]. Low frequency plateau value also indicated. f_c can also be written as f_0 .

$$s(f) = \frac{k_B T}{\pi^2 \beta (f^2 + f_0^2)}$$

Equation 3:8

The roll-off frequency determination determines the trap's stiffness in each axis in Equation 3:9. However, this requires that the fluid's viscosity and the size of the trapped particle be known. These are not required by the equipartition method described in section 3.3.2.1 [100].

$$k_i = 2\pi f_0 \beta$$

Equation 3:9

Depending upon the proximity of the trapped particle to a surface, this can mean that the β factor used in the calibration of the tweezers be altered to use Equation 3:10 in place of Equation 3:7 [101].

$$\beta = \frac{6\pi\eta r}{1 - \frac{9r}{8h} + \frac{1}{2} \left(\frac{r}{h}\right)^3 - \frac{57}{100} \left(\frac{r}{h}\right)^4 + \frac{1}{5} \left(\frac{r}{h}\right)^5 + \frac{7}{200} \left(\frac{r}{h}\right)^{11} - \frac{1}{25} \left(\frac{r}{h}\right)^{12}}$$

Equation 3:10

Once the $\frac{h}{r}$ ratio (the ratio of the distance from the centre of the trapped sphere to the flat surface (h) and the sphere's radius(r)) exceeds ~ 3 , the impact of the surface is small. Therefore, when this distance criterion is true this factor can be neglected, allowing the standard beta to be used, shown in Equation 3:9 [94], [102].

It is also possible for a particle to be subjected to movement from an outside source, typically the stage, in a known fashion. This sine or triangular wave movement provides a way to more directly measure the stiffness of forces applied to the trapped particle and, therefore, the trap [93].

3.3.3 Applicability of Hooke's Law

Once the stiffness of the trap has been determined, the net force applied to the trapped particle can be measured. The force applied to a particle causes a specific displacement from the equilibrium position in the linear response region. This can be likened to the movement of a spring, which is described using Hooke's Law shown in Equation 3:11 [97].

$$F_i = k_i x_i$$

Equation 3:11

The stiffness is dependent on the exact tweezing setup used, i.e., different particle material sizes and materials, laser power and the numerical aperture of the focusing objective, ideally the stiffness of the trap should be independent from the direction in which it is measured. When the stiffness of each axis is significantly different from the others, this can be a sign of issues with the tweezers, such as the beam diverging from the expected Gaussian profile.

3.4 Laser-Induced Heating

Shortly following the use of optical tweezers it was noticed that their use can cause the temperature in the region surrounding the focus to rise [103]. Heating can impact the trapping conditions as one key factor that is temperature dependent is viscosity of the suspension material. In majority of cases these changes are ignored in simple analysis. Many crystallisation processes are very temperature sensitive and therefore if the use of the tweezers will cause the local temperature to rise, if it cannot be avoided then at least the magnitude must be known.

3.4.1 Heating Models

Controlling the temperature of the sample being tweezed has also been the focus of research. Heating is relatively simple, performed using the tweezers themselves by examining the solvent's absorption spectrum and selecting a laser wavelength with a relatively high absorption coefficient. This could be the trapping laser, and the heating is a secondary effect. Alternatively, a second laser could be used for this purpose. It has been possible to fit each objective lens of a tweezing system with a hollow copper plate within which chilled water can be circulated to remove excess heat introduced by the trap if this is unwanted [104]. These setups are typically very confined. How practical this would be in a wide range of setups is still to be seen.

Multiple models exist for the localised heating induced by the focus of the tweezers. However, there are similarities between these models. Some depend on knowing at which distance radially from the centre of the trap the temperature can be considered to be ambient [104]. Another model devised by *Peterman et al.* uses the distance axially (z-axis in Figure 3:3) from the nearest surface and its temperature to determine the temperature rise at the focus of the tweezers [105]. This is given by Equation 3:12 this requires a number of factors about the trap (the wavelength of the trapping beam (λ_{Trap}) and the axial distance from the surface acting as the heatsink (D)) and the medium (the absorption coefficient at

the wavelength of the trapping laser ($\alpha_{abs}(\lambda_{Trap})$) and its thermal conductivity (K) in which it is operating.

$$\Delta T_B = \frac{\alpha_{abs}(\lambda_{Trap})}{2\pi K} \left(\ln \left(\frac{2\pi Z}{\lambda_{Trap}} \right) - 1 \right)$$

Equation 3:12

This model has been used to predict the temperature rise caused by the focus of the tweezers, performed by taking the distance between the trap's focus and the inner surface of the coverslip. However, the presence of a trapped particle can affect the expected temperature rise. Since the trapped particle, with a radius (r_p) is at the focus of a tweezer, where the highest irradiance is located, this is almost certain to have a different absorption coefficient and thermal conductivity than the suspending fluid. To account for any potential difference, a correcting factor must be applied, as seen in Equation 3:13.

$$\Delta T_P = \Delta \left(\frac{\alpha_{abs}}{2\pi K} \right) \left(\frac{\ln \left(\left(\frac{2\pi r_p}{\lambda_{Trap}} \right)^2 + 1 \right)}{2} \right)$$

Equation 3:13

Where:

$$\Delta \left(\frac{\alpha_{abs}}{2\pi K} \right) = \frac{\alpha_{absSolvent}}{2\pi K_{Solvent}} - \frac{\alpha_{absParticle}}{2\pi K_{Particle}}$$

Therefore, the temperature rise experienced when a trapped particle is held within a trap would be determined by Equation 3:14.

$$\Delta T_O = \Delta T_B + \Delta T_P$$

Equation 3:14

The models discussed here are just some of those which have previously been developed, and others developed by Walton [106] and Catala [107] do exist and have been used and do not appear to directly correct for the presence of a trapped particle.

3.4.2 Solvent Choice Considerations

Solvent choice can significantly impact the localised heating induced by the tweezers and the wavelength of the laser chosen for the same solvent using a different laser wavelength.

Altering the proportion of laser light that the solvent would absorb. This, in turn, would alter the temperature rise experienced by the solvent at the focus of the tweezers. This is a significant factor for the reported use of D₂O in a vast majority of studies which investigate nucleation induced by optical tweezers, discussed in detail in section 3.8. Measurement of the temperature at the focus of the tweezers using the implementation of Raman spectroscopy, by introducing a second probe laser to examine the shift observed, at the focus of the tweezers when monitoring the intensity ratio of Stokes-Anti-Stokes scattering [108], [109].

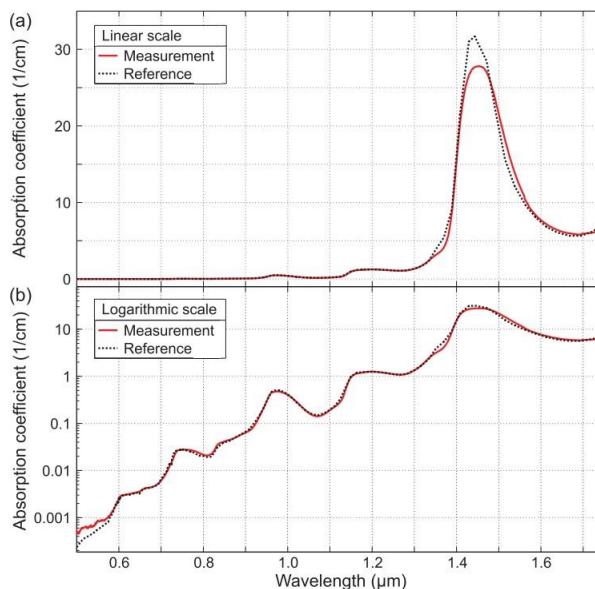


Figure 3:5: Absorption Spectrum of Water in the visible and NIR regions [110].

Figure 3:5 shows that water will absorb this in differing proportions for differing wavelengths of electromagnetic radiation over a fixed length of a medium. Using a laser in the visible region of the EM spectrum would minimise any temperature rise. However, altering the wavelength of the laser used, especially in an optical tweezing setup, can be non-trivial. This may require changing many other expensive optical components, such as beam splitters and other dichroic elements, and replacing the laser source.

The absorption coefficient can also be determined from the complex part of the refractive index using Equation 3:15. This complex part of the refractive index is the extinction coefficient [111].

$$\alpha_{abs} = \frac{4\pi n_i}{\lambda}$$

Equation 3:15

However, other factors must be considered. Even though using a 975 nm wavelength laser in decaline effectively generates no heating in proximity to the trap, other factors must be considered. Typical objects that are trapped, in aqueous suspensions, silica and polystyrene spheres, a highly common test system. The refractive index of decaline is higher than either of these two materials. Therefore, these substances would be pushed out of the trapping beam. Furthermore, the particles used must not be soluble in the liquid used. Highlighting the issue that it is possible for crystallisation experiments involving optical tweezers to have multiple, sometimes opposing constraints.

3.5 Correction for Non-Isothermal Surroundings

Due to laser-induced heating, the fluid surrounding the trapped particle is likely to no longer be isothermal. This lack of isothermal surroundings complicates thermal motion of some particles that have been studied. The surroundings are assumed to be isothermal. It requires that this be, at least, considered to accurately describe the forces to which a trapped particle is subjected. Non-isothermal surroundings can be accounted for using “Hot Brownian Motion,” which attributes a single temperature and viscosity that would have the same effect as the non-isothermal system. These are known as the Hot Brownian Motion Temperature and Viscosity [112], [113]. Assuming that the localised temperature rise is less than the starting temperature, a simplified equation can determine the Hot Brownian Motion Temperature shown in Equation 3:16. The HBM viscosity is determined by Equation 3:17 [114].

$$\frac{T_{HBM}}{T_0} = 1 + \frac{\Delta T}{2T_0} + \left(\ln \left(\frac{\eta_0}{\eta_\infty} \right) - 1 \right) \left(\frac{(\Delta T)^2}{24T_0^2} \right)$$

Equation 3:16

$$\frac{\eta_0}{\eta_{HBM}} = \frac{e^{\frac{A}{T^*}}}{\Delta T} \left(A \left(Ei \left(\frac{A}{T^* + \Delta T} \right) - Ei \left(-\frac{A}{T^*} \right) \right) + (T^* + \Delta T) e^{-\frac{A}{T^* + \Delta T}} \right) - \frac{T^*}{\Delta T}$$

Equation 3:17

Specific constants for Equation 3:16 and Equation 3:17 depend on the solvents used for deuterium oxide. The Vogel-Fulcher-Tammann constants are shown in Table 3:1. Where:

T_{HBM} Hot Brownian Motion Temperature

T^* $T - T_{VF}$

T_0 Ambient Temperature

| | |
|---------------|-------------------------------------|
| ΔT | Induced Temperature Rise |
| T_{VF} | Vogel–Fulcher–Tammann Law Parameter |
| η_{HBM} | Hot Brownian Motion Viscosity |
| η_0 | Ambient Viscosity |
| η_∞ | Vogel–Fulcher–Tammann Law Parameter |
| A | Vogel–Fulcher–Tammann Law Parameter |

Table 3:1: Vogel–Fulcher–Tammann Parameters for Deuterium Oxide. Calculated from NIST (National Institute of Standards and Technology) Webbook [115].

| | |
|---------------|----------------------------|
| A | 406.9 K |
| T_{VF} | 171.1 K |
| η_∞ | 4.46×10^{-5} Pa s |

Typically, these models are also supplied with a method for determining the variation in temperature with increasing distance from the particle's surface. However, these were created assuming that the trapped particle would have higher absorption than the surrounding medium. Since the typical case is seen with trapped silica or polystyrene, the reverse is true where these models to determine the temperature profile surrounding the particle have been discounted.

Elementary calculations have shown that potential impacts would be negligible and therefore do not require further consideration. A summary of the final outcomes is shown in Appendix I.

3.6 Alternative Traps

Multiple optical traps can be used in proximity to each other. An obvious method uses multiple sets of optical trapping apparatus near each other. However, more novel methods can allow a single beam source to generate multiple traps [116]. It is also possible to use a light beam to indirectly trap particles, as in the case of optoelectronic tweezers.

3.6.1 Time-Sharing Traps

Trapping multiple objects using a single focus is achievable by moving the focus quickly between them. However, the trapped objects impose a limit on the system to return to a specific object before it has drifted too far from its original position, requiring the trap to

cycle continuously through all the trapped objects. This system has the limitation that all trapped objects are located on the same radial (lateral) plane. The trap can be redirected using mirrors controlled using galvanometers or piezo motors. The smaller the trapped particles are the more frequently the trap would be required to 'visit' the particle. The frequency of visitation required can be limited by the setup used. Much higher frequencies can be achieved by using acousto-optic or electro-optic deflection. However, as the switching frequency increases, this also increases the trap location's resolution as much smaller movements are possible. Therefore, should multiple traps be required, the requirements of the situation will determine what methods could be used [92], [117]. Therefore, there is no solution which can be employed which would be suitable for every possible situation.

3.6.2 Beam Splitting Traps

As can be ascertained from the time-splitting traps (section 3.6.1), the ability to trap multiple objects without the limitations of the time-sharing traps would be beneficial. This is what holographic optical tweezers accomplish. Allowing multiple optical traps to be generated simultaneously. A spatial light modulator allows patterns of individual traps to be generated in arbitrary patterns, modified through time [118]. Another benefit of beam-splitting traps is that the patterns generated are not limited to the same radial (lateral) plane as 3D patterns can be accomplished. This method can generate a 3D path through which particles can travel. Multiple particles can traverse this path simultaneously, with each particle at a different point in the path [119].

3.6.3 Optoelectronic Tweezers

More recent advancements in microparticle tweezers were the development of optoelectronic tweezers. Using a chamber surrounded by hydrogenated silicon and indium tin oxide layers, an alternating current is applied. In this system, light is applied to the layer of silicon. However, this does not have the same intensity requirements as optical tweezing. Instead of using an optical force, these optoelectronic tweezers utilise a non-uniform electric field to act on a dielectric particle [120], [121]. Like tweezers, forces applied to trapped particles can be measured by observing the displacement between the particle and a plate section boundary between the silicon and indium tin oxide [121]. This form of tweezing has been used in situations where the impact of heating in tweezers must be avoided at any cost, such as the manipulation and separation of living cells and dead cells, since living cells can maintain a difference in ion concentration from their surroundings resulting in a difference in conductivity [122]. The use of optoelectronic tweezers would have the benefit of

eliminating the heating effects of the tweezing apparatus. However, examining the setup required, the indium tin oxide layers are spaced between 15 μm and 150 μm apart. This spacing poses practical limitations on the apparatus used; therefore, mounting a crystal would be impracticable without causing damage to the crystal itself [121], [123]. Also requires specifically designed and created microcells created using hydrogen-doped amorphous silicon and indium tin oxide [123]. A diagram of an optoelectronic tweezer's setup required being used to manipulate biological cells is shown in Figure 3:6

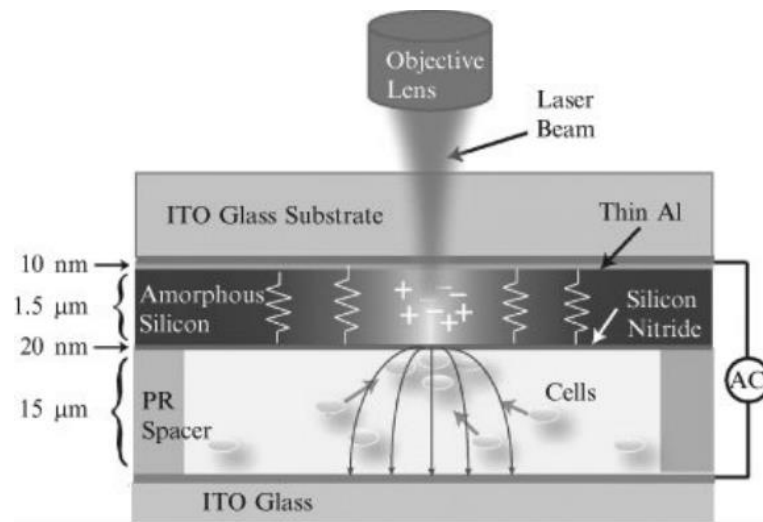


Figure 3:6: Setup required to operate optoelectronic tweezers [121].

3.7 Alternative Uses of Optical Tweezers

Optical tweezers have been extensively used in a range of other fields. However, these have been exploited extensively in investigating biological systems, down to the scale of single cells, leading to a wide range of studies investigating biological systems. An example is the studies performed on haematids (red blood cells). These have used forces directly applied by the tweezers and trappable particles. By using optical tweezers, the mechanical properties of red blood cells can be determined. This can be of use as some medical conditions cause alterations to the mechanical properties of red blood cells of effected individual's haematids, allowing optical tweezing to be used as a diagnostic tool. Optical tweezers have also been used to investigate the side effects of common medications, as the drug Atorvastatin, used to lower cholesterol, has been observed to "soften" the cell membrane of red blood cells [91].

Optical tweezers also allow for the holding and manipulation of micromachines. In one case, a basic pump was created and controlled when two spherical birefringent particles were held

on either side of a narrow channel [124], [125]. These particles can be rotated as the circularly polarised light possesses angular momentum, transferred to the trapped particles [124]–[126]. By altering the trapping power of the laser used, the rotation frequency of the trapped particles could be altered. The flowrate of the “pump” was monitored using a tracer particle. Where the speed at which the tracer moved through the channel was linearly proportional to the frequency of trapped particles’ rotation.

3.8 Optical Tweezing and Crystallisation

Using optical tweezers, the nucleation and growth of substances can be impacted to induce this to occur in places that can be controlled.

3.8.1 Optical Tweezing-Induced Nucleation

In a similar fashion to pulsed laser-induced nucleation (section 2.7.1), the original work which discovered nucleation induced by optical tweezers required the solutions used to be aged [127], [128].

3.8.1.1 *Theory and Proposed Mechanism*

The mechanism by which tweezers can induce nucleation from solution is still a matter of active debate. However, there are several hypotheses which currently exist. One major proposal suggests that the tweezing focus can “gather” solute material clusters from the solution’s bulk. When the focus is located at the air solution interface, this alters the relationship between the two forces applied to a trapped object by the tweezing focus. In that, the scattering force, which typically pushes objects out of the focus, acts to push objects towards the interface, from which there is nowhere else to go. The gradient force still acts the same attracting objects radially around the tweezing beam. In this scenario, the two forces that usually work against each other are working together [129]. A diagram of this scenario is shown in Figure 3:7. This factor of accelerating particles towards the interface was used in cases where the numerical aperture was not strong enough to generate the gradient force.

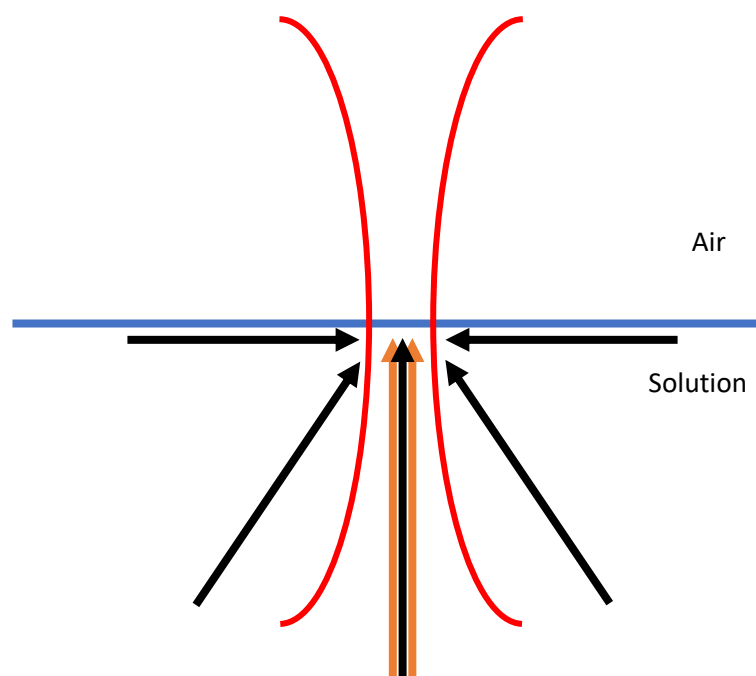


Figure 3:7: Schematic diagram of the forces operating at flat solution interface. Solution air interface (Blue), tweezing beam focus (Red Hyperbola), Gradient force direction (Black Arrows) and Scattering force direction (Orange Arrows). The gradient force would operate rotationally around the axis of the beam, this cannot be shown in this 2D diagram, this would have the effect of drawing objects into the plane shown from in front and behind the plane of this diagram..

The ability of molecular clusters, small numbers of molecules which are in proximity and exhibit a localised degree of structuring/order[18], to be trapped has been a point of debate, mainly with regards over whether the net trapping force supplied by the tweezers would be sufficient to overcome Brownian motion [130]. But it has been observed optical tweezing can suppress the Brownian motion experienced by low-mass molecules, as observed using fluorescent dyes [131], [132].

Nevertheless, this has been rebutted by Liao et al. has been countered by the suggestion that any forces from laser-induced heating would be much greater than any trapping forces [130]. This heating has commonly been minimised using D₂O in many cases. However, the trapping of even single atoms has been observed (rubidium) to act as a quantum qubit [133]. Therefore, the magnitude that these effects (trapping forces and increased thermal motion) would have compared with each other would be critical in determining the ability to trap a particle.

Calculations show that it would be possible to attract clusters to the centre of the focus at distances orders of magnitude greater than their own size dimension [18] [134].

Other observations have shown that it is possible to separate the components of a binary mixture where these two components have a difference in refractive index when operating in proximity to specific points in the phase diagram, where the depletion of one component following the cooling, after the deactivation of the tweezers. Since the diffusion of mass is approximately three orders of magnitude slower than the diffusion of heat, this allows the phase to become metastable. This effect can be directly observed when fluorescence microscopy shows a region of enhanced concentration of a single component compared to the rest of the mixture surrounding the focus of the tweezers [135]. The 'collecting' of polymer molecules could be measured using a second laser integrated into the optical setup whose high-angle backscattering was measured. From this, the signal increased as the trapping laser was active [136]. With more recent work showing that concentration of fluorescence tagged lysozyme is concentrated at and surrounding the focus as irradiation time increased as measured by an increase in fluorescence in the region surrounding the focus of the optical tweezers, giving further weight to the idea that optical tweezers are able to selectively concentrate a component of a mixture around the focus [137]. With the concentration enhancement surrounding the focus occurring more rapidly with increasing laser power and bulk solution concentration.

The significant mechanisms discussed so far, in essence, work on the same principle that the tweezing focus can selectively gather one component of the solution or mixture based on the difference in the refractive index between the components.

A completely different hypothesis exists where it has been posited that optical tweezers are only capable of acting upon already existing relatively large amorphous solute molecular clusters, which was determined to be the case through measurement of the Raman spectra produced in situ from the object seen entering the focus, as the Raman spectrometer was integrated into the tweezing optics [108]. Following a period trapped by the focus, this amorphous cluster is observed to become crystalline through the change of the spectra observed, where the amorphous glycine cluster is determined to be transformed into either the α or γ polymorph [108] which are observed to grow in the solution.

One other hypothesis is that the use of the optical tweezers requires the addition of an additional term ($-I_0n^2$), where I_0 is the laser intensity and n is the refractive index, to the free energy equation, which if assumed to be determined by CNT would be adding the term ($-I_0n^2$) to Equation 2:9, this would further reduce the system's free energy, increasing the

favourability of the crystalline state [138]. This has the additional advantage in that this does not require interactions or even the presence of molecular clusters, which is a point of debate and would be a universally applicable factor [129], [130].

3.8.1.2 Experimental Observations

When the focus of an optical trap is positioned on the air-solution interface, nucleation is observed. In contrast, when the trap's focus is elsewhere on the solution, nucleation is not observed to occur, including at the solution-container interface [139]. At the solution-container interface, the trap's activation leads to a small region of increased concentration. This region will continue to be present, provided the tweezers remain activated. This "bead" of higher concentration can be made to crystallise instantaneously if the bead is then moved to the solution-air interface [140], suggesting that operating at or in-close proximity to the interface is key. The hypothesis is that the tweezers can generate a region of increased supersaturation because nucleation can be induced to occur in undersaturated solutions [141]. This hypothesis is supported by measurements of the increase of refractive index of the solution at the focus of the tweezers and DLS (Dynamic Light Scattering) confirming an increase in the concentration of large molecular clusters [134], [140]. Tweezers have also been observed to "collect" polystyrene particles from the bulk of solutions, with the number of individual particles increasing with time [142].

3.8.1.3 Heating Effects

To limit the effects of laser-induced heating discussed in section 3.4, deuterium oxide is typically used as the solvent when experimenting with nucleation and crystal growth directly caused by optical tweezers. If the EM radiation used for the optical trap not be focused near to the diffraction limit, the laser induced heating can be neglected [128], [143]. An extensive range of optical tweezing-induced nucleation and crystal growth have been performed using a laser with a 1064 nm wavelength, performed to limit the possible heating effects and alter the solubility experienced by the solute, thereby the supersaturation [144].

3.8.1.4 Polymorph and Pseudopolymorph Control

Optical tweezers allow for the position of the nucleation event to be controlled and the polymorph of the nucleated crystal. Optical tweezers have been observed to selectively nucleate both α and γ polymorphs of glycine. Depending upon the solution's supersaturation, altering the trap's power and the laser's polarisation can alter the polymorph produced as different light polarisation states are thought to the different behaviour possible when trapping different cluster forms [145], [146]. When $S \geq 1$, linearly polarised light produces

the α polymorph, whereas circularly polarised light produces the γ polymorph. However, optical tweezers can induce nucleation in undersaturated solutions [141]. When the solutions are exposed to a tweezing focus, the polymorph produced depending upon the polarisation is reversed. In undersaturated solutions, linearly polarised light produced γ glycine, and circularly polarisation produced the α polymorph. As well as the ability to control crystal polymorph, pseudo-polymorph control is also possible on either side of the saturation line regardless of the laser power or polarisation that only one pseudo-polymorph will form when $S < 1$ the monohydrate form of L-Phenylalanine, however when $S > 1$ the anhydrous crystal form will be produced. The proportion of each pseudo-polymorph produced when saturated solution is used can be altered depending upon the laser power and polarisation used to generate the tweezers [147]. Not only can the chemical form be controlled, but the morphological form of the crystal produced can be impacted to allow some control over this by being able to have some impact on the morphological form of potassium chloride [148]. With work now beginning to explore the possibility of enantiomorph control [149].

Most research that has been performed upon optical tweezing-induced nucleation was performed in organic molecules, especially amino acids such as glycine [128], [139], [141], [145], [150], L-phenylalanine [151]–[153] and lysozyme [154]–[156]. Nucleation induced by optical tweezers is not only limited to organic substances. Lead halide perovskites have been observed to nucleate from N, N-dimethylformamide [157].

3.8.2 Crystal Growth Influenced by Optical Tweezing

The crystalline growth of a single crystal can also be altered using the focus of an optical trap. When the focus of the trap is positioned in proximity to a crystal not generated by irradiation by the tweezers, the growth rate of individual crystal faces can be altered. It is suspected this is caused by the trap causing pre-existing clusters to gather at and surround the focus of the trap locally. This is partly supported by a hypothesis presented by *Tu et al.* [154], where it is proposed that the tweezing focus is surrounded by a region that has become enriched in the solute compared to the bulk solution, as evidenced by the increase in crystal growth rate that is experienced. However, this region can also be highly regimented, as evidenced by the fact that at first, the growth rate measured when under the influence of the tweezers is partially inhibited and that the enhancement of the growth rate only occurs following a structural “reorganisation” of the trapped clusters in to a less organised or fixed pattern [154], [158]. The crystal face growth rates change depending upon laser power and the length of time of irradiation [154]. The hypothesis that the trap contains and is surrounded by a region of

higher concentration of crystal-forming units is supported by work performed by *Yuyama et al.* and *Singer et al.* [136], [151].

3.8.3 Indirectly Influenced Nucleation with Optical Tweezers

Optical tweezing can also influence nucleation outside of the trap's focus following the cessation of irradiation. A 2018 study was performed by *Yuyama et al.* to investigate the position of nuclei generated surrounding the location of the focus of the tweezers following the irradiation [155]. When a hen egg white lysozyme sample was irradiated for one hour for 1064 nm radiation, the number of nuclei generated was equal to the number generated in 24 hours in a non-irradiated sample while altering the position where nucleation events occurred within the control volume. Use of the tweezers caused the average distance where nuclei were observed as the average distance between the nuclei and the focus at the centre decreased from 4.7 mm to 2.3 mm though using the tweezers. This also caused the standard deviation of the distance to the chamber's centre to halve from 2.4 mm to 1.2 mm. Visual observation of the nucleation in the absence of the tweezers could describe the position of the nuclei as random. In contrast, when the tweezers were used, the position of the nuclei was highly concentrated around the position where the trap focus was located.

4 Methodology and Materials

This chapter describes the equipment used in this thesis to perform the experimental work contained.

4.1 Crystal16

The Crystal16, manufactured by Technobis, is a piece of equipment that monitors the transmissivity of a beam of light passing through a sample of known composition. This can run four sets of four 1 mL samples. Each set of samples can be set to run through a pre-programmed temperature and agitation cycle. Measurement of clear and cloud points allows the determination of solubility curves, metastable zone widths, and induction times, depending upon the programmed cycles. The Crystal16 is shown in Figure 4:1.



Figure 4:1: The Crystal16 Apparatus.

4.2 Crystalline

The Crystalline, manufactured by Technobis, has eight individual reactors which can hold an 8 ml glass vial. The temperature and stirring profile of each reactor can be controlled individually. Each reactor can monitor the transmissivity of the vessel used as well as monitoring the size and number of solid particles through image analysis. Agitation can be performed using a stirrer bar or overhead stirring, allowing different forms of agitator to be used depending upon circumstances. The Crystalline apparatus is shown in Figure 4:2.



Figure 4:2: The Crystalline Apparatus.

4.3 ThorLabs Modular Optical Tweezers

The Modular Optical Tweezers manufactured by ThorLabs were used for tweezing experiments in this project. The tweezers were supplied with a 330 mW 975 nm trapping laser was brought to a focus using a 100x NA=1.25 oil-immersion objective lens. The original setup is shown in Figure 4:3 with a schematic of the base set up, including the additional units detailed in section 4.4, is shown in Figure 4:4.

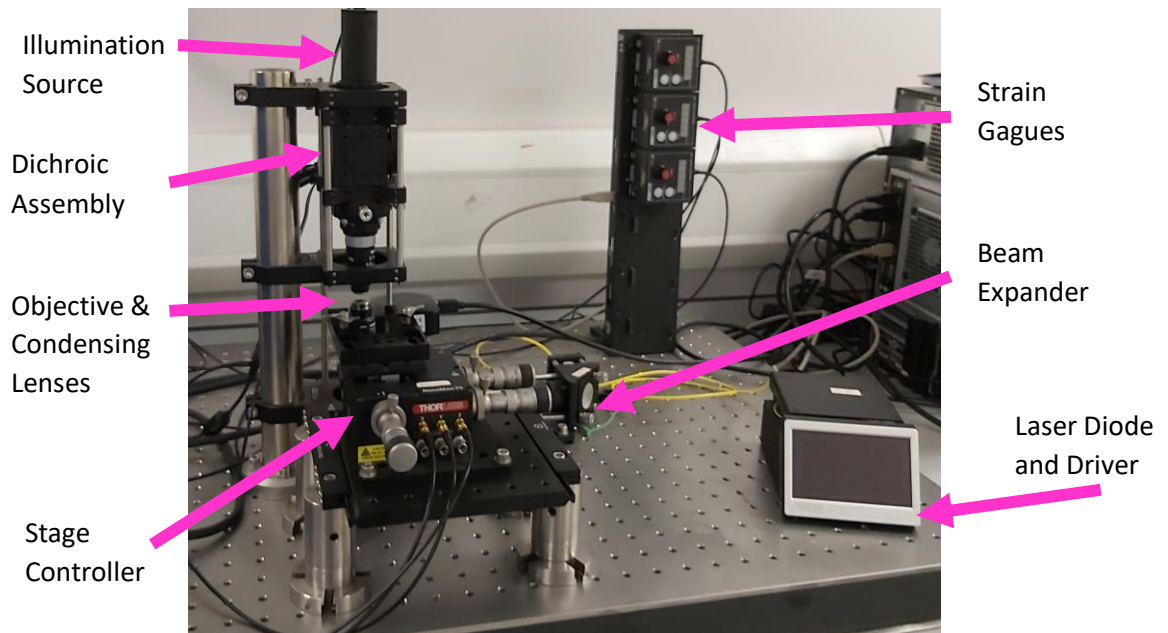


Figure 4:3: The Base setup of the ThorLabs OTKB/M modular optical tweezers.

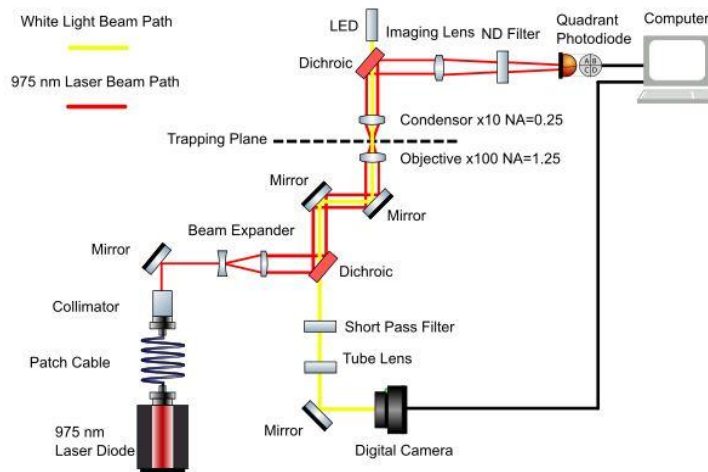


Figure 4:4: Schematic diagram of base optical tweezers OTKB/M, OTKBFM and OTKBFM-CAL

In the base setup of the tweezers the beam path begins at the diode which is connected to a collimator using a single mode patch cable. The beam path is then passed through a beam expander and then redirected vertically, following a short pass dichroic, using a pair of dielectric mirrors after which it is passed through the objective lens to the trapping plane. Following the trapping plane the condensing lens will capture the beam following trapping, from here the beam is redirected horizontally again using a short pass dichroic. Once horizontal again the beam passes through an imaging lens and neutral density filter to position the forward scattering of the trapping beam on to the quadrant photodiode. The recorded signal from the quadrant photodiode is then sent to an accompanying PC. The visual light to allow video to be recorded is counter propagated to the trapping beam. Following the imaging LED source, the light passes through the short pass dichroic and then through the condensing and objective lens, then through the steering mirrors and the first short pass dichroic that the trapping beam passed through. After this dichroic the light passes through a short pass filter, there to protect the camera from laser induced damage, and a tube lens to allow imaging to be performed. The video captured is recorded by the same PC used to monitor the voltage signal from the quadrant photodiode.

4.4 Optical Tweezers Additional Units

The two additional installed modules (OTKBFM and OTKBFM-CAL) do not come with the base Modular Optical Tweezing setup. The Back Focal Plane Detection Module (OTKBFM) consists of a quadrant photodiode used to determine the displacement of any trapped particle from the equilibrium position. Strain gauges allow the stage to operate in closed-loop mode to get total control regarding the positioning of the stage. The Force Acquisition Module (OTKBFM-

CAL) is a device that interfaces between the entire optical tweezing setup and a computer to allow calibration of the trap and the logging of data from the system, made up of the ThorLabs OTKBFM and the OTKBFM-CAL modules. Allowing the tweezer's stiffness to be calibrated according to the PSD method also allows the detector's sensitivity in each axis to be determined. Photographs of these units are shown in Figure 4:5 and Figure 4:6, respectively.

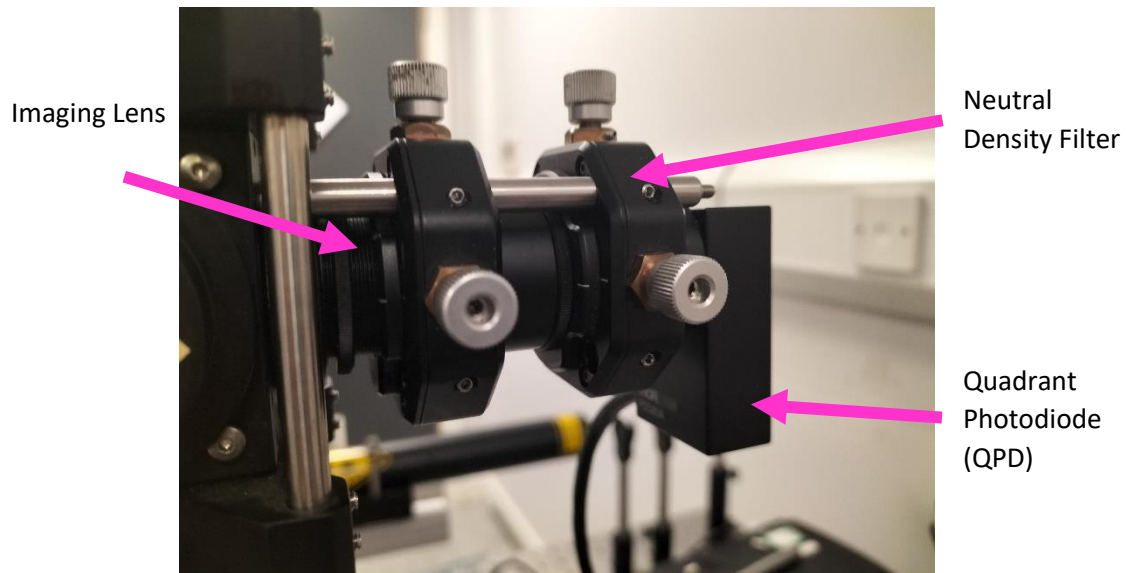


Figure 4:5: ThorLabs OTKBFM.

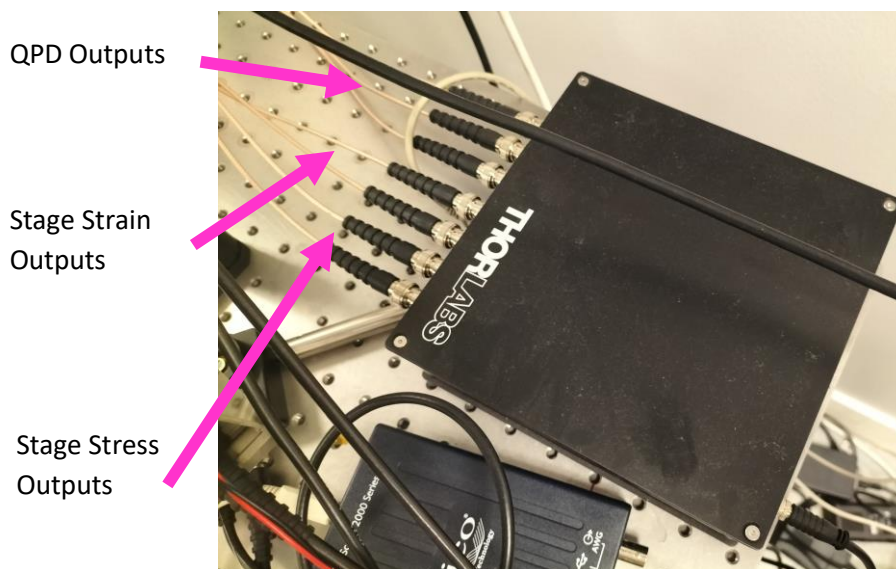


Figure 4:6: ThorLabs OTKBFM-CAL.

4.5 Modified Optical Tweezers

To allow a more powerful laser to be used in conjunction with the existing setup, slight modifications were introduced to allow the 1064 nm laser to be introduced to the beam path. The used laser was supplied by CNI and is shown in Figure 4:7. The existing optics and other components supplied with the base OTKB and two additional units OTKBFM and OTKBFM-CAL were also suitable for use with the laser as the quadrant photodiode was still relatively sensitive at 1064 nm.



Figure 4:7: 2 W CNI 1064 nm Gaussian Laser.

4.6 Crystal Cell

Solutions exposed to the tweezers focus or being tested examined using only the microscopy available with the tweezers was done using a cell constructed of a Grace Bio-Labs Press-To-Seal-Silicone Isolator, without pressure seal adhesive, seals were achieved by applying pressure between the coverslip and isolator. These have a 13 mm diameter well that was 2.5 mm deep. Each side of this well was closed using a 22 mm by 22 mm #1.5 thickness borosilicate glass coverslip. If the cell was to be seeded, this was added following washing, and then the solution of interest was pipetted into the well using a Gibson pipette with a maximum volume of 200 μ L. An empty uncovered well, lower coverslip in place, is shown in Figure 4:8 as well as a schematic diagram of the complete isolator used in Figure 4:9. How the crystal cell is arranged with respect to the objective and condensing lenses is also shown in Figure 4:10.

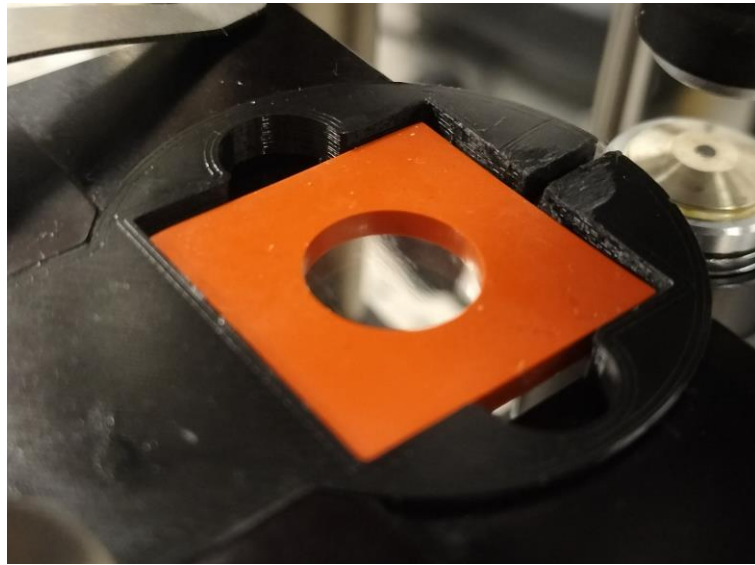


Figure 4:8: Crystal Cell Apparatus within a custom 3D-printed mount.

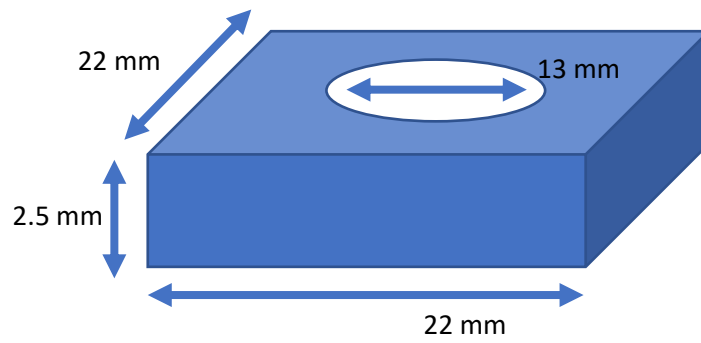


Figure 4:9: Schematic diagram of silicon isolator used.

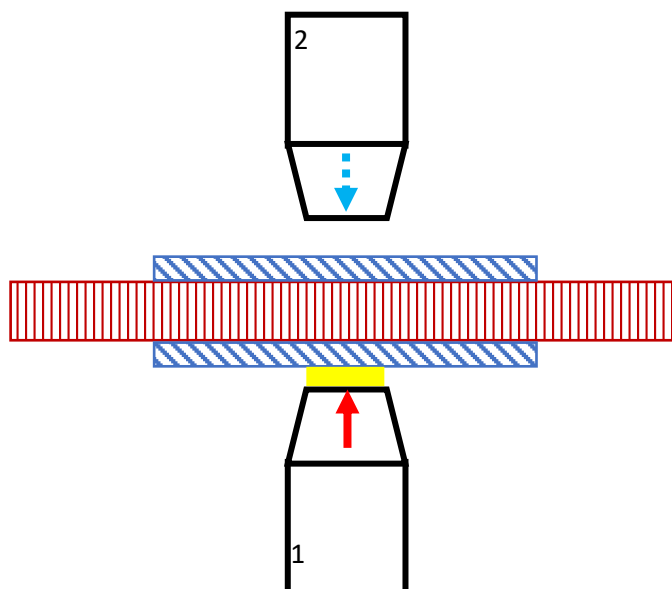


Figure 4:10: Schematic diagram of the wider trap set-up. Number 1, Objective Lens (Nikon x100 NA=1.25) used for focusing trapping laser; Number 2, Condensing Lens (x10); Yellow Solid, Immersion Oil; Blue Diagonal Stripes, Number 1.5 thickness silica microscope coverslips and Brown Vertical Stripe, Silicone Gasket. Red Solid Arrow, Path of Trapping Laser and Blue Dashed Arrow, Path of Light Source for Imaging Illumination.

4.7 Polar Bear Plus Crystal

A Polar Bear Plus Crystal, shown in Figure 4:11, was used to put small volumes of solution not subjected to agitation through temperature cycles. A machined aluminium block covered by an insulating rubber was used on the heating pad to hold and surround the vials used to hold a supersaturated solution. The temperature within the block was controlled using a thermocouple placed into a drilled hole used to control the block's temperature by altering the plate's temperature. The Plus Crystal version of this equipment is programmable to perform a specific temperature cycles.



Figure 4:11: The Polar Bear Apparatus.

4.8 Cary5000

The Cary5000 Photospectrometer manufactured by Agilent can measure absorption from the UV region of the EM spectrum to the NIR wavelengths. This equipment can measure the absorption of both solids and liquids. In cases where this has been used here, measurements were performed on solutions. These solutions are held within a Hellma 3.5 mL (Optical Glass, optical path length 10 mm) cuvette. The form of cuvette used can differ depending upon the measurement made. The choice of cuvette is typically dependent upon the region of the EM spectrum under investigation; in this case of this thesis, the cuvette material was optical glass. The Cary5000 is shown in Figure 4:12, and the Hellma cuvette in Figure 4:13.



Figure 4:12: The Cary5000 Photospectrometer.



Figure 4:13: Hellma Optical Glass Cuvette (1 cm Path length).

measurements were made using the Cary5000 spectrophotometer. This required smaller volumes of solution (~3.5 ml) to be tested. Samples were run using a Hellma optical glass cuvette with an optical path length of 10 mm. Testing was performed using an averaging time of 0.1 s and data interval of 1 nm at a scanning rate of 600 nm/min between a 1200 nm and 800 nm. A zero-baseline correction was used where two baselines were collected, where 100 % transmission measurement was taken where the spectrophotometer was empty. The second baseline was taken using a 0 % transmission measurement where the beam's path

was blocked using an opaque plastic puck. Measurements were again taken in random order. Since the cuvette was reused before the solution to be measured was inserted, measures to wash the cuvette were taken. When solutions with a deionised water solvent were used, the cuvette was first rinsed three times using deionised water, then twice using the test solution to be measured. The cuvette was filled for a third time using the test solution, and only then was this inserted into the spectrophotometer for measurements to be made. When the solution used deuterium oxide as a solvent was measured, the solution was first removed from the cuvette. This was then rinsed three times using deionised water, then twice using acetone. The acetone was then left to evaporate. Once the cuvette was completely dry, the following sample was pipetted into the cuvette. In all cases, a new pipette tip was used for each solution to prevent any potential cross-contamination between samples. To eliminate the cuvette's impact on absorption measurements, dry, empty cuvette measurements were taken to correct this impact.

4.9 Matrix-F

The Matrix-F, manufactured by Bruker, is a NIR spectrometer that can measure multiple properties, including but not limited to transmission or transreflectance in the NIR region of the electromagnetic spectrum, as shown in Figure 4:14. The Matrix-F operates using a Falcata XP 12 probe manufactured by Hellma, with multiple tips that can be utilized, allowing the optical properties of different path lengths to be measured. The probe is shown in Figure 4:15.



Figure 4:14: The Matrix-F Spectrometer.



Figure 4:15: Falcata XP 12 Transflectance Probe.

Measurements with the Matrix-F, the Falcata-12 XP probe was used with the 5 mm path length tip. Samples were tested by inserting the probe tip into a volume of solution. Samples were tested with a background of air, with 32 scans for both the background and sample with a scan resolution of 8 cm^{-1} between 12000 cm^{-1} and 4000 cm^{-1} (833 nm to 2500 nm). Samples were tested in a random order to eliminate any potential systematic error. Between each sample, the probe tip was washed using multiple deionised water rinses. The probe tip was dried using paper towels and left to dry entirely before insertion into the following sample.

Since the tip of the Falcata-12 probe is tightened each time this is used, there is the possibility that the path length deviates slightly from the advertised path length. Therefore, the path length used for calculations was determined from the pure water measurement at the wavelength of interest, 975 nm. Multiple absorption measurements allow linear best-fit trends to be determined.

4.10 Tensor II

The Tensor II, manufactured by Bruker, is a Fourier Transform Infrared spectrometer, this was used to measure infrared absorption of solid samples, powders, and single solid particles. By measuring absorption across a wide spectral range of a sample, which can be used to determine the form (i.e., the polymorph) of the present material. The Tensor II is shown in Figure 4:16.



Figure 4:16: The TensorII FTIR Infrared Spectrometer.

Measurements were examined with FTIR using an average of 32 scans at a resolution of 1 cm^{-1} between 4000 cm^{-1} and 400 cm^{-1} for the background as well as the actual material scan.

4.11 XRPD

X-ray powder diffraction was performed using a D8 Discover, manufactured by Bruker, this utilizes $\text{Cu K}\alpha_1$ and $\text{Cu K}\alpha_2$ radiation. This uses a multiwell plate where the samples are supported using $7.5\text{ }\mu\text{m}$ thick Kapton film secured to the plate using silicon grease. Samples were prepared by manual grinding in a pestle and mortar. Ground samples were loaded into the wells to an individual uniform single sample height. Intensity data was collected on a θ/θ transmission-based geometry with a focusing global mirror.

XRPD analysis was performed using $\text{Cu K}\alpha_1$ and $\text{K}\alpha_2$ radiation from the Bruker D8 Discover diffractometer between the 2θ angles of 4° and 35° using a step size of 0.017° with a scan time of 0.5 s per step, on a multiwall plate supported by Kapton film ($7.5\text{ }\mu\text{m}$).

4.12 Power Meter

The laser beam power was measured by a ThorLabs PT160T laser, where the meter was first calibrated using the cover supplied when set to the wavelength of the laser being tested. This is shown in Figure 4:17.



Figure 4:17: ThorLabs PT160T Power Meter.

4.13 Contact Angle

Measurement of contact angles was performed using a DSA30 manufactured by Kruss. A 0.8 mm outer diameter non-bevelled needle allows a single droplet of liquid or solution to be dropped onto the surface of interest. The accompanying software allowed the contact angle to be determined automatically by determining a baseline, where ellipse fitting is used in conjunction with the sessile droplet orientation. The DSA30 is shown in Figure 4:18



Figure 4:18: The Kruss DSA30 Contact Angle.

4.14 Materials

A range of materials were used to study the effect of particles and optical tweezing focuses' on nucleation from solution.

4.14.1 Glycine

Glycine is a small organic molecule that has been used for a range of nucleation studies [30], [159] as it is the simplest amino acid. This has also been used in a large range of studies involving crystallisation induced by optical tweezers [128], [139], [141], [145], [150]. All of the glycine used in this thesis was sourced from Sigma Aldrich (< 99 %, for electrophoresis, powder) was used without further purification.

4.14.2 Sodium Chloride

NaCl was used in this these to act as an inorganic comparison to the experiments involving glycine as well to be a system that was not subject to isotope exchange when dissolved in

D₂O. The NaCl used in this thesis was sourced from Sigma Aldrich (ACS Reagent, $\geq 99\%$, powder) was used without further purification.

4.14.3 Sodium Bromate

Further to the tweezing experiments performed using glycine and NaCl as a test substance, testing was performed with sodium bromate to determine whether it could nucleate individual chiral crystal forms selectively [160]. This compound was selected to allow for in situ determination of the chiral form without any offline testing. Factors examined included the trapping beam polarisation, solution concentration, solvent isotopologue, and the relative position of the beam focus within the solution droplet. The NaBrO₃ used in this thesis was bought from Sigma Aldrich (for synthesis, $\geq 99\%$, powder) and used without further purification.

4.14.4 Silica Particles

Silica particles were supplied as a suspension from Duke Scientific, via Fisher Scientific (Series 8000 Silica Particle Size Standards, 8150) for the purpose of determining their impact on the crystallisation of NaCl and glycine from solution when agitated and being held by optical tweezing focus. These particles had a diameter of $1.57\ \mu\text{m} \pm 0.02\ \mu\text{m}$ supplied as suspension in H₂O at a concentration of 2 % silica, these were used as supplied.

4.14.5 Polystyrene Particles

To determine the impact of the material of the particle a second particle material was sought as close in size to the original. These polystyrene particles were sourced from microparticles GMBH. The particles used were $1.59\ \mu\text{m} \pm 0.05\ \mu\text{m}$ diameter particles supplied in a 10 % solids suspension in H₂O (Monodisperse Particles for Research Purposes, PS-R-KM178), and were used as supplied.

4.14.6 Water

De-ionised water was taken from one of two in house sources; Millipore Ultrapure (18.2 M Ω cm) and Millipore Elix 5 (> 5 M Ω cm).

4.14.7 Deuterium Oxide

To act as a comparison to regular water deuterium oxide (D₂O) was used. This was chosen as this is also typically used in optical tweezing setups to eliminate laser induced heating as much as possible. Deuterium Oxide (> 99.9 % D Atom, Sigma Aldrich) was used in all cases where D₂O was used in this thesis without further purification.

5 Heat Absorption of Tweezing Beams and Trapping Particles

This chapter primarily examines the temperature effects caused by optical tweezing focuses and associated trapped particles. Using a pre-existing Peterman heating model [105], absorption measurement at tweezing wavelengths were performed to estimate the temperature rises at tweezing focuses. This was performed to determine the potential for temperature rises on any tweezing experiment performed. Work later in this thesis examines the suitability for substrates for crystallisation experiments in optical tweezers using mainly optical criteria particularly when doped with third material microparticles.

Shortly following the development of optical tweezers, it was noticed that optical traps can increase the temperature in proximity to the trap's focus [85], [103]. This poses a question regarding the temperature that would be in the focus of a highly focused Gaussian beam, especially when dealing with highly temperature-sensitive systems/fields. In many cases, this temperature rise could impact the trap stiffness as this is dependent on temperature. However, when investigating crystallisation from solution, this temperature rise can affect the supersaturation experienced when the focus of an optical trap is activated in a solution. The solubility of the dissolved species depends on temperature. Therefore, knowing the effects of optical tweezers on local temperature is necessary, as temperature control is critical during crystallisation operations.

5.1 Impact of Temperature on Solubility

To allow nucleation studies to be meaningful requires that the conditions under which the kinetics are observed be well defined and for the nucleation to occur within a observable timeframe (not over vast periods) Since it can be observed in section 5.7 that optical tweezers can increase the local temperature which in turn effects the solubility that any solute would experience, thereby changing the ascribed supersaturation and as can be seen from Figure 5:18 and Figure 5:19 these temperature rises have the potential to be significant.

To determine how sensitive the supersaturation was to changes in temperature, the supersaturation of a range of fixed concentration solutions with supersaturations between $1.16 \leq S \leq 1.24$ at $20\text{ }^{\circ}\text{C}$ was calculated at temperatures up to $30\text{ }^{\circ}\text{C}$. One of the examples shown in Figure 5:1 had a $S = 1.24$ at $20\text{ }^{\circ}\text{C}$ which was reduced to $S = 1.16$, the level of the secondary nucleation threshold (SNT) of glycine in water [30] as defined through the method initially described by Briuglia et al. [29]), when the temperature was raised $2.5\text{ }^{\circ}\text{C}$ to $22.5\text{ }^{\circ}\text{C}$. This decrease in supersaturation is due to an increase in solubility with increasing

temperature as indicated with the fall in supersaturation from arrow 1 to 2 as indicated in Figure 5:1.

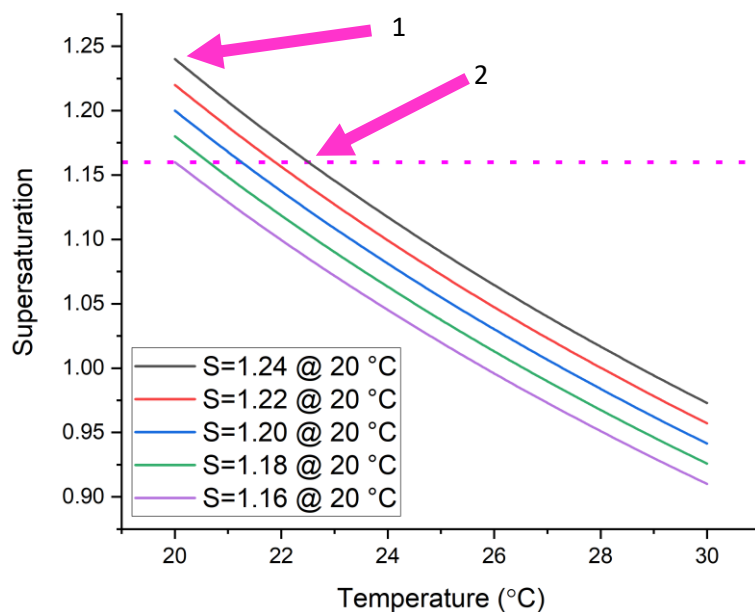


Figure 5:1: Impact of Temperature on Supersaturation of Alpha Glycine in Deuterium Oxide (Calculated using Solubility data from [161])

In the case of the sodium chloride solution in deuterium oxide, the supersaturation's sensitivity is much less sensitive to changes in temperature. Exemplified by the greater than 10 K temperature rise needed to reduce the supersaturation by 0.01, from 1.04 to 1.03, as seen in Figure 5:2.

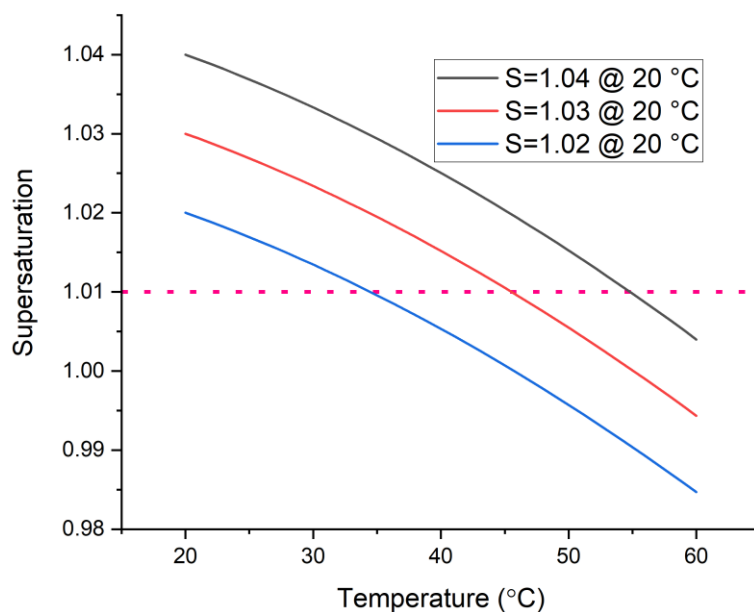


Figure 5:2: Impact of Temperature on Supersaturation on Sodium Chloride in Deuterium Oxide (Calculated using solubility data from [162])

It is observed that supersaturation levels are much more stable with respect to temperature in solutions of NaCl than glycine due to the much shallower solubility curve.

Estimates of the effects on supersaturation based of this heating model are shown in chapter 8, using measurements of the solubility of glycine and NaCl in both H₂O and D₂O made in chapter 6.

5.2 Solubility Impacted by Solvent Isotopologue

Optical properties are not the only difference that can be observed between isotopologues of the same chemical substances. When crystallising from solution, the critical factor which needs to be controlled is solubility, which can be different when using different isotopologues of the same solvent [161].

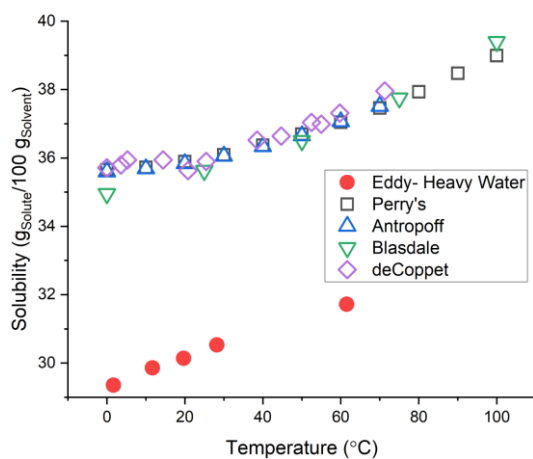


Figure 5:3: Comparison of Solubility of NaCl in Normal Water and Heavy Water (Data from Perry's [180]; Eddy [162]; Antropoff [181]; Blasdale [182] & de Coppet [183]). Hollow symbols indicate solubility in water, and filled symbols indicate deuterium oxide.

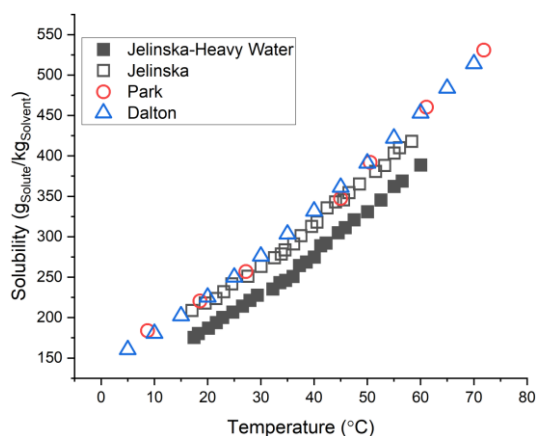


Figure 5:4: Comparison of Solubility of glycine in different isotopes of water (Data from Jelińska-Kazimierczuk [161] and Park [184]) Hollow symbols indicate solubility in water, and filled symbols indicate deuterium oxide.

Figure 5:3 and Figure 5:4 shows the solubility of sodium chloride and glycine in different isotopologues of water. In these solutes, the solubility is lower when deuterium is used as a solvent than in regular water. The solubility changes for both solutes appears to be a fixed amount when above 20 °C for each solute when the isotope of the solvent is switched from H₂O to D₂O. In the case of glycine, the spread of results that exists above a solubility of approximately 350 g_{solute}/kg_{solvent} is consistent with other results that have been published that are included in Figure 5:4 and other research publications.

5.3 Solvent and Particle Absorption

Different suspension and trapping materials will have different absorption coefficients depending on the trapping laser's wavelength, and at the same wavelengths, varied materials have different absorption coefficients.

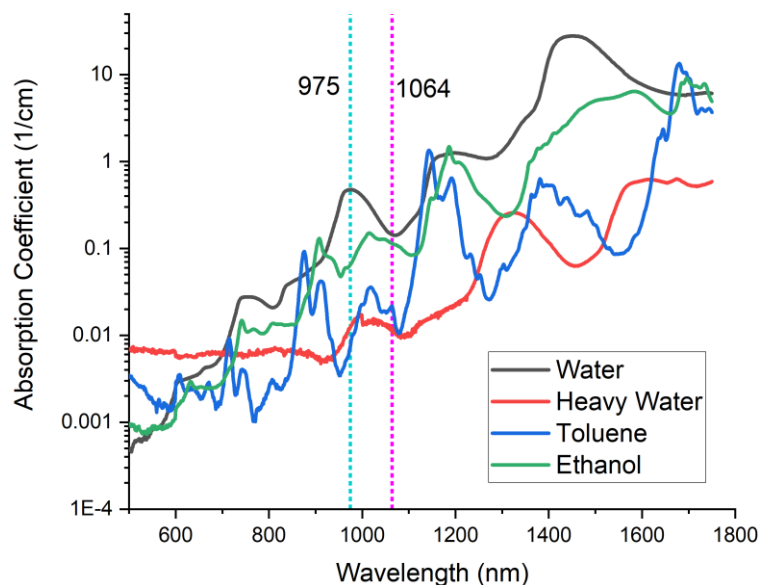


Figure 5:5: Absorption Coefficient of Selected Common Solvents (Water, Heavy Water, Toluene and Ethanol) [110]. The two trapping laser wavelengths used are indicated.

Figure 5:5 shows the differences between absorption coefficients across a range of common trapping wavelengths, highlighting the used trapping lasers' wavelengths (975 nm or 1064 nm), see chapters 8 and 9. Deuterium Oxide, shown in red, has a much lower absorption coefficient at the trapping wavelengths, as shown in Figure 5:5. Since it is clear that the use of optical tweezers can induce heating [103]; which in many cases does not pose such a significant impact, but this is not the case as temperature control is key in crystallisation processes. One way of minimising the temperature rise is to use a solvent/laser combination with a low absorption coefficient at the wavelength of the trapping laser. The values shown in Figure 5:5 only apply to pure solvents, the addition of solute impacts the overall absorption coefficient, which is discussed in section 5.5. The two solvents used in this thesis (H_2O and D_2O) are shown alongside two alternates that are also common solvents to provide additional context however it seems like at either of the trapping wavelengths that one of the non-used solvents would offer a much lower absorption but can be rejected on grounds of thermal conductivity (ethanol) or safety (toluene).

Should we desire to trap a particle, this trapped material will have its own absorption coefficient for the trapping laser's wavelength. Figure 5:6 shows these absorption coefficients for four selected common trapping materials, again highlighting the wavelengths of the trapping laser. This shows that although the silica particles have the lowest absorption of the selected common trapping materials this is not the only criterion for suitability as the refractive index must be higher than that of the solvent or solution to which these particles are suspended, other criteria may also have to be considered depending upon the exact chemical systems chosen.

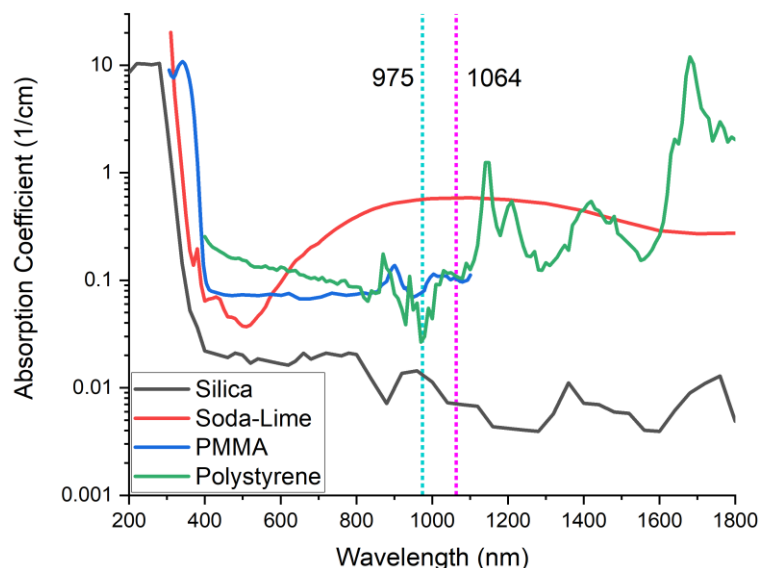


Figure 5:6: Absorption Coefficient of Selected Common Trapping Materials. Silica [163]. Polystyrene [164]. Soda Lime [165]. PMMA [166].

As previously stated, with the solvents indicated, one way to minimise the potential temperature rises when holding a particle is to trap a particle whose absorption coefficient is low at the wavelength of the trapping laser. However, this is not the only factor which must be considered. Investigations performed for micro-rheological studies have used lasers with a wavelength of 830 nm [167] or 532 nm [168], [169]. When trapping using a 532 nm laser, water use would be preferable to heavy water as this has a lower absorption coefficient. Alternatively, in situations where limitations are caused by a lack of alternative optics and diodes when water would be used as a solvent, this would require that deuterium oxide be substituted. D₂O has been widely utilised in studies where sets of optical tweezers have been used to directly induce nucleation with the trap's focus [128], [145], indicating that no one optical tweezing set-up would be suitable for all tests which could be envisaged. Therefore, due to having the lowest absorption the silica particle would be the ideal candidate for the

use when trapping this has the additional benefit of simplifying the calculations used in determining the temperature rises, this is discussed later in section 5.6.

5.4 Refractive Index of Solvents and Particles

Since many tweezing experiments involve holding a spherical particle at the focus of the tweezers. To allow the trapping to occur the refractive index of this particle must be greater than that of the suspension material. The refractive indices of common solvents are shown in Figure 5:7.

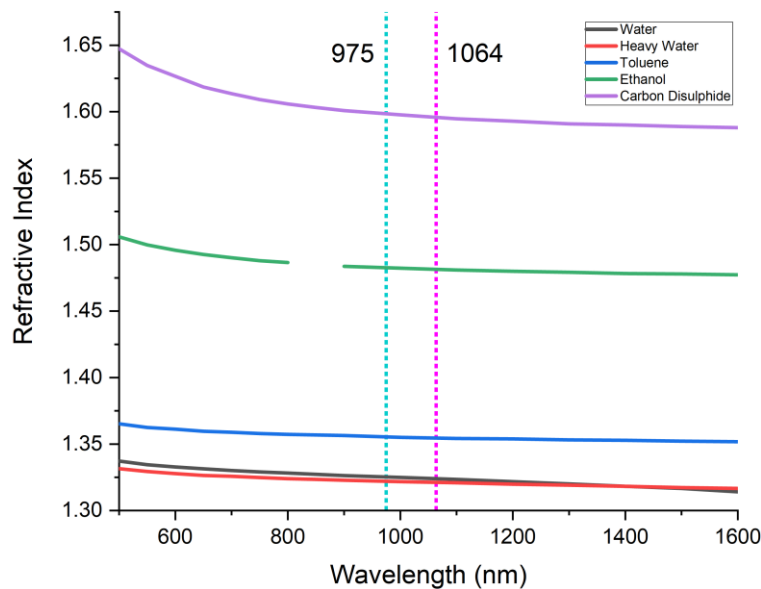


Figure 5:7: Refractive Index of Selected Solvents [110]

Over the range of wavelengths considered from 500 to 1600 nm, the refractive index is stable for these selected common solvents, with each slightly decreasing as the wavelength of the EM radiation passing through these mediums increases, as shown in Figure 5:7. One aspect to note is the refractive indices of normal water and deuterium oxide. At the shorter end of the wavelengths examined, normal water has a higher refractive index than D_2O . Whereas at the longer end of the wavelengths examined, the regular water's refractive index is lower than that of the D_2O . Comparing the refractive indices of both the trapped particle and the liquid in which it is suspended is essential to trap a particle. However, across the range of wavelengths examined, the value of the refractive index was approximately equal, and therefore not significant.

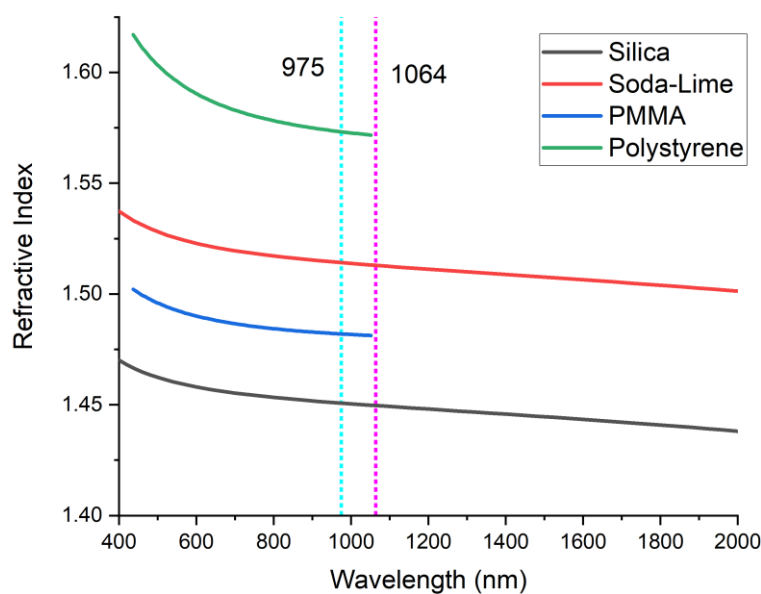


Figure 5:8: Refractive indices of selected trapping materials. (Data from Silica [170]; Polystyrene [171]; PMMA [171]; Soda-Lime [165])

For investigations involving particle trapping in aqueous systems, silica particles should be suitable as this has a low absorption coefficient and a higher refractive index than the surrounding media at the trapping laser's wavelength. However, this would not be suitable for carbon disulphide. As indicated in Figure 5:7 the refractive index of the carbon disulphide is higher than any of the common trapping materials shown in Figure 5:8, this is even before there chemical compatibility is considered.

One potential scenario is when trapping a particle in an ethanol-based suspension media requiring a strong trap, it would first be thought of to use a polystyrene particle to have a particle whose refractive index is higher than the surrounding fluid for this difference to be as large as possible. Even though it could be thought to work, it would not, due to polystyrene being soluble in ethanol, requiring an alternate particle material to be used and compensated for using a higher laser power to generate a trap with enough stiffness. This does not even account for any limitations imposed by laser-induced heating, which could be highly situationally dependent.

Under standard trapping conditions, using a Gaussian beam would not permit particles (of the materials shown in Figure 5:8) to be trapped firmly in carbon disulphide, even without accounting for laser-induced heating.

Therefore, given the conditions discussed in this section and section 5.3 use of silica suspended in D₂O based solutions would be the case where it would have the lowest impact.

5.5 Impact of Solute on Refractive Index and Absorption Coefficient

The absorption coefficient of the solvent may be the main component of the absorption coefficient of the suspending solution. However, it is not the only factor as the solute can impact the overall coefficient, depending on the solute material and quantity dissolved and the wavelength of interest.

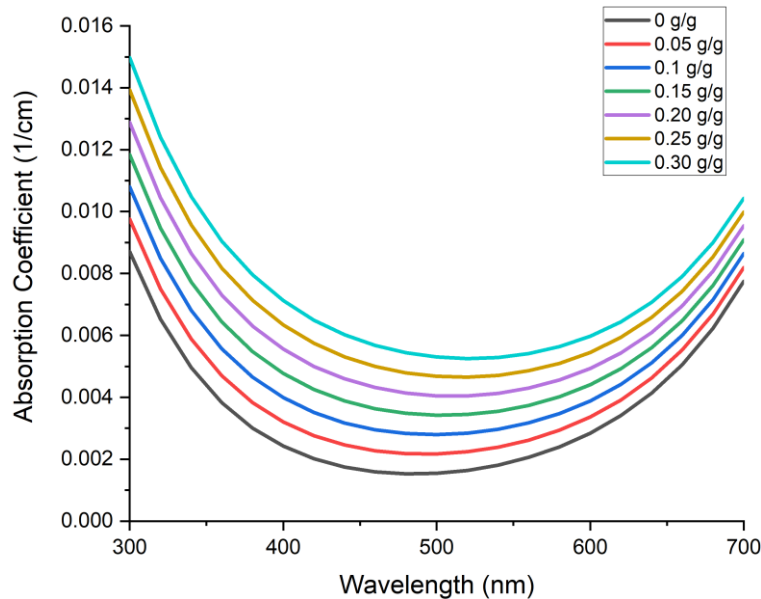


Figure 5:9: Absorption coefficient of aqueous sodium chloride solution at a range of concentrations between 0 and 0.360 g/g [172]. Determined by examining the transmissivity and reflected light through a sample of a known thickness of a solution of known concentration.

From Figure 5:9 concentration of sodium chloride directly impacts the absorption coefficient, as determined from the complex component of the refractive index. Although the impact of the concentration is independent of the wavelength within the range examined in Figure 5:9 on the refractive index's complex component. When the complex component is converted to determine the absorption coefficient the absorption has some slight dependence on wavelength due to way the conversion involves wavelength as seen from Equation 3:15.

However, Li et al. [172] do not provide constants for equations detailing the complex component of the refractive index, at 975 nm or 1064 nm. Thereby preventing estimates of the associated temperature rises being made from this source. To allow temperature rise estimates to be made for the trapping wavelengths of the laser used in this thesis absorption measurements were required to be performed, which are reported in section 5.7 and have not been performed for glycine solutions at either of the wavelengths of interest.

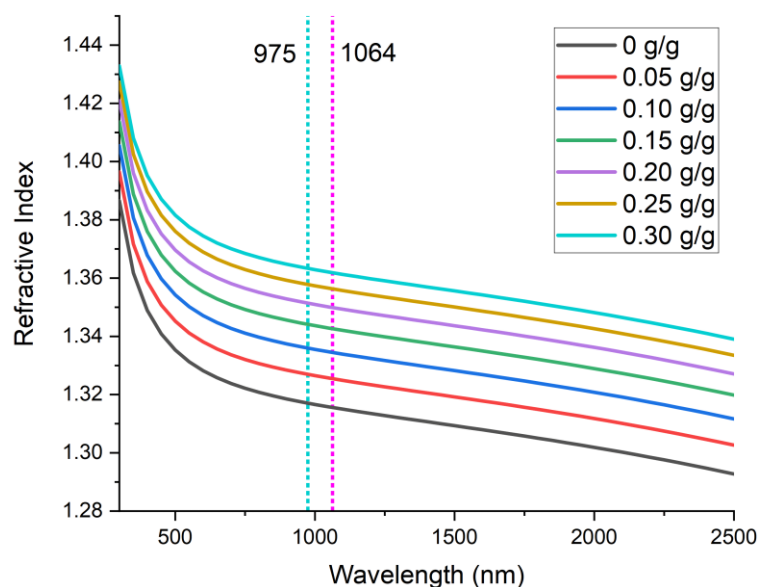


Figure 5:10: Refractive Index of Aqueous Sodium Chloride Solution [172] (Determined by examining the transmissivity and reflected light through a sample of a known thickness of a solution of known concentration.)

The refractive index of the pure solvents is the first step that must be considered to trap particles. In this case, it may be possible for a particle to be trapped in a pure solvent. However, this may change depending on whether solute is dissolved into the solvent, what that solvent is, and the wavelength under examination. In the case of sodium chloride solution, even at concentrations nearing the solubility, the refractive index, shown in Figure 5:10, will be below that of any of the particles shown in Figure 5:6, indicating that any of these materials could be trapped using a laser at the wavelength of 975 nm or 1064 nm. It is possible that this increase in refractive index of the solution could limit the ability of inducing nucleation from solution as one stated hypothesis relies on a difference in refractive index to allow the separation to occur [138].

5.6 Peterman Heating Model

The theoretical model developed by *Peterman et al.* models the temperature experienced at the trap's centre [105] by modelling the light cone geometry and incorporating the heat generated by absorption of the fluid as well as that of the trapped particle, which appears to be more important than the particle itself. This prediction first neglects any trapped particle's presence and then considers this as a correcting factor applied to the temperature rise predicted when using a laser with a Gaussian profile. Equation 5:1 and Equation 5:2 can be written regarding the temperature rise per watt of laser power used. The temperature rises that this heating model predict are with reference to the coverslip's interior temperature shown in Figure 5:11, this was the environment temperature. Models that have been

developed by others (*Mao et al.* and *Haro-Gonzalez et al.*) do not directly account for the impact of any trapped particle [104], [173]. These models (*Mao et al.* and *Haro-Gonzalez et al.*) appear not to be as suitable as trapping either occurs in an exceptionally thin liquid chamber [173], or unlike this setup where the trapping occurs much closer to one surface than the other as this is a limitation of the tweezing equipment as was used in chapters 8 and 9. Furthermore, the model developed by *Mao et al.* determines temperature based on horizontal temperature change, which is more difficult to determine with the setup as used in this thesis [104]. The *Peterman* model estimates the temperature at the trap's centre, or when a particle is trapped at the trapped particle's centre, indicated by the red rhombus in Figure 5:11. This temperature rise is determined by adding the rises predicted by Equation 5:1 and Equation 5:2, therefore $\Delta T_P + \Delta T_B = T_0 - T_D$ where T_D and T_0 are the heat sink and trap centre temperatures, respectively. How this related to the trap geometry setup is shown in Figure 4:10.

$$\Delta T_B = \frac{\alpha_{Liq}}{2\pi K_{Liq}} \ln\left(\frac{2\pi Z}{\lambda} - 1\right) P$$

Equation 5:1 [105]

Where:

- ΔT_B Temperature Rise Component from Beam (K)
- α_{Liq} Absorption Coefficient of Suspension Material (1/m)
- K_{Liq} Thermal Conductivity of Suspension Material (W/ (m K))
- Z Distance to Heat Sink (m)
- λ Wavelength of Trapping Laser (m)
- P Power of Trapping Laser (W)

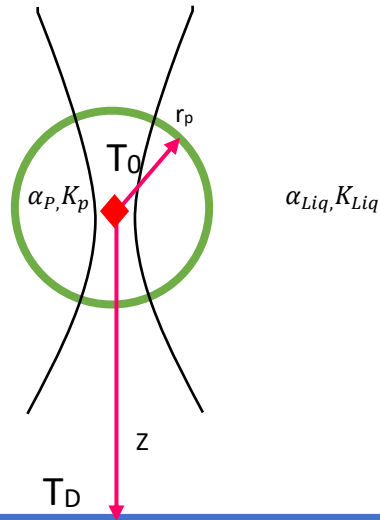


Figure 5:11: Geometry Used by Peterman Heating Model [105]. Green Circle, Particle trapped by Laser; Blue Line, Interior Surface of Glass Coverslip acting as a heat sink; Black Curves, Focused Trapping Laser and Red Rhombus, centre of Trap Geometry. T_0 , temperature at the trap's centre and T_D , the temperature at the coverslips inside surface acting as the heatsink. Diagram not to scale. A larger-scale diagram of the trapping apparatus is shown in Figure 4:10.

When a particle is trapped, the correcting factor that is required:

$$\Delta T_P = \Delta \left(\frac{\alpha}{2\pi K} \right) \frac{\left(\ln \left(\frac{2\pi r_p}{\lambda} \right)^2 + 1 \right)}{2} P$$

Equation 5:2 [105]

ΔT_P

Temperature Rise Component from Particle (K)

$$\Delta \left(\frac{\alpha}{2\pi K} \right) = \frac{\alpha_P}{2\pi K_P} - \frac{\alpha_{Liq}}{2\pi K_{Liq}}$$

Difference between brackets contents of particle and suspension Material

α_P

Particle Absorption Coefficient (1/m)

K_P

Particle Thermal Conductivity (W/ (m K))

r_p

Particle Radius (m)

Measurements of the heating induced by a 975 nm laser found that the temperature rises when trapping a 1000 nm radius silica particle observed using Stokes' drag methods are comparable to the predictions made by the *Peterman* model in the same circumstances, where the force required to move a particle of a known size a determined speed is used to determine the viscosity, therefore the temperature of the suspending fluid. This temperature rise is an order of magnitude higher in comparison to trappings performed in deuterium

oxide [104]. The implications of individual solvent and particle choice on the heating induced by using the trapping laser are discussed in section 5.7.

However, this is not the temperature that the solution would experience at the interface with the particle, as indicated by the green circle in Figure 5:11. As the distance from the centre of the trap increases, the temperature elevation from that of the heat sink decreases. This change in temperature within the particle can be ignored when the calculations involve silica particles as seen in Figure 5:12. This was explained by the fact that the value of α/K for silica is low and that most of the absorption occurs in the surrounding suspension medium [105]. The absorption coefficients and the thermal conductivities of the pure solvent materials and the particle materials are given in Table 5:1, as well as a factor used to compare systems at individual wavelengths.

Table 5:1: List of Absorption Coefficients and thermal conductivity at 293 K of solvents and common trapping materials.

| Material | | (α) Absorption Coefficient at 975 nm (m^{-1}) | (α) Absorption Coefficient at 1064 nm (m^{-1}) | (K) Thermal conductivity at 293 K (W/ (m K)) | $\left(\frac{\alpha}{K}\right)_{975}$ (K/W) | $\left(\frac{\alpha}{K}\right)_{1064}$ (K/W) |
|------------------|------------------|--|---|---|--|---|
| Solvents | Water | 47.6 [110] | 14.4 [110] | 0.590 [115] | 80.68 | 24.41 |
| | D ₂ O | 1.26 [110] | 1.16 [110] | 0.589 [115] | 2.14 | 1.97 |
| | Ethanol | 6.56 [110] | 1.14 [110] | 0.167 [174] | 39.28 | 6.83 |
| | Toluene | 0.794 [110] | 2.16 [110] | 1.358 [174] | 0.58 | 1.59 |
| Particles | Silica | 1.32 [163] | 0.71 [163] | 1.4 [174] | 0.94 | 0.51 |
| | Soda Lime | 56.6 [165] | 57.5 [165] | 0.98 [174] | 57.766 | 58.67 |
| | Polystyrene | 2.82 [164] | 7.89 [164] | 0.12 [105] | 23.5 | 65.75 |
| | PMMA | 8 [166] | N/A | 0.19 [175] | 42.1 | N/A |

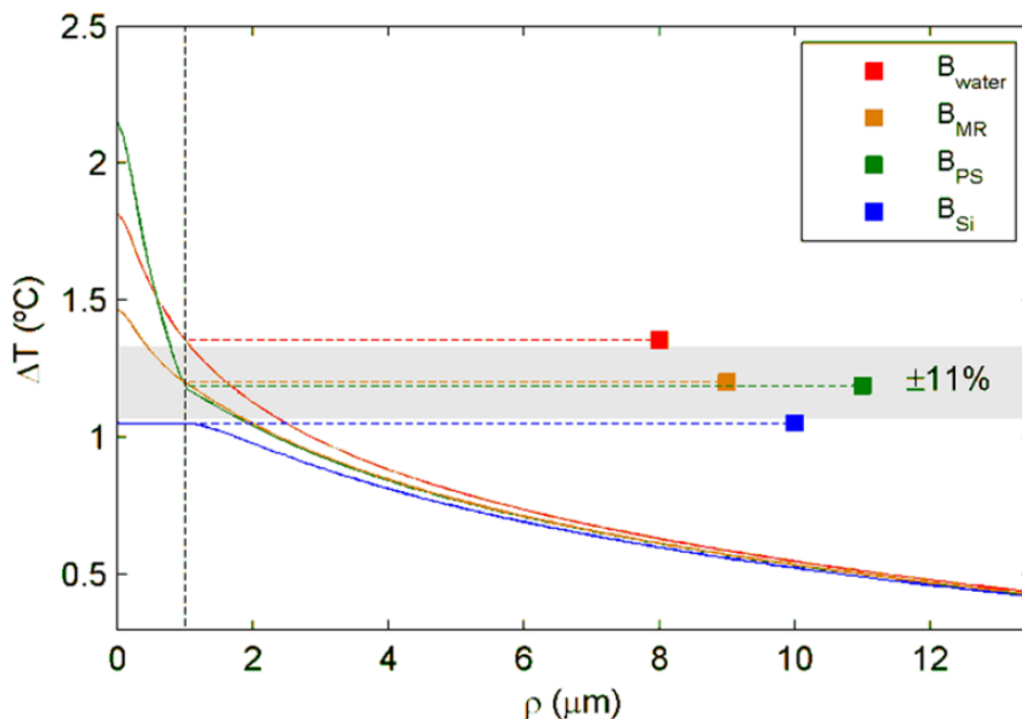


Figure 5:12: Simulated temperature profile as a function of ρ (lateral plane (x - y plane from Figure 3:3) displacement) from the centre of the trap geometry of 2-micron diameter particles of selected materials. Also shown are measurements of the temperature rise when trapping particles of various material, Filled squares. Orange Solid, Melamine Resin (MR); Green Solid, Polystyrene (PS); Blue Solid, Silica (Si); Red Solid (Water), absence of particle. The grey band indicates the standard deviation observed in the polystyrene measurements [176]. B is a measurement of the temperature rise.

The use of silica particles allows the temperature at the particle-solution interface to be determined without additional considerations, see section 5.7.3, as it is equal to the ‘core’ temperature. However, these simulations may require validation against in situ temperature rises under various conditions. Figure 5:12 also shows that when using a 1064 nm wavelength laser, the temperature observed at the interface between the particle and the surrounding suspension medium is for the materials observed approximately equal (within an order of magnitude). When the temperature rises shown in Figure 5:12 are compared with those in Figure 5:13, the solvent material significantly impacts the heating. The creators also made this observation regarding the heating model [105].

Measurements of temperature rises shown in Figure 5:12 and Figure 5:13 were made using a trap with a wavelength of 1064 nm. At the wavelength of 1064 nm, glycerol and water have an absorption coefficient of 0.214 cm^{-1} [176] and 0.144 cm^{-1} , respectively [110].

However, as shown in Equation 5:1, thermal conductivity also plays a role in the temperature rise and can make what would otherwise be a low-heating scenario be highly heating, as can be seen with the case at 975 nm, with ethanol and water. Even though the absorption of ethanol is much lower than that of H₂O, the thermal conductivity is also lower in ethanol, which also has an impact on the temperature rise predicted.

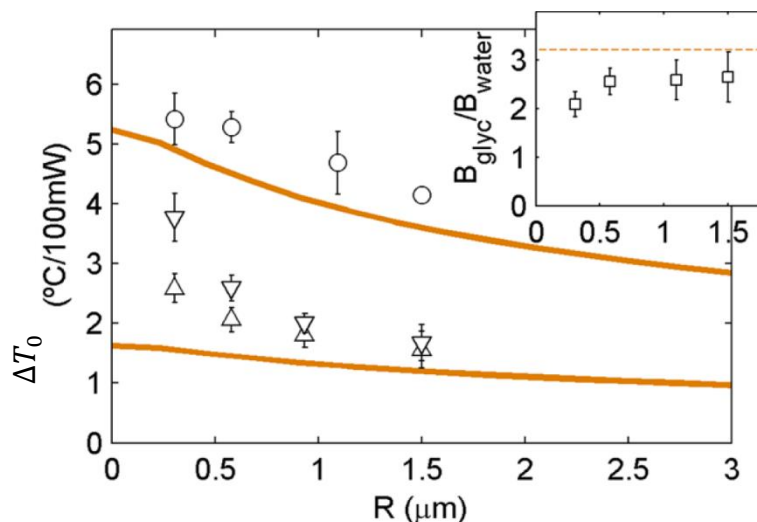


Figure 5:13: Comparison between the Peterman model and actual temperature measurements made through viscosity measurements via Stokes drag [176]. Orange lines are predictions made using the Peterman model trapping polystyrene particles of varying sizes with two solvents: upper; glycerol, and lower water. Individual points are physical measurement of temperature rises when polystyrene particles of a selection of radii were suspended in water trapping using an objective with a NA = 1.2 (Triangles) and NA = 1.3 (Inverted Triangles) and when suspended in glycerol and trapped using a NA = 1.2 objective (Circles).

Figure 5:13 compares the heating observed with an actual particle trapped in a beam and the predicted temperature rise observed by the Peterman model. Although the Peterman et al. model's predictions offer a reasonably accurate method that appears to improve in water with increasing particle size, this allows an estimate of the temperature at the interface between the suspending solution and the particle to be determined within reasonable accuracy.

Although some discrepancy exists between the temperature rise predicted by the Peterman model and the measurements made in Figure 5:13 however it would appear that this model can at least determine the order of magnitude of the heating produced. Furthermore, this temperature rise would also have minimal impact on the solubility provided the substance has a low dependence upon temperature, which is detailed in section 5.1. This slight temperature rise would have a minor impact on the stiffness of the trap, this is discussed in section 5.7.2.

5.7 Predicted Temperature Effects in Tweezer Experiments from Measurement of Absorption

Using Peterman's model, as examined in section 5.6 allows the temperature rises when tweezing in experimental conditions to be estimated. This requires that absorption measurements be made of solutions at the range of solution conditions which were to be used in the tweezers to examine nucleation and growth as these have not been determined previously before temperature rise estimates can be performed.

5.7.1 Absorption of Solutions

Absorption of solutions was measured using two independent methods to verify each other and allow averages to be calculated at each concentration evaluated to determine the trends. Since the absorption of the pure solvents (H_2O and D_2O) are well known, this allows for any systematic error to be corrected [110].

Known concentrations of sodium chloride and glycine solutions in H_2O and D_2O were made up. The solutions' absorption was tested on two pieces of equipment, the Cary5000 UV-Vis-NIR Spectrophotometer and the Bruker Matrix-F spectrometer.

Samples which used deuterium oxide as the solvent were not performed using the Matrix-F due to the prohibitive nature of the large solution volume required for testing.

The absorption coefficient for sodium chloride solutions in water and deuterium oxide are shown in Figure 5:14 and Figure 5:15 alongside the relative changes of absorption coefficient as the concentration of the solvent was increased with reference to the base pure solvent.

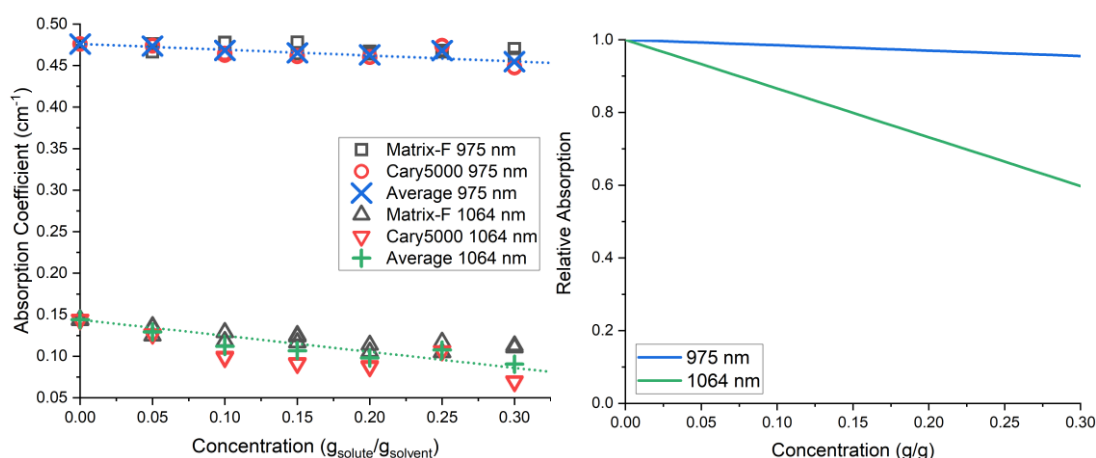


Figure 5:14: Left; Absorption Coefficient of Solutions of Sodium Chloride in Deionised water between concentrations of 0 g/g and 0.3 g/g at 975 nm and 1064 nm. Right: relative change of absorption coefficient from the pure solvent with increasing solute concentration.

In the case of each wavelength examined here, as the concentration of sodium chloride increases, the absorption of the solution decreases. The concentration increase impacts the measurements made at 1064 nm as the magnitude of the decrease is greater.

Although the base absorption when using D₂O is lower than when using H₂O, the addition of NaCl to the D₂O still causes the absorption coefficient to fall with increasing concentration of NaCl at both wavelengths examined, as shown in Figure 5:15. The relative change between the two wavelengths was much reduced in the examination of solutions in D₂O than H₂O.

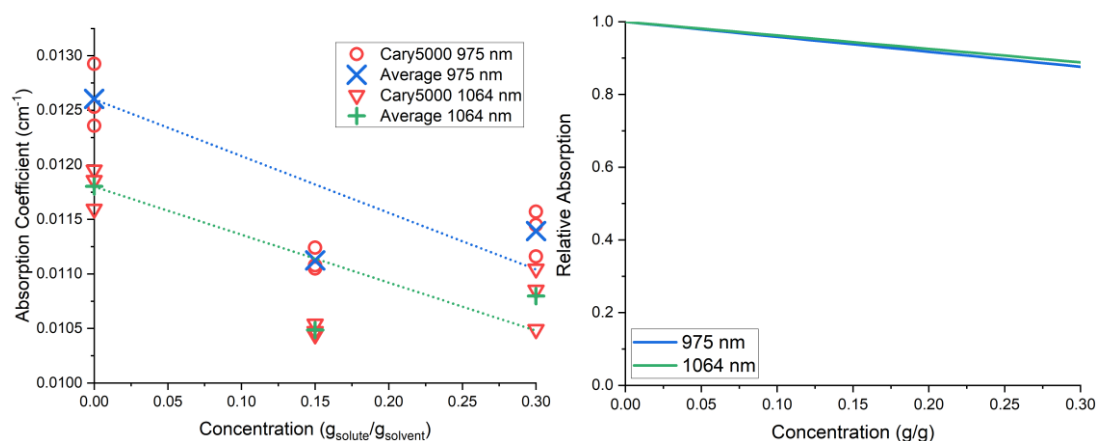


Figure 5:15: Left; Absorption Coefficient of Solutions of Sodium Chloride in Deuterium Oxide between concentrations of 0 g/g and 0.3 g/g at 975 nm and 1064 nm. Right: relative change of absorption coefficient from the pure solvent with increasing solute concentration.

Figure 5:14 and Figure 5:15 shows linear or almost linear changes in absorption coefficient are in line with the previous measurements, as determined for a range of concentrations of sodium chloride in water between 300 nm and 700 nm [172]. However, at the wavelength of 975 nm, it appears that, unlike the measurements between 300 nm and 700 nm at 975 nm, increasing the concentration causes the absorption coefficient to decrease almost linearly with concentration across a wide range of wavelengths. However, the relative increase in absorption decreases as the wavelength increases from approximately 460 nm to 700 nm [172]. When examining the relative change in the case of both solvents, however, at the same concentrations, both the absorption of the wavelengths is different, and the relative impact of the presence of sodium chloride is different. The primary reason for this difference is the order of magnitude difference observed in both pure solvents at this wavelength (975 nm) [110]. Another set of runs has been completed using glycine in water to compare different solutes on the absorption of the pure solvent. This is shown in Figure 5:16 and Figure 5:17

for glycine solutions in H₂O and D₂O, respectively alongside relative changes of the trends determined.

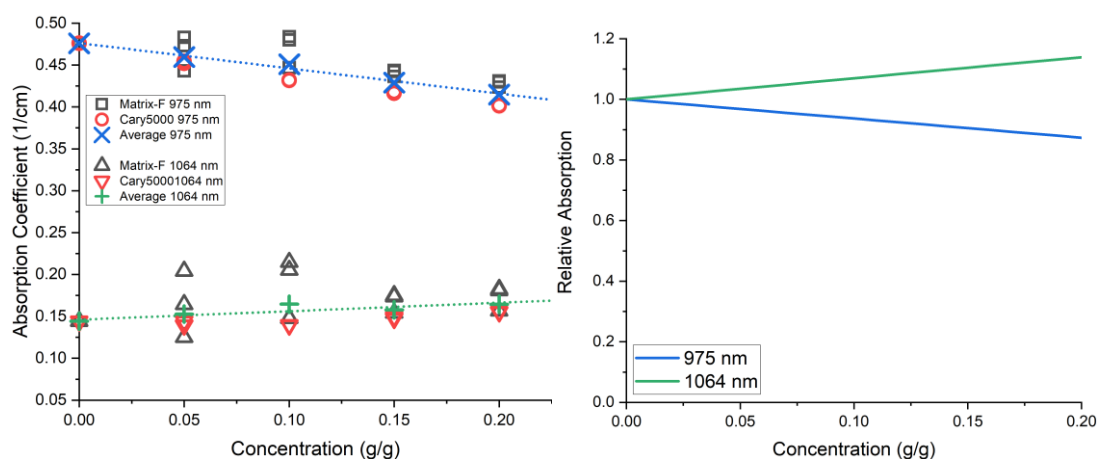


Figure 5:16: Left; Absorption Coefficient of glycine solutions in deionised water between concentrations of 0 g/g and 0.2 g/g at 975 nm and 1064 nm. Right: relative change of absorption coefficient from the pure solvent with increasing solute concentration.

When examining solutions of glycine in H₂O increasing the concentration of the solute, the effect on the absorption appears to depend on the examined wavelength, as shown in Figure 5:16. As at 975 nm, the absorption coefficient decreases, and it increases at 1064 nm with increasing concentration of glycine from the pure solvent value. However, when glycine solution based on D₂O were examined at the two wavelengths, the absorption appeared to decrease with increasing concentration. At the same time, the change's magnitude depended on the wavelength of the light being used for testing, where the decrease was much greater when testing with 975 nm than 1064 nm, as shown in Figure 5:17.

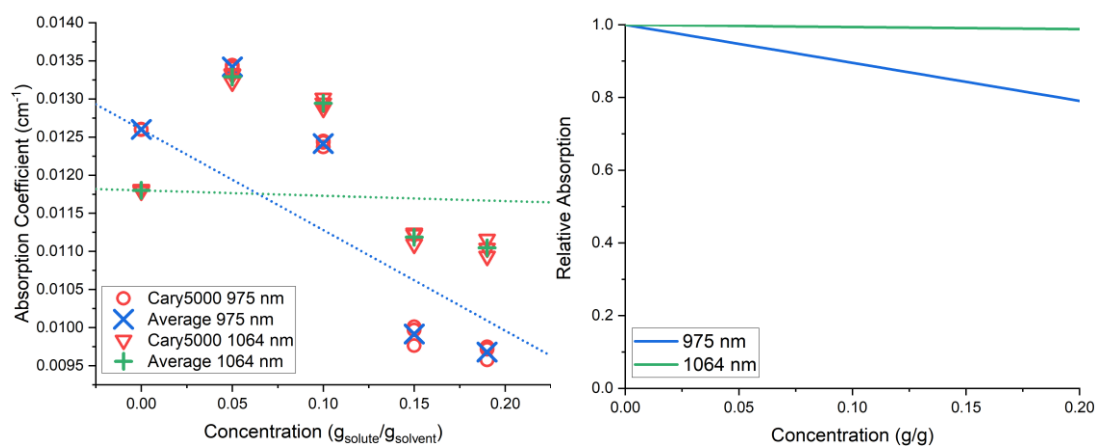


Figure 5:17: Left; Absorption Coefficient of glycine solutions in deuterium oxide between concentrations of 0 g/g and 0.2 g/g at wavelengths of 975 nm and 1064 nm. Right: relative change of absorption coefficient from the pure solvent with increasing solute concentration.

The measurement of the solutions' absorptions allows temperature rises to be estimated from the linear fits of the data gathered for concentrations that were not directly examined. It may be said that the linear fit for the data Figure 5:17 may not be entirely suitable but was decided that it would be used due to the use of linear fittings on the remainder of the absorption data which gave decent fittings to the data gathered. The fittings of the absorption coefficient when using D₂O were not performed with as many data points as those performed with H₂O, therefore it is likely that the errors involved with the fittings are higher than that those when H₂O was tested. Although since the changes in the temperature rise that are predicted when altering concentration are small, even if significant errors are made with the exact nature of the trend. It is highly unlikely that this would have a meaningful impact on the temperature rises predicted.

5.7.2 Impact of Changing Solvent

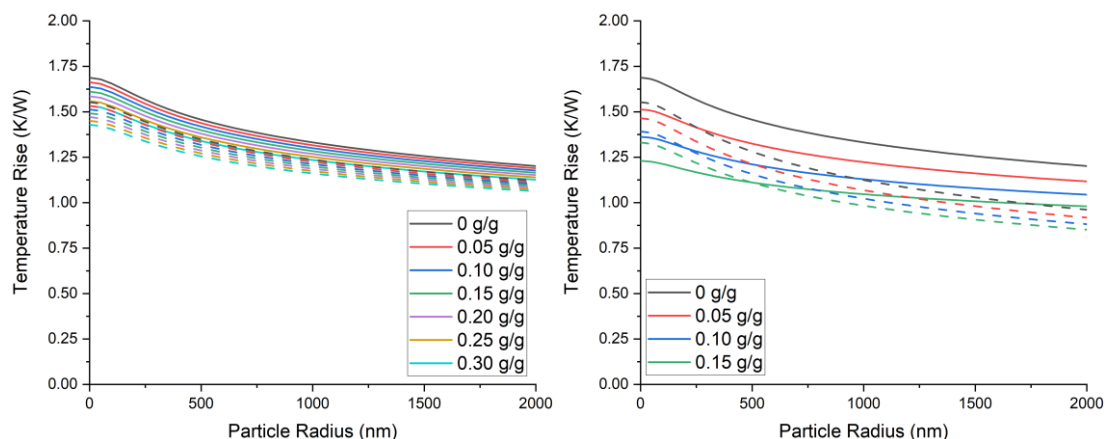


Figure 5:18: Left; Predicted temperature rise from Peterman model at the interface of silica particles in suspension medium of a sodium chloride solution in deuterium oxide at different concentrations of sodium chloride (0-0.30 $g_{solute}/g_{solvent}$). Trapped using a 975 nm laser (Solid Lines) and 1064 nm laser (Dashed Lines). Right; Predicted temperature rise from Peterman model at the interface of silica particles in suspension medium of a glycine solution in deuterium oxide at different concentrations of glycine (0-0.15 $g_{solute}/g_{solvent}$). Trapped using a 975 nm laser (Solid Lines) and 1064 nm laser (Dashed Lines)

Using the determined absorption for the ranges of solutions reported in section 5.7.1 as well as the known thermal conductivities of these species in solution [177], [178], the Peterman model used in Equation 3:14 was used to determine the temperature rises with and without the presence of particles held at the centre of the trap geometry. In all cases examined, the ‘pure’ solvent cases were the “worst-case scenarios” for laser-induced heating where the increasing concentration caused the temperature rise predicted to decrease. If a silica particle was introduced to a particle free trap this would reduce the overall temperature rise that would be observed across the range of concentrations examined. When trapping a particle of any size in this range, it can also be observed that increasing the concentration of the solution will decrease the observed temperature rise. With the maximum possible laser power of the two lasers used in this thesis being 330 mW and 2 W for 975 nm and 1064 nm respectively could result in a ~ 0.5 K when using the 975 nm laser and a ~ 4 K for the 1064 laser, before accounting for any power losses in the transmission of the laser through the optics of the tweezers.

When normal water (H_2O) is used in place of deuterium oxide (D_2O), the temperature rise that would be observed would be approximately 2-3 higher. This is shown in Figure 5:19. One point of note would be that even though the absorption of solutions of glycine in water at 1064 nm increases with concentration, the predicted temperature rise decreases, due to the also increasing thermal conductivity increasing to more than enough to compensate for this

increasing absorption, therefore it is clear that factors other than the absorption must be considered.

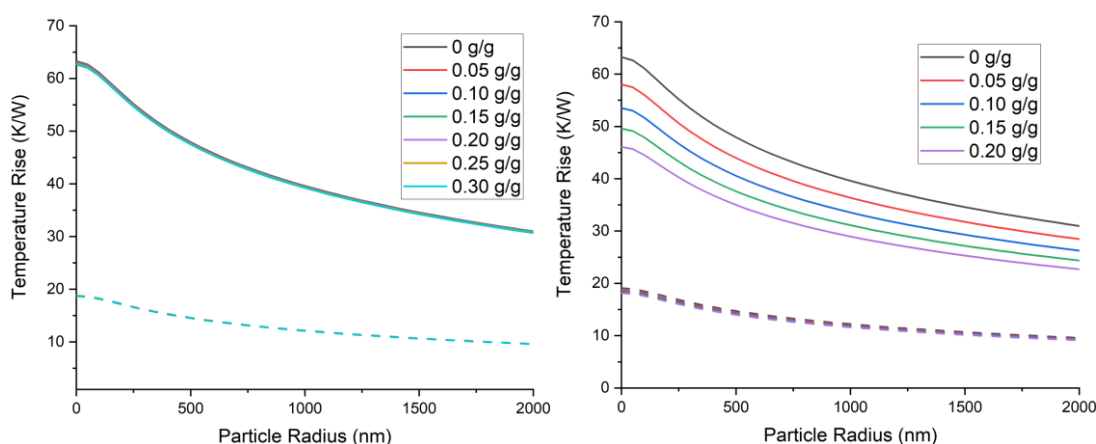


Figure 5:19: Left; Predicted temperature rise from Peterman model at the interface of silica particles in suspension medium of a sodium chloride solution in water at different concentrations of sodium chloride (0-0.30 $g_{solute}/g_{solvent}$). Trapped using a 975 nm laser (Solid Lines) and 1064 nm laser (Dashed Lines). Right; Predicted temperature rise from Peterman model at the interface of Silica Particles in suspension medium of a glycine solution in water at different glycine concentrations (0-0.20 $g_{solute}/g_{solvent}$). Trapped using a 975 nm laser (Solid Lines) and 1064 nm laser (Dashed Lines)

To allow a direct comparison the maximum possible temperature rises, per Watt of laser power in the case of each pure solvent isotopologue wavelength combination are shown in Table 5:2 when operating at the maximum possible trapping distances, the vertical distance from the coverslip to the centre of the trap geometry, as the maximum possible distance would maximise any potential temperature rise, the case of the objective lens supplied with the OTKB setup this was 60 μm as determine from the working distance of the objective lens and the thickness of the coverslip used.

Table 5:2: Predicted maximum temperature rises in pure solvent per Watt of laser power used.

| Predicted Temperature Rises (K/W) | Wavelength (nm) | |
|-----------------------------------|-----------------|------|
| | 975 | 1064 |
| H ₂ O | 63.3 | 19.1 |
| D ₂ O | 1.7 | 1.6 |

These slight increases in temperature would have a minimal impact on the determined trap stiffness and the dissolved substance's solubility. If it were to be assumed that the trap stiffness determined is using the equipartition method. Linking the variance in a trapped particle's position in one axis to the absolute temperature experienced by the system:

$$\frac{1}{2}k_B T = \frac{1}{2}k_i \langle x_i \rangle^2$$

If assumed that the variance in position is determined through measurements, the only other factor that must be determined is temperature. Since this is in the units of Kelvin and occurring at room temperature (20 °C or 293.15 K)

$$k_i = \frac{k_B T}{\langle x \rangle^2}$$

$$\Delta k_i = A \Delta T$$

$$\frac{\Delta k_i}{k_i} = \frac{A \Delta T}{A T}$$

$$\frac{\Delta k_i}{k_i} = \frac{\Delta T}{T}$$

Where:

$$A = \frac{k_B}{\langle x \rangle^2}$$

Therefore, each Kelvin of heating that the system would be subjected to would only result in a 0.34 % change in trap stiffness. Therefore, when the trap-induced heating is low, this would result in a minimal change to the trap's stiffness. And in the cases of the temperature rises given in Table 5:2 the change in the trap stiffness that would occur at the maximum powers (330 mW for 975 nm and 2 W for 1064 nm, with the additional assumption that the variance in the position of the particles would be fixed to allow a comparison) of the lasers from a solution that would exist before the action of the tweezers at 25 °C is given in Table 5:3.

Table 5:3 Example Changes in Trap Stiffness with increases in temperature.

| Change in Trap Stiffness (%) | Wavelength (nm) | |
|------------------------------|-----------------|------|
| | 975 | 1064 |
| H ₂ O | 7 | 13 |
| D ₂ O | ~0 | 1 |

This ability to neglect the temperature increase caused by the laser is similar to other investigations in crystallisation directly induced by optical tweezers [128], [145]. Measurements of temperature rises in deuterium oxide caused by a 1064 nm laser using fluorescence where the absorption coefficient is approximately equal to that at 975 nm show that temperature rises were found to be on the same order of magnitude predicted by the *Peterman* model [143]. Examinations of conductance in a nanopore have agreed with temperature rises predicted by the *Peterman* model [179]. Even if this temperature rise were used as the prediction, the laser's low power would still only give rise to less than a 1 K rise in temperature, which would have a negligible impact on the stiffness of the trap.

Since sodium chloride has very minimal temperature dependence, i.e. large changes in temperature has very little impact on the solubility experienced [180]–[183] while glycine would be more impacted due to the solubility being more temperature dependent. This temperature rise would also have a negligible impact on the solubility experienced this is discussed more in section 5.1.

5.7.3 Impact of Trapping Material and Trapping Distance

As demonstrated by *Catala* [107], shown in Figure 5:12 when materials other than silica are used as trapping media the internal structure of the trapped bead is no longer isothermal. Therefore, the temperature at the centre of the trapped bead would be different to that at its surface with the suspension medium. This adds a further layer of complexity where the model developed by *Peterman et al.* [105] deals with the temperature at the centre of the trap geometry. This would not be the temperature that would be experienced by the solution in contact with the surface of the bead. This surface temperature would be the accurate temperature to use to determine what the solubility and therefore the supersaturation would be of the solution at this point. In the soda-lime glass calculation, the calculation of the interface temperature involves an additional step than that of the silica, as the soda-lime glass has not been demonstrated to be isothermal through the radius of the trapped particle, as was the case with silica as shown in Figure 5:12 [176]. The interface temperature between the liquid/solution and sphere was approximated using the geometry in Figure 5:20, where R_1 is the radius from the centre of the geometry to the radius of the volume of the focus [105], [107], R_2 is the radius of the trapped particle (r_p in Figure 5:11, and requires that $r_2 > r_1$, due to the assumptions made in the model's development as the particle has to have a larger radius than the focus) and R_3 is the distance from the centre of the trap geometry to

the heat sink (Z in Figure 5:11). This heatsink was assumed to be present in the suspending substance in all directions at Z distance away from the centre of the trap geometry which would exist at T_3 , in essence the vast relative quantity of material further away from the trap's centre at greater distances was assumed to be equivalent to the heatsink. In this system, the rate of energy transfer is assumed to be constant. This heat transfer was considered in two separate sections: the transfer through the particle (Q_{1-2}) and the transfer through the surrounding fluid (Q_{2-3}) [143]. Were T_1, T_2 & T_3 are the corresponding temperatures at positions r_1, r_2 & r_3 respectively. The temperature at r_1 is approximated with the temperature at centre as determined by the *Peterman* model where at radii less than r_1 the temperature is assumed to be isothermal. This model also assumes a point source for the heat supplied therefore $Q_{1-2} = Q_{2-3}$.

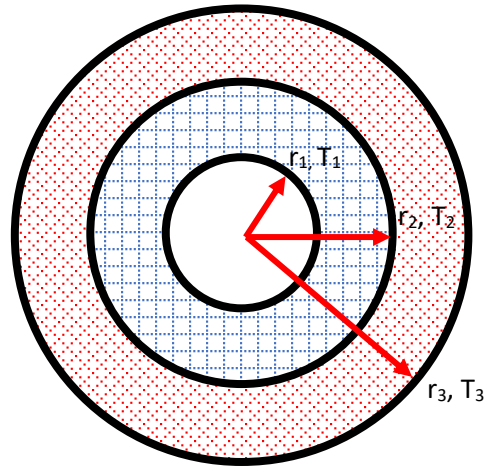


Figure 5:20: Simplified Geometry of the thermal system of a trapped particle and its surrounding suspension material. Blue Vertical Grid Area, solute subject to soda lime thermal conductivity (K) and Red Diagonal Grid Area, volume subject to suspension materials thermal conductivity of the suspension material. Explanation of Dimensions and Temperatures given above in the text. R_1 ; radius of trap centre volume (155 nm for 975 nm laser and 169 nm for 1064 nm). R_2 ; radius of trapped particle. R_3 ; radius of spherical shell at the distance of the coverslip acting as the heat sink, assumed to be 60 μm .

$$Q_{1-2} = \frac{(4\pi k_{SL} r_1 r_2 (T_1 - T_2))}{(r_2 - r_1)}$$

$$Q_{2-3} = \frac{(4\pi k_{Liq} r_2 r_3 (T_2 - T_3))}{(r_3 - r_2)}$$

$$Q_{1-2} = Q_{2-3}$$

$$\frac{(4\pi k_{Liq} r_2 r_3 (T_2 - T_3))}{(r_3 - r_2)} = \frac{(4\pi k_{SL} r_1 r_2 (T_1 - T_2))}{(r_2 - r_1)}$$

$$\frac{(k_{Liq} r_3 (T_2 - T_3))}{(r_3 - r_2)} = \frac{(k_{SL} r_1 (T_1 - T_2))}{(r_2 - r_1)}$$

$$\frac{k_{Liq} r_3}{(r_3 - r_2)} T_2 - \frac{k_{Liq} r_3}{(r_3 - r_2)} T_3 = \frac{k_{SL} r_1}{(r_2 - r_1)} T_1 - \frac{k_{SL} r_1}{(r_2 - r_1)} T_2$$

$$\frac{k_{Liq} r_3}{(r_3 - r_2)} T_2 + \frac{k_{SL} r_1}{(r_2 - r_1)} T_2 = \frac{k_{SL} r_1}{(r_2 - r_1)} T_1 + \frac{k_{Liq} r_3}{(r_3 - r_2)} T_3$$

$$T_2 \left(\frac{k_{Liq} r_3}{(r_3 - r_2)} + \frac{k_{SL} r_1}{(r_2 - r_1)} \right) = \frac{k_{SL} r_1}{(r_2 - r_1)} T_1 + \frac{k_{Liq} r_3}{(r_3 - r_2)} T_3$$

Where:

k_{SL} Thermal Conductivity of the Trapped Particle (W/(m K))

k_{liq} Thermal Conductivity of the Suspension Material; (W/(m K))

When Q_{1-2} and Q_{2-3} are considered equal; this allows the interface temperature to be determined by:

$$T_2 = \frac{\left(\left(\frac{k_{SL} r_1}{r_2 - r_1} \right) T_1 + \left(\frac{k_{liq} r_3}{r_3 - r_2} \right) T_3 \right)}{\frac{k_{SL} r_1}{r_2 - r_1} + \frac{k_{liq} r_3}{r_3 - r_2}}$$

In the case of soda-lime glass, the predicted temperature rise at the particle solution interface is shown in Figure 5:21. It can be seen that the absorption and thermal properties of the surrounding liquid or solution have a much more significant impact than that of the trapped particle, as the modelling for a particle with a significantly higher absorption only has a minor impact on the maximum temperature that would be experienced at the interface of the suspension fluid and the particle.

Based upon the work the *Peterman* model it has been possible to determine the temperature that would exist at the centre of the trap geometry, however as this would not be what would be experience at the surface of the particle and therefore by the solvent directly in contact with the trapped particle.

Figure 5:21 describes the associated temperature rise estimate from that of the heatsink at the surface of the non-silica, and therefore non isothermal, particles, as this would be the

maximum temperature that would be experienced by the suspending material, which in the case of a crystallising system what would be the source of the nuclei, when trapping was performed using either a 975 nm or 1064 nm laser. Where the temperature appears to peak regardless of the concentration used at ~ 5.5 K/W when trapping a ~ 400 nm radius sphere. Due to the assumptions that were made in the development of the model determining the temperature rises for smaller particles is not possible as this requires that the radius attributed to the focal volume be smaller than that of the particle ($r_2 > r_1$), therefore this is a limitation of this model. This limiting factor also applies to the rises determined in Figure 5:22.

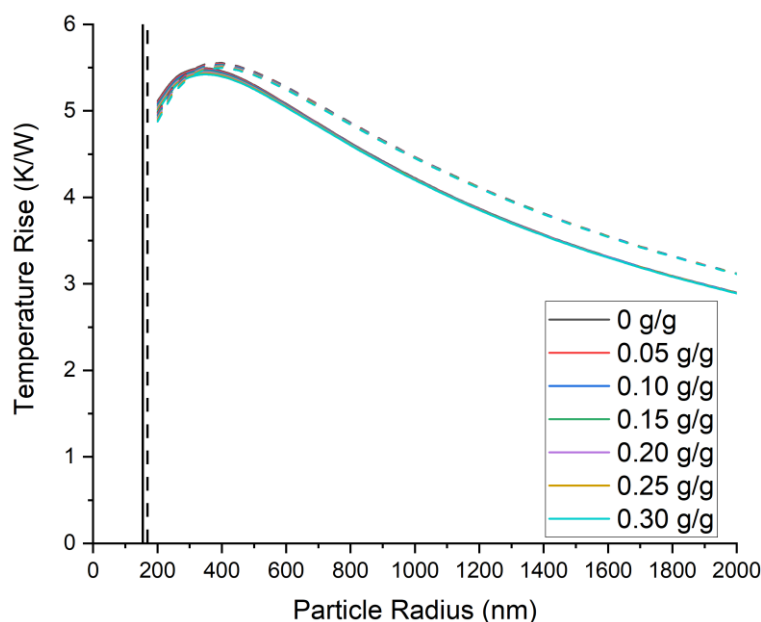


Figure 5:21: Temperature rise predicted at the interfaces of soda lime particles at their interface with the suspension media. Calculated in this case of solutions of NaCl in D_2O up to a concentration of 0.30 g/g when the focus is located $60 \mu m$ from the heatsink with the trapping performed using a 975 nm laser (solid vertical line, giving an $r_1 = 155$ nm) and 1064 nm laser (dashed vertical lines, giving an $r_1 = 169$ nm).

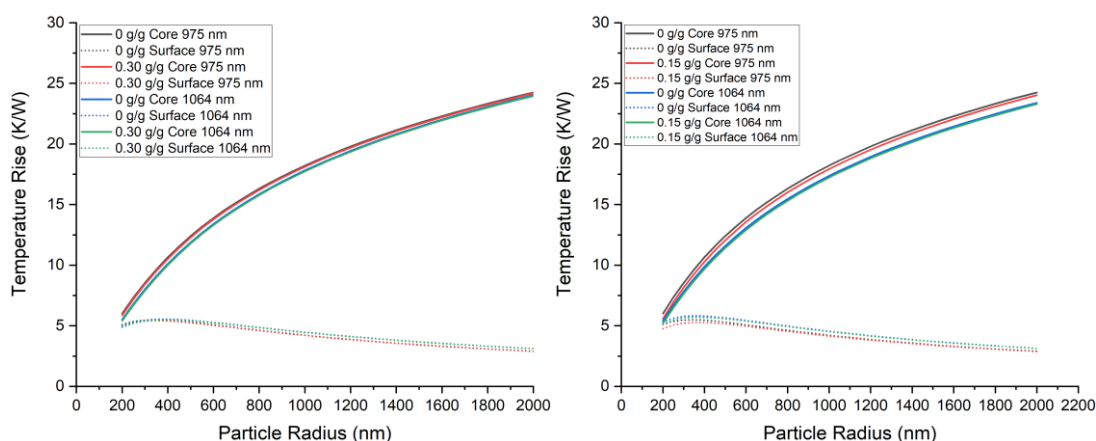


Figure 5:22: Left; Comparison between the centre temperature rise from that of the heatsink of a trapped soda-lime particle and the temperature that would exist at the interface with suspension solution when trapped using a 975 nm laser in a 0 and 0.30 $\text{g}_{\text{solute}}/\text{g}_{\text{solvent}}$ solute of NaCl using D2O as a solvent. Right; Comparison between the centre temperature rise from that of the heatsink of a trapped soda-lime particle and the temperature that would exist at the interface with suspension solution when trapped using a 975 nm laser in a 0 and 0.15 $\text{g}_{\text{solute}}/\text{g}_{\text{solvent}}$ solute of Glycine using D2O as a solvent.

From Figure 5:22, it is important to note that the temperature at the centre of the trapped particle increases steadily as the particle's radius increases. This is due to the particle's higher absorption and lower thermal conductivity. However, the temperature at the interface between the particle and the suspension material does not increase continuously with size. When NaCl is added as a solute at a concentration of 0.30 $\text{g}_{\text{solute}}/\text{g}_{\text{solvent}}$, there is minimal impact on either temperature, indicating minimal change due to the dissolved species. One aspect of this that is highlighted by Figure 5:22 is that as the particle continues to grow in size the temperature experience at the core continues to rise given equivalent trapping conditions therefore this may limit the power that can be used to trap such particles as they may become unstable due to the heating experienced.

The estimates of temperature rises made in Figure 5:18, Figure 5:19, Figure 5:21 and Figure 5:22 were made using the maximum theoretical trapping distance (60 μm) possible using the Modular Optical Tweezers. It was also assumed that this heatsink temperature existed in all directions surrounding the centre of the optical tweezers, partially due to this being the closest surface and in all other directions the environment would continue much further than in the direction to the heatsink.

Figure 5:23 shows that as the distance between the trapped object and the inner surface decreases, the temperature rises for any given situation decreases. Therefore, in any actual trapping experiments, these temperatures rise are the maximum expected to occur. This has the built in assumption that since the lower coverslip is in contact with the relatively large

mass of the tweezing optomechanics and is therefore isothermal in nature, allowing this to be modelled as an isothermal heat sink.

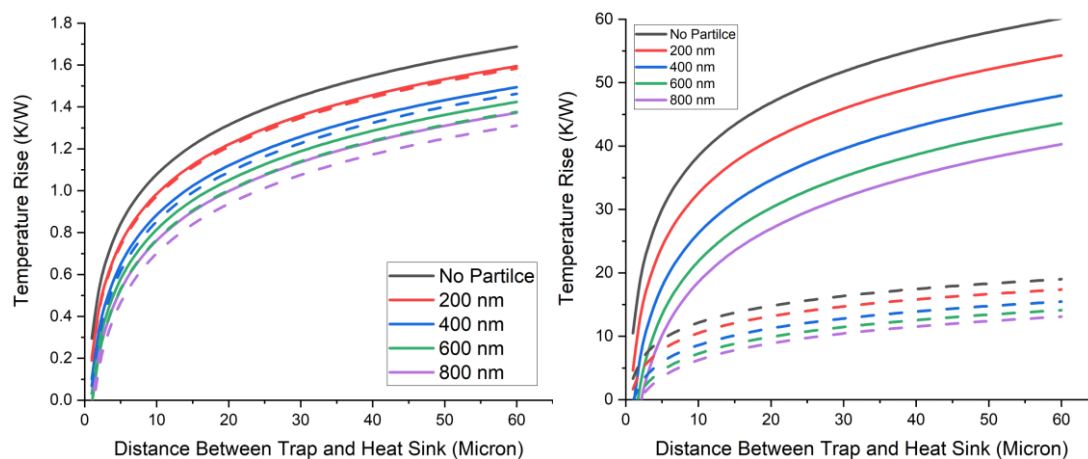


Figure 5:23: Left; Predicted Temperature Rise of Differing Radius Silica Particles in Pure Deuterium oxide at various trapping distances trapped using a 975 nm laser (Solid Lines) and a 1064 nm laser (Dashed Lines). Right; Predicted Temperature Rise of Differing Radius Silica Particles in pure water at various trapping distances trapped using a 975 nm laser (Solid Lines) and a 1064 nm laser (Dashed Lines).

Although it is important to understand heat transfer in the geometry surrounding the tweezing focus, Figure 5:23 highlights the ability of a nearby surface acting as a heatsink to dominate this relationship. Therefore, this distance (between the focus and heatsink) becomes one of the most important factors. Varying this distance can induce significant differences, especially when using H₂O as a solvent (suspension medium), which is ever more needed when using a highly heating wavelength (975 nm).

5.8 Conclusions

To allow crystallisation to be studied in the context of optically trapping including with spherical particles requires multiple considerations not usually part of the design of any crystallisation process. The main two being the refractive indices and absorption of components to one allow any trapping to occur and to determine the magnitude of any laser induced heating, respectively. In an ideal situation, this would allow a wavelength to be chosen to allow the trapping to occur while minimising the predicted temperature rise. However, in typical situations, the main restriction placed upon systems is the lasers and other optics available. Therefore, standard water can be substituted with deuterium oxide in aqueous systems for common trapping wavelengths should the laser wavelength caused excessive heating. The heating caused can be estimated in these situations, and its effects are considered. Therefore, based on the calculations in this chapter it would be possible to

neglect any heating when using D₂O as the base solvent. Due to the low temperature elevations predicted in cases of typically trapping powers.

6 Comparison of Nucleation and Growth Kinetics in Water and Deuterium Oxide

Sections of this chapter have been published as part of

J. Hoffmann, **J. Flannigan**, A. Cashmore, M.L. Briuglia, R.R.E. Steendam C.J.J. Gerard, M.D. Haw, J. Sefcik, J.H. ter Horst. The Unexpected Dominance of Secondary over Primary Nucleation. *Faraday Discussions*, 2022, 235, 109-131. DOI: 10.1039/D1FD00098E

To allow any results from the optical tweezers to be fully understood within the appropriate context, any impact of non-typical solvent isotopologues, in this case, deuterium oxide (D_2O), on crystallisation characteristics (solubility, nucleation and growth) must be fully understood on its own. Since it is possible that the effects on crystallisation can be highly specific to individual solvent/solvent systems, each of these is required to be explored to some extent. In this chapter, two solutes (NaCl and glycine) were tested to understand the impact of deuterium oxide on their crystallisation from solution compared to regular 'light' water (H_2O). In addition to allowing results elsewhere in this thesis to be interpreted within an appropriate context, these results are of interest in their own right as the effect of D_2O are not typically studied in other general crystallisation investigations.

6.1 Experimental

6.1.1 Solubility and Metastable Zone Width

Metastable zone width measurements were performed with two different solutes (glycine and NaCl) using two different solvents (H_2O and D_2O), using the Crystal16 apparatus, where 1 g of solvent was added to a 1.5 ml HPLC glass vial. An appropriate mass of solute was added to each vial to get the range of concentrations required to determine solubility and metastable zone width. Each vial was subjected to the heating and cooling cycle shown in Figure 6:1, where the temperature is altered at a rate of 0.3 K per minute, increasing and decreasing after reaching 70 °C the first time. Holds at both 70 °C and 5 °C were held for 30 minutes, with the first rapid heating ramp not used for analysis.

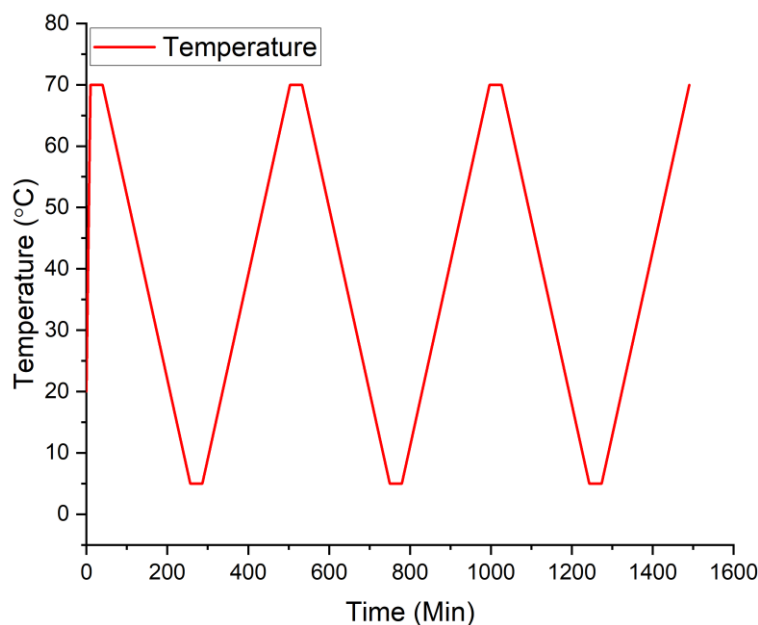


Figure 6:1: Temperature Cycle used for Solubility and Metastable Zone Width Determinations.

Through the cycle shown in Figure 6:1, each vial was agitated using a 2 mm Teflon-coated magnetic stirrer bar set at 700 RPM. Transmissivity measurements were taken at one-second intervals. At the end of each high-temperature hold, the instrument was tuned (the transmissivity reading taken at that point was considered to be 100 % transmissivity). To be considered valid, measurements, changes in transmissivity for cloud points (MSZW) and clear points (Solubility) had to have occurred during the temperature ramps, and measurements of clear or cloud points (changes in transmissivity) during either hold, low or high temperatures, were not considered valid and were excluded from the analysis.

6.1.2 Induction Time Measurements

From the solubilities measured in section 6.1.1, supersaturations were selected according to the indicated Van't Hoff fits (fitting the natural logarithm of the mole fraction against the inverse of the absolute temperature), and induction time measurements made at the two solvent scales (Crystal 16, 1 g and Crystalline, 3 g) [185].

6.1.2.1 Agitated Induction Time Measurements

Induction times were measured using the temperature profile shown in Figure 6:2, where all measurements of induction times were performed at 25 °C. This temperature cycle consisted of temperature ramps of 5 K per minute, 30-minute holds at 70 °C, and 4-hour holds at 25 °C. Similarly, to the metastable zone width measurements, tuning was performed at the end of each high-temperature hold. A uniform agitation speed was not applied to all induction time measurements and is therefore detailed individually where induction times are reported.

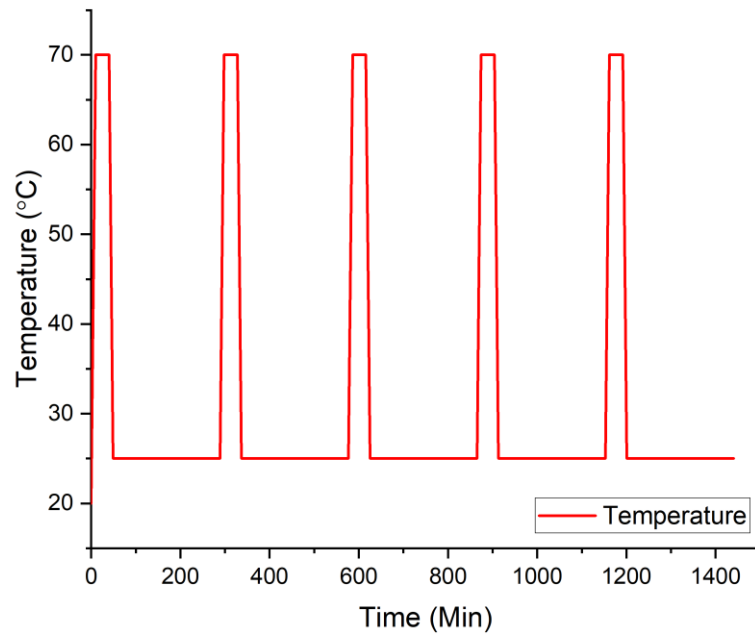


Figure 6:2: Temperature Cycle used for agitated induction time measurements.

Induction times were measured using the transmissivity measurements in Crystalline and the Crystal16. Transmissivity measurements were taken at one-second intervals for both instruments. The Crystalline also allows analysis to be performed on the particles through image analysis taken at no less than 30-second intervals. These images were taken to determine the secondary nucleation and growth rates detailed in sections 6.5 and 6.4, respectively.

Although measuring multiple inductions at small volumes where the distribution observed can be used to determine nucleation rates and growth times using the model developed by Jiang and ter Horst [48] where a primary nucleation rate (J) and growth time (t_g), to account for the time delay between the occurrence of nucleation and detection, are determined. using a small number of individual induction time measurements can result in significant errors in the nucleation rates and growth times calculated [49]. However, even large datasets are still subject to significant error, requiring vast data sets to have any appreciable impact on error reduction.

In the measurement of individual induction times, during individual cycles, monitoring the nucleation could have three outcomes: nucleation occurred during the 4-hour isothermal hold at the investigated supersaturation, nucleation occurred during cooling, or nucleation did not occur during that cycle. Only results where nucleation occurs during the 4-hour hold period are used in determining the distribution and, therefore, the primary nucleation rate.

Nucleating before the isothermal hold at 25 °C is indicated by the cumulative probability distribution having an above zero value at time 0. These are not included in the determination of primary nucleation rates. Indication of vials not nucleating by the end of the isothermal period is indicated by the data points by not reaching $P(t) = 1$ at a time equal at 240 minutes on the cumulative probability distribution.

6.1.2.2 Quiescent Induction Time Measurements

Quiescent testing was also performed at this scale. Where samples of known weight of NaCl were weighed into 1.5 mL HPLC vials, into which 1 g of solvent was added. The vials were then sealed using a basic cap. These vials were then subjected to a known temperature profile, unagitated, shown in Figure 6:3, using the Polar Bear Plus Crystal produced by Cambridge Reactor Design. Afterwards, the vials were transferred to an incubator to be observed using webcams, which took still images at regular intervals of the state of the vials.

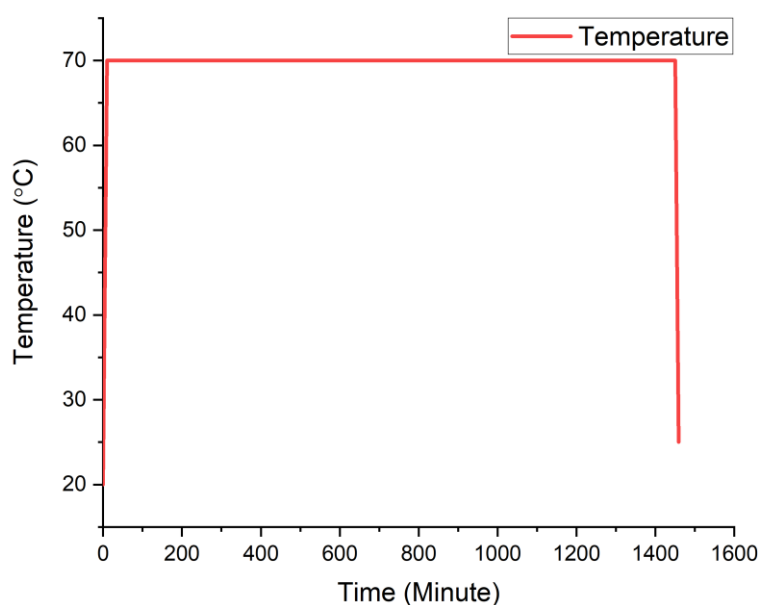


Figure 6:3: Quiescent Temperature Cycle for Polar Bear Plus Crystal

When these vials were observed at the end of the 24-hour high-temperature hold, some solid NaCl was still visible in the vials, rendering this run void. The procedure was modified as agitation was required to ensure that the solute could be fully dissolved for another run. A known mass of sodium chloride was added to a laboratory bottle, to which a known mass of solvent was added to make the final solution to the desired supersaturations. These solutions were then held at 70 °C for 4 hours while agitated using a large Teflon-coated magnetic stirrer bar using a magnetic stirring hotplate. The temperature was monitored using a thermocouple and an IR thermometer.

At the end of this temperature cycle, a mass of solution, to give 1 g of solvent within each vial, was pipetted into a 1.5 mL HPLC vial, and then closed using a basic cap within a temperature-controlled incubator at 50 °C once all of the vials were loaded and in place, the temperature was reduced to 25 °C. These vials were then monitored using webcams which took images of the vials at 5-minute intervals for 12 hours. Throughout this isothermal period, the temperature was monitored using a pair of thermocouples within the incubator. These images were then examined for the presence of crystalline material.

6.1.3 Seed Production

In addition to allowing primary nucleation to occur within the vials, a number of experiments were subjected to seeding, where a single washed crystal was introduced into the supersaturated solutions, to allow kinetic parameters to be determined (sections 6.4.2.2 & 6.5) in a more consistent way, without requiring primary nucleation to occur. To generate these seed crystals, a saturated sodium chloride solution in deionised water was created at 20 °C. This saturated solution was emptied into a petri dish and left in a fume hood to allow the liquid to evaporate. Over 24-48 hours, crystals that formed and had grown to a specific size were removed and stored for future use. The seeds used were cuboidal in shape and measured approximately 3 mm by 3 mm by 2 mm.

6.1.4 Seeded Secondary Nucleation and Growth Experiments

Seeds produced according to the procedure in section 6.1.3 were used for studies where only secondary nucleation kinetics was desired to be known, isolated from any potential effect of primary nucleation. For this section, supersaturated samples were prepared by weighing a known mass of sodium chloride into a Crystalline 8 ml vial and the correct mass of either deionised water or deuterium oxide depending upon what solvent system and supersaturation were being studied. These vials were then subjected to a single cycle of the temperature profile shown in Figure 6:4. The temperature profile used for the seeded runs is shown in Figure 6:4 as only a single temperature cycle can be performed to prevent the dissolution of the seed during the following heating ramps and high temperature holds altering the concentration of the NaCl dissolved. Where samples are heated from 20 °C to 70 °C at a rate of 5 °C per minute and held there for 30 minutes, at the end of which the software was tuned. Samples are then cooled down to 25 °C at a rate of -5 °C per minute. Samples were then held at 25 °C for 60 minutes. When samples reached 25 °C, each vial was temporarily removed to add the seed. Before adding the seed, each seed was washed via

immersion in ambient temperature pure solvent to remove any particles from the surface that would potentially initiate initial breeding [35], [36].

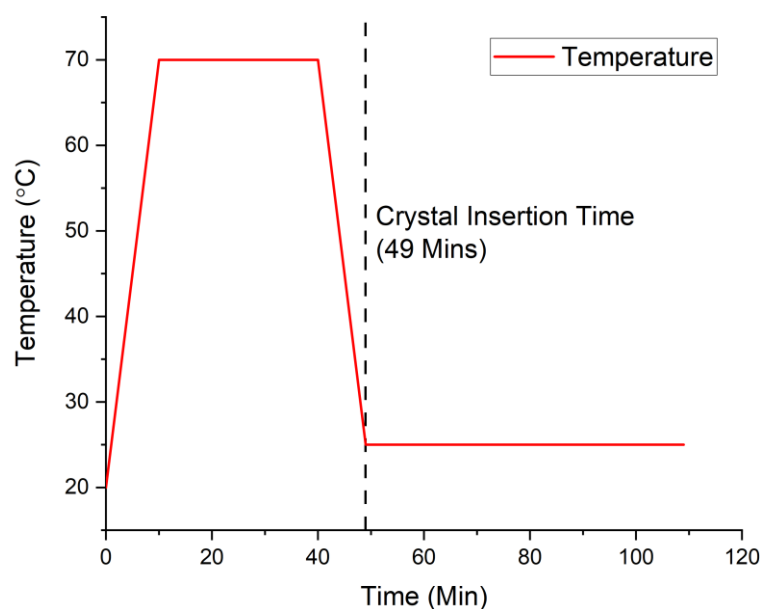


Figure 6:4: Temperature Cycle used for seeded Secondary Nucleation Studies

All seeded experiments were agitated using the short shaft three-blade overhead propeller, at a speed of 1250 RPM, as used in sections 6.3.1.3 and 6.3.2.2. This was done to prevent damage to the crystal as using a stirrer bar that could grind and break apart the brittle sodium chloride crystals used following seeding [186], [187]. The reasoning for using the overhead stirring at 1250 RPM is discussed in section 6.3.1.3.

Crowning, the formation of crystals above the liquid level within the vial, was observed sometimes with D₂O, likely due to a lower fill level in the vial since the D₂O density is higher and hence volume required for given mass is lower [49]. Therefore, when agitated, this is less able to 'sweep' the side of the vials, thereby being able to remove solid materials from the side of the vessel. Therefore, vessels were visually inspected for the presence of crowning before the seeds were added to the supersaturated solution. If crowning was observed after the temperature cycle, this data was excluded, and the cycle restarted.

No seeded experiments were performed involving glycine due to the impact that isotope exchange could have between the deuterium oxide and glycine molecules in solution [188]. Seeded studies of glycine in H₂O have been performed by *Cashmore et al.* [189]. This is the benefit of sodium chloride, as there is no possibility of solvent exchange between the solvent and the crystallising substance when using D₂O.

6.2 Solubility and Metastable Zone Widths

6.2.1 Sodium Chloride

Like most other substances, sodium chloride has a temperature-dependent solubility. However, it must be noted that this dependence is much weaker than many other solutes/solvent systems. It can be noted that the solubility of sodium chloride is lower in D₂O than in H₂O, as can be seen in Figure 6:5 across the temperature range examined. One point of note is that since the measurement of solubility was performed over a small concentration range (less than a difference of 0.02 g/g across the entire range of points) errors in measurement become important, therefore masses of solids and liquids were individually weighed to 4 decimal places, therefore the concentrations are known to a tiny uncertainty, e.g. a concentration of 0.3600 g/g would have a potential error of ± 0.0001 g/g.

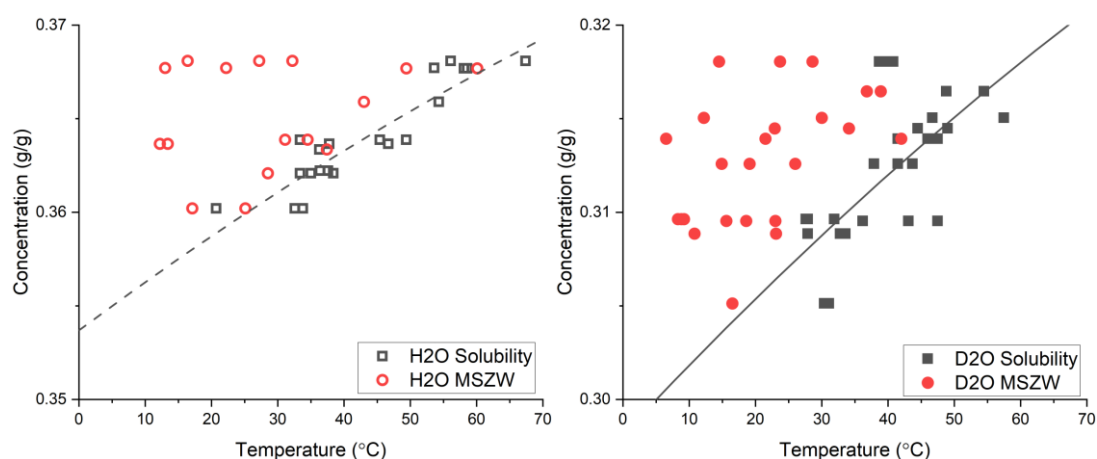


Figure 6:5: Left; Solubility, from clear points (Black Hollow Squares) and Metastable Zone Width (MSZW), from cloud points (Red Hollow Circles) of Sodium Chloride in Water. Van't Hoff fitting applied to solubility points (Black Dashed Line). Right; Solubility (Black Squares) and Metastable Zone Width (Red Circles) of NaCl in Deuterium Oxide (Black Line). Van't Hoff fitting applied to solubility points (Black Solid Line) [185].

Only limited metastable zone width measurements exist in literature for NaCl in H₂O when subject to agitation. However, these only examined the MSZW of solutions whose saturation temperature is elevated from room temperature in H₂O (50 °C – 60 °C) [190], [191]. In 1993, *Ginde et al.* reported that the metastable zone width of sodium chloride, when agitated at a speed of 100 RPM when cooled at a rate of 10 °C per hour, was 3.6 °C [190], which compared to the conditions used for the measurement of the MSZW is cooling more rapidly, however agitation is occurring more slowly, suggesting that the agitation speed used in the case of aqueous NaCl is more important than the cooling rate.

Nevertheless, this smaller MSZW should not be unexpected as the agitation speed used here was 700 RPM since increasing agitation speed has been shown to shrink the MSZW [192].

Temperature also impacts the average metastable zone width as this region shrinks with increasing saturation temperature. The determined MSZW is similar when measured in D₂O. Figure 6:6 shows good agreement between the solubility data gathered here and previously determined values sources [3], [162], [181]–[183], [193], including the data gathered when using deuterium oxide as a solvent. The data gathered here has the additional benefit of the entire experimental conditions are known unlike some of the previous sources shown in Figure 6:6. It should be noted that the previously available data when using D₂O as a solvent is much more limited as some of the sources used and detailed in Table 6:1 are multiple decades old and gathered from secondary sources. There is reasonable agreement between the data gathered here and the results from literature for the solubility in deuterium oxide [162]. However, these relate to temperatures outside the region of interest in this thesis, 25 °C – 70 °C. Overall, there is good agreement with previously published solubility data for both solvent isotopologues [180], [181].

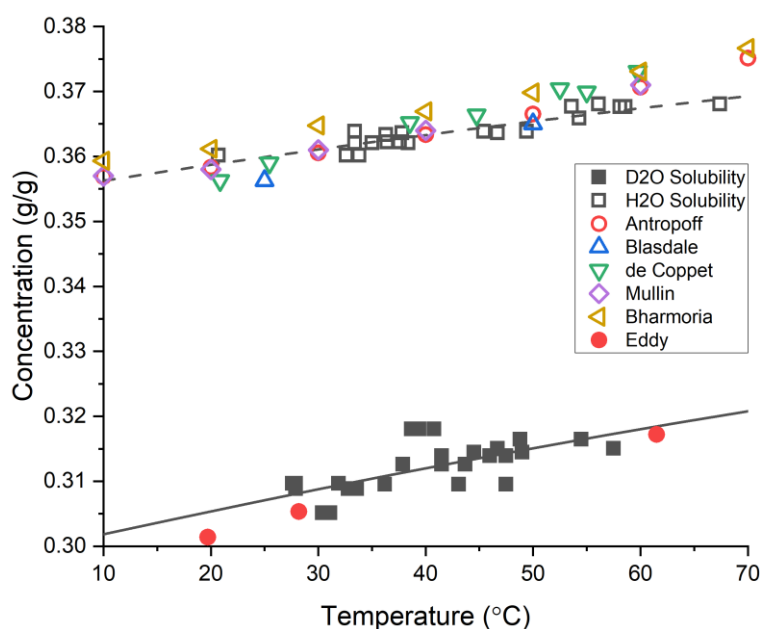


Figure 6:6: Comparison of Solubility points and Van't Hoff fittings of NaCl in H₂O (Open Symbols and Dashed Line) and D₂O (Filled Symbols and Solid Line). Also shown are various sources of solubility data from previously published sources Antropoff [181], Blasdale [182], de Coppet [183], Mullin [3], Bharmoria [193] and Eddy [162]. Methods used to determine solubility from previously published sources are shown in Table 6:1.

Table 6.1: Limited Details of reference papers for solubility of sodium chloride in water and deuterium oxide

| Reference | Method |
|-----------------|---|
| Antropoff [181] | Unknown; data gathered from Detherm Database |
| Blasdale [182] | Titration of chloride ion |
| de Coppet [183] | Unknown; data gathered from Detherm Database |
| Mullin [3] | Unknown; does not detail source of data. |
| Bharmoria [193] | Gravimetric methods |
| Eddy [162] | Sealed solubility apparatus using naked eye confirmation [194]. |

6.2.2 Glycine

Figure 6:7 reports solubility of glycine in water and deuterium oxide (clear points) and metastable zone width (cloud points) in water and deuterium oxide and a comparison of the two sets of solubility data is shown in Figure 6:8.

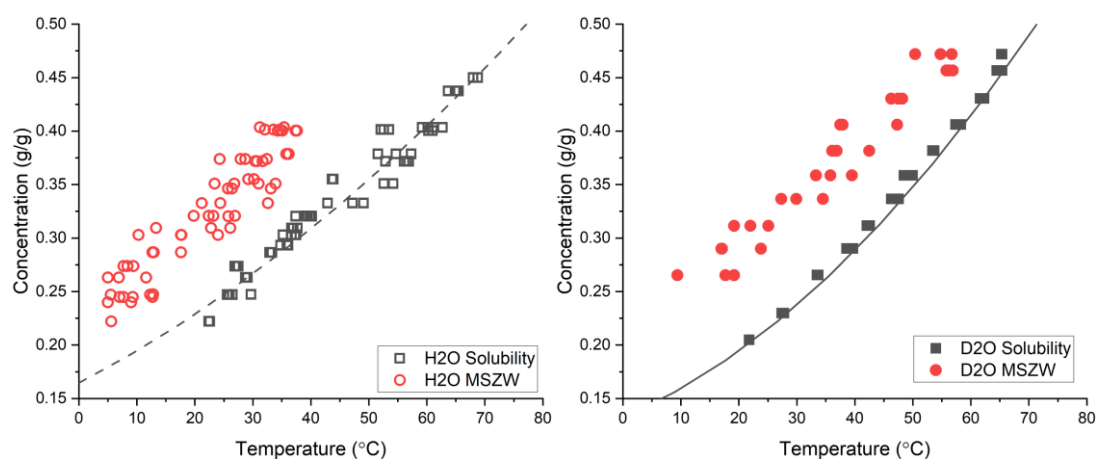


Figure 6:7: Left; Solubility from clear points (Black Hollow Squares) and Metastable Zone Width from cloud points (Red Hollow Circles) of Glycine in Water. Van't Hoff fitting applied to solubility points (Black Dashed Line). Right; Solubility (Black Squares) and Metastable Zone Width (Red Circles) of Glycine in Deuterium Oxide. Van't Hoff fitting applied to solubility points (Black Line) [185].

The solubility of glycine in H₂O agrees with a range of previous data. It was assumed that since these measurements were performed when undergoing agitation, the α polymorph of glycine was produced on crystallisation from solution [16]. The data concerning the solubility in D₂O is also in reasonable agreement when at the lowest temperatures examined. Although it could be understood as a general “rule of thumb” that substances have lower solubilities in D₂O than H₂O including amino acids [161] and carbohydrates [195], there are some exceptions to this rule, e.g. lithium fluoride [196]. The slight discrepancy between the solubility results reported for glycine in D₂O here and those in *Jelinska-Kazimierczuk et al.*

[161] may be due to their use of fully pre-deuterated solutes and solvents. Under typical circumstances of the situations examined here approximately 10 % of the deuterium atoms present in the solvent could be exchanged for the hydrogen atoms present in the glycine molecules.

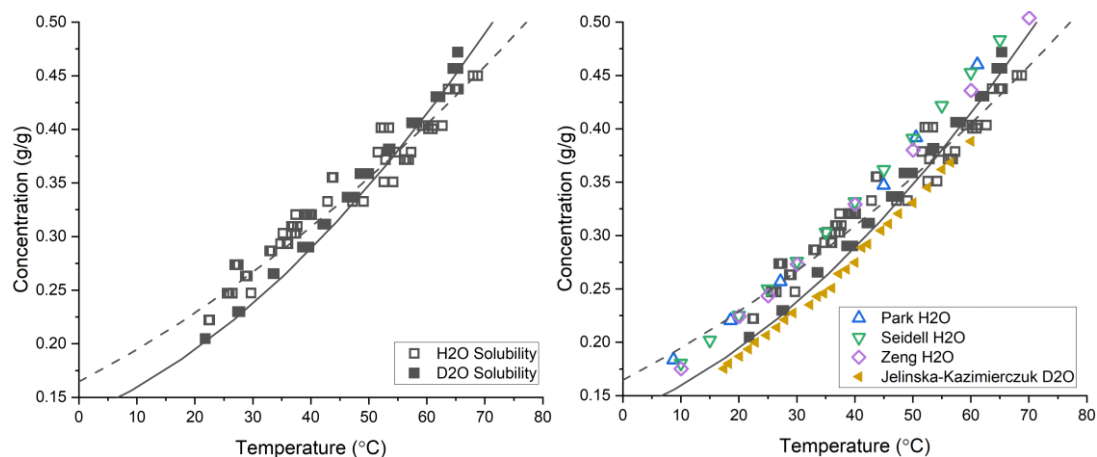


Figure 6:8: Left; Comparison of Solubility points and Van't Hoff fittings of Glycine in H₂O (Open Symbols and Dashed Line) and D₂O (Filled Symbols and Solid Line). Right; Comparison of Solubility points and Van't Hoff fittings of Glycine in H₂O (Open Symbols and Dashed Line) and D₂O (Filled Symbols and Solid Line). Also shown are various sources of solubility data from previously published sources: Park [184], Seidell [197], Zeng [198] and Jelinska-Kazimierczuk [161]. Measurement techniques of solubility for reference sources are shown in Table 6:2.

Table 6:2: Details of Glycine solubility in water Sources

| Reference | Method |
|-----------------------------|-----------------------------------|
| Park [184] | Differential Scanning Calorimetry |
| Seidell [197] | Unknown |
| Zeng [198] | Gravimetric Measurement |
| Jelinska-Kazimierczuk [161] | Refractive Index Measurements |

6.2.3 Polymorphic Effects

In previous studies of crystallising glycine from aqueous solution show that when the solution is agitated using a Teflon coated magnetic stirrer bar, the α polymorph is produced. If this stirrer bar is left in the sample unagitated, the γ polymorph is crystallised [16]. However, previous reports of solubility data for glycine in D₂O did not mention the polymorph to which this data applied [161]. Therefore, FTIR analysis was performed on the crystals produced at the end of the temperature cycle shown in Figure 6:1. Crystals were recovered from the seven highest concentration vials used for the solubility when measured in D₂O. The two polymorphs of glycine that can be produced from water by heating and cooling without

adding third chemicals, α & γ , are typically identified from a pair of absorption peaks. Both polymorphs share an absorption peak at $\sim 887\text{ cm}^{-1}$. The additional peak observed is dependent on the polymorph examined, found at wavenumbers of $\sim 910\text{ cm}^{-1}$ or $\sim 930\text{ cm}^{-1}$ for the α and γ polymorphs, respectively [16], [199]. An example of these absorbance peaks (from an α form crystal, shown in black and a crystal produced from solution in D_2O , shown in blue) is shown as the traces in Figure 6:9, with the wavenumbers used to identify specific polymorphs highlighted. When the samples were generated from solution in D_2O , the solid was removed immediately following generation as if α was formed it is possible that as it may transform to γ , as the likelihood of producing γ increases as soon as the proportion of deuterium increases beyond the natural background level of deuterium in normal water [200].

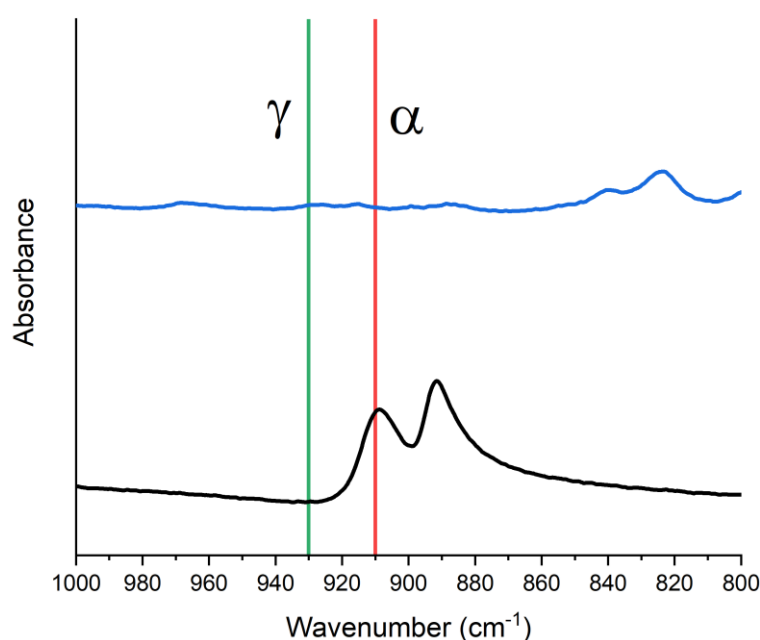


Figure 6:9: FTIR Absorbance of the glycine before dissolution in the solvent, identified as α (Black) and the Glycine recovered from solution in deuterium oxide (Blue). Vertical lines show locations of expected peaks used for non-deuterated polymorph identification of alpha (Red) and gamma (Green).

However, since these peaks were not observed in the glycine extracted from crystallisations in D_2O , this is believed to be caused by the deuteration of the crystalline glycine and therefore other peaks in the IR spectrum were first proposed to identify the polymorph of the glycine produced, as the peaks associated with certain wavenumbers are moved to alternate positions [201]. In the case of the d_3 -glycine, which is produced by the dissolution and recrystallisation of glycine in D_2O , the method used here, peaks which are associated with particular polymorphs are located at wavenumbers between $3151\text{--}2971\text{ cm}^{-1}$, $1180\text{--}1165$

cm^{-1} and $828\text{--}762\text{ cm}^{-1}$ for the α polymorph and $3094\text{--}2971\text{ cm}^{-1}$, $1167\text{--}1153\text{ cm}^{-1}$ and $824\text{--}787\text{ cm}^{-1}$ for the γ polymorph [188], [202]. A peak can be observed in the trace produced by the deuterated sample as shown by the blue line in at $\sim 825\text{ cm}^{-1}$ this could be recorded by either polymorphic form so was not an indicator of one particular polymorph.

Since these peaks largely overlap, it was decided that another entirely different technique would be required to identify the polymorph of deuterated glycine samples. When the dried crystalline samples were tested using FTIR were not ground to powder as this has been observed to initiate a γ to α polymorph transition [203], [204]. To confirm the polymorph of the remainder of same 7 examined using FTIR, X-Ray Powder Diffraction (XRPD) was performed on the remaining amount of the individual samples. The α polymorph of glycine has characteristic peaks at 19.5° and 29.7° , while the γ polymorphs peaks are present at 21° and 25.3° [16]. The XRPD pattern produced by the deuterated glycine samples were compared to a collection of simulated α and γ traces of non-deuterated glycine using the Mercury software package with data deposited in Cambridge Structural Database [205], shown in Figure 6:10 and Figure 6:11, respectively alongside the starting glycine material used to highlight if a polymorph transformation occurred. Multiple traces from the simulated data are shown for the α & γ polymorphs as multiple different depositions of have been placed in the database for each polymorph. The traces produced show that the glycine recovered from the end of the Crystal16 solubility experiments was γ in the seven cases where solid recovery was achieved. Deuteration of the solid glycine has a virtually undetectable effect on the PXRD spectra, with minimal differences that may only be detectable using an ultra-high-resolution scan, with the possibility of miniscule shifts in the positions of the peaks (i.e. $< 0.1^\circ$) [206], however, it is definitive with regards towards polymorph determination, which was the goal of PXRD testing. From Figure 6:10 and Figure 6:11 slight differences exist between the simulated α and γ traces exist as when measurements were performed there would be some experimental error and it is possible that some of the larger discrepancies could be due to sample misalignment as the differences in angle are very small [207].

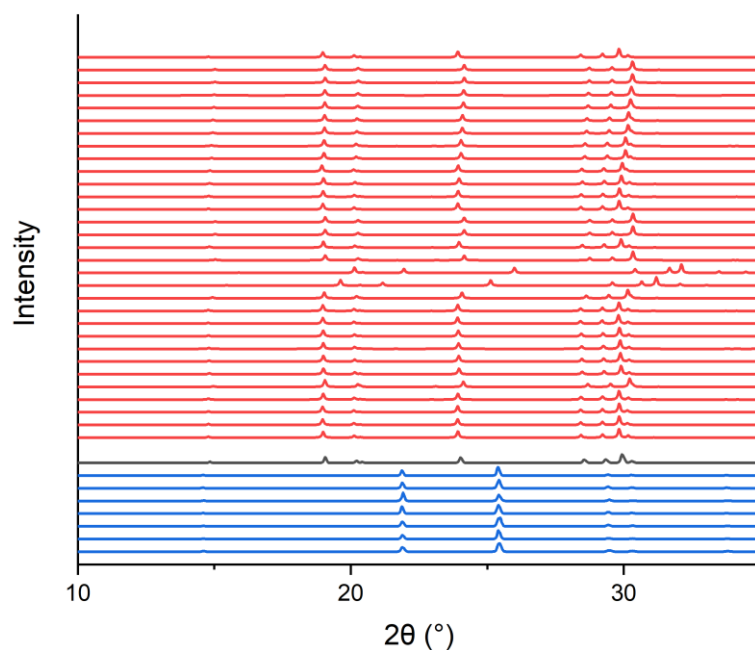


Figure 6:10: Comparison of simulated PXR D curves of alpha glycine (Red), PXR D curve of glycine for electrophoresis, Sigma Aldrich (Black) and Glycine extracted from the end of solubility testing after natural cooling in non-agitated deuterium oxide (Blue).

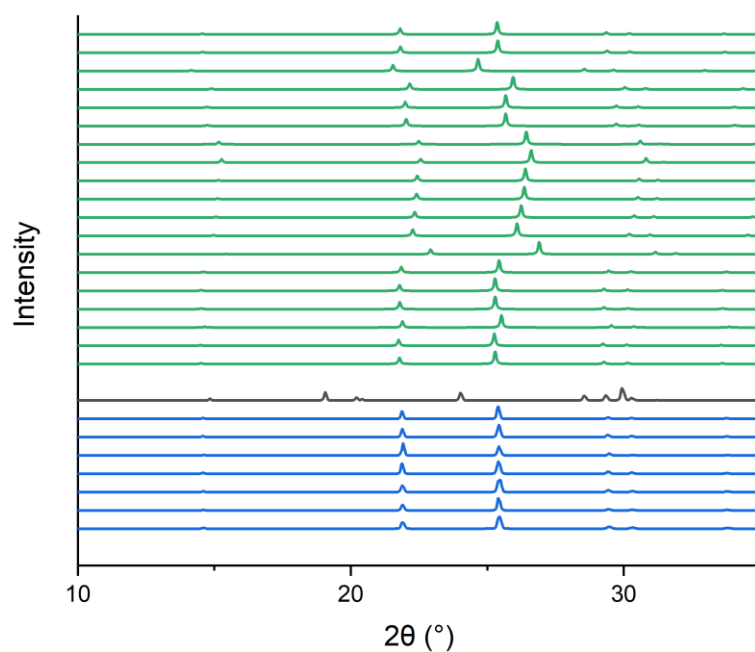


Figure 6:11: Comparison of simulated PXR D curves of gamma glycine (Green), PXR D curve of glycine for electrophoresis, Sigma Aldrich (Black) and Glycine extracted from the end of solubility testing after natural cooling in non-agitated deuterium oxide (Blue).

Using either of these techniques individually would not have been sufficient to fully identify both the deuteration of the glycine molecules, not highlighted by the PXR D and the polymorph, not identified by the FTIR.

Several explanations explain why the glycine recovered was the γ polymorph. Firstly, since the crystals were recovered following the completion of the temperature and agitation cycle where the solutions were allowed to cool naturally in the presence of a still Teflon coated stirrer bar or, secondly, due to the deuterium oxide solvent increasing the probability of the γ polymorph forming on its own [16], [200]. Finally, due to an unavoidable delay (See Appendix B), the time between the samples being generated and tested using XRPD was several months, when polymorph transformation could have occurred [208]. So, to be definitive in determining what polymorph is forming under the conditions experienced in the Crystal16 during MSZW and solubility measurements, it is necessary to, in essence, catch the crystals in the act of crystallising from solution while subject to the same agitation conditions as was used in the solubility experiments.

To be definitive with regards to which polymorph was formed when subjected to the conditions used when determining the MSZW and solubility, a single hot/cold temperature cycle was carried out where the goal was to determine only the polymorph that forms under Teflon-coated magnetic stirrer bar agitation at a speed of 700 RPM. Immediately upon crystallisation of the glycine, the solid material produced was removed, dried and ground. The resulting PXRD traces are shown in blue in Figure 6:12 and Figure 6:13, comparing those to the same set of simulated α and γ traces as shown in Figure 6:10 and Figure 6:11, from the recovered 9 vessels where nucleation occurred (the nine highest concentrations tested between 0.313 g/g and 0.500 g/g) before reaching the low-temperature hold as the blue traces in both Figure 6:12 and Figure 6:13.

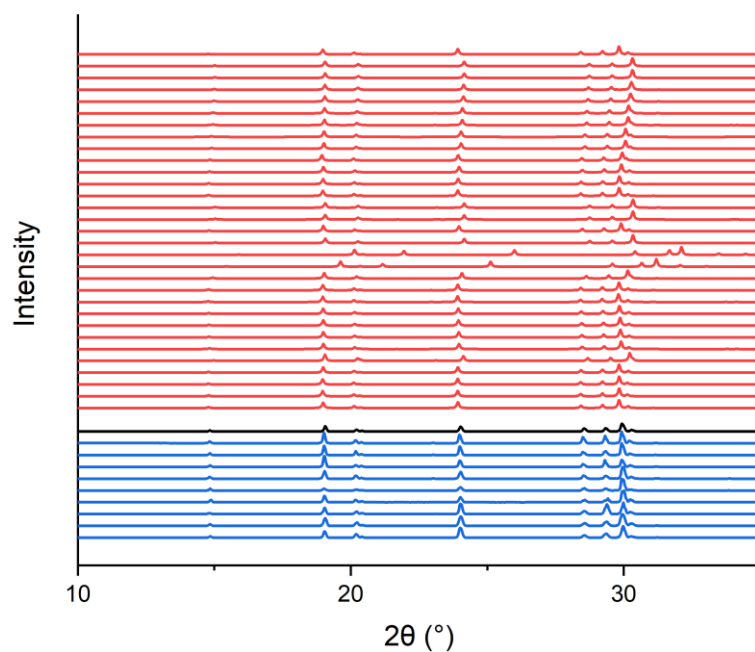


Figure 6:12: Comparison of simulated PXRD curves of alpha glycine (Red), PXRD curve of glycine for electrophoresis, Sigma Aldrich (Black) and glycine extracted from the cooling ramp while agitated (Blue).

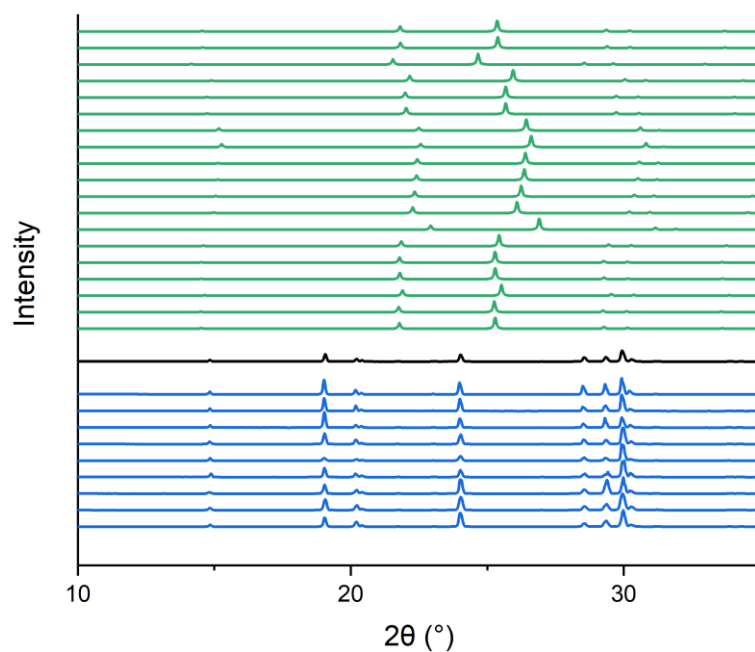


Figure 6:13: Comparison of simulated PXRD curves of gamma glycine (Green), PXRD curve of glycine for electrophoresis, Sigma Aldrich (Black) and glycine extracted from the cooling ramp while agitated (Blue).

From Figure 6:12 and Figure 6:13, it can be that, in contrast to the previous testing, the α form glycine in all circumstances. Therefore, it is reasonable to conclude that the solubility determined, shown in Figure 6:8, for the glycine in D_2O applied to the α polymorph. It can therefore be concluded that the presence of the γ form glycine was not the result of the use of the deuterated solvent, the exact source of γ form glycine would require further testing,

but since the goal was to determine the polymorph form during the agitated temperature ramps, which was determined, this was not performed.

6.3 Induction Time Measurements

6.3.1 Sodium Chloride

Measurement of induction times of sodium chloride has not been reported previously in H₂O and D₂O. However, this is of interest in its own right and can be used to guide the analysis of secondary nucleation characteristics and contextualise many other results.

The solubility data shown in section 6.2.1 allowed various supersaturations to be determined to produce the various concentrations required at 25 °C. For example, the solubility of NaCl at 25 °C was determined to be 0.3599 g_{NaCl}/g_{H₂O} and 0.3071 g_{NaCl}/g_{D₂O}. The compositions of the solutions used for induction time measure are shown in Table 6:3 when using the Van't Hoff fittings.

Table 6:3: Composition of solutions used for induction time measurements of NaCl.

| Solvent | Concentration (g/g) | Supersaturation at 25 °C (S) |
|--|---------------------|------------------------------|
| Water C* = 0.3599 g/g at 25 °C | 0.3608 | 1.0025 |
| | 0.3617 | 1.005 |
| | 0.3635 | 1.01 |
| | 0.3671 | 1.02 |
| Deuterium Oxide C* = 0.3071 g/g at 25 °C | 0.3079 | 1.0025 |
| | 0.3086 | 1.005 |
| | 0.3102 | 1.01 |
| | 0.3132 | 1.02 |
| | 0.3163 | 1.03 |
| | 0.3194 | 1.04 |

Higher supersaturations could not be examined in H₂O due to the limitations of the solubility of NaCl in water at 70 °C, as this would have required an alternative heating and cooling profile to be used, limiting the ability to compare results. This self-imposed upper-temperature limit depends on the operated equipment and the solvents used, as the complete dissolution of higher concentrations could not be guaranteed. It should be noted that there appear to be some issues with the methods of analysis developed by *Jiang and ter*

Horst [48] due to a number of vials nucleating before reaching isothermal conditions, a critique of the possible sources of problems that could occur when performing this form of analysis is detailed in section 6.3.1.5. This critique discusses issues that may exist with the underlying assumptions made in the development of the model by Jiang and ter Horst that may not apply in this case [48]. However, this now standard analysis is still presented in sections 6.3.1.1 and 6.3.1.3.

6.3.1.1 Crystal16 Scale Agitated

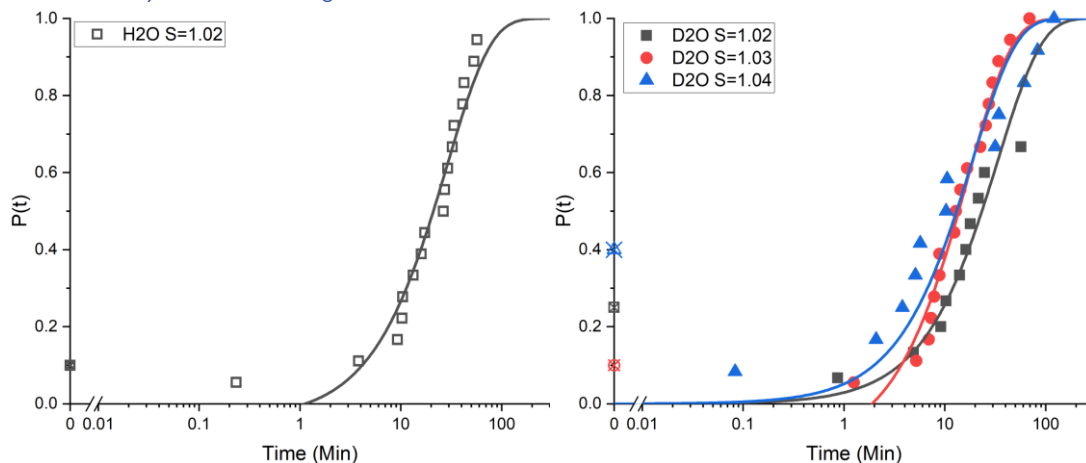


Figure 6:14: Left; Cumulative Probability Distribution Plot of Induction Time Measurements of NaCl in Water, agitated using a stirrer bar at 700 RPM at S at 1.02. Right; Cumulative Probability Distribution Plot of Induction Time Measurements of NaCl in Deuterium Oxide agitated using a stirrer bar at 700 RPM at S between 1.02 and 1.04. Crossed Symbols indicate the proportion of total vials which nucleated before reaching isothermal conditions. Lines indicate fitting according to Jiang and ter Horst [48].

Figure 6:14 highlights the difference in the range of supersaturations that can be examined with a maximum of $S = 1.02$ and $S = 1.04$ for NaCl in H_2O and D_2O , respectively. The highest possible supersaturations were tested first at this small scale as this would allow the extreme possible cases to be tested first to provide an upper bound. Where comparison can be made, at $S = 1.02$, the proportion of vials which nucleate within the low-temperature hold is significantly lower when using D_2O , as can be seen by the fewer number of black squares in Figure 6:14 right than left. To get an approximately equal number of vials to nucleate in D_2O , an $S = 1.03$ would have to be used compared to $S = 1.02$ in regular water.

6.3.1.2 Crystal16 Scale Quiescent

When examining $S = 1.01$ and $S = 1.02$ solutions in H_2O , no crystals formed within any of the 22 vials examined over the 12-hour observation period for either supersaturation. The absence of nucleation was also the case when this was repeated using D_2O as a solvent at S

= 1.01 and 1.02. None of the 22 vials examined at either supersaturation contained any solid material at the end of the observation period.

This significant reduction in the proportion of occasions where nucleation was observed highly suggests that the NaCl/Water and NaCl/Deuterium Oxide systems are highly susceptible to the agitation conditions used. Therefore, it may be possible to determine induction times should the vessels be observed for periods longer than 12 hours when quiescent conditions are used for the low temperature holds. High sensitivity to shear/agitation conditions is not unique to NaCl as this very high sensitivity to any form of shear has also been observed in urea [19].

6.3.1.3 Crystalline Scale

Since one goal is to determine sodium chloride's secondary nucleation characteristics when seeded, using a magnetic stirrer bar with an existing sodium chloride crystal is inadvisable. Due to sodium chloride's brittle nature, being an ionic substance [186], [187], therefore, the same supersaturations examined with the stirrer bar in this subsection and section 6.3.1.1 were investigated when agitated by overhead stirring. This will allow a comparison of seeded and unseeded samples and different agitation methods and, therefore, shear stresses, with the experiments performing dual purposes.

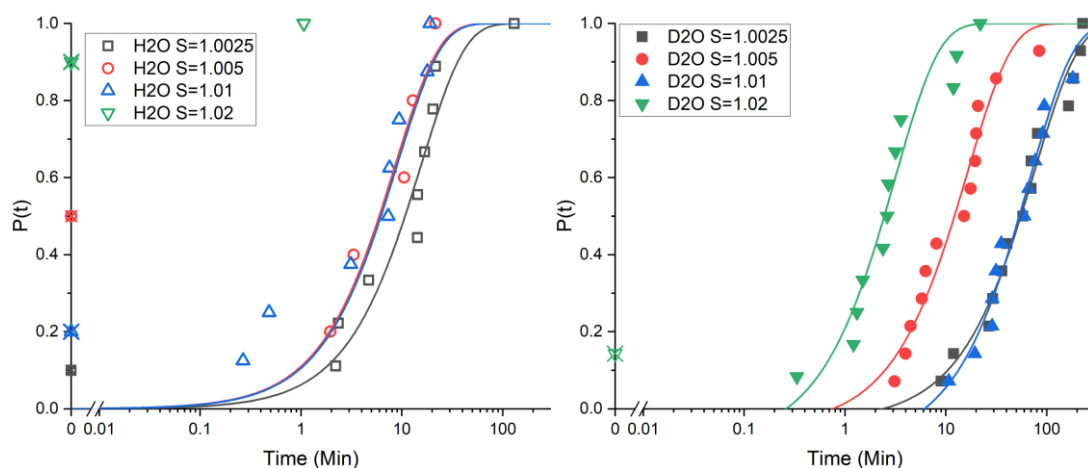


Figure 6:15: Left; Cumulative Probability Distribution Plot of Induction Time Measurements of NaCl in Water, agitated using a stirrer bar at 700 RPM at S between 1.0025 and 1.02. Right; Cumulative Probability Distribution Plot of Induction Time Measurements of NaCl in Deuterium Oxide agitated using a stirrer bar at 700 RPM at S between 1.0025 and 1.02. Crossed Symbols indicate the proportion of total vials which nucleated before reaching isothermal conditions. Lines indicate fitting according to Jiang and ter Horst [48].

Like the results seen at the smaller scale of 1 g of solvent in Figure 6:14, the same trend can be seen in Figure 6:15, at the larger scale of 3 g of solvent. At the supersaturation of 1.02, 90 % of samples prepared using H₂O as a solvent had nucleated before reaching the low-

temperature hold. A table where the times required at the low-temperature hold point for the range of supersaturations tested is shown in Table 6:4.

Table 6:4: Time after which 90 % of all samples had nucleated when examining the NaCl nucleating from H₂O and D₂O at the scale of 3 g of solvent.

| Supersaturation | Time required for Induction to be observed in 90 % of samples (Min). | | % Increase in time required for observation in D ₂ O than H ₂ O. |
|-----------------|--|------------------|--|
| | H ₂ O | D ₂ O | |
| 1.0025 | 21.65 | 214.4 | 890 |
| 1.005 | 7 | 84.7 | 1105 |
| 1.01 | 17 | N/A | N/A |
| 1.02 | 0 | 12.8 | N/A |

Solutions of $1.0025 \leq S \leq 1.02$ in H₂O were subjected to induction time measurements when agitated using overhead stirring at 700 RPM. None of the samples at any of the supersaturations examine were recorded as having nucleated. It was eventually suspected that this was due to the inability to suspend NaCl using overhead stirring at 700 RPM. This measurement issue resolved itself once the agitation speed was increased to 1250 RPM (the maximum possible on the Crystalline). To check that this was indeed the issue offline testing was performed as the Crystalline device itself prevented imaging of the entire contents of the vial at agitation speeds up to 1250 RPM using suspensions of NaCl in H₂O at $S = 1.06$. Examples of the suspensions being agitated at a range of speeds are shown in Figure 6:16.

Secondary confirmation was checked using a crystalline vial containing a saturated sodium chloride solution in deionised water that was agitated using a magnetic stirrer bar. The bar's speed was controlled using an external magnetic stirrer. At the agitation speed of 700 RPM, the seeds added remained at the bottom of the vial and were repeatedly struck by the stirrer bar. This repeated striking remained when the speed was increased to the Crystalline's maximum (1250 RPM). Only when the speed was increased to 2000 RPM, this was possible as this was performed using a separate overhead stirrer, beyond the Crystalline's maximum, was the crystal suspended in solution. However, this was not advisable as the crystal was repeatedly struck before being suspended. These experiments could not be performed in the Crystalline itself due to the low number of large particles in suspension. The Crystalline's cameras are best suiting to very high numbers of tiny particles.



Figure 6:16: Photographs of NaCl suspended in saturated NaCl solution at different agitation rates using a downward flow three-blade propeller (100 RPM, 250 RPM, 500 RPM, 700 RPM, and 1250 RPM; Left to Right)

It can be seen from the images in Figure 6:16, even the typical agitation speed of 700 RPM for magnetic bar agitation, when using this overhead stirring does not allow for a significant enough proportion of the crystalline material present to be suspended to block the beam used for transmissivity measurements. However, when examined using the highest agitation speed possible on the crystalline (1250 RPM), a much higher proportion of the solid crystalline material is suspended in the solution. Nevertheless, even this speed still permits a fraction of the solid NaCl to remain stationary at the bottom of the vial. The measurement technique used to measure induction times through transmissivity measurements where only a single laser beam is utilised can cause issues when a small quantity of crystalline material would be expected to crystallise from the solution. As would be the case in NaCl/H₂O and NaCl/D₂O, only small supersaturations can be generated and returned to low temperatures before nucleating.

A vial that was visually confirmed to contain a crystalline solid was agitated to observe the measured transmissivity. At a speed of 700 RPM, the transmissivity was not impacted and remained at 100 %. However, when the agitation speed was increased to 1250 RPM, this caused a decrease in the transmissivity recorded. Furthermore, the decrease in the transmissivity observed in these cases were not total, where the transmissivity falls from 100 % to 0 %, this could be due to a small number of small crystals being present intermittently in the path of the beam blocking it, this would be consistent with a partial decrease in the

transmissivity and fluctuating around this decrease value , which was confirmed using the crystalline equipment itself.

To ascertain that the agitator was not inducing cavitation and introducing turbidity. A pure deionised water version setup was used. This was tested at the highest speed available on the agitator overhead, 2000 RPM. The appearance of the vial at this agitation speed is shown in Figure 6:17.



Figure 6:17: Photograph of 8 ml crystalline vial agitated at 2200 RPM using a downward flow three-blade propeller.

Figure 6:17 shows that when the contents of the vials are subjected to overhead agitation of 2000 RPM, cavitation is not present, therefore it can be assumed not to occur at the lower speed of 1250 RPM and therefore can be discounted as a possible concern.

Induction time measurements of sodium chloride in water and deuterium oxide when agitated using an overhead propeller at a speed of 1250 RPM are shown in Figure 6:18.

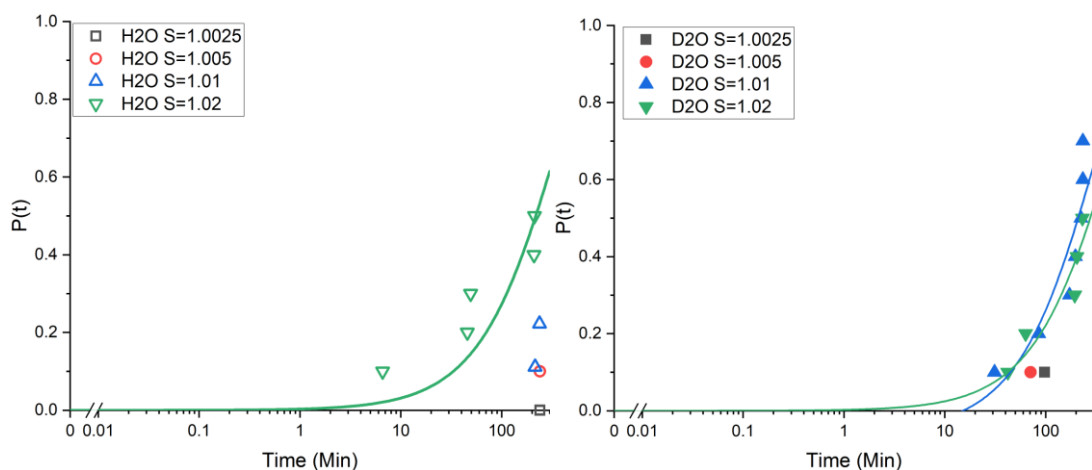


Figure 6:18: Left; Cumulative Probability Distribution Plot of Induction Time Measurements of NaCl in Water, agitated using an overhead propeller at 1250 RPM at S between 1.0025 and 1.02. Right; Cumulative Probability Distribution Plot of Induction Time Measurements of NaCl in Deuterium Oxide agitated using an overhead propeller at 1250 RPM at S between 1.0025 and 1.02. Lines indicate fitting according to Jiang and ter Horst [48].

Overhead stirring with a three-bladed propeller shows a marked difference in the induction times observed by examining the proportion of samples exhibiting nucleation than when using a magnetic stirrer bar. This is best exemplified by the $S = 1.02$ regular and heavy water samples. This can be done by comparing Figure 6:15 and Figure 6:18. When using a stirrer bar, 90 % and 14 % of solutions in H₂O and D₂O had already nucleated at this supersaturation before reaching isothermal conditions. All samples had nucleated before the end of the low-temperature hold. When using the less violent overhead stirring with a three-bladed downflow propeller, no samples nucleated before reaching the low-temperature isothermal hold. Half of each case's total samples had nucleated before the end of the low-temperature hold. Furthermore, when solutions of lower supersaturation were used, the number nucleated when using this less-vigorous agitation was significantly reduced.

All samples that nucleated from solution when using the Crystalline were also checked through the captured images if any doubt existed in the transmissivity traces. Images were examined to ensure the solid included in the vial dissolved and was nucleated from the solution. In a small number of individual temperate cycles, the morphology of the crystalline material which appeared in view was different from that of most individual induction time measurements. The morphology appeared like the particulate solid that appears in view when the vials are first agitated. Suggesting an issue with the agitation did not allow a material suspension to dissolve fully for the next cycle, when this occurred that particular cycle was removed from the analysis and repeated, this was not a common issue (occurring only 3 occasions across all of the overhead samples run with NaCl dissolved in D₂O) and

therefore was not a problem of any real significance. Photographs taken of various appearances are shown in Figure 6:19, Figure 6:20 and Figure 6:21 show images of sodium chloride before full dissolution, a false positive of a nucleation event where undissolved material was suspended at a temperature that would not permit its dissolution, and sodium chloride crystals which were formed through nucleation and crystal growth, respectively.

Figure 6:19 shows a wide distribution of particle sizes and morphologies, ranging from a large number of tiny particles to a smaller number of large (~100s of microns in diameter) round smooth particles. This is similar to the NaCl particles imaged in Figure 6:20 which were initially thought to be a nucleation event but this did not fit what would be expected to be seen upon nucleation of NaCl from aqueous solution as was observed in Figure 6:21. In the case of an actual nucleation from solution where all of the images of the particles showed that they are small, roughly the same size, and cubic in habit.

In the first interval in Figure 6:20, between images one and two of the top row, shows differences in brightness across the image's background, typically seen when differences in density are observed. This is a feature associated with differences in concentration in the photographed section.

Seeded studies require a period in which primary nucleation will not occur to ensure the seed deposited into each vial is the observed nuclei source. This is impossible when using the magnetic stirrer bar, as even at the lowest supersaturation used with H₂O allows nucleation to occur before isothermal conditions, as seen in Figure 6:15. Another reason for using the overhead stirring is the period where isothermal conditions exist before nucleation occurs where a seed can be placed into each vial, as seen in Figure 6:18.

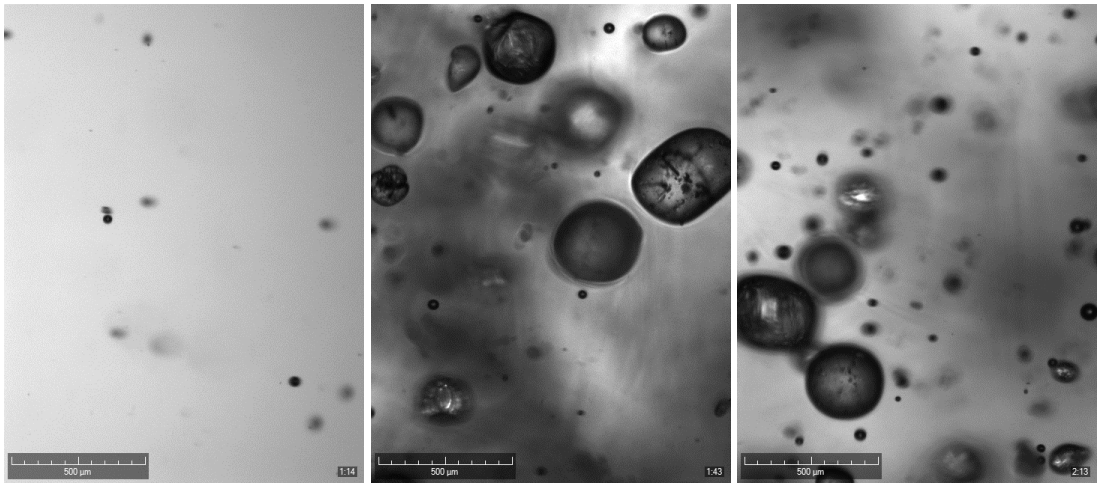


Figure 6:19: Crystalline Camera Images of Sodium Chloride before full dissolution in H_2O . Images were taken at 30-second intervals, left to right. Scale bar in each image is 500 microns.

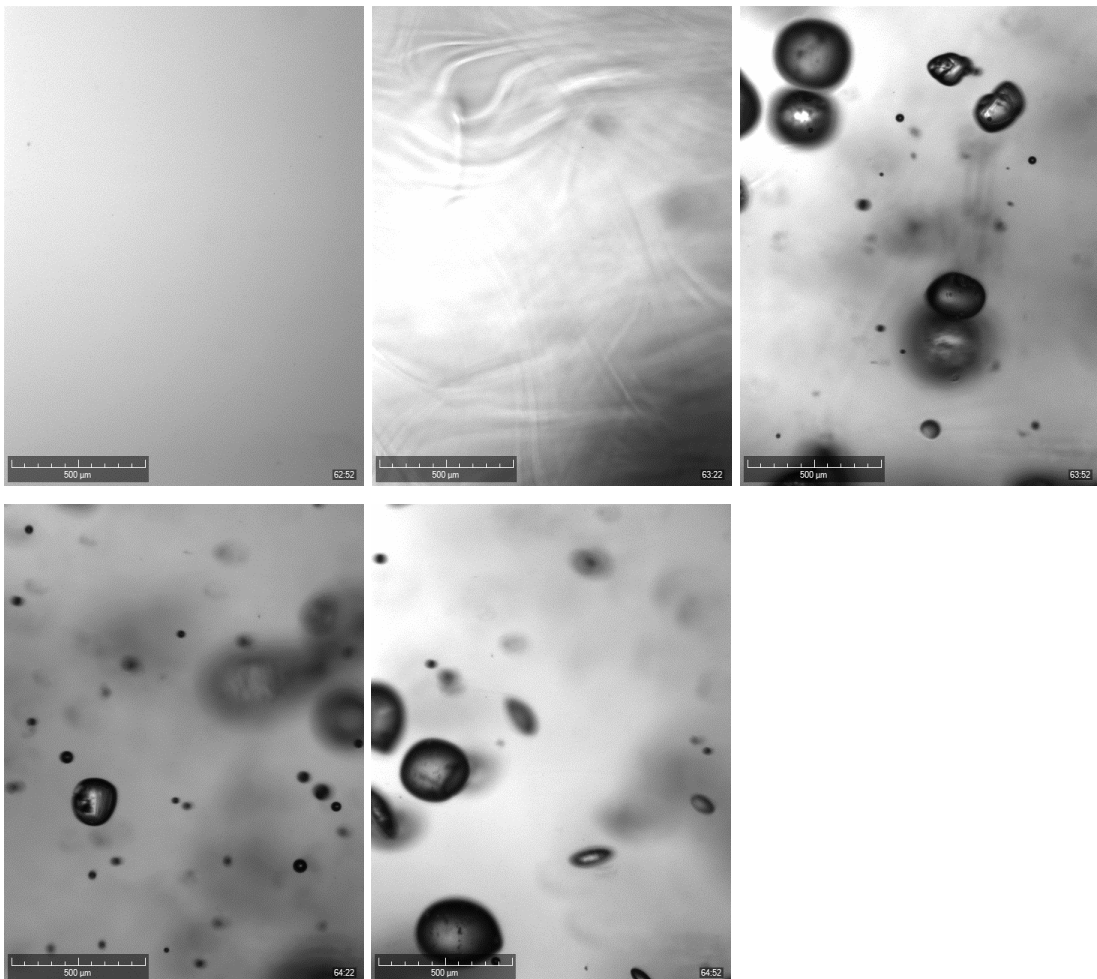


Figure 6:20: Crystalline images of a false positive nucleation event of sodium chloride in H_2O , where undissolved NaCl has become suspended in the solution, giving the appearance of nucleation. Images were taken at 30-second intervals left to right in each row, then continuing from the left-hand side of the row below. Scale bar in each image is 500 microns.

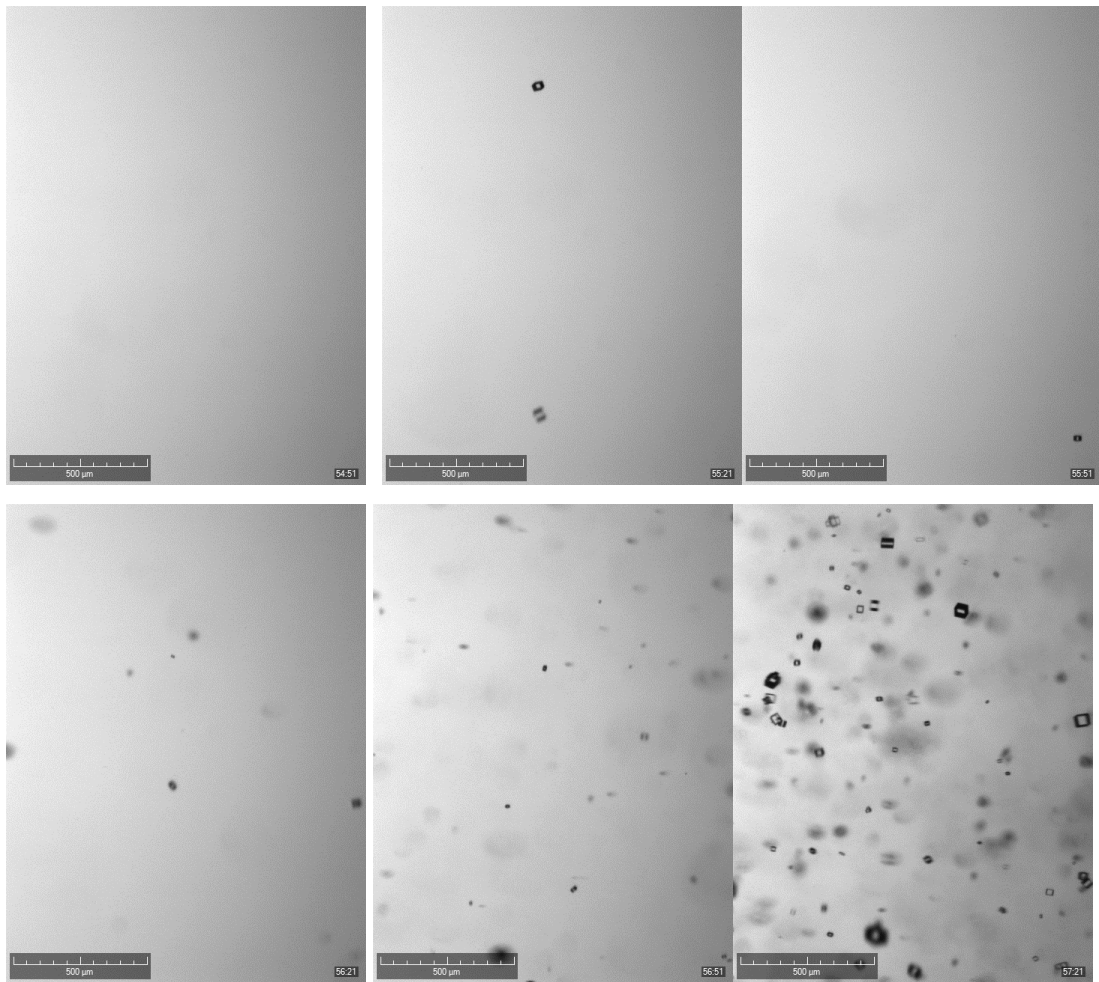


Figure 6:21: Crystalline Images of Sodium Chloride, which has nucleated from solution. Images were taken at 30-second intervals from left to right in each row, then descending in rows from top to bottom. Scale bar in each image is 500 microns.

6.3.1.4 Primary Nucleation Rate and Growth Times

Where possible, the model developed by *Jiang and ter Horst* has been used to determine the primary nucleation rates for the examined conditions [48]. This is indicated by the trendline for each supersaturation in Figure 6:14, Figure 6:15 and Figure 6:18. These associated nucleation rates and growth times are shown in Table 6:5.

Table 6:5: Nucleation Rates and Growth Times of Sodium Chloride Solutions in water and heavy water. Where a cell contains [-], a value cannot be calculated. Tolerances indicate standard error determined from the fitting of the model. 1 mL solvent scale experiments were performed in the Crysstat16, and 3 mL experiments were performed in the Crystalline.

| Solvent | Solvent Scale | S | Agitation Type | Agitation Speed (RPM) | J ($\text{m}^{-3} \text{s}^{-1}$) | t_g (min) |
|------------------|---------------|--------|----------------|-----------------------|-------------------------------------|-------------|
| H ₂ O | 1 mL | 1.02 | Bar | 700 | 580±37 | 1.12±0.95 |
| D ₂ O | 1 mL | 1.02 | Bar | 700 | 1149±139 | 0±1.79 |
| D ₂ O | 1 mL | 1.03 | Bar | 700 | 1084±63 | 1.90±0.51 |
| D ₂ O | 1 mL | 1.04 | Bar | 700 | 981±207 | 0±1.40 |
| H ₂ O | 3 mL | 1.0025 | Bar | 700 | 358±56 | 0±1.27 |
| H ₂ O | 3 mL | 1.005 | Bar | 700 | 644±144 | 0±1.07 |
| H ₂ O | 3 mL | 1.01 | Bar | 700 | 619±118 | 0±0.78 |
| H ₂ O | 3 mL | 1.02 | Bar | 700 | [-] | [-] |
| D ₂ O | 3 mL | 1.0025 | Bar | 700 | 81±6 | 2.37±2.83 |
| D ₂ O | 3 mL | 1.005 | Bar | 700 | 375±35 | 0.75±0.76 |
| D ₂ O | 3 mL | 1.01 | Bar | 700 | 90±7 | 6.13±2.6 |
| D ₂ O | 3 mL | 1.02 | Bar | 700 | 1952±267 | 0.27±0.21 |
| H ₂ O | 3 mL | 1.0025 | Overhead | 1250 | [-] | [-] |
| H ₂ O | 3 mL | 1.005 | Overhead | 1250 | [-] | [-] |
| H ₂ O | 3 mL | 1.01 | Overhead | 1250 | [-] | [-] |
| H ₂ O | 3 mL | 1.02 | Overhead | 1250 | 17±5 | 0±29 |
| D ₂ O | 3 mL | 1.0025 | Overhead | 1250 | [-] | [-] |
| D ₂ O | 3 mL | 1.005 | Overhead | 1250 | [-] | [-] |
| D ₂ O | 3 mL | 1.01 | Overhead | 1250 | 22±5 | 15.1±29.4 |
| D ₂ O | 3 mL | 1.02 | Overhead | 1250 | 15±3 | 0±30.62 |

In the cases where comparisons can be made at the same scale and supersaturation the relative change in the in the primary nucleation rate are shown in Table 6:6.

Table 6:6: Comparison of Nucleation Rates of Sodium Chloride from Deionised Water and Deuterium Oxide at the Crystalline scale with bar agitation

| Supersaturation | % Increase in primary nucleation rate of NaCl nucleating from solution H ₂ O compared to D ₂ O. |
|-----------------|---|
| 1.0025 | 339 |
| 1.005 | 72 |
| 1.01 | 629 |

There appears to be a difference in the nucleation rates observed. However, no apparent trend is present with the effect of the supersaturation. These calculated primary nucleation rates are compared to other previously published literature for nucleation from water; however, none are readily available for nucleation from deuterium oxide. These are shown in Figure 6:22 [209]–[213].

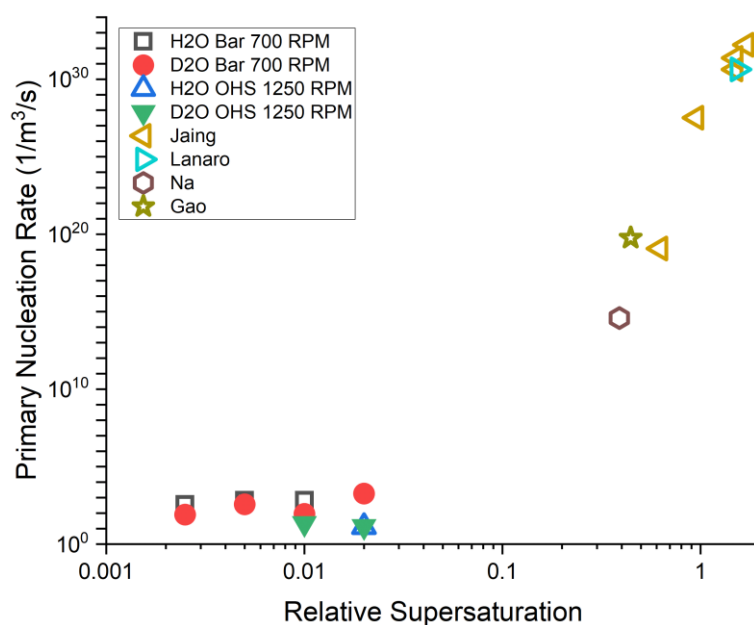


Figure 6:22: Comparison of Primary Nucleation Rate of Sodium Chloride as function of relative supersaturation ($\sigma = S - 1$) at Crystalline Scale from previously published data [209]–[213]. Solubility of all points based upon fitted Van't Hoff curves in Figure 6:6.

Figure 6:22 shows that the primary nucleation rates are many orders of magnitude lower than those previously published. Using the solubility curve determined here, the other studies were performed at much greater relative supersaturations. The studies in this thesis were performed at much lower levels of supersaturation. Therefore, it should be expected

that the nucleation rates would be lower. Moreover, when comparing just the data previously published, small changes in relative supersaturation result in changes in the primary nucleation rate of many orders of magnitude, had this trend continued, measurement of the primary nucleation rate at the supersaturations tested here would be impossible to determine. Therefore, the fact that the nucleation rate is so low compared to these other situations does seem realistic. Measurement at the supersaturations previously published does not appear to be possible when agitation was applied by magnetic stirrer bar due to the number of vials that nucleated before isothermal conditions were reached. It may be possible to examine higher supersaturations in some cases if the rate of cooling that can be achieved can be significantly increased. It was only possible to measure the primary nucleation rates when $\sigma > 0.2$ due to the scale of the crystallisations occurring as this was performed within microcapillaries. Overhead stirring had the opposite issue: few vessels nucleated in the prescribed observation time. It must also be noted that a significant difference in nucleation rate in previously published experimental data for primary nucleation rate of NaCl from H₂O (many orders of magnitude) exists [210], [214]. However, previous work has shown that the scale can significantly affect crystallisation as rates determined from microfluidic droplets are orders of magnitude higher than those in stirred glass vials [215]. And it has been noticed that more generally precious little is known about the NaCl-saturated NaCl solution especially regarding how common this system is worldwide [216].

6.3.1.5 Issues with Analysis

Although it would be straightforward to apply the kinetic model from *Jiang and ter Horst* [48], this would be to ignore a key point which could be made that there appears to be no clear significant difference in the cumulative probability distribution when altering the supersaturation (as seen in a wide range of situations [29], [50], [160]) when agitated using the magnetic stirrer bar at the two scales examined (see Figure 6:14 and Figure 6:15) opposed to those examined when using the overhead agitation, Figure 6:18. One potential explanation for this is in this case that the limiting factor in these scenarios is not the nucleation from solution. It could be proposed that the nucleation occurs quickly (and is therefore not the rate-determining step), and the induction times, in this case, are monitoring the growth at the lower end of the growth rate dispersion. The method used here for the determination of nucleation could require the smallest particles to grow to a size that allows them to be detected, due to the way that nucleation is measured in the Crystal16 and Crystalline. The

distribution of times is actually a reflection of the growth rate dispersion of NaCl, which has been observed in a wide range of chemical species [217]. Although using a fixed growth time (t_g) may not be ideal, a lack of meaningful alternatives means the primary nucleation rates estimated using the model developed by *Jiang and ter Horst* [48] are still reported here.

One other point of contention is that those cumulative distributions that have a proportion of the total samples nucleated before reaching isothermal are, in effect, conditional (on reaching the low-temperature isothermal hold without nucleating) cumulative probability distributions and that this could potentially impact the already suspect primary nucleation rates. When the model developed by *Jiang and ter Horst* is applied to the non-conditional values from the alternative versions of the cumulative probability distributions, this can indicate that vials have nucleated before reaching isothermal conditions if $P(0) > 0$ and vials not nucleating before reaching the end of the isothermal hold when $P(240) < 1$.

Another point is that the model developed by *Jiang and ter Horst* [48] could be applied to the alternate forms of the distribution shown in Appendix F.1, where distributions are shown on a non-conditional basis, e.g. if 10 % of the samples nucleate before reaching isothermal conditions this is accounted for in the fitted model. This would still allow a primary nucleation rate to be calculated. In this case, the determined widths of the tolerance for the determined rates largely overlap with those shown in Table 6:5. A second set of alternative analysis is also presented in Appendix F.2 where a more general categorisation was applied to the induction time measurements. Only reporting the section of the temperature profile where the nucleation occurred, if at all. All results were sorted into three categories, nucleation occurring during the cooling ramp, nucleation occurring during the isothermal hold or nucleation did not occur.

6.3.2 Glycine

Like the NaCl, the composition of the solutions used to measure induction time measurements was determined using the Van't Hoff fittings of the clear point data in section 6.2.2. The saturation concentration (solubility) at 25 °C was determined to be 0.2471 $\text{g}_{\text{glycine}}/\text{g}_{\text{H}_2\text{O}}$ and 0.2148 g of $\text{g}_{\text{glycine}}/\text{g}_{\text{D}_2\text{O}}$ from the fittings shown in Figure 6:6.

Table 6:7: Composition of solutions used for induction time measurements of glycine.

| Solvent | Concentration (g/g) | Supersaturation at 25 °C (S) |
|--|---------------------|------------------------------|
| Water $C^* = 0.2471 \text{ g/g at } 25 \text{ °C}$ | 0.2866 | 1.16 |
| | 0.2916 | 1.18 |
| | 0.2965 | 1.20 |
| | 0.3015 | 1.22 |
| | 0.3064 | 1.24 |
| | 0.3113 | 1.26 |
| Deuterium Oxide $C^* = 0.2148 \text{ g/g at } 25 \text{ °C}$ | 0.2492 | 1.16 |
| | 0.2535 | 1.18 |
| | 0.2578 | 1.20 |
| | 0.2621 | 1.22 |
| | 0.2664 | 1.24 |
| | 0.2706 | 1.26 |

6.3.2.1 Crystal16 Scale

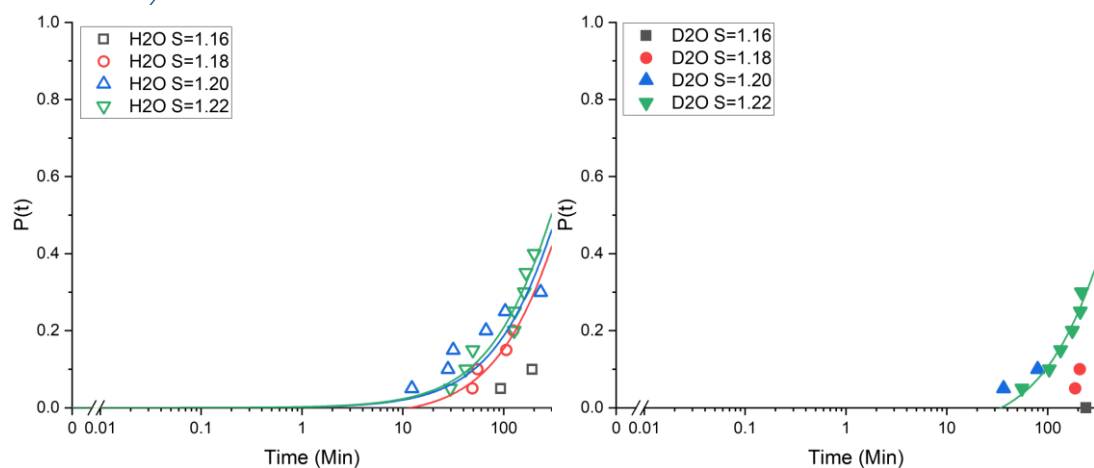


Figure 6:23: Left; Cumulative Probability Distribution Plot of Induction Time Measurements of Glycine in Water, agitated using a stirrer bar at 700 RPM at S between 1.16 and 1.22. Right; Cumulative Probability Distribution Plot of Induction Time Measurements of Glycine in Deuterium Oxide agitated using a stirrer bar at 700 RPM at S between 1.18 and 1.22. Lines indicate fitting according to Jiang and ter Horst [48].

To determine the difference in nucleation characteristics when using a different solvent isotopologue initial induction time experiments were performed with both solvent isotopologues using the Crystal16. At this scale (1g of solvent, ~1ml), Figure 6:23 shows that the supersaturations chosen to determine induction times are not high enough to allow most samples to nucleate within the observation period. Even at this scale's highest

supersaturation ($S = 1.22$), less than 50 % of samples nucleated within the 4-hour low-temperature observation period. The number of samples nucleated within this period decreased as the supersaturation decreased. In comparing the solvent isotopologue, deuterium oxide in the place of water causes induction times to increase. At all supersaturations assessed, the number of nucleated vials decreased when using the heavier solvent isotopologue, and the time before the shortest induction time measured also increased. This change can be highlighted at the $S = 1.20$, where none of the vials where the solvent used was D_2O nucleated within four hours of the isothermal conditions beginning. Therefore, higher supersaturations were used when testing progressed to the larger scale of the Crystalline ($\sim 3\text{ml}$ of solvent), as shown in 6.3.2.2. Quiescent testing was not performed at this scale as this method has previously been examined at approximately equal supersaturations [159].

6.3.2.2 Crystalline Scale

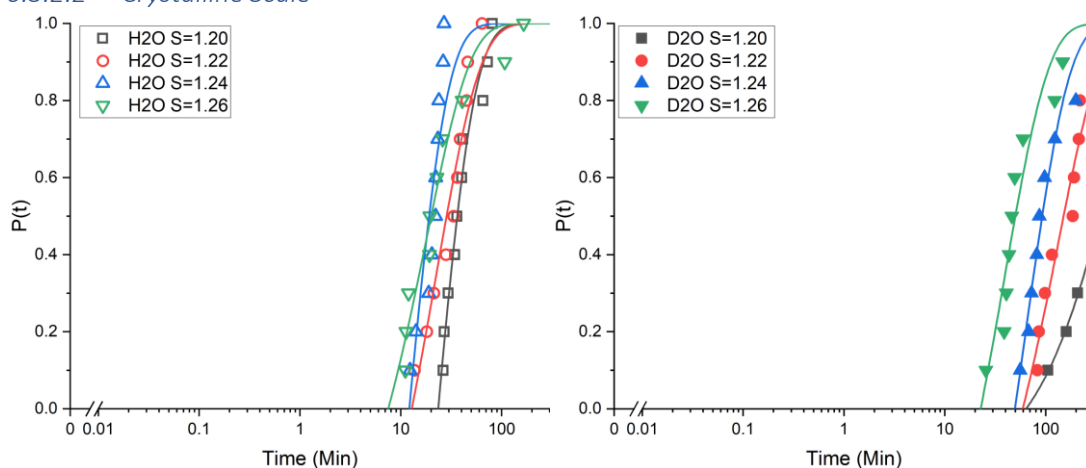


Figure 6:24: Left; Cumulative Probability Distribution Plot of Induction Time Measurements of Glycine in Water, agitated using a stirrer bar at 700 RPM at S between 1.20 and 1.26. Right; Cumulative Probability Distribution Plot of Induction Time Measurements of Glycine in Deuterium Oxide agitated using a stirrer bar at 700 RPM at S between 1.20 and 1.26. Lines indicate fitting according to Jiang and ter Horst [48].

Like in the smaller scale induction time measurement shown in section 6.3.2.1, a marked increase in induction time is observed when using D_2O as a solvent at an equal level of supersaturation. It appears to be a clearer example than the induction time measurements made using the Crystal16. All the samples tested nucleated within four hours of the isothermal conditions beginning for both solvents, as shown in Figure 6:24. The time after which 50 % of samples had nucleated is shown in Table 6:8. A longer observation period would have allowed the samples using the $S = 1.20$ to be compared using this metric.

Table 6:8: Time after which 50 % of samples nucleated for glycine in water and deuterium oxide agitated by a magnetic stirrer at a speed of 700 RPM.

| Supersaturation | Induction of 50 % of samples depending upon solvent (Min) | | % Increase |
|-----------------|---|---------------------------|------------|
| | H ₂ O | D ₂ O | |
| 1.20 | 36.2 | N/A (Only 30 % Nucleated) | N/A |
| 1.22 | 33.4 | 186.4 | 458 |
| 1.24 | 22.2 | 86.6 | 290 |
| 1.26 | 19.5 | 46.3 | 137 |

For the three supersaturations where a comparison can be made, a substantial increase in the induction times can be observed; however, it also appears that this increase, decreases in relative terms as the supersaturation increases. At the supersaturations examined at this scale using this agitation method, the proportion of nucleation events that occurred also fell as the supersaturation decreased when using D₂O as a solvent in comparison to 100 % nucleation observed when using H₂O as the solvent.

However, these systems (glycine in H₂O and D₂O) are susceptible to agitation conditions used during crystallisation. Therefore, comparing the two solvents used when agitation is supplied using the overhead propeller allows some of the impact of the agitation to be determined.

The most obvious comparison for the impact of the agitation can be seen when comparing the H₂O solvent runs for each of these agitation methods, using the stirrer bar 100 % of samples at these supersaturations. Using overhead stirring, this decreased to 50 % in the case of the highest supersaturation examined ($S = 1.26$) and 10 % in the lowest ($S = 1.20$). This decrease is also noted when comparing agitation methods using D₂O 90 % nucleated using stirrer bar agitation. As at $S = 1.20$ and $S = 1.26$, 0 % of the vials tested when subjected to overhead stirring, opposed to the 30 % and 90 % of the vials, respectively, which exhibited nucleation when agitated via magnetic bar stirring. This decrease was also observed at the other supersaturations tested ($S = 1.22$ and $S = 1.24$) but the decrease observed was less significant.

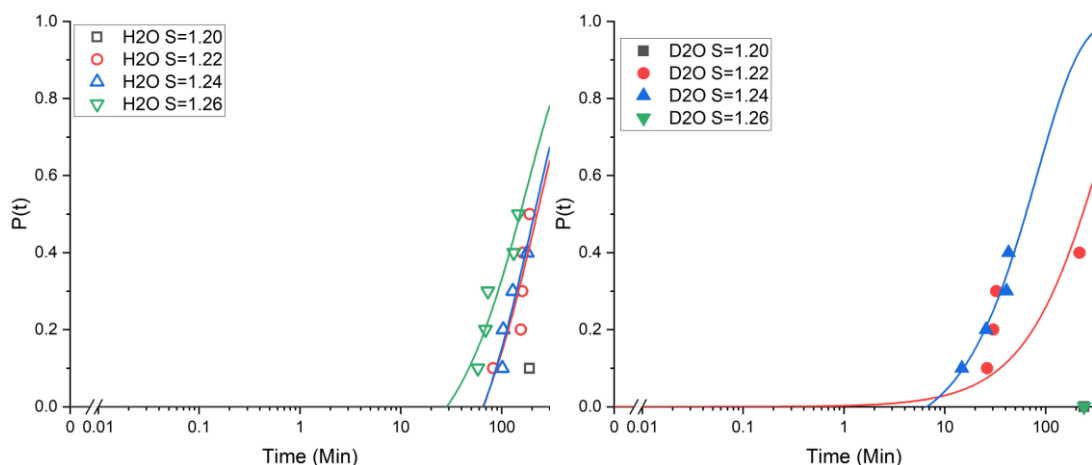


Figure 6:25: Left; Cumulative Probability Distribution Plot of Induction Time Measurements of Glycine in Water, agitated using an overhead propeller at 700 RPM at S between 1.20 and 1.26. Right; Cumulative Probability Distribution Plot of Induction Time Measurements of Glycine in Deuterium Oxide agitated using an overhead propeller at 700 RPM at S between 1.20 and 1.26. Lines indicate fitting according to Jiang and ter Horst [48].

Due to the decreased fluid shear, it is possible that a few large crystals were produced using the overhead stirring method, as experiments showed nucleation within unagitated vials was in the form of a single large crystal [159]. These larger crystals may not be able to be suspended by the overhead agitation. This smaller number would also lower the likelihood of one of these crystals passing through the beam long enough to impact the measured transmissivity. Like the case wherein one of the final temperature cycles resulted in a slight decrease in transmissivity. Following the entire heating and cooling cycle, several large crystals were observed when the vial was removed from the apparatus. However, the nature of the setup where the same vial was subjected to repeated temperature cycles, for four of the five observation periods, the vial was reheated to the dissolution temperature of 70 °C, which would result in these large crystals that could have been formed being dissolved. Therefore, this could not be confirmed, and the proportion of overhead agitated vessels having nucleated may have been undercounted.

Like in sodium chloride, where possible, the model developed by Jiang and ter Horst [48] has been applied to the induction times measured to determine the nucleation rate and the associated growth times [48]. For glycine solution systems, these nucleation rates and growth times are shown in Table 6:9. The ability to determine a primary nucleation rate from fitting the Jiang and ter Horst model [48], is also indicated in the cumulative probability distributions by the presence of a trendline.

Table 6:9: Nucleation Rates and growth times of glycine in water and heavy water. Where a cell contains [-], a value cannot be calculated. Tolerances indicate standard error as determined from the model fitting.

| Solvent | Solvent Scale | S | Agitation Type | Agitation Speed (RPM) | J ($\text{m}^{-3} \text{s}^{-1}$) | t_g (min) |
|------------------|---------------|------|----------------|-----------------------|-------------------------------------|-------------|
| H ₂ O | 1 mL | 1.16 | Bar | 700 | [-] | [-] |
| H ₂ O | 1 mL | 1.18 | Bar | 700 | 32±7 | 11.98±16.01 |
| H ₂ O | 1 mL | 1.20 | Bar | 700 | 23±10 | 0±25.51 |
| H ₂ O | 1 mL | 1.22 | Bar | 700 | 39±4 | 0±12.41 |
| D ₂ O | 1 mL | 1.16 | Bar | 700 | [-] | [-] |
| D ₂ O | 1 mL | 1.18 | Bar | 700 | [-] | [-] |
| D ₂ O | 1 mL | 1.20 | Bar | 700 | [-] | [-] |
| D ₂ O | 1 mL | 1.22 | Bar | 700 | 32±3 | 34.53±12.13 |
| H ₂ O | 3 mL | 1.20 | Bar | 700 | 301±32 | 23.53±0.97 |
| H ₂ O | 3 mL | 1.22 | Bar | 700 | 246±30 | 12.85±1.54 |
| H ₂ O | 3 mL | 1.24 | Bar | 700 | 553±110 | 12.14±1.25 |
| H ₂ O | 3 mL | 1.26 | Bar | 700 | 308±42 | 7.51±1.19 |
| D ₂ O | 3 mL | 1.20 | Bar | 700 | 15±1 | 63.93±6.98 |
| D ₂ O | 3 mL | 1.22 | Bar | 700 | 47±7 | 59.25±9.4 |
| D ₂ O | 3 mL | 1.24 | Bar | 700 | 100±13 | 49.69±3.78 |
| D ₂ O | 3 mL | 1.26 | Bar | 700 | 156±32 | 22.69±4 |
| H ₂ O | 3 mL | 1.20 | Overhead | 700 | [-] | [-] |
| H ₂ O | 3 mL | 1.22 | Overhead | 700 | 24±8 | 65.01±28.2 |
| H ₂ O | 3 mL | 1.24 | Overhead | 700 | 27±8 | 65.96±17.63 |
| H ₂ O | 3 mL | 1.26 | Overhead | 700 | 31±7 | 28.54±13.64 |
| D ₂ O | 3 mL | 1.20 | Overhead | 700 | [-] | [-] |
| D ₂ O | 3 mL | 1.22 | Overhead | 700 | 18±12 | 0±46.89 |
| D ₂ O | 3 mL | 1.24 | Overhead | 700 | 75±15 | 6.63±4.78 |
| D ₂ O | 3 mL | 1.26 | Overhead | 700 | [-] | [-] |

When using the crystalline (3mL solvent scale) agitated with the magnetic bar a full set of four supersaturations allowed a primary nucleation rate to be calculated, the nucleation rate calculated increases in both the H₂O and D₂O solvents as the supersaturation increases, and

the calculated growth times decrease with increasing supersaturation. When equal supersaturations are compared between each solvent, the nucleation rate is noticeably lower when using deuterium oxide than normal deionised water. In addition, the growth times calculated are longer when using D₂O as a solvent when compared to regular deionised water. The impact on the nucleation rate and the growth time seems to diminish with increasing supersaturation as the percentage increases in nucleation rate and growth time are shown in Table 6:10

Table 6:10: Comparison of Nucleation Rates and Growth Times of Glycine at the Crystalline Scale agitated using a bar.

| Supersaturation | % Increase of nucleation rate comparing H ₂ O and D ₂ O | % Increase of growth Time comparing D ₂ O and H ₂ O |
|-----------------|---|---|
| 1.20 | 1908 | 172 |
| 1.22 | 426 | 361 |
| 1.24 | 454 | 309 |
| 1.26 | 97 | 202 |

Comparing nucleation rates for identical conditions of solvent and supersaturation also allows the impact of the agitation on the nucleation rates to be explored. For the cases where a comparison can be made, using a stirrer bar instead of the overhead stirrer bar increased the nucleation rate by 1000 % when using H₂O as a solvent. This increase observed when using D₂O was less, between ~360 % and ~30 %, this could be potentially due to the differences observed in density and viscosity between the two isotopologues which are greater in pure D₂O than H₂O [218]. However, due to the few data points collected, a sound conclusion cannot be made. Future examinations may prove to be more fruitful.

6.4 Crystal Growth Rates

Crystal growth rates can be calculated using the image analysis software that is part of the Crystalline's operating software. For each image taken of the vial section, the software can size each particle visible and determine the size distribution histogram. Particles are divided into 3 µm wide bins up to a size of 300 µm. When stills were taken, the number of particles in each of these bins can be processed using a pre-existing tested MATLAB script to determine the volume-weighted D-90 size of the distribution of particles visible in each image

[30]. It is found that even without crystals the identified particle number fluctuates between 0 and 10 due to impurities such as dust, while for particle numbers > 160 the image processing becomes unreliable due to particle overlaps. Therefore, all analysis is limited to images with between 10 and 160 particles, the volume-weighted D-90 size is plotted against time, and the slope of this line is taken as the growth rate of crystalline material present.

Due to equipment limitations when unseeded runs were carried out, the maximum file size image analysis was only performed every 30 seconds. However, when seeding was performed, only a short single temperature cycle was used. Therefore, image analysis could be performed more frequently, every 5 seconds.

Although the primary goal of the unseeded Crystalline studies was to determine the solvent's impact on the primary nucleation, the data gathered by the crystalline also allows the secondary nucleation characteristics to be determined when nucleation occurred. Unseeded secondary nucleation, where primary nucleation triggers subsequent secondary from the first primary nucleus is discussed above in sections 6.3.1.3 and 6.3.2.2 for sodium chloride and glycine, respectively.

6.4.1 Glycine

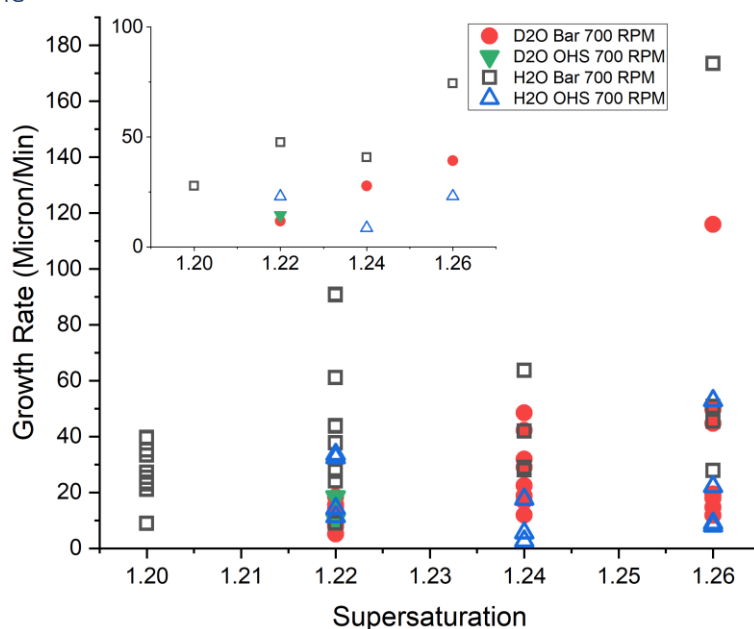


Figure 6:26: Growth Rates of Glycine determined through image analysis grown from supersaturated solutions in H₂O and D₂O when agitated using a magnetic stirrer bar agitation (Bar) and overhead stirring agitation (OHS). Trendlines shown are linear best fits of data points. Averages of each set of points at each supersaturation are shown in the insert graph using the same symbols.

Figure 6:26 shows the glycine crystal's growth rates at supersaturations range between 1.20 and 1.26 in deuterium oxide and deionised water, with the averages shown within the insert graph. These averages are shown again in Figure 6:27 alongside some previously published results of glycine in H₂O as no such measurements of the growth rate of glycine in D₂O have been published [219], [220]. Overhead agitation was able to be used at 700 RPM, unlike the higher speed of 1250 RPM required for NaCl experiments, as this could suspend the glycine crystals produced.

In cases where comparisons can be made between different solvent isotopologue and agitation conditions, at least two conclusions can be drawn. Firstly, when comparing the effect of the solvent isotopologue, glycine crystals grown from deuterium oxide grow on average at a slower rate than those grown from regular water at the same supersaturation as shown by the average growth rates of glycine which were measured at $S = 1.26$ in H₂O as this was $74 \mu\text{m}/\text{min}$ when agitating using the stirrer bar and only $39 \mu\text{m}/\text{min}$ when the base solvent was D₂O. This is the case for both forms of agitation used. Secondly, the agitation conditions themselves had influence on the growth rates observed. It also appears that when using the magnetic stirrer bar, the crystals grow faster on average than when the agitation was applied using the overhead propellers as again best shown by the measurements made when testing at $S = 1.26$ as the growth rate measured in H₂O based solutions when agitated using magnetic stirring was $74 \mu\text{m}/\text{min}$ whereas when the overhead stirring was used in the same solution the growth rate measured was $23 \mu\text{m}/\text{min}$. Since the overhead agitation is gentler than that provided by the bar, this would result in a lower Reynolds number that would be considered for the case of a crystal growing according to that proposed in *Duroudier* [72]. Therefore, this lower Reynold's number would give a larger layer across which glycine would have to diffuse from the bulk. According to Noyes and Whitney, this larger layer would then cause a decrease in the rate at which mass deposited onto the surface of a crystal that had formed [70].

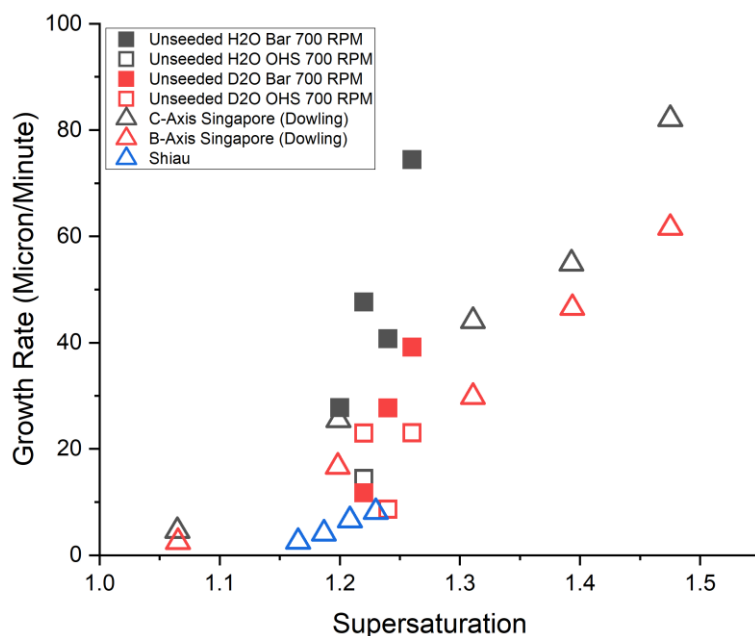


Figure 6:27: Comparison of growth rates of glycine to those previously published. All literature values are for glycine growth in water [219], [220].

6.4.2 Sodium Chloride

6.4.2.1 Unseeded

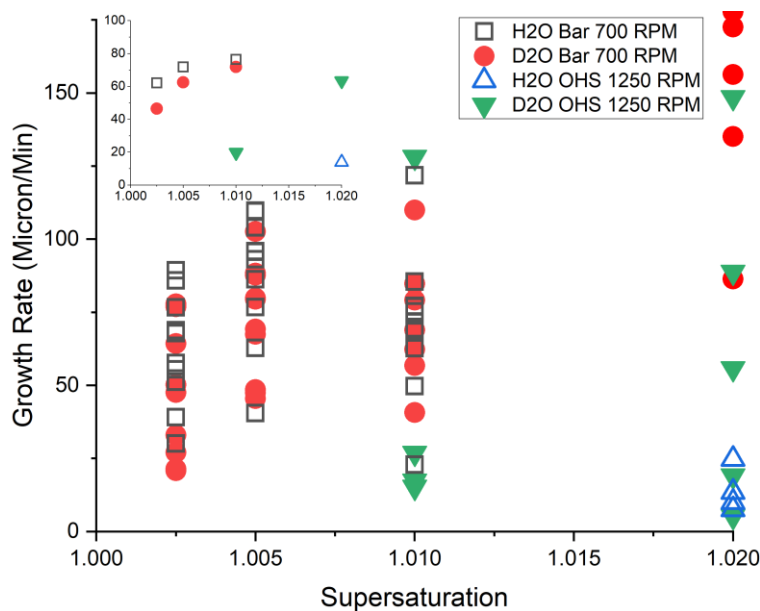


Figure 6:28: Growth Rate of Sodium Chloride Crystals calculated from image analysis of a section of solution where crystallisation occurred, supersaturation between $S = 1.0025$ and $S = 1.02$ solvents of deionised water and deuterium oxide. Vessels agitated using Teflon coated stirrer at a speed of 700 RPM and with overhead agitation at 1250 RPM. Averages are shown in the insert graph using the same symbols.

As expected from increasing the supersaturation in Figure 6:28, the growth determined through analysis of the volume-weighted D-90 values through time shows that in the case of both solvents increasing the supersaturation increases the growth rate. In the cases where

an average growth rate could be calculated for both solvents, the growth rate was lower for crystals grown in deuterium oxide than in regular deionised water for the same supersaturation. Although particle counts were available for crystals growing in solutions meant to be at $S = 1.02$ in H_2O when using magnetic stirring, the particle counts, and the D-90 calculated began increasing before isothermal conditions in 90 % of samples preventing an average from being calculated. The overall effect of the use of D_2O is that at equal supersaturation the crystal growth rates experienced are lower, this difference can appear to be small when using highly aggressive agitation as would be present when using the magnetic stirrer bar. Even though the supersaturations are the the same in each case, the concentration driving force for crystal growth would be lower when using the deuterium oxide as a solvent due to sodium chloride's decreased solubility in D_2O compared to H_2O .

6.4.2.2 Seeded

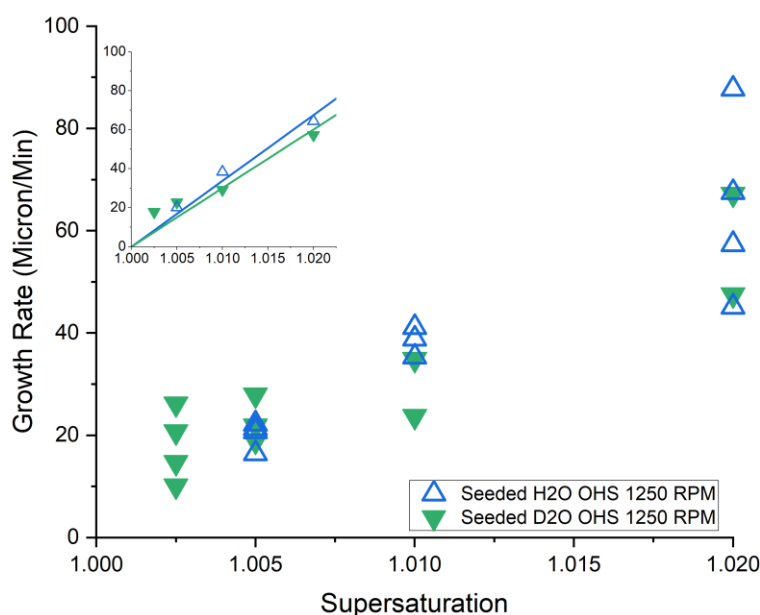


Figure 6:29: Growth Rate of Sodium Chloride calculated from image analysis of a section of solution where crystallisation was occurring with supersaturations between $S = 1.0025-1.01$ for the solvents deionised water and deuterium oxide. Solutions used were seeded with a washed crystal. Vessels agitated with overhead stirring propeller at a speed of 1250 RPM. Averages are shown in the insert graph using the same symbols. Linear fitting is constrained to equal 0 growth at $S=1$.

Unlike the unseeded growth studies in most of the supersaturations examined in Figure 6:29, where a comparison is possible, D_2O as a solvent increased the growth rate. However, compared to regular water, this effect is minimal. Any difference observed here is likely due to the spread experienced when measuring a value multiple times. Although the conditions are more controlled some spread in the growth would be expected some spread would still be expected [30].

6.4.2.3 Literature Comparison

Results obtained from seeded and non-seeded studies are mostly similar in the growth rate of the previously published data. However, since growth conditions are not directly comparable in these literature sources as one of these sources is growth taking place under stagnant conditions and fluidised bed crystallisers [221]–[223]. Growth rates at elevated supersaturation levels ($S \geq 1.1$ or $\sigma \geq 0.1$, where σ is relative supersaturation, $S-1$) were possible when crystal growth within microcapillaries was examined [224]. A comparison of the crystal average growth rates of sodium chloride shown in Figure 6:29, with growth rates published, is shown in Figure 6:30.

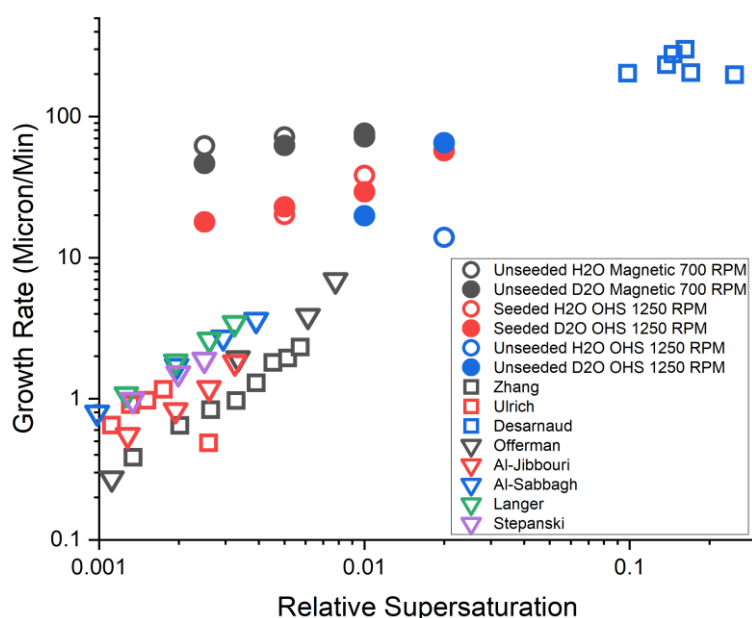


Figure 6:30: Comparison of Sodium Chloride crystal growth of a crystal dimension [221]–[224].

Comparing the average growth rates determined by the analysis of the volume-weighted D-90, the growth rates determined here are up to two orders of magnitude larger than those previously published. Previous growth rates with comparable growth rates have been gained from relative supersaturations much higher than those measured in this work.

However, the growth rate measurements were calculated by examining the rate of change of the volume-weighted D-90 values. This is not a fixed requirement, although *Cashmore et al.* [189] have found that this value appears suitable for measuring the growth of glycine in this fashion; this work supports that hypothesis. *Brown et al.* [225] suggested monitoring the volume-weighted D-75 as an in-situ growth rate measurement to minimise the impact of newly nucleating particles. This may still be too high to reflect the actual growth rate experienced accurately of NaCl growing from aqueous solution. It could be suggested that no

single diameter value can be used across all solute/solvent systems. To confirm that a selected 'D' value suitable other methods of measurement of the crystal growth rate may be required. Therefore, the growth rates were also examined by tracking the D-25 values. Although using this lower 'D' value to calculate the growth rates may provide growth rates more in line with previously published results [221]–[224], its use may give artificially low results for what could be considered the 'true' growth rate here to the greater influence of newly nucleated particles. It is also worth noting that damaged crystals (caused by either mechanical damage or laser ablation [226], [227]) have been observed growing at significantly higher rates than non-damaged crystals. In the case of laser ablation, this may not even require physical damage to the surface of the crystal. Therefore, since previous measurements are unlikely to cause damage to the crystals measured, and the measurements performed here were subjected to mechanical agitation, it should not be surprising when viewed with these comparisons in the context of *Tominaga et al.* [226] and *Schiele et al.* [227] where ablated or damaged crystals have been observed or determined to have enhanced growth rates approximately 90 % above [227] that of non-damaged crystals.

The other issue that could be the case is that growing crystals are subject to a growth rate dispersion [217], which also indicates that the largest particles are the fastest growing and could be responsible for further shifting the averages further above the trend established by the others in single crystal and fluidised-bed experiments. Since the 'D-90' was used for the growth rates here, another potential issue is with the analysis presented in this section. Multiple competing factors exist make it difficult to determine a 'real' estimate of the growth rate. The first being that as NaCl systems in which the growth rates were measured are also nucleating, which would have the effect of shifting the growth rates measured to provide an underestimate of the true growth rate, which is why a large 'D' value is taken. However the dispersion of growth rates that exist show that the largest crystals within a size distribution will be the fastest growing, which would result in a overestimate of the growth rate [217]. Although it would add great complexity monitoring how multiple 'D' values of the distribution evolve over time may provide a more accurate description of how the crystals grow in suspension.

Examining all the growth rates in Figure 6:30 adds further weight to the nucleation proposal by *Cashmore et al.* that there does not appear to be a certain supersaturation below which crystal growth or secondary nucleation would not occur. And it is likely that in the cases

where solutions are supersaturated but below the level of what would traditionally be defined as the secondary nucleation threshold, that nucleation levels would be too low to detect [30]. However, in the case of sodium chloride, the precision required to measure the growth of very low supersaturation levels is heightened by the low dependence of solubility on temperature [189].

6.5 Secondary Nucleation Rate

Secondary nucleation rates can be determined by analysing stills taken at regular intervals at a small section of the volume of the solution in which the crystallisation occurs. These photographs are analysed by the Crystalline software to output the number in each bin size of those visible. Thus, the number of solid particles visible can be converted into the number of particles present per unit volume of the solution in the Crystalline system vial setup. This calibration has been performed previously using a range of concentrations of 50 μm diameter polystyrene microspheres suspended in water for which the number of visible particles in focus within the field of view of the cameras monitoring a portion of the Crystalline's individual reactors [29]. This data was fitted to a second order polynomial to allow a wide range of concentrations to be examined the fitted trendline is shown by Equation 6:1 [29]:

$$N_p = 10 + 134.33N + 3.98N^2$$

Equation 6:1

Where N_p is the number density in particles per mL of volume, and N is the number of particles visible in the images taken by the cameras monitoring the vials in the crystalline reactors. The same limitations that applied to the particle counts in the discussion of growth rates also applies to the determinations of secondary nucleation rates, this is given in full detail in section 6.4. The number of particles per unit volume was plotted against time, an example of which is included in Appendix D. The linear trendline gradient of the volumetric number concentration was defined as the secondary nucleation rate [29]. The same limitations, with regards to the frequency of image analysis, to the growth rate analysis in section 6.4 are also applicable to secondary nucleation rate calculations.

6.5.1 Glycine

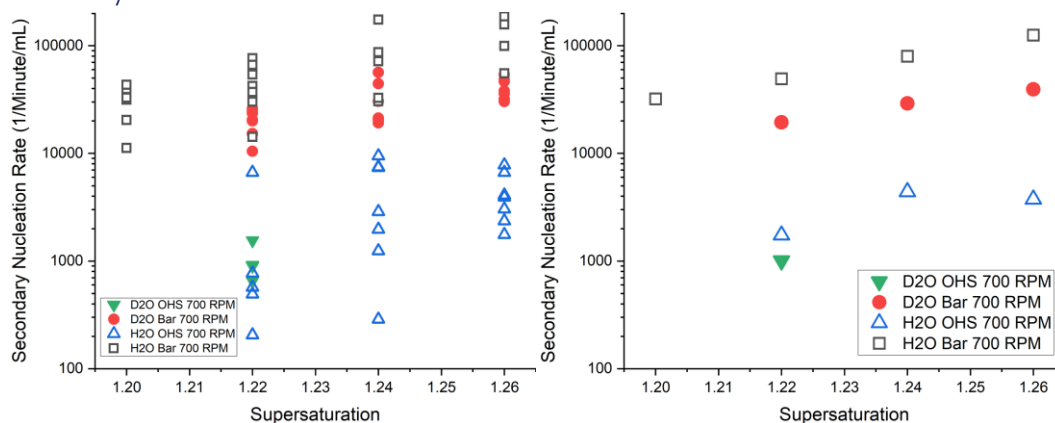


Figure 6:31: Left; Secondary Nucleation rates of glycine nucleating from supersaturated solutions in H₂O and D₂O. Right; Average secondary nucleation rates.

Similarly, to the growth rates of glycine examined in section 6.4.1, using a different solvent isotopologue can impact the secondary nucleation rate determined. Again, two non-trivial conclusions can be drawn from Figure 6:31. The impact of the solvent isotopologue is also clear when examining the samples that were agitated using the magnetic bar. The secondary nucleation rate was reduced by using D₂O when compared to solutions whose solvent was H₂O. For example at $S = 1.26$ the secondary nucleation rates were $125000 \text{ min}^{-1} \text{ mL}^{-1}$ and $39000 \text{ min}^{-1} \text{ mL}^{-1}$ for H₂O and D₂O based solutions, respectively. The large spread of data seen in the secondary nucleation rates of glycine in H₂O and D₂O should not be unexpected as this has been observed previously by Cashmore [30], it is the case that when unseeded the spread of secondary nucleation rates have been observed being spread across multiple orders of magnitude for secondary nucleation rates measured at the same supersaturation, it may be due to differences that would occur in the generation of the first crystal, through primary nucleation.

This is observed by examining the averages from the nucleation rates determined using a magnetic stirrer bar. However, this is also the case at $S = 1.22$ when using overhead stirring, the only supersaturation using overhead stirring where comparison is possible. Secondly, the impact of the agitation is also apparent as the use of the gentler agitation through overhead stirring significantly reduces the secondary nucleation observed on average by approximately an order of magnitude. It can also be seen that increasing supersaturation used for testing gives a higher secondary nucleation rate regardless of the agitation used.

6.5.2 Sodium Chloride

The secondary nucleation of sodium chloride was examined under two conditions: vials were seeded with a pre-existing crystal made through the process described in section 6.1.3, and unseeded samples where primary nucleation was allowed to occur as the vials were observed for a longer period (4 hours).

6.5.2.1 Unseeded NaCl Secondary Nucleation

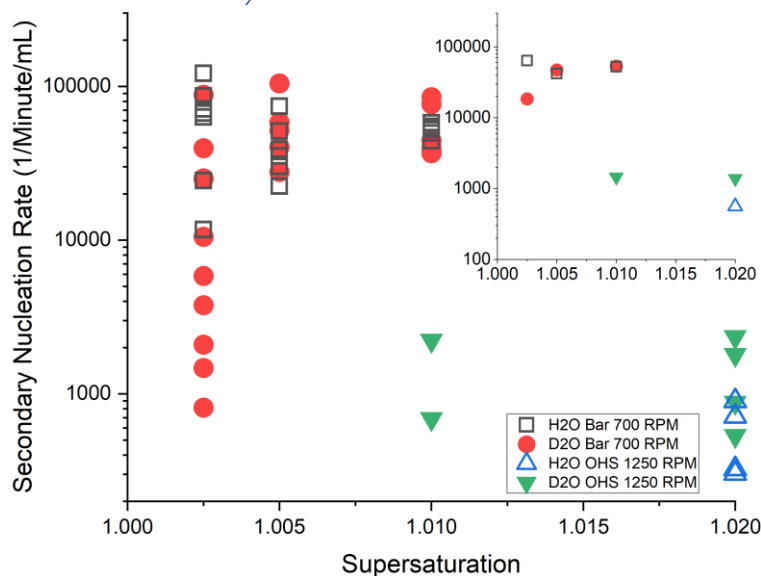


Figure 6:32: Average Secondary Nucleation rate calculated from multiple supersaturations between $S = 1.0025$ and 1.02 for both solvents deionised water and deuterium oxide shown on a logarithmic scale. Vials were not seeded and required primary nucleation to occur first. Averages are shown in the insert graph using the same symbols.

By examining the averages of each unseeded case as shown by Figure 6:32, it does not appear to be much of a trend when secondary nucleation of sodium chloride in water was agitated by a Teflon stirrer bar at 700 RPM. However, when comparing agitation conditions, the agitation conditions are also heavily influential on the secondary nucleation rate observed. Comparing the trends observed when comparing the agitation where magnetic stirring produced much higher rates of secondary nucleation at lower S than were achieved when using overhead agitation, however this was drawn from experiments performed at $S = 1.01$ due to the lack of data at other supersaturations.

Therefore, the decision was made to seed several vessels using saturated sodium chloride solution ($S = 1$) and see the impact on the number of particles observed. This was performed using the same procedure for secondary nucleation measurements for supersaturated sodium chloride solution in water, examined in section 6.5.2.3.

6.5.2.2 Seeded NaCl Secondary Nucleation

Using a three-blade downflow propeller at a speed of 1250 RPM secondary nucleation was investigated in vials containing solutions of NaCl in H₂O and D₂O which were seeded, the calculated secondary nucleation rates determined are shown in Figure 6:33.

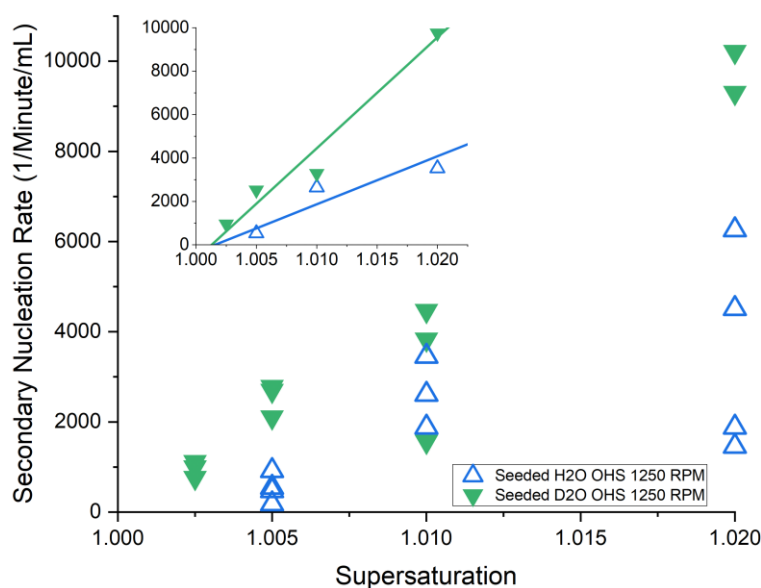


Figure 6:33: Average Secondary Nucleation rate calculated from multiple seeding experiments where a washed crystal was added between supersaturations $S = 1.0025$ and 1.02 for both solvents deionised water and deuterium oxide shown on a linear scale. Averages are shown in the insert graph using the same symbols. Linear trendlines shown are of average values.

Cases where seeded runs were performed, seen in Figure 6:33 that at supersaturations above ~ 1.0015 , the secondary nucleation rate trend is higher when utilising D₂O as a solvent when compared to regular H₂O. The trends indicate that a certain level of supersaturation is required before secondary nucleation will occur in the seeded studies. This occurred at a supersaturation of $S \approx 1.0015$ for both isotopologues of the solvent.

It must also be noted that the appearance of this supersaturation below which secondary nucleation does not occur depends on fluid shear conditions [192]. From this, it could be extrapolated that the secondary nucleation threshold's magnitude decreased as the agitation increased. Since the secondary nucleation threshold, in this case which would be defined as $S \approx 1.0015$, is so close to saturation under these conditions, it may be possible that under certain conditions, secondary nucleation is possible at even the lowest levels of supersaturation, below the value of what would typically be defined as the secondary nucleation threshold and due to the way that secondary nucleation rates have been calculated here very low rates of secondary nucleation would be difficult to quantify.

The examination of the nucleation rate of α -glycine when seeded still suggests that secondary nucleation is possible below what would be described as the 'secondary nucleation threshold'; however, like that suggested by *Cashmore et al.*, the level of secondary nucleation below this supersaturation may not be of any practical use for the generation of crystalline materials [189]. Measurement of secondary nucleation at lower supersaturations than the $S = 1.0015$ used may pose a difficulty as the current method used to perform calculations only examines a small portion of the total volume. In addition, the exceptionally low supersaturation leaves a minimal mass of solute available to form crystals and grow to a large enough size to be registered by the image analysis.

The particle count numbers also allow for assessing the period when the seed is inserted into the vial when the low-temperature hold is reached and the appearance of several particles above the level (above 10) of any potential interference from third material particles (e.g., dust). This is defined as the delay time. The data shown in Figure 6:34 shows that as the supersaturation increases when using deionised water as a solvent, the delay time decreases for all the supersaturations tested. Since a comparison can be made with only three of the four supersaturations using these supersaturations to form a basis, the same trend appears. With increasing supersaturation, the delay time shrinks.

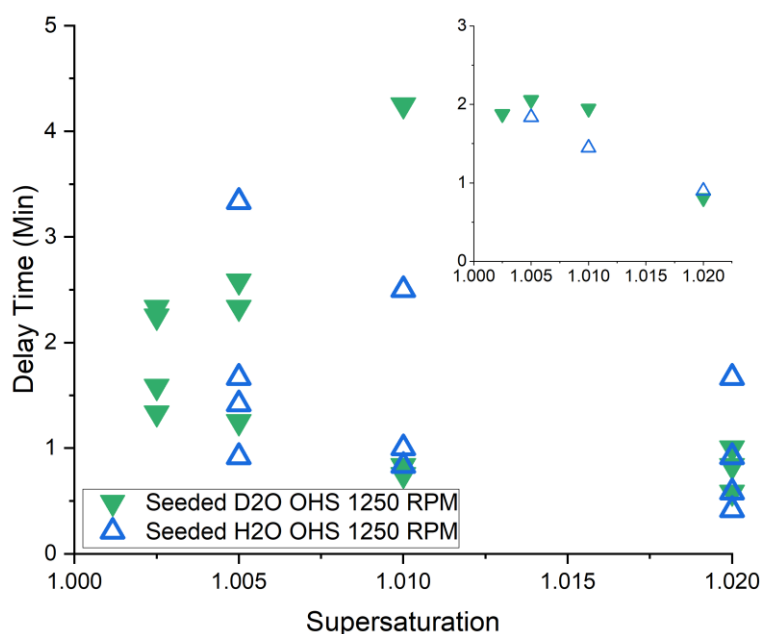


Figure 6:34: Secondary Nucleation Delay Times for seeded studies in deionised water and deuterium oxide between the supersaturations $S = 1.0025$ and 1.02 . Averages are shown in the insert graph using the same symbols.

Previous studies have suggested that introduced seeds require a brief period before producing secondary nuclei; during this period, suggested to be due a solute layer which forms surrounding the seed [30]. The increased growth rate associated with higher supersaturations allows this layer to form quicker. Thus, this layer can be more easily removed under fluid shear conditions and collisions. The results here support this hypothesis suggested previously [228]. This is further reinforced by examining Figure 6:35, the average delay time trend and the corresponding average growth rate. It can be seen when using regular water, and a linear trend appears that as the delay time increased, this was accompanied by a decrease in the growth rate experienced in both solvents. However, when examining the solutions that used deuterium oxide as a solvent, this trend is less certain, but it still is generally apparent, suggesting that the region of new crystal growth that is required before has to grow a certain amount before secondary nucleation can be observed occurring.

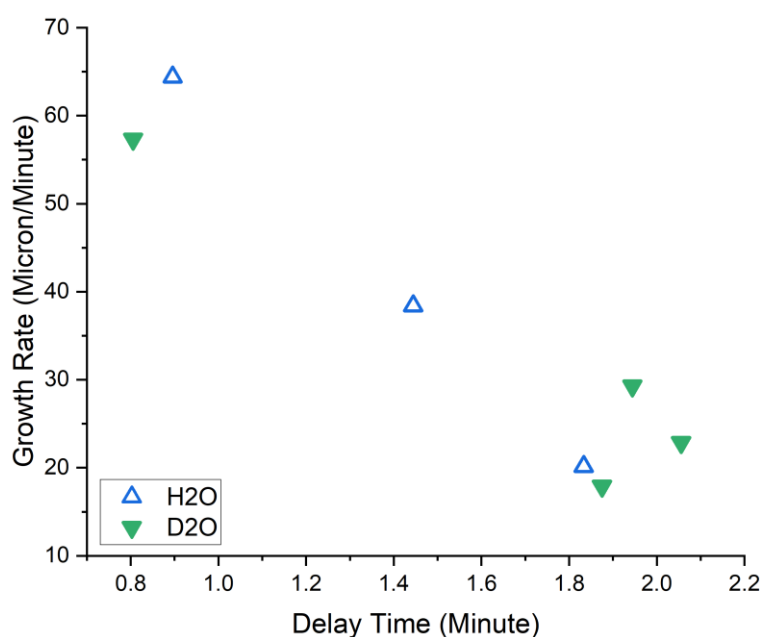


Figure 6:35: Comparison of the average growth rate determined from the trend in D-90s and the corresponding delay time after seeding with a single crystal of sodium chloride in supersaturated sodium chloride solutions in water and deuterium oxide.

6.5.2.3 Secondary Nucleation from Attrition

To check for the presence of seed attrition, experiments were carried out at $S = 1$ so that there should be no new nucleation or growth of crystals that should come from the solution. Examples of the nuclei produced through attrition are shown in Figure 6:36 and Figure 6:37.

In the seeded runs where a saturated solution is used, the very fact that the solution is not supersaturated means that these new nuclei cannot originate from nucleation from the

solution. Therefore, these particles can only be generated from the mother seed crystal. Furthermore, since the solution is saturated, these particles cannot dissolve, as no solute in the solution can form nuclei allowing them to be imaged.

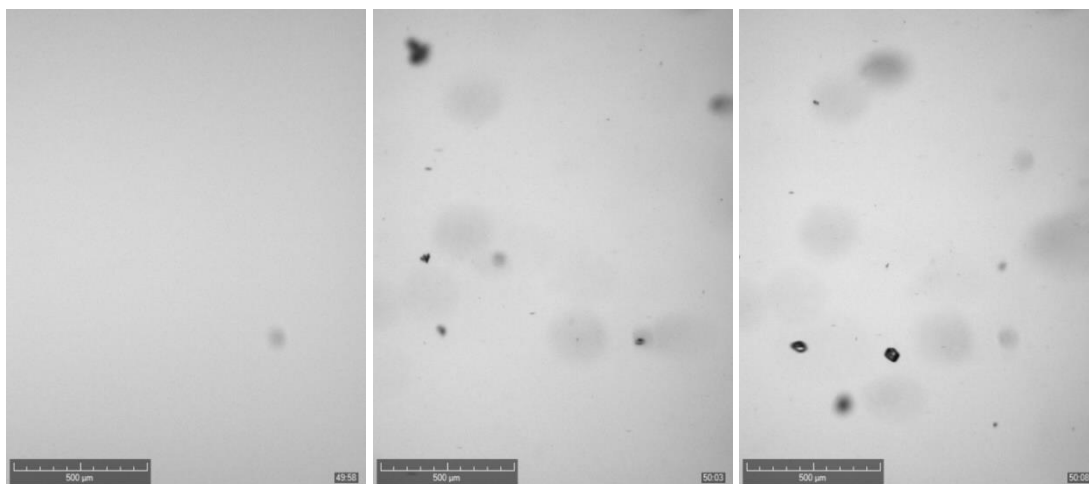


Figure 6:36: Nuclei generated from the attrition of sodium chloride in saturated water. Images taken at five-second intervals; left most image taken first.

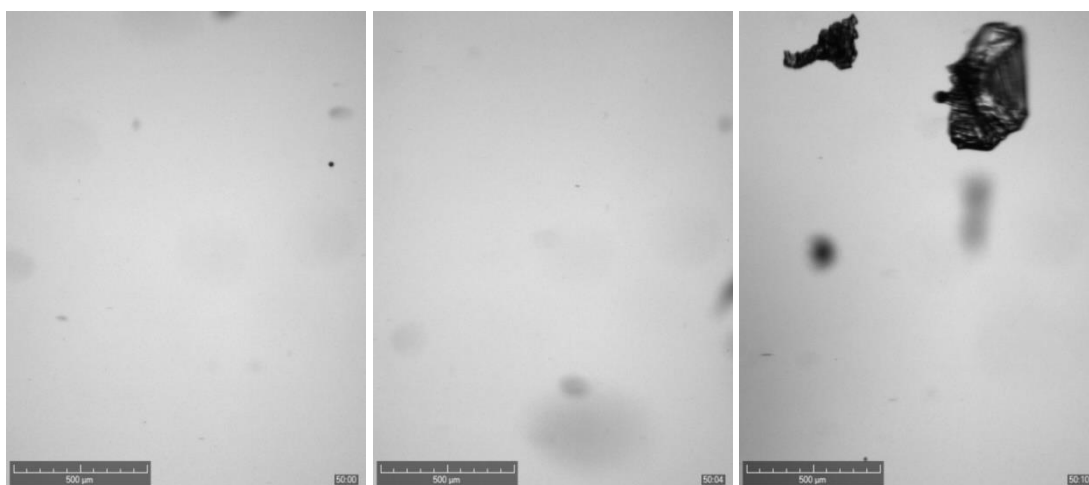


Figure 6:37: Nuclei generated from the attrition of sodium chloride in saturated deuterium oxide. Images taken at five-second intervals; left most image taken first.

The damage that can be done to seed crystals includes fragmentation, as one of the seeds used for a run-in water saturated by sodium chloride was broken into two large pieces. This was discovered at the end of the temperature cycle when the vial was removed from the Crystalline reactor.

One of the seeds used in seeding the saturated solution in water was pictured by chance, shown in Figure 6:38.

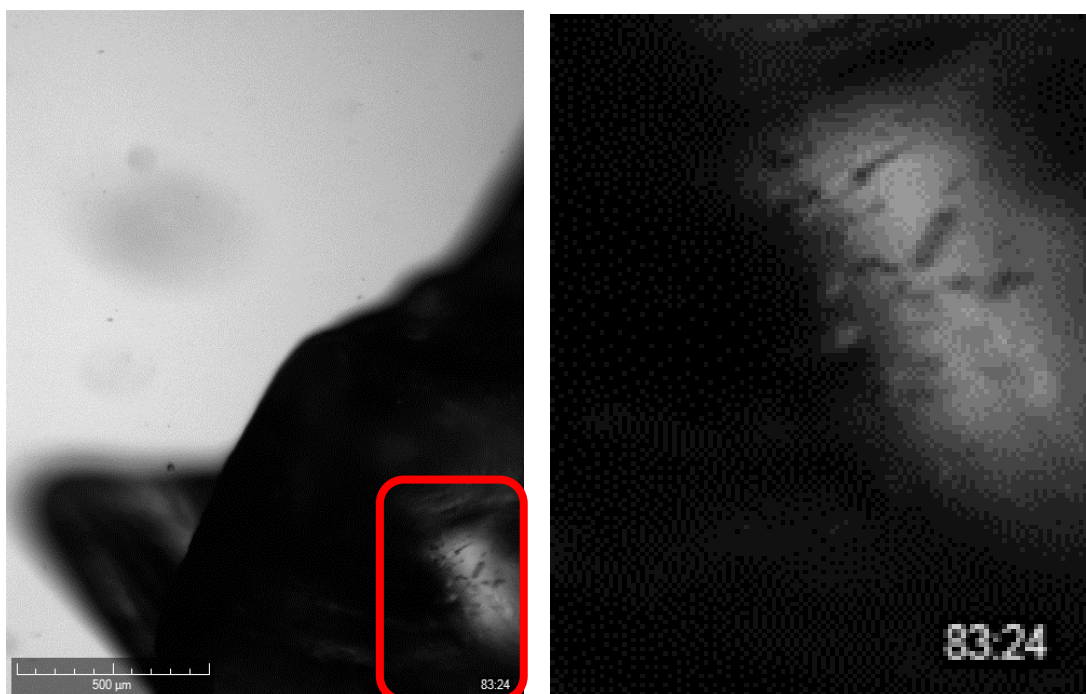


Figure 6:38: Left; Image of the seed crystal. Right; enlarged view of the section enclosed in red in the left image.

In the lower right-hand section of the right image of Figure 6:38, a rough region populates the crystal. Damage caused by the collisions that occur in the vial between the stirrer bar and the crystal and between the crystal and the walls of the glass vial—further supporting the idea that the source of the particles visible in Figure 6:36 and Figure 6:37 are coming from the mechanical damage caused by the stirrer bar used to agitate the solution in each vial. It was fair to conclude that this damage came from the action of the magnetic stirrer bar since the seeds were immersed in pure H₂O prior to insertion for at least 10 seconds, which from the results later discussed in section 8.2.

6.6 Connection between Growth and Nucleation

To discern if any direct correlation exists between the secondary nucleation rate and the D-90 determined growth rate, both were plotted against one another on a log-log scale for each solute system as performed by *Cashmore* [189]. Where the solvent was either water or deuterium oxide, in the case where the crystallising substance was glycine and sodium chloride, these comparisons are shown in Figure 6:39 and Figure 6:40, respectively. From Figure 6:39 it can be seen that there is some correlation between the secondary nucleation rate and the growth rate of the crystal distribution examined where increasing one also causes the other factor to increase. It also appears that the major factor when deciding where on this general trend a certain point will fall is due to the agitation employed.

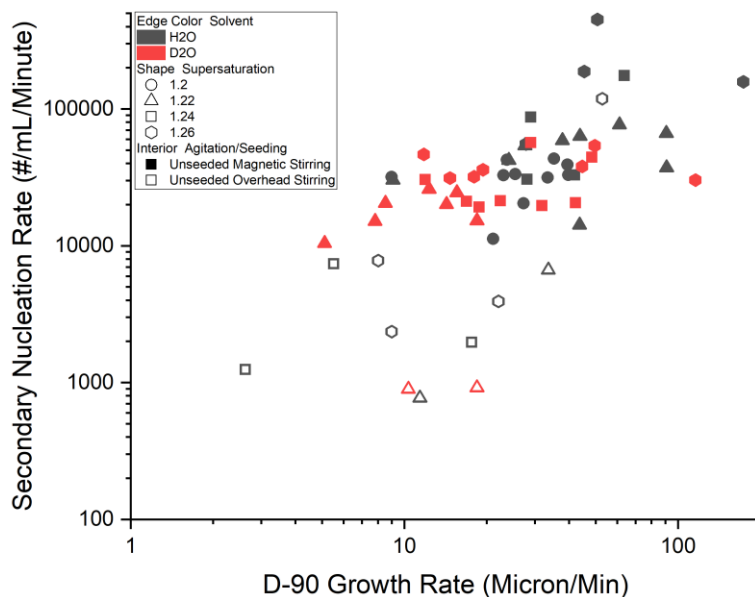


Figure 6:39: Comparison of Secondary Nucleation Rates and Growth Rates of Glycine from solution in water and deuterium oxide between $S = 1.20$ and $S = 1.26$, when subjected to agitation using magnetic and overhead stirring. Determined at the Crystalline Scale (3 g of solvent). Colour indicates the solvent isotopologue used; H_2O (Black) and D_2O (Red). Shape indicates the supersaturation used; 1.20 (Circles), 1.22 (Triangles), 1.24 (Squares) and 1.26 (Hexagons). The interior state indicates the agitation used; Magnetic Bar Stirring (Filled) and Overhead Stirring (Hollow).

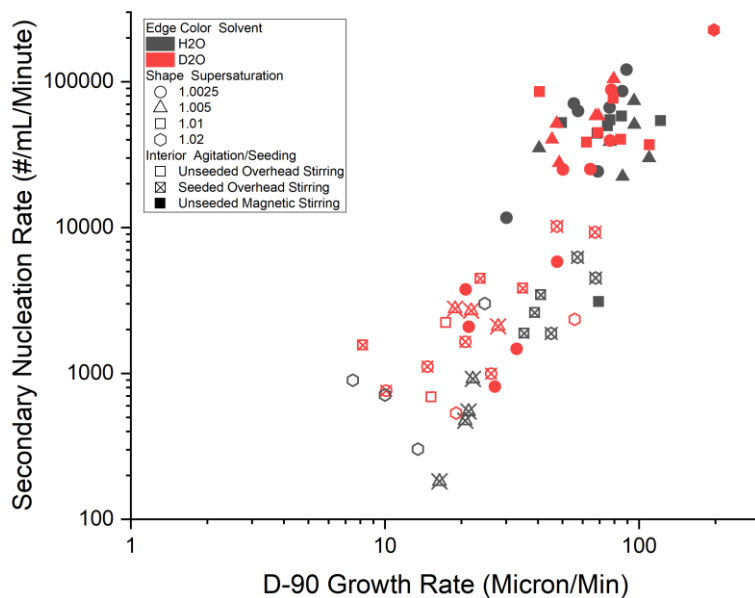


Figure 6:40: Comparison of secondary nucleation rates and growth rates of NaCl from solution in water and deuterium oxide between $S = 1.0025$ and $S = 1.02$ when subjected to magnetic bar agitation and overhead agitation when unseeded, and overhead agitation when seeded. Determined at the Crystalline scale (3 g of solvent). Colour indicates the solvent isotopologue used; H_2O (Black) and D_2O (Red). Shape indicates the supersaturation used; 1.0025 (Circles), 1.005 (Triangles), 1.01 (Squares) and 1.02 (Hexagons). The interior state indicates the agitation used; Magnetic Bar Stirring (Filled) and Overhead Stirring (Hollow). Seeding is indicated by crossed symbols.

Figure 6:40 shows a band within with all the points determined for the crystallising NaCl fall where a high degree of correlation exists between the D-90 growth rate and the secondary

nucleation rate. The low nucleation and low growth end are mainly populated with runs where overhead stirring was used either with or without seeding. In contrast, this band's higher nucleation and growth end are exclusively where magnetic bar agitation was utilised. The main factor in delivering high nucleation rates and substantial growth rates was not supersaturation or seeding but the agitation used. The same form of relationship proposed by *Cashmore* [30] is observed here, shown in Figure 6:40.

6.7 Conclusions

The solvent isotopologue's impact depends on the system that is under examination. For glycine, using deuterium oxide compared to regular water appears to reduce the primary and secondary nucleation rate and the rate at which the crystal of glycine grows at equal supersaturation. However, deuterium oxide's use as a solvent in sodium chloride appears to decrease the primary nucleation rate, increase the secondary nucleation rate, and have an insignificant impact on the crystal growth rate. Since the effects of the isotopes are not consistent across the systems, therefore it may be necessary to examine systems individually for now and it may be reasonable to suggest that this effect may be similar to the kinetic isotope effect.

7 Impact of Particles on Nucleation Characteristics

It is well known and understood that additional third material in suspension with a crystallising solution can influence the nucleation rates observed, depending on numerous factors. These additional particles typically reduce the energy barrier required for nucleation [58]. The reductions in the energy barriers are quantifiable using the contact angle between the heterogeneous particle, solution, and the solid crystallising material [3].

The precise effect of non-crystallising solid material, sometimes called a template, depends on its concentration and composition. Therefore, it is critical to understand the effects that any particles required for tweezing would have on crystallisation, especially nucleation, if these particles are used to investigate crystallisation when particles are also tweezed when in suspension in a solution. This data in addition to providing additional context for the results reported in chapters 8 and 9. But additionally this work is also of great interest on its own as it provides an additional way in which nucleation can be controlled through a range of conditions including solvent choice, solute concentration and particle material and loading, in addition to further exploration of a relatively methods to measure nucleation by determining the onset of nucleation.

7.1 Experimental

7.1.1 Solvent Particle Suspension Preparation

Before the solutions of NaCl or glycine were made up using the solvent with the suspended microparticles, the base particle suspension had to be produced. Two different particles were used in testing: silica (Duke Scientific, 1.57 μm diameter) and polystyrene (microparticles GMBH, 1.59 μm diameter). Details of the particle suspensions used when testing the effects on glycine and NaCl nucleating from solution are summarised below in Table 7:1. Different particle concentrations were used for the two solutes as these were performed as part of two separate experimental campaigns, due to unavoidable circumstances, see Appendix B for more detail.

Table 7.1: Summary of the particle suspensions used to test the effects of particle dopings on primary nucleation behaviour.

| Solute | Particle Material | Mass Concentration (mg _{particle} /g _{solvent}) | Number Concentration ¹ (#/g _{Solvent}) |
|---------|-------------------|---|--|
| Glycine | Silica | 1 | 2.5x10 ⁸ |
| | | 2 | 5x10 ⁸ |
| | Polystyrene | 0.5 | 2.5x10 ⁸ |
| NaCl | Silica | 0.12 | 3x10 ⁷ |
| | Polystyrene | 0.06 | 3x10 ⁷ |

The lowest of these number concentration ($3 \times 10^7 \text{ g}_{\text{Solvent}}^{-1}$) of particles that was used when testing the effect of the tweezers on crystal growth and nucleation as examined in chapters 8 & 9. This concentration was decided upon as this allowed a small number (low single digits) of individual particles to be visible with the field of view of the optics at any one time, as determined by examining suspensions at a range of suspension concentrations using the microscopy section of the optical tweezers.

The suspensions were manufactured by diluting the suspensions supplied by either Duke Scientific (for silica suspensions) or microparticles GMBH (for polystyrene suspensions). Depending on the particle and solute being tested, a known mass of supplied suspension was added to a laboratory bottle. This was then diluted down using pure solvent, depending on the tested solvent. Particle suspensions were made up to have 20 g of pure solvent (H₂O or D₂O). These were then closed using the supplied lid, sealed using parafilm, and stored for later use.

7.1.2 Metastable Zone Width Impacted by Particles

Each vial was prepared by adding a known mass of solute into each 1.5 mL HPLC vial by difference, to which a known mass of solvent suspension was added to give a mass of pure solvent with each vial of 1 g. Following this, a 2 mm Teflon-coated magnetic stirrer bar was added to each vial. These were then closed using a basic cap. Using the Crystal16 each set of vials was subjected to a temperature cycle between 5 °C and 70 °C, where the temperature was changed using ramps of 0.3 °C per minute, where the temperature holds at 5 °C, and 70

¹ Number concentration determined by assuming a uniform distribution of particles through the volume and the calculated mass of a single particle to determine the number of particles present per gram of solvent.

°C were held for 30 minutes upon reaching each of these ramp-end temperatures, this temperature profile is shown in Figure 7:1. Throughout this temperature profile, the contents of the vials were agitated using the added magnetic stirrer bar at 700 RPM. This temperature and agitation profile are the same used for testing when measurements of the MSZW when in the absence of particles, as reported in section 6.1.1, allowing direct comparisons to be made.

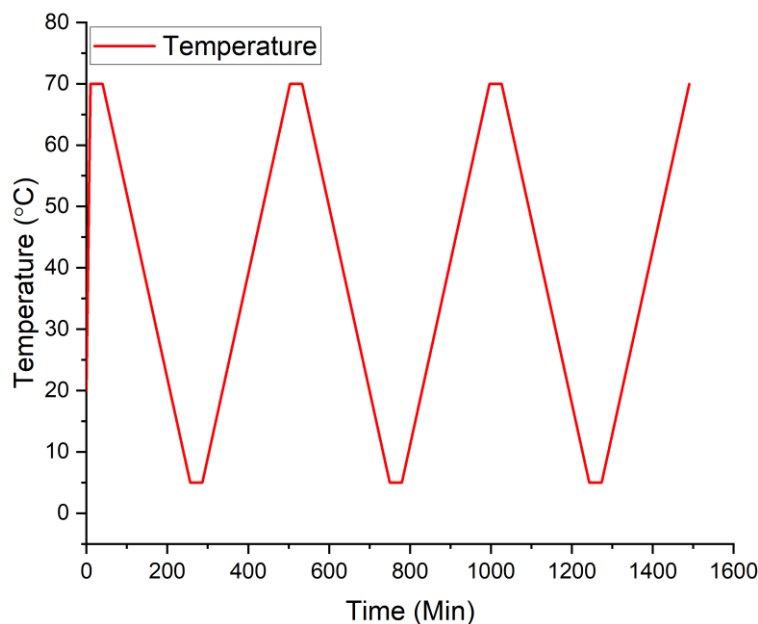


Figure 7:1: Temperature Cycle used to determine the Effect of Microparticles on the MSZW. This is the same profile used in section 6.1.1 as shown in Figure 6:1.

At the end of each high-temperature hold, the Crystal16 device was tuned. This is commonly used to signal that the samples being tested are undersaturated. Therefore, no solid crystalline test material would be present, resulting in the transmissivity reading at this point jumping to 100 % through this calibration step. However, this did not necessarily occur when the particles were included. This is discussed in greater detail in section 7.4, depending on the particle's concentration and material.

7.1.3 Induction Time Distributions Impacted by Particles.

Like in the testing of the MSZWs, the impacts of microparticles on induction time distributions (and therefore primary nucleation rates) were tested on the same range of solutions evaluated in section 6.2. The supersaturations tested for NaCl and glycine in H₂O and D₂O are shown in Table 7:2 and Table 7:3, respectively.

Table 7:2: Concentrations of NaCl in H₂O and D₂O used to determine the effects of particles on primary nucleation characteristics.

| Solvent | Concentration (g/g) | Supersaturation at 25 °C (S) |
|--|---------------------|------------------------------|
| H₂O C* = 0.3599 g/g at 25 °C | 0.3608 | 1.0025 |
| | 0.3617 | 1.005 |
| | 0.3635 | 1.01 |
| | 0.3671 | 1.02 |
| D₂O C* = 0.3071 g/g at 25 °C | 0.3079 | 1.0025 |
| | 0.3086 | 1.005 |
| | 0.3102 | 1.01 |
| | 0.3132 | 1.02 |

Table 7:3: Concentrations of Glycine in H₂O and D₂O used to determine the effects of particles on primary nucleation characteristics.

| Solvent | Concentration (g/g) | Supersaturation at 25 °C (S) |
|--|---------------------|------------------------------|
| H₂O C* = 0.2471 g/g at 25 °C | 0.2866 | 1.16 |
| | 0.2916 | 1.18 |
| | 0.2965 | 1.20 |
| | 0.3015 | 1.22 |
| D₂O C* = 0.2148 g/g at 25 °C | 0.2492 | 1.16 |
| | 0.2535 | 1.18 |
| | 0.2578 | 1.20 |
| | 0.2621 | 1.22 |

To determine the effects of microparticles on primary nucleation rates the, the conditions examined in section 6.3, were used as a basis to compare doped and non-doped runs. This testing initially using the same concentrations of particles as was used to examine the effects on the MSZW. Induction times were measured at 25 °C, using the temperature and agitation cycle shown in Figure 7:2. Where temperature ramps of 5 °C / min between the high and low temperatures of 70 °C and 25 °C, and high-temperature holds were 30 minutes in length. In contrast, low-temperature holds were 4 hours, where the vial contents were agitated throughout the temperature cycle using an included 2 mm Teflon-coated magnetic stirrer bar at 700 RPM. In essence these tests are being performed using the same concentrations

and procedures as was used in chapter 6, with the only difference being the presence of the silica or polystyrene microspheres.

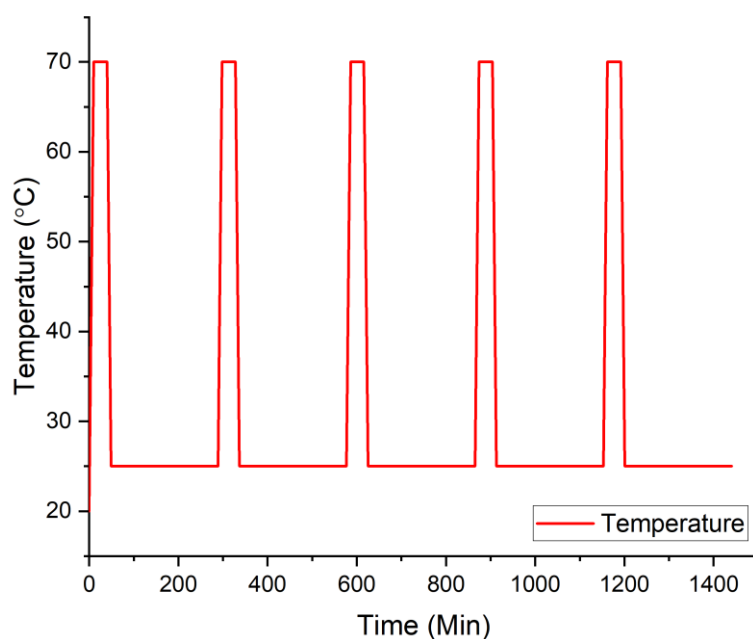


Figure 7:2: Temperature profile used to determine the effects of microparticles on induction time distribution. This is the same profile used in section 6.1.2 as shown in Figure 6:2.

7.2 Impact of Particles on MSZW

Since added solid non-soluble materials would be required for typical tweezing experiments, the effect that common tweezing particles would have in non-tweezing scenarios would be required to be known to allow the effects that these and the tweezers would have to be fully understood within their full context. However, it is also important to regard the concentration, size, polymorph, and functionalisation status of the non-soluble material [50], [60].

7.2.1 MSZW of Glycine in H₂O and D₂O with Silica and Polystyrene Particles

The effect of the silica particles at a 1 mg_{silica}/g_{solvent} in the H₂O-based solution, shown in Figure 7:3, is best described as one-sided shrinkage in the prediction band, suggesting that that the onset of nucleation is promoted once the same point is passed. Suggesting that the presence of the particles does not increase the maximum temperature at which the glycine in H₂O would nucleate. However, once this point is crossed, dependent upon the concentration of the solution used, nucleation is more likely at a lower level of supersaturation. This is shown in Figure 7:3. However, in the case of glycine dissolved in D₂O, there is a general shift of the metastable limit towards higher temperatures indicating that nucleation is more likely to

occur at higher temperatures when in the presence of the silica size standard microparticle, as indicated by the general shift in the prediction band.

The gradient of the metastable limit is not impacted as the linear fit shown in Figure 7:3 shows that the gradient of the trendlines are equal when examining the silica-doped and particle-free runs in both H₂O and D₂O, suggesting that the impact that these silica particles have is effectively equal across the range of concentrations examined. The indicated undersaturated region (shown in green) was determined in all cases in the absence of any particulate/template material in all cases indicated in section 7.2.

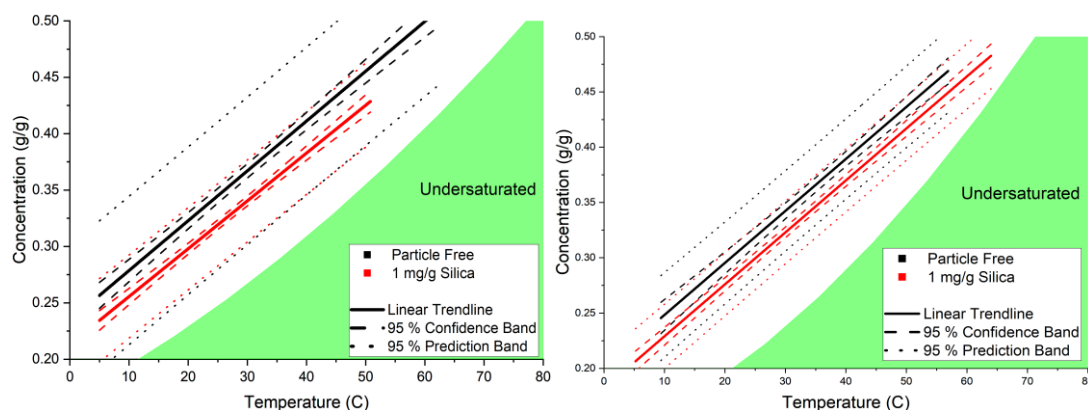


Figure 7:3: Left; Effect of 1 mg_{silica}/g_{water} 1.57-micron diameter silica microspheres on the MSZW of Glycine nucleating from solution in H₂O. Right; Effect of 1 mg_{silica}/g_{deuterium oxide} 1.57-micron diameter silica microspheres on the MSZW of Glycine nucleating from solution in D₂O. Addition of silica particles (Black to Red) shrinks the MSZW.

However, when an equivalent situation was examined using polystyrene particles at the same number concentration in place of silica (half of the mass concentration due to the 50 % reduction in density from silica to polystyrene), these had a different impact on the MSZW of glycine in H₂O and D₂O. It must be noted that the presence of these polystyrene particles did impact the transmissivity measurements, discussed in detail in section 7.4.2. The impact of the polystyrene particles on glycine in H₂O and D₂O is shown in Figure 7:4. The impact appeared to be different depending upon the solvent isotopologue used. In the case of solutions made up using H₂O appeared to shrink the width of the metastable zone at lower saturation temperatures. In comparison, at higher temperatures, the width appeared slightly wider than in the absence of particles. This suggests that at these lower temperature that the presence of the polystyrene greatly promotes the nucleation of glycine from solution and that this promotion of nucleation falls away as the temperature increases in the case of suspension in H₂O. Whereas there does not appear to be any promotion of nucleation when suspended in D₂O and if anything, there may be some slight inhibition of nucleation which

increases with increasing saturation temperature as indicated by the increased gradient of the fitted curve in red compared to that in black.

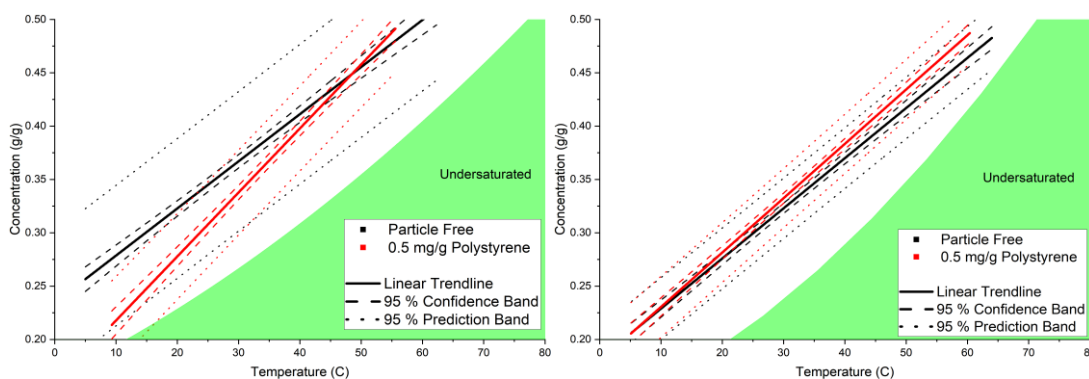


Figure 7:4: Left; $0.5 \text{ mg}_{\text{polystyrene}}/\text{g}_{\text{water}}$ 1.57-micron diameter Polystyrene microspheres on the MSZW of Glycine nucleating from solution in H_2O . Right; $0.5 \text{ mg}_{\text{polystyrene}}/\text{g}_{\text{Deuterium Oxide}}$ 1.57-micron diameter Polystyrene microspheres on the MSZW of Glycine nucleating from solution in D_2O . Addition of particles (Black to Red) induces a shift in the gradient of the MSZW.

Using D_2O resulted in a slightly different change to the characteristics of the metastable zone limit at the lower concentrations. As the concentration of the glycine was increased, this had a slight impact on the width of the metastable zone as this increased with increasing concentration. There appeared to be effectively zero impact induced by the presence of the polystyrene particles.

7.2.2 MSZW of NaCl in H_2O and D_2O with Silica and Polystyrene Particles

Unlike the effect of the silica particles on the metastable limits of glycine, Figure 7:5 shows a shift to higher temperatures is observed and an increased gradient, resulting in a comparatively smaller MSZW at equal solute concentrations. However, it also appears that the confidence band within which the best fit linear trendline is expected to fall is also shrunk, suggesting that the point where nucleation is expected to occur is also more concentrated around a specific temperature dependent upon the concentration. This is the case when using either solvent isotopologue.

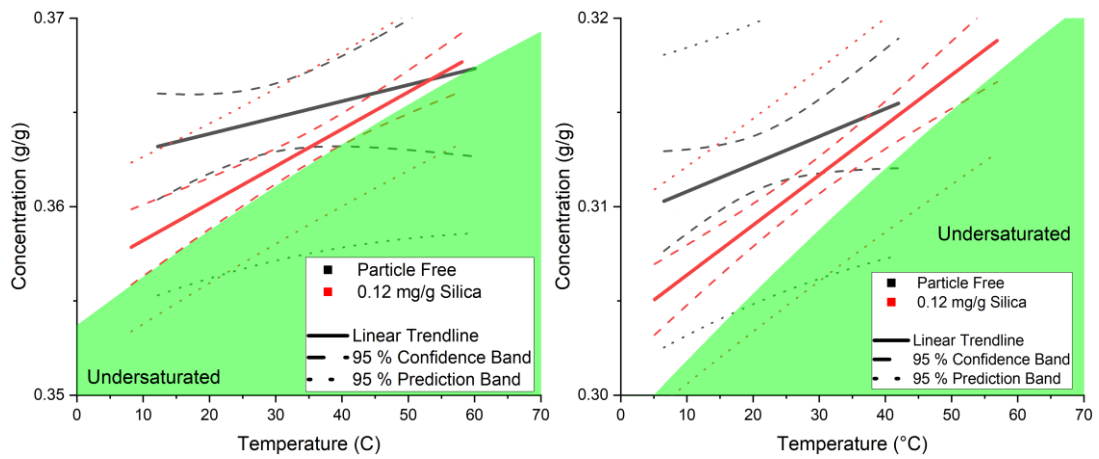


Figure 7:5: Left; Effect of $0.12 \text{ mg}_{\text{silica}}/\text{g}_{\text{water}}$ 1.57-micron diameter silica microspheres on the MSZW of NaCl nucleating from solution in H_2O . Right; Effect of $0.12 \text{ mg}_{\text{silica}}/\text{g}_{\text{Deuterium Oxide}}$ 1.57-micron diameter silica microspheres on the MSZW of Glycine nucleating from solution in D_2O . Addition of particles (Black to Red) causes both a shrinkage of the MSZW and for this boundary to become steeper.

To allow for a comparison based upon the particle material alone MSZW measurements were carried out using polystyrene particles, it had a similar impact to the silica particles, where the width of the MSZW was shrunk at lower concentrations of NaCl. As the concentration of NaCl was increased, the width was slightly wider than in the absence of any polystyrene microparticles.

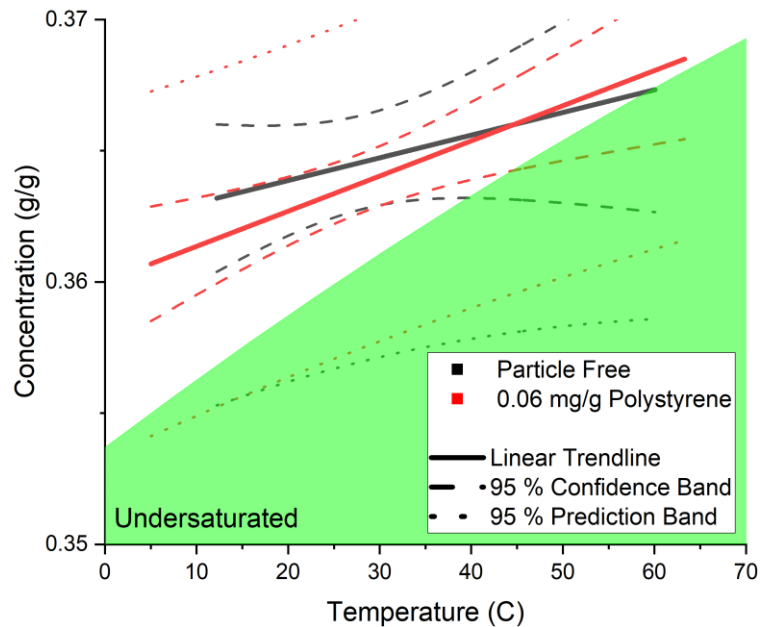


Figure 7:6: $0.06 \text{ mg}_{\text{polystyrene}}/\text{g}_{\text{water}}$ 1.57-micron diameter Polystyrene microspheres on the MSZW of NaCl nucleating from solution in H_2O . Addition of particles (Black to Red) cases the MSZW to become narrower at the lower end of the saturation temperatures examined as the gradient of the MSZW is increased.

Although not shown here, an experiment was carried out to determine the width of the MSZW of NaCl in D_2O in the presence of polystyrene particles. This resulted in very few of

the individual vial temperature cycles inducing nucleation within the vials before reaching the low-temperature hold. Therefore, the reliability that could be ascribed to any such trend would be significantly lower than the other situations reported. However, this does suggest in the case of NaCl in D₂O nucleation is at least partially inhibited by the presence of polystyrene microparticles in suspension. This could be thought to be unexpected as the presence of solid particles in suspension in a solution that is nucleating would typically be expected to increase the nucleation rate. However, this is not a universally applicable rule as particular surface groups on functionalised particles can be observed to increase the time taken for nucleation to occur, while other surface groups on the same base particle can show a decrease in the time taken for nucleation to occur [65]. This may be situationally dependent and could require individual system investigation to arrive at a definitive conclusion. It should be of note that the particles used in this study were not functionalised and were charge stabilised and therefore did not require surfactant to be added to allow the particles to remain in suspension without clumping together.

7.3 Impact of Particles on Induction Time Distributions

7.3.1 Induction Time Distributions of Glycine in H₂O and D₂O with Silica and Polystyrene Particles

To show the impact of the particles, when the induction time distributions are reported when microparticles are included, the particle-free equivalents are shown as open symbols in the induction time distributions in this chapter and particle doped are indicated by closed. Figure 7:7 shows the effect of the inclusion of 1 mg_{silica}/g_{solvent} in glycine solutions in H₂O and D₂O. In the cases of both solvent isotopologues, the inclusion of the silica shifted the induction times to shorter times. It increased the proportion of the runs where nucleation within the vial was observed. In the case of the D₂O counterparts, the same effect is observed where the induction time distribution is shifted to shorter times with a greater proportion of the total number of vials nucleating. However, the nucleation rates observed in D₂O-based solutions are lower than in particle-doped H₂O-based ones when doped with silica particles at equal supersaturation. The new data reported here, particle-doped induction time distributions, have been fitted to the model developed by *Jiang and ter Horst* to determine the primary nucleation rates [48]. The fitted curves are shown on the induction time cumulative probability distributions in the same colour as the points to which the curve is fitted. The *Jiang and ter Horst* fittings for the particle-free runs are not included to improve the included graphs' clarity.

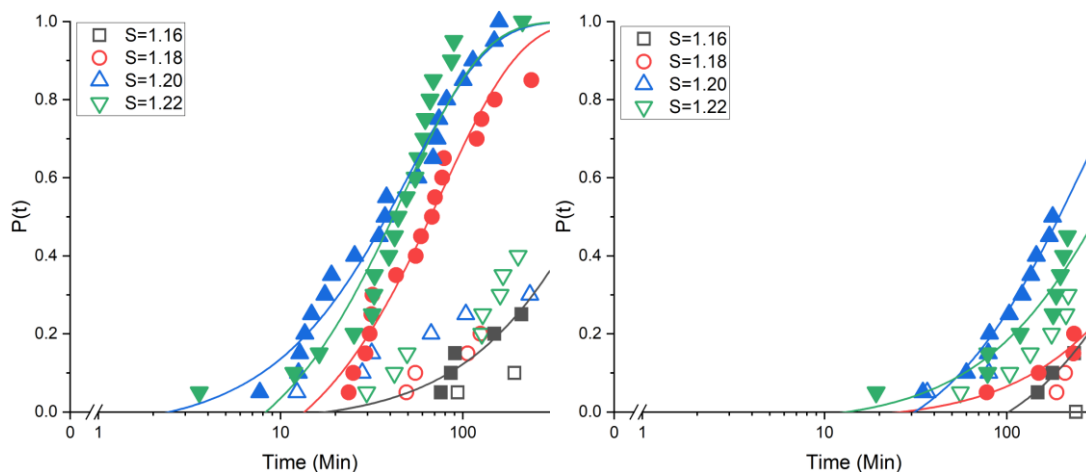


Figure 7:7: Both; Cumulative Probability Distribution Plot of Induction Times of Glycine doped and undoped with silica microspheres, agitated using a stirrer bar at 700 RPM at S between 1.16 and 1.22. Pure Solution (Hollow Symbols), $1 \text{ mg}_{\text{silica}}/\text{g}_{\text{Solvent}}$ dispersion (Filled Symbols). Jiang and ter Horst fitting [48] only shown in systems doped with silica. Left; Glycine in H_2O . Left; Glycine in D_2O .

Similarly, to doping with silica, adding polystyrene particles also decreased induction times and increased the proportion of vials within which nucleation is observed. Another similarity between the two doping materials is that the effect of introducing the polystyrene microspheres. The D_2O -based doped solutions from inspection indicate lower nucleation rates than their H_2O -based counterparts as shown in Figure 7:8.

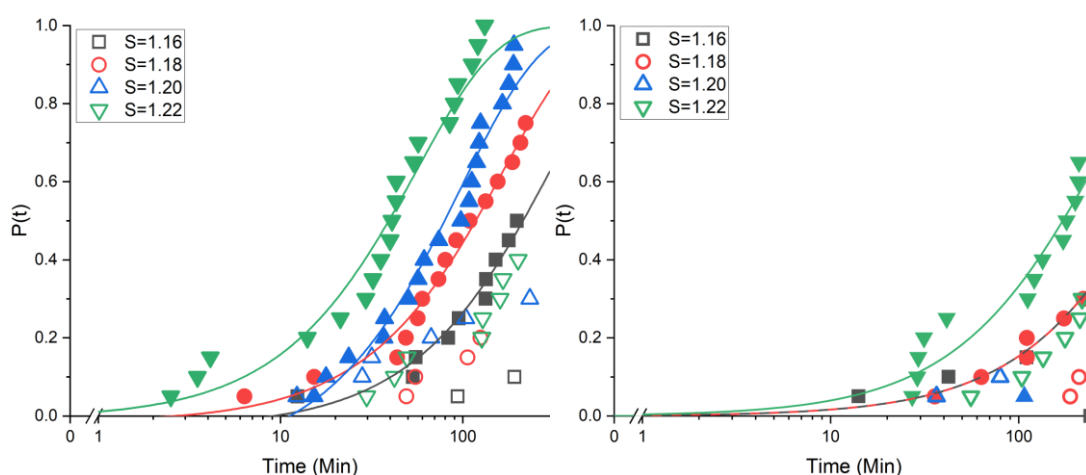


Figure 7:8: Both; Cumulative Probability Distribution Plot of Induction Times of Glycine doped and undoped with polystyrene microspheres, agitated using a stirrer bar at 700 RPM at S between 1.16 and 1.22. Pure Solution (Hollow Symbols), $0.5 \text{ mg}_{\text{Polystyrene}}/\text{g}_{\text{Solvent}}$ dispersion (Filled Symbols). Jiang and ter Horst fitting [48] only shown in systems doped with silica. Left; Glycine in H_2O . Left; Glycine in D_2O .

The effect of solid particulate material of aqueous glycine solutions shifted the induction time distributions to shorter times, indicating higher nucleation rates than in the absence of the particle suspension. The determined primary nucleation rates are shown in Figure 7:9. The nucleation rate was also higher in particle doped D_2O at the one supersaturation where

comparison was possible. Although very few non-particle doped runs where D₂O was used as the solvent nucleated suggests that a greater proportion of the vials nucleated when doped within the observation period shows a higher nucleation rate than in their absence.

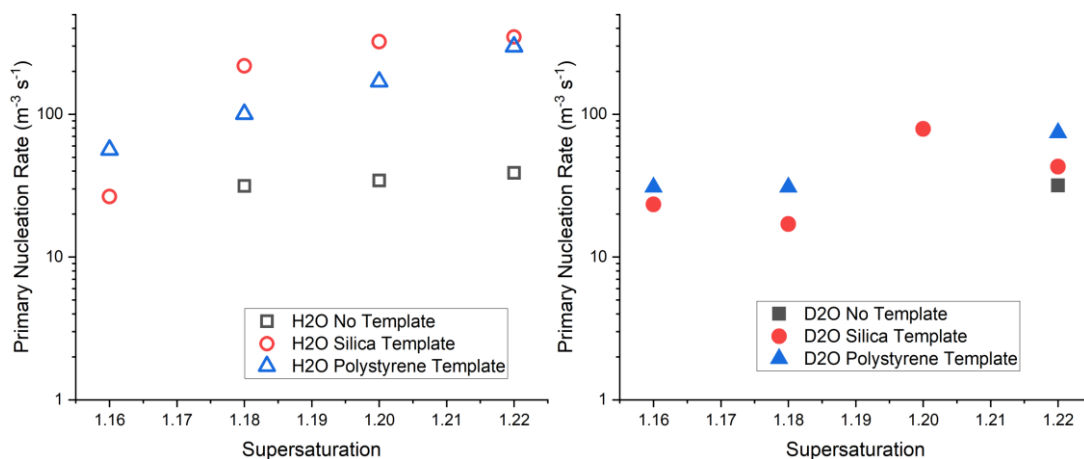


Figure 7:9: Effect of Silica and Polystyrene micro-particles on the primary nucleation rates of Glycine from H₂O and D₂O. Calculated using the fitting model published by Jiang and ter Horst [1].

In the case where glycine was examined in H₂O it appears that the silica particles induced a greater nucleation rate that equally sized polystyrene equivalents. When the glycine nucleation rates were examined in D₂O the reverse was true that from the more limited data, the polystyrene was a greater promoter of nucleation than silica.

7.3.2 Induction Time Distributions of NaCl in H₂O and D₂O with Silica and Polystyrene Particles

The effect of doping with particles of silica and polystyrene was also measured in NaCl solutions. In both cases, using either H₂O or D₂O as the solvent, induction times were shifted to shorter times. This also showed that a greater proportion of the vials tested nucleated before reaching isothermal conditions, as indicated by a symbol shown in the induction time distributions at zero time in Figure 7:10.

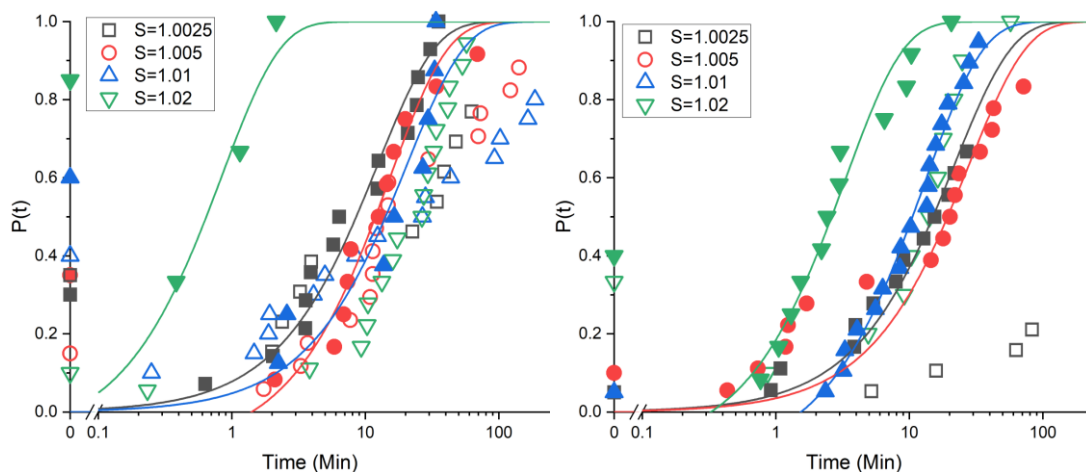


Figure 7:10 Both; Cumulative Probability Distribution Plot of Induction Times of NaCl doped and undoped with silica microspheres, agitated using a stirrer bar at 700 RPM at S between 1.0025 and 1.02. Pure Solution (Hollow Symbols), $0.12 \text{ mg}_{\text{silica}}/\text{g}_{\text{solvent}}$ dispersion (Filled Symbols). Jiang and ter Horst fitting [48] only shown in systems doped with silica). At time 0, the proportion of total vials nucleated before isothermal conditions is indicated using the same symbols. Left; NaCl in H_2O . Right; NaCl in D_2O .

However, comparing the silica dispersion runs from Figure 7:10. It can be seen that the ones where D_2O was used as a solvent were still at longer times at equal supersaturation. Therefore, this appears to be a more general trend, even in the presence of the particles, indicating higher nucleation rates when the solutions are made up of H_2O than D_2O as was found to be the case when determining the rates of particle free samples from Table 6:5.

Unlike the other three scenarios of solute and particle material, the introduction of particulate polystyrene had the opposite effect than it had when introduced to aqueous glycine solutions than when silica was introduced to NaCl solutions by shifting the distributions to longer induction times than can be seen in their absence, as evidenced by Figure 7:11. Although initially unexpected, particles can induce this response depending on the surface groups that are presented to the solution can cause the time taken for nucleation to occur to be longer than without the particles being present [65]. This phenomenon was previously reported when particles had been functionalised with surface groups acting as chelating agents where the non endcapped setup were dispersed in an aqueous solution of calcium chloride. In this case, the exact cause warrants further investigation, as it was not the question being investigated at the time, but it should be noted that polystyrene particles were not used in any tweezing experiment performed in Chapters 8 and 9.

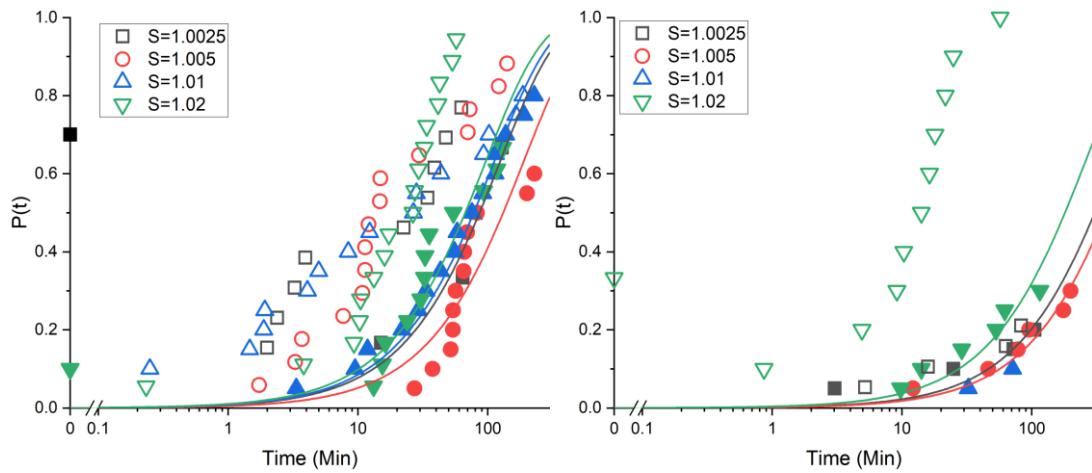


Figure 7:11: Both; Cumulative Probability Distribution Plot of Induction Times of NaCl doped and undoped with polystyrene microspheres, agitated using a stirrer bar at 700 RPM at S between 1.0025 and 1.02. Pure Solution (Hollow Symbols), $0.06 \text{ mg}_{\text{Polystyrene}}/\text{g}_{\text{Solvent}}$ dispersion (Filled Symbols). Jiang and ter Horst fitting [48] only shown in systems doped with silica). At time 0, the proportion of total vials nucleated before isothermal conditions is indicated using the same symbols. Left; NaCl in H_2O . Left; NaCl in D_2O .

Comparing the results from Figure 7:6, which examined the MSZW and those for the nucleation times shown in Figure 7:11, are partially in conflict with each other as the results for the NaCl solutions. When doped with polystyrene particles are suggest two opposite things in that when examining the MSZW the presence of these particles does appear to “promote” nucleation while examining the induction time distributions suggest that like all of the results when using D_2O .

When the NaCl solutions were made using H_2O across the range of supersaturations examined, the addition of silica microparticles had the effect of increasing the primary nucleation rate, while the polystyrene particles caused a decrease in the primary nucleation rate, as shown in Figure 7:12. When examining those made up in D_2O the situation becomes less clear due to the fewer nucleation rates from particle free runs that could be determined. At $S = 1.02$, where rates for all three scenarios could be calculated, the same effect as shown in H_2O was observed.

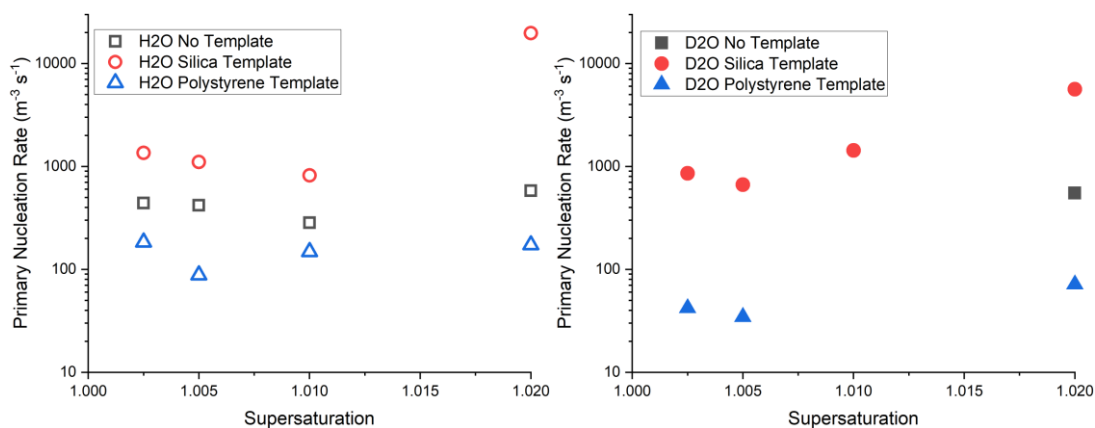


Figure 7:12: Effect of Silica and Polystyrene micro-particles on the primary nucleation rates of NaCl from H₂O and D₂O. Calculated using the fitting model published by Jiang and ter Horst [1].

If this trend is the case for the other three supersaturations tested when using D₂O, then the no particle (template) points would be between the silica and polystyrene points on the graph. Unlike when testing with glycine, it cannot be claimed that these rates are too low to be determined as they should still be above the polystyrene doped runs determining rates, which are visible. Alternatively, it could be possible that in D₂O-based solutions in the solutions where $S < 1.02$, the particle-free runs would have a lower nucleation rate than those where polystyrene microparticles were present. A definitive conclusion is therefore not possible in this case of NaCl nucleating from solution in D₂O.

7.4 Measurement Issues for Systems with Added Particles

The suspended solid material's presence impacts the crystallisation characteristics and the measurement methods used to determine the point where nucleation from solution occurs.

7.4.1 High Concentration of Silica Particles

Since the systems used to measure transmissivity are based upon a laser beam being transmitted when crystals are not present in the vial and blocked by the crystals when present. The addition of heterogeneous particles can impact the signals determined when conducting MSZW or induction time measurements. However, a minimum concentration is required to see this effect on the traces. A sample of affected traces from the measurement of the MSZW is shown in Figure 7:13 . The second set of standard traces is shown in Figure 7:14 from a low particle concentration, $1 \text{ mg}_{\text{Silica}}/\text{g}_{\text{Solvent}}$ is not high enough to interfere with transmissivity measurements. "Tuning" is performed during each cycle at the end of the high-

temperature hold, where the transmissivity reading taken at that time is taken as 100 % transmissivity. When the tuning step was performed, its effect was visible when the transmissivity value suddenly increased at the end of the first high-temperature hold; it should result in the transmissivity increasing to 100 %, but it can be seen in Figure 7:13 that this did not occur. However, after the tuning point (the sudden rise in transmissivity measurements during the first cooling ramp), it is evident that the transmissivity increases stepwise until a sudden drop in the transmissivity occurs when it falls to 0 %.

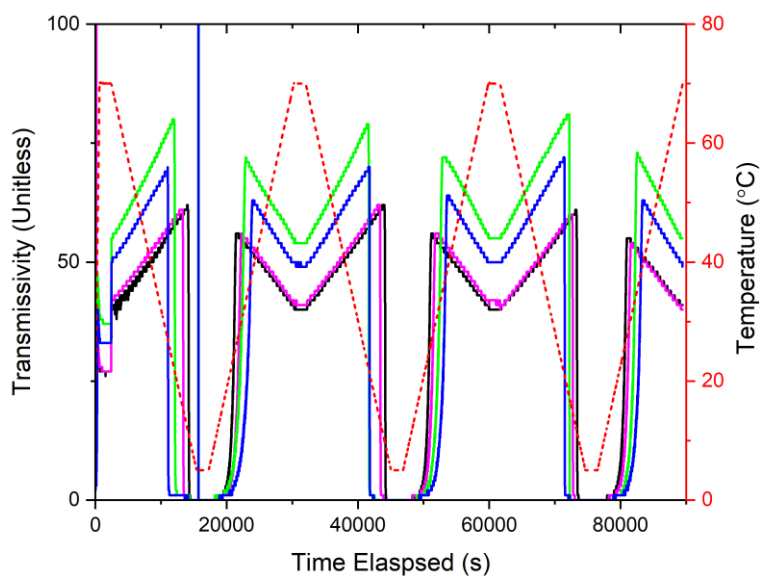


Figure 7:13: Transmissivity for samples containing added particles at 2 mg/g of glycine in H₂O at different concentrations of glycine 0.245 g/g (Black Solid), 0.265 g/g (Magenta Solid), 0.290 g/g (Green Solid) and 0.313 g/g (Blue Solid). Temperature is shown on the secondary y-axis, temperature profile (Red Dashed).

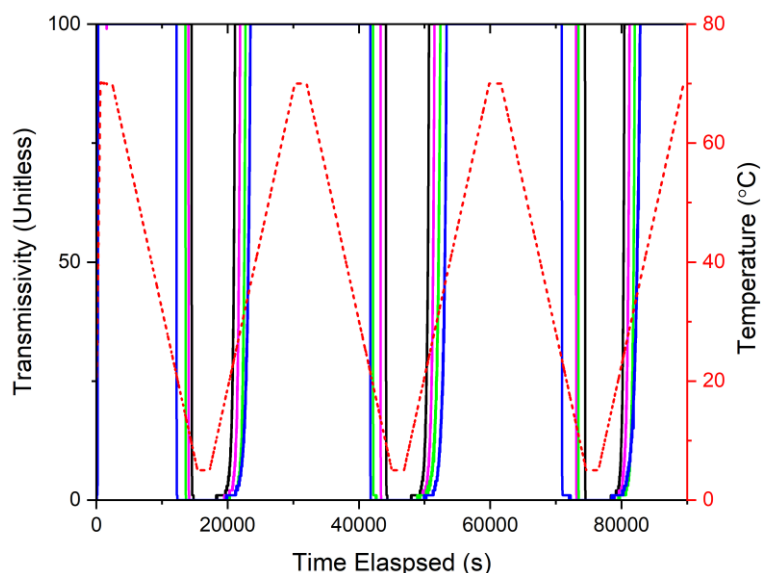


Figure 7:14: Transmissivity for samples containing added particles at 1 mg/g of glycine in H₂O at different concentrations of glycine 0.242 g/g (Black Solid), 0.264 g/g (Magenta Solid), 0.288 g/g (Green Solid) and 0.311 g/g (Blue Solid). Temperature is shown on the secondary y-axis, temperature profile (Red Dashed).

In cases where template concentration is high enough to interfere with transmissivity-based measurements, this could cast doubt on the use of this method to determine clear and cloud points. In the case of the 2 mg/g loadings (as shown in Figure 7:13) of silica particles it was not possible to use a single value criterion for the measured transmissivity to determine the onset of nucleation. Although these runs cannot use a standardised transmissivity percentage as the chosen transmissivity reading for determining the onset of nucleation. However, even if the highest point of the sudden change in transmissivity is used, this still may provide a reasonably accurate measurement, as these changes in transmissivity happen suddenly and still occur at a representative temperature should a low enough temperature gradient be used.

However, alternative measurement methods of the onset of nucleation exist that would be more suitable for particle-doped systems. It is not based on light transmission methods but on a temperature change observed when a solute crystallises from solution [50]. This alternative method requires a temperature probe to determine the temperature within each of the individual volumes of crystallising substance. This could aid nucleation through additional heterogeneous pathways unless the temperature within the vials could be monitored through non-invasive methods. Such testing was performed and is reported in section 7.5 Another issue is that a certain mass of substance must crystallise with a high enough heat of crystallisation to cause a temperature spike to either increase or decrease

the temperature to distinguish this spike from background temperature fluctuations, as has been demonstrated with aqueous solutions of glycine [50]. This could be an issue if there is only the potential for tiny masses of solid to nucleate from the solution, as in the cases of some of the NaCl solutions reported in this work. Therefore, although useful, this relatively novel method does have some limitations.

7.4.2 Polystyrene Particles

Since the refractive index of polystyrene is higher than that of silica [163], [171], it should not be surprising that an equal particle number concentration of particles that the polystyrene doped samples would have a more significant impact on the transmissivity measurements from the samples tested, as shown in Figure 7:15 due to the increased scattering that the higher refractive index particles would induce at the same number concentration. In comparing Figure 7:15 and Figure 7:13, the difference between the two is the material of the particle used when polystyrene was used as a template particle. This had a much more significant impact on the transmissivity measurements; however, sudden drops in transmissivity are visible, although the magnitude of the decrease is significantly reduced.

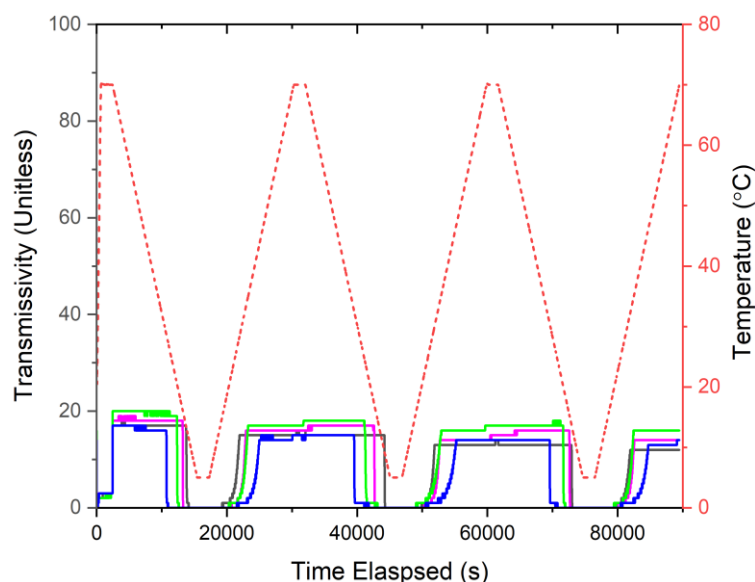


Figure 7:15: Individual transmissivity traces of glycine in H₂O at different concentrations of glycine 0.242 g/g (Black Solid), 0.264 g/g (Magenta Solid), 0.288 g/g (Green Solid) and 0.311 g/g (Blue Solid). Temperature is shown on the secondary y-axis, temperature profile (Red Dashed). Solutions contained 0.5 mg_{Polystyrene}/g_{water} of 1.59-micron diameter polystyrene microspheres.

This highlights another factor that must be considered when examining the impact of microparticles when measuring for the presence of crystals in suspension through transmissivity measurements. The particle material must also be factored into any

considerations, especially when the difference in refractive index becomes greater. This is another circumstance when the measurement of primary nucleation characteristics, through transmissivity, is not ideal, especially as the difference in refractive index between the particle and solvent becomes greater.

7.5 Induction times determined using individual vial temperature.

On the basis that the use of temperature monitoring method of determining induction times was reliable, the temperature method proposed by *Olalere et al.* was used in place of light transmission methods [50].

Temperatures were monitored in each vial of the Crystal16 using type-K thermocouples using a pair of TC-08 picologgers. This allowed the temperature to be monitored throughout the temperature cycling. Although this also monitored the vials as they were put through the same temperature cycle as shown in Figure 7:2, the use of these probes allows any minor deviations from the low temperature hold to be identified and measured where and when these temperature rises associated with the crystallisation from solution occur [229]. However, the use of the probes poses two separate questions, the first being how consistent these two methods would be with one another and whether the presence of the probes alone increases the nucleation rates observed.

To answer these questions, a particle-free run was performed where the temperature probes were present to determine the point in time at which a small temperature peak would be observed during the low-temperature hold and compared to those times determined through more standard transmissivity methods using solutions of glycine in H₂O between $S = 1.16$ and 1.22 prepared using the same methods as detailed in section 7.3, where the vials also included a type-K thermocouple. The comparison of induction times determined using either the light transmission or temperature monitoring methods is shown in Figure 7:16.

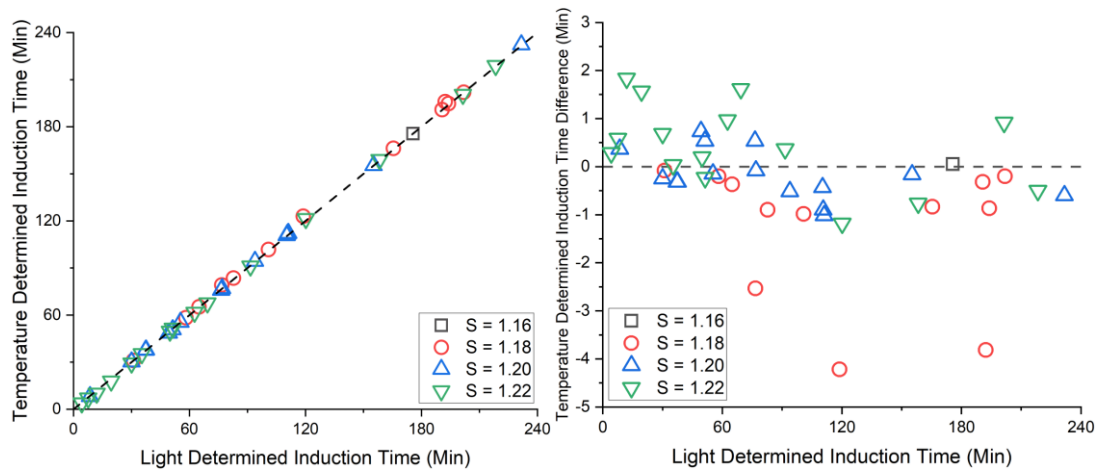


Figure 7:16: Comparison of Induction times as determined using the transmission of light and the monitoring of individual vial temperature. Induction times of glycine solutions in H_2O between the supersaturations of 1.16 and 1.22 at 25 °C. The dashed black line indicates the equal time line.

Figure 7:16 indicates that there are minimal differences between the individual induction times when measured using either of the methods (transmission or temperature) as indicated by the proximity to the points to the equal time line, where some minor discrepancies exist in the induction times determined using the temperature method are slightly longer than those determined by the transmission of light. However, this does not show if there is any general increase in nucleation rates caused by the presence of the temperature probes themselves. Requiring that the nucleation rates be determined for the induction time distributions using the model developed by *Jiang and ter Horst* [48], the induction time distributions runs performed with and without the inclusion of the

temperature probes are shown in Figure 7:17, the calculated primary nucleation rates are indicated in Figure 7:19.

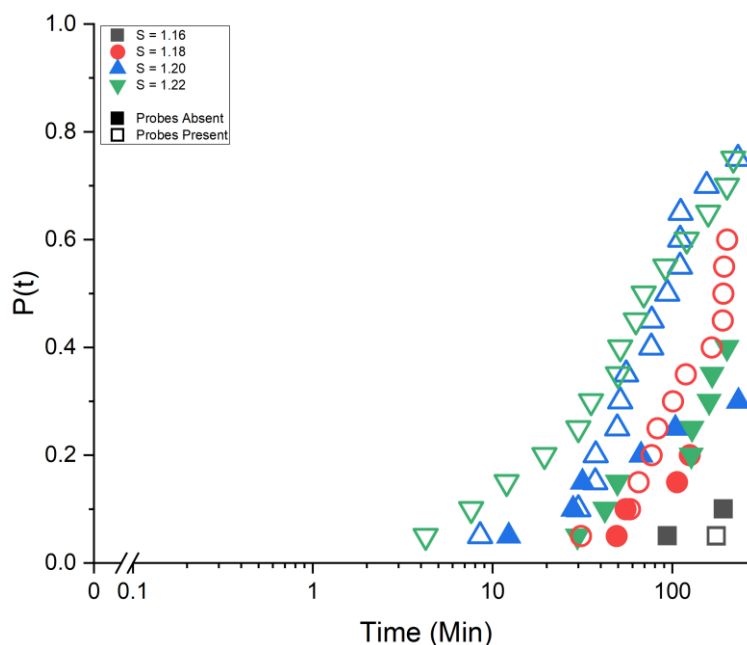


Figure 7:17: Comparison of cumulative probability distributions of glycine solutions in H_2O between $S = 1.16$ and 1.22 when measured in the absence and presence of the temperature probe using light transmission to determine the crystallisation point.

Figure 7:17 highlights that the inclusion of the thermocouple probes to the vials increases the proportion of the vials which nucleated before the end of the isothermal low-temperature hold, as well as shifting the distribution to shorter times. Indicative of an increase in the primary nucleation rate.

Now with a method of being able to accurately measure the nucleation time when a concentration of a particulate material would significantly interfere with the transmission of light through the vial, using the temperature probes. This novel method and the more traditional method based on the opacity of the solution produce good agreement when in situations where both can be measured together, although the determined nucleation rates measured are higher than in the absence of the probes. Allowing concentrations that would be unreliably measured using transmissivity to be measured using temperature changes.

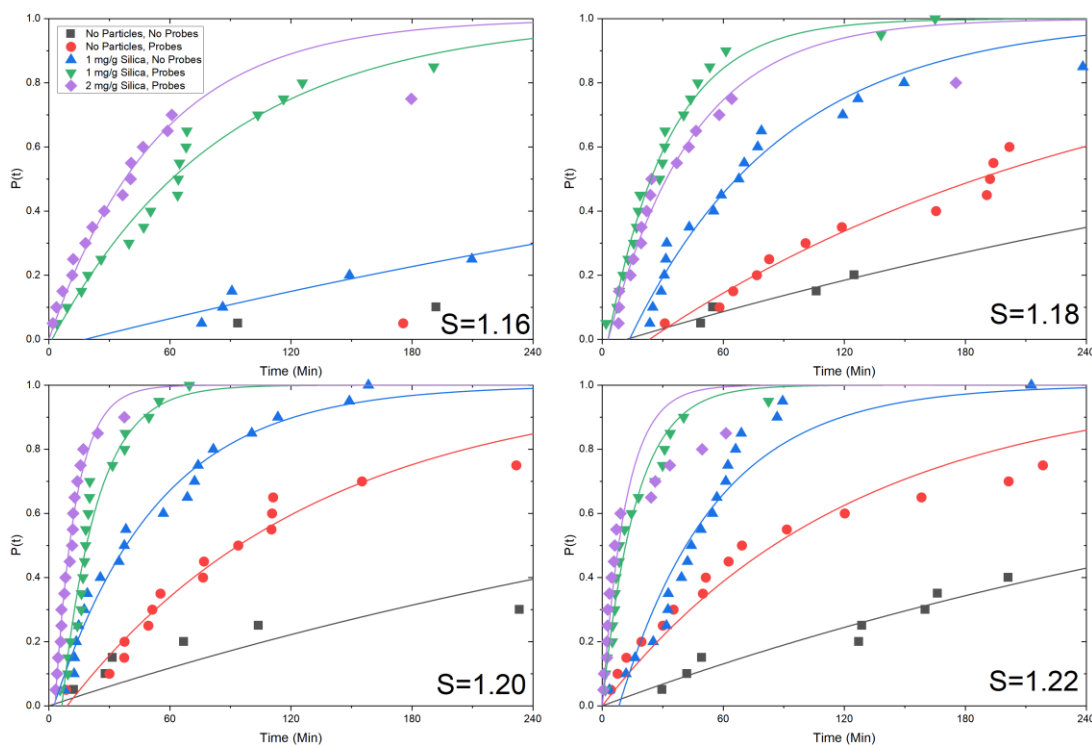


Figure 7:18: Comparison of cumulative probability distributions of glycine solutions in H_2O , between $S = 1.16$ and 1.22 using dopings of $1.57 \mu m$ diameter silica particles of 1 mg/g, 2 mg/g, and particle free.

Figure 7:18 shows two separate effects, one of which can also be seen in chapter 6. Whereas the supersaturation of the solution is increased, the induction time distribution is shifted to shorter times. This is the case across three concentrations of particle loadings (0 mg/g, 1 mg/g, and 2 mg/g). As well as the effect of altering the loading of silica was increasing the concentration of silica in suspension in the glycine solution, shifting the induction time distribution to shorter times and increasing the proportion of vials which nucleate in comparison to those which did not include the silica particles.

The calculated primary nucleation rates across the range of circumstances examined with glycine in H_2O are shown in Figure 7:19, from which several insights can be gained. Firstly, the inclusion of the temperature probes is enough to significantly increase the nucleation rates on their own, much like the presence of spherical microparticles, whose presence can also increase the primary nucleation rate. The concentration and material of the particle used in doping a solution also plays a key role. As the concentration of the particle used increases, so does the primary nucleation rate. Different particle material also has some impact at the same concentration. But critically these results show that it is indeed possible to use temperature probes to detect nucleation occurring within small volumes and use this data to determine nucleation rates.

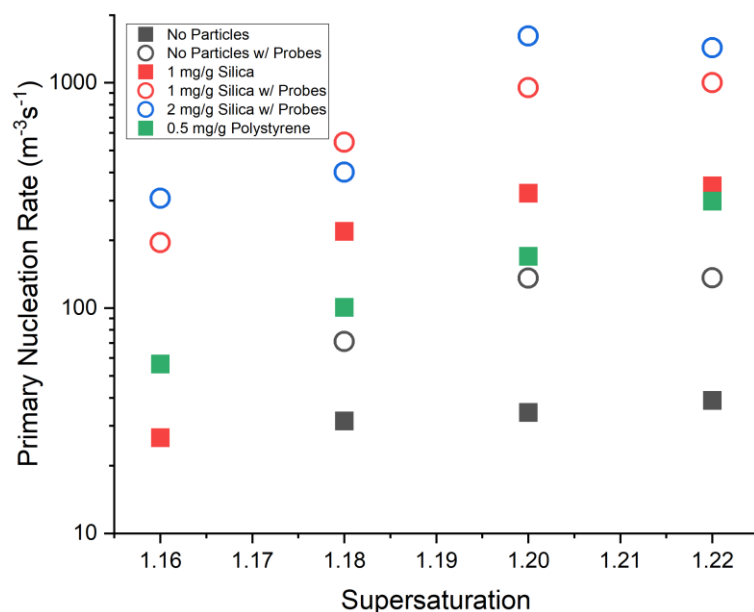


Figure 7:19: Primary nucleation rates of glycine from solution in H₂O under all previously examined conditions when in suspension with silica and polystyrene, measured using light and temperature methods. Hollow Symbols indicated the presence of the temperature probes.

7.6 Conclusions

While the impact of polystyrene microparticles appears to be more complex, and changes depend on the system and property under examination. The presence of microparticles does appear to impact the primary nucleation characteristics of glycine and NaCl in H₂O and D₂O. In both solutes, the presence of silica particles has the effect of shrinking the width of the metastable zone width and increasing the primary nucleation rate. When polystyrene was introduced to glycine solutions, this had the same effect as the silica microparticles, where the MSZW was shrunk, and the primary nucleation rate was increased. However, when polystyrene particulate material was introduced to NaCl solutions, the MSZW was shrunk while appearing to decrease the primary nucleation rate where comparisons could be made.

Depending on the concentration and material of the doping particles used, there is the possibility of interference exists for the determination of cloud points when using 'standard' transmission-based method of detection as was the case when doing was performed using silica at 2 mg/g. This required that an alternative method be used to detect the onset of nucleation. The use of temperature probes is one such possibility which has been demonstrated to be consistent with transmissivity measurement during simultaneous testing. But the inclusion of the probes did cause an increase in the nucleation rate compared with the absence of the probes.

8 Effects of the Proximity of an Optical Tweezing Focus near a Pre-existing Crystal.

A previous body of work examines how optical tweezing can impact the growth of microscopic crystals induced to nucleate from solution through the action of the tweezers or elsewhere in the tiny volumes of solution [154], [158], [230]. However, the effect of optical tweezers on macroscopically large crystals has not been investigated previously. Therefore, this provides us with a series of investigations that could be performed to examine previously untested phenomenology.

In this chapter we first discuss some preliminary results examining the impacts of washing seed crystals to determine the impact that this has on their surfaces, by examining the roughness and the presence of additional particles on the surface of the seeds before examining how the presence of an optical tweezing focus can impact on the kinetics of the crystal front growth including when trapping a silica particle and examining if it was possible to use this trapped particle to cause secondary nucleation to occur through shear in proximity to the surface of the seed.

8.1 Experimental

8.1.1 Seed Washing

To limit the initial breeding particle's impact before the seeds are introduced to the cell, as these have the potential to separate off from the main crystal to which they are attached and grown in bulk and also potentially induce nucleation. To combat the presence of these surface particles the seeds were washed via immersion in a pure solvent volume in either quiescent H₂O or D₂O, an example of the surface of a NaCl seed before washing is shown in Figure 8:1 at x20 magnification. This washing was performed by holding the individual crystals submerged in quiescent pure solvent (H₂O or D₂O) using a pair of tweezers for a selected period of time, up to 10 s. Before and after washing seeds were placed on a glass microscopy slide and imaged at a range of magnifications up to x50. These images were then used to form a comparison of the condition of the surface of the seeds and the effect of washing for different periods. Stills were taken using a Zeiss Axioskop microscope, where images were taken using a Bresser MikroCam II 12 MP. Photographs showing the surface of seeds before and after washing are shown in Appendix C for immersions occurring in H₂O and D₂O, respectively, for immersions lasting 1, 5, and 10 seconds.

8.1.2 Measurement of Single Crystal Growth Rates in proximity to Tweezing Focuses

Understanding the impact of tweezing focuses on a macroscopically large NaCl seed required observing it in the presence and absence of the tweezer to determine the optical trap's impact.

A seed crystal (approximately measuring 3 mm x 3 mm x 2 mm) was washed via 10 s of immersion in the pure solvent at 20 °C. Following washing, the seed was then placed in a closed well filled with 200 µL solution, suspension, or pure solvent, consisting of a silicone isolator with a 13 mm diameter and 2.4 mm deep well (Grace Bio-Labs), closed using a pair of glass coverslips 22 mm by 22 mm number 1.5 thickness.

Using a Mikrocam II, a video of the growing seed was recorded, and growth rate measured via the motion of the seed surface across the field of view, calibrated using a microscope graticule. While the time taken to travel this distance was taken as the timestamp from individual frames used to measure distances. Unlike images taken when examining the effect of the washing, all growth rate measurements were performed on the OTKB optical tweezers setup.

Although these measurements could have been performed in another non-tweezing setup, this allows for a more direct comparison without compensating for any differences in the setups used.

8.2 Seed Washing

Images of the seed surface following immersion are shown in Appendix C. In all the images in this section, with scale bars; red scale bars indicate 200 µm in length, and black scale bars indicate 50 µm.

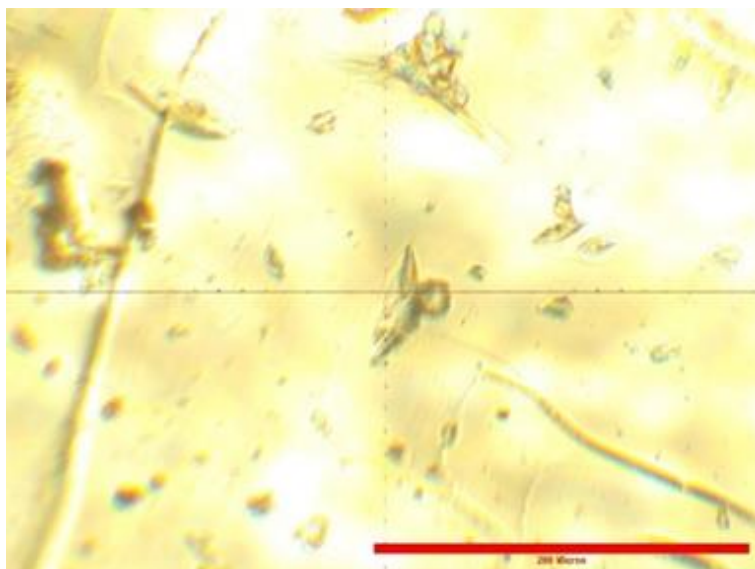


Figure 8:1: Example image showing the surface of a NaCl Crystal prior to immersion washing. Image taken at x20 magnification, Red scale bar is indicative of 200 microns.

Generally, from the series of images, in either solvent (H_2O or D_2O), increasing the immersion time increases the effectiveness of washing away/dissolving the surface-attached particles and/or dust seen on the surface at a relatively low magnification x5. Short washing periods, such as 1 s, initially could be considered suitable for eliminating these surface deposits until viewed at a much higher magnification (x50) when submerged in either H_2O or D_2O . Extending this period to 5 s appears to remove any surface deposits at even the highest level of magnification used to examine the washed seeds. Nevertheless, to examine the effects of extending this further, the immersion period was doubled to 10 s. This immersion time found that these crystals were free from surface deposits and showed a smoother surface, due to the seed crystal partially dissolving in the pure solvent, than pre-immersion. 10 s of immersion was used moving forward for two main reasons. Although 5 s seconds were enough to remove the surface particles from the faces of the crystals examined, the 10 s was chosen to guarantee this fact and the fact that this immersion time left the surface of the seed crystal with smoother surface.

8.3 NaCl Crystal Growth and Dissolution Rate

Without the laser being active, the microscopic growth was examined under two circumstances: when suspended in a “pure” solution and a silica dispersion as shown in section 8.4.1. Dissolution rates were only examined under the solution conditions.

This first acts as a control experiment to allow the impacts of the growth rates to be determined. Growth and dissolution rates of NaCl crystals in quiescent solutions using H₂O and D₂O as the base solvent at a range of supersaturation ratios is shown in Figure 8:2.

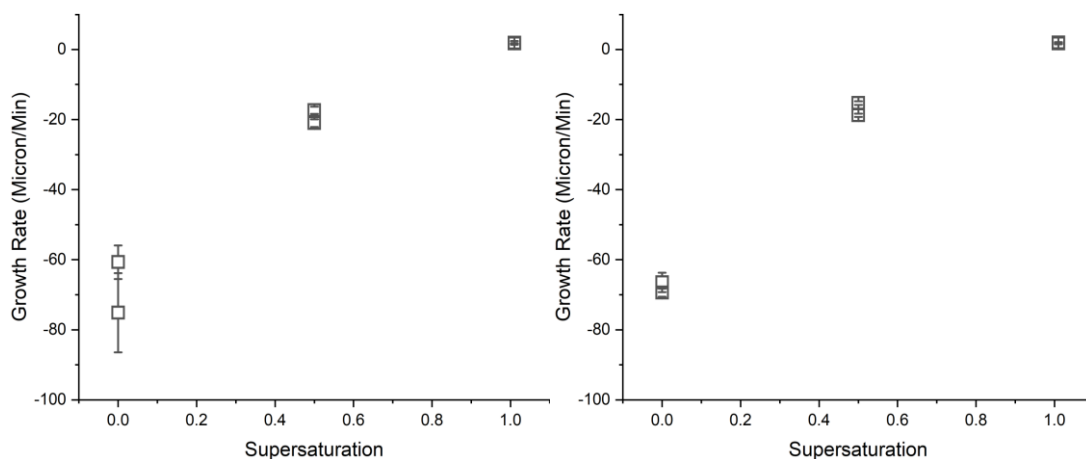


Figure 8:2: Growth and Dissolution Rates of NaCl in solutions of NaCl in either H₂O (left) or D₂O (right) at concentrations up to $S = 1.01$. Each point indicates the growth or dissolution calculated by tracking the crystal front over a period of time, extracted from equally time spaced stills from the recorded video. Error bars indicate a 95 % confidence interval of the rate determined from a linear fit of the individual displacements.

Below saturation, at $S = 0$ and $S = 0.5$, the crystal dissolves back into solution as indicated by the 'negative growth rate'. This dissolution rate decreases as the concentration of sodium chloride increases in the solution. However, once the $S > 1$, as in the measurements made at $S = 1.01$, the crystal begins to grow in solution. The growth rates found here are comparable to rates published previously [221], [224], [231].

8.4 Growth in Proximity to Tweezing Focuses

A tweezing focus could alter the local supersaturation by altering the temperature of the fluid surrounding the focus without even considering the ability of the focus to alter the local supersaturation, as suggested by a range of previous works. It is possible that laser induced temperature rises and localised enhanced concentration play a role depending upon the system to which the tweezers act upon [151], [152]. Therefore, it is essential to know how the focus of optical tweezers can alter the growth of a NaCl crystal grown from solution when the tweezing focus is in proximity to the existing crystal [148], [158]. Estimates of the tweezers effect on the supersaturation through laser induced heating are shown in Appendix J.

8.4.1 Impact of Tweezing Focus Power and Proximity on Crystal Growth Rate

Two major factors were investigated to determine their impact on the growth rates of crystal fronts when a tweezing focus was located in proximity, these were the laser power and the lateral distance between the focus and the crystal front. In the cases where the laser power was altered the (300 nm diameter) tweezing focus was positioned 10 μm away from the crystal front and the crystal was allowed to grow towards the optical tweezing focus, this was repeated at a number of laser powers. The other factor that was investigated was the distance between the focus and the crystal front, in these cases the power was kept the same and the distance at which the crystal was positioned was varied up to 30 μm . When referring to these distances the word initially is used here as the distance was not kept constant through the test as the distance was measured at the start and the crystal was allowed to grow towards the focus of the tweezers. For example, during the 10 μm run using a power of 300 mW, the tweezing focus was located at a distance of 10 μm away from the 300 mW optical tweezing focus when the analysis was begun. These growth rates were determined when the bulk solution was $S = 1.01$ are shown in Figure 8:3, by tracking the position of the crystal front over a period of up to 1 minute across stills extracted from individual videos.

When using solutions made from H_2O , it appears as if the growth rate reduces as the laser's power increases. This should not be unexpected when examining the impact of the laser on the local supersaturation. As the power increases, the local temperature rises, increasing sodium chloride's solubility, lowering the supersaturation, and thereby reducing the growth rate. However, in the case of D_2O , where the growth rate appears to increase with laser power cannot be explained by the effects of temperature as the effect would be significantly reduced in magnitude due to the much lower absorption coefficient of D_2O in comparison to H_2O at 975 nm [110]. It may be possible to explain this increase in local concentration as clusters of solute molecules or ions are "collected" in and around the focus of the trapping beam [154], [158].

However, when this was performed initially using hen egg-white lysozyme (HEWL) in D_2O , the growth rate in proximity to optical tweezing focuses first decreased and then only increased after an extended period of irradiation with the tweezers [158]. It is not unreasonable that different solute-solvent systems would take various times to transition from the period where growth is reduced to the point where growth is increased. If this

period, as has been suggested, exists for sodium chloride, it is on the scale of seconds rather than tens of minutes, as was when measurements were made in HEWL. Only two data points could be collected for each set of conditions due to uncontrollable external factors, see Appendix B for further details. The data errors associated with each point are for the single points themselves as each is determined from a trendline of individually determined positions. The errors associated with an average calculated from a pair of points would not have been very insightful.

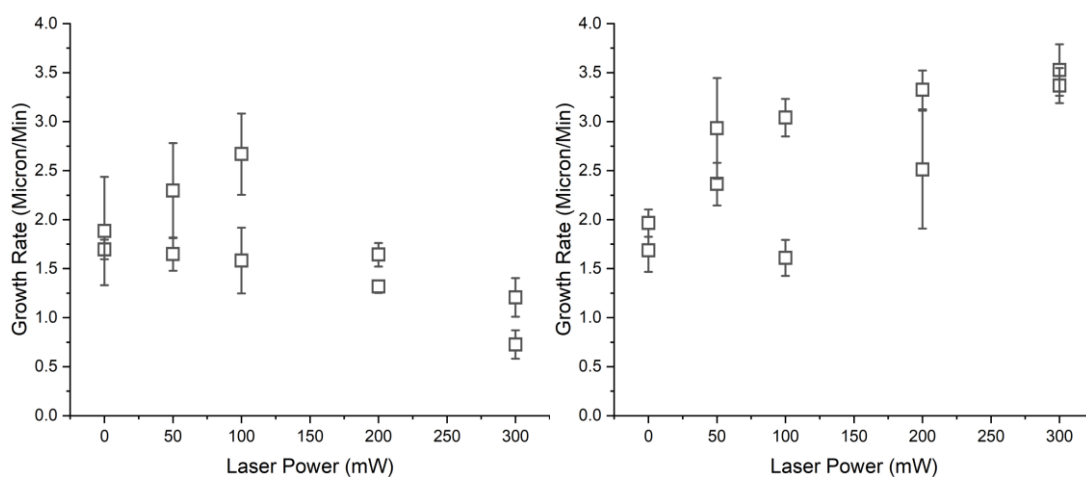


Figure 8:3: Growth rate of a NaCl crystal in $S=1.01$ solution made from H_2O (left) and D_2O (right). An optical tweezing focus of various powers is initially located 10 microns from the front of the crystal face. Error bars indicate a 95 % confidence interval calculated by determining a linear fit of the displacement positions of the crystal front, the gradient of this trendline was taken as the growth rate.

The other aspect that was investigated is the distance between the trap's centre and the crystal front. Again, the impact of altering the distance between the crystal front and the tweezing focus depends on the solvent isotopologue shown in Figure 8:4. With H_2O solvent, increasing distance results in increased growth rates as the distance between the tweezing focus and the crystal front increased. This is not unexpected as the laser-induced heating at the solution crystal interface would be reduced as the temperature elevation would decrease with increasing distance from the trap's centre modelled as a point source [176], however this may require additional testing to be definitive due to the errors associated with calculated growth rates from the fittings as only a small number of points could be captured for each set of variables. It may be the case that when using D_2O as the solvent causes the growth rate to decrease as the distance from the focus is increase, however due to the small sample size gathered it could also be argued that the trend is flat and that the distance does not have any significant effect. Again, like altering the power used to generate the trap, this cannot be explained through temperature effects. As the region of increased supersaturation

surrounding the tweezing focus can only be so big and cannot extend indefinitely as the centre of the region is moved further away from the crystal front, it would be the case that this would have a reduced impact with the average distance between the two points of interest [154], [158]. However, this region could appear at least 30 μm from the trap's centre as the growth rate was still elevated above the baseline observed in the absence of the laser, however this could be debated due to the associated errors. The fact that this region appears to extend beyond the focal volume of the tweezers can be supported by more recent fluorescence based measurements which shown a concentration enhancement effect far outside the focal volume [137], as it has been demonstrated that tweezers are able to capture objects at distances much greater than the dimension of the object itself [134]

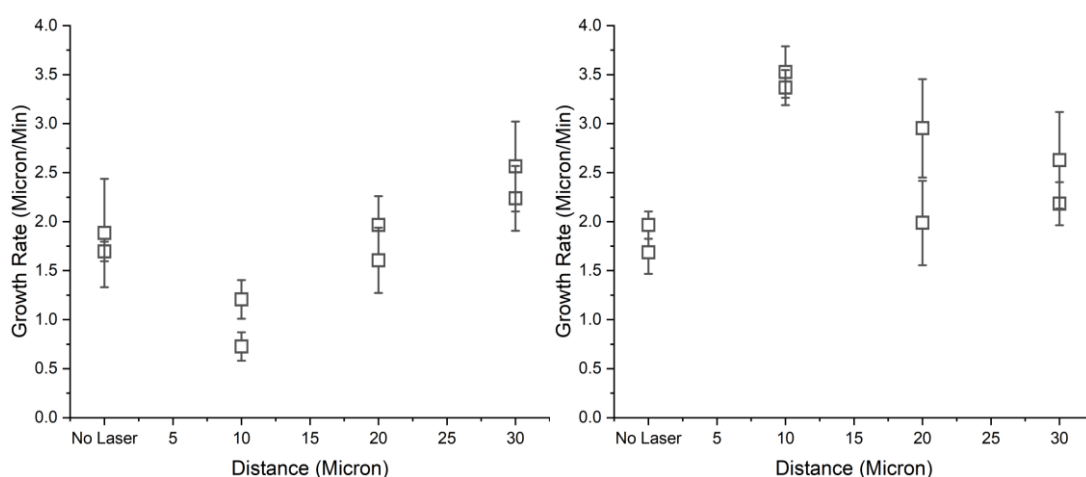


Figure 8:4: Growth rate of a NaCl crystal in $S = 1.01$ solution made from H_2O (left) and D_2O (right). An optical tweezing focus set to a power of 300 mW initially at the distance indicated was used. Error bars indicate a 95 % confidence interval calculated by determining a linear fit of the displacement positions of the crystal front, the gradient of this trendline was taken as the growth rate Impact of presence of silica particles in dispersion.

It is possible that the presence of particles typically held in tweezing focuses could potentially impact the growth crystal used for seeding. Therefore, this effect was examined in the absence of any laser. The growth rate determined compared to the growth rates in the absence of silica particles is shown in Figure 8:5. Although it appears less evident in the H_2O results than in the D_2O , the presence of the silica particles has a negligible effect as there appears to be no significant difference between the rates measured in the absence and presence of the silica particles. As it is possible that the presence of the silica particles could induce heterogeneous nucleation, lowering the supersaturation below the level to which the solution is made up, as the presence of particles can and has been observed increasing the primary nucleation rate of NaCl from H_2O and D_2O , as demonstrated by chapter 7, however at the scale examined with the optical tweezers it does not appear to be an issue. It could be

possible that agitation is required before the full effect of the particles observed in chapter 7 is observed.

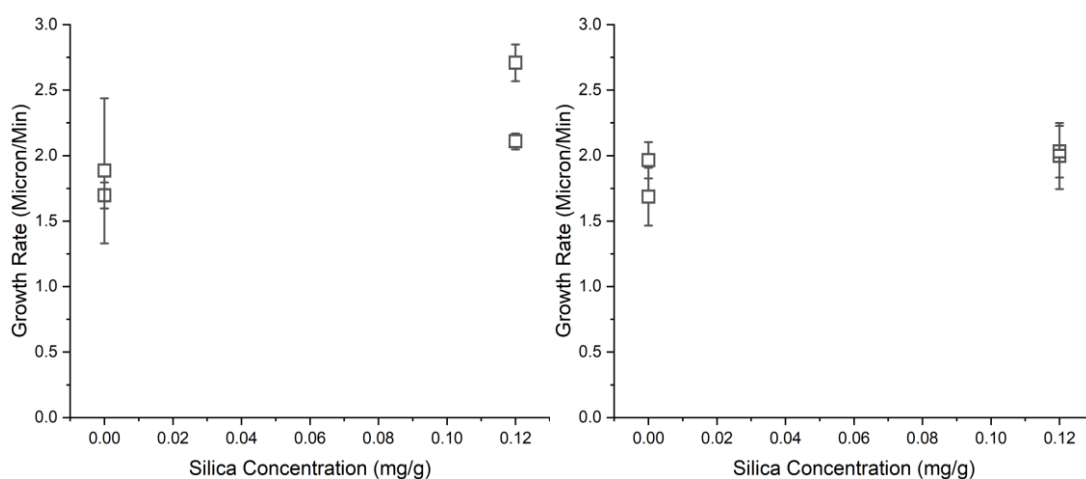


Figure 8:5: Growth Rates of a NaCl crystal grown from a solution at $S = 1.01$ in H_2O (left) and D_2O (right). The solution used also contains 0.12 mg of silica per g of solvent. Error bars show a 95 % confidence interval of the displacement rate of the crystal front as determined from still images extracted from a video of the growing crystals.

The subsequent analysis stage examines the combination of the optical tweezing focus and silica particles in dispersion rather than just a NaCl solution. The presence of the silica particles alone does not affect the growth of the sodium chloride seeds, as indicated by Figure 8:5. However, the presence of the tweezer alone can impact the growth of NaCl crystals, which depends upon the laser power used and its distance from the front of the crystal front, as seen in section 8.4.1. Therefore, the second set of experiments was conducted in which growth was investigated in with the same silica suspension as was used in chapter 7 ($0.12 \text{ mg}_{\text{silica}}/\text{g}_{\text{solvent}}$).

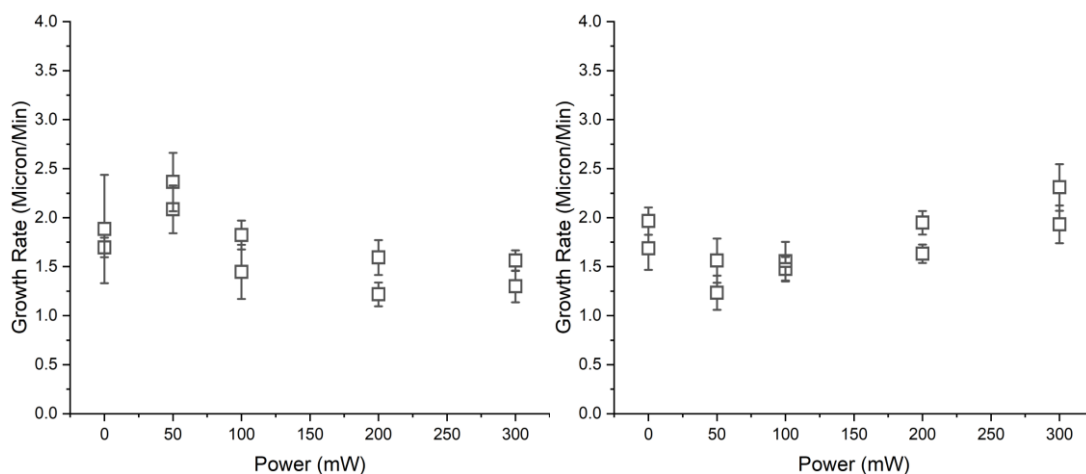


Figure 8:6: Growth rate of a NaCl crystal in $S=1.01$ $0.12 \text{ mg}_{\text{silica}}/\text{g}_{\text{solvent}}$ silica dispersion made from H_2O (left) and D_2O (right). An optical tweezing focus of various powers is initially located 10 microns from the front of the crystal face. Error bars show a 95 % confidence interval calculated from the gradient of the displacement of the crystal front.

Again, like the rates observed in the silica-free solution, the same trends can be seen in increasing the power of the laser used to impact the rate of the growing crystal while in dispersion with silica in Figure 8:6. In suspensions made up of H_2O , increasing the laser power reduces the crystal growth rate. However, the effect does appear to be more subdued when silica is present in dispersion. While the opposite effect is observed in D_2O , increasing laser power appears to increase the rate at which crystals grow in proximity to the focus of optical tweezers.

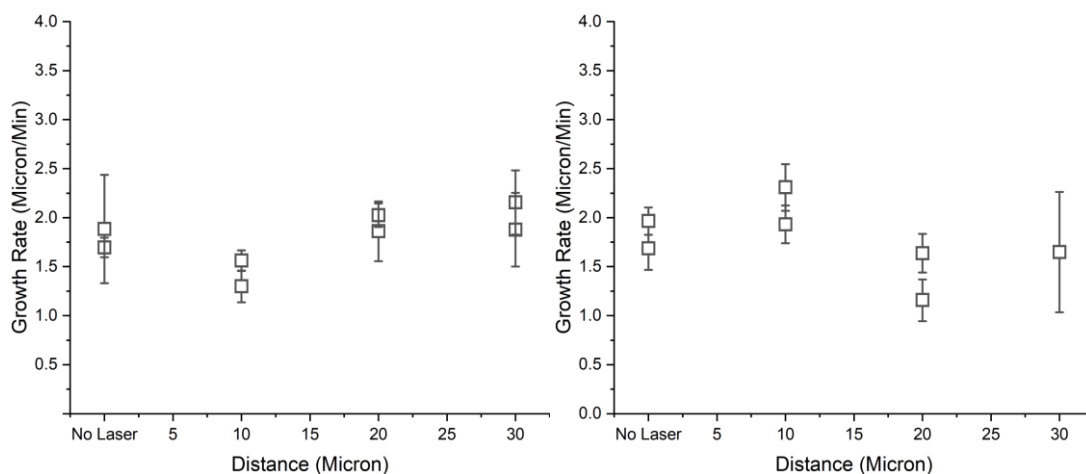


Figure 8:7: Growth rate of a NaCl crystal in $S = 1.01$, $0.12 \text{ mg}_{\text{silica}}/\text{g}_{\text{solvent}}$ silica dispersion made H_2O (left) and D_2O (right). An optical tweezing focus set to a power of 300 mW initially at the distance indicated was used. Error bars show a 95 % confidence interval calculated from the gradient of the displacement of the crystal front.

Again, like those measurements made in silica-free solutions when considering the distance between the crystal front and the optical tweezing focus, the same trends appear in the

suspension when the supporting medium is H₂O, as shown in Figure 8:7. There is a slight increase in the growth rate as the initial distance between the crystal front and the trap's focus increases. The presence of silica in dispersion/suspension has no meaningful impact on the observed trends compared to a pure solution free of silica microspheres when operating in proximity to the crystal front.

The final set of experiments that was conducted is to see the impact that one of the silica particles was previously only in suspension, now with one of these particles being held in the focus of the trap, while near the surface of a growing macroscopic crystal.

While a particle is trapped in the focus of the tweezers like in all other situations tested where the solution/suspension was made up of H₂O, where power is increased while the distance of the tweezers is initially at 10 μm the rate of crystal growth decreases with increasing power as seen in Figure 8:8. Nevertheless, it can also be seen that as the initial distance between the crystal and the tweezing focus increases, the tweezer's impact on the growth rate decreases.

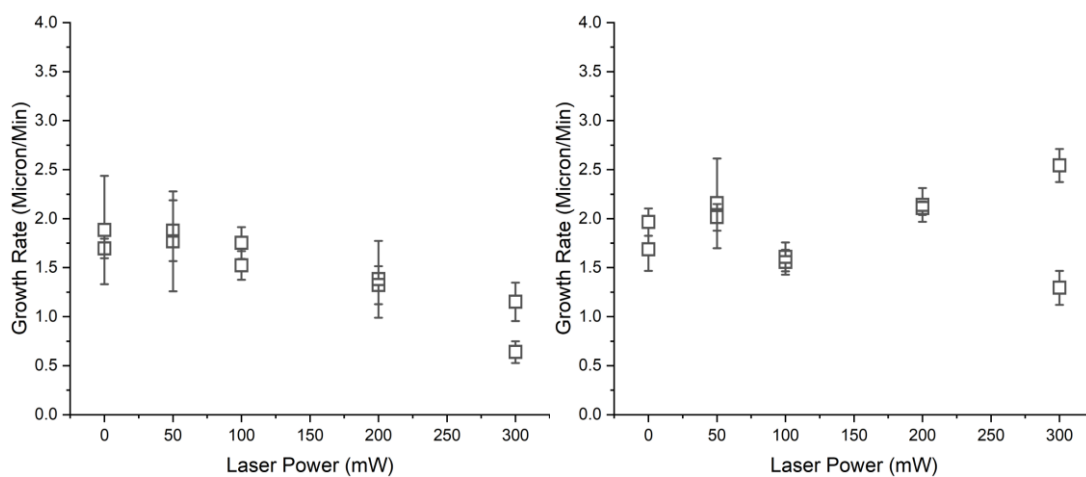


Figure 8:8: Growth rate of a NaCl crystal in $S=1.01$, $0.12 \text{ mg}_{\text{silica}}/\text{g}_{\text{solvent}}$ silica dispersion where a single silica particle was held by the tweezers, made from H₂O (left) and D₂O (right). An optical tweezing focus of various powers is initially located 10 microns from the front of the crystal face. Error bars show a 95 % confidence interval calculated from the gradient of the displacement of the crystal front.

This suggests that the intensity of the beam would be highest in the centre of the beam (where the particle would be located) therefore suggesting that the fluid surrounding the particle may still be able to be heated enough to have an impact on the local supersaturation, in the case of the H₂O. When examining the effect of varying the laser power used to impact solutions/suspension where H₂O was the base solvent/suspension medium, as the power is increased the growth rate of the crystal decreases. Whereas when using D₂O the opposite

effect is generally observed where increasing the laser power increases the growth rates. However it may be the case that the presence of the silica trapped by the focus partially mutes this effect, this at least partially supports the hypothesis presented by *Tu et al.* [154], [158], where the focus of the tweezers is considered critical to the mechanisms behind the concentrating effects observed.

However, when examining the impact of the initial distance (Figure 8:9) when using H₂O, a single particle was held using the optical trap while a NaCl crystal was growing in the proximity of the trap-held particle. Increasing the distance between the particle and the crystal front from 10 microns to 30 microns appears to allow the crystal growth rate to return to the level seen in the absence of the trap.

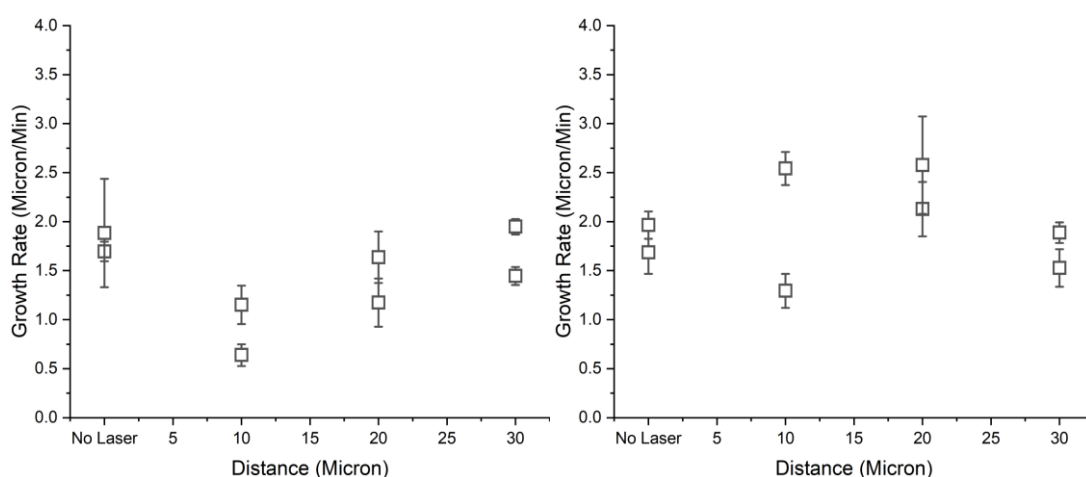


Figure 8:9: Growth rate of a NaCl crystal in $S = 1.01$, $0.12 \text{ mg}_{\text{silica}}/\text{g}_{\text{solvent}}$ silica dispersion where a single silica particle was held by the tweezers, made from H₂O (left) and D₂O (right). An optical tweezing focus set to a power of 300 mW initially at the distance indicated was used. Error bars show a 95 % confidence interval calculated from the gradient of the displacement of the crystal front.

Much like the D₂O dispersion, where no particle was being trapped, where varying the power, no discernible trend can be observed when altering the initial distance between the trap's centre and the seed's surface. Nevertheless, when using H₂O, the same trend is observed regardless of the situation; whether particles are present in the system or trapped by the laser, the growth rate increases as the initial distance between the trap's centre and the seed surface is increased. One explanation that could explain the effect when a particle is trapped in the focus located near the surface of a crystal is that the heating effect of the laser is still present, which would impact the two solvent isotopologues differently as the H₂O based samples would be subjected to significantly greater degrees of heating than the D₂O based samples. And secondly the presence of the trapped particle interferes with the formation of

the region of enhanced supersaturation. When both of these effects are taken together it is possible that the H₂O samples would result in partial inhibition of growth, while the D₂O samples might not see much of an effect as they would not be significant as the concentration enhancement would be prevented, and the heating would be minimal.

Both tests using a trapped particle when using D₂O as the solvent can drastically alter the power-dependent trends, with a particle having a definite but not fully defined effect.

8.5 Growth through Tweezing Focuses

In addition to growth in proximity to the focus of the tweezer, the crystal's growth through the centre of the trap geometry can also be examined when using a macroscopically large crystal.

8.5.1 Crystal Growth of NaCl from solution through the focus of an Optical Trap

From Figure 8:11, when a growing through the focus of an optical tweezer at low laser powers, it does not appear as if altering the laser power below a particular value significantly impacts the growth rate observed. Furthermore, neither does the growth rate appear to be altered by the relative direction of the growth about the centre of the trap geometry, either towards or away from the focus centre. A diagram further explaining growth towards the focus and away from it is shown in Figure 8:10.

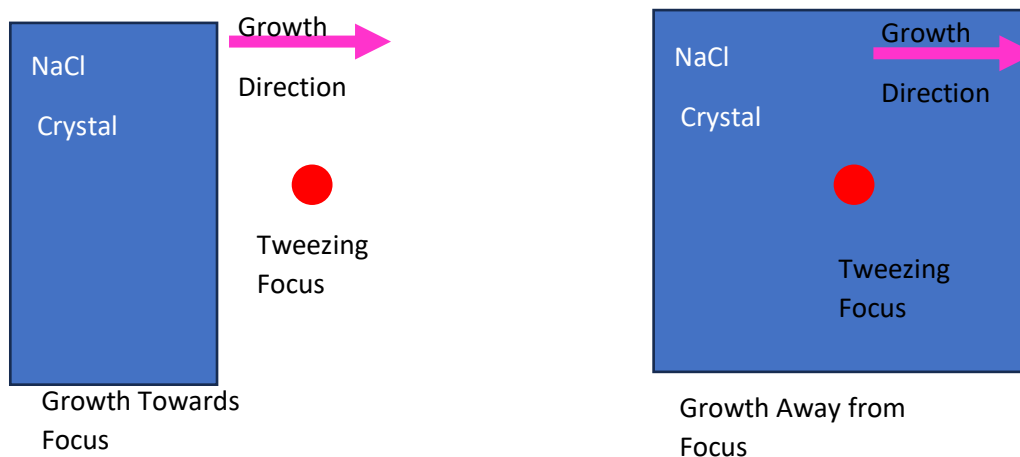


Figure 8:10: Geometry of crystal growing towards and away from the optical tweezing focus.

Here it is surprising that with the trends observed when the tweezing focus is located 10 – 30 μm from the surface of the growing seed, where the growth rates decrease as the distance decreases, however when operating even closer as was tested when growing through the focus where the growth rates increased back up again. At these distances, heating and increased localised concentration could compensate for each other, while at

greater distances, the heating has a significant influence. However, if this is the case, it is only valid up to a “critical” point with regards to the laser power delivered, as shown by the case examined in Figure 8:12 as seen by the effect seen at a set laser power of 300 mW, this supports the reasoning provided by *Yuyama et al.* that the laser power used must be above a certain critical value before any effect can be observed [232].

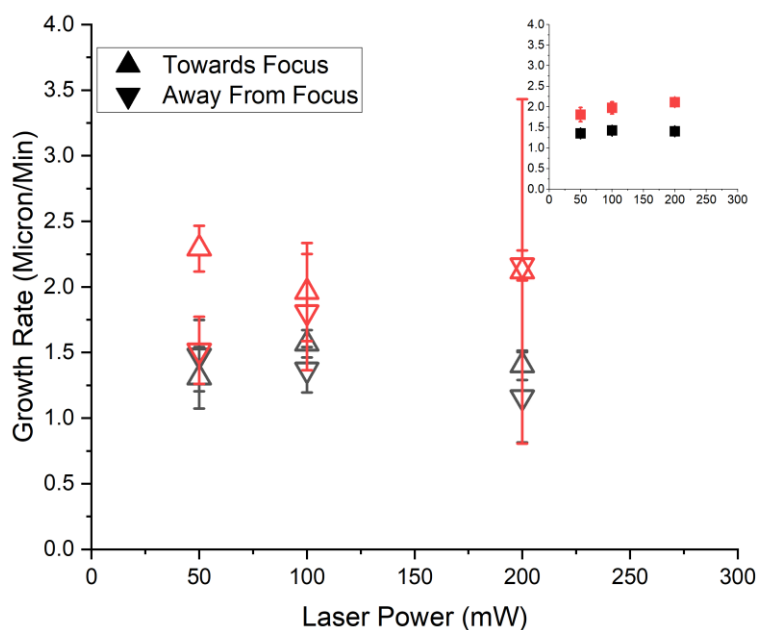
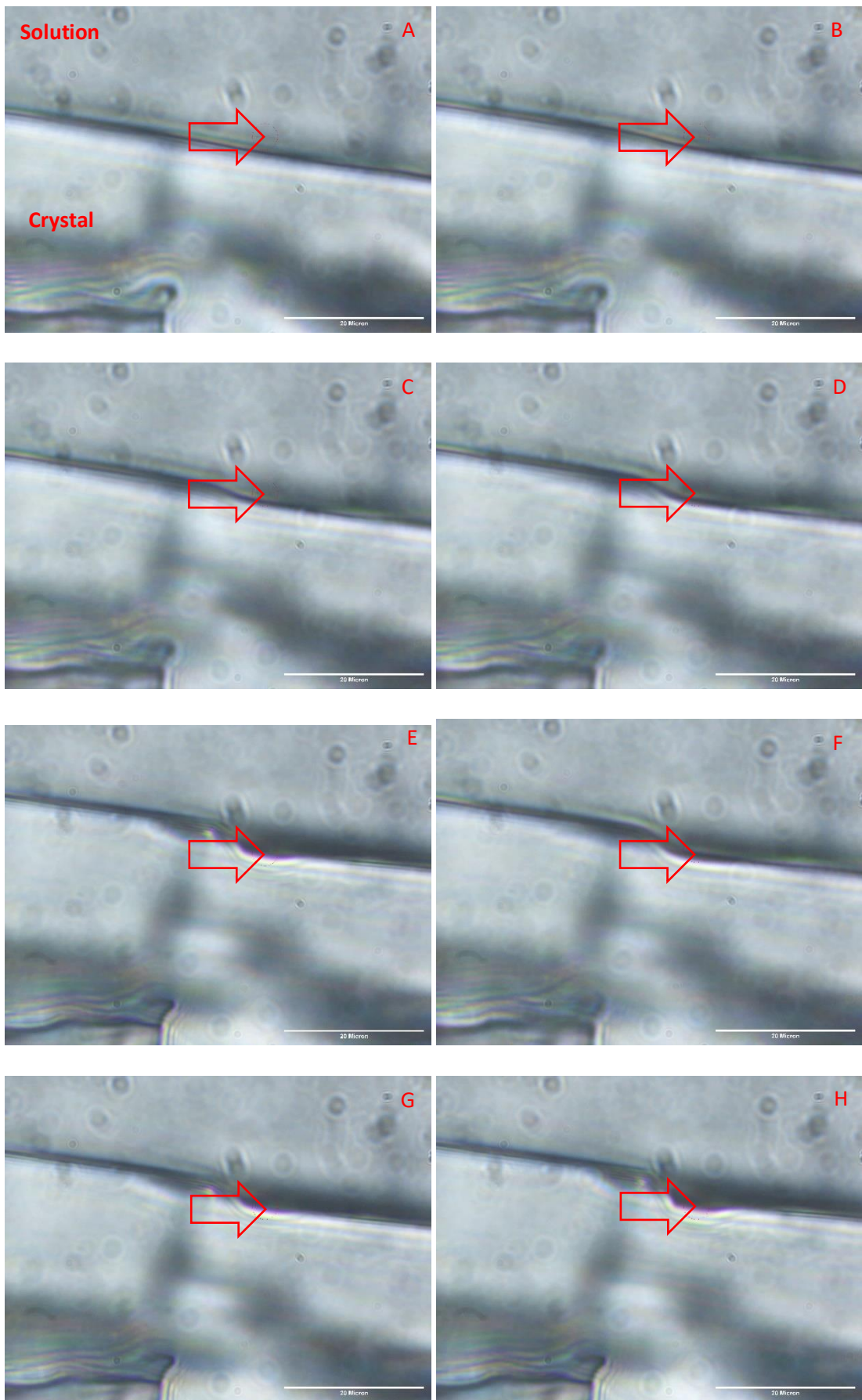


Figure 8:11: Growth rate of NaCl crystal through a focus of an optical tweezer of a NaCl crystal in $S = 1.01$ solution in H_2O at various laser powers. The growth rate was analysed under three circumstances, towards the focus (triangles) and away from the focus (inverted triangles) overall growth rates are shown in the insert; linked runs are indicated using the same symbol colour. Error bars indicate a 95 % confidence interval in the gradient of the points analysed in each scenario. Symbols shown in the same colour at the same laser power were determined from a single experiment. Geometric relationship of towards focus and away from the focus is shown in the diagram in Figure 8:10.

8.5.2 Inhibition of NaCl Crystal Growth

A set laser power of 300 mW, which appears to be above a certain critical power required to inhibit growth, was used when close to the crystal suspended in a solution made from H_2O . In the period when the crystal was growing towards the focus of the tweezers. Growth was suspended in the region near the focus, while growth continued on the left and right-hand sides of the focus. Leaving a concave section on the surface of the crystal, shown in Figure 8:12.



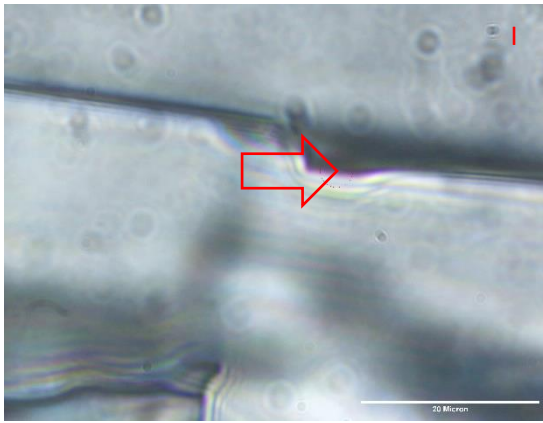
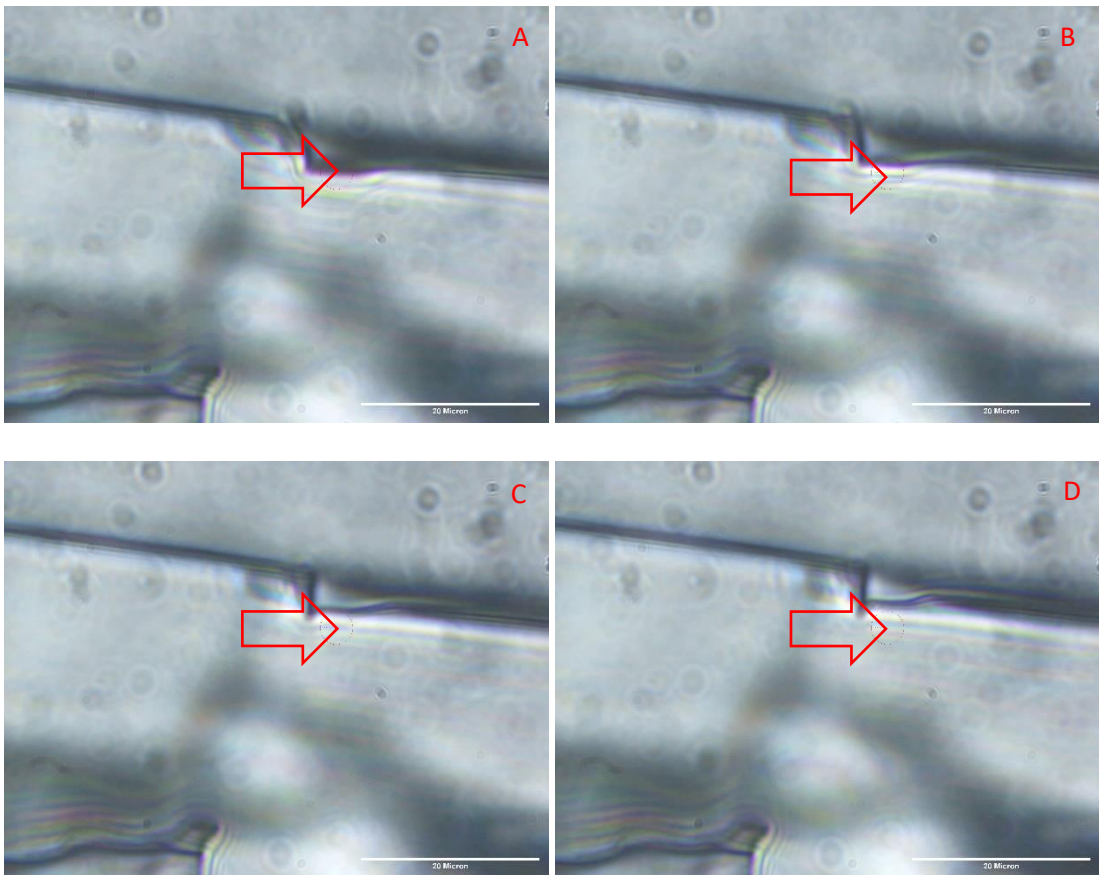


Figure 8:12: Growth of a NaCl Crystal suspended in $S = 1.01$ solution in H_2O through the Focus of an Optical Trap at 300 mW set power. Images A-I were taken at 30-second intervals where the focus was activated at time 0 when image A was taken. White scale bars show 20 microns. The Position of the tweezing focus in the images is indicated by the red arrow in each image.

Following the cessation of the irradiation using the tweezers, growth resumes in the region where the tweezing focus had previously prevented it at this set laser power (300 mW). As the growth fills the concave region, evidence of this previously inhibited growth is present as a flaw in the surface is introduced where it was not previously present. This period of growth is shown in Figure 8:13.



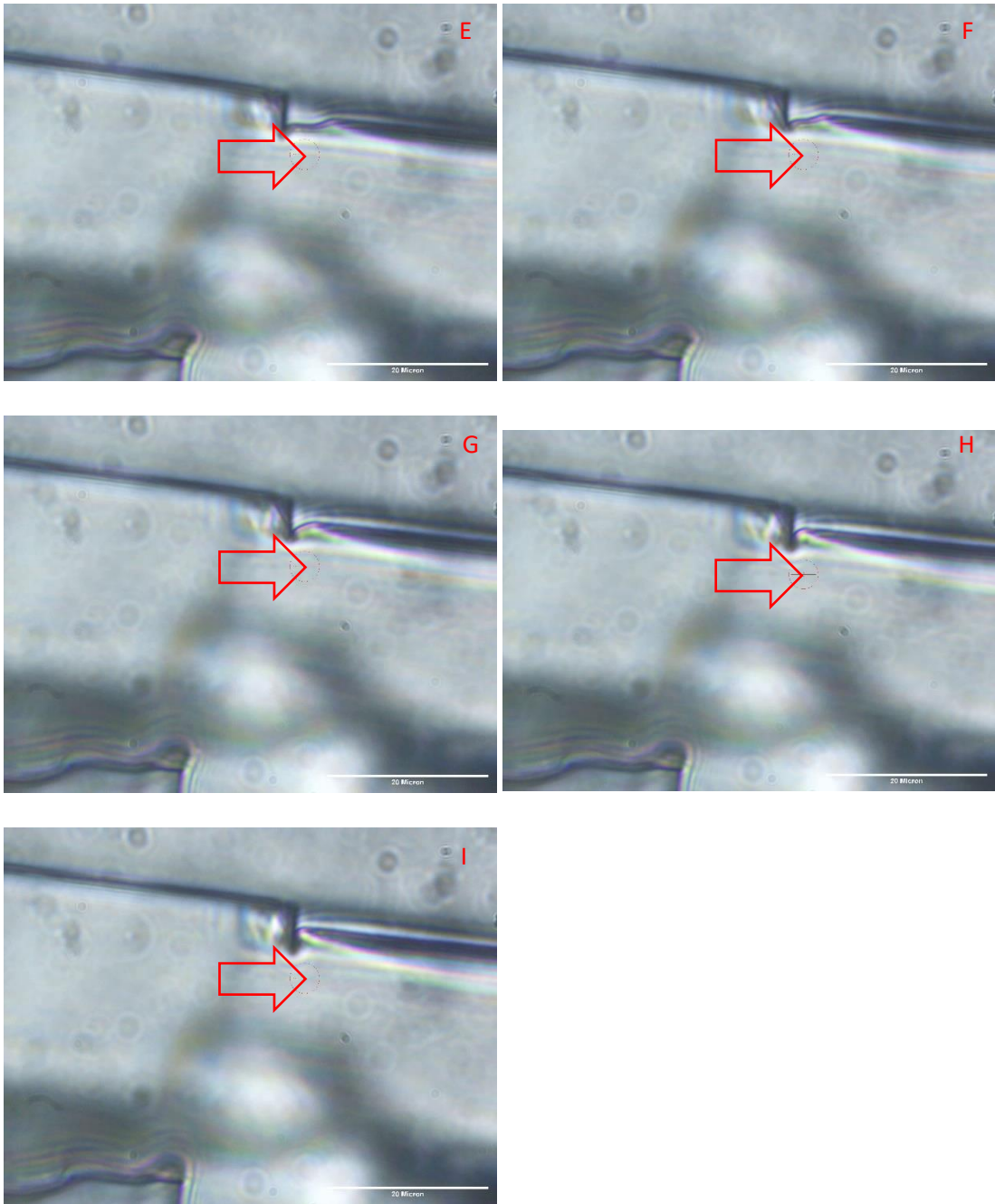


Figure 8:13: Growth of a NaCl Crystal in $S = 1.01$ H_2O based NaCl Solution in H_2O following deactivation of an optical trap with a set laser power of 300 mW. Images A-I were taken at 30-second intervals following activation when image A was taken. White scale bars show 20 microns. Position of where the tweezing focus was located in the image is indicated by the red arrows.

The observation shown by Figure 8:13 is combined with the predicted supersaturation, estimated from temperature rises from the model derived by *Peterman* [105]. The laser power delivered to the focus plane is 124 mW when a set power of 300 mW should not reduce the supersaturation below $S = 1$, as indicated by the calculations shown in Appendix J, where the effects of the heating caused by the tweezing focus on the calculated

supersaturation without accounting for any potential localised concentration enhancement. At least two elementary explanations exist for why this occurs: the first is that the model derived by *Peterman et al.* estimates temperature rises that are lower than the actual temperature rises produced. This discrepancy would be in line with observations made by others when examining the viscosity of the fluid in the proximity of the focus. Therefore, suggesting an even more significant difference between the temperature rises predicted by the *Peterman* model and the actual temperature rise [176]. The other is that the solubility curve is steeper than was found to be the case, as shown in section 6.2.1 as clear points indicated at the higher end of the temperatures tested were lower than those of previous other measurements [3], [181], [183], [193].

Of note is what happens when this experiment is repeated using D₂O as a solvent, where the growth rates were observed to decrease with increasing laser power, as seen in Figure 8:14. Since this was performed in D₂O, this cannot be explained by laser-induced heating altering the local supersaturation, which has been demonstrated to be minimal, at the laser powers used in this work, the same effect observed in H₂O when operating at 300 mW is not observed when using D₂O as shown by the presence of calculable growth rates at this laser power.

It may even be the case that holding the tweezing focus this close to the surface of a macroscopic crystal disrupts any attempt to generate a region of enhanced supersaturation.

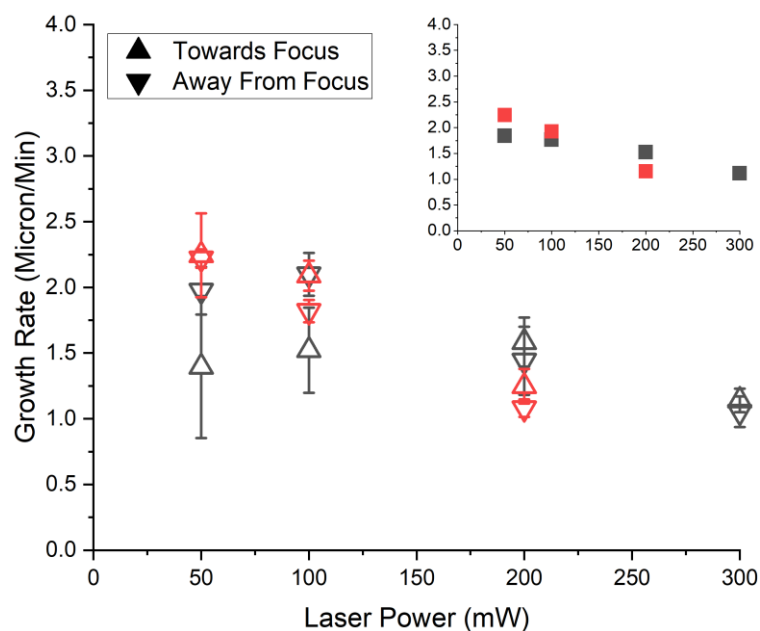


Figure 8:14: Growth rate of NaCl crystal through a focus of an optical tweezer of a NaCl crystal in $S = 1.01$ solution in D_2O at various laser powers. The growth rate was analysed under three circumstances, and towards the focus (triangles) and away from the focus (inverted triangles) overall growth rates are shown in the insert; linked runs are indicated using the same symbol colour. Error bars indicate a 95 % confidence interval in the gradient of the points analysed in each scenario. Symbols shown in the same colour at the same laser power were determined from a single experiment.

8.5.3 Growth Through an Optical Trap Containing a Silica Particle

Noticeably, if a particle was held within the trap, the power's impact on the solvent isotopologue is switched as it grows through the focus. Power delivered impacts crystal growth rates if D_2O is used and not H_2O . From Figure 8:15, compared to measurements made where a particle was not present within the focus of the trap, holding one in that position causes the growth rate through the focus of a trap to become dependent upon the laser power used. The growth rates determined by sodium chloride/silica solution/dispersion are shown in Figure 8:15 and Figure 8:16 for H_2O and D_2O , respectively.

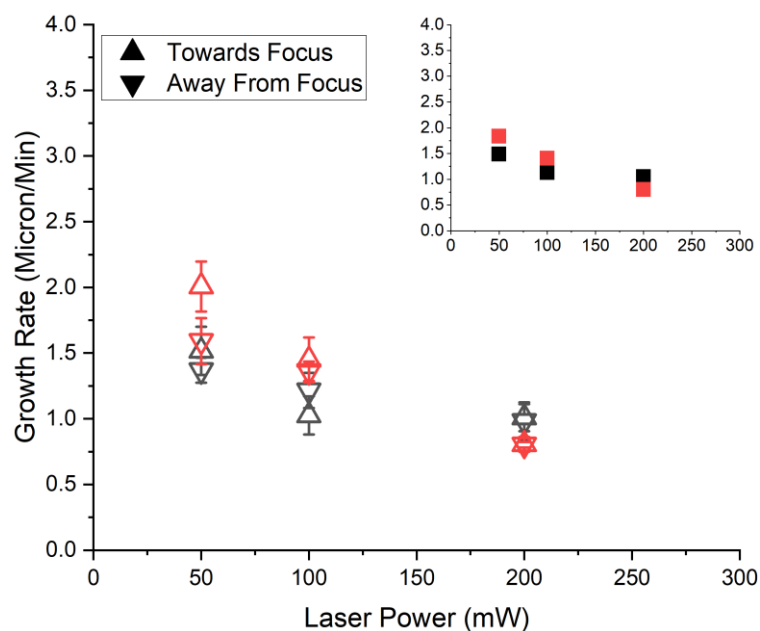


Figure 8:15: Growth rate of NaCl crystal through a focus of an optical tweezer of a NaCl crystal in $S = 1.01$ in H_2O with silica in suspension at a concentration of $0.12 \text{ mg}_{\text{silica}}/\text{g}_{\text{solvent}}$ at various laser powers, where a silica particle is held in the focus of the tweezers. The growth rate was analysed under three circumstances, and towards the focus (triangles) and away from the focus (inverted triangles) overall growth rates are shown in the insert; linked runs are indicated using the same symbol colour. Error bars indicate a 95 % confidence interval in the gradient of the points analysed in each scenario. Symbols shown in the same colour at the same laser power were determined from a single experiment.

Where again the use of the H_2O results in a lowering of the determined growth rates, however since the effect is small and the error bars shown do somewhat overlap the soundness of this conclusion cannot be guaranteed. As previously mentioned, when the growth in proximity was being examined, this could be due to the competing factor of the localised increase in concentration not being able to occur due to the centre of the trap being “occupied” by the silica particle and the heating that occur in the surrounding geometry.

This idea where a highly organised interlinked structure, proposed by *Yuyama et al.* [152], can form when something, i.e. a silica particle, is not present, could require the core of the trap to allow this to occur when little to no effect is seen when growth is observed in a D_2O based suspension.

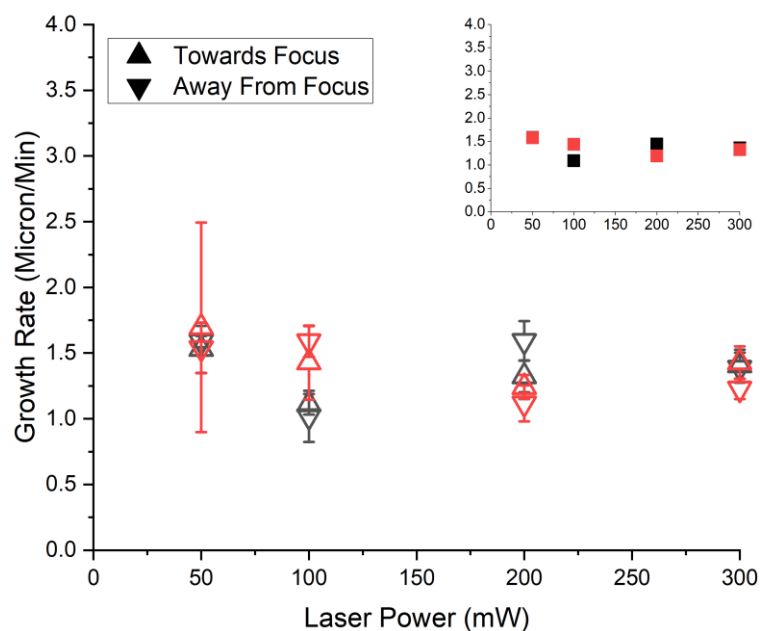


Figure 8:16: Growth rate of NaCl crystal through a focus of an optical tweezer of a NaCl crystal in $S = 1.01$ in D_2O with silica in suspension at a concentration of $0.12 \text{ mg}_{\text{silica}}/\text{g}_{\text{solvent}}$ at various laser powers, where a silica particle is held in the focus of the tweezers. The growth rate was analysed under three circumstances, and towards the focus (triangles) and away from the focus (inverted triangles) overall growth rates are shown in the insert; linked runs are indicated using the same symbol colour. Error bars indicate a 95 % confidence interval in the gradient of the points analysed in each scenario. Symbols shown in the same colour at the same laser power were determined from a single experiment.

8.6 Impact on Secondary Nucleation by optical Tweezing focuses

The presence of optical tweezing focus can alter nucleation both in the focus directly and in proximity to the beam itself [128], [155]. However, this has tended to focus on the effects of the beam directly causing or impacting primary nucleation. Nothing has been found to indicate that work has been conducted to investigate the impact of tweezing on secondary nucleation and if indeed, this is possible using this solute/solvent system using the forces that can be generated at this region of relatively low laser powers. In this section we examine the impact that trapped particles agitated in proximity to already existing macroscopic seeds can have on secondary nucleation.

8.6.1 Seeded Agitation Testing

To see if it were possible to induce secondary nucleation from a microscopically large NaCl seed suspended in supersaturated condition using a base solvent of D_2O , to minimise any potential heating effects, a range of individual circumstances were tested. This involved an investigation of shearing the solution in close proximity to the surface of the seed in a variety of forms. This required that a particle be oscillated parallel and perpendicularly, with reference to the edge of the crystal seed suspended in the solution, over amplitudes between

1 - 3 μm at frequencies between 1 - 3 Hz at 2 μm from the surface of the washed seed suspended in $S = 1.01$ D_2O based solution. Diagrams explaining the motion of the particle is shown in Figure 8:17. Agitation conditions were chosen to examine conditions over the range that the equipment and control software allowed that were found to be accurate through a manual check of performed with a microscope graticule.

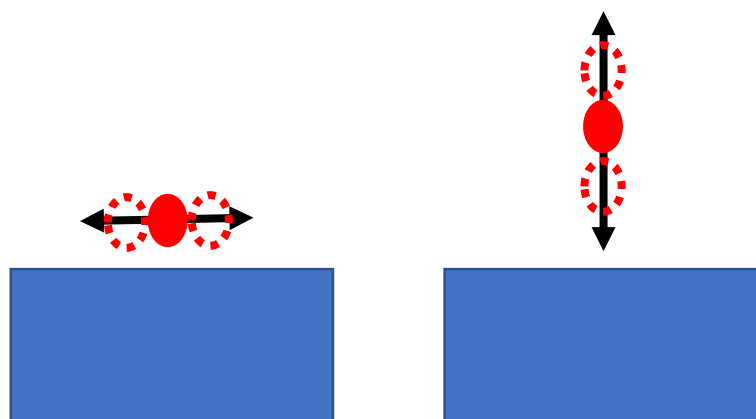


Figure 8:17: Schematic of agitation applied to the surface of a NaCl seed. Left; Parallel agitation. Right; Perpendicular agitation.

Each individual combination of circumstances was tested 5 times and on not a single occasion of any of the testing conditions was secondary nucleation observed. It is possible that the levels of shear that were generated were not high enough to induce secondary nucleation. However, these experiments were not a total write off as this allowed the growth rates to be examined when the particle in proximity to the surface was not stationary, these growth rates are shown in section 8.6.1.1.

8.6.1.1 Growth of Seed Crystals in Supersaturated Solutions Impacted by Agitated Particles

The testing to determine if the presence of agitation would impact secondary nucleation of tiny crystalline particles from or near the surface of the existing macroscopic crystal also allowed the growth of the surface to be examined to see if this would have any impact on the surface. Also, allowing the growth of these faces in all the tests performed to be examined to see if the agitation's magnitude, frequency, or direction would impact the crystal surface growth rate. In all cases, when using supersaturated solution, the seeds appeared to grow, confirming that the solution itself was supersaturated. From Figure 8:18 and Figure 8:19, altering the agitation conditions could impact the growth rate determined of the crystal front of the washed NaCl crystal. First, examining the direction of the agitation,

agitation in the perpendicular direction to the crystal front causes the growth rate of the crystal to be higher than agitation in the parallel direction. Examining the amplitude of the agitation shows that as the amplitude increases, the growth rate of the crystal front also increases. As can be clearly seen the presence of any agitation near to the surface of the growing crystal appears to lower the growth rates measured on average as can be seen by the blue lines being above the levels of the bars in Figure 8:19.

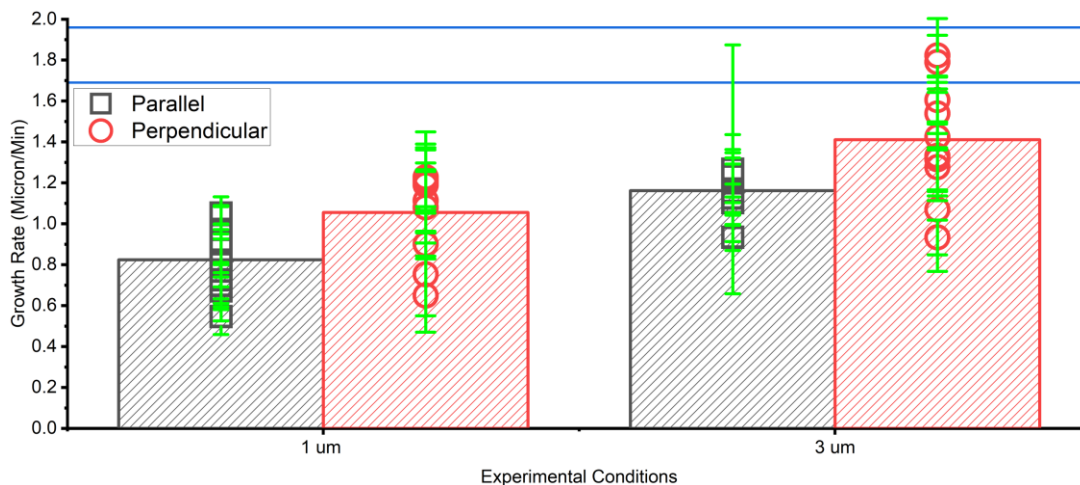


Figure 8:18: Growth Rates of NaCl Crystals in proximity to an agitated silica microsphere, held using a 975 nm laser at a set power of 300 mW, examined by altering the direction, amplitude, and frequency of agitation. The subdivision of agitation frequency is not shown. Points show individual measurements with 95 % Confidence Intervals. Bars indicate averages of points. Blue lines indicate growth rate of NaCl in $S = 1.01$ D_2O based solution in absence of any outside influence.

However, when examining the frequency of the agitation, as highlighted in Figure 8:19, shows that in most of the cases examined at the frequencies shows minimal impact as the agitating at 1 Hz and 3 Hz as there was typically no significant difference between the two frequencies. Most of the subsets of the rates determined are, on average equal when the amplitude and direction of agitation are equal, however, when using an amplitude of 3 μm , when agitated in a perpendicular direction to the surface of the crystal surface on average this subset of conditions had the closest growth rate to that of the control experiment where the growth was examined in the absence of any agitation in the silicone well. Which itself is surprising however when looked at in isolation as the frequency or the amplitude of the agitation increased the growth rate also increased, which is in line with previous knowledge including work performed in chapter 6.

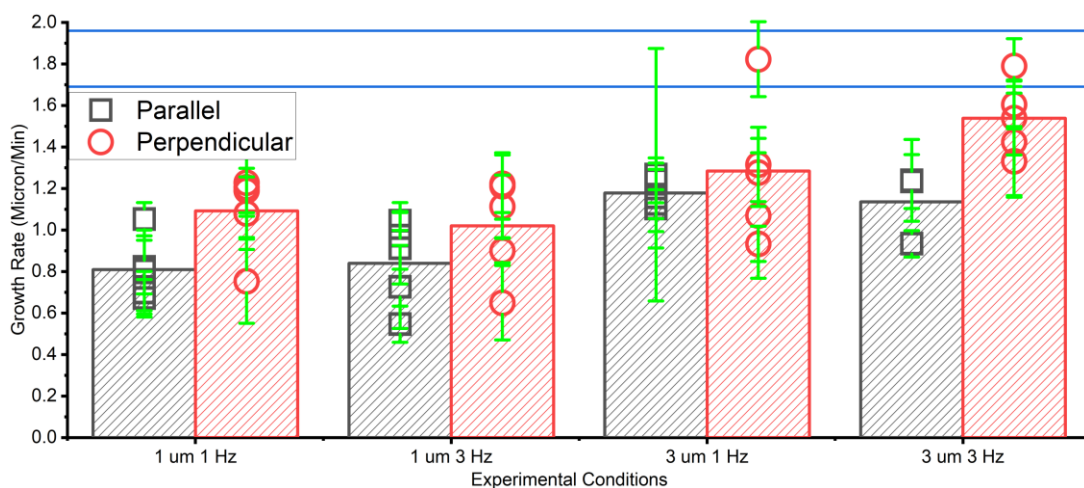


Figure 8:19: Growth Rates of NaCl Crystals in proximity to an agitated silica microsphere, held using a 975 nm laser at a set power of 300 mW, examined by altering the direction, amplitude, and frequency of agitation. Points show individual measurements with 95 % Confidence Intervals. Bars indicate averages of points. Blue lines indicate growth rate of NaCl in $S = 1.01$ D_2O based solution in absence of any outside influence.

8.6.1.2 Well Filling Testing

Since the goal of this section is to determine the effects of secondary nucleation, it is necessary to ensure that the methods used to fill the well are not themselves causing nucleation to occur unduly as any particles generated by the filling method which become visible in tested could be incorrectly attributed to the action of the laser itself or the particle inducing the agitation. The well created by the silicon isolator and glass coverslip was filled via pipette in an incubator above the saturation temperature of the solution being tested (50 °C). The well was then closed using a second pre-warmed glass coverslip. The solution was then allowed to cool down naturally in situ on the tweezing setup. Testing showed if the well was overfilled, even slightly, caused the layer between the top of the isolator and glass coverslip to dry out within minutes and induce crystallisation in the well's main volume.

Therefore, to eliminate the possibility of this occurring, the volume of the well had to be slightly underfilled. The wells were then filled with 200 μ L of undersaturated solution and allowed to cool down to become supersaturated to a level of $S = 1.01$. However, this did introduce an air solution interface within the well. Figure 8:20 shows that it takes more than 24 hours before any crystals were observed within the volume of solution in the isolator well. With the images shown in Figure 8:20, this is observed by the presence of bright spots within the wells in images A2 and B2 that are not present in the corresponding A1 and B1 image.

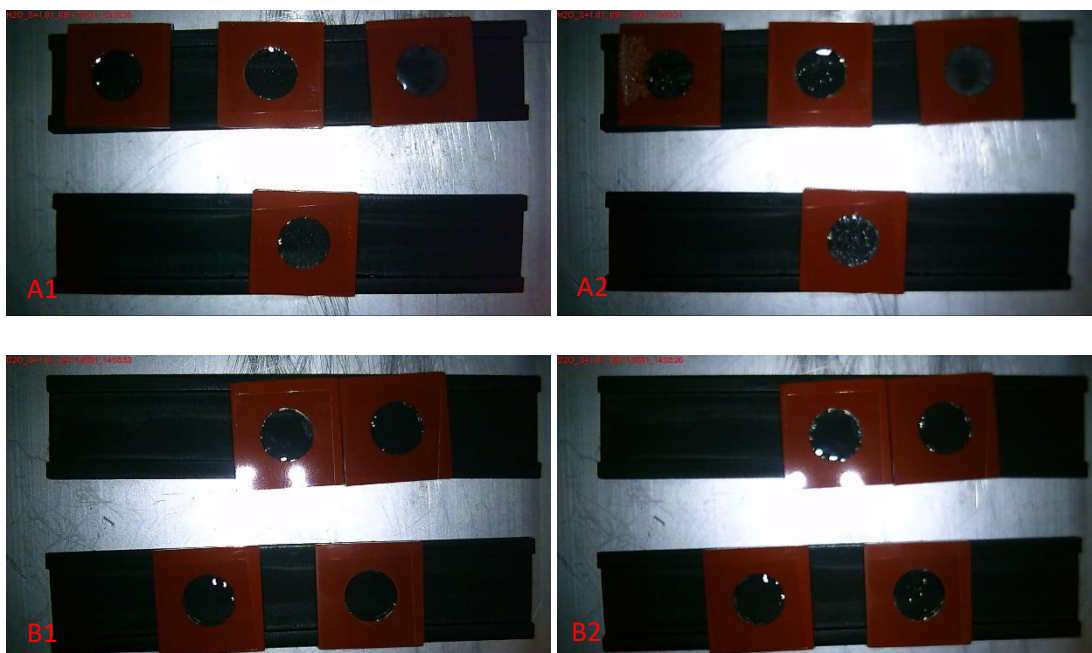


Figure 8:20: Pictures taken of Silicon Isolator well-filling tests. Row A; NaCl in H_2O . Row B; NaCl in D_2O . Column 1; Initial appearance. Column 2; Appearance after 24 hours.

8.7 Conclusions

Combining temperature rises with solubility curves allows supersaturations to be estimated using the tweezers when impacted by laser-induced heating. Allowing predictions to be compared to actual observations when holding a tweezing focus near an existing macroscopic crystal. Whereas in a supersaturated solution, the growth experienced by the crystal can be inhibited or enhanced depending on the conditions used, such as the laser power, solvent isotopologue and the presence of a silica microsphere. However, when applying agitation this can impact the effect of the tweezers when close to the existing crystal.

9 Nucleation from Solution Induced by Optical Tweezing

9.1 Tweezing Set-Up

Higher laser powers are required to determine the impact of the optical tweezers directly on nucleation from solutions than are required to influence growth, as indicated by work previously performed by Yuyama et al. and Tu et al. [145], [154]. Requiring the setup of the optical tweezers to be altered slightly from what was previously used to accommodate the use of a higher power 2 W 1064 nm laser (MLL-H-1064-2W-5, CNI Lasers), the new altered setup is shown in Figure 9:1. The switch to 1064 nm had the additional benefit that at equal trapping power the laser-induced heating would be reduced in H₂O and D₂O [105] in comparison to 975 nm. When using the 1064 nm wavelength laser the diameter of the focus was approximately 300 nm/

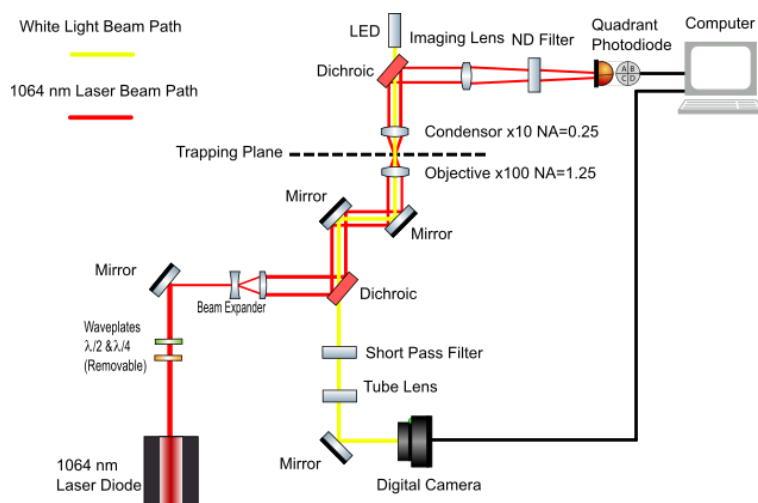


Figure 9:1: Schematic of Modified Optical Tweezer Set-Up. Component library provided by Alexander Franzen [233].

9.2 Experimental

9.2.1 Contact Angle Measurements

Since nucleation was going to be induced using optical tweezing at or near the edge of solution droplets, understanding the geometry of the trinary interface point of the droplet edge is critical.

Contact angle measurements were performed using the Kruss DSA30 in combination with a 3 mL syringe using a 0.8 mm OD flat-ended needle to drop a single sessile drop onto the surface of the examined cover glass. This allowed an image to be taken to measure the contact angle made between the liquid and the cover glass. This was utilised to characterise

the cover glasses' surface energy and the physical geometry that sessile drops would form on the surface of the coverslip.

9.2.2 Tweezed Droplet Set-Up

To allow nucleation when acted upon with the optical tweezers to be studied in the specific geometry of a sessile drop at a controllable location within its volume requires an in-house setup to be used. This consists of a silicone isolator (Grace Bio Labs) with an open well (13 mm Diameter, 2.2 mm thick) that is closed using a pair of # 1.5 thickness 22 mm x 22 mm borosilicate cover glasses previously tested to determine the surface energy and the geometry of the droplet on the surface. A diagram of the setup of the point where tweezing was conducted is shown in Figure 9:2, as well as the wider setup including the silicon isolator. A photograph of the wider setup is shown in Figure 4:8.

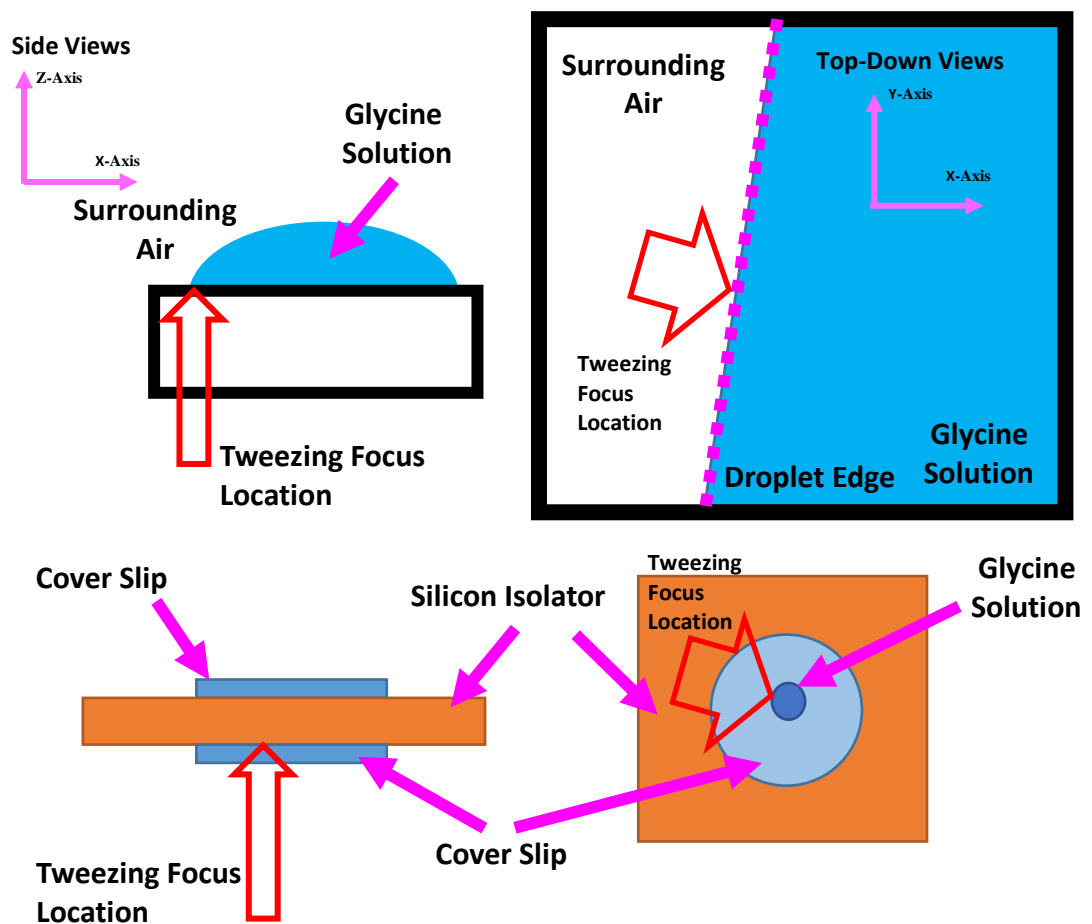


Figure 9:2: Schematic diagram of the sessile droplet within the silicon isolator and coverslip assembly showing a side view and top-down when the tweezing focus was located at the droplet edge. Wider setup including silicon isolator show. Other non-test droplets placed on to the surface not shown.

The exact position of the tweezing focus within the sessile droplet depended on the scenario being investigated. In the experiments the tweezer position relative to the contact line was

varied to test the effect of proximity to the interface on induced nucleation. A single 20 μL droplet of the solution was pipetted onto the upper surface of the lower coverslip using a Gibson pipette performed within an incubator set at 50 $^{\circ}\text{C}$. The well within the silicon isolator was then sealed using a second identical coverslip.

The solutions were manufactured by weighing a known mass of solute (Glycine, NaCl or NaBrO_3) by difference into a 1.5 mL HPLC vial into which 1 g of solvent (either H_2O or D_2O) was also added. A 3 mm Teflon-coated stirrer bar was added, and the vials were sealed using a basic cap. Complete dissolution was ensured using a magnetic stirring hotplate set to 65 $^{\circ}\text{C}$, where the solution was held for 30 minutes to ensure dissolution. The compositions of the solutions tested are shown in Table 9:1 for glycine solutions in H_2O and D_2O . The solubility of glycine at 20 $^{\circ}\text{C}$ was 0.2286 $\text{g}_{\text{glycine}}/\text{g}_{\text{H}_2\text{O}}$ and 0.1943 $\text{g}_{\text{glycine}}/\text{g}_{\text{D}_2\text{O}}$ for the two solvents used.

Table 9:1: Compositions of Glycine Solutions used for nucleation testing using optical tweezers.

| Solvent | Concentration (g/g) | Supersaturation at 20 $^{\circ}\text{C}$ |
|---|---------------------|--|
| Water $C^* = 0.2286 \text{ g/g at } 20^{\circ}\text{C}$ | 0.3429 | 1.50 |
| | 0.2858 | 1.25 |
| | 0.2286 | 1.00 |
| | 0.2057 | 0.90 |
| | 0.1943 | 0.85 |
| | 0.1829 | 0.80 |
| | 0.1715 | 0.75 |
| Deuterium Oxide $C^* = 0.1943 \text{ g/g at } 20^{\circ}\text{C}$ | 0.2915 | 1.50 |
| | 0.2429 | 1.25 |
| | 0.1943 | 1.00 |
| | 0.1749 | 0.90 |
| | 0.1652 | 0.85 |
| | 0.1554 | 0.80 |
| | 0.1457 | 0.75 |

Testing using NaCl was only performed at one supersaturation $S = 1.01$ due to the practical limitations of transferring higher supersaturation solutions from the incubator to the optical tweezers. Where the concentrations were 0.3623 $\text{g}_{\text{NaCl}}/\text{g}_{\text{H}_2\text{O}}$ and 0.3084 $\text{g}_{\text{NaCl}}/\text{g}_{\text{D}_2\text{O}}$ for solutions

in water and deuterium oxide, respectively, at 20 °C. Concentrations used for testing with sodium bromate are shown in Table 9:2.

Table 9:2: Compositions of Sodium Bromate Solutions used for nucleation testing using optical tweezers.

| Solvent | Concentration (g/g) | Supersaturation at 20 °C |
|---|---------------------|--------------------------|
| Water C* = 0.3664 g/g at 20 °C | 0.5130 | 1.4 |
| | 0.4763 | 1.3 |
| Deuterium Oxide C* = 0.2904 g/g at 20 °C | 0.4066 | 1.4 |
| | 0.3775 | 1.3 |

Testing nucleation using the optical tweezers involved altering the distance (both laterally, x or y axis displacement in Figure 9:2 and vertically, z axis in Figure 9:2, from the droplet edge) and other factors, such as the beam polarisation and the presence of a silica particle, explored in section 9.5. Using the droplet edge as a reference point from which locations within the geometry of the droplet are defined from, e.g., 10 µm is laterally 10 µm into the bulk of the droplet from the edge. 10 repeat tests were performed to determine the time taken from the activation of the tweezers and the appearance of a crystal. The observation was not carried out indefinitely until the point where nucleation was observed. From a small number (~15) of preliminary experiments, it was decided that an observation period of 10 minutes should be used from preliminary experiments performed at the droplet edge using glycine in H₂O at S = 1.50, where all the samples tested had nucleated before reaching 10 minutes of irradiation at 775 mW. If this period had elapsed without the tweezers inducing nucleation, the tweezers were deactivated. The setup was reset, with a fresh drop of test solution, for the next sample to be tested while recording a failure to induce nucleation. If nucleation was observed within 10 minutes, the laser was deactivated shortly following the appearance of the crystal and reset to allow the repeat to be performed. This also allowed the growth rate of the crystals produced by the action of the tweezers to be measured, this is discussed in detail in section 9.10. Experiments were performed with linearly polarised light unless otherwise stated.

In addition to measuring the nucleation time, the images captured at this point allowed the morphology of the crystal produced to be determined. This is discussed in greater detail in section 9.5.1.2. In the periods following nucleation, crystals were allowed to continue to grow while within the focus. This allowed the growth rates as conditions were varied without

requiring a separate experiment to be performed at each value of lateral distance, supersaturation etc., 10 repeat experiments were performed with a new droplet for each experimental condition tested. From these repeats cumulative nucleation probability distributions vs time could then be generated for each scenario to determine the effects of altering factors. One disadvantage of this setup is that all experiments had to be performed in series and that nothing was parallelisable.

9.3 Suspending Cover Glass Characterisation

The surface energy of the coverslips used when performing tweezing experiments can be determined by measuring the contact angles that circular droplets of a small range of selected solutions make with the borosilicate glass surface (used as supplied) at room temperature representing the same conditions when performing nucleation experiments using the optical tweezers. This was performed using three liquids: deionised water, diiodomethane and ethylene glycol. The results of the contact angles measured for these three test liquids can be seen in Figure 9:3.

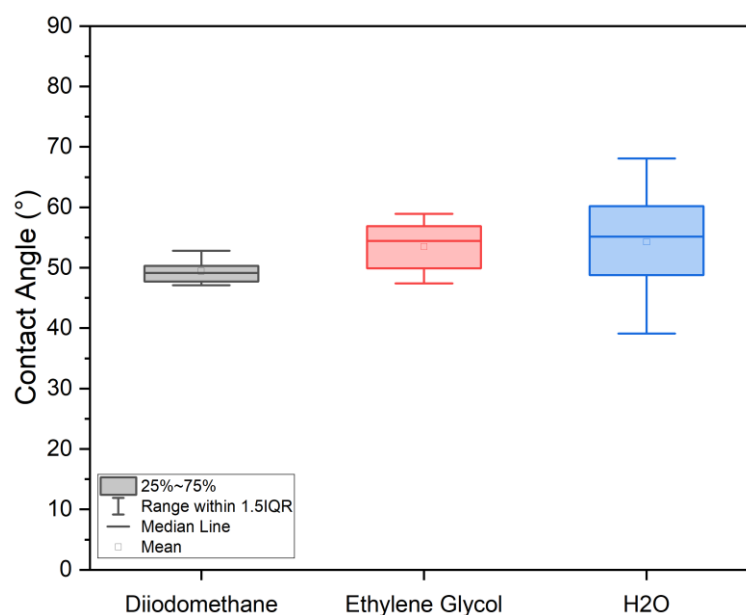


Figure 9:3: Box plot of the contact angle measurements of three liquids to determine the surface energy of the coverslips used in the tweezing experiments. Distributions were determined from 10 measurements of contact angle at 20 °C. 50 % of points are within the box, outer quartiles are within the bars. The median is indicated with the line, and the mean is highlighted using the indicated point.

These measurements allow the surface energy of the coverslips used to be determined as the Lifshitz van der Waals (LW) (γ^{LW}) and the Lewis acid (γ^+) and base (γ^-) characteristics of each are well known. Table 9:3 shows these components of each test liquid used to determine the surface energy of the coverslips used.

Table 9:3: Surface energy parameters of test liquids [234].

| Liquid | γ_L^{LW} (mJ m ⁻²) | γ_L^+ (mJ m ⁻²) | γ_L^- (mJ m ⁻²) | γ_L (mJ m ⁻²) |
|-----------------|---------------------------------------|------------------------------------|------------------------------------|----------------------------------|
| Diiodomethane | 50.8 | 0 | 0 | 50.8 |
| Ethylene Glycol | 29.0 | 1.92 | 47.0 | 48.0 |
| Water | 21.8 | 25.5 | 25.5 | 72.8 |

Where the overall surface energy of a substance can be determined using Equation 9:1 [235], [236] from a combination of the component parts.

$$\gamma_i = \gamma_i^{LW} + 2\sqrt{\gamma_i^+\gamma_i^-}$$

Equation 9:1

Where:

- γ_i Overall surface energy term of substance *i*
- γ_i^{LW} Lifshitz Van der Waals component of substance *i*'s surface energy
- γ_i^+ Lewis acid component of substance *i*'s surface energy
- γ_i^- Lewis base component of substance *i*'s surface energy

When two substances touch each other the angle at which these two make contact is dependent upon the each of these surface energy components for the two substances. Using a liquid, or in this case a series of liquids whose LW and Lewis surface energy averages are known allow these same components to be calculated for another whose are unknown. This also requires that angle (θ) at which the two make contact be determined. In this case, of a solid surface (in this case the cover glass) denoted in Equation 9:2 with the S subscript (γ_S) and that of the probe liquid used denoted by the subscript L (γ_L), component parts of the surface energy can be determined for the cover glasses used, and thereby the overall surface energy using Equation 9:1.

$$\gamma_L(1 - \cos(\theta)) = 2\sqrt{\gamma_L^{LW}\gamma_S^{LW}} + 2\sqrt{\gamma_L^+\gamma_S^-} + 2\sqrt{\gamma_L^-\gamma_S^+}$$

Equation 9:2

Table 9:4: Surface Energy Components of the Cover glasses

| Material | γ_S^{LW} (mJ m ⁻²) | γ_S^+ (mJ m ⁻²) | γ_S^- (mJ m ⁻²) | γ_S (mJ m ⁻²) |
|--------------------------|---------------------------------------|------------------------------------|------------------------------------|----------------------------------|
| Borosilicate Cover glass | 34.75 | 0.11 | 38.94 | 38.89 |

9.4 Contact Angles of Tested Solutions

In addition to determining the surface energy of the coverslips used throughout this chapter, as this factor can influence any potential nucleation, by lowering the free energy barrier required for nucleation. Contact angle measurements were also performed on a selection of the solutions later probed using optical tweezers. These measurements were performed to ascertain the confined geometry within which the focus of the tweezers was located when attempting to induce nucleation from solution.

In both solvent isotopologues, the contact angle increases as the supersaturation of the NaCl solution tested increases. There appeared to be an insignificant impact between the isotopologues, with a considerable overlap of the standard errors, as seen in Figure 9:4 when comparing the isotopologues at the same supersaturation. In general, these measurements showed a slight increase in the average contact angle (although the overlap of the error bars may cast some doubt, this could be clarified by greater sample sizes in future measurements) when comparing the solutions to the base solvent. Only concentrations up to saturation were tested due to the difficulties associated with keeping and maintaining a supersaturated solution through the apparatus required to test contact angles, testing performed showed that any use of supersaturated solutions resulted in the solution crystallising within the syringe or needle.

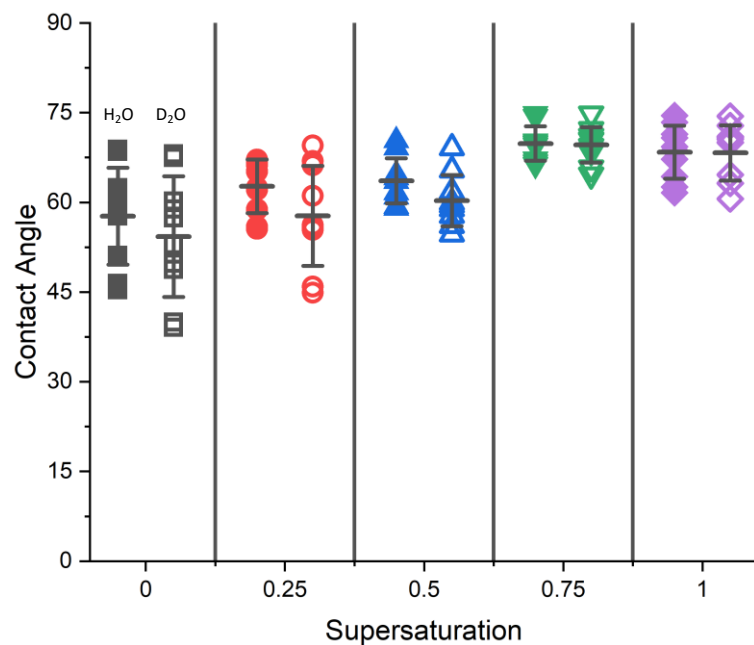


Figure 9:4: Contact angle measurements of sodium chloride solutions in water (Hollow Symbols) and deuterium oxide (Filled Symbols) of a range of supersaturation at 20 °C based on a solubility of 0.3623 g_{NaCl}/g_{Water} and 0.3084 0.3623 g_{NaCl}/g_{Deuterium Oxide}. Black bars indicate the mean and the standard error for each concentration in each solvent.

Unlike the measurements performed using sodium chloride solutions, those done when using glycine showed a decrease in contact angle from the base solvent in both solvent isotopologues, as seen in Figure 9:5. However, this trend appears to reverse itself once the solution becomes saturated. The contact angle generally increases as the solution increases supersaturation in H₂O and D₂O, however the overlapping error bars may cast some doubt on this.

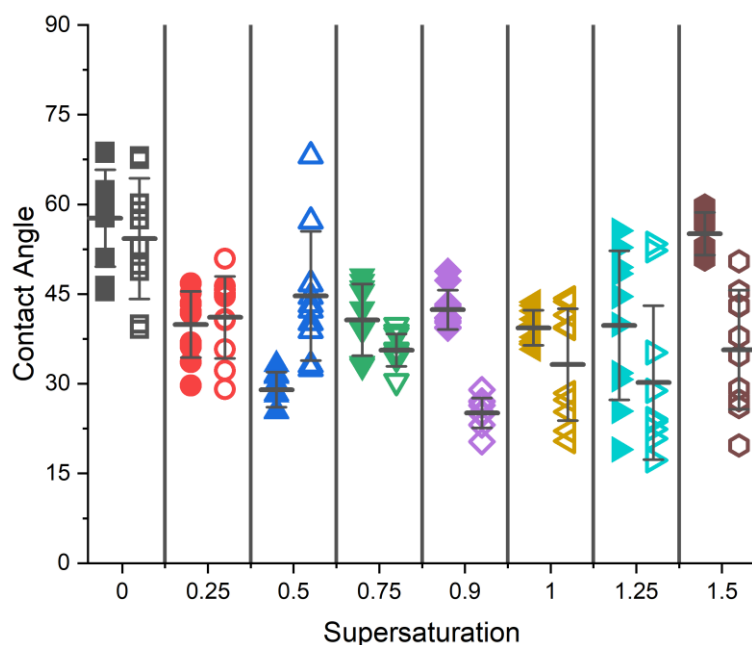


Figure 9:5: Contact angle measurement of glycine solutions in water (Hollow Symbols) and Deuterium Oxide (Filled Symbols) of a range of supersaturation at 20 °C using the solubilities of 0.2286 g_{glycine}/g_{water} and 0.1943 g_{glycine}/g_{deuterium oxide}. Black bars indicate the mean and the standard error for each concentration in each solvent.

9.5 Induced Nucleation from Glycine Solutions using Optical Tweezers

9.5.1 Effect of Solution Supersaturation

One of the most obvious factors that can be altered is the bulk supersaturation of the solution that the tweezers act on, in addition to the laser power used to generate the trap.

9.5.1.1 Nucleation Time Distributions

With the tweezer focussed fixed at the droplet edge, of which a selection of examples are shown in Figure 9:6, the solution concentration was altered to determine the impact that this could have on the distribution of nucleation times observed. In the absence of the tweezing focus no crystals were observed to nucleate within the field of view using $S = 1.50$ solutions using either H₂O or D₂O, therefore it is reasonable to conclude that the appearance of any crystal within the field of view of the tweezing is due to the action of the tweezing beam. These control experiments were performed at both the droplet edge and in the bulk of the droplet.

In Figure 9:7, the impact of altering the glycine concentration when using two separate trapping beam powers 775 mW (left) and 650 mW (right). It was possible to ensure that the trap's focal volume was located at the points required, in this case, the droplet edge, as the

trap would have an approximate diameter of 0.3 microns, based upon the term used to quantify the volume of the focus of the trap [105].

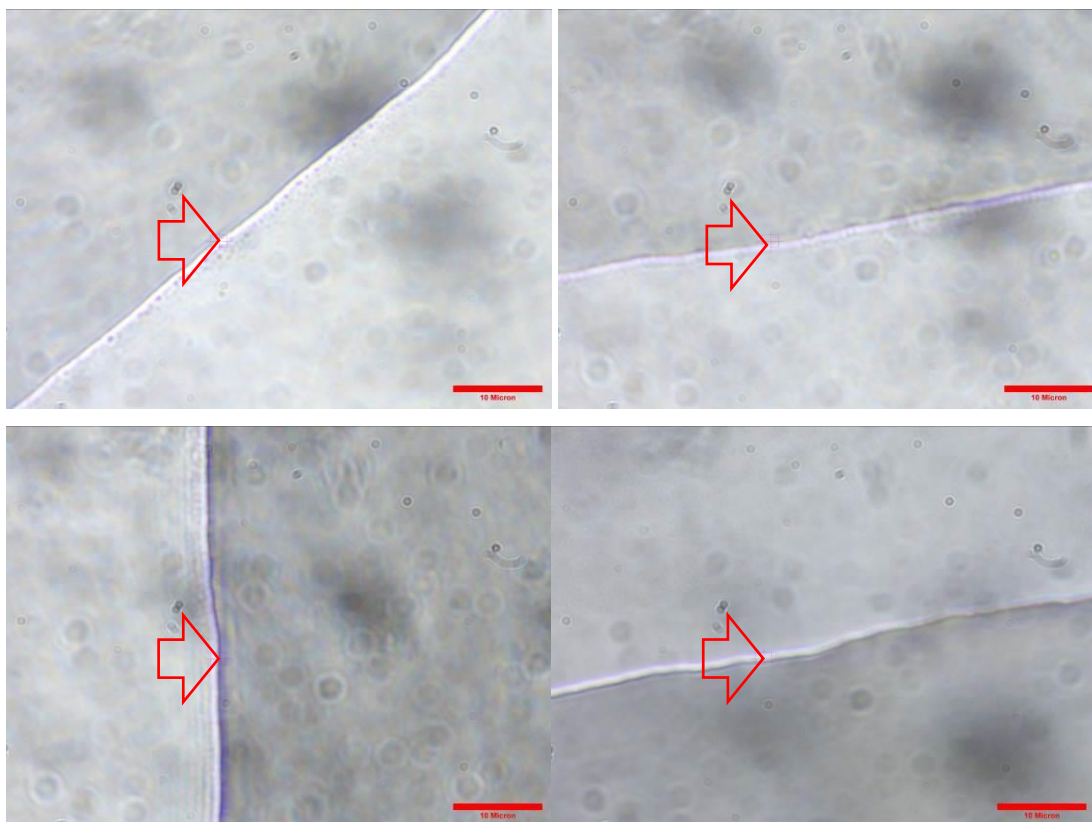


Figure 9:6: Examples of the droplet edge before nucleation, solutions of $S = 1.5$ in H_2O . Solution is located within the darker portion of the image, and the surrounding air is within the lighter half. Scale Bar indicates 10 microns. Red arrows indicate location of tweezing focus.

Figure 9:7 shows that when using the 775 mW trapping beam, the concentration did not make a qualitative impact until the supersaturation dropped to $S = 0.75$, as evidenced by the fact that the proportion of vessels that nucleated dropped from 90 % at $S=0.80$ to 0 % at $S = 0.75$ when exposing the solutions to a 775 mW trapping beam. One feature of note from the results show is the inducement using optical tweezers of nucleation of glycine from solution in undersaturated H_2O , previously unreported to the author's best knowledge. Several reports where nucleation of glycine induced by optical tweezers from solution in D_2O have noted that the reason for using D_2O was to minimise any laser-induced heating [145]. It is possible that operating the optical tweezing focus in such proximity to the coverslip (as performed here, which acts as a heatsink) renders any significant effect of the laser-induced heating insignificant. As the predicted temperature rise falls sharply when operating in such proximity to the heat sink (within 10 μm), as shown in Figure 5:20. This is also supported that the use of H_2O does not appear to be an issue when L-serine is induced to nucleate from H_2O

based solutions in similar circumstances to those used here for glycine [149], when operating the tweezing focus at the edge of the sessile droplet.

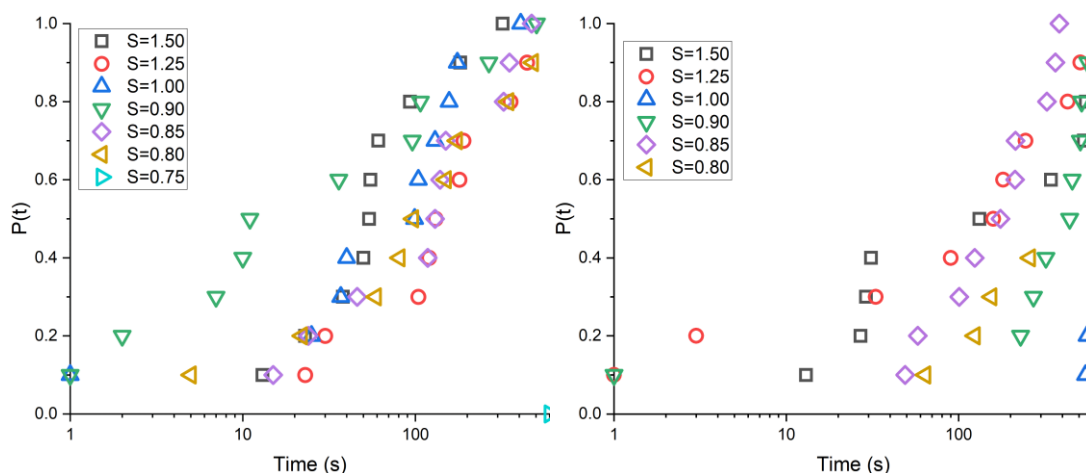


Figure 9:7: Cumulative probability distributions of the nucleation times located at the droplet edge for a range of glycine solutions in H_2O . Trapping power 775 mW (left) and 650 mW (right) of linearly polarised beam. A total of 10 repeat experiments were performed at each power and supersaturation combination.

The same range of supersaturations was examined using D_2O (shown in Figure 9:8) as the base solvent rather than the more abundant isotopologue H_2O . Like those situations examined when using H_2O , a similar behaviour was observed where there appeared to be a minor impact on the distribution within a specific range of supersaturations. However, once the lower bound of this range is crossed, becoming apparent when supersaturation drops below $S = 0.85$, as above or equal to this supersaturation, as 78 % of samples examined nucleated within the observation period. Whereas at $S = 0.80$, only 30 % of the samples nucleated within the observation period, and as it was reduced again to $S = 0.75$, the proportion fell to 10 %. When using the lower trapping power of 650 mW, slightly different behaviour was observed where the proportion of samples which nucleated slowly reduced as the supersaturation dropped from $S = 1.5$, which is summarised in Table 9:5.

Table 9:5: Percentage of times nucleation was observed when focused at the edge of a droplet of glycine solution in D₂O at a range of supersaturation at 775 mW and 650 mW.

| Supersaturation (Unitless) | Laser Power Used (mW) | |
|-------------------------------|-----------------------|-----|
| | 775 | 650 |
| 1.50 | 90 | 90 |
| 1.25 | 70 | 100 |
| 1.00 | 70 | 80 |
| 0.90 | 70 | 70 |
| 0.85 | 90 | 60 |
| 0.80 | 30 | 40 |
| 0.75 | 10 | N/A |

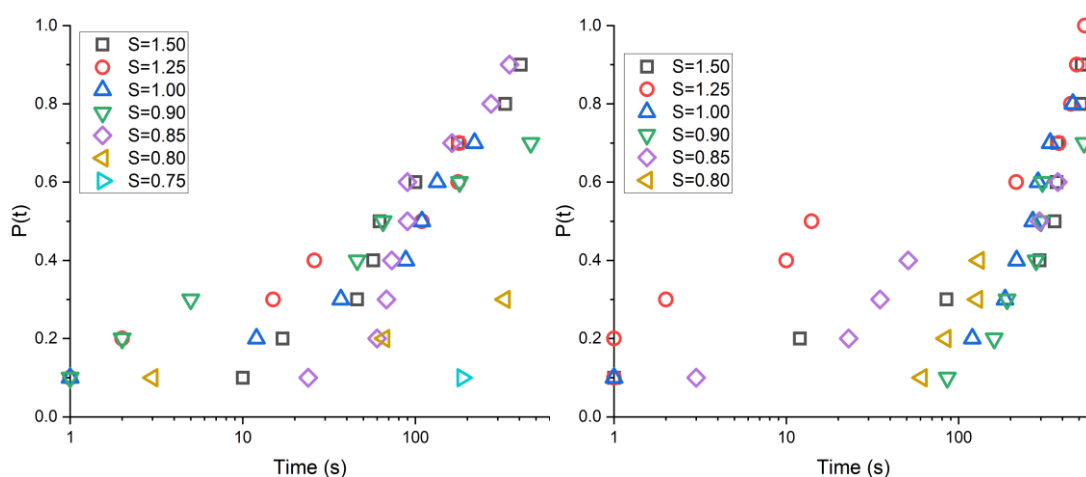


Figure 9:8: Cumulative probability distributions of the nucleation times for a range of glycine solutions in D₂O. Trapping beam 775 mW (left) and 650 mW (right) of linearly polarised 1064 nm. A total of 10 repeat experiments were performed at each power and supersaturation combination.

One conceivable way to compare each supersaturation quantitatively is to fit a numerical model to the cumulative probability distribution of the observed crystallisation times, described in small vial studies, like those in section 6.3, as induction times. One model that is typically used in small-scale nucleation studies is that developed by *Jiang and ter Horst* [48], as shown in Equation 9:3.

$$P(t) = 1 - \exp(-JV(t - t_g))$$

Equation 9:3

However, this would require some modification as the nucleation is induced to occur at a single point within the volume of the solution and not in the rest of the droplet, as here it was not possible to monitor what was occurring in the rest of the vial and secondary nucleation was not being encouraged through agitating the control volumes contents as was the case in chapters 6 and 7. To allow a model to be applied, the JV term was grouped into a single term (K_1 , with the units of s^{-1}) that would be used to quantify the slope of the cumulative probability distribution and the t_g term can be removed as this is present to account for the production of the secondary nuclei necessary for that method to work. The form of the equation used to fit the data here is given in Equation 9:4. Similar models have been used in modelling the effects of lasers and mechanical shock on nucleation from solution [237], [238].

$$P(t) = 1 - \exp(-K_1(t))$$

Equation 9:4

An example of the fitting of this model to the $S = 1.25$ H₂O samples measured when induced to nucleate by a 775 mW focus in Figure 9:9 when the tweezing focus was located at the droplet edge. The determined K_1 term for each of the supersaturations examined is shown in Figure 9:10, where it appears that in 3 of the 4 cases examined, the supersaturation of the solution used did not appear to make a significant difference to the value of the K_1 term determined by the fitting. However, the lack of nucleation, with one exception, below $S = 0.80$, suggests that this could be a supersaturation threshold that must be “crossed” before the tweezers can induce nucleation. This also highlights the effect of the reduction of laser power and the effect of changing solvent isotopologue. When the laser power is reduced from 775 mW to 650 mW, the value of the average K_1 term determined decreases. While the switch to D₂O from H₂O also shows the same trend where the K_1 term decreases at both laser powers examined. Again like the induction time distributions examined in chapters 6 and 7 any determined primary nucleation rate, or in this case determined characteristic K_1 coefficient would be susceptible to significant errors. Even doubling the sample size would not have a significant effect on the errors observed and would require at least a sample size an order of magnitude larger than what has been used here [49]. However, with the way the nucleation times have to be generated when acted upon by the laser requires all samples to be measured sequentially and not simultaneously, therefore it becomes highly impractical to measure very large sample sizes.

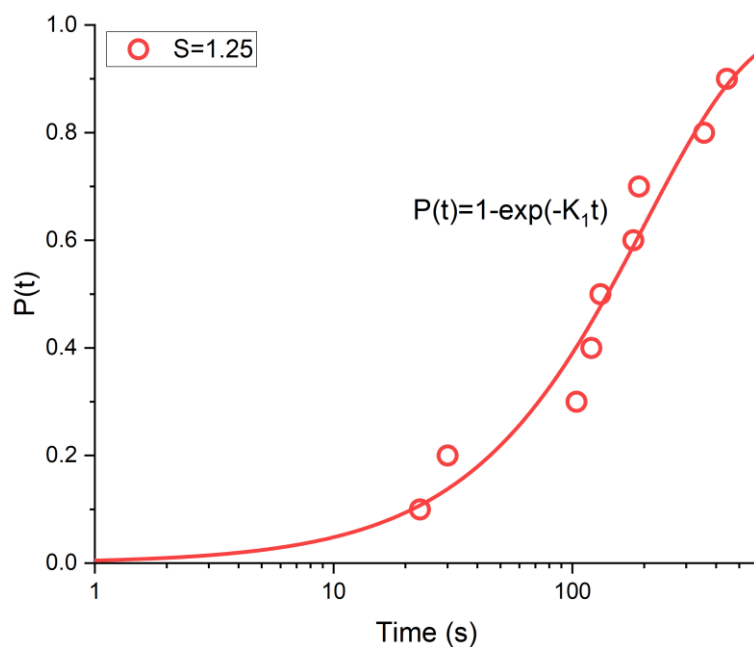


Figure 9:9 Example of model shown in Equation 9:4 fitting to cumulate probability distribution of crystallisation times of glycine in H₂O being induced to nucleate using a 775 mW optical focus located at the droplet edge.

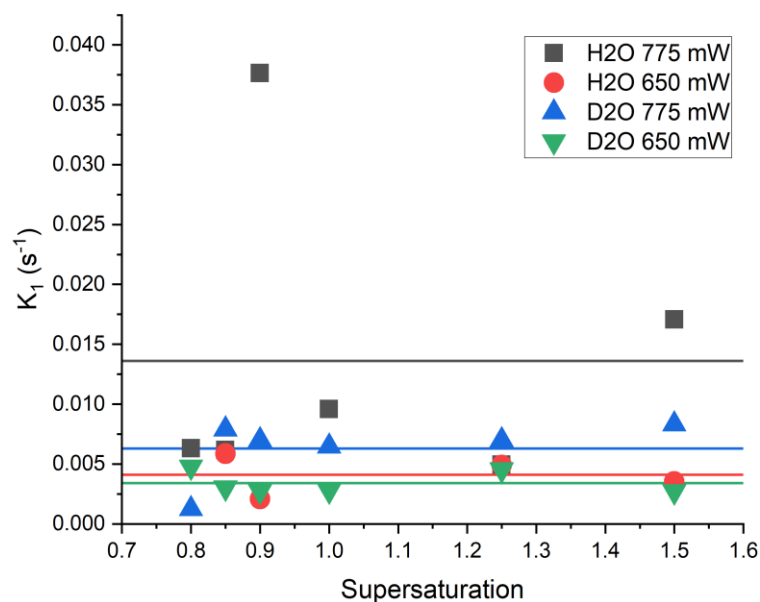


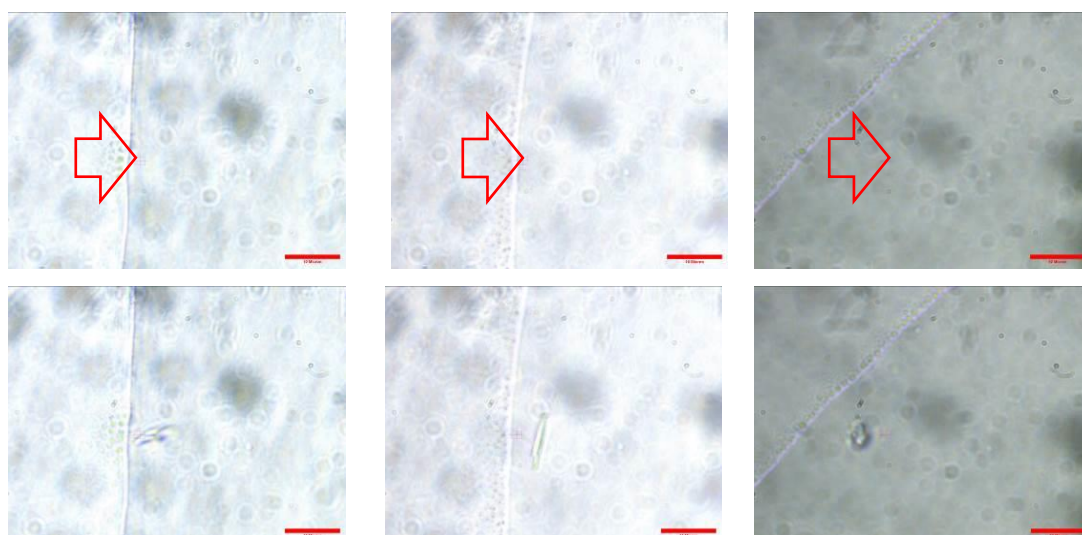
Figure 9:10 Determined values of K_1 from fittings of Equation 9:4 to the cumulative probability distributions when examining the effect of altering the supersaturation of the solution used for testing while remaining at the droplet edge with the optical tweezers. Points show individual values determined, and lines indicate the averages across the range of supersaturations tested using the same solvent isotopologue and laser power.

This form of model has been used by others when examining the inducement of nucleation of KBr and KCl from aqueous solution when monitoring the proportion of occasions in which nucleation is observed when varying the peak power density of the pulse used to induce said nucleation [238]. Much like the supersaturation examined here there also appear to be another critical limiting factor that was explored by *Ward et al.* as fittings indicate that a

minimum power may be required to cause an inducement for nucleation, however, to determine that lower powers than the two powers (775 mW and 650 mW) would have to be examined to determine what this would be for this system under this form of examination. This form of model has also been seen to fit other forms of inducement of nucleation such as mechanical inducement through direct impact on the container of solution [237]. One outlying point can be observed in Figure 9:10 when examining the $S = 0.90$ in H_2O using a 775 mW beam power, this is due to most of the samples tested nucleating within 30 seconds of the activation of the tweezers. Indicating that the stochastic nature associated with nucleation at low volume still plays some role in the distributions reported here, and that the tweezers are influential enough to be a powerful but not total influence.

9.5.1.2 Form of Nucleation Observed

It was noticed over many tests that crystal morphology of glycine that evolved upon nucleation was one of three forms, termed here as “plate,” “needle,” and “cluster.” An example of the appearance of each of these forms evolving over 0.5 s intervals is given in Figure 9:11, with the plate form being the morphology nucleated most of the time. One point of note is that the morphological form termed “cluster” could also be described as a collection of multiple “needle” forms of crystal nucleating within the tweezers at the same time, suggesting that it is possible that multiple individual crystals can form at the same time from within the tweezer’s focus simultaneously.



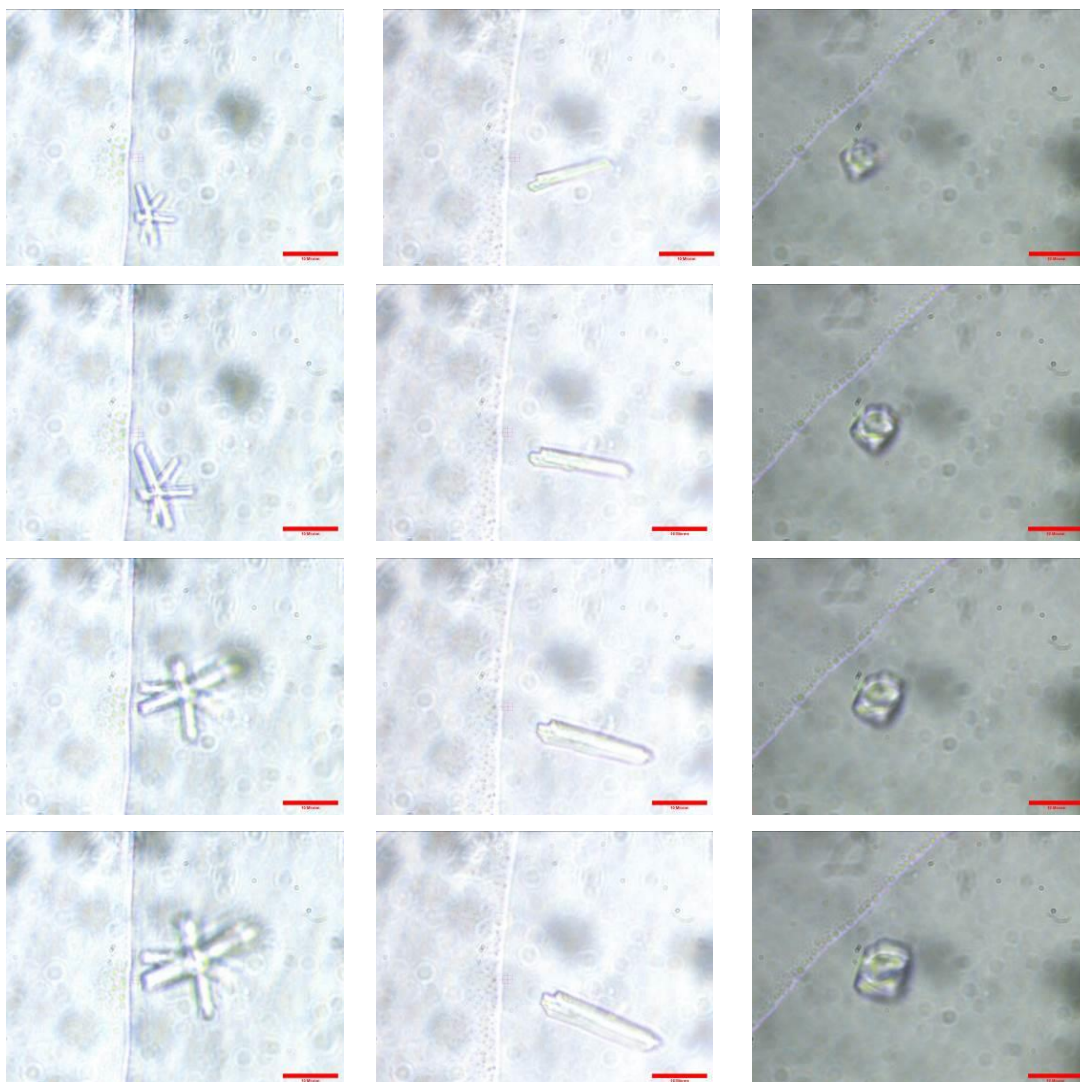


Figure 9:11: Example of Morphology of Glycine nucleating from $S = 1.5$ in D_2O when the focus of the tweezers was no more than 10 microns from the droplet edge. Cluster form (Left), Needle form (Centre) and Plate form (Right). Descending rows show 0.5 s evolution in the morphology of the crystals nucleating. Red scale bars indicate 10 microns. Red arrows indicate the location of the tweezing focus in the first image of each sequence.

On a small minority of occasions when nucleation did occur, the evolved morphological form could not be determined as the crystal produced did not remain held by the trap long enough for the morphological form to be determined by moving out of the field of view rapidly. In cases such as this, the morphological form was termed to be undetermined, but it was certain that nucleation did occur, as confirmed by the quadrant photodiode signal, which is discussed in section 9.6. In Figure 9:12 and Figure 9:13, the proportion of morphological form of nucleation or lack of it is indicated for both solvent isotopologues at both powers examined. This characterisation is used throughout the other factor examined in this chapter when categorising the form morphological form of nucleation observed when examining the nucleation of glycine. One point that must be made is that since the video only captures a 2D

perspective the morphology of the crystals which nucleate, where a needle could appear a plate crystal when viewed from the smallest projected area plane. However, it is likely that a crystal in this orientation would disrupt the profile of the edge of the droplet, and this was not observed.

When using the higher laser power of 775 mW within the range in which nucleation is observed ($S > 0.75$), the plate form appears to be the dominant morphology observed, as shown in Figure 9:12, with a minority of needles and clusters. Using a lower laser power of 650 mW did not appear to have a significant impact on the major characteristics of the nucleation morphology, where the plate form was the majority across the range of concentrations examined. One minor change observed was the introduction of a few cases where the morphological form was undetermined, as the newly formed crystal did not remain within the field of view for more than a single frame. One possible explanation is that the lower laser power does not produce a trap strong enough to hold some of the produced crystals long enough to be characterised morphologically. This is consistent with the general features of optical trapping, where higher power traps can hold particles within the focus when subject to higher forces acting upon the trapped particle.

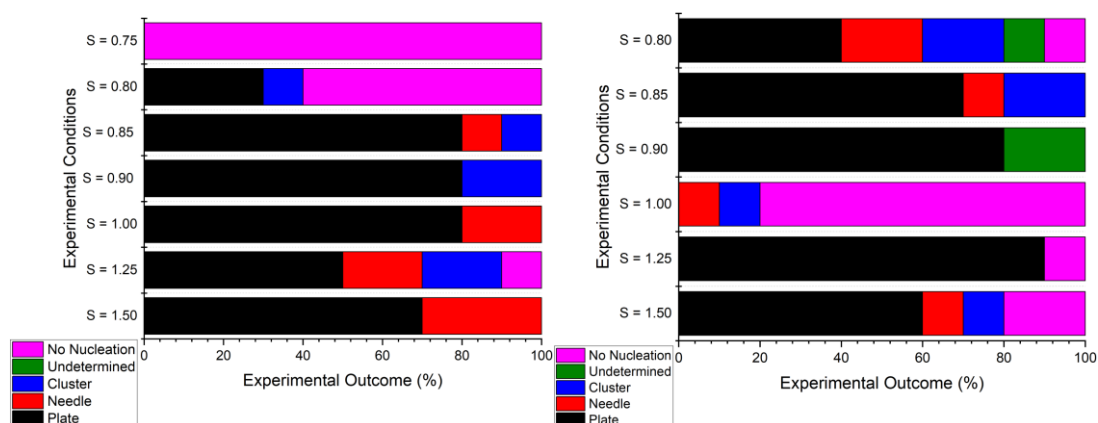


Figure 9:12: Form of crystal morphology nucleated from a range of supersaturations of glycine in H₂O when acted upon at the droplet edge using optical tweezers generated using a linearly polarised 1064 nm laser at a trapping plane power of 775 mW (left) and 650 mW (right).

Figure 9:13 shows the complementary morphological determinations when the solution used D₂O as the solvent. Similarly, to the H₂O, across the range of supersaturations tested again, the plate form was produced most, with a small proportion of the other two forms forming. One aspect that can be highlighted is that it can also be easily observed with Figure 9:13, is the decrease in the overall proportion of nucleation occurs as the supersaturation is reduced, mainly when operating at 650 mW. Furthermore, when testing $S = 1.50$ when using the lower

laser power, it was possible to have an occasion where the morphological form could not be determined, as the newly formed crystal did not remain in the field of view long enough to be identified.

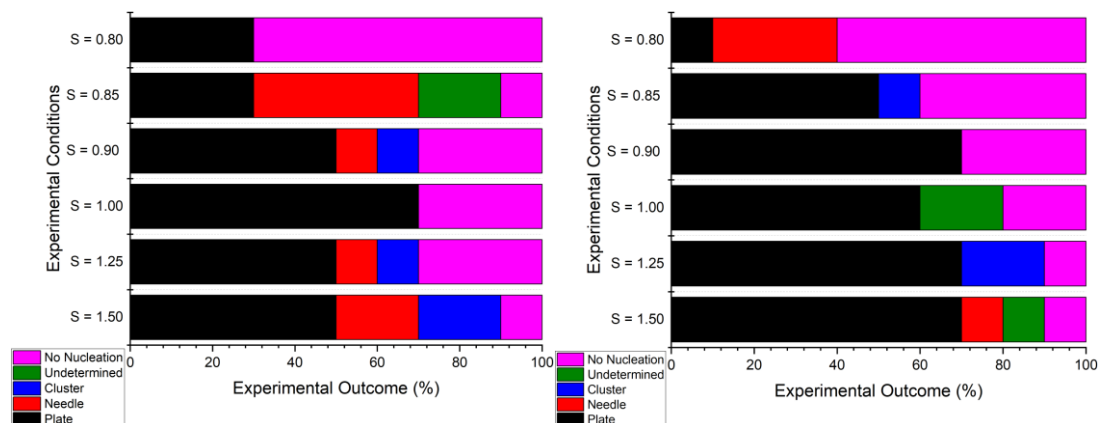


Figure 9:13: Form of crystal morphology nucleated from a range of supersaturations of glycine in D_2O when acted upon at the droplet edge using optical tweezers generated using a linearly polarised 1064 nm laser at a trapping plane power of 775 mW (left) and 650 mW (right).

9.5.2 Effect of Focus Position

One factor that others have not studied when investigating nucleation induced by optical tweezers is the effect of changing the relative position of the optical tweezing focus within the confined geometry of the solution where the crystallisation is induced.

9.5.2.1 Nucleation Time Distribution

As well as exploring a range of concentrations of the solution used in its effect on the distribution of nucleation times, the position of the focus of the optical tweezers relative to the edge of the sessile drop was also examined to determine its effects. This was first performed at a selected range of locations either at or with reference to the edge of the sessile drop used to examine the impact of nucleation, most of which involved changing the horizontal distance between the edge of the droplet and the tweezing focus while remaining at the same 'elevation' within the droplet as the droplet edge. This was first examined in $S = 1.5$ solutions of glycine in H_2O , as shown in Figure 9:14, at the same two laser powers (775 mW and 650 mW) used to examine the effect of changing the concentration in 9.5.1. In this case, all of the points examined existed on the elevation plane of the triple contact point of the air, solution, and the cover glass, except those which has the focus located at a distance of 10 microns laterally (horizontally) into the bulk from the droplet edge and 10 microns vertically up from the surface of the glass coverslip, this 10 micron change in "elevation" was altered using the z-axis micrometer which controlled the stage position the calculated

average position of the interface in these cases is detailed in Figure 9:17. Samples, where an elevation change was also employed of 10 microns up into the axial (vertical) direction, were also used. When using the higher laser power again, the effects on the supersaturation zone proximal to the droplet edge existed where there was negligible impact on the distribution of induction times. Once this range was exceeded, an impact was observed where the proportion of nucleation samples decreased, shifting the distributions to longer times. This zone within the droplet where nucleation could be triggered was approximately 15–20 microns wide which is many times larger than the diameter of, depending upon the power used to generate the trap in this case. At even greater distances, at a minimum of 50 microns, no nucleation was observed at all at 775 mW.

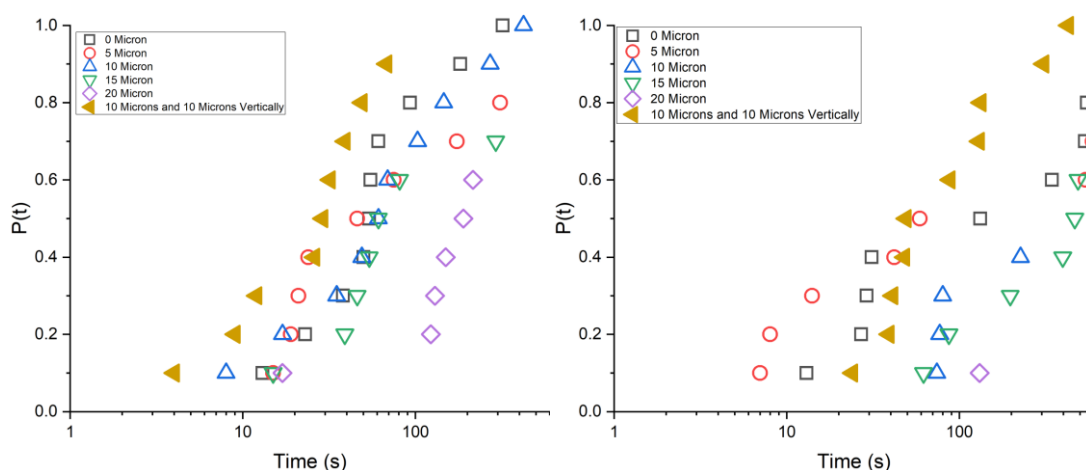


Figure 9:14: Cumulative probability distributions of the nucleation times of $S=1.5$ solutions of glycine in H_2O at selected positions within a sessile drop. Trapping beam 775 mW (left) and 650 mW (right) of linearly polarised 1064 nm. No nucleation was observed for the full 600 seconds of the experiment when focussing trap in bulk (centre of the droplet) or anywhere in the sample when trap was not operated. A total of 10 repeat experiments were performed at each position and power combination.

To ensure that the nucleation observed was indeed induced by the tweezers, a set of control experiments were performed where the edge of a sessile droplet was observed without the activation of the tweezers since, in these cases, no nucleation was observed in any case. Therefore, the nucleation observed can be attributed to the tweezers rather than spontaneous nucleation occurring in the observed location. Since this was performed using $S = 1.5$ (the highest supersaturation tested) is also reasonable that this would also be the case when using the lower supersaturations.

One point of note is the testing runs that included a change in elevation from the plane of the tri-phase intersection point in space, where there was a shift to shorter nucleation times that was observed at the droplet edge (0 Microns). This was also the case when using the

650mW laser power, especially when examining the higher values of the cumulative probability distribution. The same general trends were also observed when D₂O was used as the base solvent. Depending upon the laser power and solvent isotopologue used. It does appear that by inspection of Figure 9:15 that the zone within which nucleation can be achieved appears to be narrower when using lower laser powers and the D₂O solvent isotopologue, heavily suggesting that any potential heating induced through the use of H₂O could be a key factor. The fact that nucleation seems to be enhanced when the focus was moved away from the three-phase contact plane suggests that that it is the air-liquid interface that is key, which has also been suggested by Sugiyama et al. [150]. These observations are supported by the trends discussed in Figure 9:16.

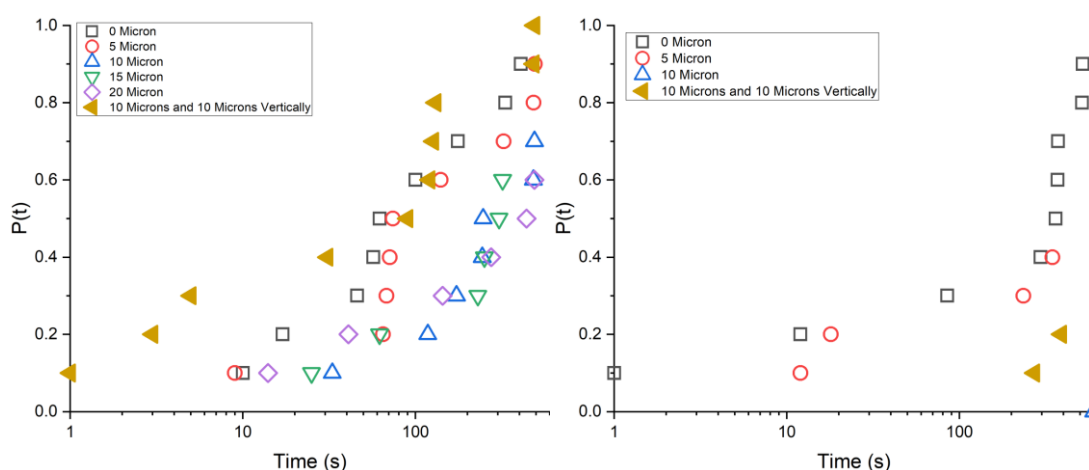


Figure 9:15: Cumulative probability distributions of the nucleation times of $S=1.5$ solutions of glycine in D_2O at selected positions within a sessile drop. Trapping beam 775 mW (left) and 650 mW (right) of linearly polarised 1064 nm. No nucleation was observed when operating in bulk or in the absence of the laser. A total of 10 repeat experiments were performed at each position and power combination.

Using the same model, given in Equation 9:4, as used when comparing the supersaturations, this allows a qualitative comparison of the various positions of the optical tweezing focus in reference to the edge of the droplet. Where in the situations examined, increasing the distance between the droplet edge and the tweezing focus decreases the determined K_1 term linearly. This inverse relationship suggests that there would be a distance from the droplet edge for a given laser power that nucleation would not be observed for a given observation period. This supports the hypothesis that at a great distance from the droplet edge, nucleation would not occur. It would seem from this analysis that any further increase in the lateral distance from the droplet edge would cross into the zone where nucleation would not occur. As well as supporting the point that the width of the zone where nucleation could potentially occur shrinks with decreasing laser power. While the switch to D₂O from

H₂O also has the same effect as reducing the laser power at the same laser power, the value of the K_1 term is reduced. The use of higher laser powers may allow the horizontal distance from the droplet edge where nucleation to be increased. However, some previous testing has indicated there is a trapping power beyond which the proportion of nucleation events observed decreases [145].

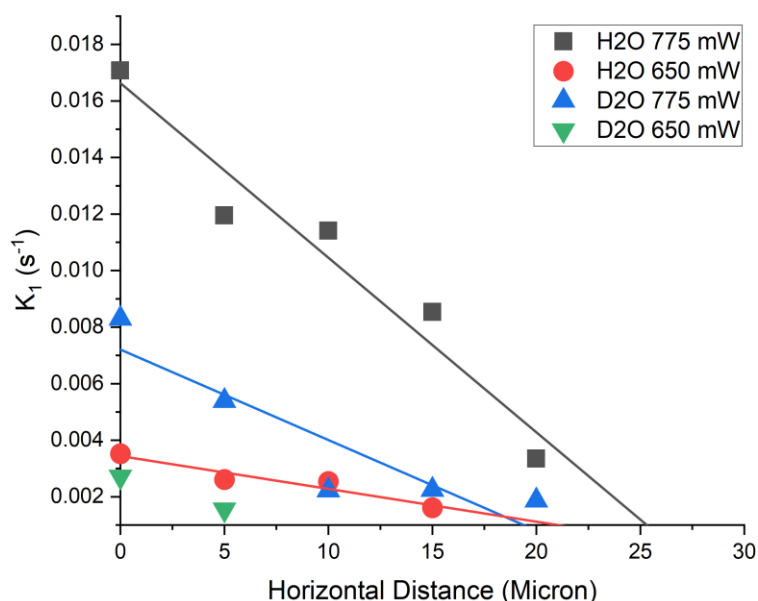


Figure 9:16: Determined values of K_1 from the fitting of Equation 9:4 to the cumulative probability distributions when examining the effect of altering the position of the optical tweezing focus with respect to the droplet edge while keeping the bulk $S = 1.5$. Points show the individual values determined at a range of positions. Lines indicate linear trendlines.

One other factor that was explored was the change in the vertical elevation of the tweezing, the values of which are shown in Table 9:6. Where shifting the elevation up from the surface of the droplet edge increases the value of the determined K_1 constant, when remaining at the same horizontal distance from the droplet edge. Since the contact angles of the solutions were measured as well, this allows the relative height between the focus of the trap and the predicted surface of the liquid to be determined when using D₂O and H₂O, as the average contact angle that these solutions make are different at the same saturation used for testing $S = 1.5$, a schematic diagram of the predicted arrangements is shown in Figure 9:17. The total volume of the rest droplet use was 20 μL and had a diameter of ~ 3 mm. Any potential difference in the axial change in the position was not accounted for when moving into the bulk of the droplet away from the edge.

Table 9:6: Determined values of the K_1 from the fitting of Equation 9:4 to the cumulative probability distributions when altering the vertical distance when the horizontal distance between the tweezing focus and the droplet edge is 10 microns when the bulk solution is $S = 1.5$.

| Solvent Isotopologue & Laser Power | K_1 (s^{-1}) | |
|------------------------------------|--------------------|------------|
| | Vertical Elevation | |
| | 0 micron | 10 microns |
| H ₂ O, 775 mW | 0.0114 | 0.0288 |
| H ₂ O 650 mW | 0.0025 | 0.0123 |
| D ₂ O, 775 mW | 0.0022 | 0.0098 |

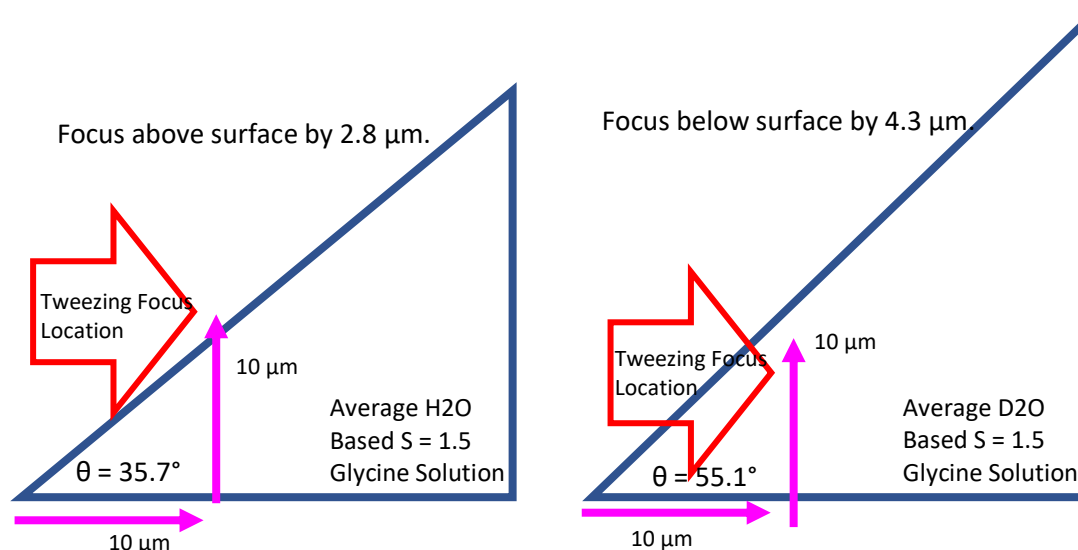


Figure 9:17: Schematic diagram of the droplet edge, showing a side view and the approximate position of the tweezing focus when the focus was moved 10 μm horizontally in from the droplet edge and 10 μm vertically up from the interface of the droplet and the cover glass. Left, H₂O-based solution where the focus would be 2.8 μm above the droplet's surface and right, D₂O-based solution where the focus would be 4.3 μm below the droplet's surface.

Figure 9:17 shows another surprising feature of the optical tweezing-induced nucleation in that not only does it appear that the focus does not have to be directly focused on the interface of the solution already shown by this section, but it can either be above it, out of the crystal suspension material, as is the case where 10 microns of vertical displacement was used in combination with 10 microns of lateral movement into the bulk of the droplet. Suggesting that the rest of the tweezing hyperboloid and not just the focal volume at the diameter of ~300 nm can induce nucleation. Also, with moving the “elevation” of the trap will alter the energy that the solution would absorb. Given the nucleation mechanism that are discussed in section 9.9, this should not be surprising. The linear approximation of the

edge of the droplet is realistic as the surface of the droplet only begins to deviate from the linear nature at 10 % of the total distance of the diameter. In the case of the ~ 3 mm diameter droplets used this would be at $300 \mu\text{m}$ which is much greater than the distances probed with the tweezers.

9.5.2.2 Form of Nucleation Observed

Again, much like the forms of nucleation morphology produced when examining the effect of altering supersaturation, the main form observed was the plate form with a small proportion of the other two defined forms, needle, and cluster. At a laser power of 775 mW of laser power of the other two forms observed, the needle form was much more common than the cluster morphology again, these graphs can also be used to highlight the reduction of the proportion of times nucleation is observed as the lateral distance between the trap, and the droplet edge is increased, this is more visible when using the lower of the two laser powers (650 mW). It should also be noted that as the power is reduced, a greater proportion of those times when nucleation does occur, it is the plate form that is produced, as shown in Figure 9:18.

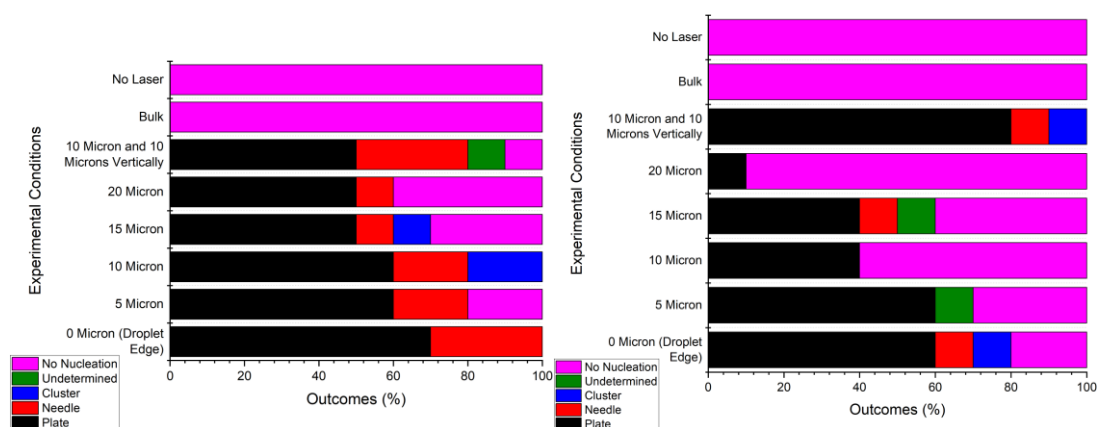


Figure 9:18: Form of crystal morphology nucleated from $S = 1.5$ glycine in H_2O at a range of positions with reference to the droplet edge when acted upon using optical tweezers generated using a linearly polarised 1064 nm laser at a trapping plane power of 775 mW (left) and 650 mW (right).

Again, like those performed using H_2O , the plate form is the most common form produced across the range of positions examined when using D_2O as the solvent, even while the lateral distance between the droplet edge and the tweezing focus is increased, as shown in Figure 9:19. Again, this highlights the effect of reducing the laser power with the marked reduction in the proportion of times nucleation is observed within the observation time, this also sees a reduction in the proportion of times where nucleation that it a form other than the plate form that is produced. However, a small number of times where indeterminate forms were

produced, as opposed to the absence of indeterminate times nucleation, was observed when the higher 775 mW of laser power was used.

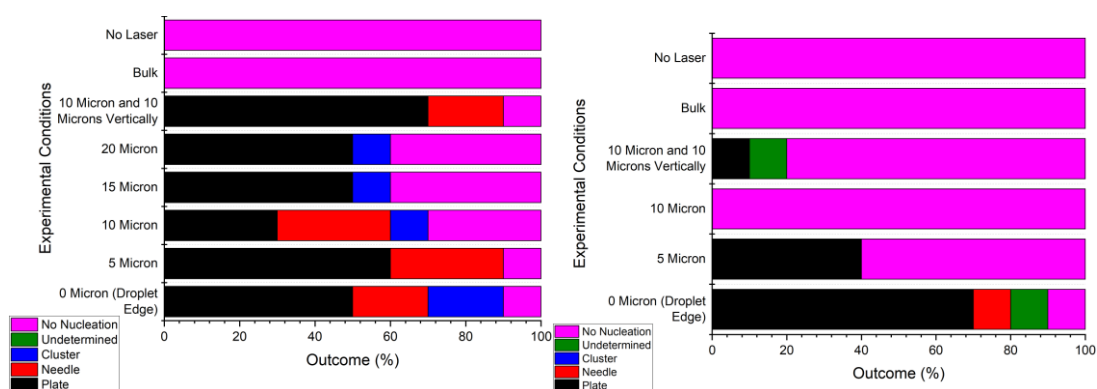


Figure 9:19: Form of crystal morphology nucleated from $S = 1.5$ glycine in D_2O at a range of positions with reference to the droplet edge when acted upon using optical tweezers generated using a linearly polarised 1064 nm laser at a trapping plane power of 775 mW (left) and 650 mW (right).

9.5.3 Effect of Light Polarisation

Laser light is commonly also defined as having a particular polarisation. This is how the electric waves align with one another in the direction of beam propagation. In all the previous experiments, this has been done with linearly polarised (LP) light vertically aligned at the source, where the peaks and troughs of the electric wave when viewed from their source from a line. However, light can have other polarisations. One possible orientation is left-handed circular polarisation (CP), where the peak of a particular electric field wave forms a helix as it travels along its beam path. The circular polarisation was produced by putting a zero-order quarter wave ($\lambda/4$) plate in the path of the laser where the fast axis of the quarter-wave plate and the polarisation axis of the trapping beam are offset 45° from each other. Power was recalibrated at the trapping plane with the additional optics in place to keep trapping power constant with the addition of the waveplate.

9.5.3.1 Nucleation Time Distributions

To see if any difference exists in the nucleation behaviour when altering the polarisation of the tweezing beam used to induce nucleation from solution. A comparison showing the nucleation time distributions comparing the same position with the droplet when probed using linearly polarised and circularly polarised light is shown in Figure 9:20. When the solutions' tested solvent was H_2O , it appeared that there was not a significant, consistent difference between the trapping beam polarisations. Some differences were observed when the solutions were made using D_2O when the focus of the tweezers was moved away from

the edge of the droplet, where the use of circularly polarised light shifts the distribution to shorter times as well as generally increasing the proportion of nucleation events observed. When the focus was located at the droplet edge (0 Micron) in a D₂O-based solution, no significant difference was observed. One point of note the orientation of the beam's linear polarisation was not controlled with reference to the edge of the droplet. Other work has controlled the relative orientation of beam polarisation when examining the growth of microscopic crystals in proximity to a tweezing focus [154].

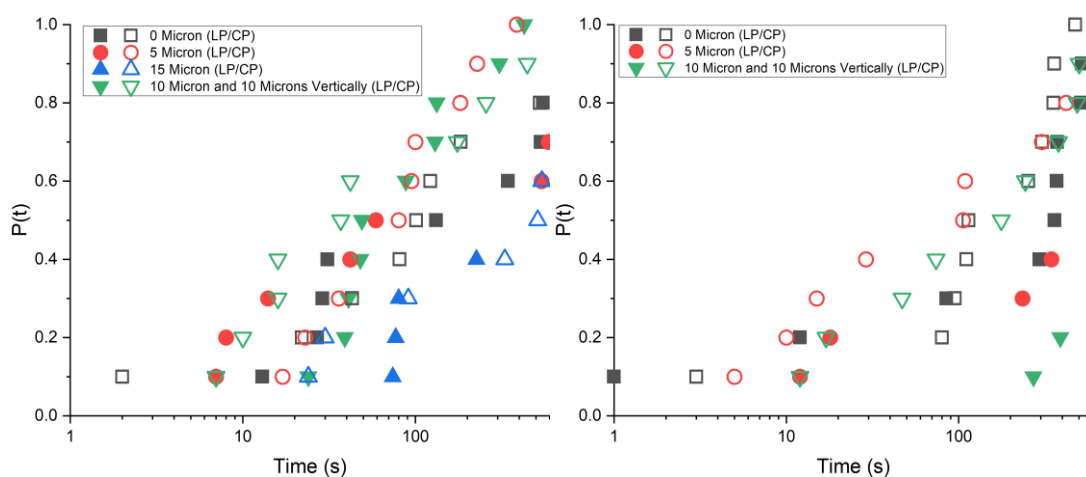


Figure 9:20: Cumulative probability distribution of nucleation of $S=1.5$ solutions of glycine in H₂O (left) and D₂O (right) in various positions with the sessile droplets. Trap generated using a power of 650 mW using linearly polarised light (Closed Symbols) and circularly polarised light (Open Symbols). A total of 10 repeat experiments were performed at each polarisation and position combination.

Since the other major factor that was examined when using linearly polarised light was the bulk solution concentration. Like those samples influenced by linearly polarised light in section 9.5.2, the bulk supersaturation was altered while positioning the tweezing focus at the droplet edge while using circularly polarised light to generate the trap, the results of which are shown in Figure 9:21.

When operating at the droplet edge differences between the nucleation behaviour only exist when the bulk $S \leq 1$. While the effect of switching the polarisation being dependent upon the solvent isotopologue. In H₂O based solutions circularly polarised light generally increased the proportion of times in which nucleation is observed and shifts the distribution to shorter nucleation times. Whereas when using D₂O appears to slightly shift this distribution to longer times. Since these shifts appear to be small and could be associated with the stochastic nature of nucleation as may not be eliminated entirely, to be completely conclusive much

larger data sets would be required, taking much extended periods to perform, due to the sequential nature in which they have to be performed.

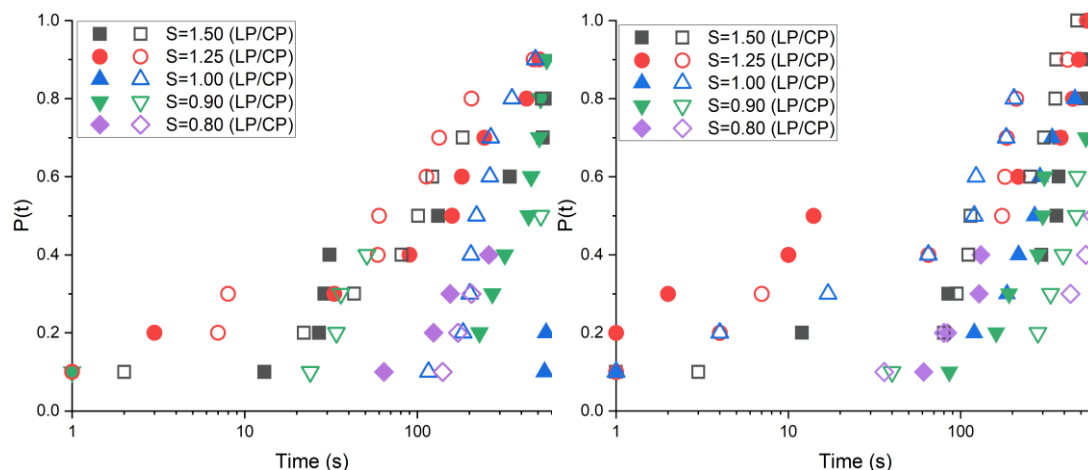


Figure 9:21: Cumulative probability distribution of nucleation of solutions of glycine in H₂O (left) and D₂O (right) based solutions examining a range of concentrations where the tweezing focus is located at the edge of the sessile droplet (tri-point interface). Trap generated using a power of 650 mW using linearly polarised light (Closed Symbols) and circularly polarised light (Open Symbols). A total of 10 repeat experiments were performed at each polarisation and supersaturation combination.

Overall, when circularly polarised light is used, the same general trends are seen when using linearly polarised light. Whereas the concentration of the solution tested was reduced, the distributions were shifted to the right, indicating that it took longer for nucleation and that fewer samples tested showed nucleation to occur within the observation period.

Again, using Equation 9:4 allows the K_1 constant to be determined from the cumulative probability distributions when using circularly polarised light when exploring the same factors of supersaturation and position relative to the droplet edge. From Figure 9:22, when examining the effect of altering the horizontal distance, it may be the case that the use of circularly polarised light (compared to linearly polarised) produces a reduction in the K_1 parameter from Equation 9:4 when operating within 5 microns of the droplet edge when the bulk supersaturation is kept at $S = 1.5$. However, once this horizontal distance is increased to 15 microns, the effect appears to disappear, as the determined value for K_1 when using either polarisation is approximately equal. When varying the supersaturation when operating at the droplet edge, saturation ($S = 1$) acts as a dividing line where different effects are observed on either side. When $S > 1$, the use of circularly polarised light results in an increase of the K_1 parameter in comparison to LP. Whereas below saturation generally, the reverse is true where using CP light results in a reduction in K_1 in comparison to LP.

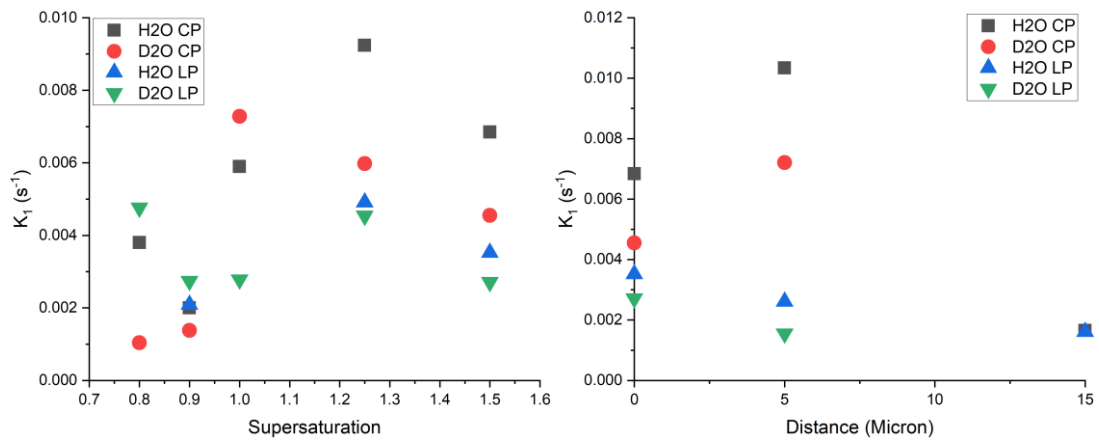


Figure 9:22: Determined values of K_1 from the fitting of Equation 9:4 to the cumulative probability distributions when examining the effect of altering the polarisation of the laser beam used to generate the tweezing focus. When altering the supersaturation when remaining the droplet edge (left) and altering the horizontal distance between the focus and the droplet edge when keeping the bulk supersaturation at 1.5 (right). Using a laser power of 650 mW. Error bars are smaller than the symbols.

9.5.3.2 Form of Nucleation Observed

Although not the primary information that is designed to be gained from Figure 9:23 moving away from the edge of the droplet and towards the bulk, reduces the proportion of times nucleation is observed.

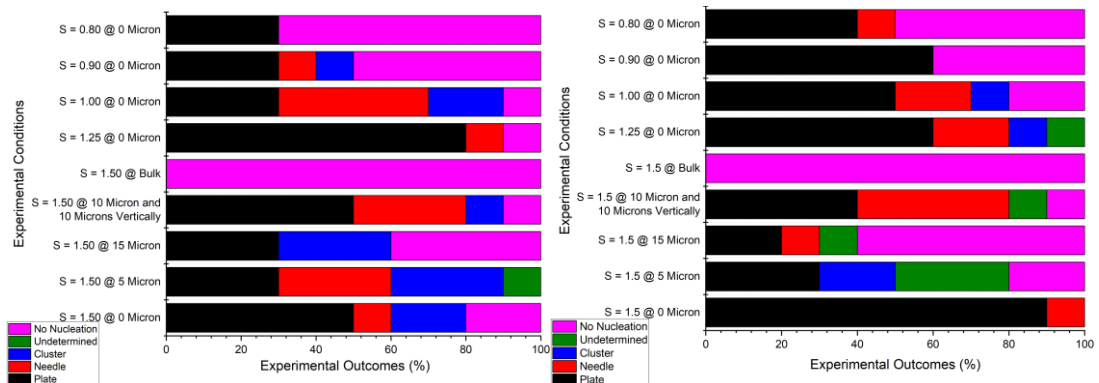


Figure 9:23: Form of crystal morphology nucleated when using a circularly polarised 1064 nm laser at a trapping plane power of 650 mW when in solutions of H_2O (left) and D_2O (right). At a range of positions relative to the edge of the droplet at an $S = 1.50$ and at other supersaturations when located at the droplet edge.

Across all of the circumstances (supersaturation and position combinations) examined, there appeared to be a decrease in the number of occasions in which the plate morphology is observed resulting in an increase number of occasions observing the needle and cluster morphology when compared to tests performed in H_2O as seen in Figure 9:24. As well as a general increase in the proportion of nucleation events that are observed when using circularly polarised light in $S = 1.50$ solutions in D_2O when away from the droplet edge, which

also showed in two of the three cases a significant increase in the proportion of non-plate morphology observed.

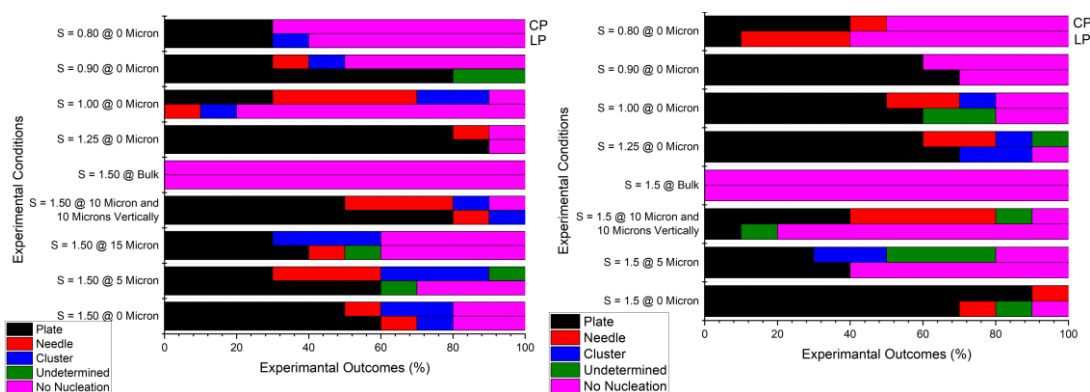


Figure 9:24: Comparison of the crystal morphology nucleated under a range of conditions varying the supersaturation when located at the droplet edge and $S = 1.5$ solution when in a solution of H_2O (left) and D_2O (right) using circularly polarised, CP, (upper bars) and linearly polarised, LP, (lower bars) of 1064 nm laser at a trapping plane power of 650 mW.

9.5.4 Effect of the Presence of Trapped Silica Particles

Since the primary use of optical tweezers is to hold particles or biological cells at the focus of the tweezers, one other factor that could be investigated was to see if the presence of any trapped particle would have an impact on the time taken for nucleation to occur and the morphology of the crystal produced when induced to nucleate by the tweezers. This is a factor that others have not previously explored. The closest others have come to performing a similar experiment was to add microparticles following nucleation [153].

9.5.4.1 Nucleation Time Distributions

From Figure 9:25, the presence of the particles in the absence of the laser does not have the effect of inducing nucleation to occur within the field of view that would surround the focus of the tweezers at the edge of the droplet, as the presence of the silica particles did not induce nucleation themselves on any occasions. Therefore, when nucleation occurred when the tweezers were active, the nucleation can be attributable to the presence of the tweezers and not the suspended particles. As the presence of the spherical particles alone are not enough to induce nucleation at the droplet edge within the field of view examined. At the closest point to the droplet edge where testing was performed (5 microns), the presence of the silica microparticle held within the ~ 300 nm diameter tweezing focus shifted the distribution to longer nucleation times in both solutions based on H_2O and D_2O . However, as the displacement between the tweezing focus and the droplet edge increased, the effect of

the particle was diminished as at 10 microns, an equal proportion of nucleation events were observed whether a silica particle was present being held by the tweezers.

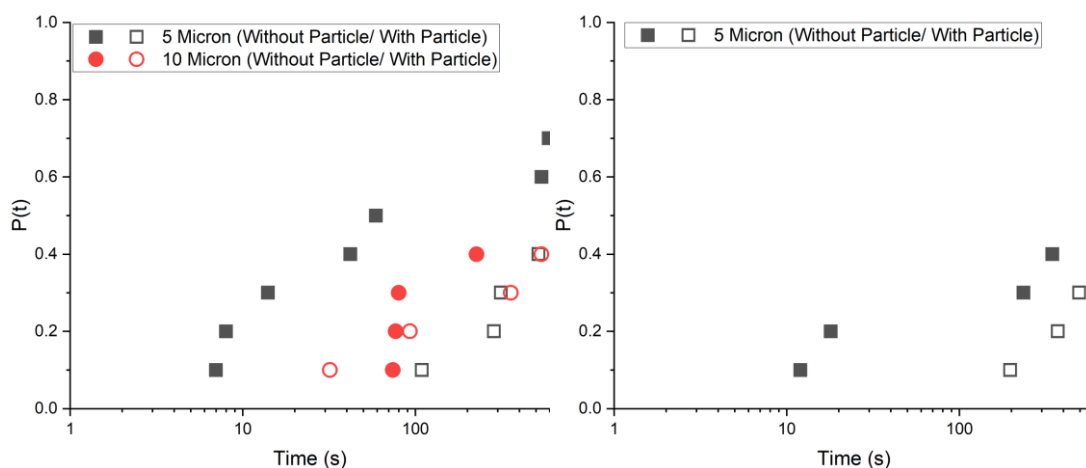


Figure 9:25: Cumulative probability distributions of nucleation times of $S = 1.5$ glycine in H_2O (left) and D_2O (right) at selected positions within a sessile drop. The trapping beam had a trapping plane laser power of 650 mW linear polarised 1064 nm laser light holding a $1.57 \mu m$ diameter silica particle (Open Symbols). Also shown are particle-free runs for comparison (Filled Symbols). No nucleation was observed when operating in bulk or in the absence of the laser. A total of 10 repeat experiments were performed at each position and particle presence combination.

Although it was initially envisaged that testing would also be conducted at the droplet edge (0 Microns), this was attempted; however, in the attempt, it was not possible to trap and manoeuvre it to the edge of the liquid droplet while keeping the particle trapped. Therefore, this comparison could not be made. Again, like the rest of the factors examined, Equation 9:4 is a quantitative comparison of when the trap was holding a particle and not. In the cases of both solvent isotopologues, the presence of a single trapped silica particle within the focus results in a sharp reduction in the determined K_1 value, at both distances from the droplet edge, examined as seen in Figure 9:26. No experiments were possible with polystyrene

particles as when tested with glycine solutions in H₂O and D₂O it was not possible to stably trap a polystyrene particle.

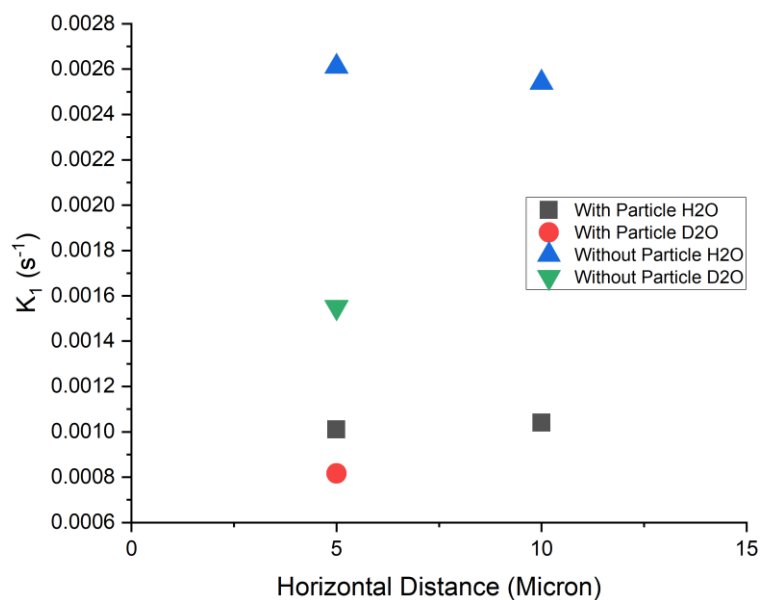


Figure 9:26: Determined values of K_1 from the fitting of Equation 9:4 to the cumulative probability distributions when examining the effect of the presence of a 1.57 μm diameter silica sphere using a 650 mW trapping beam. Performed in $S = 1.5$ solutions of glycine in H₂O and D₂O.

9.5.4.2 Form of Nucleation Observed

The form of nucleation morphology was observed when the tweezing focus held a 1.57 μm diameter silica (Duke Scientific), shown in Figure 9:23. Once again, it highlights that no nucleation happened without the laser and holding a silica particle in the bulk of the droplet of the solution. When nucleation occurred, the morphology was dependent upon the isotopologue of the solvent. When using H₂O, the non-plate forms were the dominant form of nucleation morphology when nucleation occurred. When D₂O was used as the solvent, the plate form was the only morphological form produced when nucleation occurred.

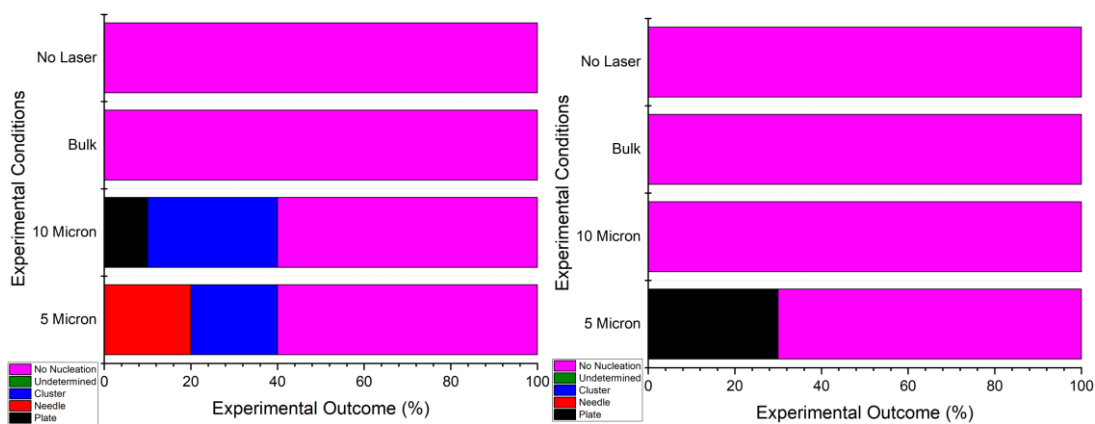


Figure 9:27: Form of crystal nucleation morphology when $S = 1.5$ of glycine in H_2O (left) and D_2O (right) at various positions with the sessile drop with reference to the edge of the sessile drop tested. The trapping beam held a $1.57 \mu m$ diameter silica spherical particle, trapping laser used linearly polarised 1064 nm with a trapping plane power of 650 mW.

The direct comparison of the morphology of the nucleation with and without the particles being held by the tweezing focus is shown in Figure 9:28. Comparing the effect of the presence of the particle in H_2O -based solutions, the morphology is altered from the presence of the silica particle as in most of the cases where nucleation occurred it was the cluster and needle form that was produced. In contrast, in the absence of the particle, the plate form nucleated from solution, which occurred at both the distances from the droplet edge tested where nucleation occurred. However, when D_2O was used, no morphology change was observed when nucleation occurred.

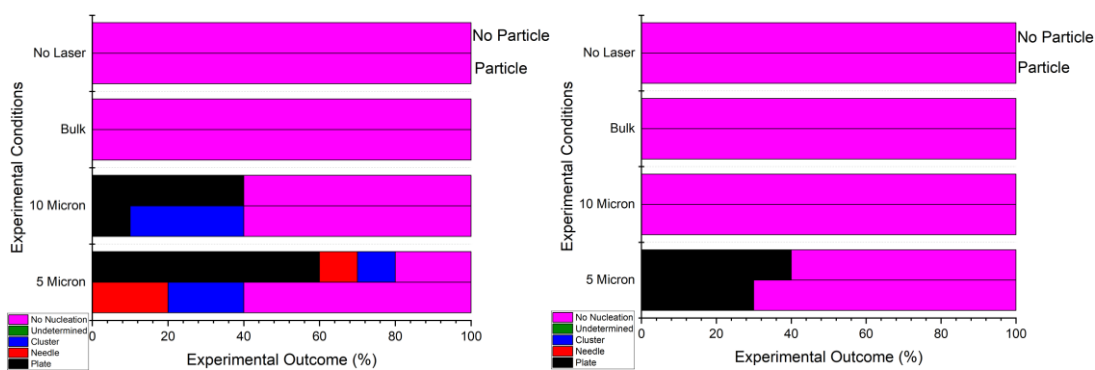


Figure 9:28: Comparison of crystal nucleation morphology of the crystal of glycine formed from an $S = 1.5$ solution in H_2O (left) and D_2O (right). The trapping beam used a linearly polarised 1064 nm laser with a trapping plane power of 650 mW. $1.57 \mu m$ diameter silica spheres were held in the tweezers (Lower Bars) and silica particle free tweezers (Upper Bars).

9.6 Quadrant Photodiode Results

The use of the silicon isolator and cover glass setup has the additional benefit of allowing the forward scattering from the trapping beam to be measured using a four-quadrant photodiode (QPD). Alternative setups may have limited this, as using a bottle with a lid/cap would block the beam path [152]. The QPD was set to monitor the sum voltage rather than the difference between section pairs. It was noticed that upon the nucleation of a crystal, the sum voltage measured fell. A range of examples of the recorded sum QPD voltage recorded at the point when nucleation occurred is in Figure 9:29.

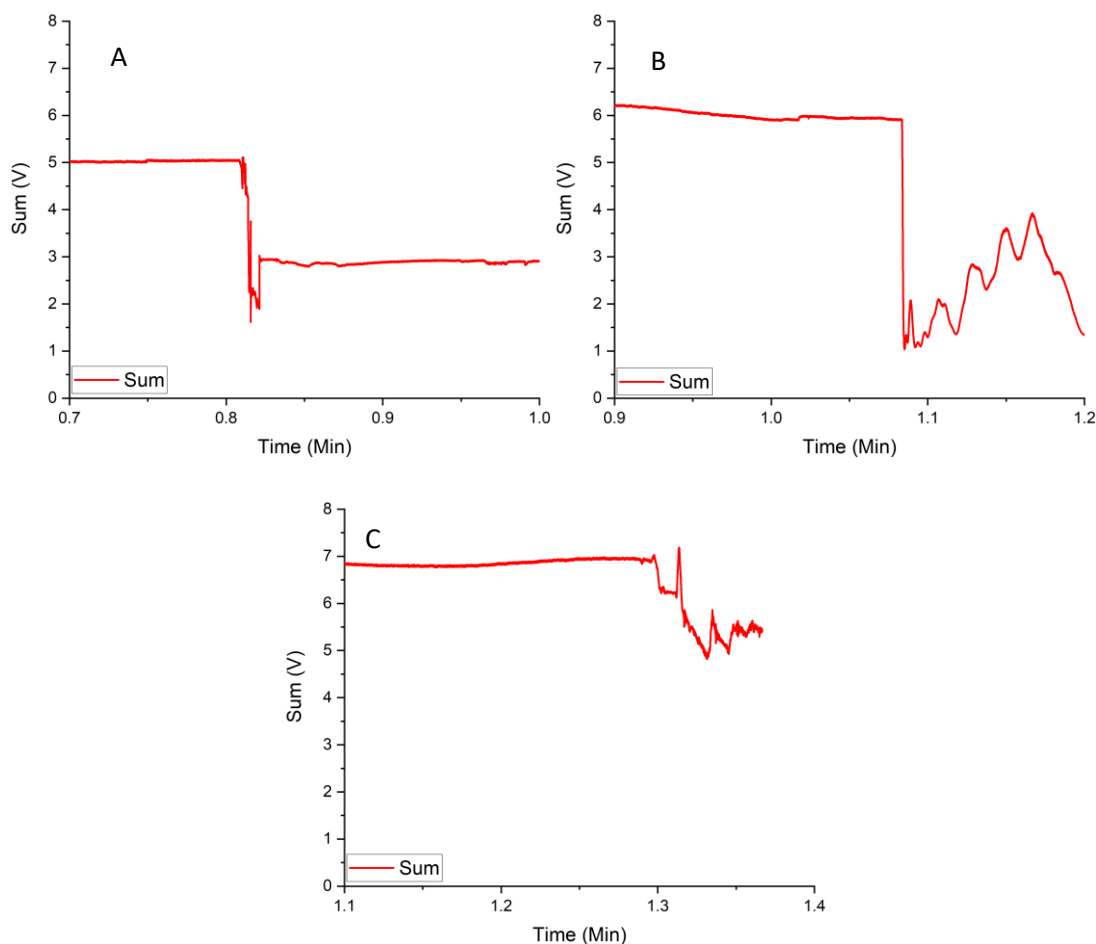


Figure 9:29: QPD sum voltage extract produced when nucleation was observed using $S = 1.50$ glycine in H_2O (A & B) and D_2O (C) when using a trapping plane power of 775 mW when the focus was located at the droplet edge (0 Micron). A, B and C are the QPD sum voltages for different experiments.

This was observed in the wide range of scenarios tested in the absence of any silica particle (position, concentration, polarisation etc.), with the same sudden fall in sum QPD voltage being observed. This could act as secondary confirmation that nucleation did occur and cross-check that nucleation time was observed. This sudden fall in sum QPD voltage is similar to

what would be expected if a trace were to be recorded where a single spherical particle would enter the trap. This would be similar to the reasoning proposed by *Liao et al.* where an amorphous particle of the solute would first have to enter the trap focus to allow nucleation to occur [108]. Although the QPD traces in this instance were used as corroboration for the visual assessment it may be possible that these signals in future could provide a more direct way of determining the onset of nucleation. This was not possible in this thesis, as all of the aspects involved in probing the test liquid had to be performed manually, e.g., activating the laser and beginning the two forms of recording performed, video and QPD signal.

9.7 Sodium Chloride Solutions

Since it was possible to investigate several factors using glycine, it was decided to see if these same trends could be observed using another solute material. Since the growth of NaCl in proximity to optical tweezing focuses has already been examined, here it would be prudent to examine nucleation in NaCl as well, using a higher power laser than was used to investigate the effect on growth rates.

Like the investigation performed using the solute glycine, the effect of H₂O and D₂O was examined to determine if any difference existed and to quantify the difference between the two isotopologues.

Previous testing involving a similar salt (KCl) shown that significant differences in the time taken for nucleation to occur in equivalent solutions when comparing the different light polarisations tested [148], where the time required to observe nucleation was significantly reduced when using circularly polarised light in comparison to linearly polarised. Therefore, the conditions where nucleation was most likely to be observed was tested at the location of the droplet edge and in bulk to examine the comparison at a supersaturation $S = 1.01$ in both H₂O and D₂O. None of the 40 occasions for each solvent isotopologue where nucleation could have occurred when acted upon by the tweezers in each solvent did it occur. In essence, no nucleation was observed using the tweezers under any of the conditions examined. Since the testing with the glycine indicated that the droplet edge is where nucleation is most likely to occur, this is the location that was tested the most, with the bulk also being tested to ensure that there is no reversal of findings when using the NaCl in comparison to the glycine.

Unlike previous testing with KCl [148], circularly polarised light did not make any impact at all, as in both solvent isotopologue cases, no nucleation was observed in either case. Ideally,

it would have been prudent to test these conditions again using a higher supersaturation to see if tweezing-induced nucleation is possible when using NaCl. However, this is not possible to perform on this setup as testing performed when examining the impact that tweezers can have on crystal growth rates has shown that the transfer, via pipette on the glass coverslip, of the solution alone is enough to induce nucleation within the sessile droplet. While reducing the concentration of the solution used in testing would have the undesirable effect of making the observation of crystal formed by the presence of the tweezers harder to perform. The last factor that could be changed was the laser power. However desirable that would be, this is not possible to increase as these experiments were conducted at the highest laser power possible. In effect, if nucleation were going to happen at this concentration, it would have occurred using the conditions used here for this examination. Therefore, it is reasonable to conclude that it is not possible under these circumstances. Other setups in future may prove to be more fruitful in examining NaCl. It could be possible that the laser power required for the controlled nucleation of NaCl from aqueous solution is higher than the powers that could be used in this section.

9.8 Sodium Bromate Solutions

Nucleation using optical tweezers has been found to influence multiple aspects of the form crystals can take by controlling the polymorph, pseudo-polymorph, and morphology of the crystal grain formed [145], [147], [148]. However, one aspect that has not been investigated is enantiomorph since this can be of critical importance in many industrial, especially pharmaceutical processes, as demonstrated in the case of thalidomide [239]. The use of sodium bromate is a substance that allows this hypothesis to be tested as sodium bromate is achiral in solution and chiral in the solid crystalline form [160]. Each of the crystalline sodium bromate's two mirror chiral forms can be distinguished using linearly polarised light. Recent work suggests that there is some preference for different chiral forms of crystals depending on the handedness of the circularly polarised light used to act upon crystals following nucleation [240].

With experiments being performed at 20 °C, the solubility of NaBrO₃ has been previously determined to be 0.3664 g/g, while no such equivalent exists for D₂O at 20 °C [29]. Measurements comparing the solubility of sodium bromate have been performed at a lower temperature (5 °C), where an 11.9 % reduction in solubility was observed on a molar basis [241]; this was assumed to be the case for solutions at 20 °C; therefore, the solubility was

assumed to be 0.2904 g/g of NaBrO₃ in D₂O. To ensure the greatest likelihood of the observing nucleation occurring initial experiments involving the sodium bromate tests were performed at the edge of sessile droplets, as suggested by the work performed in glycine in section 9.5.

Previous work has measured induction times of supersaturated solutions of NaBrO₃ in agitated conditions at $S = 1.1$ and $S = 1.2$ at approximately equal temperatures to the work performed here [215]. This supersaturation was to be used as a starting point for where nucleation under the influence of optical tweezing would be investigated, $S = 1.4$ and 1.3 were chosen to allow a comparison to non-tweezed situations to form a comparison. However, when these were tested, the $S = 1.3$ samples were tested first. None of the 10 samples using either linearly polarised or left-handed circularly polarised light showed nucleation to occur within the 10-minute observation period.

Therefore, $S = 1.4$ ones were also run; however, the same lack of nucleation was observed in any of the 10 times using either polarisation (linear or left-handed circular) in either H₂O or D₂O.

A third set of runs at $S = 1.4$ were performed in the bulk of the solution to check if there was any difference in the conditions required for nucleation to occur than in the previous systems tested. These again did not show any nucleation occurring under the influence of the tweezers with any of the four individual combinations of solvent isotopologue and laser polarisation.

Although chiral form determination would have been possible when using NaBrO₃ since it was not possible to form any using the tweezers, here does not indicate that it is not more generally possible; nucleation induced by optical tweezers of sodium bromate may indeed be possible if longer irradiation times were used or if higher trapping powers could be utilised through a more powerful laser. Should further investigations occur, sodium bromate would be a suitable candidate for such investigations. As specific enantiomorphs could be determined by linearly polarised observation light in situ without requiring any other offline examination. Other experimental reports have shown that using sodium chlorate when acted upon by optical tweezers can produce situations where an enantiomeric excess can be produced [240], [242].

9.9 Discussion of Evidence about Nucleation Mechanism Models

From the range of work that has been performed previously by others, several hypotheses exist to explain the mechanism by which optical tweezers can induce nucleation from solution [108], [129], [138].

Recent work has been performed where it was observed by *Liao and Wynne* [108], where nucleation from solution using the optical tweezers was only observed following the entry of an amorphous particle into the focus of the tweezers which then transforms into a crystalline structure following its entry to the focus, which was determined through in-situ Raman spectroscopy monitoring the focus of the tweezers which observed changes in line with the visual observations as it was proposed that the tweezers are able to rearrange the amorphous structure into a crystalline one. This is, at minimum, similar to several observations made in the nucleation experiments performed here, where immediately prior to the appearance of the crystal, an identifiable particle can be observed approaching and then entering the location of the tweezing focus. Although it appears to be similar phenomenologically, any possible transformation in the material's structure in the focus cannot be determined as in-line spectroscopy was not employed in the tweezing setup. Adding this functionality would greatly expand the capabilities of the tweezers that were used here for future experiments, therefore, this is based purely on the visual qualitative observations made. These observations of small particles seen entering the focal point of the tweezers were made across the range where glycine nucleating from solution was investigated, see section 9.5.

One other major hypothesis that has been used to explain the ability of tweezing in nucleating is the ability of the optical tweezers to attract and hold molecular clusters leading to a localised increase in concentration above that of the bulk [150]. However, this is still subject to some debate as it has been stated that the clusters would be subject to thermal forces that would prevent their trapping [130], but it has been demonstrated that trapping single molecules is possible [131], [132]. In the cases of the systems examined here, the one that was able to be nucleated using optical tweezers has been demonstrated to produce mesoscale molecular clusters when in aqueous solution, as shown by DLS [18], and any potential clusters of NaCl, that would have been present in experiments in section 9.7 are orders of magnitude smaller [243], [244]. At first, this would seem to support the hypothesis that optical tweezers act upon present molecular clusters. However, this could not explain

how potassium chloride has been able to be nucleated from solution, where it would be reasonable to conclude that any clusters present would be on the same order of magnitude as the sodium chloride and not on the scale of the glycine mesoclusters. Therefore, based on this evidence, it could not be concluded that the solute clusters are key.

Another major factor used is the refractive indices of components that are important in the ability of optical tweezers to induce phase separation. It has been demonstrated previously and conclusively here that it is possible to nucleate glycine from aqueous solution. The refractive index of glycine, which was observed nucleating from solution in section 9.5, has been measured to be approximately 2.6 at 1064 nm [245]. Whereas the at this wavelength, the refractive index of NaCl is 1.53 [246]. If this information were viewed in isolation, it would be tempting to ascribe the nucleation behaviour to the refractive index. However, when viewed in a broader context, it has been shown possible to induce nucleation of KCl from aqueous solution [148], which has a refractive index of 1.48 at 1064 nm [246]. Therefore, this suggests that it is not the refractive index which plays a critical role as if it were possible to nucleate the KCl from solution with an even lower refractive index than the NaCl, then it would be possible to nucleate the NaCl if it were the refractive index which plays the critical role in the optical tweezing induced nucleation.

Unlike some other observations where nucleation occurred only following the deactivation of the tweezers since the diffusion of heat is orders of magnitude higher than the diffusion of mass [135], nucleation was able to occur while the tweezers were still active. Furthermore, it has been possible to demonstrate that the tweezing focus does not need to be located at the air-solution interface to induce nucleation, see section 9.5.2. However, it has also been posited that the action of the tweezers would be able to act universally by influencing the free energy that would be experienced in the path of the laser. This acts by requiring that an additional term be added to account for the “stored electromagnetic energy” on the free energy which would result in a reduction through the addition of $-n^2 I_0$ where n is the refractive index of the material in the focus and I_0 is the laser intensity. This would therefore result in a reduction in the critical size from which nucleation is involved as within the path of the beam smaller clusters would be stable, this would go a part of the way to suggest why nucleation is possible in situations that are in the bulk undersaturated. As smaller clusters are present in solution (at least in the case of aqueous glycine [18]) than would be present in solutions where nucleation would not be required to be induced through non-traditional

means. This is similar to change in free energy proposed when solutions are acted upon by nanosecond length pulses [247].

Overall, there were some similarities between the results produced here and the range of results previously produced where it has been possible to induce nucleation from a range of solutions, especially those conducted by *Sugiyama et al.* [129]. Moreover, *Liao and Wynne* made observations where there were several occasions where ‘particles’ were seen entering the focus of the tweezers shortly before nucleation [108]. Therefore, when already espoused hypotheses are examined considering the results previously published and with the results detailed herein, it is difficult to discriminate between them to decide which is critical in the inducement of nucleation from solution.

9.10 Growth Rate of Crystals that Nucleated from Solution using Optical Tweezers

In addition to determining the distribution of nucleation times from crystals that nucleated from solution when acted upon by the optical tweezers, the rate at which these crystals grow can be determined. This was measured using the same videos used to determine the nucleation times. This also captures the development of the crystal following nucleation, where the linear rate of the change in the area occupied by the newly nucleated crystal was taken as the growth rate of the crystal.

Numerous methods exist which could be used to determine this growth rate; however, some methods would be impractical to implement across the large data set produced. Therefore, it was decided that an efficient way to determine the area growth rates would be to utilise a machine learning model² (Detectron2 [248]) to one detect the presence of a crystal in the video and then, to determine the area that it occupies in each frame of the video to allow the how this area changes with time to be determined. Growth rates have been reported from previous experiments where optical tweezers have induced nucleation from solution; however, the methods used to determine the growth do not appear to have been specified [152], [153].

In the first instance, the videos were processed by an already existing machine learning model to see if this would work without having to train said model. In the first instance of

² This model was developed by others [252], [253], however the additional training was performed by Dr Christopher Boyle and myself.

the use of this model resulted in only ~10 % of videos which had nucleations during their runtime being recognised. The main issue observed when analysing the results from the processing of the videos by the model was that the model recognised either the whole section of the frame, see Figure 9:6 for an example, which contained either the surrounding air or the solution itself and not recognising the crystal, which appeared in the. Therefore, it was decided to see if any progress at all could be made to determine the growth rate of the crystals which were induced to nucleate using the optical tweezers, then model training would have to be performed.

9.10.1 Model Training

The machine learning model's training was performed to give the machine learning model definitive examples of what a crystal within the image was and how this developed over time as this grew suspended in the surrounding solutions. This was done in the environment using two sub-sets of the videos recorded where nucleation was induced to occur from $S = 1.5$ solutions in H_2O and D_2O using a 775 mW beam located at the edge of the droplet.

This involved manually outlining the crystal present within the video manually over approximately 1500 individual frames from the points in the videos captured where nucleation occurred to show the model examples of crystals in order that it be able to recognise crystals in videos that were not part of the training set and determine their growth rates, by fitting a linear trendline to the cross-sectional area of the crystal with respect to time as determined by the frame rate, in the first increase in growth experienced. Before being used the rates determined by the model were checked against manual calculations performed on the training set.

9.10.2 Determined Growth Rates

Once the model had been trained, this was then used across the entire range of videos that were produced in the nucleation study. Although the proportions of occasions where the model was able to recognise the presence of a crystal and monitor the development of its growth over time, it was unable to perform this universally, and there were many occasions where this could not be recognised. When being acted upon by the 775 mW laser at the edge of the droplet in H_2O -based solutions, the determined growth rates are shown in Figure 9:30.

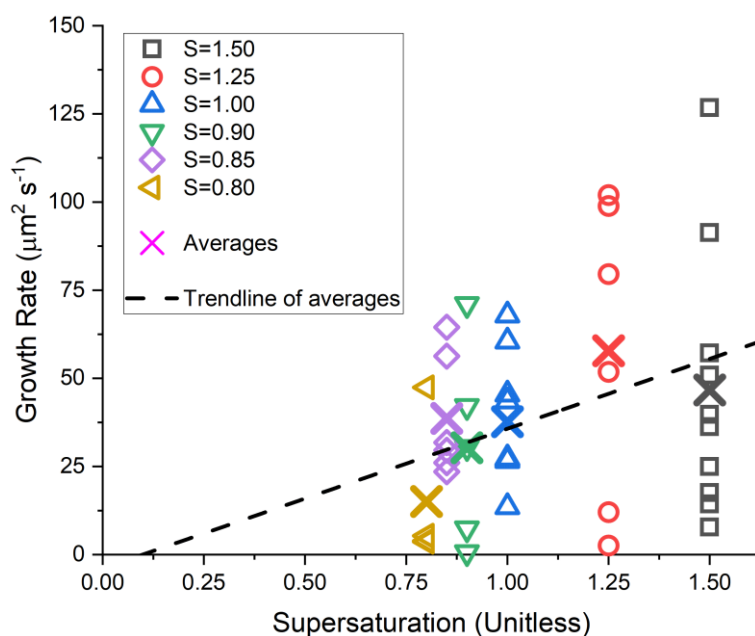


Figure 9:30: Determined growth rates (Open Points) of crystals formed from glycine solutions in H_2O between the supersaturations of 1.5 and 0.85. When the tweezing focus was located at the droplet edge when using a laser power of 775 mW. Crosses indicate averages at each supersaturation. Dashed line indicates linear fitting of average growth rate values at each supersaturation.

Where the reduction in the supersaturation of the solution evaluated shows a reduction in the average measured growth rate of the crystals once they had nucleated from solution. If this trend was to be followed linearly to a value of a zero-growth rate at a $S \approx 0.10$.

Once the lower laser power runs were examined (650 mW) in Figure 9:31 showed a change in the growth rates measured in the same supersaturations with the same isotopologue. This crosses the zero-growth line at much higher supersaturation that was measured using the higher laser power. The implication is that as the laser power is reduced, the range of supersaturations over which growth can be affected by the tweezers is reduced.

One thing of note across the samples where growth was examined was that the individual growth rates did not congregate around a specific supersaturation specific value but were spread over a broad range, this could suggest that the growth rate of the crystal imaged is susceptible to the local conditions and much larger samples of growth rates may be required to be definitive. However, growth rates, especially when measured via large dispersions, can result in dispersions (for different sizes of crystals growing at different rates and possibly the crystals of the same size growing at different speeds) in the measured growth rates [249] and as has also been measured here in section 6.4. One possible explanation is that since all other measurements have been performed at the “top of droplets” rather than at the edge that

this change in location of the tweezing focus is enough to cause this large dispersion of growth rates.

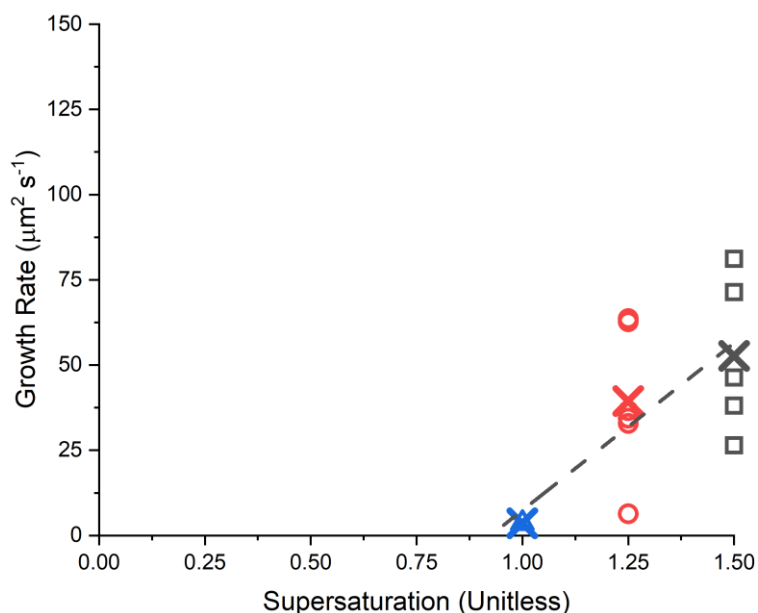


Figure 9:31: Determined growth rates of crystals formed from glycine solutions in H_2O between the supersaturations of 1.5 and 1.00. When the tweezing focus was located at the droplet edge when using a laser power of 650 mW.

Since experiments were also performed in D_2O , which also induced to nucleate by the optical tweezers, these were also examined to determine the growth rates from the deuterated solvent version, as shown in Figure 9:32. Where for most of the rates determined that as the supersaturation was decreased from $S = 1.5$ the growth rates decreased slowly at first but once $S < 1$ it appeared that in most cases that the growth rate fell sharply. However, it should be noted that when examining solutions at $S = 0.85$ there were two occasions where exceedingly high area growth rates were determined. These were checked manually and found to be accurate representations of the image of the crystal formed by the action of the tweezers. However, it is not unprecedented that there can be two separate growth behaviours when examining growth under approximately equal “tweezing conditions” [158].

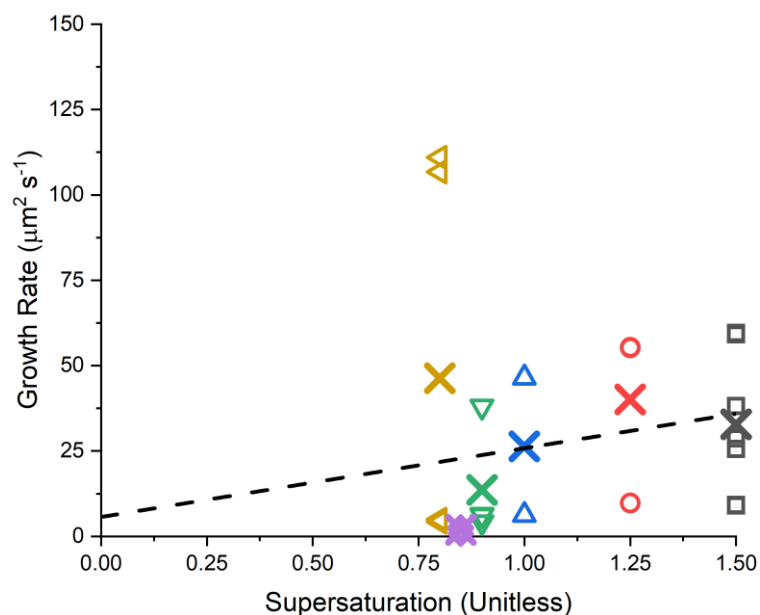


Figure 9:32: Determined growth rates of crystals formed from glycine solutions in D_2O between the supersaturations of 1.50 and 0.85. When the tweezing focus was located at the droplet edge when using a laser power of 775 mW.

Some previous measurements have been performed measuring the area growth rate of crystals which have been induced to nucleate from solution in aqueous solutions of L-phenylalanine, which showed a linear trend in the change of the area of the growing crystal (implying a constant growth rate of area) which has also been shown to be the case when examined in this work [153]. As well as this, later testing elsewhere showed that a proportional relationship existed with the growth rate measured and the laser power and solution supersaturation used, which was also found to be the case here [152]. It does appear from selected sources that have indicated measured optical tweezing-induced crystals' growth rates do not appear to specify the method by which growth rates were measured. However, it was assumed here that this was performed manually due to the large intervals between the frames analysed to determine the area covered by the crystal to determine the trendline for the growth rate [152], [153]. Whereas here, the machine learning model allows every frame of the video to be analysed to determine the area occupied by the crystal to determine the growth rate of the crystal more frequently to assign a greater degree of certainty to the growth rates determined here than elsewhere.

9.10.3 Machine Learning Issues

Although the use of the machine learning model did allow for the automation of the measurement of the growth rates of the crystals formed by being induced to nucleate from solution by tweezing action, this was by no means perfect and should be viewed within the appropriate context where, although this model could deal with the three morphological forms of crystal that could be positively identified, some issues were present. The first and most obvious is that it could not recognise the crystal formation on all occasions. This was especially true as the focus of the tweezers was moved away from the droplet edge. One plausible reason for this was the training subset of the data used, which did not feature any samples with the tweezing focus located away (i.e., anything other than 0-micron samples). This would require the machine learning model to receive additional training images signifying the crystals formed when the tweezing focus was located away from the droplet edge. This would also require that the videos be rerun through the model's processing, which is heavily computationally time intensive. The additional training would be immensely time-consuming and would have no guarantee of success in recognising crystals when the tweezing focus was located away from the droplet edge. The errors associated with the calculated growth rates when using the machine learning models would be less than those determined from the data in chapter 8 as a much greater number of frames could be analysed, a random sample was also checked manually to determine the accuracy of this model and the comparison found the rates determined by the machine learning model to be accurate.

9.10.4 Comparison to Existing Growth Rates of Glycine Crystals

To see how much impact the tweezers can have on the growth of microscopic crystals induced to nucleate using the tweezers however, this requires that the growth rates determined in 9.10.2 be processed to ensure they are “monitoring” the same property. Many previous measurements here have measured the change in one dimension, while the measurements made using the machine learning model have shown the product of the change in two dimensions. To allow a direct comparison, the square root of the change in area (as the vast majority of the samples produced square shaped plate crystals) will be compared to the range of previous measurements of the growth rate of glycine from solution, some of which were performed in chapter 6, as well as a selection of rates previously published [219], [220]. Ideally, comparing the results here with previous reports of tweezing induced nucleation, however this has not been reported for glycine and only currently exist for L-phenylalanine [151]–[153].

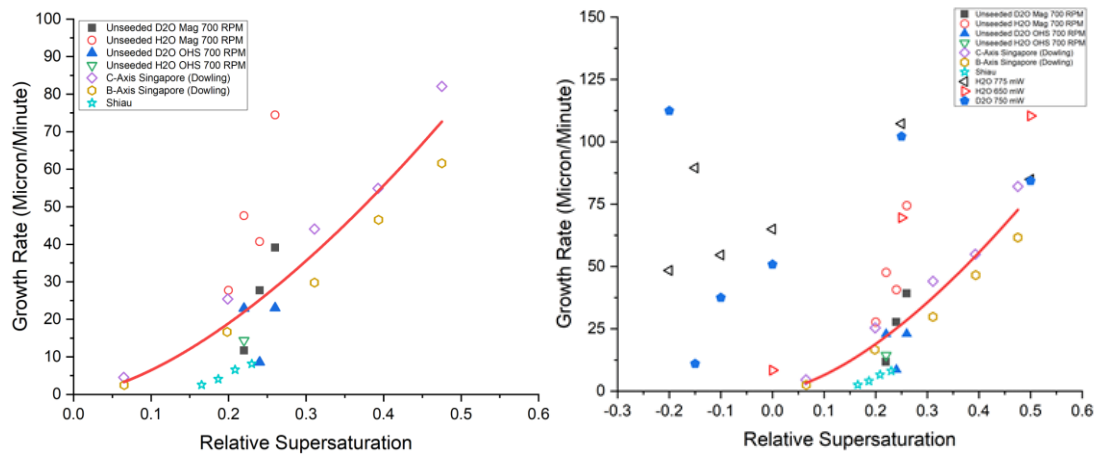


Figure 9:34: Correlation of the growth rate of glycine crystals at a range of relative supersaturations ($\sigma, S - 1$). Power law fitting is applied to all data shown. Repeat and further analysis of Figure 6:27. Left: showing previous data only. Right: Previously shown data alongside average growth rates induced by the action of the tweezing focus.

The growth of these crystals presents an opportunity to estimate the supersaturation that the optical tweezing focus is created by monitoring the growth rates of the crystals produced and using this growth rate to determine the supersaturation that would be present in the solution to cause this growth rate. Firstly, a power law correlation (as suggested by previous Equation 2:18 [75]) was fitted to a range of growth rate measurements earlier in section 6.4.1 and from literature sources, shown in Figure 9:34. Using this correlation in each individual case where the processed growth rates linear growth rates were able to be determined allowed a supersaturation that would allow that growth rate to be calculated, as shown in Figure 9:35

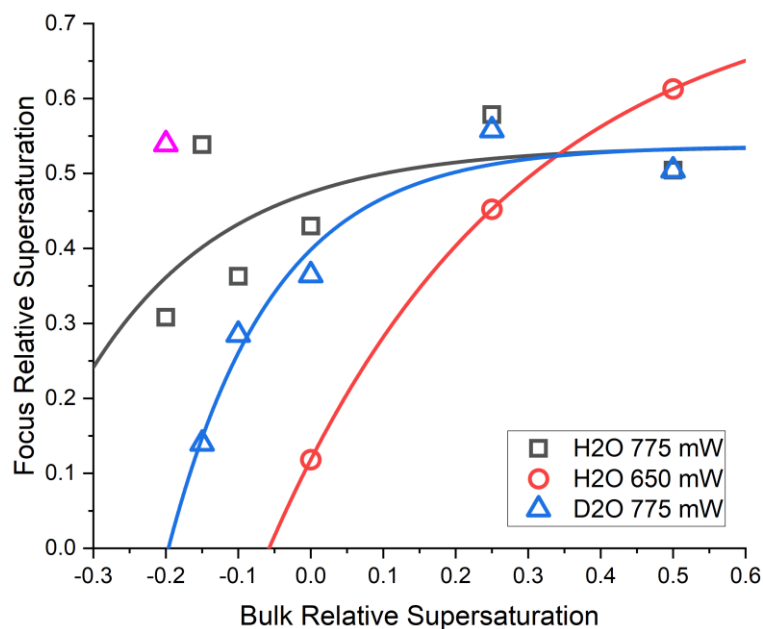


Figure 9:36: Average bulk and calculated focus relative superstation. Lines are intended only to guide eyes, elementary power low fitting. Magenta point excluded from fitting of D₂O 775 mW set.

From the approximate fittings applied to the calculated averages of the trap focus relative supersaturations, there appears to be bulk relative supersaturation would not be able to reach a positive relative supersaturation. However, the effect of the laser power examined here suggested that using a higher laser power to generate the trap would allow solutions of greater negative relative supersaturation to become supersaturated and allow crystal nucleation and growth. This analysis provides further weight to the idea that the focus of the optical tweezers can increase the solute's local concentration in and around the focus of the optical tweezers. However, it only is possible up to a certain relative supersaturation, in this case, $S \approx 1.5$ ($\sigma = 0.5$).

9.11 Conclusions

The use of optical tweezers can induce nucleation from solutions in a range of circumstances, the characteristics of which can be dependent on a range of factors, including: the solute and solvent themselves and the concentration used, the position of the tweezing focus used and its position within the solution that is used to generate the crystal, the polarisation of the laser beam used to generate the tweezers and the presence of a silica particle within the focus. The crystallisation of glycine from solution induced by optical tweezers appears to be only possible with certain supersaturation ranges ($S > 0.75$ when using 775 mW) and within specific distances of solution interfaces (up to 20 μm when using 775 mW) dependent on the laser power used. The crystallisation of NaCl or NaBrO₃ from aqueous solution was not possible with the setup used here. Other setups could prove to be more successful in this endeavour. Also, growth rates can be determined from the same videos used to determine the time at which nucleation occurred, using a machine learning model, with trends depending on laser power and the supersaturation of the bulk solution. With some cases of the linear growth rates being in line with what would be expected in the absence of the tweezers and undersaturated solutions appearing to be supersaturated in proximity to the tweezers.

10 Final Remarks

This thesis reports the steps required to comprehensively investigate crystallisation induced by or impacted by optical tweezers and particles typically trapped using optical tweezers. Beginning with considerations that must be made before ever using optical tweezers, moving to the effects of using non-standard isotopes for standard methods of crystallisation investigations and the impacts that introducing particles commonly used in tweezing experiments have on crystallisation characteristics. Finally, we determine the impact a tweezer focus can have on pre-existing crystals and when directly nucleated from solution, even when undersaturated.

10.1 Heat Absorption of Tweezing Beams and Trapping Particles

A range of factors must be considered before examining potentially crystallising systems to avoid or at least minimise the magnitude of laser-induced heating, especially in situations where particles were to be held within the tweezing focus. The most important of these factors is the laser's wavelength, although, in ideal circumstances, the tweezing system used would be designed to allow for the study of a chosen crystallising system and not vice versa. However, this is impracticable as optical components are not likely to be interchangeable due to being optimised for specific wavelengths. Therefore, the systems chosen would use D₂O and H₂O as solvents to examine the effect of the magnitude of laser induced heating and glycine and NaCl as these have different temperature dependent solubility curves.

10.2 Comparison of Nucleation and Growth Characteristics in Water and Deuterium Oxide

Different solvent isotopologues (H₂O and D₂O) can impact the crystallisation characteristics observed and altered depending on the specific isotopologue used. Changes that occur depending on the characteristic examined (primary nucleation rate, secondary nucleation rate or crystal growth rate) and the solute used. One issue that can occur in some cases isotope exchange between the solute and the solvent, making crystal polymorph determination more complicated than it would be under normal conditions. Another consideration here is that there appears to be no sudden level of supersaturation where secondary nucleation “switches off” with only growth occurring. The work here provides further evidence that it would appear to occur at levels below what would be commonly considered the secondary nucleation threshold. Especially since secondary nucleation has been observed at miniscule relative supersaturations in this work.

10.3 Impact of Particles on Nucleation Characteristics

Testing was performed to determine the impact of commonly used tweezing particles on their effects on primary nucleation characteristics. Their presence narrowed the width of the determined metastable zone in both regular H₂O and D₂O in all but one of the cases examined. In the case of primary nucleation rates, the effect appeared to depend on the solute and particle material of choice. Some combinations caused the reduction of induction times, while others lengthened it to values greater than in the absence of the particles. One issue that can present itself is the reliability of the method used to determine the presence of crystals when other third materials are already present (the solid non-soluble particle) and can block or scatter the light used to measure the turbidity typically induced by the presence of crystals from what was a transparent solution when tested without any particulate material present, should this third material not allow transmissivity measurement to be made alternative methods for determining the presence of crystals would have to be utilised.

10.4 Effect of Proximity of an Optical Tweezing Focus near a Pre-existing Crystal

The presence of an optical trap near the face of an already existing crystal can have a range of different effects depending on multiple factors. The effects of the laser power and distance between the trap and the crystal face depended on the solvent isotopologue used. When regular water was used, increasing the power, or decreasing the distance resulted in lower growth rates, whereas the opposite was true when using D₂O. Introducing a trapped silica particle also impacted the results, and the same effect was seen when examining water-based solutions. However, when using D₂O, there appeared to be a negligible effect. Some effects were also observed in some circumstances where in scenarios that could be classified as highly heating, the localised growth can be inhibited by the action of the tweezers. Microscopic agitations possible when trapping silica particles can also not induce the production of secondary nuclei from crystals suspended in supersaturated solutions.

10.5 Nucleation from Solution Induced by Optical Tweezing

The inducement of nucleation of glycine from solution to a localisable point is possible when using optical tweezers from solutions based on H₂O or D₂O. An interface or proximity to one is key to allowing the tweezer's action to induce nucleation. However, this can be impacted by a range of factors such as solutions supersaturation (nucleation is possible from an undersaturated solution), the lateral distance from the three-phase intersection line, laser polarisation and power, solvent isotopologue and the presence or absence of a silica particle

with the focus of the tweezers. To the author's knowledge, the nucleation of glycine from solution in H₂O when undersaturated using optical tweezers is reported for the first time. Nucleation induced by optical tweezers was attempted in other solute systems, in one case, to determine if it would have been possible to nucleate specific chiral forms of a substance depending upon the specific conditions of the tweezing focus, however, this was unsuccessful on this occasion.

10.6 Future Work

From the work performed here, there are several items which could warrant further investigation.

- Direct comparison of temperature rises in non-pure solvent system using predictive theory and direct measurements, using Stokes anti-Stokes scattering.
- Measuring the effects of solvent isotopologues on other solute systems, emphasising systems where the solute has increased solubility in D₂O than in H₂O.
- A more exhaustive examination of the impacts of particulate material on crystallising systems, by varying particle concentration and size and altering the material of the particle tested.
- Determining the impacts of optical tweezing on the growth of pre-existing macroscopic crystals in a small range of other settings, such as altering the systems examined and the laser polarisation used.
- Examining more widely the impacts of optical tweezers on the nucleation of substances, starting with slight alterations of situations where it has already been observed, such as testing with other amino acids. Furthermore, to further investigate the systems tested here where it was not possible to induce nucleation from solution

using optical tweezers (NaCl and NaBrO₃), such as using higher power traps and longer observation times.

References

- [1] H. M. Schoen, C. S. Grove, and J. A. Palermo, "The early history of crystallization," *J. Chem. Educ.*, vol. 33, no. 8, pp. 373–375, 1956, doi: 10.1021/ed033p373.
- [2] B. M. Couillaud, P. Espeau, N. Mignet, and Y. Corvis, "State of the Art of Pharmaceutical Solid Forms: from Crystal Property Issues to Nanocrystals Formulation," *ChemMedChem*, vol. 14, no. 1, pp. 8–23, 2019, doi: 10.1002/cmdc.201800612.
- [3] J. W. Mullin, *Crystallization*, 4th ed. Boston: Butterworth-Heinemann, 2001.
- [4] A. S. Myerson and R. Ginde, "Crystals, Crystal Growth and Nucleation," in *Handbook of industrial crystallization*, A. S. Myerson, Ed., 2nd ed. Butterworth-Heinemann, 2001, pp. 33–66.
- [5] D. Erdemir, A. Y. Lee, and A. S. Myerson, "Nucleation of crystals from solution: Classical and two-step models," *Acc. Chem. Res.*, vol. 42, no. 5, pp. 621–629, 2009, doi: 10.1021/ar800217x.
- [6] A. M. Schwartz and A. S. Myerson, "Solutions and Solution Properties," in *Handbook of industrial crystallization*, A. S. Myerson, Ed., Butterworth-Heinemann, 2001, pp. 1–31.
- [7] S. Kim and A. S. Myerson, "Metastable Solution Thermodynamic Properties and Crystal Growth Kinetics," *Ind. Eng. Chem. Res.*, vol. 35, no. 4, pp. 1078–1084, 1996, doi: 10.1021/ie950327m.
- [8] A. Lewis, M. M. Seckler, H. Kramer, and G. van Rosmalen, *Industrial Crystallization*. Cambridge: Cambridge University Press, 2015.
- [9] H. Yang, "Relation between metastable zone width and induction time of butyl paraben in ethanol," *CrystEngComm*, vol. 17, no. 3, pp. 577–586, 2015, doi: 10.1039/c4ce01625d.
- [10] J. H. Williams, "The Classification of crystals," in *Crystal Engineering How molecules build solids*, IOP Publishing, 2017.
- [11] M. M. Ripoll and F. H. Cano, "The symmetry of crystals. Representation of Bravais lattices," 2020. https://www.xtal.iqfr.csic.es/Cristalografia/parte_03_4-en.html (accessed Mar. 23, 2020).
- [12] K. J. Sypek, "Investigation of the effects of flow on crystallisation process," University of Strathclyde, 2014.
- [13] A. Nangia, "Conformational polymorphism in organic crystals," *Acc. Chem. Res.*, vol. 41, no. 5, pp. 595–604, 2008, doi: 10.1021/ar700203k.
- [14] J. D. Dunitz and J. Bernstein, "Disappearing Polymorphs," *Acc. Chem. Res.*, vol. 28, no. 4, pp. 193–200, 1995, doi: 10.1021/ar00052a005.
- [15] K. Srinivasan, "Crystal growth of α and γ glycine polymorphs and their polymorphic phase transformations," *J. Cryst. Growth*, vol. 311, no. 1, pp. 156–162, 2008, doi: 10.1016/j.jcrysgro.2008.10.084.
- [16] M. J. Vesga, D. McKechnie, P. A. Mulheran, K. Johnston, and J. Sefcik, "Conundrum of

γ glycine nucleation revisited: to stir or not to stir?," *CrystEngComm*, vol. 21, no. 13, pp. 2234–2243, 2019, doi: 10.1039/c8ce01829d.

- [17] B. Rodríguez-Spong, C. P. Price, A. Jayasankar, A. J. Matzger, and N. Rodríguez-Hornedo, "General principles of pharmaceutical solid polymorphism: A supramolecular perspective," *Adv. Drug Deliv. Rev.*, vol. 56, no. 3, pp. 241–274, 2004, doi: 10.1016/j.addr.2003.10.005.
- [18] G. Zimbitas *et al.*, "Investigation of molecular and mesoscale clusters in undersaturated glycine aqueous solutions," *Colloids Surfaces A Physicochem. Eng. Asp.*, vol. 579, no. July, p. 123633, 2019, doi: 10.1016/j.colsurfa.2019.123633.
- [19] C. Forsyth, "Influence of Controlled Fluid Shear on Glycine Crystal Nucleation from Solution," University of Strathclyde, 2015.
- [20] N. Dąbrowska, "Influence of Impurities on the Crystallisation of Pharmaceutical Materials," University of Strathclyde, 2017.
- [21] C. Valeriani, E. Sanz, and D. Frenkel, "Rate of homogeneous crystal nucleation in molten NaCl," *J. Chem. Phys.*, vol. 122, no. 19, p. 194501, 2005, doi: 10.1063/1.1896348.
- [22] P. R. ten Wolde and D. Frenkel, "Enhancement of protein crystal nucleation by critical density fluctuations," *Science (80-.)*, vol. 277, no. 5334, pp. 1975–1978, 1997, doi: 10.1126/science.277.5334.1975.
- [23] P. G. Vekilov, "The two-step mechanism of nucleation of crystals in solution," *Nanoscale*, vol. 2, no. 11, pp. 2346–2357, 2010, doi: 10.1039/c0nr00628a.
- [24] L. F. Filobelo, O. Galkin, and P. G. Vekilov, "Spinodal for the solution-to-crystal phase transformation," *J. Chem. Phys.*, vol. 123, no. 1, 2005, doi: 10.1063/1.1943413.
- [25] D. Chakraborty and G. N. Patey, "How crystals nucleate and grow in aqueous NaCl solution," *J. Phys. Chem. Lett.*, vol. 4, no. 4, pp. 573–578, 2013, doi: 10.1021/jz302065w.
- [26] Q. Sun, S. Cui, and M. Zhang, "Homogeneous nucleation mechanism of nacl in aqueous solutions," *Crystals*, vol. 10, no. 2, 2020, doi: 10.3390/cryst10020107.
- [27] G. D. Botsaris, "Secondary Nucleation — A Review," in *Industrial Crystallization*, Boston, MA: Springer US, 1976, pp. 3–22. doi: 10.1007/978-1-4615-7258-9_1.
- [28] T. L. Threlfall and S. J. Coles, "A perspective on the growth-only zone, the secondary nucleation threshold and crystal size distribution in solution crystallisation," *CrystEngComm*, vol. 18, no. 3, pp. 369–378, 2016, doi: 10.1039/c5ce01608h.
- [29] M. L. Briuglia, J. Sefcik, and J. H. ter Horst, "Measuring Secondary Nucleation through Single Crystal Seeding," *Cryst. Growth Des.*, vol. 19, no. 1, pp. 421–429, 2019, doi: 10.1021/acs.cgd.8b01515.
- [30] A. Cashmore, "Understanding and Measurement of Secondary Nucleation," University of Strathclyde, 2022.
- [31] S. G. Agrawal and A. H. J. Paterson, "Secondary Nucleation: Mechanisms and Models," *Chem. Eng. Commun.*, vol. 202, no. 5, pp. 698–706, 2015, doi: 10.1080/00986445.2014.969369.

- [32] J. Anwar, S. Khan, and L. Lindfors, "Secondary crystal nucleation: Nuclei breeding factory uncovered," *Angew. Chemie - Int. Ed.*, vol. 54, no. 49, pp. 14681–14684, 2015, doi: 10.1002/anie.201501216.
- [33] D. Zheng *et al.*, "Coupling of Contact Nucleation Kinetics with Breakage Model for Crystallization of Sodium Chloride Crystal in Fluidized Bed Crystallizer," *J. Chem.*, vol. 2019, pp. 1–11, 2019, doi: 10.1155/2019/2150560.
- [34] R. Y. Qian and G. D. Botsaris, "A new mechanism for nuclei formation in suspension crystallizers: The role of interparticle forces," *Chem. Eng. Sci.*, vol. 52, no. 20, pp. 3429–3440, 1997, doi: 10.1016/S0009-2509(97)89691-1.
- [35] L. Gora and R. W. Thompson, "Investigations of secondary nucleation by initial breeding in clear solution zeolite NaA systems," *Zeolites*, vol. 15, no. 6, pp. 526–534, 1995, doi: 10.1016/0144-2449(95)00012-U.
- [36] K. Shimizu, K. Tsukamoto, J. Horita, and T. Tadaki, "Origin of secondary nucleation as revealed by isotopic labelling," *J. Cryst. Growth*, vol. 69, no. 2–3, pp. 623–626, 1984, doi: 10.1016/0022-0248(84)90376-2.
- [37] A. Mersmann, R. Sangl, M. Kind, and J. Pohlisch, "Attrition and secondary nucleation in crystallizers," *Chem. Eng. Technol.*, vol. 11, no. 1, pp. 80–88, 1988, doi: 10.1002/ceat.270110112.
- [38] P. Ayazi Shamlou, A. G. Jones, and K. Djamarani, "Hydrodynamics of secondary nucleation in suspension crystallization," *Chem. Eng. Sci.*, vol. 45, no. 5, pp. 1405–1416, 1990, doi: 10.1016/0009-2509(90)87134-E.
- [39] R. E. A. Mason and R. F. Strickland-Constable, "Breeding of crystal nuclei," *Trans. Faraday Soc.*, vol. 62, pp. 455–461, 1966, doi: 10.1039/tf9666200455.
- [40] P. J. Frawley, N. A. Mitchell, C. T. Ó'Ciardhá, and K. W. Hutton, "The effects of supersaturation, temperature, agitation and seed surface area on the secondary nucleation of paracetamol in ethanol solutions," *Chem. Eng. Sci.*, vol. 75, pp. 183–197, 2012, doi: 10.1016/j.ces.2012.03.041.
- [41] L. G. Bauer, "Contact nucleation of magnesium sulfate heptahydrate in a continuous MSMPR crystallizer," Iowa State University, 1972.
- [42] S. M. Reeves and P. J. Hill, "Mechanisms influencing crystal breakage experiments in stirred vessels," *Cryst. Growth Des.*, vol. 12, no. 6, pp. 2748–2758, 2012, doi: 10.1021/cg200896m.
- [43] Y. Cui and A. S. Myerson, "Experimental evaluation of contact secondary nucleation mechanisms," *Cryst. Growth Des.*, vol. 14, no. 10, pp. 5152–5157, 2014, doi: 10.1021/cg500861f.
- [44] C. Y. Tai, W. L. McCabe, and R. W. Rousseau, "Contact nucleation of various crystal types," *AIChE J.*, vol. 21, no. 2, pp. 351–358, 1975, doi: 10.1002/aic.690210217.
- [45] R. W. Rousseau, W. L. McCabe, and C. Y. Tai, "The stability of nuclei generated by contact nucleation," *AIChE J.*, vol. 21, no. 5, pp. 1017–1019, 1975, doi: 10.1002/aic.690210528.
- [46] J. McGinty, N. Yazdanpanah, C. Price, J. H. ter Horst, and J. Sefcik, "Nucleation and

Crystal Growth in Continuous Crystallization,” in *The Handbook of Continuous Crystallization*, Cambridge: Royal Society of Chemistry, 2020. doi: 10.1039/9781788013581-00001.

- [47] S. S. Kadam, S. A. Kulkarni, R. Coloma Ribera, A. I. Stankiewicz, J. H. ter Horst, and H. J. M. Kramer, “A new view on the metastable zone width during cooling crystallization,” *Chem. Eng. Sci.*, vol. 72, pp. 10–19, 2012, doi: 10.1016/j.ces.2012.01.002.
- [48] S. Jiang and J. H. ter Horst, “Crystal nucleation rates from probability distributions of induction times,” *Cryst. Growth Des.*, vol. 11, no. 1, pp. 256–261, 2011, doi: 10.1021/cg101213q.
- [49] Y. Xiao, S. K. Tang, H. Hao, R. J. Davey, and T. Vetter, “Quantifying the Inherent Uncertainty Associated with Nucleation Rates Estimated from Induction Time Data Measured in Small Volumes,” *Cryst. Growth Des.*, vol. 17, no. 5, pp. 2852–2863, 2017, doi: 10.1021/acs.cgd.7b00372.
- [50] O. H. Olalere, “Phase behaviour and crystal nucleation in complex multicomponent system,” University of Strathclyde, 2019.
- [51] J. Zaccaro, J. Matic, A. S. Myerson, and B. A. Garetz, “Nonphotochemical, laser-induced nucleation of supersaturated aqueous glycine produces unexpected γ -polymorph,” *Cryst. Growth Des.*, vol. 1, no. 1, pp. 5–8, 2001, doi: 10.1021/cg0055171.
- [52] N. Javid, T. Kendall, I. S. Burns, and J. Sefcik, “Filtration suppresses laser-induced nucleation of glycine in aqueous solutions,” *Cryst. Growth Des.*, vol. 16, no. 8, pp. 4196–4202, 2016, doi: 10.1021/acs.cgd.6b00046.
- [53] A. J. Alexander and P. J. Camp, “Non-photochemical laser-induced nucleation,” *J. Chem. Phys.*, vol. 150, no. 4, p. 040901, 2019, doi: 10.1063/1.5079328.
- [54] S. Nalesso, M. J. Bussemaker, R. P. Sear, M. Hodnett, and J. Lee, “A review on possible mechanisms of sonocrystallisation in solution,” *Ultrason. Sonochem.*, vol. 57, no. February, pp. 125–138, 2019, doi: 10.1016/j.ultsonch.2019.04.020.
- [55] H. Kim and K. Suslick, “The Effects of Ultrasound on Crystals: Sonocrystallization and Sonofragmentation,” *Crystals*, vol. 8, no. 7, p. 280, 2018, doi: 10.3390/cryst8070280.
- [56] J. R. G. Sander, B. W. Zeiger, and K. S. Suslick, “Sonocrystallization and sonofragmentation,” *Ultrason. Sonochem.*, vol. 21, no. 6, pp. 1908–1915, 2014, doi: 10.1016/j.ultsonch.2014.02.005.
- [57] J. M. Kim, S. M. Chang, K. S. Kim, M. K. Chung, and W. S. Kim, “Colloids and Surfaces A : Physicochemical and Engineering Aspects Acoustic influence on aggregation and agglomeration of crystals in reaction crystallization of cerium carbonate,” *Colloids Surfaces A Physicochem. Eng. Asp.*, vol. 375, no. 1–3, pp. 193–199, 2011, doi: 10.1016/j.colsurfa.2010.11.084.
- [58] A. Cacciuto, S. Auer, and D. Frenkel, “Onset of heterogeneous crystal nucleation in colloidal suspensions,” *Nature*, vol. 428, no. 6981, pp. 404–406, 2004, doi: 10.1038/nature02397.
- [59] K. Sandomirski *et al.*, “Heterogeneous crystallization of hard and soft spheres near

- flat and curved walls," *Eur. Phys. J. Spec. Top.*, vol. 223, no. 3, pp. 439–454, 2014, doi: 10.1140/epjst/e2014-02101-7.
- [60] A. J. Malkin, J. Cheung, and A. McPherson, "Crystallization of satellite tobacco mosaic virus I. Nucleation phenomena," *J. Cryst. Growth*, vol. 126, no. 4, pp. 544–554, 1993, doi: 10.1016/0022-0248(93)90804-6.
- [61] E. Curcio, V. Curcio, G. Di Profi, E. Fontananova, and E. Drioli, "Energetics of protein nucleation on rough polymeric surfaces," *J. Phys. Chem. B*, vol. 114, no. 43, pp. 13650–13655, 2010, doi: 10.1021/jp106349d.
- [62] W. C. Chien, C. C. Lee, and C. Y. Tai, "Heterogeneous Nucleation Rate of Calcium Carbonate Derived from Induction Period," *Ind. Eng. Chem. Res.*, vol. 46, no. 7, pp. 6435–6441, 2007.
- [63] T. Lapidot, O. K. Matar, and J. Y. Y. Heng, "Calcium sulphate crystallisation in the presence of mesoporous silica particles: Experiments and population balance modelling," *Chem. Eng. Sci.*, vol. 202, pp. 238–249, 2019, doi: 10.1016/j.ces.2019.02.045.
- [64] E. Allahyarov, K. Sandomirski, S. U. Egelhaaf, and H. Löwen, "Crystallization seeds favour crystallization only during initial growth," *Nat. Commun.*, vol. 6, no. 1, p. 7110, 2015, doi: 10.1038/ncomms8110.
- [65] T. Lapidot and J. Y. Y. Heng, "Functionalized mesoporous silica for the control of crystallization fouling," *Ind. Eng. Chem. Res.*, vol. 55, no. 44, pp. 11475–11479, 2016, doi: 10.1021/acs.iecr.6b02914.
- [66] D. Han, Y. Wang, Y. Yang, T. Gong, Y. Chen, and J. Gong, "Revealing the role of a surfactant in the nucleation and crystal growth of thiamine nitrate: Experiments and simulation studies," *CrystEngComm*, vol. 21, no. 23, pp. 3576–3585, 2019, doi: 10.1039/c9ce00325h.
- [67] K. Bodnár, S. P. Hudson, and Å. C. Rasmuson, "Promotion of Mefenamic Acid Nucleation by a Surfactant Additive, Docusate Sodium," *Cryst. Growth Des.*, vol. 19, no. 2, pp. 591–603, 2019, doi: 10.1021/acs.cgd.8b00995.
- [68] S. K. Poornachary, G. Han, J. W. Kwek, P. S. Chow, and R. B. H. Tan, "Crystallizing Micronized Particles of a Poorly Water-Soluble Active Pharmaceutical Ingredient: Nucleation Enhancement by Polymeric Additives," *Cryst. Growth Des.*, vol. 16, no. 2, pp. 749–758, 2016, doi: 10.1021/acs.cgd.5b01343.
- [69] E. G. Cooke, "The influence of added impurities on the growth and nucleation of sodium chloride," *Krist. und Tech.*, vol. 1, no. 1, pp. 119–126, 1966, doi: 10.1002/crat.19660010115.
- [70] A. A. Noyes and W. R. Whitney, "The rate of solution of solid substances in their own solutions," *J. Am. Chem. Soc.*, vol. 19, no. 12, pp. 930–934, 1897, doi: 10.1021/ja02086a003.
- [71] L. Akil, "Physical analysis of solid solution formulations," University of Strathclyde, 2018.
- [72] J. P. Duroudier, "Dispersions and Dissolutions of Powders," in *Solid-Solid, Fluid-Solid, Fluid-Fluid Mixers*, London: ISTE Press, 2016.

- [73] G. Dhanaraj, K. Byrappa, V. Prasad, and M. Dudley, "Crystal Growth Techniques and Characterization: An Overview," in *Springer Handbook of Crystal Growth*, G. Dhanaraj, K. Byrappa, V. Prasad, and M. Dudley, Eds., 1st ed. Berlin, Heidelberg: Springer Berlin Heidelberg, 2010.
- [74] S. A. Stavchansky and J. A. McGinity, "Bioavailability in Tablet Technology," in *Pharmaceutical Dosage Forms Tablets Volume 2*, H. A. Lieberman, L. Lachman, and J. B. Schwartz, Eds., CRC Press, 1990.
- [75] C. F. Abegg, J. D. Stevens, and M. A. Larson, "Crystal size distributions in continuous crystallizers when growth rate is size dependent," *AIChE J.*, vol. 14, no. 1, pp. 118–122, 1968, doi: 10.1002/aic.690140121.
- [76] C. Virone, J. H. ter Horst, H. J. M. Kramer, and P. J. Jansens, "Growth rate dispersion of ammonium sulphate attrition fragments," *J. Cryst. Growth*, vol. 275, no. 1–2, pp. 1397–1401, 2005, doi: 10.1016/j.jcrysgro.2004.11.167.
- [77] A. E. D. M. van der Heijden and J. P. van der Eerden, "Growth rate dispersion: the role of lattice strain," *J. Cryst. Growth*, vol. 118, no. 1–2, pp. 14–26, 1992, doi: 10.1016/0022-0248(92)90044-J.
- [78] C. Gahn and A. Mersmann, "Brittle fracture in crystallization processes Part B. Growth of fragments and scale-up of suspension crystallizers," *Chem. Eng. Sci.*, vol. 54, no. 9, pp. 1283–1292, 1999, doi: 10.1016/S0009-2509(98)00452-7.
- [79] J. Garside and M. A. Larson, "Direct Observation of Secondary Nuclei Production," *J. Cryst. Growth*, vol. 43, pp. 694–704, 1978, doi: 10.1016/0022-0248(78)90148-3.
- [80] "The Nobel Prize in Physics 2018."
<https://www.nobelprize.org/prizes/physics/2018/summary/> (accessed Oct. 03, 2019).
- [81] A. Ashkin, "Acceleration and Trapping of Particles by Radiation Pressure," *Phys. Rev. Lett.*, vol. 24, no. 4, pp. 156–159, 1970, doi: 10.1103/PhysRevLett.24.156.
- [82] A. Ashkin and J. M. Dziedzic, "Optical levitation by radiation pressure," *Appl. Phys. Lett.*, vol. 19, no. 8, pp. 283–285, 1971, doi: 10.1063/1.1653919.
- [83] A. Ashkin, *Optical Trapping and Manipulation of Neutral Particles Using Lasers*. Hackensack: World Scientific, 2006.
- [84] A. Ashkin and J. M. Dziedzic, "Optical Levitation of Liquid Drops by Radiation Pressure," *Science (80-.)*, vol. 187, no. 4181, pp. 1073–1075, 1975, doi: 10.1126/science.187.4181.1073.
- [85] A. Ashkin, J. M. Dziedzic, J. E. Bjorkholm, and S. Chu, "Observation of a single-beam gradient force optical trap for dielectric particles," *Opt. Lett.*, vol. 11, no. 5, p. 288, 1986, doi: 10.1364/OL.11.000288.
- [86] J. E. Molloy and M. J. Padgett, "Lights, action: Optical tweezers," *Contemp. Phys.*, vol. 43, no. 4, pp. 241–258, 2002, doi: 10.1080/00107510110116051.
- [87] M. C. Müllenbroich, "Sensorless Adaptive Optics in Advanced Microscopy Techniques," University of Strathclyde, 2012.
- [88] K. Dholakia, P. Reece, and M. Gu, "Optical micromanipulation," *Chem. Soc. Rev.*, vol.

- 37, no. 1, pp. 42–55, 2008, doi: 10.1039/b512471a.
- [89] H. Felgner, O. Müller, and M. Schliwa, “Calibration of light forces in optical tweezers,” *Appl. Opt.*, vol. 34, no. 6, p. 977, 1995, doi: 10.1364/ao.34.000977.
- [90] A. Ashkin, “Forces of a single-beam gradient laser trap on a dielectric sphere in the ray optics regime,” *Biophys. J.*, vol. 61, no. 2, pp. 569–582, 1992, doi: 10.1016/S0006-3495(92)81860-X.
- [91] P. Polimeno *et al.*, “Optical tweezers and their applications,” *J. Quant. Spectrosc. Radiat. Transf.*, vol. 218, pp. 131–150, 2018, doi: 10.1016/j.jqsrt.2018.07.013.
- [92] N. B. Simpson, L. Allen, and M. J. Padgett, “Optical tweezers and optical spanners with Laguerre–Gaussian modes,” *J. Mod. Opt.*, vol. 43, no. 12, pp. 2485–2491, 1996, doi: 10.1080/09500349608230675.
- [93] K. C. Neuman and S. M. Block, “Optical trapping,” *Rev. Sci. Instrum.*, vol. 75, no. 9, pp. 2787–2809, 2004, doi: 10.1063/1.1785844.
- [94] D. G. Glass, “Optical Tweezers : A tool to control, manipulate and quantify immune cell interaction,” University of Strathclyde, 2014.
- [95] S. E. Rice, T. J. Purcell, and J. A. Spudich, “[6] Building and using optical traps to study properties of molecular motors,” *Methods Enzymol.*, vol. 361, no. 1998, pp. 112–133, 2003, doi: 10.1016/S0076-6879(03)61008-6.
- [96] M. Sarshar, W. T. Wong, and B. Anvari, “Comparative study of methods to calibrate the stiffness of a single-beam gradient-force optical tweezers over various laser trapping powers,” *J. Biomed. Opt.*, vol. 19, no. 11, p. 115001, 2014, doi: 10.1117/1.JBO.19.11.115001.
- [97] R. M. Simmons, J. T. Finer, S. Chu, and J. A. Spudich, “Quantitative measurements of force and displacement using an optical trap,” *Biophys. J.*, vol. 70, no. 4, pp. 1813–1822, 1996, doi: 10.1016/S0006-3495(96)79746-1.
- [98] K. Berg-Sørensen and H. Flyvbjerg, “Power spectrum analysis for optical tweezers,” *Rev. Sci. Instrum.*, vol. 75, no. 3, pp. 594–612, 2004, doi: 10.1063/1.1645654.
- [99] P. Parthasarathi, “Micromechanics and Dynamics of Colloids and Living Matter using Optical Techniques,” University of Bangalore, 2018.
- [100] Thorlabs, “OTKBFM-CAL Calibration and Measurement Module for OTKB / OTKBFM (Revision C).” Newton, 2018.
- [101] E. Schäffer, S. F. Nørrelykke, and J. Howard, “Surface forces and drag coefficients of microspheres near a plane surface measured with optical tweezers,” *Langmuir*, vol. 23, no. 7, pp. 3654–3665, 2007, doi: 10.1021/la0622368.
- [102] M. Andersson *et al.*, “Using optical tweezers for measuring the interaction forces between human bone cells and implant surfaces: System design and force calibration,” *Rev. Sci. Instrum.*, vol. 78, no. 7, 2007, doi: 10.1063/1.2752606.
- [103] A. Ashkin, J. M. Dziedzic, and T. Yamane, “Optical trapping and manipulation of single cells using infrared laser beams,” *Nature*, vol. 330, pp. 769–711, 1987.
- [104] H. Mao, J. R. Arias-Gonzalez, S. B. Smith, I. Tinoco, and C. Bustamante, “Temperature

- control methods in a laser tweezers system," *Biophys. J.*, vol. 89, no. 2, pp. 1308–1316, 2005, doi: 10.1529/biophysj.104.054536.
- [105] E. J. G. Peterman, F. Gittes, and C. F. Schmidt, "Laser-induced heating in optical traps," *Biophys. J.*, vol. 84, no. 2 I, pp. 1308–1316, 2003, doi: 10.1016/S0006-3495(03)74946-7.
- [106] F. A. Walton, "Mapping and Controlling Nucleation," University of Glasgow, 2019.
- [107] F. Català, "Implementation of the direct force measurement method in optical tweezers," University of Barcelona, 2018.
- [108] Z. Liao and K. Wynne, "A Metastable Amorphous Intermediate Is Responsible for Laser-Induced Nucleation of Glycine," *J. Am. Chem. Soc.*, vol. 144, no. 15, pp. 6727–6733, 2022, doi: 10.1021/jacs.1c11154.
- [109] B. Gardner, P. Matousek, and N. Stone, "Temperature Spatially Offset Raman Spectroscopy (T-SORS): Subsurface Chemically Specific Measurement of Temperature in Turbid Media Using Anti-Stokes Spatially Offset Raman Spectroscopy," *Anal. Chem.*, vol. 88, no. 1, pp. 832–837, 2016, doi: 10.1021/acs.analchem.5b03360.
- [110] S. Kedenburg, M. Vieweg, T. Gissibl, and H. Giessen, "Linear refractive index and absorption measurements of nonlinear optical liquids in the visible and near-infrared spectral region," *Opt. Mater. Express*, vol. 2, no. 11, p. 1588, 2012, doi: 10.1364/ome.2.001588.
- [111] Q. Fu, "Radiation Transfer in the Atmosphere: Cloud-Radiative Processes," *Encycl. Atmos. Sci. Second Ed.*, vol. 5, pp. 13–15, 2015, doi: 10.1016/B978-0-12-382225-3.00338-8.
- [112] P. B. Roder, "Quantitative Photothermal Heating and Cooling Measurements of Engineered Nanoparticles in an Optical Trap," University of Washington, 2015.
- [113] K. Kroy and F. Cichos, "Hot Brownian Motion," in *Diffusive Spreading in Nature, Technology and Society*, A. Bunde, J. Caro, J. Kärger, and G. Vogl, Eds., Cham: Springer, 2018.
- [114] D. Rings, M. Selmke, F. Cichos, and K. Kroy, "Theory of hot brownian motion," *Soft Matter*, vol. 7, no. 7, pp. 3441–3452, 2011, doi: 10.1039/c0sm00854k.
- [115] P. J. Linstrom and W. G. Mallard, Eds., "NIST Chemistry WebBook," *NIST Standard Reference Database Number 69*. National Institute of Standards and Technology, Gaithersburg, 2018.
- [116] R. Lynge Eriksen, V. Ricardo Daria, and J. Glückstad, "Fully dynamic multiple-beam optical tweezers," *Opt. Express*, vol. 10, no. 14, p. 597, 2002, doi: 10.1364/oe.10.000597.
- [117] T. Čižmár, L. C. D. Romero, K. Dholakia, and D. L. Andrews, "Multiple optical trapping and binding: new routes to self-assembly," *J. Phys. B At. Mol. Opt. Phys.*, vol. 43, no. 10, p. 102001, 2010, doi: 10.1088/0953-4075/43/10/102001.
- [118] J. E. Curtis, B. A. Koss, and D. G. Grier, "Dynamic holographic optical tweezers," *Opt. Commun.*, vol. 207, no. 1–6, pp. 169–175, 2002, doi: 10.1016/S0030-4018(02)01524-

9.

- [119] F. C. Cheong, B. J. Krishnatreya, and D. G. Grier, "Strategies for three-dimensional particle tracking with holographic video microscopy," *Opt. Express*, vol. 18, no. 13, p. 13563, 2010, doi: 10.1364/oe.18.013563.
- [120] M. C. Wu, "Optoelectronic tweezers," *Nat. Photonics*, vol. 5, no. 6, pp. 322–324, 2011, doi: 10.1038/nphoton.2011.98.
- [121] E. P. Y. Chiou and M. C. Wu, "Optoelectronic Tweezers," in *Micro/Nano Technology Systems for Biomedical Applications*, Oxford University Press, 2010, pp. 317–345. doi: 10.1093/acprof:oso/9780199219698.003.0009.
- [122] A. T. Ohta *et al.*, "Optoelectronic Tweezers for the Manipulation of Cells, Microparticles, and Nanoparticles," in *Recent Optical and Photonic Technologies*, InTech, 2010. doi: 10.5772/6921.
- [123] S. Zhang *et al.*, "Patterned Optoelectronic Tweezers: A New Scheme for Selecting, Moving, and Storing Dielectric Particles and Cells," *Small*, vol. 14, no. 45, pp. 1–11, 2018, doi: 10.1002/smll.201803342.
- [124] J. Leach, H. Mushfique, R. di Leonardo, M. Padgett, and J. Cooper, "An optically driven pump for microfluidics," *Lab Chip*, vol. 6, no. 6, p. 735, 2006, doi: 10.1039/b601886f.
- [125] M. Padgett and R. Bowman, "Tweezers with a twist," *Nat. Photonics*, vol. 5, no. 6, pp. 343–348, 2011, doi: 10.1038/nphoton.2011.81.
- [126] L. Allen, M. W. Beijersbergen, R. J. C. Spreeuw, and J. P. Woerdman, "Orbital angular momentum of light and the transformation of Laguerre-Gaussian laser modes," *Phys. Rev. A*, vol. 45, no. 11, pp. 8185–8189, 1992, doi: 10.1103/PhysRevA.45.8185.
- [127] B. A. Garetz, J. E. Aber, N. L. Goddard, R. G. Young, and A. S. Myerson, "Nonphotochemical, Polarization-Dependent, Laser-Induced Nucleation in Supersaturated Aqueous Urea Solutions," *Phys. Rev. Lett.*, vol. 77, no. 16, pp. 3475–3476, 1996, doi: 10.1103/PhysRevLett.77.3475.
- [128] T. Sugiyama, T. Adachi, and H. Masuhara, "Crystallization of glycine by photon pressure of a focused CW laser beam," *Chem. Lett.*, vol. 36, no. 12, pp. 1480–1481, 2007, doi: 10.1246/cl.2007.1480.
- [129] T. Sugiyama and S. F. Wang, "Manipulation of nucleation and polymorphism by laser irradiation," *J. Photochem. Photobiol. C Photochem. Rev.*, vol. 52, no. April, p. 100530, 2022, doi: 10.1016/j.jphotochemrev.2022.100530.
- [130] Z. Liao and K. Wynne, "Mesoscopic amorphous particles rather than oligomeric molecular aggregates are the cause of laser-induced crystal nucleation," *Proc. Natl. Acad. Sci. U. S. A.*, vol. 119, no. 33, pp. 2–3, 2022, doi: 10.1073/pnas.2207173119.
- [131] M. A. Osborne, S. Balasubramanian, W. S. Furey, and D. Klenerman, "Optically biased diffusion of single molecules studied by confocal fluorescence microscopy," *J. Phys. Chem. B*, vol. 102, no. 17, pp. 3160–3167, 1998, doi: 10.1021/jp9715078.
- [132] G. Chirico, C. Fumagalli, and G. Baldini, "Trapped brownian motion in single- and two-photon excitation fluorescence correlation experiments," *J. Phys. Chem. B*, vol.

106, no. 10, pp. 2508–2519, 2002, doi: 10.1021/jp013087z.

- [133] J. Beugnon *et al.*, “Two-dimensional transport and transfer of a single atomic qubit in optical tweezers,” *Nat. Phys.*, vol. 3, no. 10, pp. 696–699, 2007, doi: 10.1038/nphys698.
- [134] O. Y. Gowayed, T. Moosa, A. M. Moratos, T. Hua, S. Arnold, and B. A. Garetz, “Dynamic Light Scattering Study of a Laser-Induced Phase-Separated Droplet of Aqueous Glycine,” *J. Phys. Chem. B*, vol. 125, no. 28, pp. 7828–7839, 2021, doi: 10.1021/acs.jpcc.1c02620.
- [135] F. Walton and K. Wynne, “Using optical tweezing to control phase separation and nucleation near a liquid-liquid critical point,” *Soft Matter*, vol. 15, no. 41, pp. 8279–8289, 2019, doi: 10.1039/c9sm01297d.
- [136] W. Singer, U. J. Gibson, T. A. Nieminen, N. R. Heckenberg, and H. Rubinsztein-Dunlop, “Towards crystallization using optical tweezers,” in *Photonics: Design, Technology, and Packaging II*, D. Abbott, Y. S. Kivshar, H. H. Rubinsztein-Dunlop, and S. Fan, Eds., Dec. 2005, p. 60380B. doi: 10.1117/12.651755.
- [137] P. W. Yi *et al.*, “Two-stage optical trapping and assembling of protein at air/solution interface,” *Appl. Phys. Express*, vol. 16, no. 2, p. 025501, 2023, doi: 10.35848/1882-0786/acb3ab.
- [138] F. Walton and K. Wynne, “Control over phase separation and nucleation using a laser-Tweezing potential,” *Nat. Chem.*, vol. 10, no. 5, pp. 506–510, 2018, doi: 10.1038/s41557-018-0009-8.
- [139] H. Masuhara, T. Sugiyama, T. Rungsimanon, K. I. Yuyama, A. Miura, and J. R. Tu, “Laser-trapping assembling dynamics of molecules and proteins at surface and interface,” *Pure Appl. Chem.*, vol. 83, no. 4, pp. 869–883, 2011, doi: 10.1351/PAC-CON-10-09-32.
- [140] K. I. Yuyama, T. Sugiyama, and H. Masuhara, “Millimeter-scale dense liquid droplet formation and crystallization in glycine solution induced by photon pressure,” *J. Phys. Chem. Lett.*, vol. 1, no. 9, pp. 1321–1325, 2010, doi: 10.1021/jz100266t.
- [141] T. Rungsimanon, K. I. Yuyama, T. Sugiyama, and H. Masuhara, “Crystallization in unsaturated glycine/D₂O solution achieved by irradiating a focused continuous wave near infrared laser,” *Cryst. Growth Des.*, vol. 10, no. 11, pp. 4686–4688, 2010, doi: 10.1021/cg100830x.
- [142] S. F. Wang, T. Kudo, K. I. Yuyama, T. Sugiyama, and H. Masuhara, “Optically Evolved Assembly Formation in Laser Trapping of Polystyrene Nanoparticles at Solution Surface,” *Langmuir*, vol. 32, no. 47, pp. 12488–12496, 2016, doi: 10.1021/acs.langmuir.6b02433.
- [143] S. Ito, T. Sugiyama, N. Toitani, G. Katayama, and H. Miyasaka, “Application of fluorescence correlation spectroscopy to the measurement of local temperature in solutions under optical trapping condition,” *J. Phys. Chem. B*, vol. 111, no. 9, pp. 2365–2371, 2007, doi: 10.1021/jp0651561.
- [144] X. Yang, X. Wang, and C. B. Ching, “Solubility of form α and form γ of glycine in aqueous solutions,” *J. Chem. Eng. Data*, vol. 53, no. 5, pp. 1133–1137, 2008, doi:

10.1021/je7006988.

- [145] K. I. Yuyama, T. Rungsimanon, T. Sugiyama, and H. Masuhara, "Selective fabrication of α - And γ -polymorphs of glycine by intense polarized continuous wave laser beams," *Cryst. Growth Des.*, vol. 12, no. 5, pp. 2427–2434, 2012, doi: 10.1021/cg300065x.
- [146] X. Sun, B. A. Garetz, and A. S. Myerson, "Supersaturation and Polarization Dependence of Polymorph Control in the Nonphotochemical Laser-Induced Nucleation (NPLIN) of Aqueous Glycine Solutions," *Cryst. Growth Des.*, vol. 6, no. 3, p. 684, 2006.
- [147] C. S. Wu, P. Y. Hsieh, K. I. Yuyama, H. Masuhara, and T. Sugiyama, "Pseudopolymorph Control of L-Phenylalanine Achieved by Laser Trapping," *Cryst. Growth Des.*, vol. 18, no. 9, pp. 5417–5425, 2018, doi: 10.1021/acs.cgd.8b00796.
- [148] A. C. Cheng, H. Masuhara, and T. Sugiyama, "Evolving Crystal Morphology of Potassium Chloride Controlled by Optical Trapping," *J. Phys. Chem. C*, vol. 124, no. 12, pp. 6913–6921, 2020, doi: 10.1021/acs.jpcc.9b11651.
- [149] W. C. Wang, S. F. Wang, and T. Sugiyama, "L-serine polymorphism controlled by optical trapping with high-repetition-rate femtosecond laser pulses," *J. Chinese Chem. Soc.*, vol. 69, no. 1, pp. 200–210, 2022, doi: 10.1002/jccs.202100269.
- [150] T. Sugiyama, K. I. Yuyama, and H. Masuhara, "Laser trapping chemistry: From polymer assembly to amino acid crystallization," *Acc. Chem. Res.*, vol. 45, no. 11, pp. 1946–1954, 2012, doi: 10.1021/ar300161g.
- [151] K. I. Yuyama, D. S. Chiu, Y. E. Liu, T. Sugiyama, and H. Masuhara, "Crystal Growth and Dissolution Dynamics of L-Phenylalanine Controlled by Solution Surface Laser Trapping," *Cryst. Growth Des.*, vol. 18, no. 11, pp. 7079–7087, 2018, doi: 10.1021/acs.cgd.8b01233.
- [152] K. I. Yuyama, J. George, K. G. Thomas, T. Sugiyama, and H. Masuhara, "Two-Dimensional Growth Rate Control of L-Phenylalanine Crystal by Laser Trapping in Unsaturated Aqueous Solution," *Cryst. Growth Des.*, vol. 16, no. 2, pp. 953–960, 2016, doi: 10.1021/acs.cgd.5b01505.
- [153] K. I. Yuyama, T. Sugiyama, and H. Masuhara, "Laser Trapping and crystallization dynamics of L-phenylalanine at solution surface," *J. Phys. Chem. Lett.*, vol. 4, no. 15, pp. 2436–2440, 2013, doi: 10.1021/jz401122v.
- [154] J. R. Tu, A. Miura, K. I. Yuyama, H. Masuhara, and T. Sugiyama, "Crystal growth of lysozyme controlled by laser trapping," *Cryst. Growth Des.*, vol. 14, no. 1, pp. 15–22, 2014, doi: 10.1021/cg401065h.
- [155] K. I. Yuyama, K. D. Chang, J. R. Tu, H. Masuhara, and T. Sugiyama, "Rapid localized crystallization of lysozyme by laser trapping," *Phys. Chem. Chem. Phys.*, vol. 20, no. 9, pp. 6034–6039, 2018, doi: 10.1039/c7cp06990a.
- [156] Y. Tsuboi, T. Shoji, and N. Kitamura, "Crystallization of lysozyme based on molecular assembling by photon pressure," *Japanese J. Appl. Physics, Part 2 Lett.*, vol. 46, no. 45–49, 2007, doi: 10.1143/JJAP.46.L1234.
- [157] K. I. Yuyama, M. J. Islam, K. Takahashi, T. Nakamura, and V. Biju, "Crystallization of

- Methylammonium Lead Halide Perovskites by Optical Trapping,” *Angew. Chemie - Int. Ed.*, vol. 57, no. 41, pp. 13424–13428, 2018, doi: 10.1002/anie.201806079.
- [158] J. R. Tu, K. I. Yuyama, H. Masuhara, and T. Sugiyama, “Dynamics and mechanism of laser trapping-induced crystal growth of hen egg white lysozyme,” *Cryst. Growth Des.*, vol. 15, no. 10, pp. 4760–4767, 2015, doi: 10.1021/cg501860k.
- [159] D. McKechnie, “Heterogeneous Nucleation at Hydrophobic Interfaces,” University of Strathclyde, 2021.
- [160] J. Hoffmann *et al.*, “The unexpected dominance of secondary over primary nucleation,” *Faraday Discuss.*, vol. 235, pp. 109–131, 2022, doi: 10.1039/D1FD00098E.
- [161] M. Jelińska-Kazimierczuk and J. Szydłowski, “Isotope effect on the solubility of amino acids in water,” *J. Solution Chem.*, vol. 25, no. 12, pp. 1175–1184, 1996, doi: 10.1007/BF00972645.
- [162] R. D. Eddy and A. W. C. Menzies, “The solubilities of certain inorganic compounds in ordinary water and in deuterium water,” *J. Phys. Chem.*, vol. 44, no. 2, pp. 207–235, 1940, doi: 10.1021/j150398a007.
- [163] M. A. Khashan and A. Y. Nassif, “Dispersion of the optical constants of quartz and polymethyl methacrylate glasses in a wide spectral range: 0.2-3 μm ,” *Opt. Commun.*, vol. 188, no. 1–4, pp. 129–139, 2001, doi: 10.1016/S0030-4018(00)01152-4.
- [164] X. Zhang, J. Qiu, X. Li, J. Zhao, and L. Liu, “Complex refractive indices measurements of polymers in visible and near-infrared bands,” *Appl. Opt.*, vol. 59, no. 8, p. 2337, 2020, doi: 10.1364/ao.383831.
- [165] M. Rubin, “Optical properties of soda lime silica glasses,” *Sol. Energy Mater.*, vol. 12, no. 4, pp. 275–288, 1985, doi: 10.1016/0165-1633(85)90052-8.
- [166] Y. Lin, J. Zhang, L. Brzozowski, E. H. Sargent, and E. Kumacheva, “Nonlinear optical figures of merit of processible composite of poly(2-methoxy,5-(2’-(ethyl)hexyloxy)-p-phenylene vinylene) and poly(methyl methacrylate),” *J. Appl. Phys.*, vol. 91, no. 1, pp. 522–524, 2002, doi: 10.1063/1.1420760.
- [167] M. Tassieri *et al.*, “Microrheology with optical tweezers: Measuring the relative viscosity of solutions ‘at a glance,’” *Sci. Rep.*, vol. 5, pp. 1–6, 2015, doi: 10.1038/srep08831.
- [168] F. Watts, L. E. Tan, C. G. Wilson, J. M. Girkin, M. Tassieri, and A. J. Wright, “Investigating the micro-rheology of the vitreous humor using an optically trapped local probe,” *J. Opt. (United Kingdom)*, vol. 16, no. 1, 2014, doi: 10.1088/2040-8978/16/1/015301.
- [169] M. P. Lee, A. Curran, G. M. Gibson, M. Tassieri, N. R. Heckenberg, and M. J. Padgett, “Optical shield: measuring viscosity of turbid fluids using optical tweezers,” *Opt. Express*, vol. 20, no. 11, p. 12127, 2012, doi: 10.1364/oe.20.012127.
- [170] I. H. Malitson, “Interspecimen Comparison of the Refractive Index of Fused Silica*,†,” *J. Opt. Soc. Am.*, vol. 55, no. 10, p. 1205, 1965, doi: 10.1364/josa.55.001205.

- [171] N. Sultanova, S. Kasarova, and I. Nikolov, "Dispersion properties of optical polymers," *Acta Phys. Pol. A*, vol. 116, no. 4, pp. 585–587, 2009, doi: 10.12693/APhysPolA.116.585.
- [172] X. Li, L. Liu, J. Zhao, and J. Tan, "Optical properties of sodium chloride solution within the spectral range from 300 to 2500 nm at room temperature," *Appl. Spectrosc.*, vol. 69, no. 5, pp. 635–640, 2015, doi: 10.1366/14-07769R.
- [173] P. Haro-González *et al.*, "Quantum dot-based thermal spectroscopy and imaging of optically trapped microspheres and single cells," *Small*, vol. 9, no. 12, pp. 2162–2170, 2013, doi: 10.1002/sml.201201740.
- [174] R. C. Weast, Ed., *Handbook of Chemistry and Physics*, 56th ed. Cleaveland: CRC Press, 1975.
- [175] Goodfellow, "Polymethylmethacrylate (PMMA, Acrylic) Material Information," 2020. <http://www.goodfellow.com/E/Polymethylmethacrylate.html> (accessed Jul. 06, 2020).
- [176] F. Català, F. Marsà, M. Montes-Usategui, A. Farré, and E. Martín-Badosa, "Influence of experimental parameters on the laser heating of an optical trap," *Sci. Rep.*, vol. 7, no. 1, pp. 1–9, 2017, doi: 10.1038/s41598-017-15904-6.
- [177] A. A. Aleksandrov, E. V. Dzhuraeva, and V. F. Utenkov, "Thermal conductivity of sodium chloride aqueous solutions," *Therm. Eng. (English Transl. Teploenerg.)*, vol. 60, no. 3, pp. 190–194, 2013, doi: 10.1134/S0040601513030026.
- [178] Y. L. Rastorguev and Y. A. Ganiev, "THERMAL CONDUCTIVITY OF SOLUTIONS," *Inzhenerno-Fizicheskii Zhurnal*, vol. 14, no. 4, pp. 689–697, 1968.
- [179] U. F. Keyser, D. Krapf, B. N. Koeleman, R. M. M. Smeets, N. H. Dekker, and C. Dekker, "Nanopore tomography of a laser focus," *Nano Lett.*, vol. 5, no. 11, pp. 2253–2256, 2005, doi: 10.1021/nl051597p.
- [180] B. E. Poling, G. H. Thomson, D. G. Friend, R. L. Rowley, and W. V. Wilding, "Physical and Chemical Data," in *Perry's Chemical Engineering Handbook*, D. W. Green and R. H. Perry, Eds., 8th ed. 2007.
- [181] A. Antropoff, "The Solubilities in the ternary Systems Sodium Chloride - Sodium Hydroxide - Water and Potassium Chloride - Potassium Hydroxide - Water," *Z. Elektrochem. Angew. Phys. Chem.*, vol. 30, no. 19–20, pp. 457–467, 1924.
- [182] W. C. Blasdale, "Equilibria in solutions containing mixtures of salts. I—the system water and the sulfates and chlorides of sodium and potassium," *Ind. Eng. Chem.*, vol. 10, no. 5, pp. 344–347, 1918, doi: 10.1021/ie50101a006.
- [183] L. C. de Coppet, "Study on the solubility of chlorides, bromides and iodides of potassium and sodium," *Ann. Chim. Phys.*, vol. 30, no. 5, pp. 411–429, 1883.
- [184] K. Park, J. M. B. Evans, and A. S. Myerson, "Determination of Solubility of Polymorphs Using Differential Scanning Calorimetry," *Cryst. Growth Des.*, vol. 3, no. 6, pp. 991–995, 2003, doi: 10.1021/cg0340502.
- [185] C. Mack, J. Hoffmann, J. Sefcik, and J. H. ter Horst, "Phase Diagram Determination and Process Development for Continuous Antisolvent Crystallizations," *Crystals*, vol.

- 12, no. 8, p. 1102, 2022, doi: 10.3390/cryst12081102.
- [186] A. Kelly, W. R. Tyson, and A. H. Cottrell, "Ductile and brittle crystals," *Philos. Mag.*, vol. 15, no. 135, pp. 567–586, 1967, doi: 10.1080/14786436708220903.
- [187] T. L. Johnston, R. J. Stokes, and C. H. Li, "The ductile-brittle transition in ionic solids," *Philos. Mag.*, vol. 4, no. 48, pp. 1316–1324, 1959, doi: 10.1080/14786435908233367.
- [188] T. Rungsimanon, K. I. Yuyama, T. Sugiyama, H. Masuhara, N. Tohnai, and M. Miyata, "Control of crystal polymorph of glycine by photon pressure of a focused continuous wave near-infrared laser beam," *J. Phys. Chem. Lett.*, vol. 1, no. 3, pp. 599–603, 2010, doi: 10.1021/jz900370x.
- [189] A. Cashmore, C. J. Brown, M. Haw, M. Lee, H. Jolliffe, and J. Sefcik, "Assessment of the Secondary Nucleation and Growth Kinetics of α -Glycine," *Prep.*.
- [190] R. M. Ginde and A. S. Myerson, "Effect of impurities on cluster growth and nucleation," *J. Cryst. Growth*, vol. 126, no. 2–3, pp. 216–222, 1993, doi: 10.1016/0022-0248(93)90028-U.
- [191] A. Chianese, S. Di Cave, and B. Mazzarotta, "Solubility and metastable zone width of sodium chloride in water-diethylene glycol mixtures," *J. Chem. Eng. Data*, vol. 31, no. 3, pp. 329–332, 1986, doi: 10.1021/je00045a020.
- [192] M. Yousuf and P. J. Frawley, "Experimental Evaluation of Fluid Shear Stress Impact on Secondary Nucleation in a Solution Crystallization of Paracetamol," *Cryst. Growth Des.*, vol. 18, no. 11, pp. 6843–6852, 2018, doi: 10.1021/acs.cgd.8b01074.
- [193] P. Bharmoria, H. Gupta, V. P. Mohandas, P. K. Ghosh, and A. Kumar, "Temperature invariance of NaCl solubility in water: Inferences from salt-water cluster behavior of NaCl, KCl, and NH₄Cl," *J. Phys. Chem. B*, vol. 116, no. 38, pp. 11712–11719, 2012, doi: 10.1021/jp307261g.
- [194] A. W. C. Menzies, "A method of Solubility Measurement. Solubilities in the System SrCl₂-H₂O from 20 to 200°," *J. Am. Chem. Soc.*, vol. 58, no. 6, pp. 934–937, 1936, doi: 10.1021/ja01297a027.
- [195] M. V. C. Cardoso, L. V. C. Carvalho, and E. Sabadini, "Solubility of carbohydrates in heavy water," *Carbohydr. Res.*, vol. 353, pp. 57–61, 2012, doi: 10.1016/j.carres.2012.03.005.
- [196] W. A. Van Hook and L. P. N. Rebelo, "Isotope Effects on Solubility," in *Developments and Applications in Solubility*, T. M. Letcher, Ed., Royal Society of Chemistry, 2007.
- [197] A. Seidell, *Solubilities of inorganic and metal organic compounds: a compilation of quantitative solubility data from the periodical literature*. New York, NY: D. Van Nostrand Company, 1940.
- [198] Y. Zeng, Z. Li, and G. P. Demopoulos, "Phase equilibria for the glycine-methanol-NH₄Cl-H₂O system," *Ind. Eng. Chem. Res.*, vol. 53, no. 43, pp. 16864–16872, 2014, doi: 10.1021/ie502846m.
- [199] D. McKechnie, S. Anker, S. Zahid, P. A. Mulheran, J. Sefcik, and K. Johnston, "Interfacial Concentration Effect Facilitates Heterogeneous Nucleation from

- Solution," *J. Phys. Chem. Lett.*, vol. 11, no. 6, pp. 2263–2271, 2020, doi: 10.1021/acs.jpcllett.0c00540.
- [200] C. E. Hughes and K. D. M. Harris, "The effect of deuteration on polymorphic outcome in the crystallization of glycine from aqueous solution," *New J. Chem.*, vol. 33, no. 4, pp. 713–716, 2009, doi: 10.1039/b819199a.
- [201] D. M. Hudgins, C. W. Bauschlicher, and S. A. Sandford, "The Impact of Deuteration on the Infrared Spectra of Interstellar Polycyclic Aromatic Hydrocarbons," *Astrophys. J.*, vol. 614, no. 2, pp. 770–780, 2004, doi: 10.1086/423930.
- [202] S. Suzuki, T. Shimanouchi, and M. Tsuboi, "Normal vibrations of glycine and deuterated glycine molecules," *Spectrochim. Acta*, vol. 19, no. 7, pp. 1195–1208, 1963, doi: 10.1016/0371-1951(63)80040-5.
- [203] Z. Liu, L. Zhong, P. Ying, Z. Feng, and C. Li, "Crystallization of metastable β glycine from gas phase via the sublimation of α or γ form in vacuum," *Biophys. Chem.*, vol. 132, no. 1, pp. 18–22, 2008, doi: 10.1016/j.bpc.2007.10.003.
- [204] G. L. Perlovich, L. K. Hansen, and A. Bauer-Brandl, "The polymorphism of glycine: Thermochemical and structural aspects," *J. Therm. Anal. Calorim.*, vol. 66, no. 3, pp. 699–715, 2001, doi: 10.1023/A:1013179702730.
- [205] C. R. Groom, I. J. Bruno, M. P. Lightfoot, and S. C. Ward, "The Cambridge structural database," *Acta Crystallogr. Sect. B Struct. Sci. Cryst. Eng. Mater.*, vol. 72, no. 2, pp. 171–179, 2016, doi: 10.1107/S2052520616003954.
- [206] C. E. Hughes, S. Hamad, K. D. M. Harris, C. R. A. Catlow, and P. C. Griffiths, "A multi-technique approach for probing the evolution of structural properties during crystallization of organic materials from solution," *Faraday Discuss.*, vol. 136, pp. 71–89, 2007, doi: 10.1039/b616611c.
- [207] S. A. Speakman, "Introduction to X-Ray Powder Diffraction Data Analysis." [http://prism.mit.edu/xray/introduction to xrpd data analysis.pdf](http://prism.mit.edu/xray/introduction%20to%20xrpd%20data%20analysis.pdf) (accessed Jun. 23, 2023).
- [208] X. Yang, J. Lu, X. J. Wang, and C. B. Ching, "Effect of sodium chloride on the nucleation and polymorphic transformation of glycine," *J. Cryst. Growth*, vol. 310, no. 3, pp. 604–611, 2008, doi: 10.1016/j.jcrysgr.2007.11.072.
- [209] N. E. R. Zimmermann, B. Vorselaars, D. Quigley, and B. Peters, "Nucleation of NaCl from Aqueous Solution: Critical Sizes, Ion-Attachment Kinetics, and Rates," *J. Am. Chem. Soc.*, vol. 137, no. 41, pp. 13352–13361, 2015, doi: 10.1021/jacs.5b08098.
- [210] H. Jiang, A. Haji-Akbari, P. G. Debenedetti, and A. Z. Panagiotopoulos, "Forward flux sampling calculation of homogeneous nucleation rates from aqueous NaCl solutions," *J. Chem. Phys.*, vol. 148, no. 4, 2018, doi: 10.1063/1.5016554.
- [211] G. Lanaro and G. N. Patey, "Molecular dynamics simulation of NaCl dissolution," *J. Phys. Chem. B*, vol. 119, no. 11, pp. 4275–4283, 2015, doi: 10.1021/jp512358s.
- [212] H. S. Na, S. Arnold, and A. S. Myerson, "Cluster formation in highly supersaturated solution droplets," *J. Cryst. Growth*, vol. 139, no. 1–2, pp. 104–112, 1994, doi: 10.1016/0022-0248(94)90034-5.

- [213] Y. Gao, L. E. Yu, and S. B. Chen, "Efflorescence relative humidity of mixed sodium chloride and sodium sulfate particles," *J. Phys. Chem. A*, vol. 111, no. 42, pp. 10660–10666, 2007, doi: 10.1021/jp073186y.
- [214] N. E. R. Zimmermann *et al.*, "NaCl nucleation from brine in seeded simulations: Sources of uncertainty in rate estimates," *J. Chem. Phys.*, vol. 148, no. 22, 2018, doi: 10.1063/1.5024009.
- [215] M. L. Briuglia, "Primary and Secondary Crystal Nucleation of Pharmaceuticals," University of Strathclyde, 2017.
- [216] I. Sanchez-Burgos and J. R. Espinosa, "Direct calculation of the planar NaCl-aqueous solution interfacial free energy at the solubility limit," *Phys. Rev. Lett.*, vol. 130, no. 11, p. 118001, 2022, doi: 10.1103/PhysRevLett.130.118001.
- [217] J. Ulrich, "Growth rate dispersion — a review," *Cryst. Res. Technol.*, vol. 24, no. 3, pp. 249–257, 1989, doi: 10.1002/crat.2170240302.
- [218] F. J. Millero, R. Dexter, and E. Hoff, "Density and Viscosity of Deuterium Oxide Solutions from 5–70° C," *J. Chem. Eng. Data*, vol. 16, no. 1, pp. 85–87, 1971, doi: 10.1021/je60048a006.
- [219] R. Dowling *et al.*, "Acceleration of crystal growth rates: An unexpected effect of tailor-made additives," *Chem. Commun.*, vol. 46, no. 32, pp. 5924–5926, 2010, doi: 10.1039/c0cc00336k.
- [220] L. D. Shiau, "Determination of the nucleation and growth kinetics for aqueous L-glycine solutions from the turbidity induction time data," *Crystals*, vol. 8, no. 11, 2018, doi: 10.3390/cryst8110403.
- [221] S. B. Zhang, J. J. Yuan, H. A. Mohameed, and J. Ulrich, "The effect of different inorganic salts on the growth rate of NaCl crystallized from sea water," *Cryst. Res. Technol.*, vol. 31, no. 1, pp. 19–25, 1996, doi: 10.1002/crat.2170310105.
- [222] H. Offermann, G. Von Brachel, A. Al-Sabbagh, and F. Farelo, "Crystallization Kinetics of NaCl in Multicomponent Solutions," *Cryst. Res. Technol.*, vol. 30, no. 5, pp. 651–658, 1995, doi: 10.1002/crat.2170300511.
- [223] S. Al-Jibbouri and J. Ulrich, "The growth and dissolution of sodium chloride in a fluidized bed crystallizer," *J. Cryst. Growth*, vol. 234, no. 1, pp. 237–246, 2002, doi: 10.1016/S0022-0248(01)01656-6.
- [224] J. Desarnaud, H. Derluyn, J. Carmeliet, D. Bonn, and N. Shahidzadeh, "Hopper Growth of Salt Crystals," *J. Phys. Chem. Lett.*, vol. 9, no. 11, pp. 2961–2966, 2018, doi: 10.1021/acs.jpcclett.8b01082.
- [225] C. J. Brown *et al.*, "Enabling precision manufacturing of active pharmaceutical ingredients: workflow for seeded cooling continuous crystallisations," *Mol. Syst. Des. Eng.*, vol. 3, no. 3, pp. 518–549, 2018, doi: 10.1039/c7me00096k.
- [226] Y. Tominaga *et al.*, "Promotion of protein crystal growth by actively switching crystal growth mode via femtosecond laser ablation," *Nat. Photonics*, vol. 10, no. 11, pp. 723–726, 2016, doi: 10.1038/nphoton.2016.202.
- [227] S. A. Schiele, R. Hupfer, F. Luxenburger, and H. Briesen, "Growth of Abraded Crystals

- Tracked in Three Dimensions,” *Cryst. Growth Des.*, vol. 21, no. 11, pp. 6373–6384, 2021, doi: 10.1021/acs.cgd.1c00849.
- [228] S. Y. Wong, Y. Cui, and A. S. Myerson, “Contact secondary nucleation as a means of creating seeds for continuous tubular crystallizers,” *Cryst. Growth Des.*, vol. 13, no. 6, pp. 2514–2521, 2013, doi: 10.1021/cg4002303.
- [229] B. G. Lakatos and B. Szilágyi, “Modeling Crystallization from Solution with Heat Effects,” *Cryst. Growth Des.*, vol. 15, no. 12, pp. 5726–5737, 2015, doi: 10.1021/acs.cgd.5b00863.
- [230] T. Sugiyama, T. Adachi, and H. Masuhara, “Crystal growth of glycine controlled by a focused CW near-infrared laser beam,” *Chem. Lett.*, vol. 38, no. 5, pp. 482–483, 2009, doi: 10.1246/cl.2009.482.
- [231] J. Ulrich, H. Mohameed, S. B. Zhang, and J. J. Yuan, “Effect of Additives on the Crystal Growth Rates : Case Study NaCl,” *Bull. Soc. Sea Water Sci. Japan*, vol. 51, no. 2, pp. 73–77, 1997, doi: 10.11457/swsj1965.51.73.
- [232] K. I. Yuyama, K. Ishiguro, T. Sugiyama, and H. Masuhara, “Laser trapping dynamics of L-alanine depending on the laser polarization,” *Opt. Trapp. Opt. Micromanipulation IX*, vol. 8458, p. 84582D, 2012, doi: 10.1117/12.929381.
- [233] A. Franzen, “ComponentLibrary,” 2006. <http://www.gwoptics.org/ComponentLibrary/> (accessed Aug. 30, 2022).
- [234] R. J. Good and C. J. van Oss, “The modern theory of contact angles and the hydrogen bond components of surface energies,” in *Modern Approach to Wettability: Theory and Applications*, M. E. Schrader and G. I. Loeb, Eds., New York: Springer, 1992.
- [235] P. C. Rieke, “Application of Van Oss-Chaudhury-Good theory of wettability to interpretation of interfacial free energies of heterogeneous nucleation,” *J. Cryst. Growth*, vol. 182, no. 3–4, pp. 472–484, 1997, doi: 10.1016/S0022-0248(97)00357-6.
- [236] M. H. Derkani, “Understanding colloidal interactions at oil/rock/brine interfaces,” University of Strathclyde, 2019.
- [237] Y. Sun and A. J. Alexander, “Mechanical shock-induced nucleation in solution: Is cavitation necessary?,” *J. Cryst. Growth*, vol. 594, no. July, p. 126786, 2022, doi: 10.1016/j.jcrysgro.2022.126786.
- [238] M. R. Ward and A. J. Alexander, “Nonphotochemical laser-induced nucleation of potassium halides: Effects of wavelength and temperature,” *Cryst. Growth Des.*, vol. 12, no. 9, pp. 4554–4561, 2012, doi: 10.1021/cg300750c.
- [239] E. Tokunaga, T. Yamamoto, E. Ito, and N. Shibata, “Understanding the Thalidomide Chirality in Biological Processes by the Self-disproportionation of Enantiomers,” *Sci. Rep.*, vol. 8, no. 1, pp. 6–12, 2018, doi: 10.1038/s41598-018-35457-6.
- [240] S. F. Wang and T. Sugiyama, “Femtosecond laser-driven enantioselectivity on achiral-chiral polymorphic transition,” *Cell Reports Phys. Sci.*, vol. 4, no. 3, p. 101323, 2023, doi: 10.1016/j.xcrp.2023.101323.
- [241] E. C. Noonan, “Solubility of Salts in Deuterium Oxide,” *J. Am. Chem. Soc.*, vol. 70, no. 9, pp. 2915–2918, 1948, doi: 10.1021/ja01189a026.

- [242] K. Toyoda, H. T. Su, K. Miyamoto, T. Sugiyama, and T. Omatsu, "Chiral crystallization manipulated by orbital angular momentum of light," *Optica*, vol. 10, no. 3, p. 332, 2023, doi: 10.1364/optica.478042.
- [243] A. V. Sugonyako, D. I. Vainshtein, A. A. Turkin, H. W. Den Hartog, and A. A. Bukharaev, "Melting of sodium clusters in electron irradiated NaCl," *J. Phys. Condens. Matter*, vol. 16, no. 6, pp. 785–798, 2004, doi: 10.1088/0953-8984/16/6/009.
- [244] G. Ren and Y. Wang, "Reversible transient nucleation in ionic solutions as the precursor of ion crystallization," *Epl*, vol. 107, no. 3, 2014, doi: 10.1209/0295-5075/107/30005.
- [245] N. Sivakumar, V. Jayaramakrishnan, K. Baskar, and G. Anbalagan, "Synthesis, growth and characterization of γ -glycine - A promising material for optical applications," *Opt. Mater. (Amst.)*, vol. 37, no. C, pp. 780–787, 2014, doi: 10.1016/j.optmat.2014.09.007.
- [246] H. H. Li, "Refractive index of alkali halides and its wavelength and temperature derivatives," *J. Phys. Chem. Ref. Data*, vol. 5, no. 2, pp. 329–528, 1976, doi: 10.1063/1.555536.
- [247] A. J. Alexander and P. J. Camp, "Single pulse, single crystal laser-induced nucleation of potassium chloride," *Cryst. Growth Des.*, vol. 9, no. 2, pp. 958–963, 2009, doi: 10.1021/cg8007415.
- [248] Y. Wu, A. Kirillov, F. Massa, W. Y. Lo, and R. Girshick, "Detectron2," 2019. <https://github.com/facebookresearch/detectron2>
- [249] J. Garside and R. I. Ristić, "Growth rate dispersion among ADP crystals formed by primary nucleation," *J. Cryst. Growth*, vol. 61, no. 2, pp. 215–220, 1983, doi: 10.1016/0022-0248(83)90357-3.
- [250] C. N. Banwell, *Fundamentals of Molecular Spectroscopy*, 3rd ed. London: McGraw-Hill, 1983.
- [251] Nikon Europe B.V., "Objective Comparison." https://www.microscope.healthcare.nikon.com/en_EU/selectors/objective-comparison/-87014 (accessed Aug. 17, 2021).
- [252] K. He, G. Gkioxari, P. Dollár, and R. Girshick, "Mask R-CNN," 2017, doi: arXiv.1703.06870.
- [253] T. Y. Lin *et al.*, "Microsoft COCO: Common Objects in Context," 2014.

Appendix A Personal Outputs

A.1 Events Attended

CMAC Open Day, Virtual, Poster, An investigation of secondary nucleation at the microscale using optical tweezing, 21 October 2020 – 22 October 2020

British Crystallographic Association / British Association for Crystal Growth Joint Spring Meeting, Virtual, Poster, Primary Nucleation of Sodium Chloride from Water and Deuterium Oxide under Isothermal Agitated Conditions, 29 March 2021– 1 April 2021

CMAC Mini-Symposium– Drug Substances, Virtual, Poster, Primary Nucleation of Sodium Chloride from Water and Deuterium Oxide under Isothermal Agitated Conditions, 14 June 2021

21st International Symposium on Industrial Crystallization, Virtual, Poster, Primary and Secondary Nucleation of Sodium Chloride from Water and Deuterium Oxide, 30 August 2021– 2 September 2021

Strathclyde Chemical and Process Engineering Research Celebration Event, Glasgow; UK, Presentation, Primary and Secondary Nucleation of Sodium Chloride from Water and Deuterium Oxide, 24 November 2021

EPSRC CMAC Open Days & ARTICULAR Showcase, Glasgow; UK, Poster, Investigating Crystal Nucleation and Growth under the influence of Optical Tweezers, 16 May 2022 – 18 May 2022

EPSRC CMAC Summer School, Crieff; UK, Poster, Investigating Crystal Nucleation and Growth under the influence of Optical Tweezers, 14 June 2022 – 17 June 2022

British Association for Crystal Growth Annual Conference, Virtual, Presentation, Crystal Nucleation from Solution Induced by Optical Tweezers, 28 June 2022

A.2 Papers

I.A. Principe, B. Murdoch, **J.M. Flannigan**, A.J. Fletcher. *Decoupling microporosity and nitrogen content to optimize CO₂ adsorption in melamine–resorcinol–formaldehyde xerogels*.

Materials Today Chemistry, 10:195-205, 2018. DOI: 10.1016/j.mtchem.2018.09.006

J. Hoffmann, **J. Flannigan**, A. Cashmore, M.L. Briuglia, R.R.E. Steendam C.J.J. Gerard, M.D. Haw, J. Sefcik, J.H. ter Horst. *The Unexpected Dominance of Secondary over Primary Nucleation*. *Faraday Discussions*, 235:109-131, 2022. DOI: 10.1039/D1FD00098E

A. Cashmore, **J.M. Flannigan**, D. Innes, A. Manson, M. Lee, M.D. Haw, J. Sefcik. *High-Temperature Solubility Measurements, including the Binary Solution Triple Point*. In Preparation.

J.M. Flannigan, D. MacIver, H. Jolliffe M.D. Haw, J. Sefcik. *Nucleation and Growth in Isothermal Crystallization of Sodium Chloride from Water and Deuterium Oxide*. In Preparation.

O.H. Olalere, **J.M. Flannigan**, M.D. Haw, J. Sefcik, J.H. ter Horst. *Template Enhanced Induction Time Probability Distribution Measurements using Temperature Probes*. In Preparation.

J.M. Flannigan, J. Sefcik, M.D. Haw. *Nucleation of Glycine from Aqueous Solution using Optical Tweezers in proximity to the edge of sessile droplets*. In Preparation.

Appendix B COVID-19 Impact Statement

Even though the impact of COVID-19 has been worldwide, the impacts that this had on my research are detailed in this section.

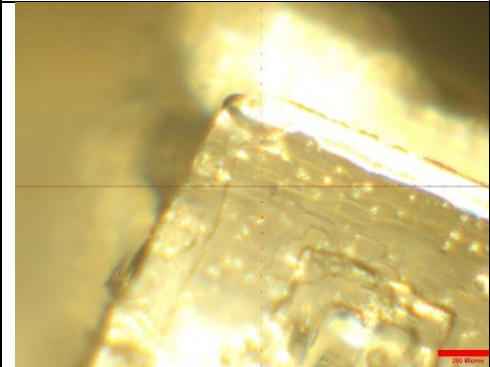
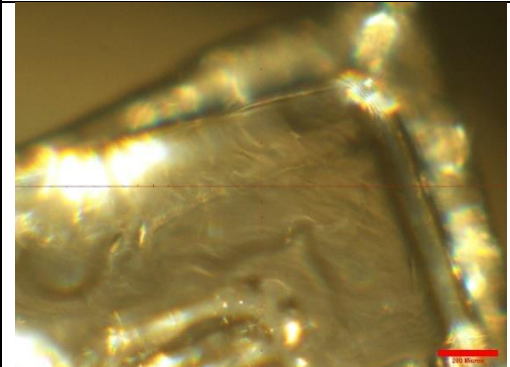
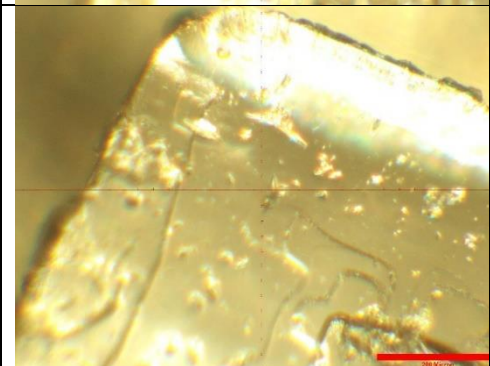
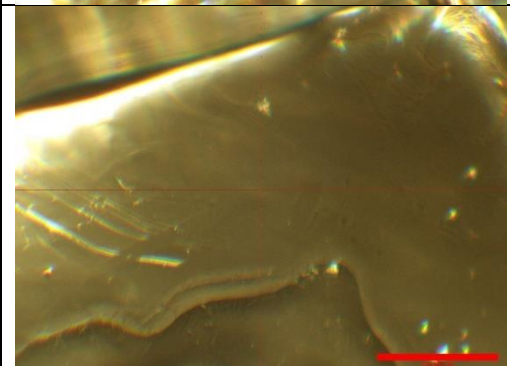
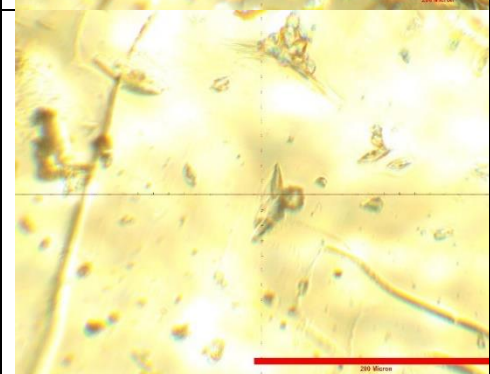
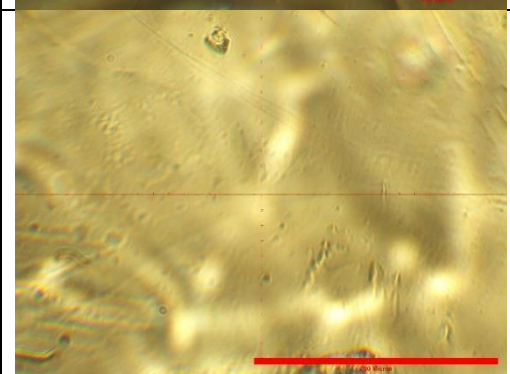
The United Kingdom first went into lockdown in March 2020. Like elsewhere, the University of Strathclyde closed. Access to the laboratory was regained in the final quarter of 2020. Due to my project's experimental nature, this time was lost and resulted in unavoidable setbacks. Although I was the only user of the Optical Tweezers for a considerable proportion of the time of my project, these were in a shared space that was subject to a maximum occupancy of one. Therefore, time in this space had to be divided equitably before the implications of officially imposed restrictions.

Time in the lab was also required to be booked in advance, and the inability to use office space within the University for a Large Proportion of the time during which restrictions were enforced. Even when access to the office space was regained, the time permitted was required to be pre-booked and, in effect, rationed.

All of this, taken together, resulted in a drastic reduction in my ability to undertake work, resulting in a less comprehensive dataset than I would have been otherwise able to produce.

Appendix C Images of Washed Seeds

C.1 Seeds Washed in H₂O

| Magnification | Before Immersion | Following 1 s Immersion |
|---------------|---|--|
| 5x |  |  |
| 10x |  |  |
| 20x |  |  |

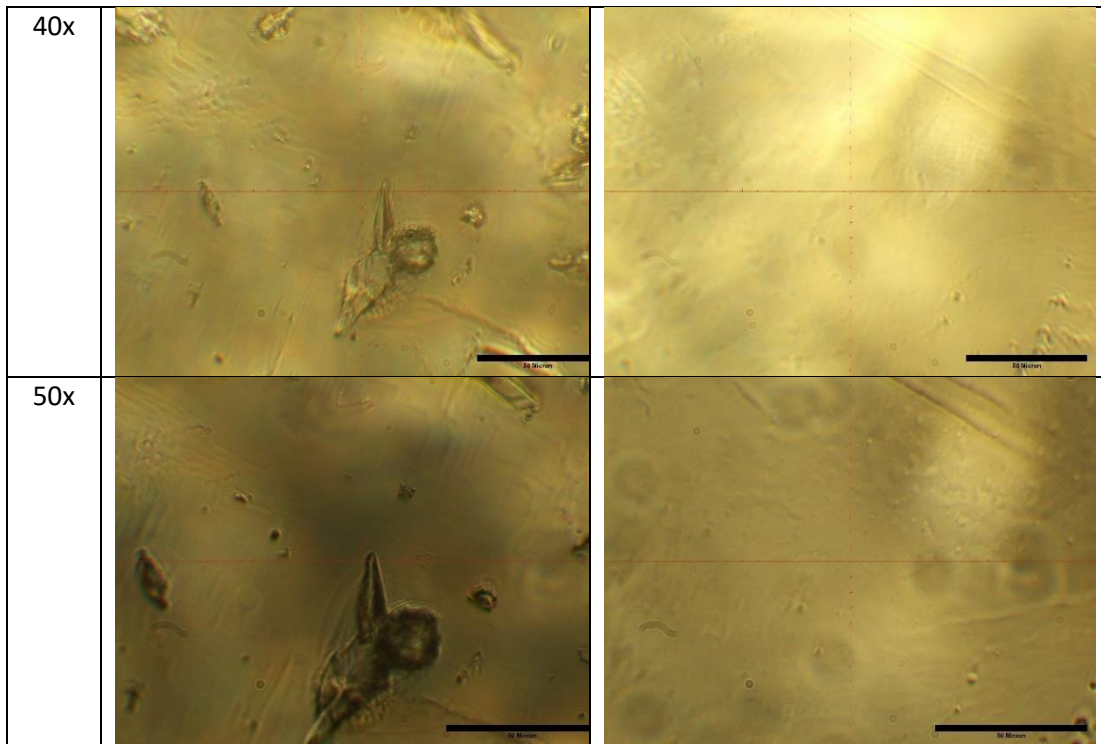
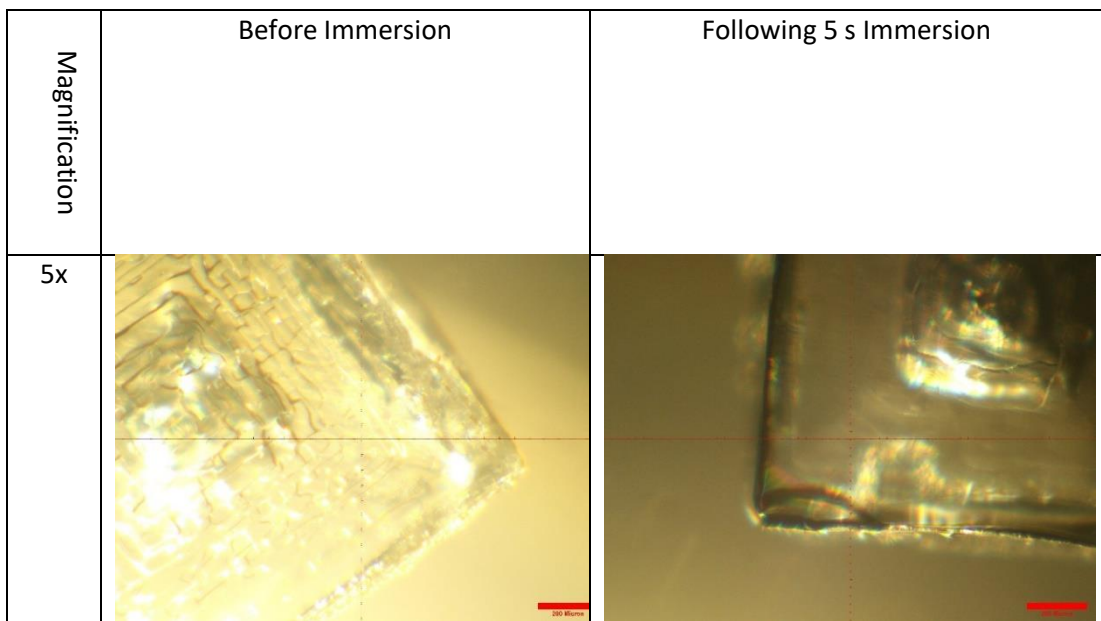


Figure C:1: Impact of Quiescent Immersion Washing in H₂O for 1 second.



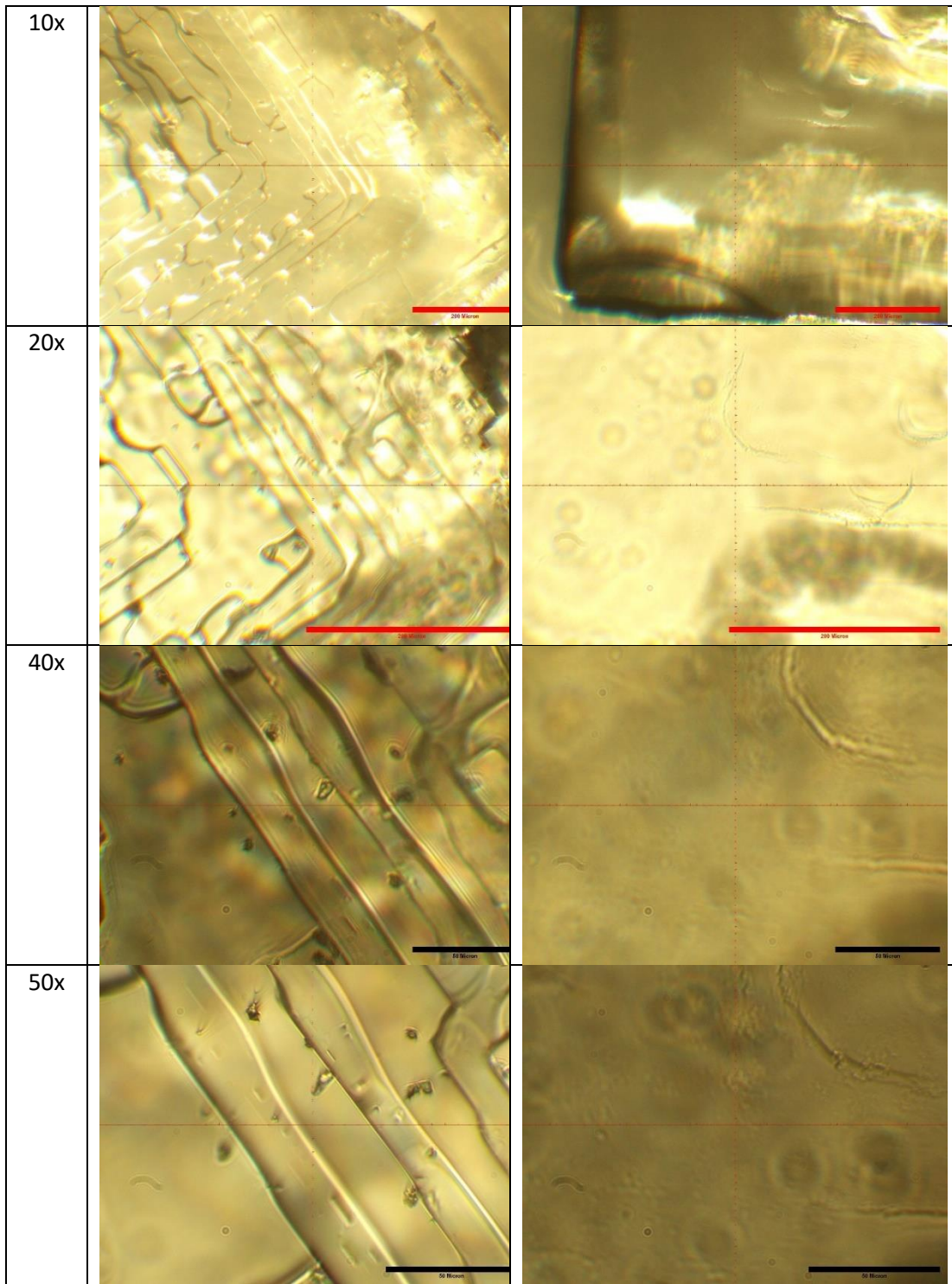

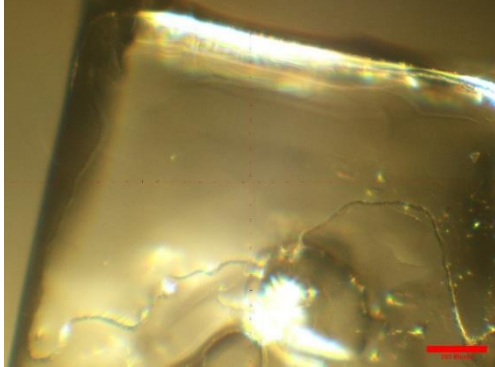
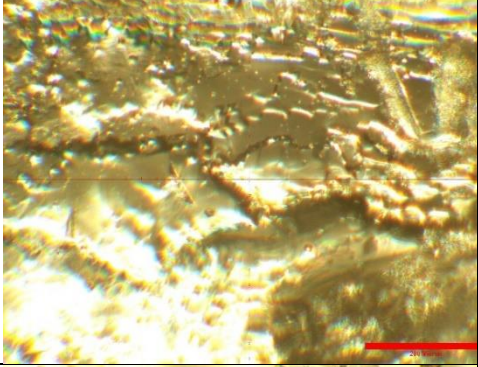
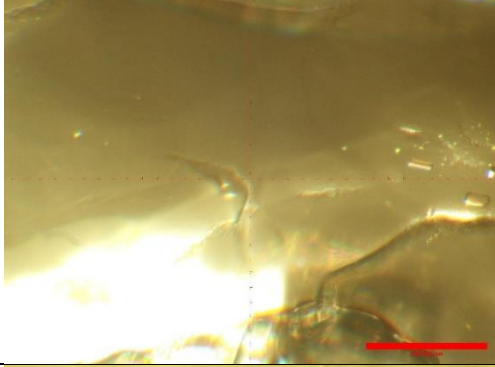
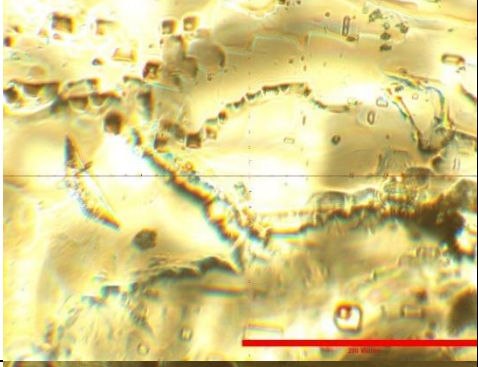
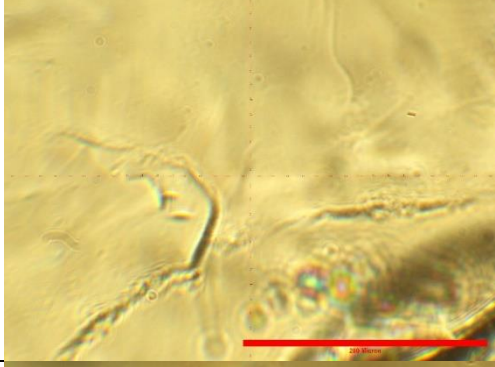
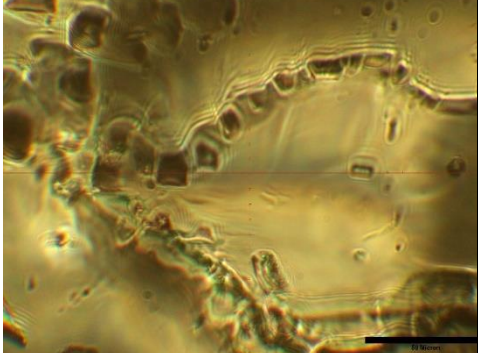
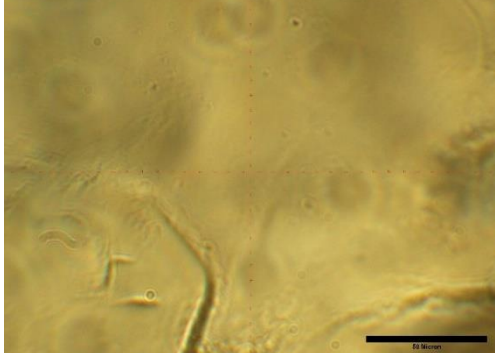


Figure C:2: Impact of Quiescent Immersion Washing in H₂O for 5 seconds.

| Magnification | Before Immersion | Following 10 s Immersion |
|---------------|---|--|
| 5x |  |  |
| 10x |  |  |
| 20x |  |  |
| 40x |  |  |

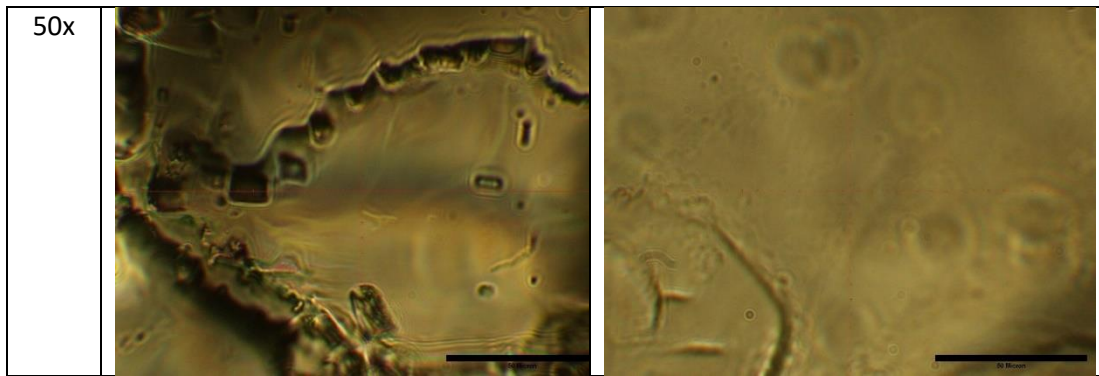
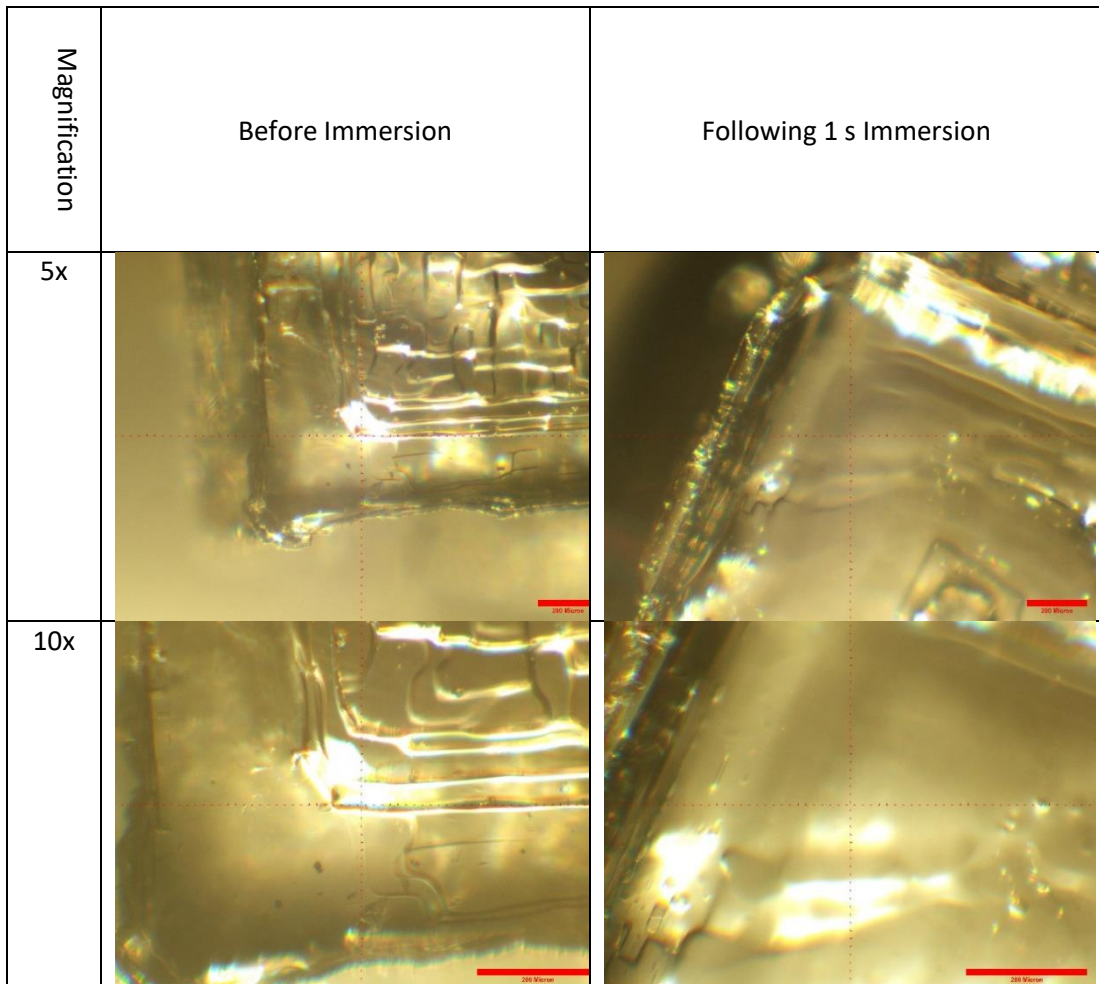


Figure C:3: Impact of Quiescent Immersion Washing in H₂O for 10 seconds.

C.2 Seeds Washed in D₂O



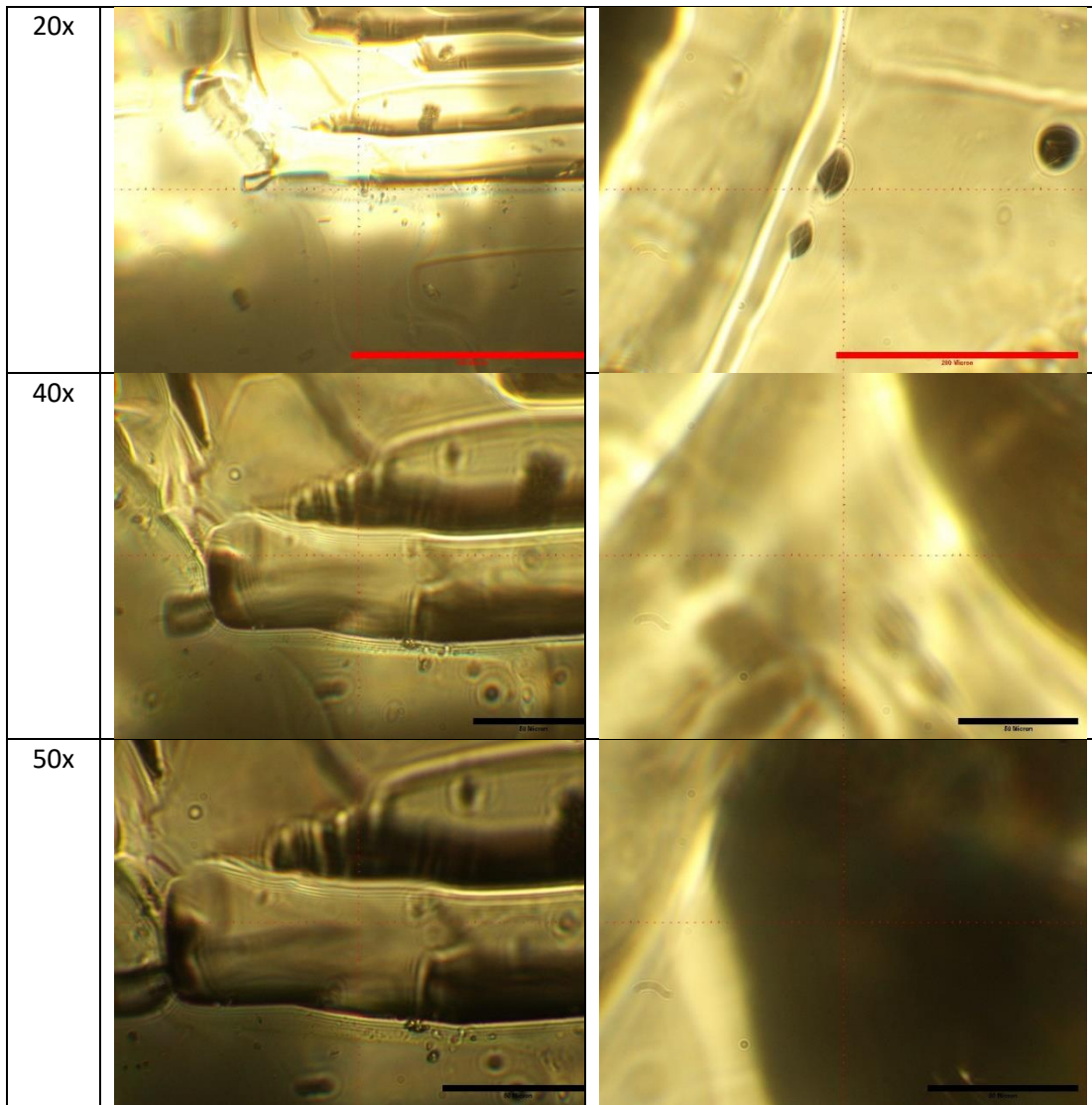
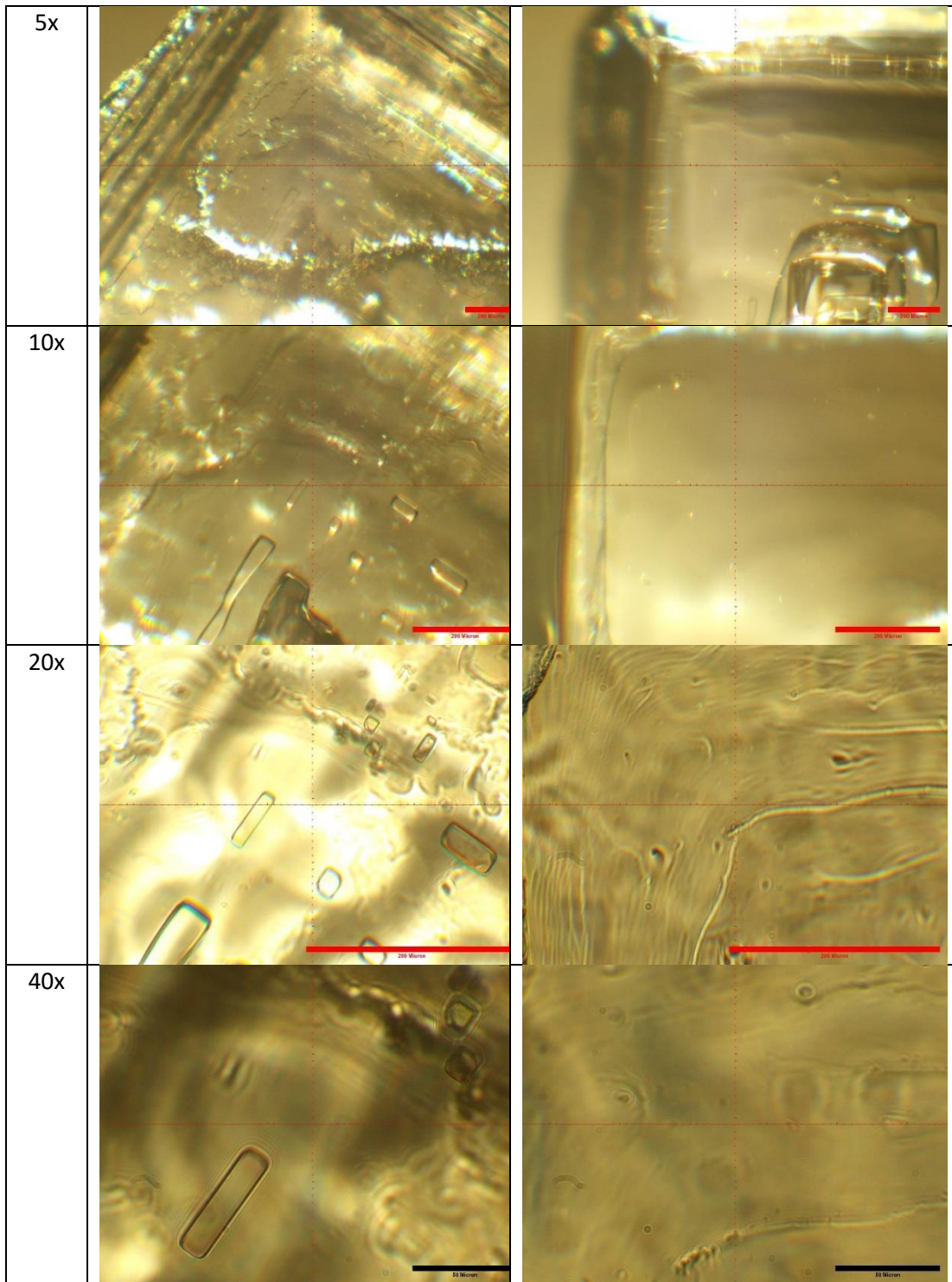


Figure C:4: Impact of Quiescent Immersion Washing in D_2O for 1 second.

| | | |
|---------------|------------------|-------------------------|
| Magnification | Before Immersion | Following 5 s Immersion |
|---------------|------------------|-------------------------|



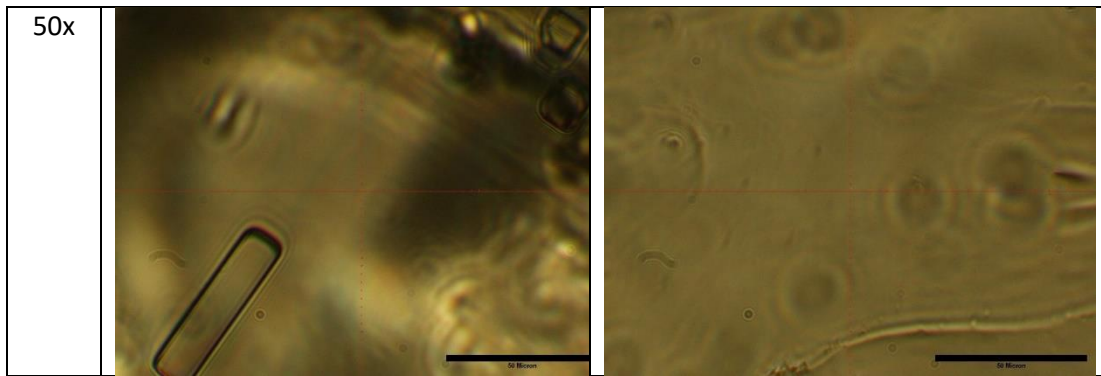


Figure C:5: Impact of Quiescent Immersion Washing in D_2O for 5 seconds.

| Magnification | Before Immersion | Following 10 s Immersion |
|---------------|------------------|--------------------------|
| 5x | | |
| 10x | | |

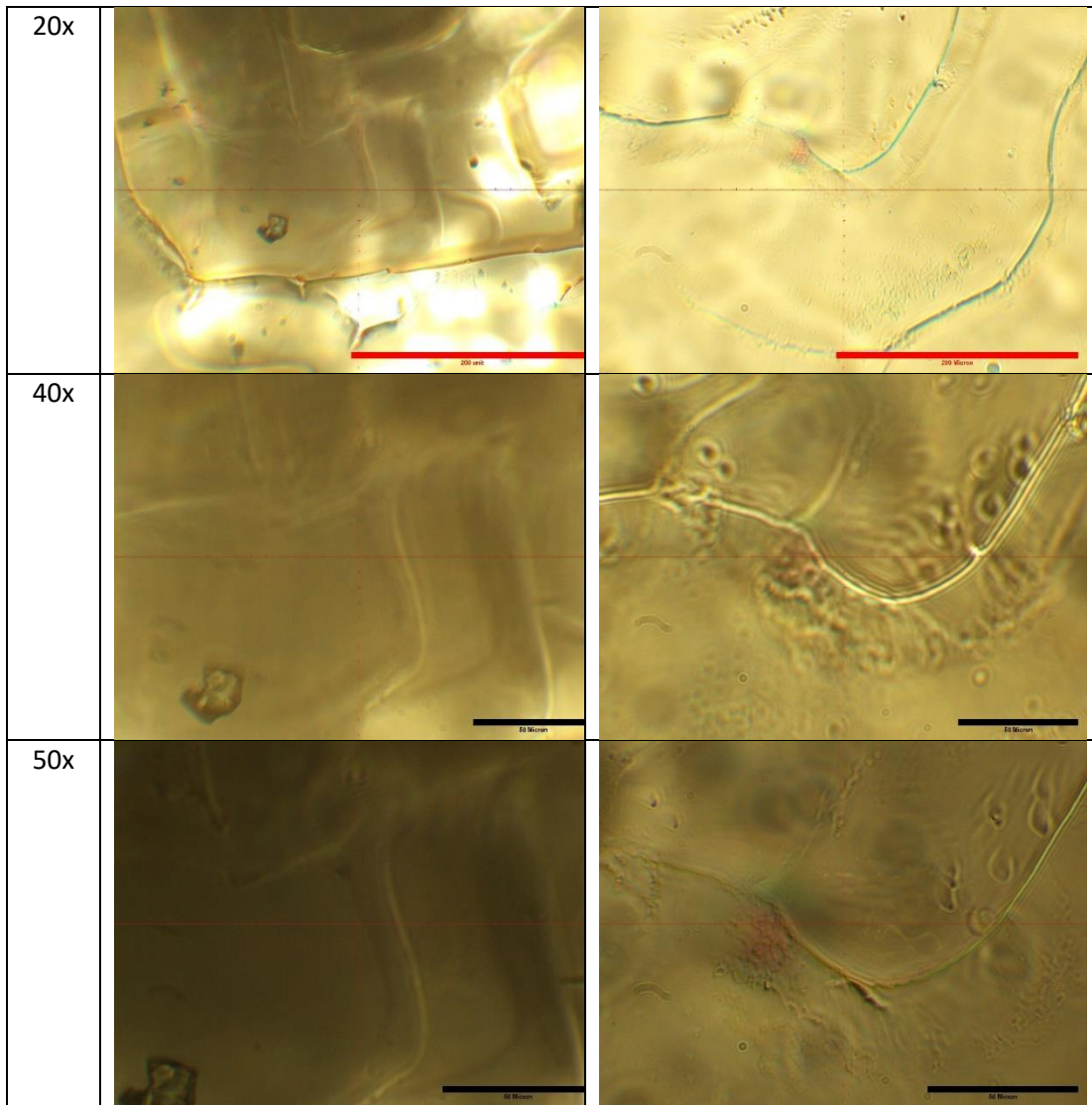


Figure C:6: Impact of Quiescent Immersion Washing in D_2O for 10 seconds.

Appendix D Crystalline Particle Number and Size Distribution Examples

This appendix contains examples of the raw particle numbers (Figure D:1), the converted particle concentration (Figure D:2) and the determined D-90 (Figure D:3) for the distribution of NaCl over the time of the experiment when a washed seed was placed into an $S = 1.01$ solution in H_2O . This was used to calculate the secondary nucleation rate and the growth rate.

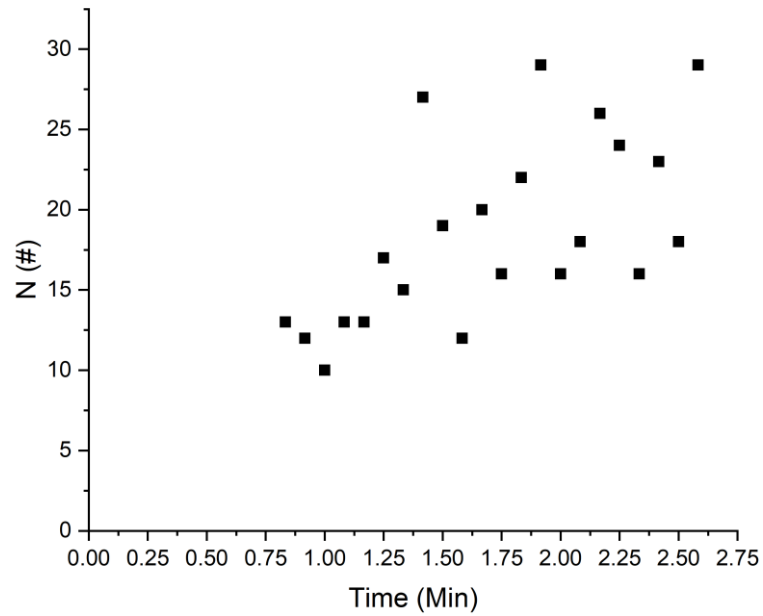


Figure D:1: Example of the number of particles visible in images captured by a Crystalline camera. Example from a seeded experiment using an $S = 1.01$ solution in H_2O , agitated using an overhead propeller at 1250 RPM. Time from the beginning of isothermal conditions.

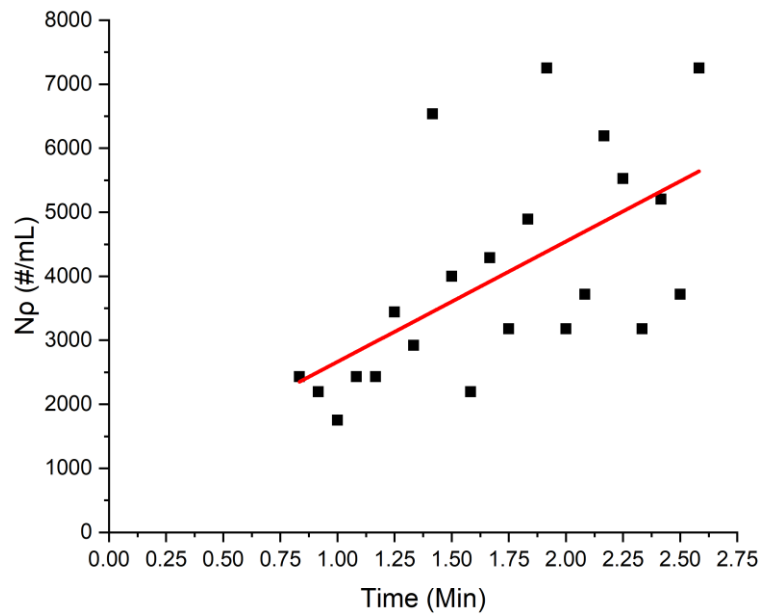


Figure D:2: Calculated number concentration of particles in suspension calculated from the number of particles imaged. Example from a seeded experiment using an $S = 1.01$ solution in H_2O , agitated using an overhead propeller at 1250 RPM. The linear fit of points is also shown. Time from the beginning of isothermal conditions.

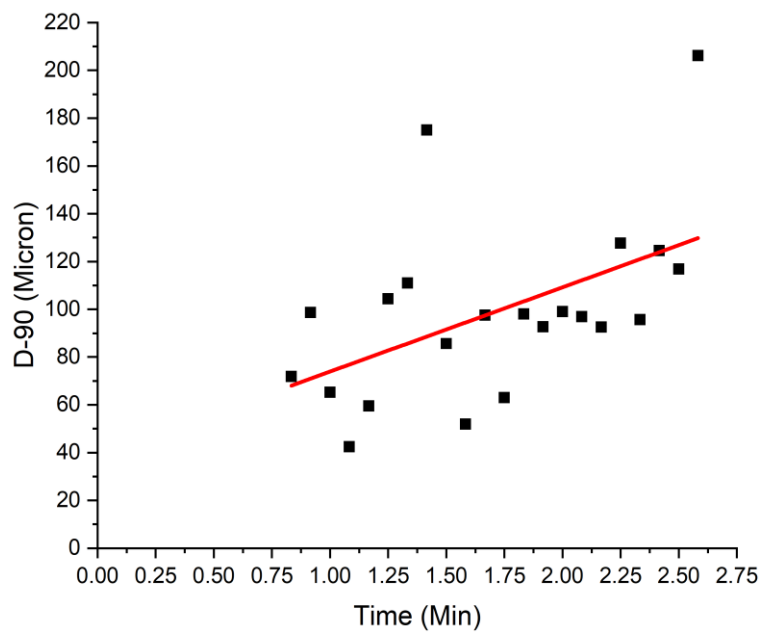


Figure D:3: Calculated D_{-90} from binned particle distributions as determined from the images taken by the internal Crystalline reactor camera. Example from a seeded experiment using an $S = 1.01$ solution in H_2O , agitated using an overhead propeller at 1250 RPM. Linear fit of points is also shown. Time from the beginning of isothermal conditions.

Appendix E Machine Learning Workspace

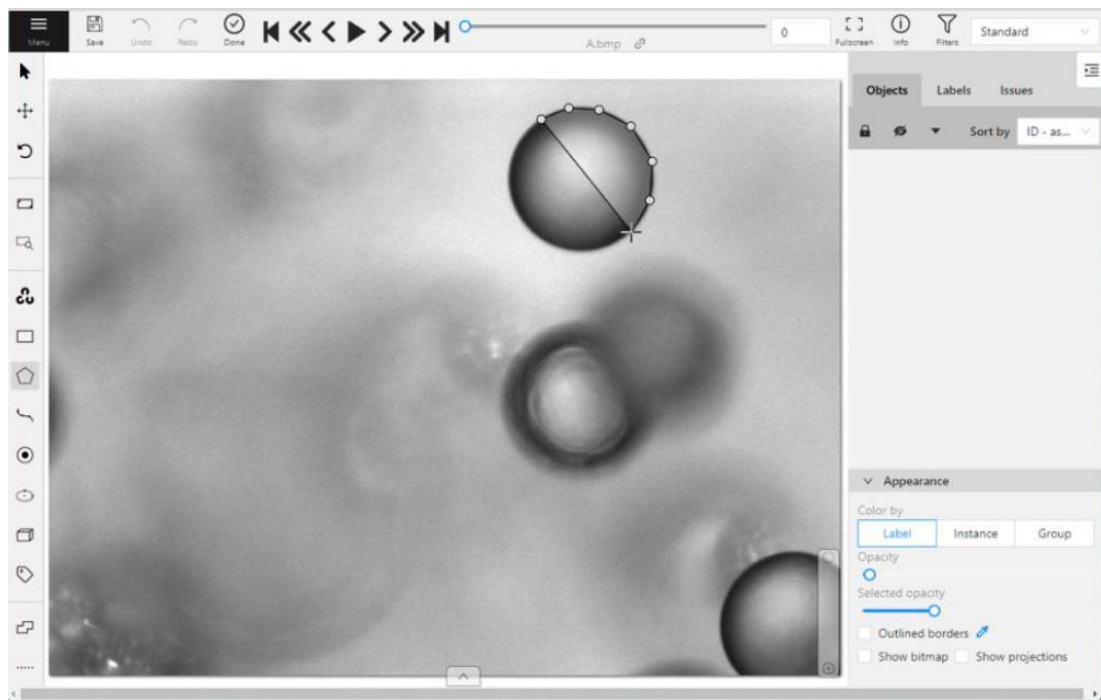


Figure E:1: Example of the machine learning workspace used CVAT, where an example of a spherical particle is midway through being outlined by the user to allow it to be identified by the algorithm.

Appendix F Alternative Frequency Distributions of Nucleation from Solution.

As mentioned in the main body of the thesis, there are several cumulative frequency distributions when examining the nucleation from solution in H₂O and D₂O. Non-conditional versions of the cumulative frequency distributions of the graphs shown in sections 6.3.1 and 7.3.2 are shown here in sections F.1.1 and F.1.2, respectively.

F.1 Cumulative Probability Distributions

F.1.1 Nucleation of NaCl from H₂O and D₂O

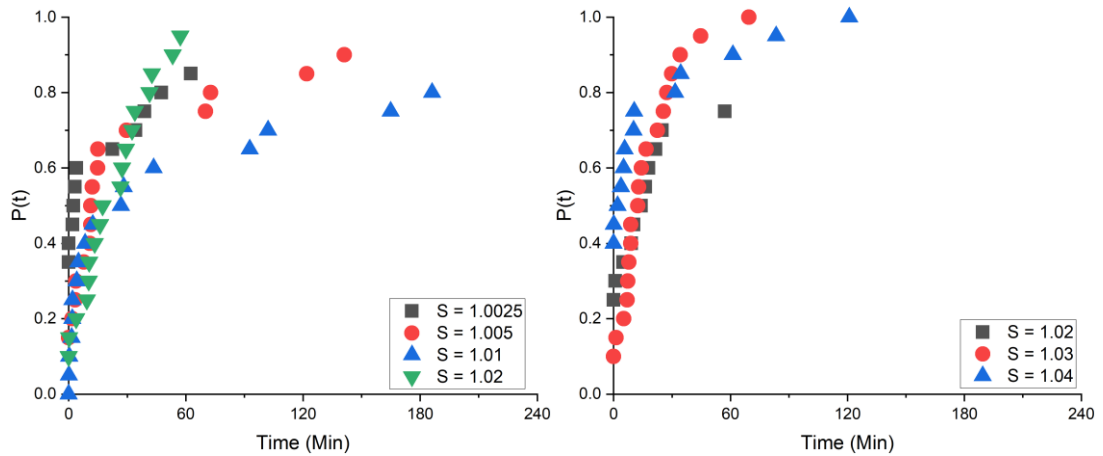


Figure F:1: Left; Cumulative Probability Distribution Plot of Induction Time Measurements of NaCl in Water, agitated using a stirrer bar at 700 RPM at S between 1.0025 and 1.02. Right; Cumulative Probability Distribution Plot of Induction Time Measurements of NaCl in Deuterium Oxide agitated using a stirrer bar at 700 RPM at S between 1.02 and 1.04.

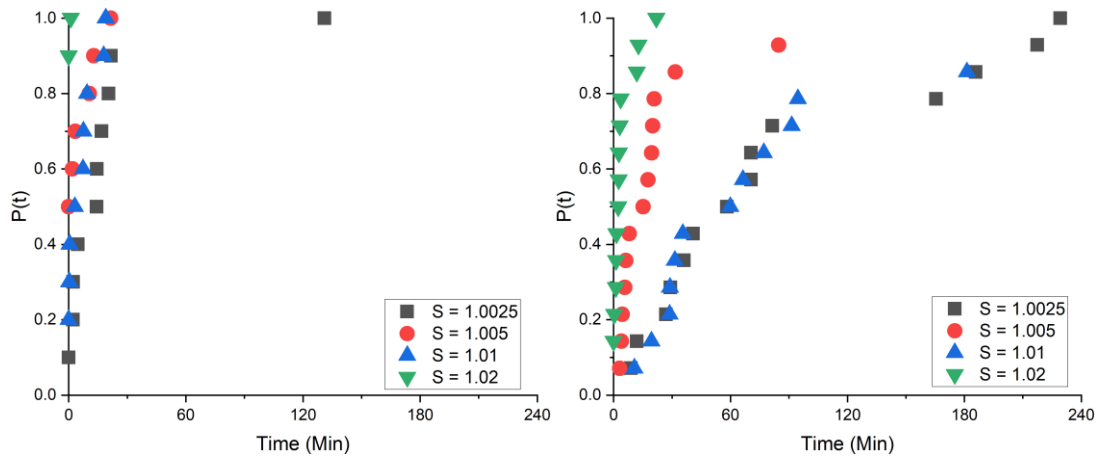


Figure F-2: Left; Cumulative Probability Distribution Plot of Induction Time Measurements of NaCl in Water, agitated using a stirrer bar at 700 RPM at S between 1.0025 and 1.02. Right; Cumulative Probability Distribution Plot of Induction Time Measurements of NaCl in Deuterium Oxide agitated using a stirrer bar at 700 RPM at S between 1.0025 and 1.02.

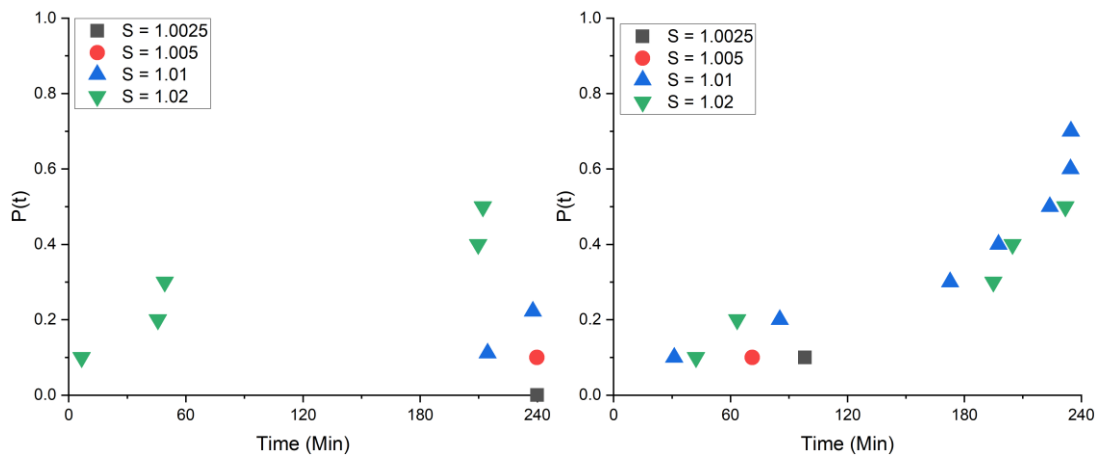


Figure F-3: Cumulative Probability Distribution Plot of Induction Time Measurements of NaCl in Water, agitated using an overhead propeller at 1250 RPM at S between 1.0025 and 1.02. Right; Cumulative Probability Distribution Plot of Induction Time Measurements of NaCl in Deuterium Oxide agitated using an overhead propeller at 1250 RPM at S between 1.0025 and 1.02.

F.1.2 Effect of Microparticles on Induction Time Distributions

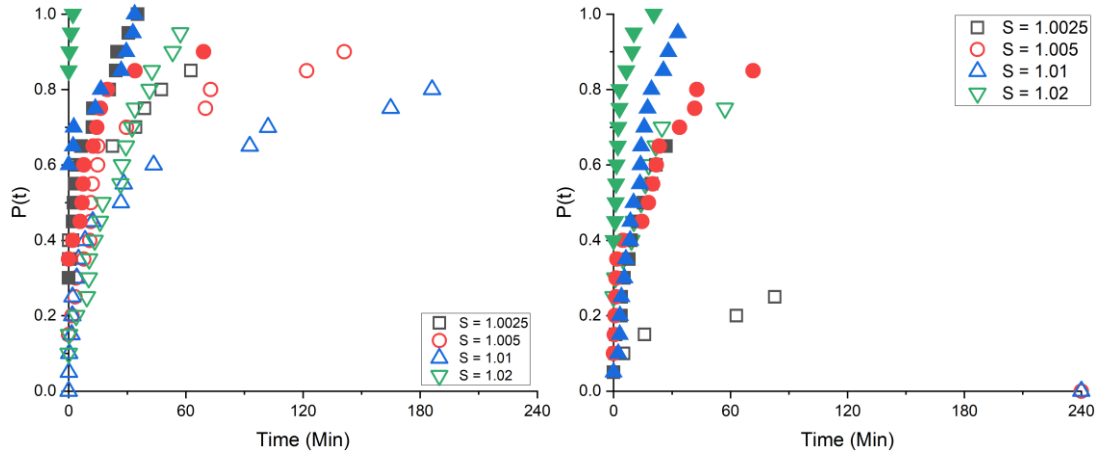


Figure F.4: Cumulative Probability Distribution Plot of Induction Times of NaCl in H_2O , agitated using a stirrer bar at 700 RPM at S between 1.0025 and 1.02. Pure Solution (Hollow Symbols), $0.12 \text{ mg}_{\text{silica}}/\text{g}_{\text{water}}$ dispersion (Filled Symbols). Right; Cumulative Probability Distribution Plot of Induction Times of NaCl in D_2O agitated using a stirrer bar at 700 RPM at S between 1.0025 and 1.02. Pure Solution (Hollow Symbols), $0.12 \text{ mg}_{\text{silica}}/\text{g}_{\text{deuterium oxide}}$ dispersion (Filled Symbols).

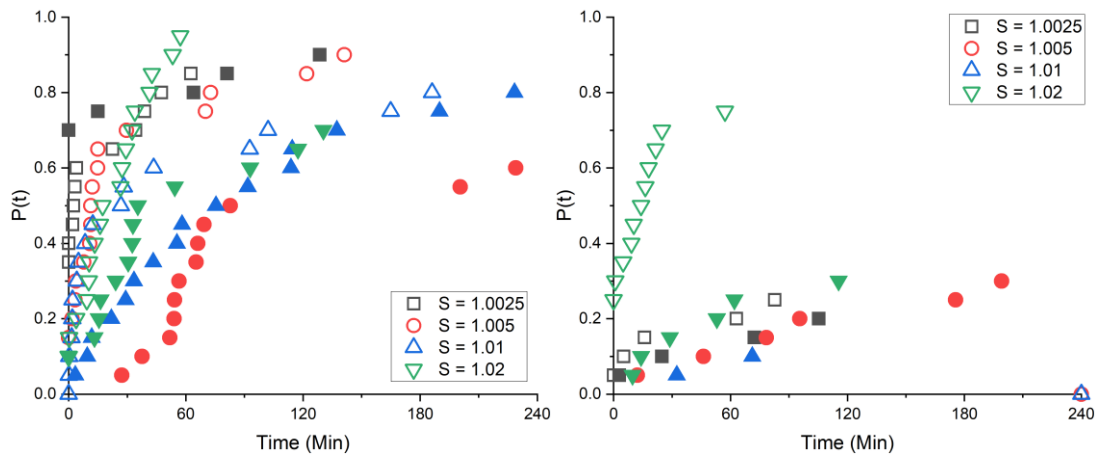


Figure F.5: Left; Cumulative Probability Distribution Plot of Induction Times of NaCl in H_2O , agitated using a stirrer bar at 700 RPM at S between 1.0025 and 1.02. Pure Solution (Hollow Symbols), $0.06 \text{ mg}_{\text{polystyrene}}/\text{g}_{\text{water}}$ dispersion (Filled Symbols). Right; Cumulative Probability Distribution Plot of Induction Times of NaCl in D_2O , agitated using a stirrer bar at 700 RPM at S between 1.0025 and 1.02. Pure Solution (Hollow Symbols), $0.06 \text{ mg}_{\text{polystyrene}}/\text{g}_{\text{deuterium oxide}}$ dispersion (Filled Symbols).

F.2 Period Indication Graphs

It has also been the case that when nucleation from solution has been examined under various heat and agitation cycles, it has also been observed that it has been categorised by region where it occurs (i.e., during the cooling ramps, during the isothermal hold, and afterwards or not at all) [16].

F.2.1 Nucleation of NaCl from H₂O and D₂O

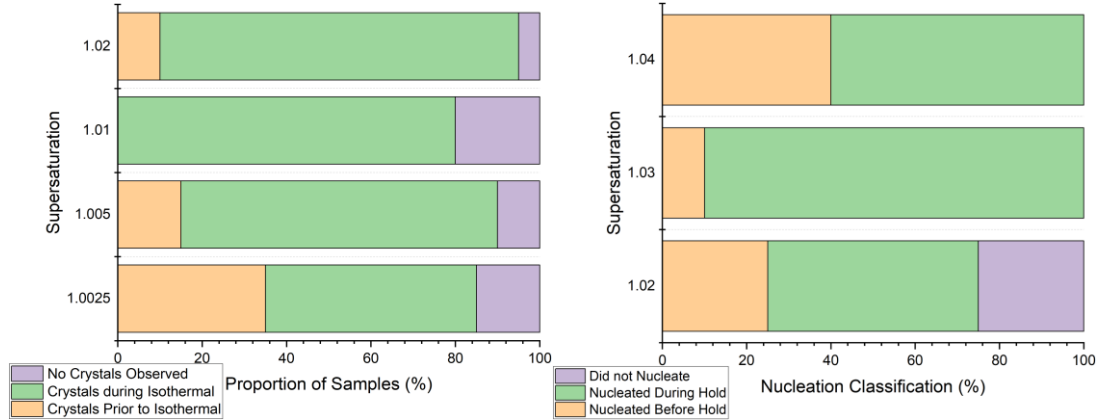


Figure F:6: Crystallisation Time Classification Plot. Left: of NaCl in Water, agitated using a stirrer bar at 700 RPM at S between 1.0025 and 1.02. Right: of NaCl in Deuterium Oxide, agitated using a stirrer bar at 700 RPM at S between 1.02 and 1.04.

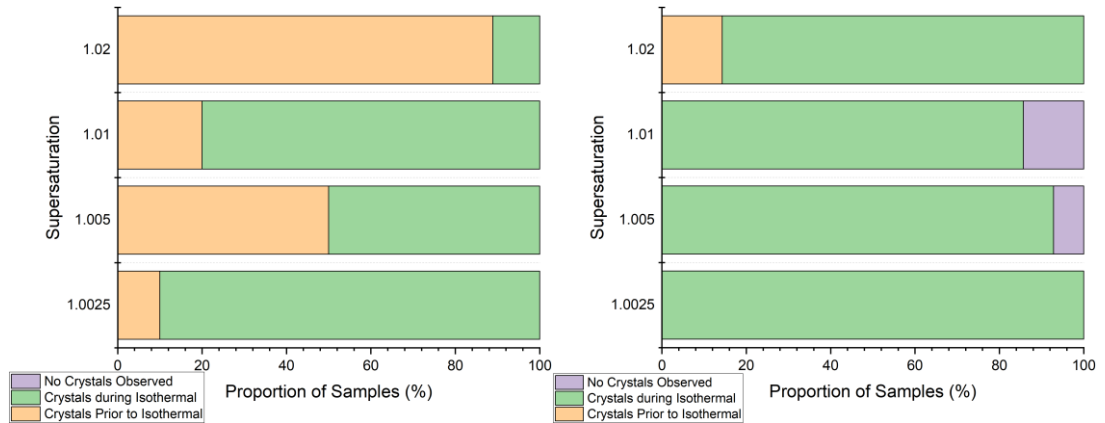


Figure F:7: Crystallisation Time Classification Plot. Left: of NaCl in Water, agitated using a stirrer bar at 700 RPM at S between 1.0025 and 1.02. Right: of NaCl in Deuterium Oxide, agitated using a stirrer bar at 700 RPM at S between 1.0025 and 1.02.

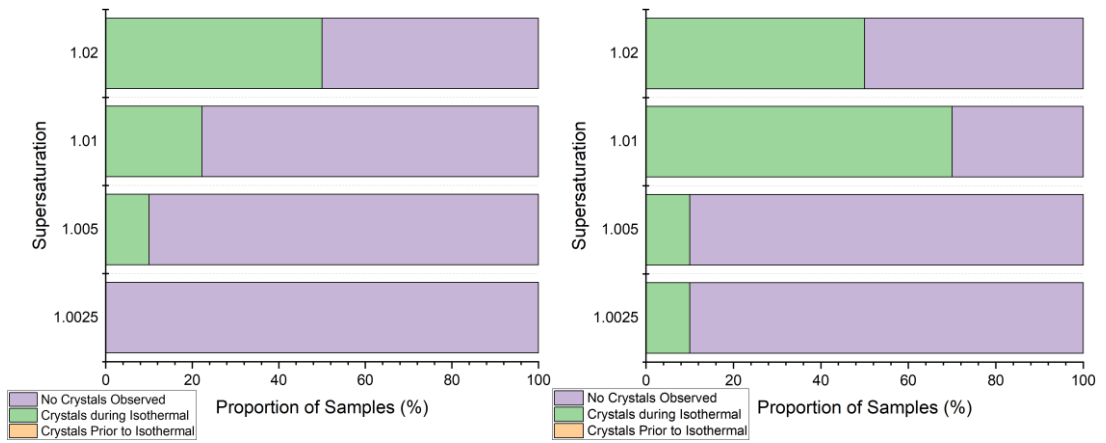


Figure F:8: Crystallisation Time Classification Plot. Left: of NaCl in Water, agitated using an overhead propeller at 1250 RPM at S between 1.0025 and 1.02. Right: of NaCl in Deuterium Oxide, using agitated using an overhead propeller at 1250 RPM at S between 1.0025 and 1.02.

F.2.2 Effect of Microparticles on Induction Time Distributions

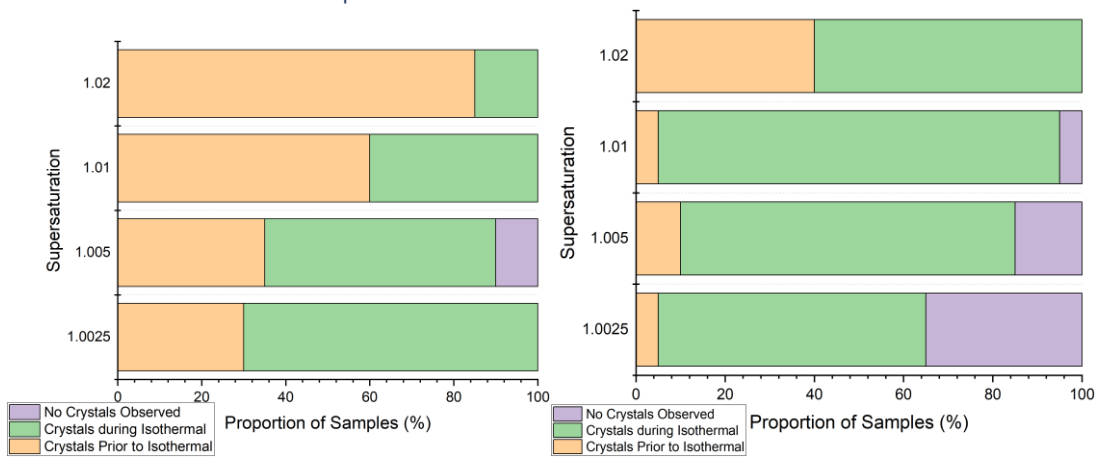


Figure F:9: Crystallisation Time Classification Plot. Left: NaCl in H_2O , agitated using a stirrer bar at 700 RPM at S between 1.0025 and 1.02 with $0.12 \text{ mg}_{\text{silica}}/\text{g}_{\text{water}}$. Right: NaCl in D_2O , agitated using a stirrer bar at 700 RPM at S between 1.0025 and 1.02 with $0.12 \text{ mg}_{\text{silica}}/\text{g}_{\text{Deuterium Oxide}}$.

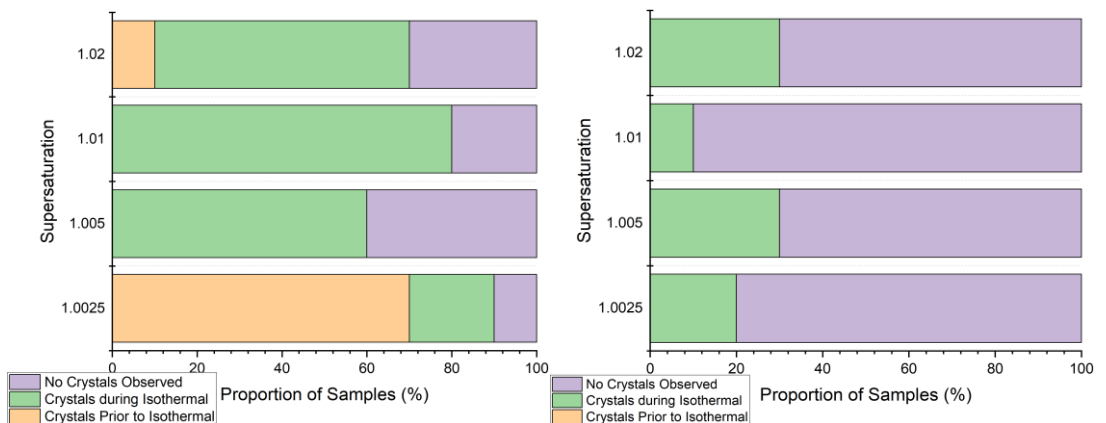


Figure F:10: Crystallisation Time Classification Plot. Left: NaCl in H_2O , agitated using a stirrer bar at 700 RPM at S between 1.0025 and 1.02 with $0.06 \text{ mg}_{\text{polystyrene}}/\text{g}_{\text{water}}$. Right: NaCl in D_2O , agitated using a stirrer bar at 700 RPM at S between 1.0025 and 1.02 with $0.06 \text{ mg}_{\text{polystyrene}}/\text{g}_{\text{Deuterium Oxide}}$.

Appendix G Alternative Frequency Distributions of Nucleation from Solution when induced by Optical Tweezers

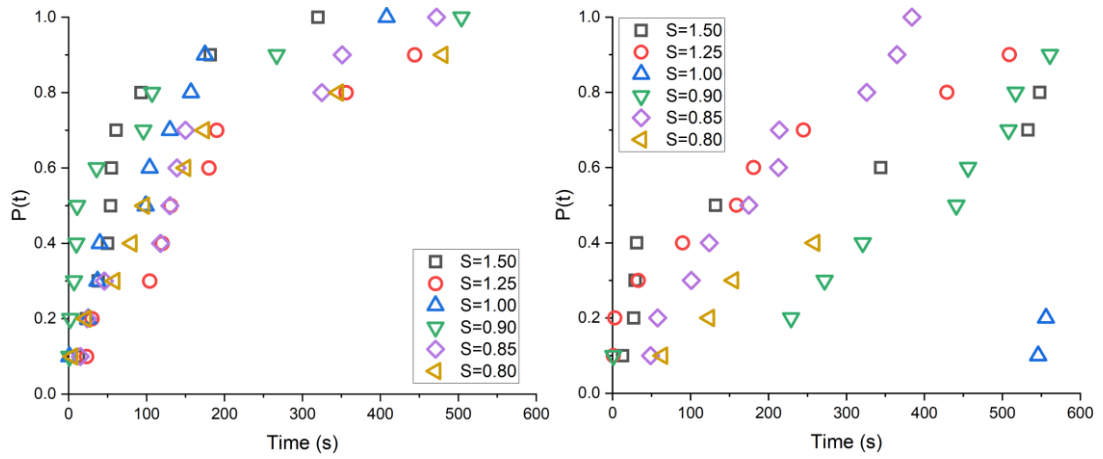


Figure G.1: Cumulative probability distributions of the nucleation times located at the droplet edge for a range of glycine solutions in H_2O . Trapping power 775 mW (left) and 650 mW (right) of linearly polarised beam.

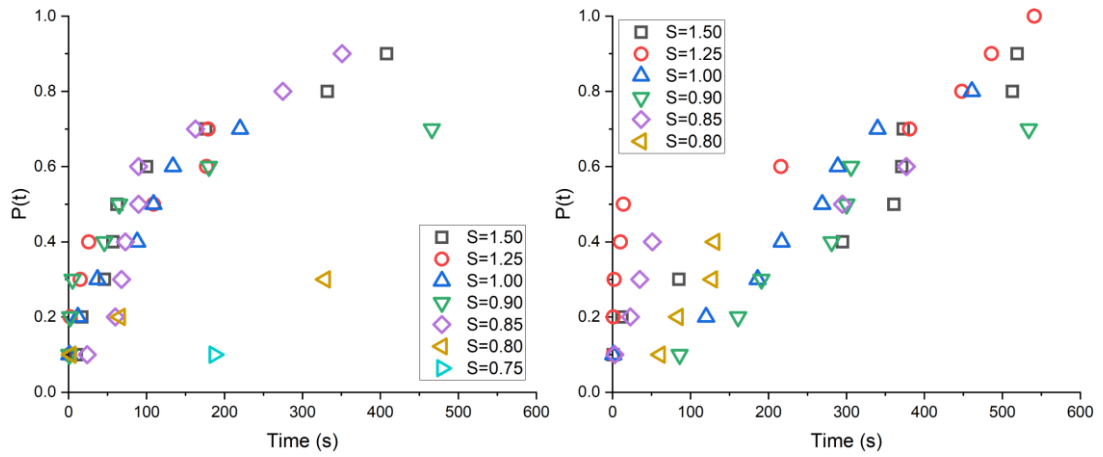


Figure G.2: Cumulative probability distributions of the nucleation times for a range of glycine solutions in D_2O . Trapping beam 775 mW (left) and 650 mW (right) of linearly polarised 1064 nm.

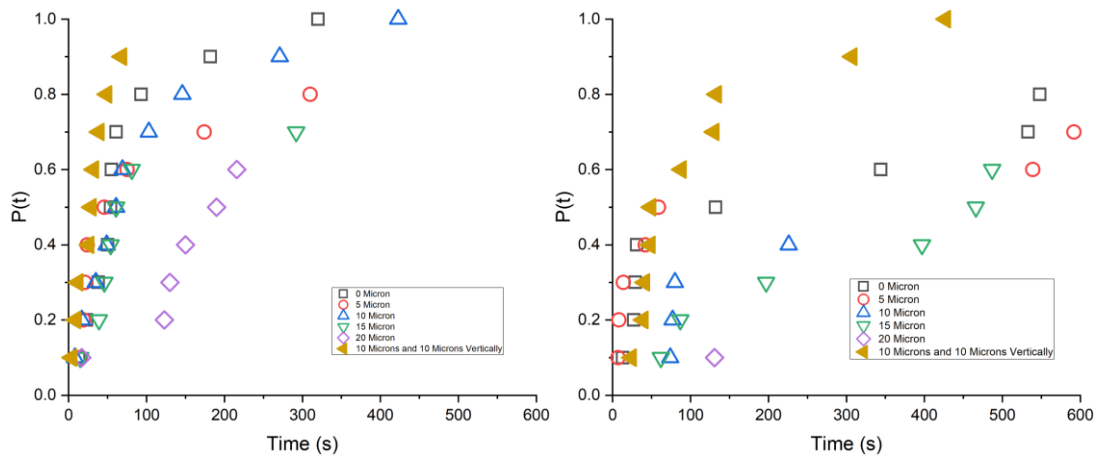


Figure G:3: Cumulative probability distributions of the nucleation times of $S=1.5$ solutions of glycine in H_2O at selected positions within a sessile drop. Trapping beam 775 mW (left) and 650 mW (right) of linearly polarised 1064 nm. No nucleation was observed when operating in bulk or in the absence of the laser.

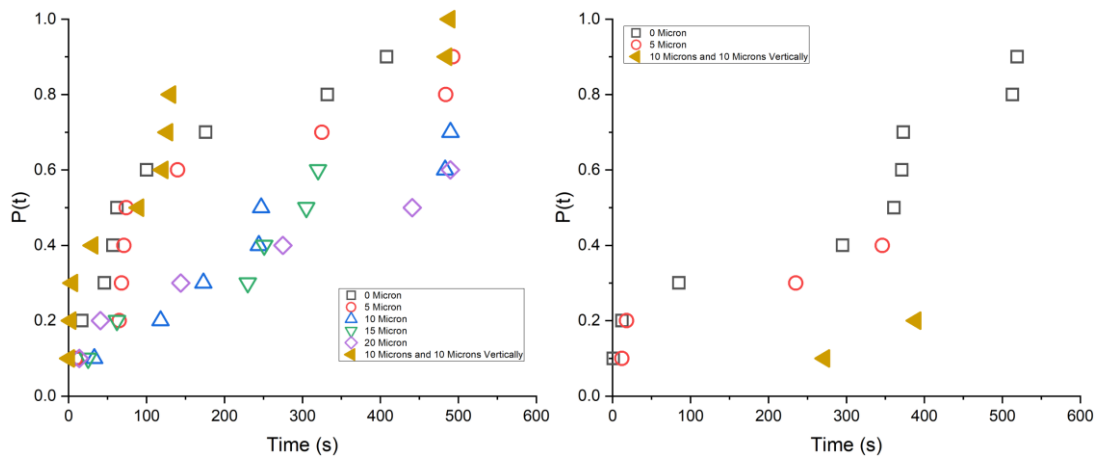


Figure G:4: Cumulative probability distributions of the nucleation times of $S=1.5$ solutions of glycine in D_2O at selected positions within a sessile drop. Trapping beam (left) and (right) of linearly polarised 1064 nm. No nucleation was observed when operating in bulk or in the absence of the laser.

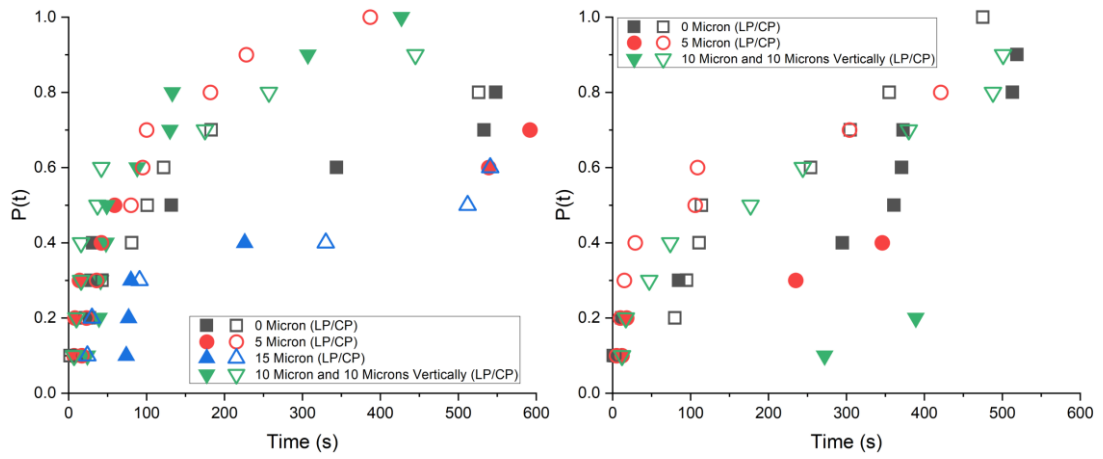


Figure G:5: Cumulative probability distribution of nucleation of $S = 1.5$ solutions of glycine in H_2O (left) and D_2O (right) in various positions with the sessile droplets. Trap generated using a power of 650 mW using linearly polarised light (Closed Symbols) and circularly polarised light (Open Symbols).

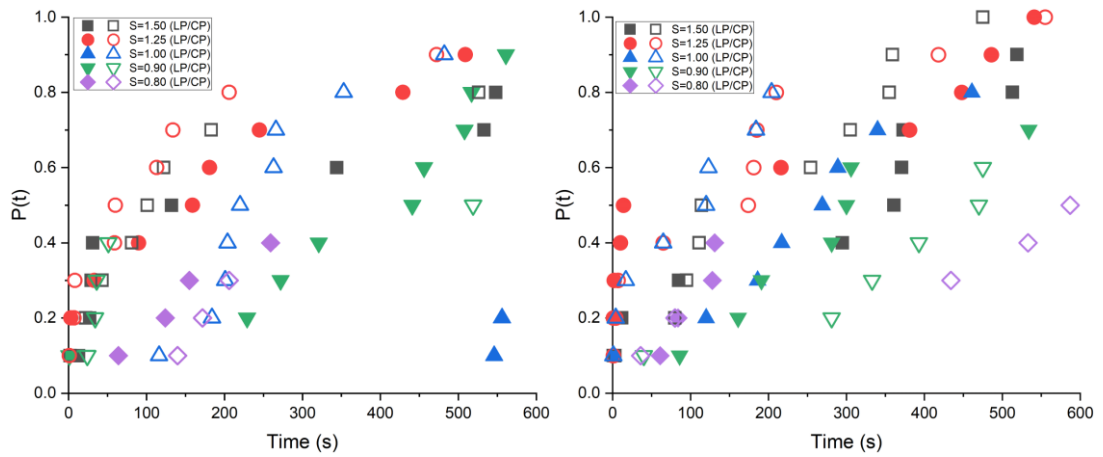


Figure G:6: Cumulative probability distribution of nucleation of solutions of glycine in H_2O (left) and D_2O (right) based solutions examining a range of concentrations where the tweezing focus is located at the edge of the sessile droplet (tri-point interface). Trap generated using a power of mW using linearly polarised light (Closed Symbols) and circularly polarised light (Open Symbols).

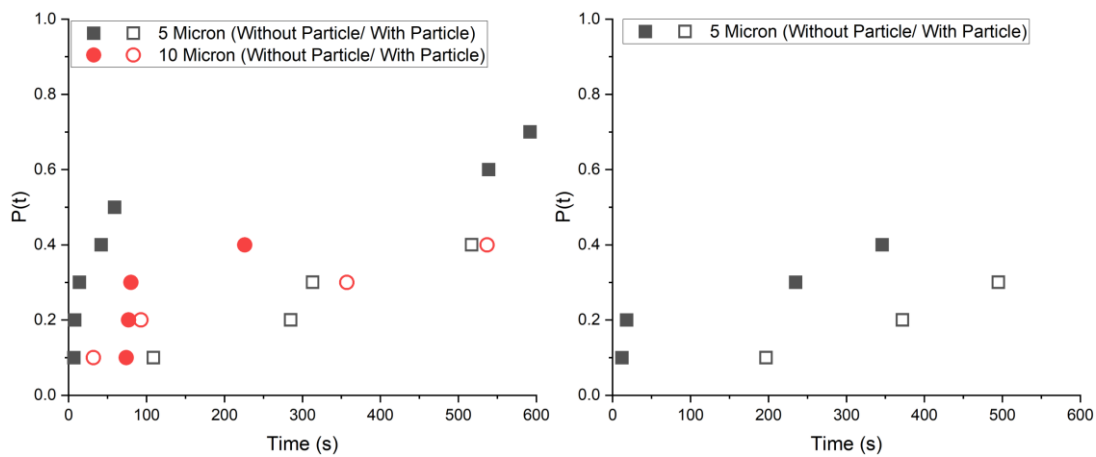


Figure G:7: Cumulative probability distributions of nucleation times of $S = 1.5$ glycine in H_2O (left) and D_2O (right) at selected positions within a sessile drop. The trapping beam had a trapping plane laser power of mW linear polarised 1064 nm laser light holding a $1.57 \mu m$ diameter silica particle (Open Symbols). Also shown are particle-free runs for comparison (Filled Symbols). No nucleation was observed when operating in bulk or in the absence of the laser.

Appendix H Beer-Lambert Law

As light passes through a substance, it can be absorbed. This absorption reduces light intensity as the path length of the light through the substance increases and depends on the wavelength of light used. Different wavelengths of light correspond to different changes in atoms or molecules in terms of energy, where at $\sim 1 \mu\text{m}$, it is said to be vibrational spectroscopy being performed [250]. This property of materials can be measured using the Beer-Lambert law given in Equation H:1.

$$\log_y \left(\frac{I_0}{I(x)} \right) = A = \alpha_{molar} c_{molar} x$$

Equation H:1

However, this can also be written where the molar components of Equation H:2 can be combined.

$$\log_y \left(\frac{I_0}{I(x)} \right) = \alpha x$$

Equation H:2

Since differing scientific fields can use different bases in the logarithm of the Beer-Lambert law, two standard bases use base 10 and base e. One method's measurements are not directly interchangeable, requiring a conversion factor. Due to the *Peterman* model [105] requiring the absorption coefficients to be determined using the natural logarithm, this standard will be used for all absorption coefficients contained in this thesis are reported in base e. Should the absorption coefficient be determined using another base, this can be converted using Equation H:3.

$$\alpha_e = \alpha_\delta \times \ln(\delta)$$

Equation H:3

Appendix I Hot Brownian Motion Calculation Outcomes

Hot Brownian motion calculations were performed to determine the outcomes of this theory to determine if it would be required to include this in any analysis performed. The final outcomes in the case of operating the 975 nm laser in deuterium oxide are shown.

$$\frac{T_{HBM}}{T_0} = 1 + \frac{\Delta T}{2T_0} + \left(\ln \left(\frac{\eta_0}{\eta_\infty} \right) - 1 \right) \left(\frac{(\Delta T)^2}{24T_0^2} \right) = 1.000939$$

$$\frac{\eta_0}{\eta_{HBM}} = \frac{e^{\frac{A}{T^*}}}{\Delta T} \left(A \left(Ei \left(\frac{A}{T^* + \Delta T} \right) - Ei \left(-\frac{A}{T^*} \right) \right) + (T^* + \Delta T) e^{-\frac{A}{T^* + \Delta T}} \right) - \frac{T^*}{\Delta T} = 1.0071$$

Appendix J Predicted Effect on Supersaturation with Laser Power

Now that the solubility of sodium chloride in H₂O and D₂O (see section 6.2.1) is known, from work performed here in both H₂O and D₂O and the impact of the tweezers on the local temperature, this can allow the tweezer's possible maximum effect on supersaturation to be estimated. This does not account for any potential localized increase in localized supersaturation due to any of the mechanisms discussed in section 9.9.

J.1 Laser Power Delivered

Although the power output by the laser is known through the calibration sheet supplied with the diode, this does not account for transmission losses through the optics of the optical tweezing setup. Ideally, the beam power would be measured after the beam exits the tweezer's objective lens; the spot size does not allow measurements to be made. Therefore, measurements were made when the beam entered the objective's rear. Using these measurements alongside the published specifications for the objective will allow an estimate to be made for laser power delivered at the trapping plane. Power measurements were performed using a Coherent PowerMax PM10V1 sensor with a FieldMate Laser Power Meter. The power measured and the associated calculated power delivered to the trapping point is shown in Figure J:1. The transmittance of the objective lens used is shown in Figure J:2 [251]. At the wavelength of the trapping laser used, at 975 nm, this is 73 %.

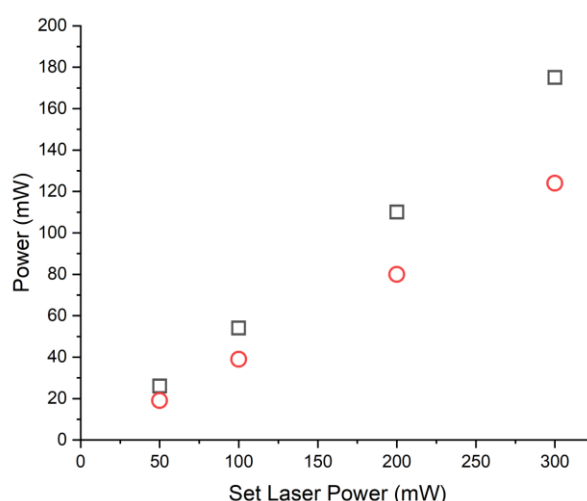


Figure J:1: Measured Power at the Back of the Objective lens and the associated power delivered at the trapping point. Measurements were taken at the rear of the objective (Black Squares) and calibrated power after the objective (Red Circles), based on transmittance at 975 nm from Figure J:2.

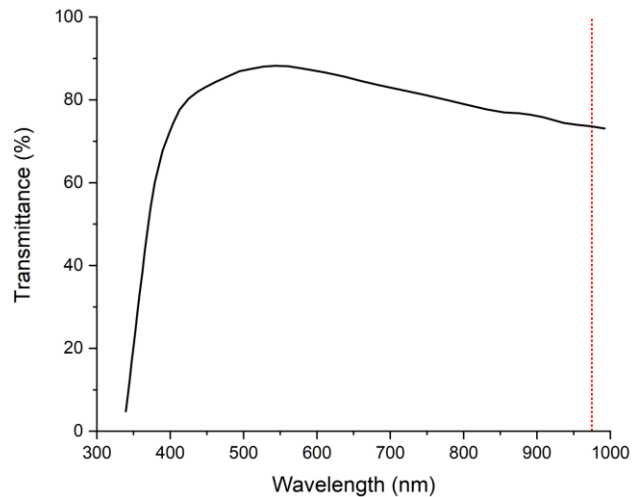


Figure J:2: Transmittance of the objective lens, Nikon E Plan 100x NA=1.25, Oil Immersion (Black). Wavelength of the trapping laser (Red Dashed Line). Taken from Nikon [251].

J.2 Effect on Supersaturation when Altering Laser Power at Fixed Displacement

When assumed that the focus of the trap is at the maximum possible distance from the inside of the surface of the lower coverslip, this allows the maximum possible temperature rise using that setup to estimate its effect on the supersaturation, I should also be noted that since this model accounts for the entire light cone if it were possible to operate further away from the heatsink temperature rises would be higher. From Figure J:3 and Figure J:4, it can be seen when using a 975 nm laser for trapping, using H₂O as a solvent causes relatively large drops in the supersaturation, increasing with laser power as the absorption coefficient is significantly higher in H₂O than D₂O at the trapping wavelengths. However, the use of D₂O results in lower drops in supersaturation. It must be noted that these drops are not zero. Although these decreases are insignificant for the laser powers available to us here, these decreases could become significant at higher laser powers. These calculations do not consider the possibility/likelihood that the tweezing focus would generate a region of localised increased supersaturation, as observations suggest in other solute-solvent systems. Previous studies have shown that nucleation can occur from undersaturated solutions in D₂O [151], [152]. However, this has not been observed in solutions of ionic substances [148], [158]. But as can also be seen from using a 1064 nm wavelength laser when operating with H₂O-based solutions also reduces the magnitude of the heating-induced drop in supersaturation.

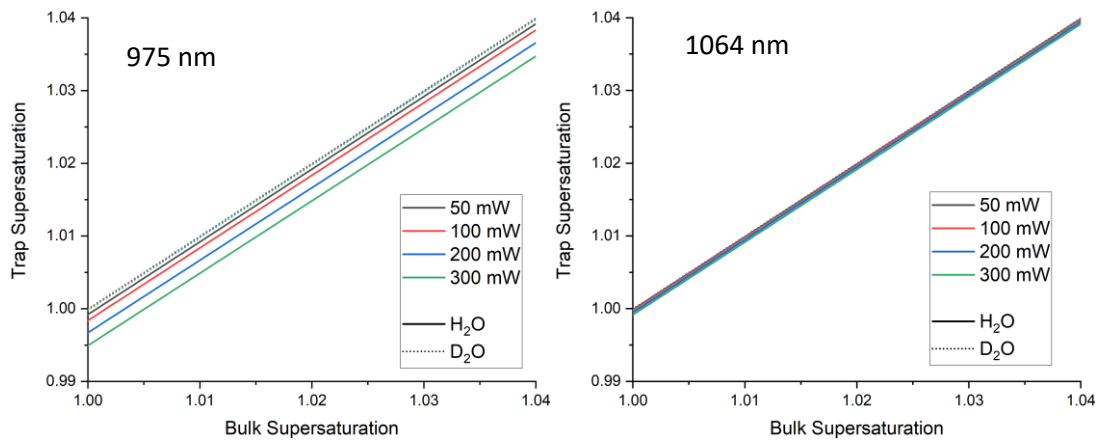


Figure J:3: Left; Bulk and Focus Supersaturation of Solutions of NaCl in H₂O and D₂O using various set powers of a 975 nm trapping laser. Power is set at the point of the driver where the effect of the supersaturation is adjusted to account for losses through the optical components. Predictions were made using H₂O (solid lines) and D₂O (dashed lines). Laser Power is shown by line colour 50 mW set power (black), 100 mW set power (red), 200 mW set power (blue) and 300 mW set power (green). Right; Bulk and Focus Supersaturation of Solutions of NaCl in H₂O and D₂O using various set powers of a 1064 nm trapping laser. Power is set at the point of the driver where the effect of the supersaturation is adjusted to account for losses through the optical components. Predictions were made using H₂O (solid lines) and D₂O (dashed lines). Laser Power is shown by line colour 50 mW set power (black), 100 mW set power (red), 200 mW set power (blue) and 300 mW set power (green).

Since some previous examinations of temperature rises in the focus of optical tweezing focuses show that the temperature measured is higher than those predicted by *Peterman et al.*

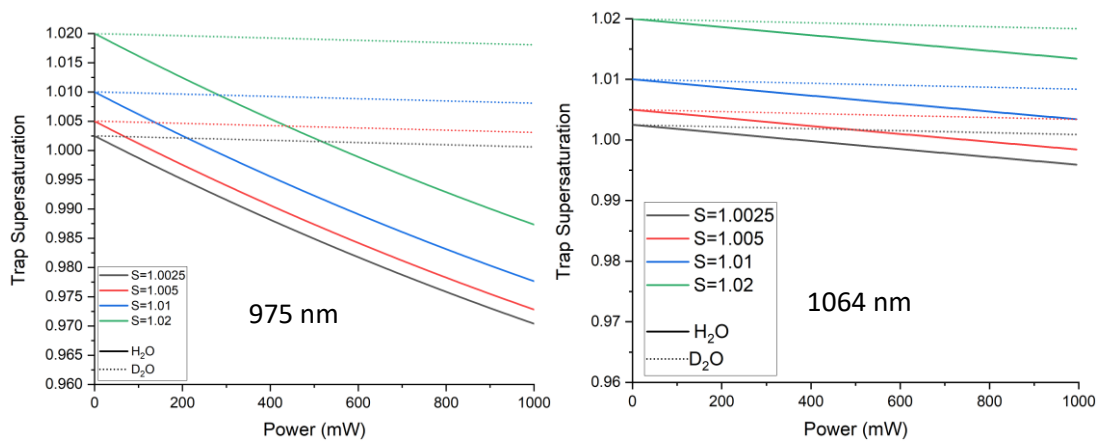


Figure J:4: Left; Trap Supersaturations for Fixed bulk supersaturations in H₂O and D₂O using a 975 nm trapping laser. Predictions were made using H₂O (solid lines) and D₂O (dashed lines). Initial Supersaturation of 1.0025 (black), 1.005 (red), 1.01 (blue) and 1.02 (green). Right; Trap Supersaturations for Fixed bulk supersaturations in H₂O and D₂O using a 1064 nm trapping laser. Predictions were made using H₂O (solid lines) and D₂O (dashed lines). Initial Supersaturation of 1.0025 (black), 1.005 (red), 1.01 (blue) and 1.02 (green).

J.3 Effect on Supersaturation when Altering Trap Displacement from the Heatsink

In the three vertical trapping distances (the distance from the upper surface of the lower coverslip and the trap's centre) where a supersaturation has been predicted, the predictions almost superimpose each other when the base solvent used is D₂O (Dotted Lines in Figure J:5). However, the axial distance between the focus of the tweezers can impact the temperature rise experienced at the focus of the tweezers. However, this depends on the solvent used, significantly impacting the supersaturation. As from Figure J:5, when using H₂O (Solid Lines) as the solvent, the supersaturations that would be experienced diverge from one another with increasing laser power, with the drop in supersaturation increasing with increasing trap distance. However, this effect is significantly lower when using D₂O as the solvent than when using H₂O. Highlighting the critical nature of solvent choice and the specific isotopologue in some cases is demonstrated by the differences observed between H₂O and D₂O. This also highlights the effect of altering the wavelength of the laser used for trapping, particularly when using H₂O as the solvent. There is a significant reduction in the drop in supersaturation when using the 1064 nm wavelength laser compared to the 975 nm, as the magnitude of the decrease is significantly reduced when using a 1064 nm laser.

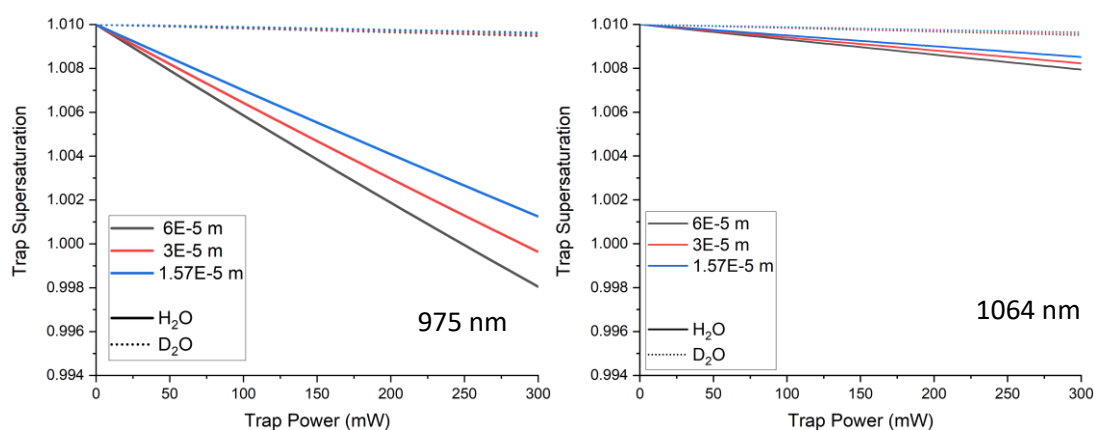


Figure J:5: Left; Predicted Impact of Trapping distance between the trap focus and the internal surface of the coverslip when using bulk $S = 1.01$ based H₂O and D₂O as solvents when using a 975 nm laser. Predictions were made using H₂O (solid lines) and D₂O (dashed lines). Distance between the trap focus and the interior of the coverslip is shown in colour 60 microns distance (black), 30 microns (red) and 16 microns (blue). Right; Predicted Impact of Trapping distance between the trap focus and the internal surface of the coverslip when using H₂O and D₂O as solvents when using a 1064 nm laser. Predictions were made using H₂O (solid lines) and D₂O (dashed lines). Distance between the trap focus and the interior of the coverslip is shown in colour 60 microns distance (black), 30 microns (red) and 16 microns (blue)